

AD A070250

DDC FILE COPY

LEVEL

406 8971

2

AFFDL-TR-76-55
Volume I

20000726132

**AERODYNAMIC STABILITY TECHNOLOGY FOR
MANEUVERABLE MISSILES**

Volume I. Configuration Aerodynamic Characteristics

MARTIN MARIETTA CORPORATION
ORLANDO DIVISION
P. O. BOX 5837
ORLANDO, FLORIDA 32805

MARCH 1979

TECHNICAL REPORT AFFDL-TR-76-55, Vol. 1
Final Report for period February 1975 - December 1976

Approved for public release; distribution unlimited.

DDC
RECEIVED
JUN 22 1979
D

AIR FORCE FLIGHT DYNAMICS LABORATORY
AIR FORCE WRIGHT AERONAUTICAL LABORATORIES
AIR FORCE SYSTEMS COMMAND
WRIGHT-PATTERSON AIR FORCE BASE, OHIO 45433

Reproduced From
Best Available Copy

NOTICE

When Government drawings, specifications, or other data are used for any purpose other than in connection with a definitely related Government procurement operation, the United States Government thereby incurs no responsibility nor any obligation whatsoever; and the fact that the government may have formulated, furnished, or in any way supplied the said drawings, specifications, or other data, is not to be regarded by implication or otherwise as in any manner licensing the holder or any other person or corporation, or conveying any rights or permission to manufacture, use, or sell any patented invention that may in any way be related thereto.

This report has been reviewed by the Information Office (OI) and is releasable to the National Technical Information Service (NTIS). At NTIS, it will be available to the general public, including foreign nations.

This technical report has been reviewed and is approved for publication.




W. H. LANE
Project Engineer
Control Dynamics Branch



R. O. ANDERSON, Chief
Control Dynamics Branch
Flight Control Division

FOR THE COMMANDER


J. R. STANLEY, Col, USAF
Chief, Flight Control Division
Air Force Flight Dynamics Laboratory

"If your address has changed, if you wish to be removed from our mailing list, or if the addressee is no longer employed by your organization please notify AFFDL/FCC, W-PAFB, OH 45433 to help us maintain a current mailing list".

Copies of this report should not be returned unless return is required by security considerations, contractual obligations, or notice on a specific document.

AIR FORCE/56780/21 May 1979 - 33

UNCLASSIFIED

SECURITY CLASSIFICATION OF THIS PAGE (When Data Entered)

REPORT DOCUMENTATION PAGE		READ INSTRUCTIONS BEFORE COMPLETING FORM
1. REPORT NUMBER AFFDL-TR-76-55-Vol-1	2. GOVT ACCESSION NO.	3. RECIPIENT'S CATALOG NUMBER
4. TITLE (and Subtitle) Aerodynamic Stability Technology for Maneuverable Missiles. Vol. I. Configuration Aerodynamic Characteristics.		5. TYPE OF REPORT & PERIOD COVERED Final Report, February 1975 to December 1976
7. AUTHOR(s) Gennaro F. Aiello Michael C. Bateman		6. PERFORMING ORGANIZATION REPORT NUMBER OR-14927
9. PERFORMING ORGANIZATION NAME AND ADDRESS Martin Marietta Corporation Orlando Division, PO Box 5837 Orlando, FL 32805		8. CONTRACT OR GRANT NUMBER(s) F33615-75-C-3052
11. CONTROLLING OFFICE NAME AND ADDRESS U.S. Air Force Flight Dynamics Laboratory Wright-Patterson Air Force Base Dayton, Ohio		10. PROGRAM ELEMENT, PROJECT, TASK AREA & WORK UNIT NUMBERS
14. MONITORING AGENCY NAME & ADDRESS (if different from Controlling Office)		12. REPORT DATE March 1979
		13. NUMBER OF PAGES 360
		15. SECURITY CLASS (of this report) Unclassified
		15a. DECLASSIFICATION/DOWNGRADING SCHEDULE
16. DISTRIBUTION STATEMENT (of this Report) Approved for public release; distribution unlimited		
17. DISTRIBUTION STATEMENT (of the abstract entered in Block 20, if different from Report)		
18. SUPPLEMENTARY NOTES		
19. KEY WORDS (Continue on reverse side if necessary and identify by block number) Transonic Supersonic High Angle Predictions		
20. ABSTRACT (Continue on reverse side if necessary and identify by block number) This study developed empirical methods to predict aerodynamic characteristics of body-tail, body-wing-tail and body-strake-tail missile configurations. Methods cover the Mach number range from 0.6 to 3.0. Methods cover the individual body and tail characteristics at angles of attack from 0 to 180 degrees. For winged bodies the methods encompass angles of attack up to about 30 degrees. All mutual interference effects are accounted for, allowing accurate prediction of force and moment coefficients.		

11/3

FOREWORD

This report was prepared for the U. S. Air Force Flight Dynamics Laboratory, Wright-Patterson Air Force Base, Dayton, Ohio, under contract number F33615-75-C-3052 as part of Project 8219. The work was performed at the Orlando Division of Martin Marietta Aerospace in Orlando, Florida. The reported effort began in February 1975 and ended with the submittal of the draft of this final report in December 1976.

The principal investigators were J. E. Fidler and G. F. Aiello. The technical monitors for the Flight Dynamics Laboratory were Dr. Robert Nelson, Lt William Miklos and Mr. William Lane.

The authors wish to express their gratitude to the aforementioned contract monitors for their guidance and support and recognize a special debt to Mr Lane for his extraordinary effort in reviewing this report and the significant contribution towards the readability and overall quality of the report. The authors would also like to express their gratitude to Mr. William Baker, Arnold Engineering Development Center, for his cooperation in providing easy access to the 180 degree, body plus tail data bank. Many sincere thanks are due the following associates at the Martin Marietta, Orlando Division: G. S. Logan, Jr., D. T. Moore and R. L. Swann.

Accession For	
DTIS GRA&I	<input checked="" type="checkbox"/>
DDC TAB	<input type="checkbox"/>
Unannounced	<input type="checkbox"/>
Justification	
By	
Distribution/	
Availability Codes	
	Avail and/or special
A	

DDC
 RECEIVED
 JUN 22 1979
 D

TABLE OF CONTENTS

	<u>Page</u>
1.0 Introduction	1
2.0 Experimental Data Sources and Models	7
3.0 Aerodynamic Data Trends	12
4.0 Formulation of the Aerodynamic Prediction Equations	35
5.0 Aerodynamic Methods	39
5.1 Isolated Components	39
5.1.1 Body Normal Force	39
5.1.2 Body Center of Pressure	61
5.1.3 Body Axial Force	77
5.1.4 Fin Normal Force	91
5.1.5 Chordwise Center of Pressure	122
5.2 Body-Tail Configurations	143
5.2.1 Tail-on-Body Normal Force	143
5.2.2 Tail-to-Body Carry-over Normal Force	161
5.2.3 Tail-to-Body Carry-over Normal Force Center of Pressure	171
5.3 Body-Strake-Tail Configurations	190
5.3.1 Incremental Normal Force Due to Strakes	190
5.3.2 Center of Pressure for Incremental Normal Force Due to Strakes	202
5.3.3 Incremental Normal Force Due to Tails	220
5.3.4 Center of Pressure for Incremental Normal Force Due to Tails	232

TABLE OF CONTENTS (Concluded)

	<u>Page</u>
5.4 Body-Wing-Tail Configurations	259
5.4.1 Incremental Normal Force Due to Wings	259
5.4.2 Effective Center of Pressure for Incremental Force Due to Wings	274
5.4.3 Tail Incremental Normal Force Due to Wing Vortex Interference	289
5.4.4 Effective Center of Pressure of the Incremental Tail Normal Force Due to Wings	306
5.5 Thrust Vector Control Effects	310
5.5.1 Incremental Body Normal Force Due to Plume Effects	310
5.5.2 Effective Center of Pressure for Incremental Body Normal Force Due to Plume Effects	323
5.5.3 Incremental Tail Normal Force Due to Plume Effects	334
5.5.4 Effective Center of Pressure of Incremental Tail Normal Force Due to Plume Effects	351
6.0 Conclusions and Recommendations	356
7.0 References	358

LIST OF ILLUSTRATIONS

<u>Figure</u>		<u>Page</u>
1a	Methodology Requirements for TVC Missiles	5
1b	Methodology Requirements for Aerodynamically Controlled Missiles	6
2	Schematic of Total Data Base	9
3a	Martin Marietta Main Body Model in the NSRDC 7' X 10' Transonic Tunnel at Sixty Degrees Angle of Attack	10
3b	Martin Marietta Tail Models	11
4	Vortices Produced by the Reattachment of Lower Surface Boundary Layer	13
5a	Fin Normal Force Coefficient (M=0.8, Aspect Ratio Effects)	19
5b	Fin Chordwise Center of Pressure (M=0.8, Aspect Ratio Effects)	20
5c	Fin Normal Force Coefficient (M=2.0, Aspect Ratio Effects)	21
5d	Fin Chordwise Center of Pressure (M=2.0, Aspect Ratio Effects)	22
6a	Fin Normal Force Coefficient (M=0.8, Taper Ratio Effects)	23
6b	Fin Chordwise Center of Pressure (M=0.8, Taper Ratio Effects)	24
6c	Fin Normal Force Coefficient (M=2.0, Taper Ratio Effects)	25
6d	Fin Chordwise Center of Pressure (M=2.0, Taper Ratio Effects)	26
7a	Fin Normal Force (Mach Effects)	27
7b	Fin Chordwise Center of Pressure (Mach Effects)	28
8a	Variation of Induced Out-of-Plane Forces and Moments (M=0.6).	29

LIST OF ILLUSTRATIONS (Cont'd)

<u>Figure</u>		<u>Page</u>
8b	Variation of Induced Out-of-Plane Forces and Moments (M=2.0).	30
9a	Out-of-Plane Forces and Moments Due to Vortex Asymmetry (AR = 0.5, $\lambda = 1.0$, d/s = 0.5)	31
9b	Out-of-Plane Forces and Moments Due to Vortex Asymmetry (AR = 0.5, $\lambda = 0$, d/s = 0.4).	32
10a	Comparison of Tail Normal Forces	33
10b	Comparison of Rolling Moments.	34
11	Comparison of Experimental and Predicted Results (C_{NB}), Mach = 0.6.	48
12	Comparison of Experimental and Predicted Results (C_{NB}), Mach = 1.15	48
13	Comparison of Experimental and Predicted Results (C_{NB}), Mach = 1.30	49
14	Comparison of Experimental and Predicted Results (C_{NB}), Mach = 2.0	49
15	Coefficients for Calculation of $C_{NB} (A_1)$	50
16	Coefficients for Calculation of $C_{NB} (A_2)$	50
17a	Curves for Transonic $C_{N\alpha}$ ($l_N/d = 1.5$).	51
17b	Curves for Transonic $C_{N\alpha}$ ($l_N/d = 2.5$).	52
17c	Curves for Transonic $C_{N\alpha}$ ($l_N/d = 3.5$).	52
18a	Curves for Supersonic $C_{N\alpha}$ ($l_N/d = 2.5$).	53
18b	Curves for Supersonic $C_{N\alpha}$ ($l_N/d = 3.0$).	53
18c	Curves for Supersonic $C_{N\alpha}$ ($l_N/d = 3.5$).	54
18c	Curves for Supersonic $C_{N\alpha}$ ($l_N/d = 4.0$).	54
19	Correlation Factor for End Effects	55
20	Variation of η with Mach Number	55
21	Curves for Determining Transonic Values of η	56

LIST OF ILLUSTRATIONS (Cont'd)

<u>Figure</u>		<u>Page</u>
22 a	Basic Values of C_{d_c}	57
22b	Crossflow Drag Coefficient (Subcritical Crossflow, $M_c \leq 0.4$).	57
23	Comparison of Experimental and Predicted Results (C_{N_B}), Mach = 0.6	57
24	Comparison of Experimental and Predicted Results (C_{N_B}), Mach = 1.15	58
25	Comparison of Experimental and Predicted Results (C_{N_B}), Mach = 1.30	59
26	Comparison of Experimental and Predicted Results (C_{N_B}), Mach = 2.0	59
27	Comparison of Experimental and Predicted Results (C_{N_B}), Mach = 2.86	60
28	Comparison of Experimental and Predicted Results (C_{N_B}), Mach = 0.85, 1.20, and 2.25.	60
29a	Transonic Tangent Ogive-Cylinder Zero Angle of Attack Centers of Pressure ($l_N/d = 3.5$)	70
29b	Transonic Tangent Ogive-Cylinder Zero Angle of Attack Centers of Pressure ($l_N/d = 2.5$)	70
29c	Transonic Tangent Ogive-Cylinder Zero Angle of Attack Centers of Pressure ($l_N/d = 1.5$)	70
30a	Supersonic Tangent Ogive Cylinder Zero Angle of Attack Centers of Pressure ($l_N/d = 4.0$)	71
30b	Supersonic Tangent Ogive - Cylinder Zero Angle of Attack Centers of Pressure ($l_N/d = 3.5$)	71
30c	Supersonic Tangent Ogive - Cylinder Zero Angle of Attack Centers of Pressure ($l_N/d = 2.5$)	71
31	Increment in Center of Pressure Between Angles of Attack of 0 and 20 degrees	72
32	Polynomial Coefficients, Low Angle of Attack	72
33	Polynomial Coefficients, High Angle of Attack.	73

LIST OF ILLUSTRATIONS (Cont'd)

<u>Figure</u>		<u>Page</u>
34	Comparisons Between Predictions and Experimental Data X_{CP} , Mach = 2.86 $\frac{d}{B}$	74
35	Comparisons Between Predictions and Experimental Data X_{CP} , Mach = 2.25 $\frac{d}{B}$	74
36	Comparisons Between Predictions and Experimental Data X_{CP} , Mach = 0.85 $\frac{d}{B}$	75
37	Comparisons Between Predictions and Experimental Data X_{CP} , Mach = 0.80 $\frac{d}{B}$	75
38	Comparisons Between Predictions and Experimental Data X_{CP} , Mach = 3.0 $\frac{d}{B}$	76
39	Variation with Mach Number of 180-Degree Axial Force Coefficient	84
40 (a-f)	Comparison Between Predicted and Experimental C_{AB} (Transonic)	85
41a	Curves for Determining $C_{A_{1b}}$ ($l_N/d = 1.5$)	87
41b	Curves for Determining $C_{A_{1b}}$ ($l_N/d = 2.5$)	87
41c	Curves for Determining $C_{A_{1b}}$ ($l_N/d = 3.5$)	88
42	Scaling Factor for $C_{A_{1b}}$	88
43	Variation of \bar{C}_A with Mach Number	89
44	Basic Curves of $f(M, \alpha)$ Calculated from Power Series	89

LIST OF ILLUSTRATIONS (Cont'd)

<u>Figure</u>		<u>Page</u>
45	Comparison Between Predicted and Experimental Data C_{A_B} (Supersonic)	90
46	Power Series Parameters for Equation (24)	104
47 (a-d)	Lift Curve Slope for Taper Ratios 0-1.0	105
48	Variation of $C_{N_T} (\pi/2)$ with Mach Number	107
49	α' , Angle of Attack Above Which ΔC_N Must be Applied (Subsonic only)	108
50	Dimensionless C_N Increment Above α'	109
51	ΔC_{N_M} , Maximum Increment of Normal Force Above α' (Subsonic Only)	110
52	Comparison of Predicted and Experimental C_{N_T} , Mach = 0.8	110
53	Comparison of Predicted and Experimental C_{N_T} , Mach = 0.98	111
54	Comparison of Predicted and Experimental C_{N_T} , Mach = 1.02	111
55	Variation of Fin Normal Force at $\alpha = 90^\circ$ with Mach No.	112
56a	Variation of Normal Force Coefficient, $C_{N_T} (30)$, with Mach No., $\alpha = 30^\circ (\lambda = 0)$	113
56b	Variation of Normal Force Coefficient, $C_{N_T} (30)$, with Mach No., $\alpha = 30^\circ (\lambda = .5)$	113
56c	Variation of Normal Force Coefficient, $C_{N_T} (30)$, with Mach No., $\alpha = 30^\circ (\lambda = 1.0)$	113
57	Variation of $C_{N_{Ta}} (30)$ with Mach Number	114
58	Power Series Parameters for Equation (26)	115
59	Comparison of Predicted and Experimental C_{N_T} from 30 to 90 degrees	116
60	Curves for Modifying C_N Method, ($\lambda = 0$, AR = 1.0, Subsonic)	116

LIST OF ILLUSTRATIONS (Cont'd)

<u>Figure</u>		<u>Page</u>
61	An Example Using ΔC_{N_T}	116
62	Comparison of Method and Test, C_{N_T} ($\lambda = 0, AR = 0.5$) . . .	117
63	Comparison of Method and test, C_{N_T} ($\lambda=0.5, AR=0.5; \lambda=0, AR=1.0$)	118
64	Comparison of Test to Methods to 180° , $M = 0.6$ (C_{N_T}) . .	119
65	Comparison of Test and Method, $M = 2.0$ (C_{N_T})	120
66	Comparison of Test and Method, $M = 2.5$ (C_{N_T})	120
67	Comparison of Test and Method, $M = 3.0$ (C_{N_T}) ($\lambda=1.0, AR=1.0$)	121
68	Comparison of Test and Method, $M = 3.0$ (C_{N_T}) ($\lambda = 0, AR=1.0$)	121
69	Chordwise Center of Pressure Variation to 180° Degrees	136
70	Chordwise Center of Pressure Variation with Taper Ratio at Alpha of 90° Degrees	136
71a	Basic Curves for $\frac{X_{CP}}{C_R}$ at Reference Mach Number 0.98 ($0-180^\circ$ Degrees, $AR = 0.5$)	137
71b	Basic Curves for $\frac{X_{CP}}{C_R}$ at Reference Mach Number 0.98 ($0-180^\circ$ degrees, $AR = 1.0$)	137
71c	Basic Curves for $\frac{X_{CP}}{C_R}$ at Reference Mach Number 0.98 ($0-180^\circ$ Degrees, $AR = 2.0$)	137
72a	Basic Curves for $\frac{X_{CP}}{C_R}$ at Reference Angle of Attack $175-180^\circ$ Degrees ($M = 0.6$ to 3.0 , $AR = 0.5$)	138
72b	Basic Curves for $\frac{X_{CP}}{C_R}$ at Reference Angle of Attack $175-180^\circ$ Degrees ($M = 0.6$ to 3.0 , $AR = 1.0$)	138
72c	Basic Curves for $\frac{X_{CP}}{C_R}$ at Reference Angle of Attack $175-180^\circ$ Degrees ($M = 0.6$ to 3.0 , $AR = 2.0$)	138
73	Power Series Constants Versus Angle of Attack	139
74	Mach Number Correction Factor for $\alpha < 90^\circ$ Degrees	140
75	Variation of $\Delta_1(X_{CP}/C_R)$ with Mach Number at Alpha of 160° Degrees	140
76	Comparison of Predicted and Experimental Center of Pressure Location, $\frac{X_{CP}}{C_R}$ $M = 1.15$	141

LIST OF ILLUSTRATIONS (Cont'd)

<u>Figure</u>		<u>Page</u>
77	Comparison of Predicted and Experimental C.P. Location, $X_{CP} \frac{C_{PT}}{C_R}$ M = 0.80	141
78	Comparison of Predicted and Experimental C.P. Location, $X_{CP} \frac{C_{PT}}{C_R}$ M = 1.3	142
79	$K_{T(B)}$ Ratio at Zero Angle of Attack	150
80	General Coefficients for Calculation of $R_{T(B)}$ (A_0)	151
81	General Coefficients for Calculation of $R_{T(B)}$ (A_1)	152
82	General Coefficients for Calculation of $R_{T(B)}$ (A_2)	153
83	Interference Factor at Angle of Attack of 90 Degrees	154
84	Comparison of Experimental and Predicted Results, $C_{N_{T(B)}}$, M = 0.6	155
85	Comparison of Experimental and Predicted Results, $C_{N_{T(B)}}$, M = 3.0	156
86	Comparison of Experimental and Predicted Results, $C_{N_{T(B)}}$, M = 2.0	157
87	Comparison of Experimental and Predicted Results, $C_{N_{T(B)}}$, M = 3.0	158
88	Comparison of Experimental and Predicted Results, $C_{N_{T(B)}}$, M = 1.15	159
89	Comparison of Experimental and Predicted Results, $C_{N_{T(B)}}$, M = 0.8	160
90	Transonic $I_{B(T)}$, Schematic	166
91a	Curves for Estimation of Transonic I_a (all λ)	167

LIST OF ILLUSTRATIONS (Cont'd)

<u>Figure</u>		<u>Page</u>
91b	Curves for Estimation of Transonic I_b (all λ and $\frac{d}{s}$)	167
91c	Curves for Estimation of Transonic I_c (all λ and M)	167
92	Comparison between Predicted and Experimental $I_B(T)$	168
93	Supersonic $I_B(T)$, Schematic	168
94a	Curves for Estimation of Supersonic I_1	169
94b	Curves for Estimation of Supersonic I_2	169
94c	Curves for Estimation of Supersonic I_3	169
95	Comparison Between Predicted and Experimental $I_B(T)$	170
96	Curves for Determining $\frac{X_{CP}}{C_R} B(T)$ with Afterbodies for Supersonic Speeds	183
97	Curves for Determining $\frac{X_{CP}}{C_R} B(T)$ for No Afterbodies at Supersonic Speeds	184
98	Curves for Determining $\frac{X_{CP}}{C_R} B(T)$ for Subsonic Speeds (Zero Leading Edge Sweep)	185
99	Curves for Determining $\frac{X_{CP}}{C_R} B(T)$ for Subsonic Speeds (Zero Trailing Edge Sweep)	186
100	Coefficients Required for Evaluation of $\frac{X_{CP}}{C_R} B(T)$	187
101	Comparison Between Predicted and Experimental Data $C_{N_{BT}}$	188

LIST OF ILLUSTRATIONS (Cont'd)

<u>Figure</u>		<u>Page</u>
102	Comparison Between Predicted and Experimental Data, $X_{CP_{BT}}$	189
103	$\Delta C_{N_{BS}}$ General Curve Form	196
104	$\Delta C_{N_{BS}}$ Peak Factor K	197
105	Coefficients for Calculating $\Delta C_{N_{BS}}$	198
106 (a-d)	Comparison of Test Data and Method, $\Delta C_{N_{BS}}$	200
107	General Curve Form, $X_{CP_{\Delta BS}}$	211
108	Strake Parameters	212
109	Polynomial Coefficients for Calculating $X_{CP_{ABS}}$	213
110	J and K Values for Calculating $X_{CP_{\Delta BS}}$	216
111	Comparison of Test Data and Method, $X_{CP_{\Delta BS}}/d$	217
112	Comparison of Test Data and Method, $X_{CP_{BS}}/d$	219
113	Coefficients for Calculation of $\Delta C_{N_{BST}}$ (A_1)	227
114	Coefficients for Calculation of $\Delta C_{N_{BST}}$ (A_2)	228
115	Coefficients for Calculation of $\Delta C_{N_{BST}}$ (A_3)	229
116	$K_{T(B)}$ and $K_{B(T)}$ Ratios (Slender Body Theory).	230
117	Comparisons of Predicted Results with Experimental Data, $\Delta C_{N_{BST}}$	231

LIST OF ILLUSTRATIONS (Cont'd)

<u>Figure</u>		<u>Page</u>
118	$K_{T(B)}$ and $K_{B(T)}$ Ratios (Slender Body Theory)	245
119	Tail Alone Center of Pressure at Subsonic Speeds	246
120	Tail Alone Center of Pressure at Supersonic Speeds	247
121	Curves for Determining $\frac{X_{CP_{B(T)}}}{C_R}$ for Subsonic Speeds (Zero Trailing Edge Sweep)	248
122	Curves for Determining $\frac{X_{CP_{B(T)}}}{C_R}$ for No Afterbody at Supersonic Speeds	249
123	Curves for Determining $\frac{X_{CP_{B(T)}}}{C_R}$ for Subsonic Speeds (Zero Leading Edge Sweep)	250
124	Curves for Determining $\frac{X_{CP_{B(T)}}}{C_R}$ with Afterbodies at Supersonic Speeds	251
125	Coefficients for Calculation of $\frac{X_{CP}}{C_R}$, (A_1)	252
126	Coefficients for Calculation of $\frac{X_{CP}}{C_R}$, (A_2)	253
127	Coefficients for Calculation of $\frac{X_{CP}}{C_R}$, (A_3)	254
128	Comparison Between Predicted and Experimental Results, $X_{CP_{BST}}/d$, $M=0.6$	355
129	Comparison Between Predicted and Experimental Results, $X_{CP_{BST}}/d$, $M=0.85$	256

LIST OF ILLUSTRATIONS (Cont'd)

<u>Figure</u>		<u>Page</u>
130	Comparison Between Predicted and Experimental Results, $X_{CP_{BST}}/d$, $M=1.2$	257
131	Comparison Between Predicted and Experimental Results, $X_{CP_{BST}}/d$, $M=2.2$	258
132	Comparisons of Existing Method Predictions with Experimental Data, $\Delta C_{N_{BW}}$	266
133	$K_{B(W)}$ Ratio at Zero Angle of Attack	267
134	Comparison Between Predicted and Experimental Results, $\Delta C_{N_{BW}}$, Configuration 2, $M=1.1$	268
135	Configurations (Body + Wing)	269
136	Comparisons Between Experimental and Predicted Results, $\Delta C_{N_{BW}}$, Configurations 1 and 3, $M=1.1$	270
137	Comparisons Between Experimental and Predicted Results, $\Delta C_{N_{FW}}$, $M=3.08$	271
138	Comparisons Between Experimental and Predicted Results, $\Delta C_{N_{BW}}$, $M=1.9$	272
139	Comparison Between Experimental and Predicted Results, $\Delta C_{N_{BW}}$, $M=0.85$	273
140	$K_{W(B)}$ and $K_{B(W)}$ Ratios (Slender Body Theory)	279
141	Wing Alone Center of Pressure at Subsonic Speeds.	280
142	Wing Alone Center of Pressure at Supersonic Speeds.	281
143	Curves for Determining $X_{CP_{B(W)}}/C_R$ at Subsonic Speeds.	282
144	Curves for Determining $X_{CP_{B(W)}}/C_R$ with Afterbody at Supersonic Speeds	283

LIST OF ILLUSTRATIONS (Cont'd)

<u>Figure</u>		<u>Page</u>
145	Configurations (Body + Wing)	284
146	Comparison Between Predictions and Experimental Data, X_{CP} / d , $M=0.85$	285
	Δ_{BW}	
147	Comparison Between Predictions and Experimental Data, X_{CP} / d , $M=1.1$	286
	Δ_{BW}	
148	Comparison Between Predictions and Experimental Data, X_{CP} / d , $M=1.9$	287
	Δ_{BW}	
149	Comparison Between Predictions and Experimental Data, X_{CP} / d , $M=2.86$	288
	Δ_{BW}	
150	Transonic Wind Tunnel Test Configurations	299
151	Wing Vortex Location	300
152	Wing Vortex Induced Tail Angle of Attack	301
153	Comparison Between Predicted and Experimental Results, $\Delta C_{N_{TW}}$, $M=1.1$	302
154	Comparison Between Predicted and Experimental Results, $C_{N_{BWT}}$, $M=0.7$	303
155	Comparison Between Predicted and Experimental Results, $C_{N_{BWT}}$, $M=0.85$	304
156	Comparison Between Predicted and Experimental Results, $C_{N_{BWT}}$, $M=2.36$	305
157	Comparison Between Predicted and Experimental Results, X_{CP} / d , $M=0.85$	308
	Δ_{BWT}	
158	Comparison Between Predicted and Experimental Results, X_{CP} / d , $M=2.36$	309
	Δ_{BWT}	

LIST OF ILLUSTRATIONS (Concluded)

<u>Figure</u>		<u>Page</u>
159	General Curve Form, $\Delta C_{N_{BP}}$	317
160	Power Series A for Calculating $\Delta C_{N_{BP}}$	318
161	Amplification Factors for Calculating $\Delta C_{N_{BP}}$	319
162 (a-e)	Comparisons Between Predictions and Experimental Data, $\Delta C_{N_{BP}}$	320
163 (a-e)	Comparison of Body Alone X_{CP} / d (Jet-On and Jet-Off)	328
164 (a-e)	Comparison Between Predictions and Experimental Data, $X_{CP_{BP}} / d$	331
165	General Curve Forms, $ \Delta C_{N_{TP}} $	343
166	Amplification Factors for Calculating $\Delta C_{N_{TP}}$	344
167a	Power Series A for Calculating $\Delta C_{N_{TP}}$, $M \leq 1.2$	346
167b	Power Series A for Calculating $\Delta C_{N_{TP}}$, $1.2 < M \leq 2.2$	347
168 (a-e)	Comparisons Between Predictions and Experimental Data, $\Delta C_{N_{TP}}$	348
169 (a-e)	Comparison Between Jet-On and Jet-Off Tail Centers of Pressure	353

LIST OF SYMBOLS

$A_0, A_1, A_2, A(\alpha)$	General coefficients
AR	Aspect ratio, $(2b)^2/S$ (2 panels)
AR_s	Strake aspect ratio
a, r	Body radius \sim inches
a_0, a_1, a_2, \dots	Polynomial expansion coefficients
$B_0, B_1, B_2, B(\alpha)$	General coefficients
b	Exposed semispan \sim inches
c_1, c_2, \dots	General coefficients
C_A	Axial force coefficient
C_{A_1}	Axial force coefficient, omitting base effects
C_{A_1b}	Basic value of C_{A_1}
$C_{A_{base}}$	Axial force coefficient due to base effects
C_{A_0}	$C_{A_1} + C_{A_{base}}$
C_d	Drag coefficient
C_m	Pitching moment coefficient
C_N	Normal force coefficient, based on S_{ref}
C_{NB}, C_{NBP}	Body alone C_N , jet-off and jet-on, respectively
C_{NBS}	Body + strakes normal force coefficient
$C_{NB(ST)}, C_{NB(ST)P}$	Total C_N on the body in the presence of strakes and tails, jet-off and jet-on.
C_{NC}	Normal force coefficient at $\alpha = 90^\circ$

LIST OF SYMBOLS (CONT'D)

$C_{NS(B)total}$, $C_{NS(B)Ptotal}$	Total C_N of four strakes in presence of body, jet-off and jet-on
C_{NT}	Single tail panel alone normal force coefficient
$C_{NT(B)total}$, $C_{NT(B)Ptotal}$	Total C_N of four tails in presence of body, jet-off and jet-on
$C_{NT(B)}$, $C_{NT(B)P}$	Single tail panel normal force coefficient in the presence of a body, jet-off and jet-on
C_R	Root chord ~ inches
C_{RS}	Strake root chord length ~ inches
C_s	Base stagnation pressure coefficient
d	Body cross-sectional diameter ~ inches
d_{noz}	Nozzle exit diameter ~ inches
K_{55} , K_{110} , K_{160}	Amplification factor at $\alpha = 55^\circ$, 110° , and $160^\circ = f(M)$
K_{70}	Value of $\Delta C_{N_{BP}} / M_R$ at $\alpha = 70^\circ$ [$=f(M)$]
K_{145}	Value of $\Delta C_{N_{BP}} / M_R$ at $\alpha = 145^\circ$ [$=f(M)$]
$F(MACH)$	Mach number correction used in conjunction with $\Delta \frac{X_{CP}}{C_R} \Big _{\alpha < 90}$
h	Vertical distance between wing vortex core and tail surface at l_s
$I_{a,b,c}$	Coefficients for transonic range of $I_{B(T)}$
$I_{1,2,3}$	Coefficients for supersonic range of $I_{B(T)}$
$I_{B(S)}$, $I_{B(S)P}$	Strake contribution to carryover C_N on body, jet-off and jet-on
$I_{B(T)}$, $I_{B(T)P}$	Tail contribution to carryover C_N on body, jet-off and jet-on
$I_{B(ST)}$, $I_{B(ST)P}$	Total carryover C_N on body due to strakes and tails, jet-off and jet-on

LIST OF SYMBOLS (CONT'D)

J_1	$\Delta C_{N_{BS\alpha}} @ \alpha = 0^\circ = (K_{B(W)} + K_{W(B)}) \left(\frac{S_s}{S_{ref}} \right) \left(\frac{\pi AR_s}{2} \right)$
J_2	Scale factor for $X_{CP_{\Delta BS}}$ at $\alpha = 60^\circ$
K_a	Amplification factor, peak value of ΔC_{NBS} at $\alpha = 57^\circ$ and 135°
K_b	Scale factor for $X_{CP_{\Delta BS}}$ at $\alpha = 60^\circ$
K_1	Value of X_{CP_B} / d_{REF} at $\alpha = 120^\circ$
$K_{T(B)}$	Ratio of normal force on tail in the presence of body to tail alone normal force
$K_{B(T)}$	Ratio of normal force on body due to tails to tail alone normal force
$K_{B(W)}$	Ratio of normal force on body due to wings to wing alone normal force
$K_{W(B)}$	Ratio of normal force on the wing in the presence of body to wing alone normal force
L	Mean value of $\Delta C_{N_{BS}}$, $80^\circ \leq \alpha \leq 120^\circ$
l	Length ~ inches
l/d	Fineness ratio
l	Missile total length ~ inches
l_A	Length of missile cylindrical section ~ inches
l_N	Missile nose length ~ inches
l_s	Distance between wing trailing edge and tail leading edge at a lateral distance \bar{Y}_W
M	Freestream Mach number
M_R	Jet momentum ratio = q_j / q_∞
M.S.	Missile station (inches from the nose)
N	Normal force ~ lbf

LIST OF SYMBOLS (CONT'D)

p	Tail semispan, measured from body centerline ~ inches
q_J	Jet dynamic pressure at nozzle exit ~ lbs/sq. ft.
q_∞, q	Freestream dynamic pressure ~ lbs/sq. ft.
R	Tangent ogive nose radius, or value of $\frac{X_{CP_S}}{d}$ at $\alpha = 60^\circ$ ~ inches
R_e	Reynolds number
R_T	Tail area ratio = S_T/S_{ref}
$R_{T(B)}$	Interference factor ($C_{N_{T(B)}}/C_{N_T}$)
$R_{W(B)}$	Interference factor ($C_{N_{W(B)}}/C_{N_W}$)
r	Body radius ~ inches
r_v	Radial distance measured from vortex core ~ inches
S	Area ~ sq. ft.
S_p	Body planform area ~ sq. ft.
S_{ref} , or S_B	Reference area = $\frac{\pi d^2}{4}$ ~ sq. ft.
S_{RS} , or S_s	Strake single span exposed area ~ sq. ft.
S_{S+B}	Area of two strakes + planform area of body between strakes
S_T	Tail single panel exposed area ~ sq. ft.
S_W	Wing single panel exposed area ~ sq. ft.
s	Total tail span including body
T	Value of $\frac{X_{CP_S}}{d}$ at $\alpha = 120^\circ$
V_t	Vortex tangential velocity at a distance r
X	Axial distance ~ inches
\bar{X}	Distance to center of planform area ~ inches
\bar{X}_A	Location of forward strake segment centroid relative to LE

LIST OF SYMBOLS (CONT'D)

\bar{x}_B	Location of aft strake segment centroid relative to LE
\bar{x}_S	Location of net strake centroid relative to LE
$x_{CP_{B(T)}}$	Center of pressure of carry-over loading on body measured from tail root chord leading edge
x_{CP_T}	Center of pressure of the tail measured from the body nose
$x_{CP_{T(B)}}$	Chordwise center of pressure of tail in the presence of a body measured from tail root chord leading edge
x_{CP_0}	Strake CP location at $\alpha = 0^\circ$
$x_{CP_B} \cdot x_{CP_{BP}}$	Body alone center of pressure station, jet-off and jet-on, relative to the nose
$x_{CP_{BS}}$	Body + strakes center of pressure, relative to the nose
$x_{CP_{BST}} \cdot x_{CP_{BSTP}}$	Center of pressure of a body-strake-tail combination, jet-off and jet-on
$x_{CP_I} \cdot x_{CP_{IP}}$	Effective center of pressure (M.S.) of total carryover C_N due to strakes + tails, jet-off and jet-on
$x_{CP_{I(S)}} \cdot x_{CP_{I(S)P}}$	Effective center of pressure (M.S.) of strake carryover on body C_N , jet-off and jet-on
$x_{CP_{I(T)}} \cdot x_{CP_{I(T)P}}$	Effective center of pressure (M.S.) of tail carryover on body C_N , jet-off and jet-on
x_{CP_S}	Center of pressure of $\Delta C_{N_{BS}}$, relative to strake LE
$x_{CP_{\Delta BS}}$	Center of pressure of $\Delta C_{N_{BS}}$, relative to the nose
$\frac{x_{CP_{\Delta BST}}}{C_R}$	Center of pressure of $\Delta C_{N_{BST}}$ as a percentage of root chord measured from the wing root chord leading edge
$\frac{x_{CP_{\Delta BW}}}{d}$	Center of pressure of $\Delta C_{N_{BW}}$ measured in diameters from the nose

LIST OF SYMBOLS (CONT'D)

$X_{CP \Delta TWV}$	Effective center of pressure of $\Delta C_{N \Delta TWV}$
X_{CP}/C_R	Chordwise center of pressure (nondimensionalized by panel root chord, C_R)
$\left. \frac{X_{CP}}{C_R} \right _{\alpha=1}$	Center of pressure at $\alpha = 1$ degrees
$\left. \frac{X_{CP}}{C_R} \right _{\substack{\alpha = 160 \\ M = 0.98}}$	Tail center of pressure at $\alpha = 160^\circ$ for basic Mach = 0.98
$\left. \frac{X_{CP}}{C_R} \right _{\alpha = 160}$	Tail center of pressure at $\alpha = 160^\circ$ corrected for Mach number
	$\left. \frac{X_{CP}}{C_R} \right _{\substack{\alpha = 160^\circ \\ M = 0.98}} + \Delta 1 \frac{X_{CP}}{C_R}$
$X_{CP \text{ BS}(T)}$	Effective center of pressure of the incremental force on a body strake-configuration due to the addition of a tail
$\frac{\left. \frac{X_{CP}}{C_R} \right _{\alpha=160} - \left. \frac{X_{CP}}{C_R} \right _{\alpha=90}}{\left(\frac{70}{180}\right)\pi}$	Initial slope of tail chordwise center of pressure at $\alpha = 160^\circ$
X_{LE}	Strake leading edge station from nosetip
α	Angle of attack
α'	Angle at which linear variation of $X_{CP \text{ B}}$ begins
β	$\sqrt{1-M^2}$ or $\sqrt{M^2-1}$
$\Delta C_{N \text{ BP}}$	Incremental C_N on body alone due to jet = $C_{N \text{ BP}} - C_{N \text{ B}}$
$\Delta C_{N \text{ BS}}$	Incremental normal force coefficient due to strakes
$\Delta C_{N \text{ BS } \alpha}$	Slope of $\Delta C_{N \text{ BS}}$ vs α curve = $\partial \Delta C_{N \text{ BS}} / \partial \alpha$

LIST OF SYMBOLS (CONT'D)

$\Delta C_{N_{RW}}$	Increment in normal force due to the addition of wings to a body
ΔC_{NS}	Incremental C_N on strakes due to jet = $C_{N_{SP}} - C_{N_S}$
ΔC_{NT}	Incremental C_N on tails due to jet = $C_{N_{TP}} - C_{N_T}$
$\Delta C_{N_{T(BS)}}$	Increment in normal force due to the tails of a body-strake-tail configuration
$\Delta C_{N_{TP}}$	Total incremental C_N on body + tails configuration due to jet effects on tails = $(C_{N_{TP}} + I_{B(T)P}) - (C_{N_T} + I_{B(T)})$
$\Delta C_{N_{TW}}$	Incremental normal force coefficient produced on a tail due to wing vortex interference
$\Delta I_{B(ST)P}$	Incremental interference C_N on body due to jet effects on strakes and tails = $I_{B(ST)P} - I_{B(ST)}$
$\Delta I_{B(T)P}$	Incremental interference C_N on body due to jet effects on tails = $I_{B(ST)P} - I_{B(T)}$
\bar{y}_w	Spanwise distance between wing root and location of trailing vortex
$\Delta X_{CP_{IP}}$	Change in CP location of strake + tail interference C_N due to the jet = $X_{CP_{IP}} - X_{CP_I}$
$\Delta X_{CP_{I(S)P}}$	Change in CP location of strake-on-body interference in C_N due to the jet = $X_{CP_{I(S)P}} - X_{CP_{I(T)}}$
$\Delta X_{CP_{IP(S)}}$	Change in CP location of strake + tail interference C_N due to jet effects on X_{CP_S}
$\Delta X_{CP_{IP(T)}}$	Change in CP location of the strake + tail interference C_N due to jet effects on X_{CP_T}
$\Delta X_{CP_{SP}}$	Change in strake CP location due to jet effects = $X_{CP_{SP}} - X_{CP_T}$

LIST OF SYMBOLS (CONCL'D)

$\Delta X_{CP_{TP}}$	Change in tail CP location due to jet effects = $X_{CP_{TP}} - X_{CP_T}$
$\Delta \frac{X_{CP}}{C_R} \Big _{\alpha < 90}$	Difference between tail chordwise centers of pressure at $\alpha = 90^\circ$ and any $\alpha < 90^\circ$, $\frac{X_{CP}}{C_R} \Big _{\alpha=90} - \frac{X_{CP}}{C_R} \Big _{\alpha < 90}$
$\Delta \frac{X_{CP}}{C_R} \Big _{\alpha > 90}$	Difference between tail chordwise centers of pressure at $\alpha = 175^\circ$ and 160° , $\frac{X_{CP}}{C_R} \Big _{\alpha=175} - \frac{X_{CP}}{C_R} \Big _{\alpha=160}$
$\Delta_1 \left(\frac{X_{CP}}{C_R} \right)$	Mach number correction used at $\alpha = 160^\circ$
Δx	Change in center of pressure
ϵ	Vortex induced angle of attack at the tail
η	Crossflow drag proportionality factor
Δ	Sweep angle
λ	Taper ratio, tip chord/root chord
X	Nondimensionalized center of pressure = X_{CP}/d

SUBSCRIPTS

A	Afterbody
B	Body
base	Base
Basic, b	Basic
BS	Body-strake
BST	Body-strake-tail
BT	Body plus tail
B(T)	Body in the presence of the tail
BW	Body plus wing

SUBSCRIPTS (CONT'D)

B(W)	Body in the presence of a wing
BWT	Body plus wing plus tail
c	Crossflow
D.P.	Double panel
e	Exposed
I	$I_{B(T)}$
i	General indicator
L.E.	Leading Edge
N	Nose
n	Nonlinear
p	Planform area
POT	Potential
ref	Reference
S	Strake
SF	Skin friction
S.P.	Single panel
T	Tail
T(B)	Tail in presence of body
T.E.	Trailing edge
V	Vortex
W	Wing, or wave drag
W(B)	Wing in the presence of a body
α	Denotes differentiation with respect to α
ΔBW	$\Delta C_{N_{BW}}$
$\pi/2$	$\alpha = 90^\circ$
π	$\alpha = 180^\circ$

SUBSCRIPTS (CONCL'D)

0	$\alpha = 0^\circ$
16	$\alpha = 16^\circ$
20	$\alpha = 20^\circ$
160	$\alpha = 160^\circ$

SUMMARY

This report describes the construction and use of methods for predicting the pitch plane aerodynamic characteristics of a class of missile configurations. The configurations include body alone, body-tail, body-strake-tail and body-wing-tail configurations at high angles of attack. An assessment is also provided of the effects of a rocket exhaust plume on the pitch plane characteristics for a range of thruster conditions.

The methods, semi-empirical in nature, were developed through correlation of test data obtained during several independent test programs. These data, when taken together, form a rather extensive data bank in which configuration geometries and flow conditions are systematically varied. Except for the methods pertaining to winged missile configurations, which are limited to 30 degrees angle of attack, all methods are applicable to angles of attack between 0 and 180 degrees. In several instances lack of test data imposed Mach number limitations; however, in the majority of cases the methods apply to Mach numbers between 0.6 and 3.0.

Methods are provided to predict the characteristics of isolated components and interference effects produced when various components are combined. The methods pertain to bodies of circular cross-section. When tails are added, they are mounted in cruciform (plus attitude) with the tail trailing edges in line with the base of the body and undeflected. Forward lifting surfaces (strakes or wings) can also be added.

The methods enable the user to estimate the normal force and center of pressure of a variety of configurations by calculating the characteristics of individual missile components and their mutual interactions

produced when in combination. Where possible, predictions have been compared against data which were not used in the development of models. In general, these comparisons have demonstrated good agreement.

1.0 INTRODUCTION

A recurring problem in missile engineering is the lack of accurate methods for predicting configuration aerodynamic characteristics, for all Mach numbers, at high angles of attack. The situation is aggravated by the long term trend toward increased missile maneuverability and angle of attack. Historically, maximum angle requirements have increased steadily. The greatest increase has occurred relatively recently to meet advanced air-launched system maneuverability requirements. These now dictate angles of attack to 90 and even 180 degrees.

The missiles which fly at these very high angles are usually of the slewing type, i.e., their angle of attack is generated by thrust vector control (TVC) (for example, AIR SLEW and AGILE). Aerodynamically they tend to be somewhat simpler than missiles which achieve high maneuverability through use of aerodynamic surface deflection because of the large control forces available from the deflected TVC nozzle. Non-TVC missiles usually can deploy wings and canards as well as tails, and their maximum angles of attack are limited to about 40 degrees. Air slew missiles usually deploy tails, but any forward lifting surfaces are generally small (e.g., strakes). Basic aerodynamic prediction methods are required for both types of vehicles.

The aerodynamic performance of TVC type vehicles is further complicated by plume interference; therefore a method is required for calculating this effect in addition to methods for estimating the basic aerodynamics.

It has been well-established (References 1, 2, 3, and 4) that the best

means of constructing methods for estimating basic aerodynamic characteristics at high angles of attack is through correlation of experimental data generated by testing over systematically-varied ranges of the relevant geometric and aerodynamic parameters (Reference 1). This report describes the generation of methods using that technique. The methods deal with the aerodynamics of aerodynamically controlled missiles and TVC missiles with and without plume effects. A summary of the data used in the development of the methods is presented in Reference 5.

The objective of this work was to evaluate existing methods, to improve upon these existing methods if possible, and, where necessary, to develop new methods to predict the pitch-plane aerodynamic characteristics for aerodynamically controlled and TVC missiles. The methods addressed were applicable to the configurations, angle of attack and Mach number ranges indicated in Table I.

Table I
Scope of Methodology Requirements

CONFIGURATION	Control Mechanism		
	Aerodynamically Control $\alpha = 0^\circ - 30^\circ$ $M = 0.6 - 3.0$	TVC $\alpha = 0^\circ - 180^\circ$ $M = 0.6 - 3.0$	Jet Interference Effects Included
Body Alone	✓	✓	✓
Body-Wing-Tail (Canard)	✓		
Body-Tail	✓	✓	✓
Body-Strake		✓	✓
Body-Strake-Tail		✓	✓

Prediction of the aerodynamic characteristics for the configurations indicated in Table I requires methods for predicting the aerodynamics of individual components and mutual interference effects. Figures 1a and 1b show the extent of existing capabilities prior to this contract with respect to total methodology requirements.

Although it is not shown in Figures 1a and b, a certain level of capabilities existed in each of the areas indicated. In general, the accuracy of these methods is poor at angles greater than a few degrees; therefore, these methods were not indicated. Under the present work, methodology was developed to fill in the gaps indicated in the overall requirements of Figures 1a and b. The methods developed are of an engineering type and include charts, graphs and formulations which facilitate ease of use by hand.

By and large the methods are empirical and therefore are limited to the range of test conditions and geometric parameters tested. The specific conditions tested are discussed in Section 2.0 and the Mach number range of interest, namely 0.6 to 3.0 is adequately covered. However, as is usually the case, the flight combinations of Mach and Reynolds numbers were not achieved in the wind tunnel test programs. Therefore the resulting methods do not contain all the effects of Reynolds number variation that might be desired. Until better matching of flight conditions is achieved in wind tunnel tests, the user of such methods must exercise care and judgement with regard to this point.

Finally it is noted that methodology was developed to predict induced yaw forces and moments and induced rolling moments, and was provided as part of this program. Reference 39 describes the development of the methods and the computerized version of the methods.

The general layout of the report is as follows: First, a general description of the equipment and models used in data generation is given in Section 2.0. Then a limited amount of data analysis is presented in Section 3.0. Following this, Section 4.0 describes the formulation of the aerodynamic prediction equations and the terms for which methods are constructed. The methods themselves are described in Section 5.0. Where applicable each description includes background discussions, treatment of data, approach of construction, use of methods, and where possible, checks of method accuracy against data not used in the construction.

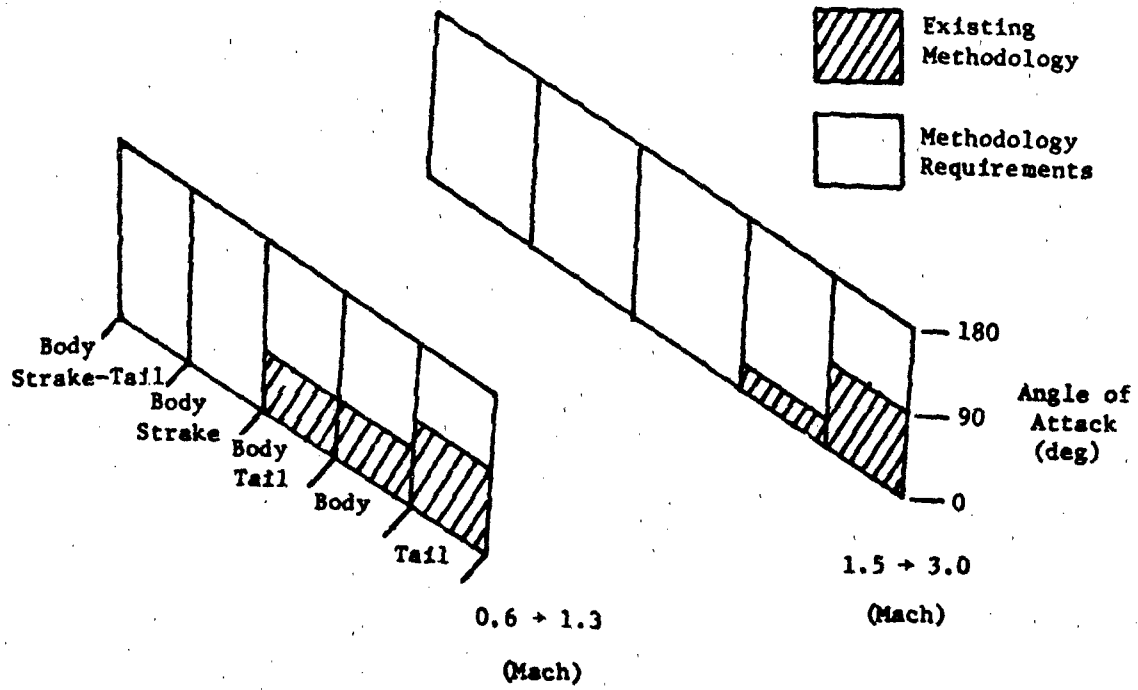


Figure 1a. Methodology Requirements for TVC Missiles

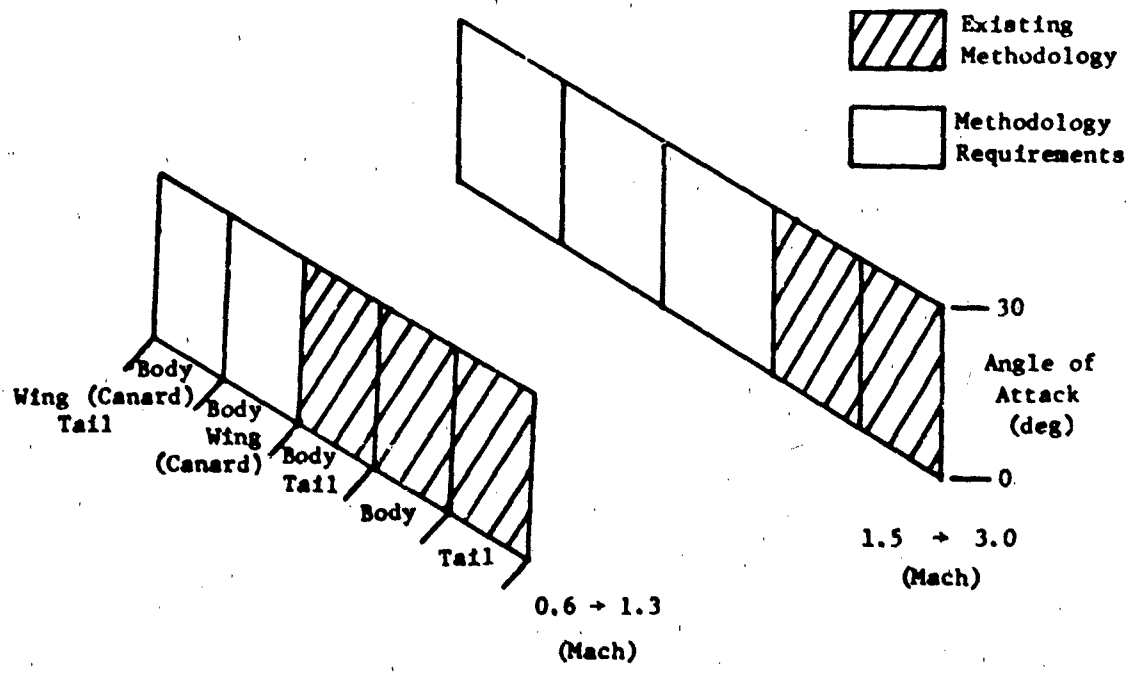


Figure 1b. Methodology Requirements for Aerodynamically Controlled Missiles

2.0 EXPERIMENTAL DATA SOURCES AND MODELS

The majority of data available for correlation (see Figure 2) were generated using either U.S. Air Force or Martin Marietta, Orlando Division, supplied models. Reference 13, which is based on 485 hours of testing in tunnels 4T and A at AEDC, is the primary source of data. The TVC data are taken from a 312 hour test program in tunnels 16T and 16S at AEDC. Typical missile components were tested separately and in combination. A Martin Marietta supplied reflection plane and fins were tested to provide isolated fin data to 180 degrees angle of attack. Isolated body and non-rolled body tail data were generated using both Air Force and Martin Marietta models. The Martin Marietta main body model is shown in Figure 3a with the selection of tails which can be mated to the body shown in Figure 3b. The Air Force and Martin Marietta models are both 10 calibers in length with tangent ogive noses but the Air Force nose is 2.5 calibers compared to 3.0 calibers for the Martin Marietta nose. The Air Force and Martin Marietta model diameters are 1.25 and 3.75 inches, respectively. Tails of identical planform geometry, arranged in cruciform and undeflected, were tested on each body. Tail taper ratios, aspect ratios and diameter to span ratios were varied between 0 - 1.0, 0.5 - 2.0 and 0.3 - 0.5, respectively. Angles of attack varied from 0 to 180 degrees. The maximum angle of attack attained by the Martin Marietta sting mounted model was limited to 60 degrees. Through a combination of stings and struts, the Air Force model was tested to 180 degrees. The Martin Marietta model was equipped with four 3-component tail balances compared to a single tail balance for the Air Force model. These

balances measured tail normal force, hinge moment and root bending moment.

Six-component main balance data were available from each model.

Body-wing-tail configurations were tested to 30 degrees angle of attack at a non-rolled altitude using the Martin Marietta model. Data consisted of 6-component main balance and 3-component fin balance outputs. This model can accommodate sets of half wings mounted in cruciform at several different axial stations between the shoulder and after body section containing the tail balances. The wings are not attached to recording balances. Wings tested were of constant aspect ratio 2.0 and taper ratio 0.0 with diameter to span ratio varying between 0.35 and 0.5.

A more complete description of the sources of test data, test conditions and model configurations is contained in the Data Report (Reference 5) submitted as part of this study contract (CDRL Item No. A005).

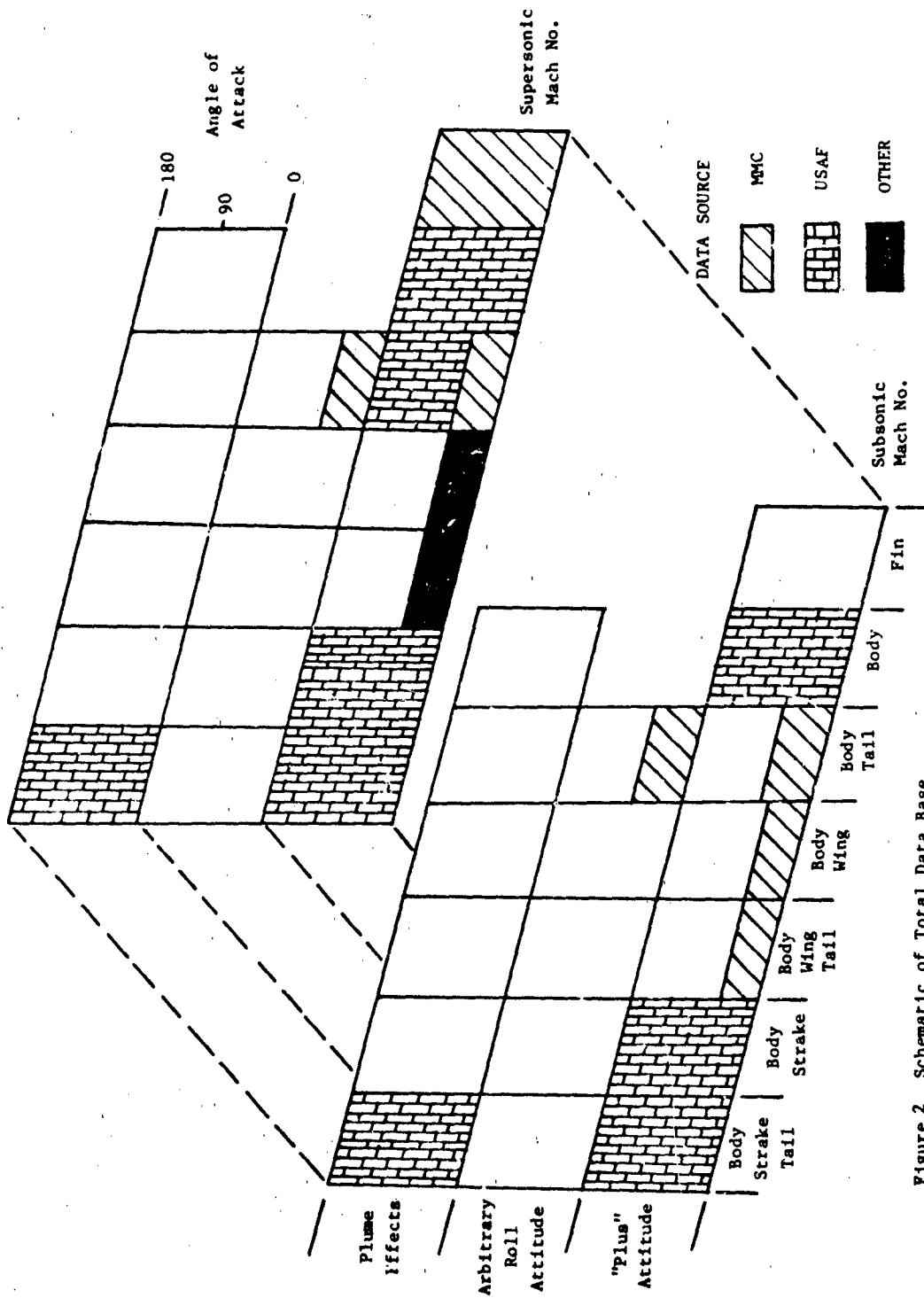


Figure 2 Schematic of Total Data Base

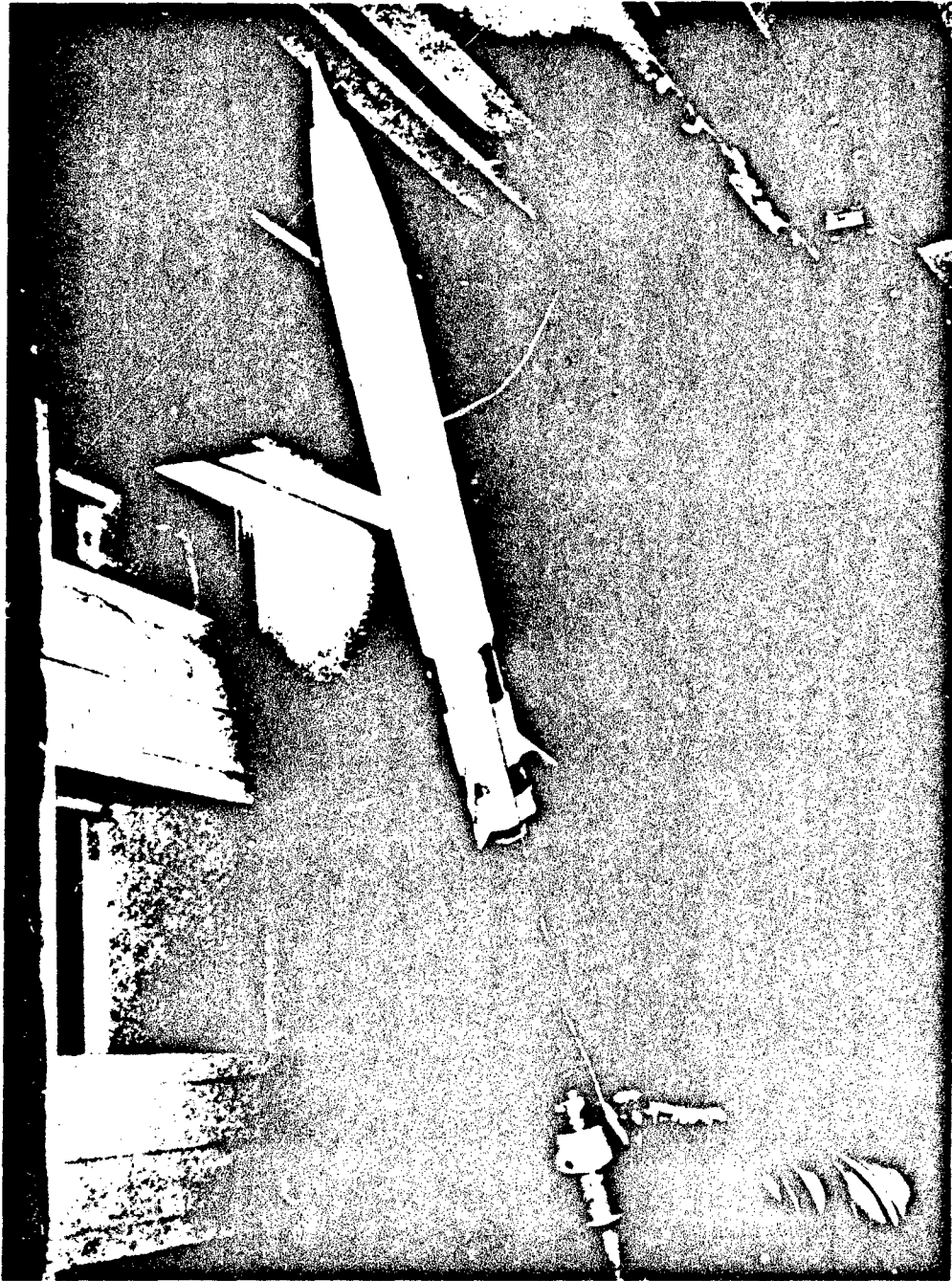


Figure 3a. Martin Marietta Main Body Model in the NSRDC 7'x10' Transonic Tunnel at Sixty Degrees Angle of Attack

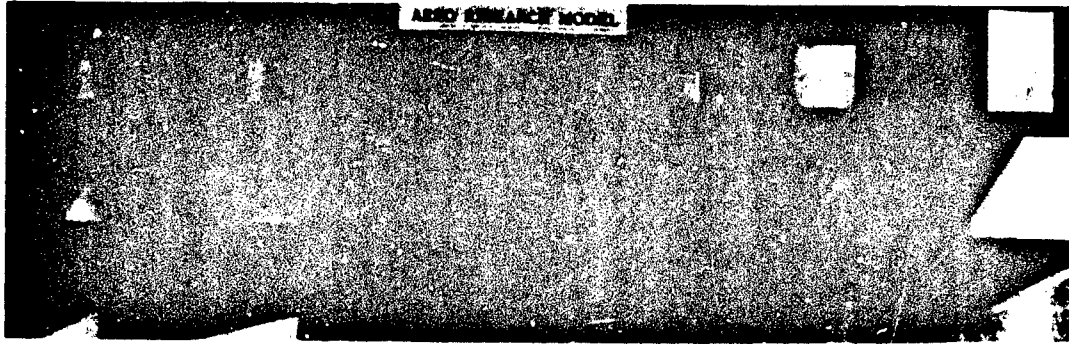


Figure 3b. Martin Marietta Tail Models

3.0 AERODYNAMIC DATA TRENDS

Before proceeding to the various methods, a qualitative analysis of some of the test data will be presented. The discussions are intended to illuminate the basic phenomena underlying model aerodynamic behavior and provide the user with more than simply a recipe for calculating the various force and moment quantities. Many of the basic ideas used were presented in References 2 and 3. They will be summarized here for the sake of convenience. The discussions here will be limited to isolated fins and bodies and body plus tail configurations.

3.1 Fin Aerodynamics

Most of the discussions in this section are based upon those of Reference 2. No attempt will be made to reproduce all of the previous material. The reader is referred to the original document for a detailed treatment.

The discussions center on the effects of fin geometry (planform taper and aspect ratios) and Mach number on the aerodynamic characteristics. Fin flow patterns are discussed briefly along with the associated stall characteristics. The implications for fin normal force coefficient and chordwise center of pressure location are outlined. Discussions begin with a consideration of delta fins.

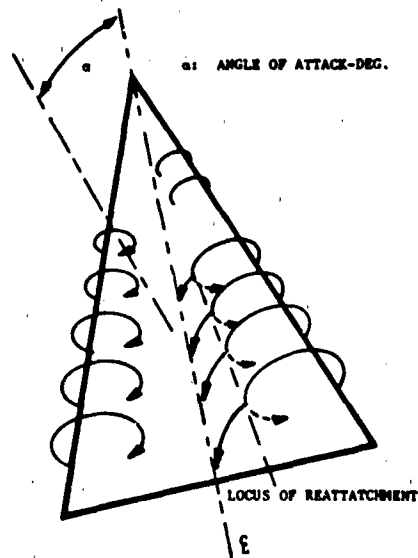


Figure 4. Vortices Produced by the Reattachment of Lower Surface Boundary Layer

At high angles of attack the flow around delta fins is characterized by the presence of large upper surface vortices fed with vorticity from the boundary layers which separate at the leading edges (See Figure 4). Stall on such wings is brought about by vortex "bursting". This is accompanied by a breakdown of the well-ordered vortex flow and a sudden pressure increase at and downstream of the "burst" point. Upstream the pressure in the vortex remains low and produces a suction which increases the normal force. As angle of attack is increased the "burst" point moves upstream towards the trailing edge. When it crosses the edge, stall begins and is characterized by a loss of normal force and a forward movement of the center of pressure. As aspect ratio increases, the stalling angle of attack decreases. These effects are shown in Figures 5a and 5b at transonic speeds. The figures also show the following:

- i) The normal force curve slopes, $C_{N\alpha}$, at $\alpha = 0^\circ$ and 180° are numerically equal - this result is predicted by Slender Body Theory.
- ii) At $\alpha = 90^\circ$, the centers of pressure and of area very nearly coincide. This is intuitively obvious.
- iii) At $\alpha = 180^\circ$, the centers of pressure of these delta fins lie right at the "leading" edge. This bears out the Slender Body Theory result that all of the loading on a fin occurs over the region where the fin span is changing (increasing). The predicted effect of retreating side edges (i.e., to push the center of pressure upstream) is not evident. A similar result is found for non-delta fins also.

Still confining the discussions to delta fins, Figures 5c and d show their behavior at supersonic speeds. It will be seen that no stalling is visible at this Mach number. During the reflection plane tests from which these data were obtained, it was found that near $\alpha = 90^\circ$ at supersonic Mach numbers, the fins behaved like forward facing steps, resulting in low values of C_N . Accordingly, the C_N value at $\alpha = 90^\circ$ was obtained from Reference 6 and the data faired through that point as shown. Also worthy of note is the center of pressure behavior, particularly near $\alpha = 180^\circ$.

When the fin planform is not triangular, the upper surface vortices referred to earlier are modified or joined by yet other rotating flows.

For rectangular fins, the large suction-producing vortices now spring from the side edges, while a laminar separation bubble can exist at the leading edge. When stall occurs on such a fin, it is frequently a result of laminar bubble lengthening, spreading low-velocity, high pressure flow over the upper surface. The result is a loss of normal force and a rearward shift of center of pressure. A clipped delta fin displays behavior somewhere between that of a delta and a rectangular fin. This behavior is shown in Figures 6a and b at transonic speeds. Note the centers of pressure for the rectangle at $\alpha = 0^\circ$ and 180° . They lie right at the "leading" edge as predicted by Slender Body Theory. At $\alpha = 180^\circ$, all three fins show this predicted behavior. As before, the supersonic data show no visible stalling and have been faired through $C_{N_{\pi/2}}$ from Reference 6, Figures 6c and d.

The effect of increasing Mach number on a delta fin is to move the vortex "burst" point downstream. Thus a fin which is stalled at one Mach number may be unstalled by simply increasing Mach. This behavior is shown in Figures 7a and b for an AR = 2.0 delta fin. The stalling behavior at $M = 0.8$ is entirely removed at $M = 1.3$ and higher.

3.2 Body Aerodynamics

As in the case of fins, the aerodynamic characteristics of bodies at high angles of attack are largely influenced by viscous, separated flows. The discussions below deal with these, especially in the case where the body wake takes the form of an asymmetric vortex pattern. This phenomenon has recently become of considerable interest for high

incidence missiles (Reference 7).

When a slender missile body is placed at angle of attack in a uniform flow, the boundary layer generally separates on either side of the body and forms a lee-side wake. Separation usually begins near the rear when the missile reaches about 6 degrees angle of attack. The wake takes the form of a pair of symmetrically-disposed, counter-rotating vortices fed by vorticity shed from the separating boundary layer. As angle of attack increases, the axial extents, sizes and strengths of vortices increase also.

When the body angle of attack reaches about 25 degrees, the symmetrical nature of the wake disappears. The two vortices are joined by a third, beginning again at the body rear, and the wake becomes asymmetric. As angle of attack is increased further, more vortices join the flow until the wake contains several which have been shed from the body. A section taken through the wake shows it to resemble the von Karman vortex street, well known in the literature on two-dimensional flows.

The asymmetric nature of the wake produces an asymmetric distribution of pressure forces along the body. This results in out-of-plane forces and moments being induced, whether the body has lifting surfaces deployed or not. These forces and moments can be significantly large, requiring special means to be found to counteract or remove their effects (Reference 8). Figure 8a shows the force and moment coefficients induced on a body at $M = 0.6$. The effect of increasing Mach number to supersonic values is usually to reduce those effects to negligible proportions. This may be seen in Figure 8b for $M = 2.0$. Later discussions will illustrate the

additional effects of adding lifting surfaces to such a body. The steady, asymmetric wake persists up to angles of about 50 to 60 degrees. At higher angles the wake becomes unsteady and vortices are shed asymmetrically.

3.3 Body Tail Configuration Aerodynamics

The addition of tails to a body generally increases the out-of-plane forces and moments induced by asymmetric vortex effects as well as producing rolling moments. Several examples will be given of these important effects. Figures 9a and b show out-of-plane quantities at $M = 0.6$ for two typical sets of cruciform tails fixed to the 10:1 caliber body ("plus" attitude). It is of interest to note the correspondence between the peaks of force and moment. The angle of attack has generally been limited to 90 degrees because:

- i) By 90 degrees the wake flow is unsteady and the out-of-plane quantities fluctuate rapidly.
- ii) Above 90 degrees, the presence of the strut support might cause alterations in the wake pattern and its effects.

By the time Mach number has reached 2.0, no induced effects are visible (not shown here).

Another illustration of the asymmetric wake effect is contained in Figures 10a and b. Previous testing on a MMO model with four instrumented tails yielded the forces and moments on the individual tails. Complete configuration rolling moment was obtained from separate (main balance) instrumentation. Figure 10a shows the tail forces for a "cross" configuration ($\phi = 45^\circ$) at angles of attack to 60 degrees. If the moments of these tail

forces about the missile axis are summed and the result compared with the main balance reading, the comparison of Figure 10b is obtained. Clearly, the induced roll is generated by the unequal tail forces, which themselves are induced by the asymmetric wake.

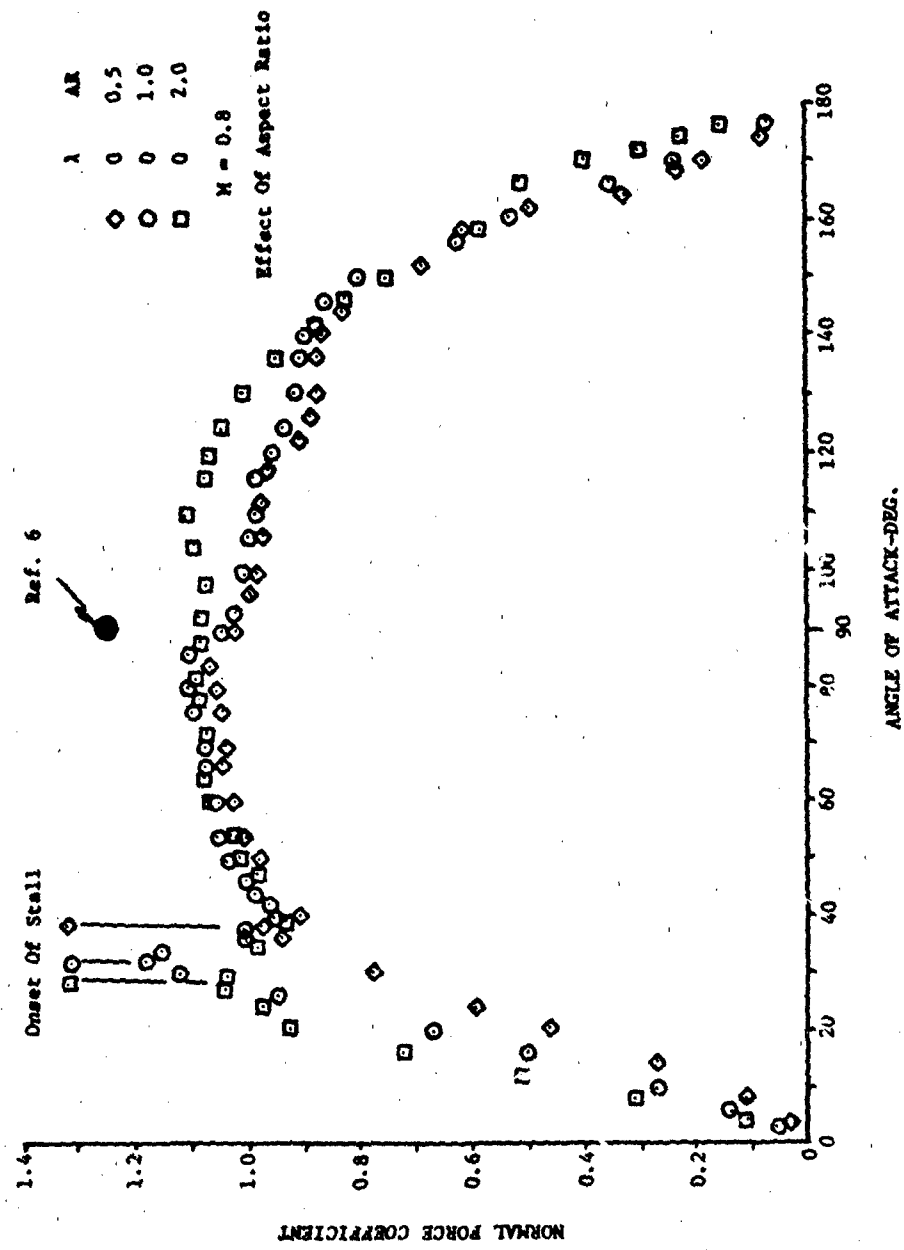


Figure 5a. Fin Normal Force Coefficient, $M = 0.8$

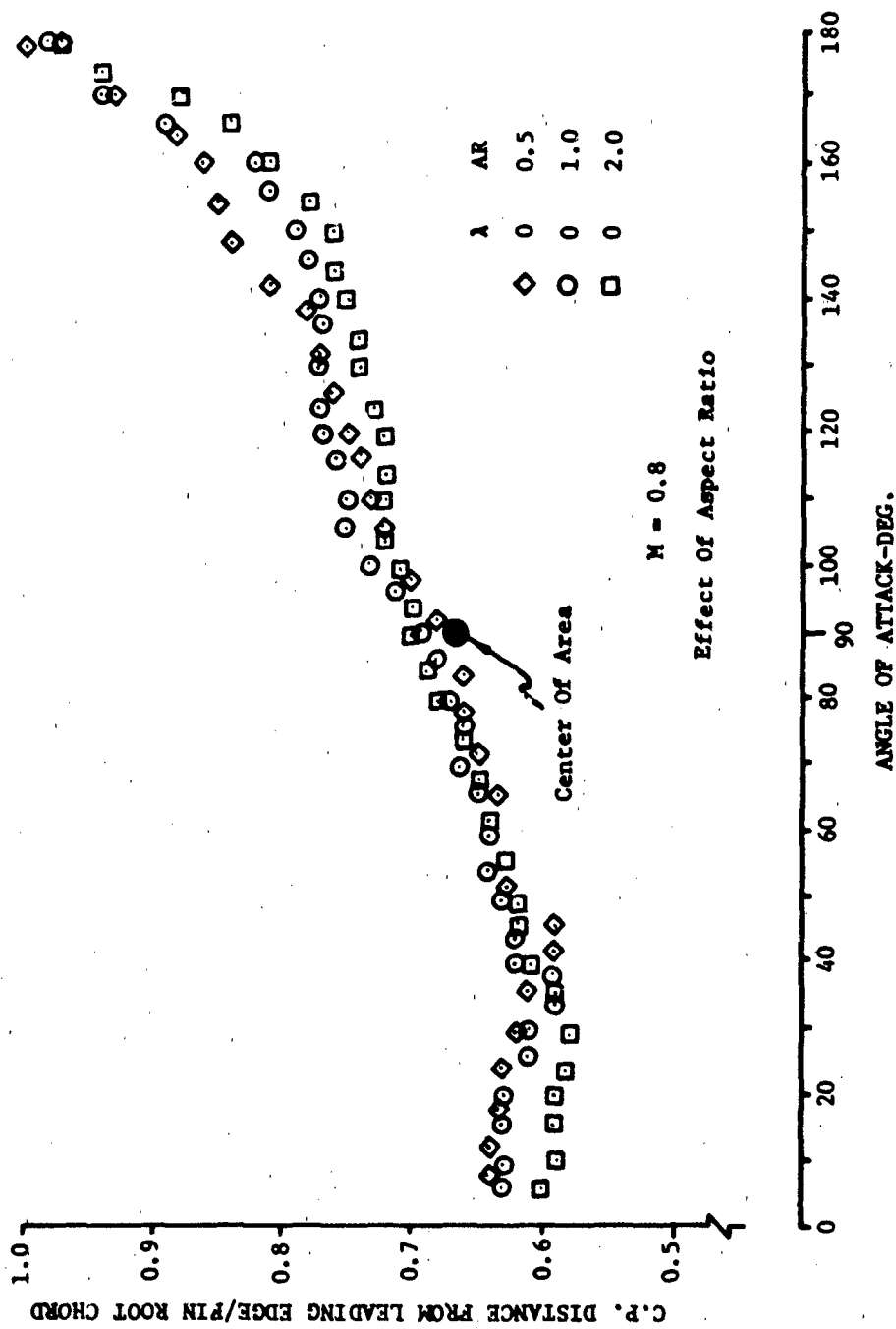


Figure 5b. Fin Chordwise Center of Pressure, M = 0.8

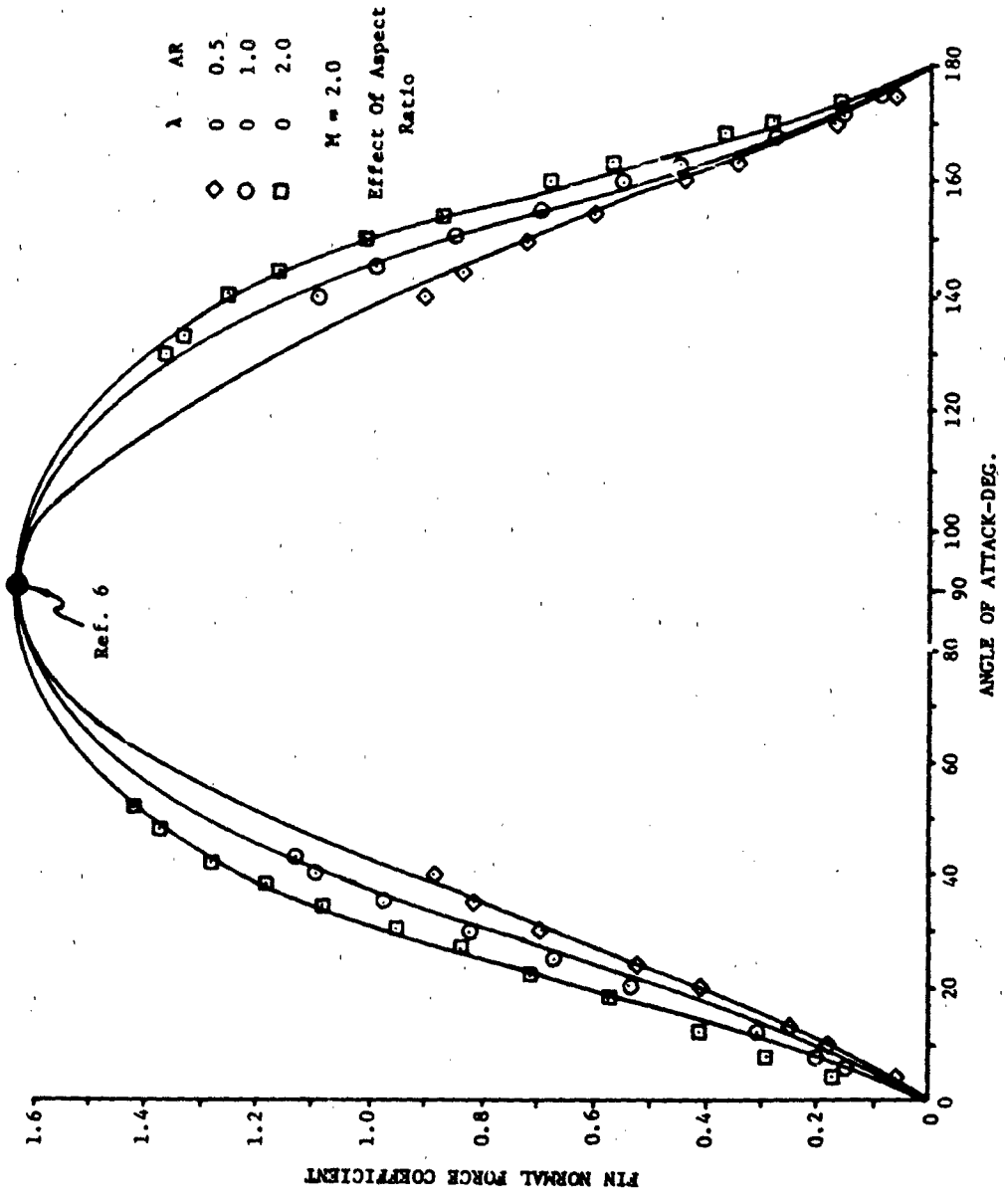


Figure 5c. Pin Normal Force Coefficient, M = 2.0

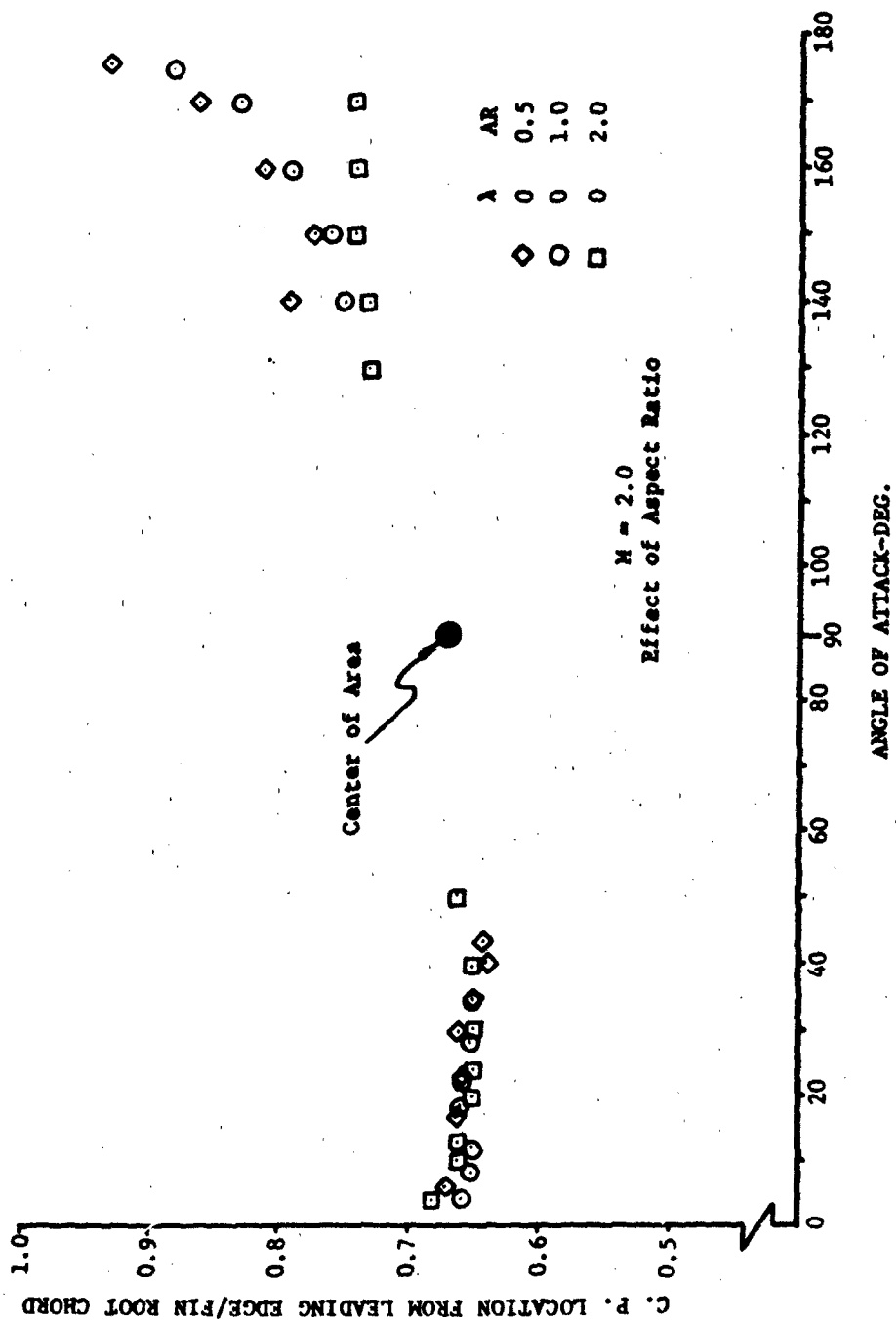


Figure 5d. Fin Chordwise Center of Pressure, M = 2.0

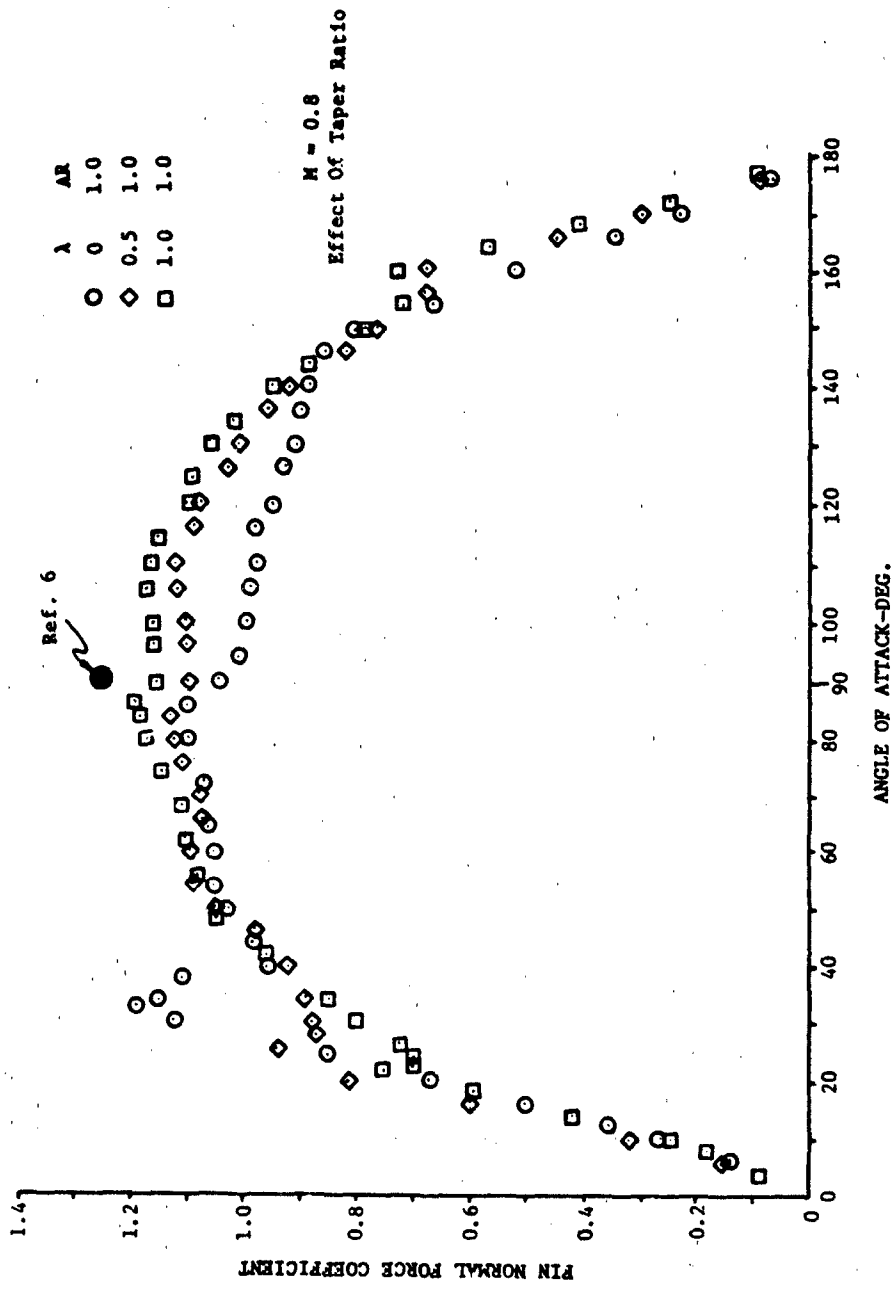


Figure 6a. Fin Normal Force Coefficient, M = 0.8

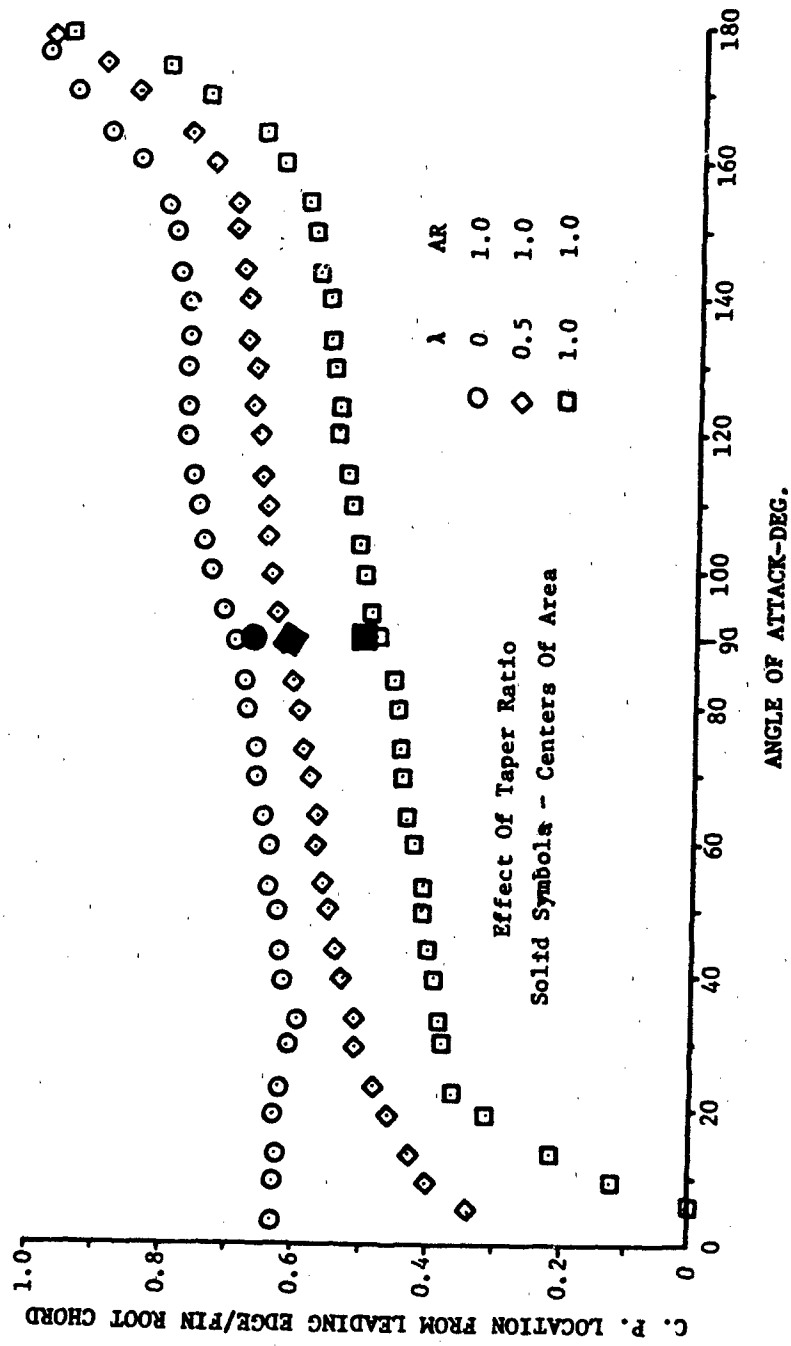


Figure 6b. Fin Chordwise Center of Pressure, $M = 0.8$

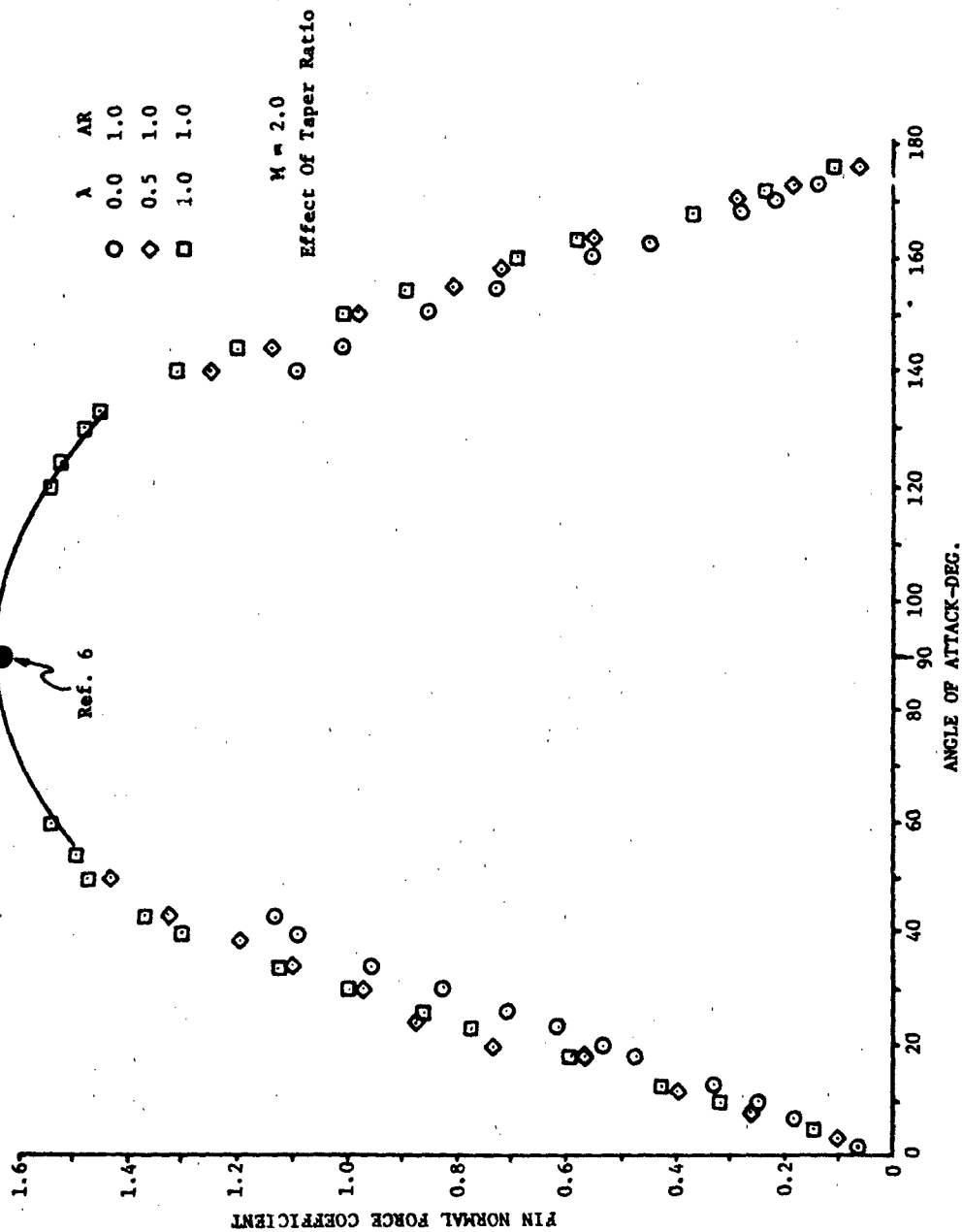


Figure 6c. Fin Normal Force Coefficient, $M = 2.0$

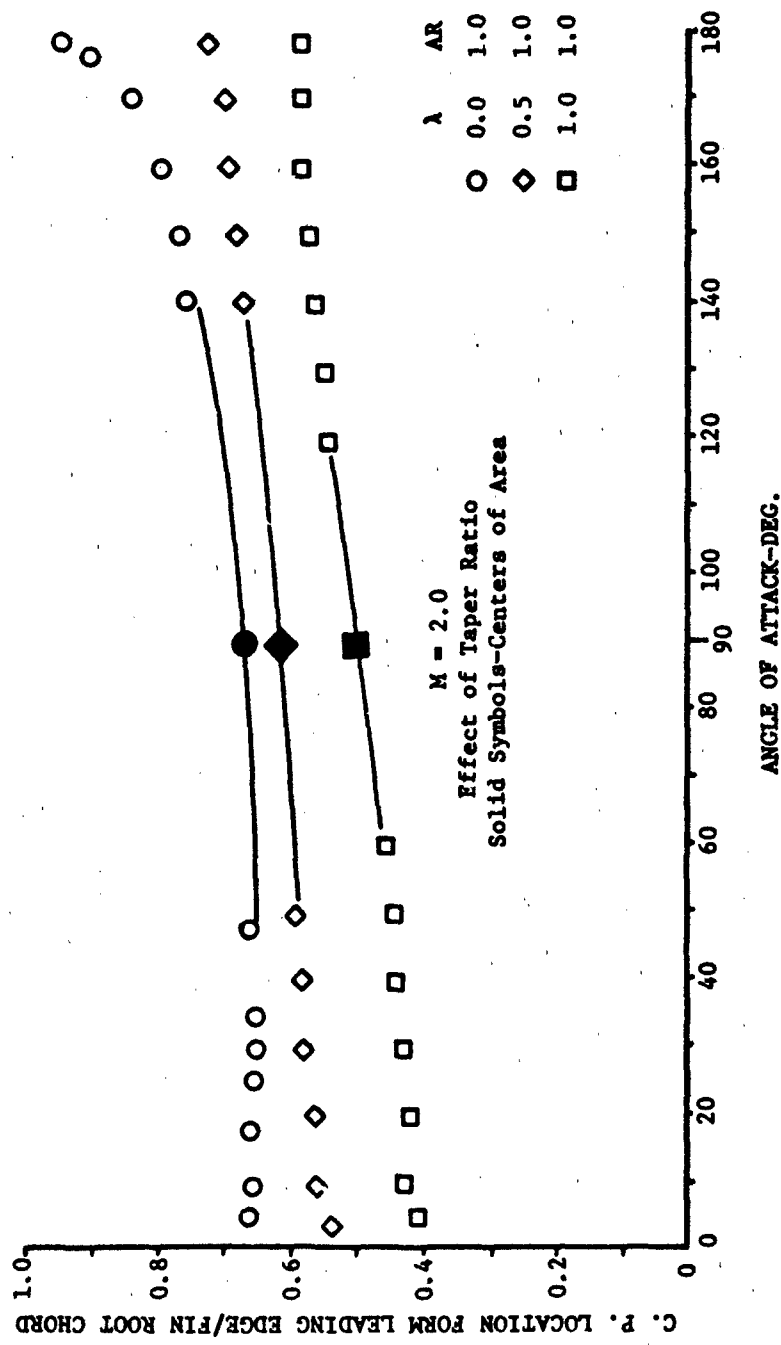


Figure 6d. Fin Chordwise Center of Pressure, M = 2.0

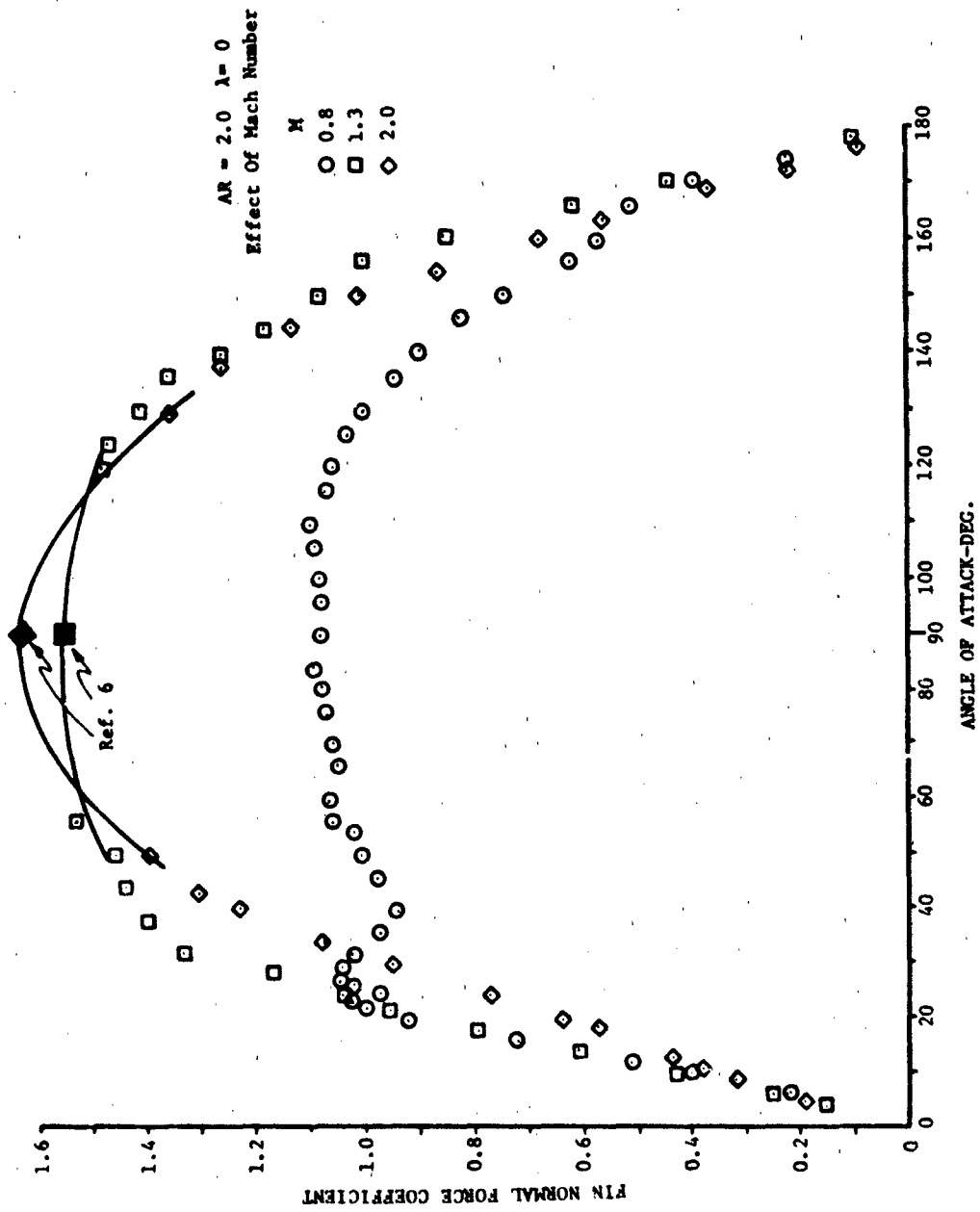


Figure 7a. Fin Normal Force Coefficient

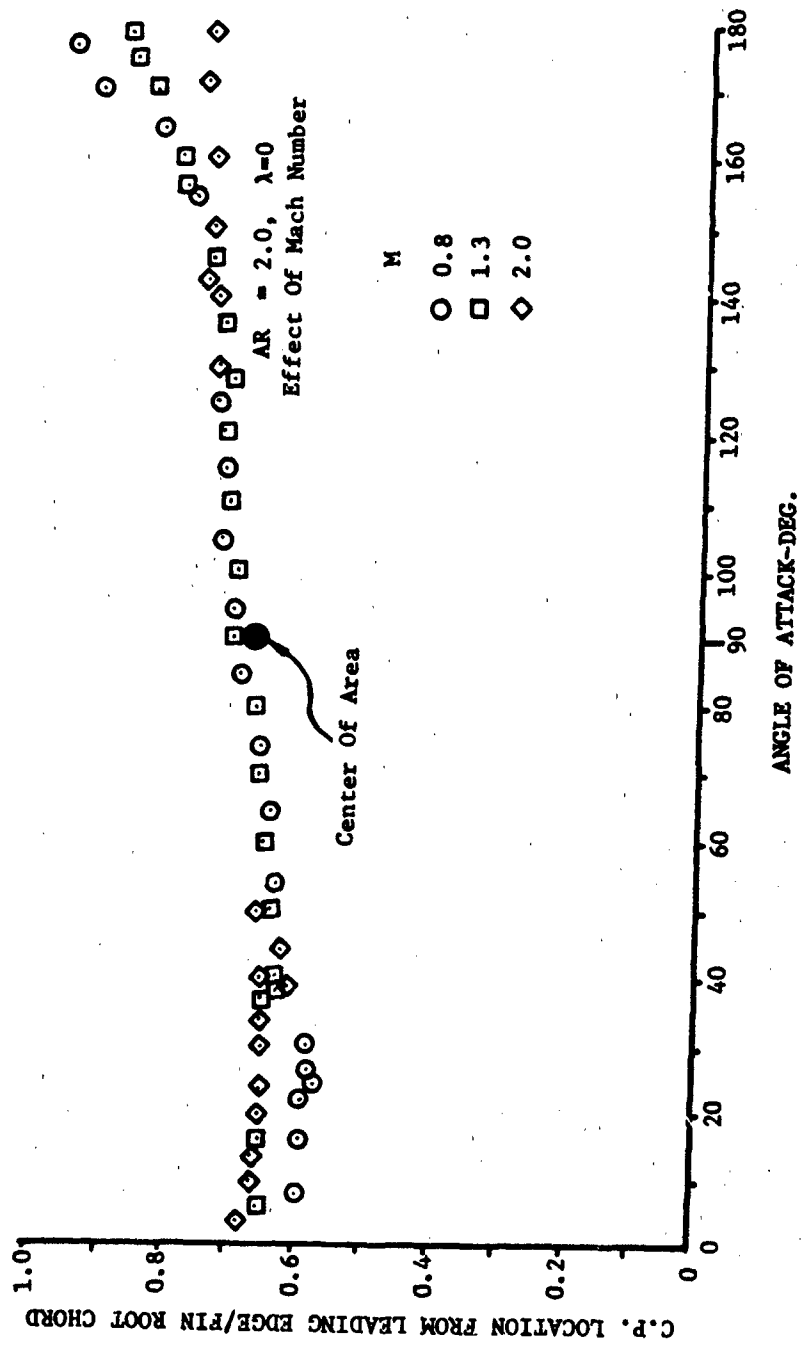


Figure 7b. Fin Chordwise Center Of Pressure

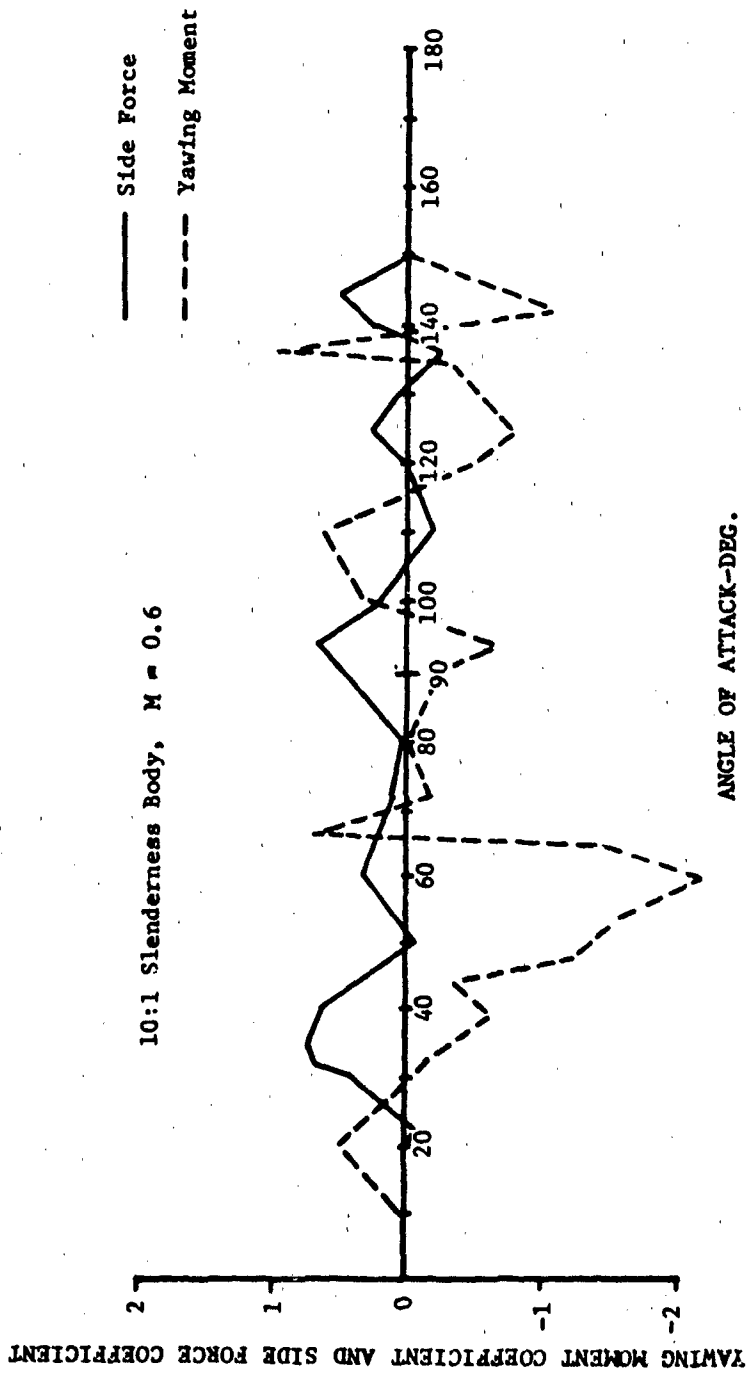


Figure 8a. Variation of Induced Out-of-Plane Force and Moment, $M = 0.6$

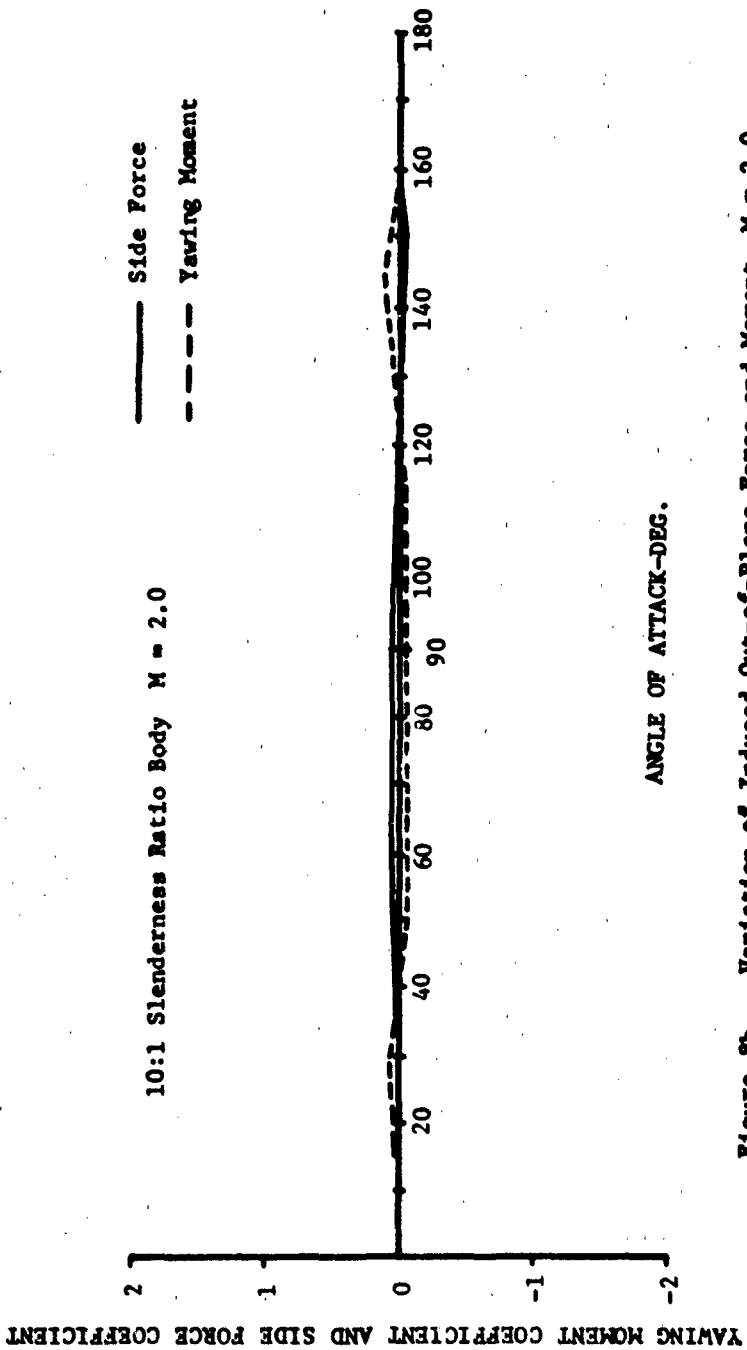


Figure 8b. Variation of Induced Out-of-Plane Force and Moment, $M = 2.0$

Plus Tail

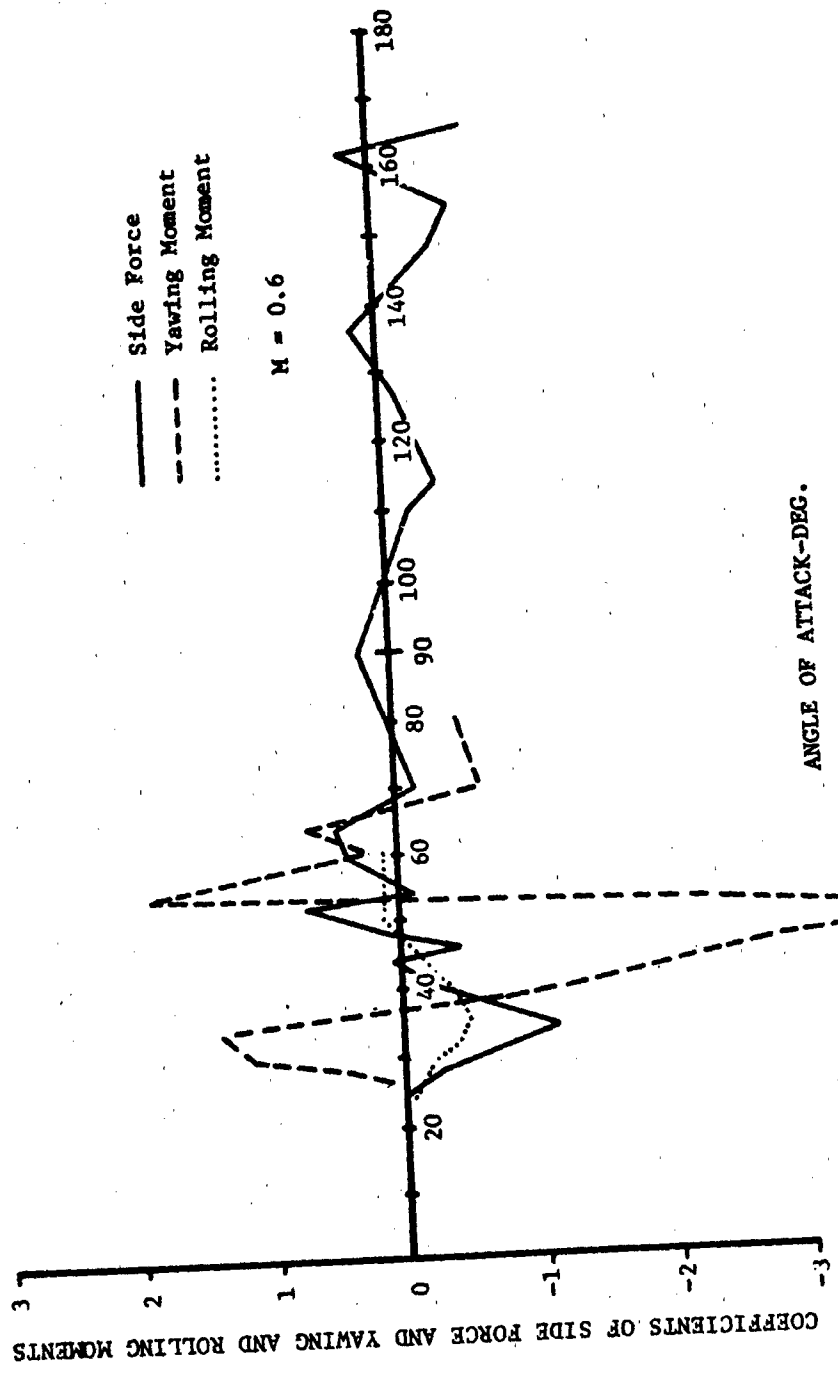


Figure 9a. Out-Of-Plane Forces And Moments Due To Vortex Asymmetry
Plus Tail, AR = 0.5, $\lambda = 1.0$, $d/s = 0.5$

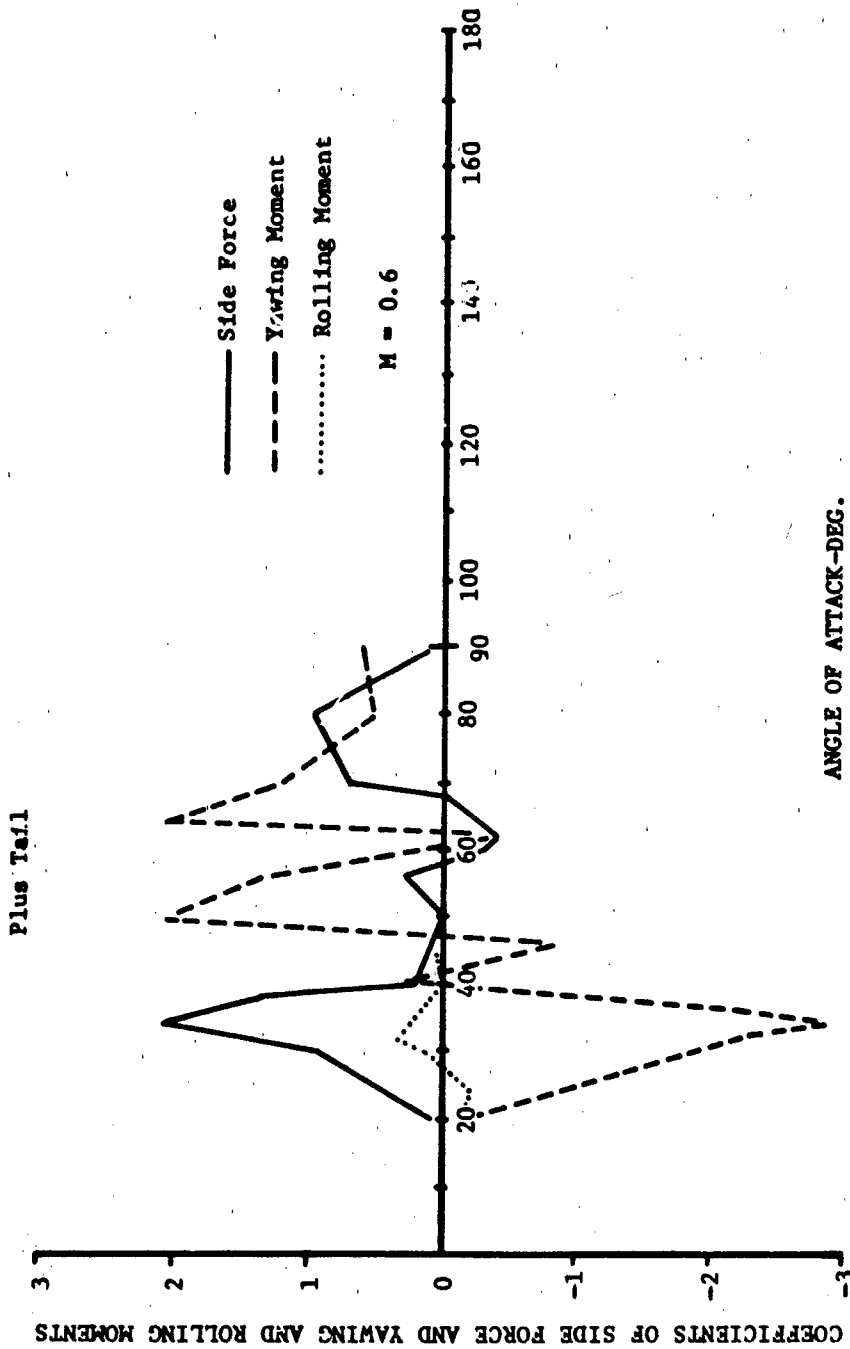


Figure 9b. Out-Of-Plane Forces And Moments Due To Vortex Asymmetry Plus Tail, AR = 0.5, $\lambda = 0.0$, $d/s = 0.4$

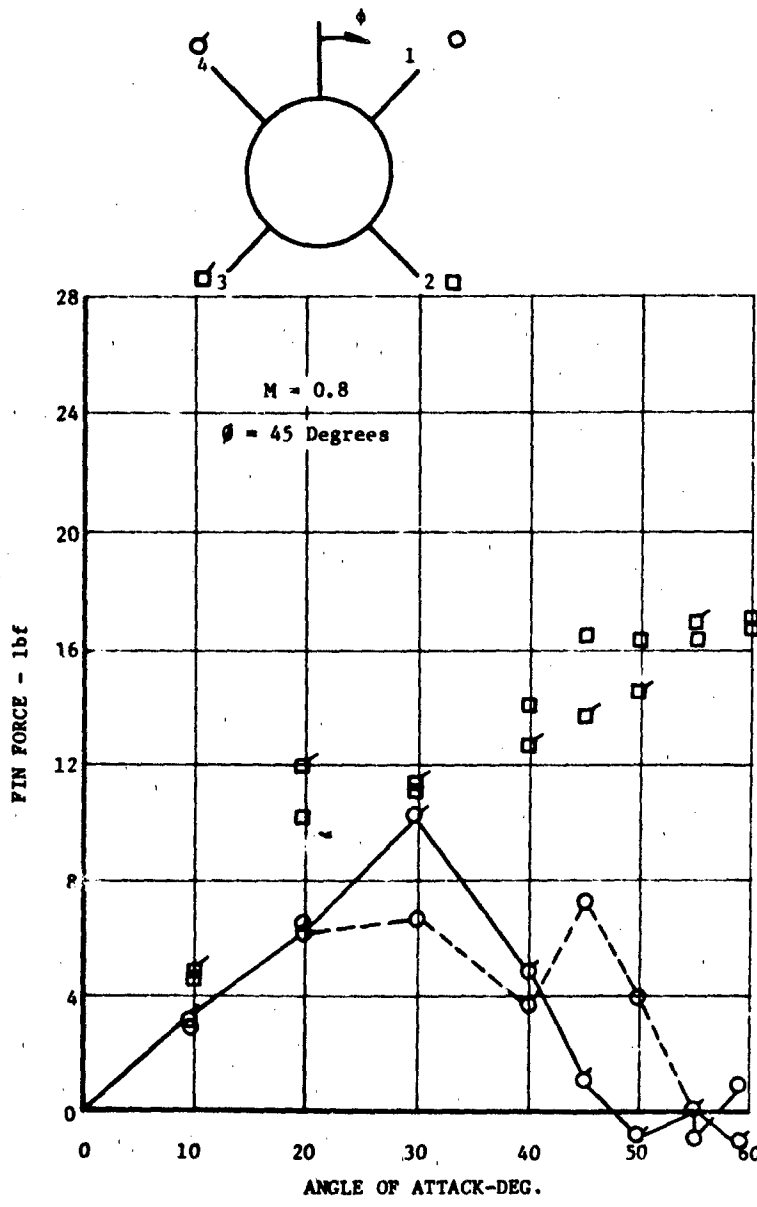


Figure 10a. Comparison Of Tail Normal Forces

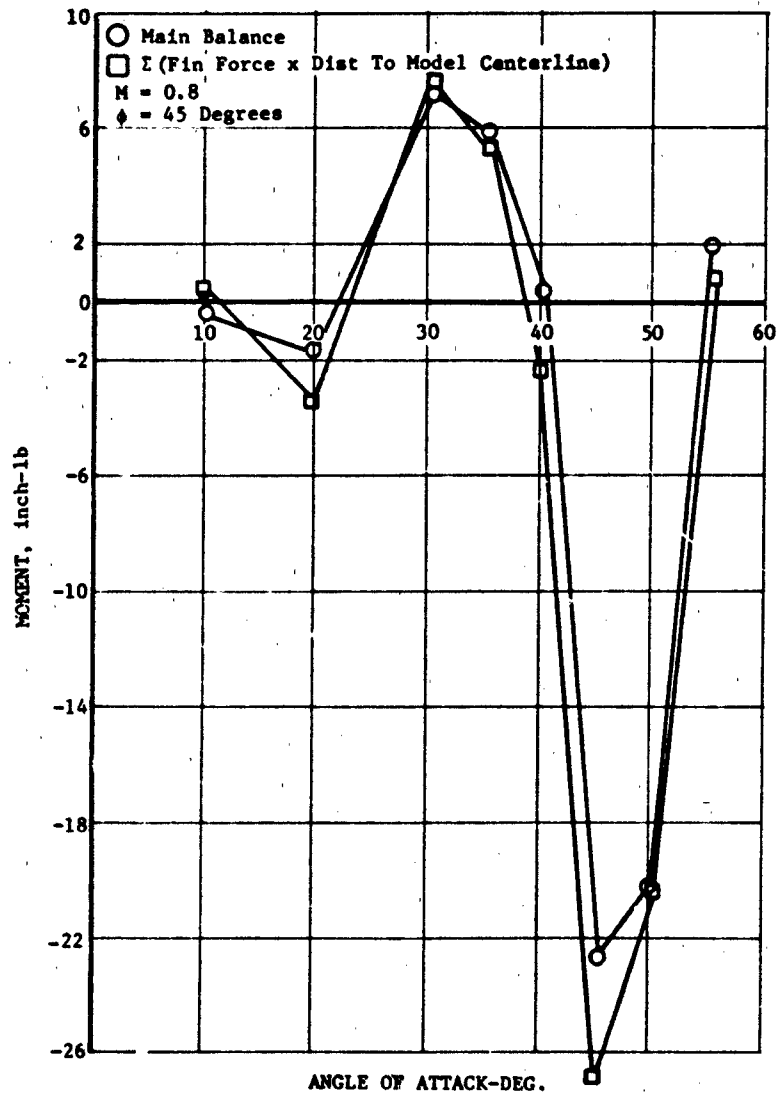


Figure 10b. Comparison Of Rolling Moments

4.0 FORMULATION OF THE AERODYNAMIC PREDICTION EQUATIONS

Because of the nature of the information available, the following formulations of body-tail, body-strake-tail and body-wing-tail configuration pitch-plane aerodynamic characteristics are necessary. These formulations will vary depending on whether the configurations are to be aerodynamically or thrust vector controlled (TVC).

Aerodynamically Controlled

Body-Tail

$$C_{N_{BT}} = C_{N_B} + 2 C_{N_T} R_{T(B)} \frac{S_T}{S_B} + I_{B(T)} \quad (1)$$

$$C_{m_{BT}} = C_{N_B} \frac{X_{CP_B}}{d} + 2 C_{N_T} R_{T(B)} \frac{S_T}{S_B} \frac{X_{CP_{T(B)}}}{d} + I_{B(T)} \frac{X_{CP_{I(T)}}}{d} \quad (2)$$

Body-Strake-Tail

$$C_{N_{BST}} = C_{N_B} + \Delta C_{N_{BS}} + \Delta C_{N_{BST}} \quad (3)$$

$$C_{m_{BST}} = C_{N_B} \frac{X_{CP_B}}{d} + \Delta C_{N_{BS}} \frac{X_{CP_{\Delta BS}}}{d} + \Delta C_{N_{BST}} \frac{X_{CP_{\Delta BST}}}{d} \quad (4)$$

Body-Wing-Tail

$$C_{N_{BWT}} = C_{N_B} + \Delta C_{N_{BW}} + 2 C_{N_T} R_{T(B)} \frac{S_T}{S_B} + I_{B(T)} + \Delta C_{N_{T WV}} \quad (5)$$

$$C_{m_{BWT}} = C_{N_B} \frac{X_{CP_B}}{d} + \Delta C_{N_{BW}} \frac{X_{CP_{\Delta BW}}}{d} + 2 C_{N_T} R_{T(B)} \frac{S_T}{S_B} \frac{X_{CP_{T(B)}}}{d} + I_{B(T)} \frac{X_{CP_{I(T)}}}{d} + \Delta C_{N_{T WV}} \frac{X_{CP_{\Delta TWV}}}{d} \quad (6)$$

Thrust Vector Controlled

Body-Tail

$$C_{N_{BT}} = C_{N_B} + \Delta C_{N_{BP}} + 2 C_{N_T} R_{T(B)} \frac{S_T}{S_B} + \Delta C_{N_{TP}} + I_{B(T)} \quad (7)$$

$$C_{M_{BT}} = C_{N_B} \frac{X_{CP_B}}{d} + \Delta C_{N_{BP}} \frac{X_{CP_{BP}}}{d} + 2 C_{N_T} R_{T(B)} \frac{S_T}{S_B} \frac{X_{CP_{T(B)}}}{d} + \Delta C_{N_{TP}} \frac{X_{CP_{TP}}}{d} + I_{B(T)} \frac{X_{CP_{I(T)}}}{d} \quad (8)$$

Body-Strake-Tail

$$C_{N_{BST}} = C_{N_B} + \Delta C_{N_{BP}} + \Delta C_{N_{BS}} + \Delta C_{N_{BST}} + \Delta C_{N_{TP}} \quad (9)$$

$$C_{M_{BST}} = C_{N_B} \frac{X_{CP_B}}{d} + \Delta C_{N_{BP}} \frac{X_{CP_{BP}}}{d} + \Delta C_{N_{BS}} \frac{X_{CP_{ABS}}}{d} + \Delta C_{N_{BST}} \frac{X_{CP_{ABST}}}{d} + \Delta C_{N_{TP}} \frac{X_{CP_{TP}}}{d} \quad (10)$$

Hence, the following quantities are required in order to conduct aerodynamic analyses on body-tail, body-wing-tail, or body-strake-tail configurations which are either aerodynamically or thrust vector controlled. The section of this report in which each quantity is developed is listed as follows.

<u>Quantity</u>	<u>Section</u>	<u>Page</u>
C_{N_B}	5.1.1	39
X_{CP_B}	5.1.2	61
C_{N_T}	5.1.4	91
X_{CP_T}	5.1.5	122
$R_{T(B)}$	5.2.1	143
$I_{B(T)}$	5.2.2	161
$X_{CP_{I(T)}}$	5.2.3	171
$\Delta C_{N_{BS}}$	5.3.1	190
$X_{CP_{\Delta BS}}$	5.3.2	202
$\Delta C_{N_{BST}}$	5.3.3	220
$X_{CP_{\Delta BST}}$	5.3.4	232
$\Delta C_{N_{BW}}$	5.4.1	259
$X_{CP_{\Delta BW}}$	5.4.2	274
$\Delta C_{N_{TWV}}$	5.4.3	289
$X_{CP_{TWV}}$	5.4.4	306

Use in either
Aerodynamically Controlled
or TVC modes

<u>Quantity</u>	<u>Section</u>	<u>Page</u>	
$\Delta C_{N_{BP}}$	5.5.1	310	} TVC Mode Only
$X_{CP_{BP}}$	5.5.2	323	
$\Delta C_{B_{YP}}$	5.5.3	334	
$X_{CP_{TP}}$	5.5.4	351	

As indicated above, certain of the quantities are applicable to the equations for aerodynamic control as well as the equations for TVC. Others are used only in the TVC model. Limits of applicability for each method are indicated in the appropriate sections.

5.0 AERODYNAMIC METHODS

5.1 Isolated Components

5.1.1 Body Normal Force

Summary

A method is presented for predicting body normal force coefficients, C_{N_B} , for angles of attack between 0 and 180 degrees and Mach numbers from 0.6 up to 3.0. Comparisons between predicted results and experimental data show good agreement. This method represents an improvement over existing methods in that it accurately predicts C_{N_B} both transonically and supersonically.

Background

The aerodynamic force directed normal to a body in its pitch plane can be separated into potential and viscous flow contributions. Using slender body theory, Munk found the potential flow contribution to be equal to $\sin 2\alpha$, where 2 is the slope of the normal force coefficient curve at $\alpha = 0$ degrees. In later work by Ward (Reference 9), it was shown that this force is actually directed midway between the normal to the stream and the normal to the body axis. Taking this into account, potential contributions to body normal force can be expressed as:

$$C_{N_{POT}} = \sin 2\alpha \cos \frac{\alpha}{2} \quad (11)$$

At very low angles of attack, this potential term dominates body normal force. However, for angles of attack greater than 6 degrees, viscous effects are introduced and rapidly become the dominating factor. Existing theories do not adequately predict viscous effects. Empirical procedures

have been developed based on the early work by Allen and Perkins¹⁰ and Kelly¹¹ which introduced the concept that the viscous crossflow around inclined bodies of revolution is analogous to the flow around a circular cylinder normal to the flow. In accordance with standard notation, these empirical procedures relate the viscous normal force contribution to C_{d_c} , the crossflow drag coefficient defined by analogy with two-dimensional flow. Thus

$$C_{N_c} = C_{d_c} \eta \frac{S_p}{S_{ref}} \sin^2 \alpha \quad (12)$$

Experimental data have shown C_{d_c} to be a function of both Reynolds and crossflow Mach numbers. Values of η have been determined empirically from two-dimensional and finite length cylinder data.

Combining the theoretical potential and empirical viscous contribution results in the following expression for body total normal force coefficient:

$$C_N = \sin 2\alpha \cos \frac{\alpha}{2} + C_{d_c} \eta \frac{S_p}{S_{ref}} \sin^2 \alpha \quad (13)$$

This is the same expression used by Jorgensen¹² to predict transonic and supersonic values of C_N for angles of attack between 0 and 180 degrees.

The procedure outlined by Jorgensen in Reference 12 was found to be inaccurate at transonic Mach numbers when predicted results were compared with the data of Reference 13. These comparisons are presented in Figures 11 through 14. Accuracy is only fair when all Mach numbers and angles of attack are considered, but does improve with increasing Mach number.

Two avenues are available to improve accuracy. First, develop a new method to improve transonic capabilities. The second, and perhaps most

desirable approach, would be to develop a single procedure which would be accurate both transonically and supersonically.

Method Development

A power series approach is used to develop a method which predicts the combination of potential and viscous effects on body total C_N . Boundary conditions were sought which would adequately define the characteristics of C_N between angles of attack of 0 and 180 degrees. Values of C_N and $\frac{\partial C_N}{\partial \alpha}$ at $\alpha = 0, \pi/2,$ and π were taken as boundary conditions. Experimental data indicated that values of C_N at $\alpha = 0$ and $\alpha = \pi$ are zero. Also from experimental data, it was observed that $\frac{\partial C_N}{\partial \alpha} = 0$ at $\alpha = \pi/2$ and π . The remaining boundary conditions, i.e., C_N at $\alpha = \pi/2$ and $\frac{\partial C_N}{\partial \alpha}$ at $\alpha = 0,$ were retained as free variables.

Applying these boundary conditions to the expression:

$$C_{N_B} = a_0 + a_1\alpha + a_2\alpha^2 + a_3\alpha^3 + a_4\alpha^4 + a_5\alpha^5$$

yielded

$$C_{N_B} = \left[\alpha - \frac{6\alpha^2}{\pi} + \frac{13\alpha^3}{\pi^2} - \frac{12\alpha^4}{\pi^3} + \frac{4\alpha^5}{\pi^4} \right] C_{N_\alpha} + \left[\frac{16\alpha^2}{\pi^2} - \frac{32\alpha^3}{\pi^3} + \frac{16\alpha^4}{\pi^4} \right] C_{N_{\pi/2}}$$

which can be rewritten as

$$C_{N_B} = A_1 C_{N_\alpha} + A_2 C_{N_{\pi/2}}; \quad S_{ref} = S_{base} \quad (14)$$

where

$$A_1 = \alpha - \frac{6\alpha^2}{\pi} + \frac{13\alpha^3}{\pi^2} - \frac{12\alpha^4}{\pi^3} + \frac{4\alpha^5}{\pi^4}$$

$$A_2 = \frac{16\alpha^2}{\pi^2} - \frac{32\alpha^3}{\pi^3} + \frac{16\alpha^4}{\pi^4}$$

Values of A_1 and A_2 are plotted as functions of angle of attack in Figures 15 and 16. Values of C_{N_α} and $C_{N_{\pi/2}}$ still require definition.

Transonic values of C_{N_α} presented in Figure 17 as a function of Mach number, nose length and afterbody length were taken from References 14 and 15. Supersonic values of C_{N_α} presented in Figure 18 were taken from Reference 16 as a function of Mach number, nose length and afterbody length. The data of Figures 17 and 18 represent improvements over existing correlations. Linear interpolation is required for values of C_{N_α} between Mach 1.2 and 1.5.

Values of $C_{N_{\pi/2}}$ can be calculated with Equation 13 recognizing that the "potential" term goes to zero and utilizing the published data for values of η (Reference 17) and C_{d_c} (Reference 12). The available values of η (shown as η_0 in Figure 19) are derived from subsonic test data and are typically assumed to apply up to crossflow Mach number (M_c) equal 1.0. Above Mach one η is normally assumed to be 1.0. Rather than continue to use such a discontinuous representation, a procedure is employed here which produces an estimate of the variation of η with M_c through the transonic regime. The transonic variation of η is developed as follows:

The potential component of normal force is still defined as in Equation 11 with the change that C_{N_α} replaces the 2. The intent is to make use of the test data (Reference 13) as a source for C_{N_α} rather than rely on the theoretical value of 2. Then the viscous contribution to the normal force is defined as $C_{N_{VIS}}$ as follows:

$$C_{N_{VIS}} = C_N - \sin(C_{N_\alpha} \alpha) \cos(\alpha/2)$$

C_N and C_{N_α} are both obtained from the test data. Then

$$\eta C_{D_C} = \frac{C_{N_{VIS}}}{\frac{S_p}{S_{ref}} \sin^2 \alpha}$$

The quantity ηC_{D_C} was calculated utilizing this expression at crossflow Mach numbers ranging from 0.2 to 2.0. Values of C_{D_C} were taken from Reference 10 at the corresponding Mach numbers to permit solving for η . The curve faired through the values of η which result from this exercise is shown in Figure 20. The subsonic value is seen to apply up to about $M_c = 0.8$ with the upward trend continuing to about $M_c = 1.4$. A polynomial expression was then derived as follows to represent the variation of η with M_c .

$$\frac{\partial \eta}{\partial M_c} = 0.0 \text{ at } M_c = 0.8 \text{ and } 1.4$$

$$\eta = \eta_0 \text{ at } M_c = 0.8$$

$$\eta = 1.0 \text{ at } M_c = 1.4$$

Applying these boundary conditions to the following expansion:

$$\eta = a_0 + a_1 M_c + a_2 M_c^2 + a_3 M_c^3$$

yielded

$$\eta = \eta_0 (-9.0741 + 31.1111 M_c - 30.5556 M_c^2 + 9.2593 M_c^3) + (10.0741 - 31.1111 M_c + 30.5556 M_c^2 - 9.2593 M_c^3)$$

which can be rewritten as:

$$\eta = B_0 \eta_0 + B_1 \tag{16}$$

where

$$B_0 = -9.0741 + 31.1111 M_c - 30.5556 M_c^2 + 9.2593 M_c^3$$

$$B_1 = 10.0741 - 31.1111 M_c + 30.5556 M_c^2 - 9.2593 M_c^3$$

Equation 16 is applicable to crossflow Mach numbers between 0.8 and 1.4. Values of η_0 are contained in Figure 19. Values of B_0 and B_1 are presented in Figure 21.

Values of C_{d_c} from Reference 13 modified on the basis of the results of Reference 3 are presented in Figure 22. These data cover a wide range of crossflow Mach numbers and come from a number of different sources.

Using the above information and Equation 12, it is now possible to calculate the value of $C_{N_{\pi/2}}$ required for the calculation of C_N between $\alpha = 0$ and 180 degrees.

Method Evaluation

Check cases were made using the same configuration and conditions represented in Figures 11 through 14. Figures 23 through 26 show comparisons between these predictions, experimental data, and predictions using Jorgensen's procedure (Reference 12). These comparisons indicate improved accuracy at high angles of attack in the transonic Mach regime and equally good accuracy at all angles of attack in the supersonic regime.

Use of Method

The method for predicting isolated body normal force is applied in the following way.

- 1 Depending upon the Mach number, use either Figure 17 or 18 to determine C_{N_α} as a function of nose and afterbody length.
- 2 Calculate the value of $C_{N_{\pi/2}}$ using Equation 12.
 - a Use Figure 22 to determine C_{d_c} .
 - b Depending upon the Mach number, determine the value of η .
 - . For $M_c \leq 0.8$, use Figure 19 to determine η as a function of l/d .
 - . For $0.8 < M_c < 1.4$, use Equation 16 and Figure 19.
 - . For $M_c > 1.4$, $\eta = 1.0$.
- 3 Using Equation 14, the results of steps 1 and 2, and Figures 15 and 16, calculate the values of C_{N_B} from 0 to 180 degrees.

Numerical Example

Calculate C_{N_B} between 0 and 180 degrees at $M = 2.86$ for a body with the following characteristics:

$$\frac{l_N}{d} = 3.0 \text{ (tangent ogive)}$$

$$\frac{l_A}{d} = 6.0$$

$$\frac{S_P}{S_{ref}} = 10.2$$

- 1 Using Figure 18b, $C_{N_\alpha} = 3.05/\text{rad}$
- 2 Use the following equation to calculate $C_{N_{\pi/2}}$

$$C_{N_{\pi/2}} = C_{d_c} \eta \frac{S_P}{S_{ref}}$$

a From Figure 22, $C_{dc} = 1.34$

b For $M = 2.86$, $\eta = 1.0$

c Therefore $C_{N_{\pi/2}} = 13.67$

3 Using the following equation and Figures 15 and 16, calculate

$$C_{NB} = A_1 C_{Na} + A_2 C_{N_{\pi/2}}; S_{ref} = S_{base}$$

α°	A_1	A_2	C_N
0	1.0	0.0	0.0
5	0.074	0.01	0.36
10	0.123	0.045	0.989
15	0.153	0.095	1.76
20	0.167	0.155	2.63
30	0.162	0.305	4.66
40	0.13	0.475	6.89
50	0.09	0.645	9.09
60	0.051	0.79	10.95
70	0.023	0.905	12.44
80	0.005	0.975	13.34
85	0.001	0.99	13.54
90	0.0	1.0	13.67
95	0.001	0.99	13.54
100	0.004	0.975	13.34
110	0.015	0.905	12.44
120	0.026	0.79	10.88
130	0.034	0.645	8.92
140	0.037	0.475	6.61
150	0.033	0.305	4.27
160	0.022	0.155	2.19
165	0.014	0.095	1.34
170	0.007	0.045	0.636
175	0.002	0.01	0.143
180	0.0	0.0	0.0

Data Comparisons

The results of the numerical example are compared with experimental data (Reference 18) in Figure 27. Because these data were not involved in the development of the method, this comparison represents an independent check of the method. Agreement is quite good throughout the angle

of attack range transonically. Figure 28 represents further independent checks of predicted results against experimental data from Reference 19. Comparisons between predicted results and experimental data have shown the method of this section to be more accurate than the Jorgensen method in the majority of cases. However, the Jorgensen method has proven more accurate in the 0 to 40 degree angle of attack range transonically. Therefore, it is recommended that the Jorgensen method be used in this region and the method of this section in all others.

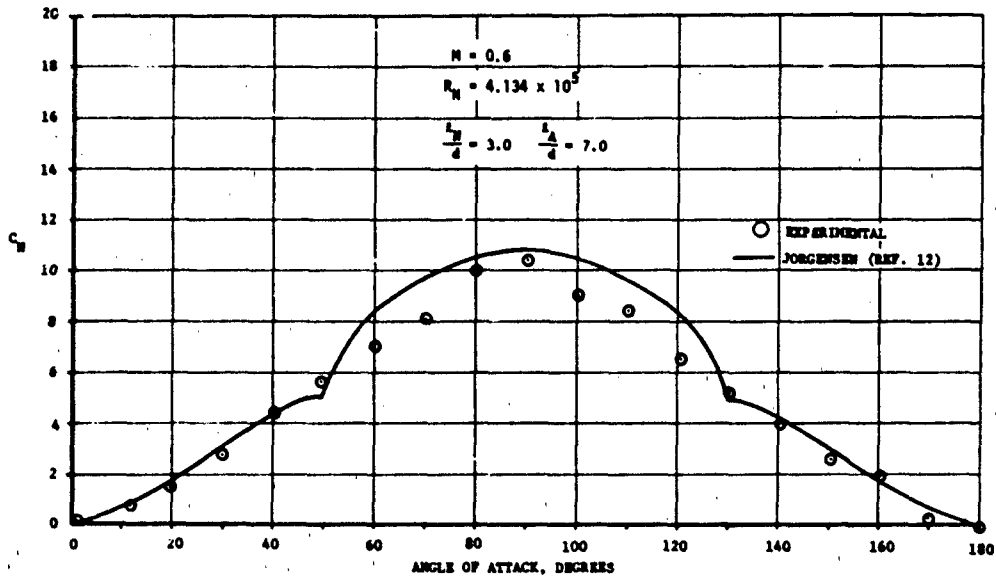


Figure 11. Comparison of Experimental and Predicted Results (C_{N_B}), Mach = 0.6

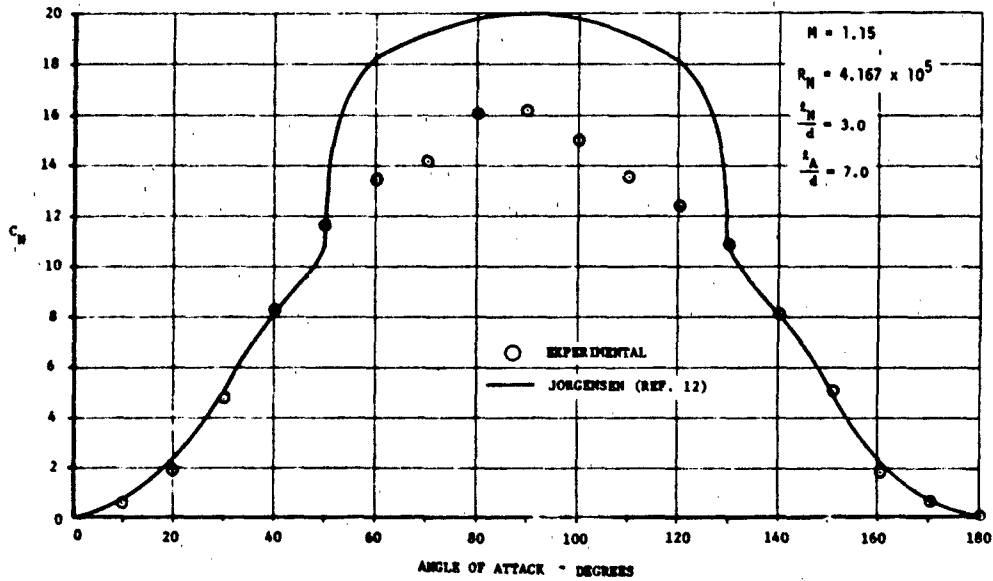


Figure 12. Comparison of Experimental and Predicted Results (C_{N_B}), Mach = 1.15

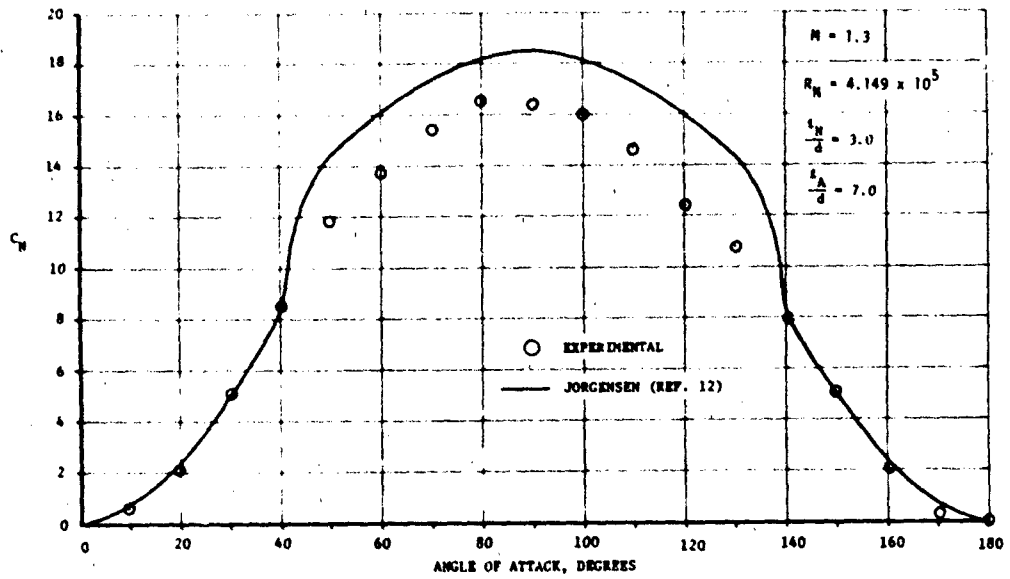


Figure 13. Comparison of Experimental and Predicted Results (C_{N_B}), Mach = 1.30

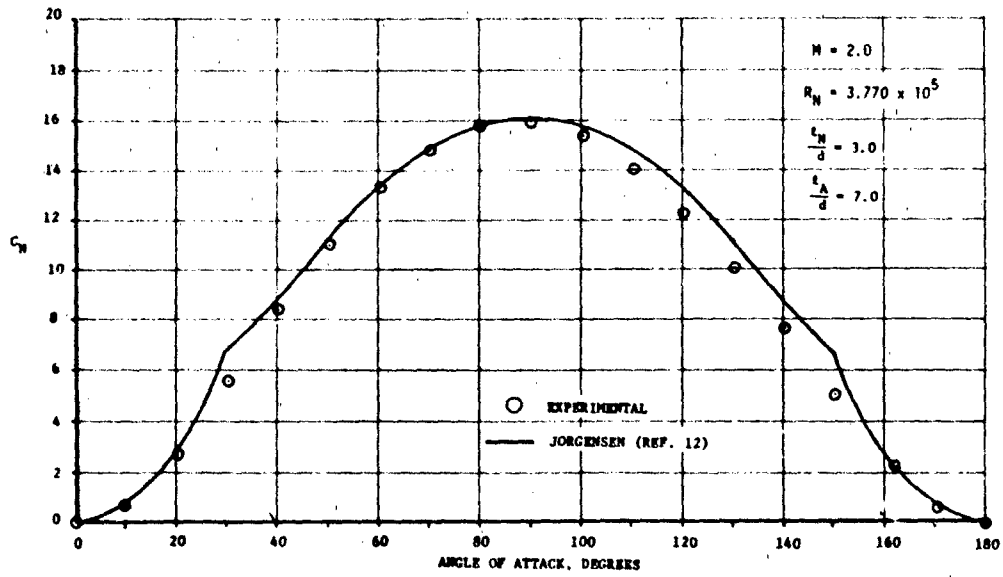


Figure 14. Comparison of Experimental and Predicted Results (C_{N_B}), Mach = 2.0

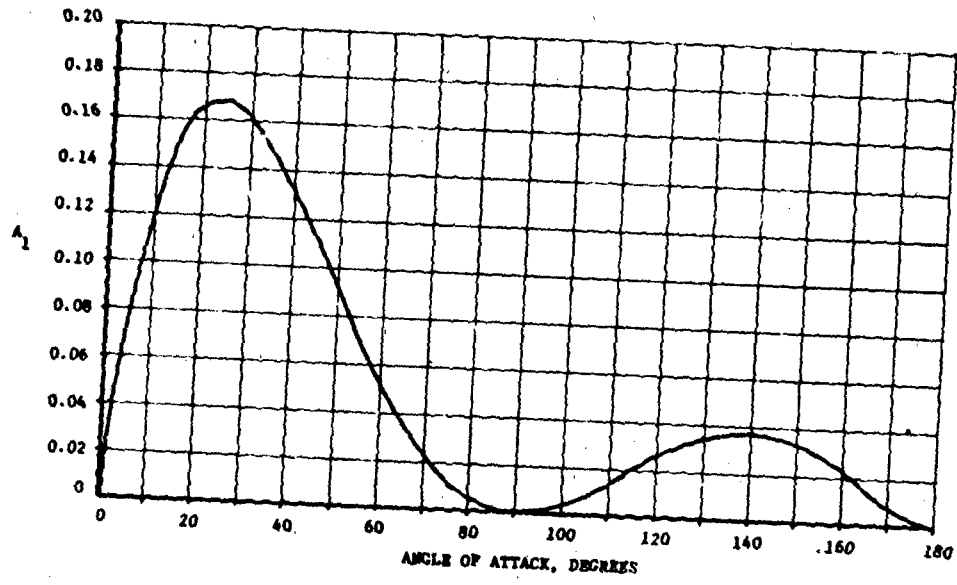


Figure 15. Coefficients for Calculation of C_{N_B}

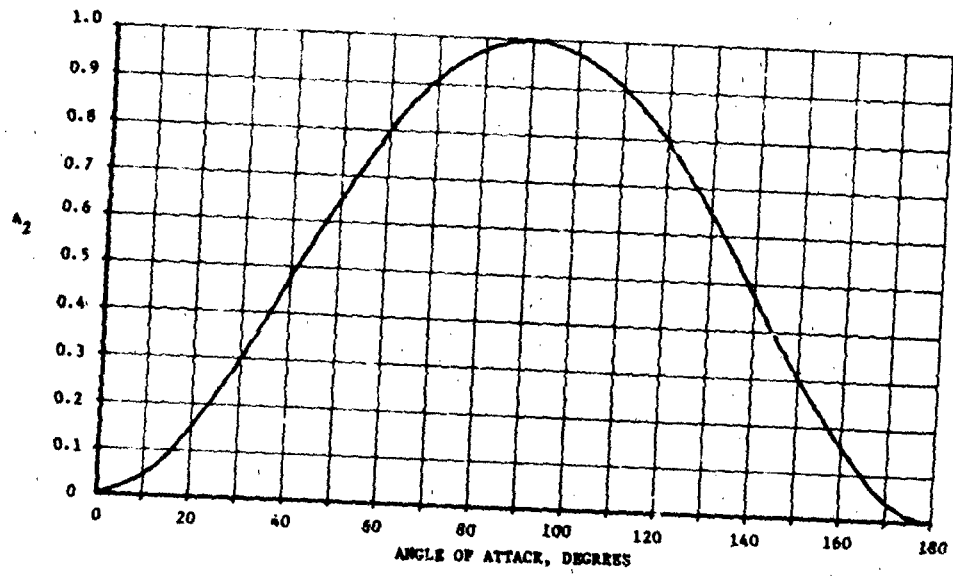


Figure 16. Coefficients for Calculation of C_{N_B}

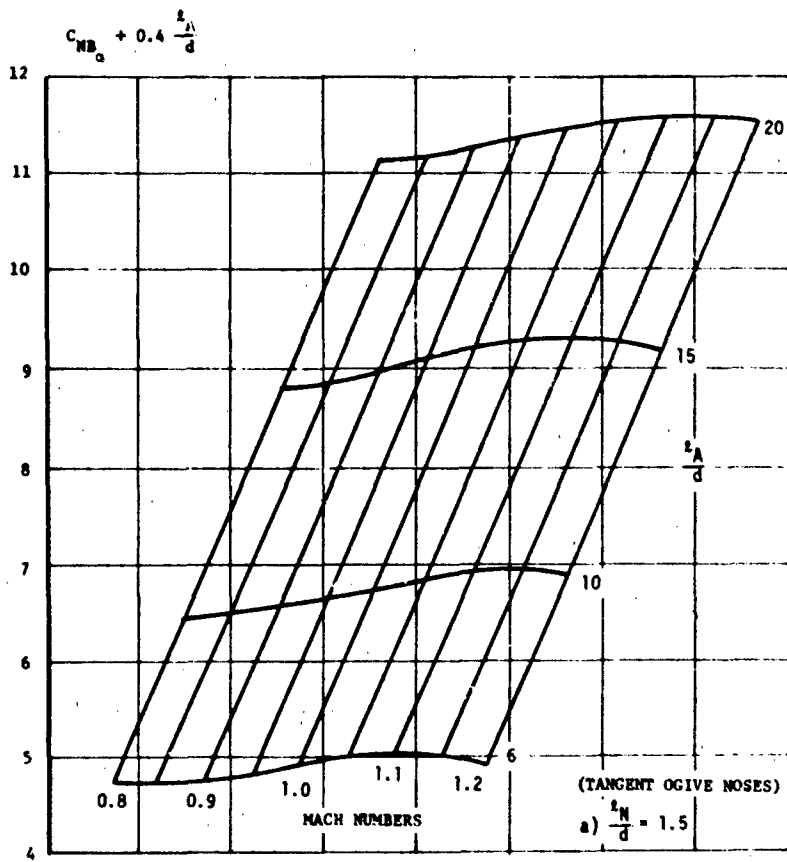


Figure 17a. Curves for Transonic C_{NB_a} ($\frac{l_N}{d} = 1.5$)

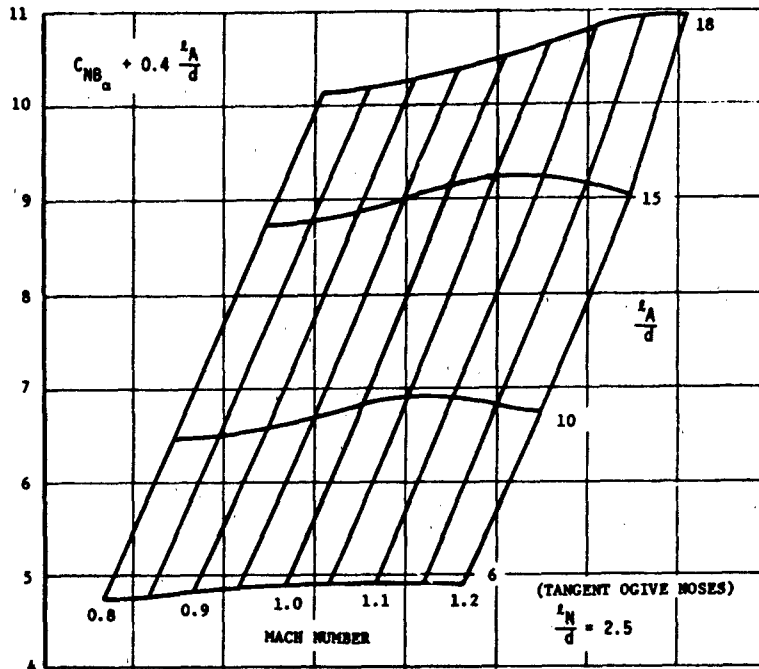


Figure 17b. Curves for Transonic $C_{N\alpha}$ ($l_N/d = 2.5$)

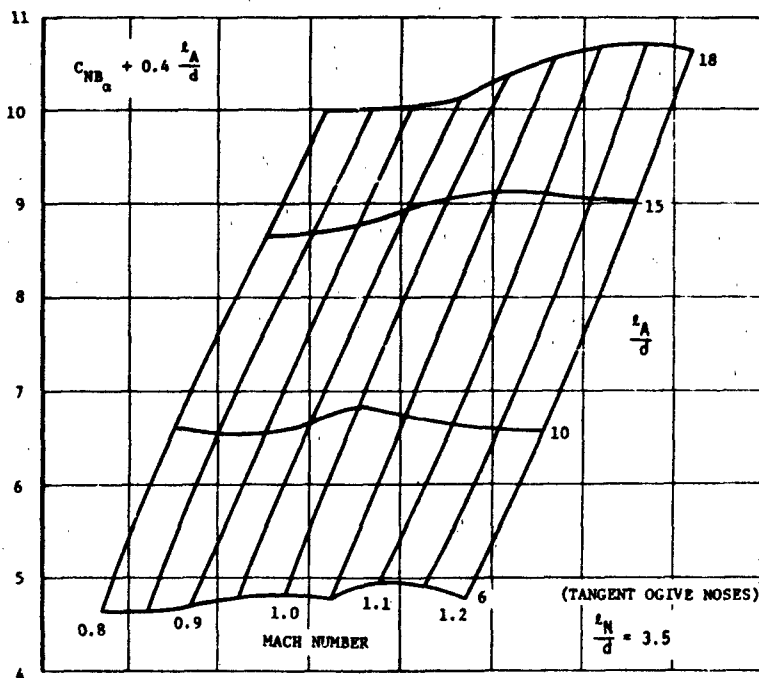


Figure 17c. Curves for Transonic $C_{N\alpha}$ ($l_N/d = 3.5$)

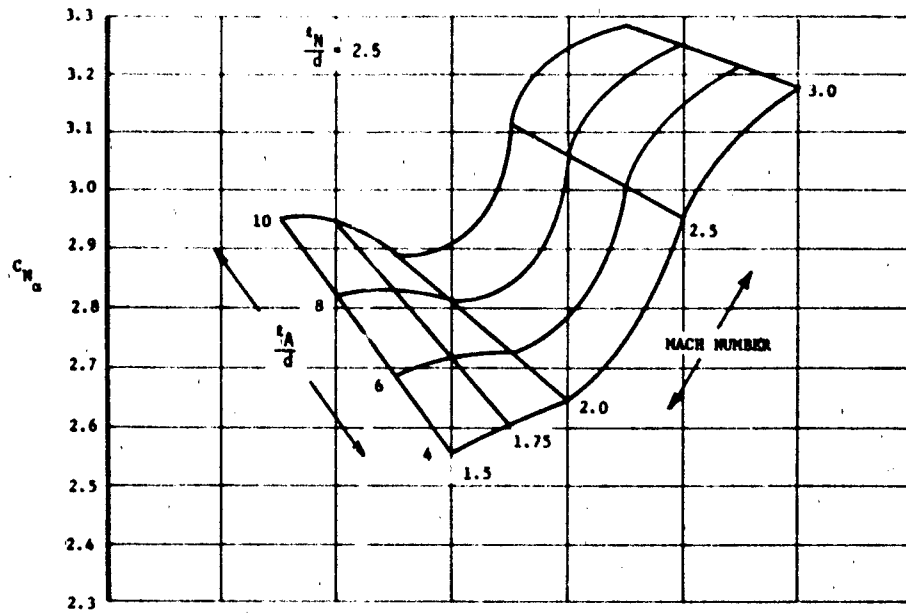


Figure 18a. Curves for Supersonic C_{N_α} ($l_N/d = 2.5$)

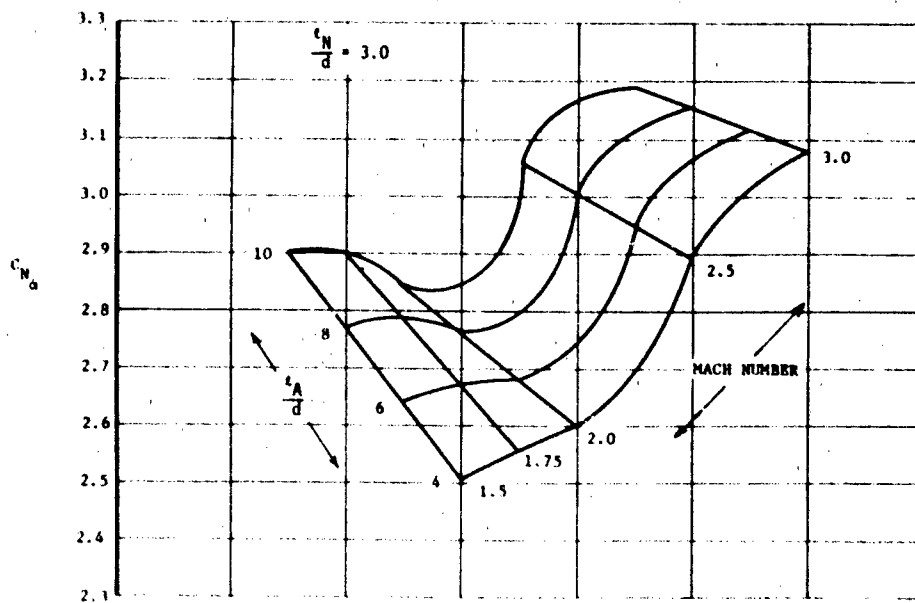


Figure 18b. Curves for Supersonic C_{N_α} ($l_N/d = 3.0$)

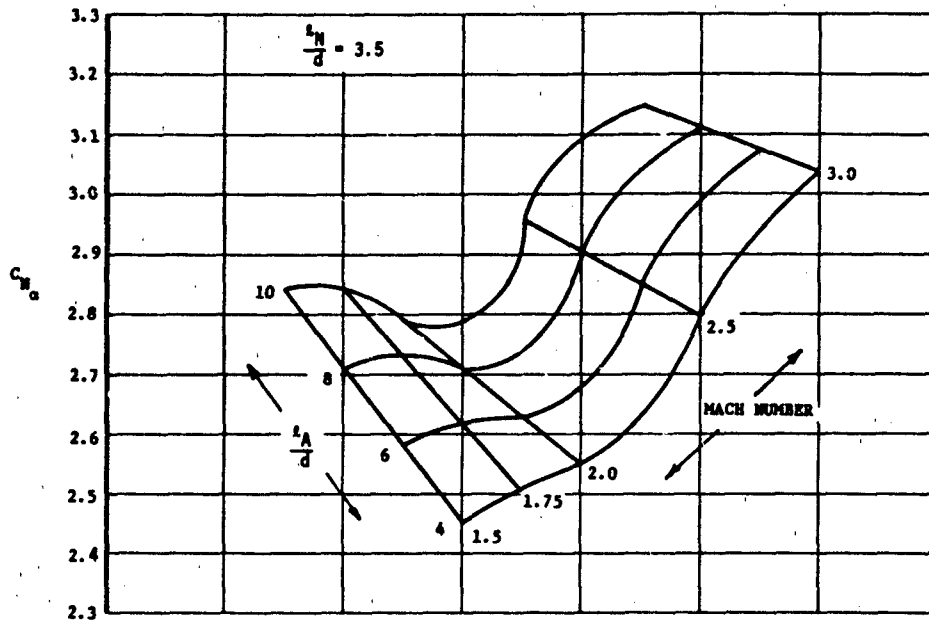


Figure 18c. Curves for Supersonic C_{N_α} ($l_N/d = 3.5$)

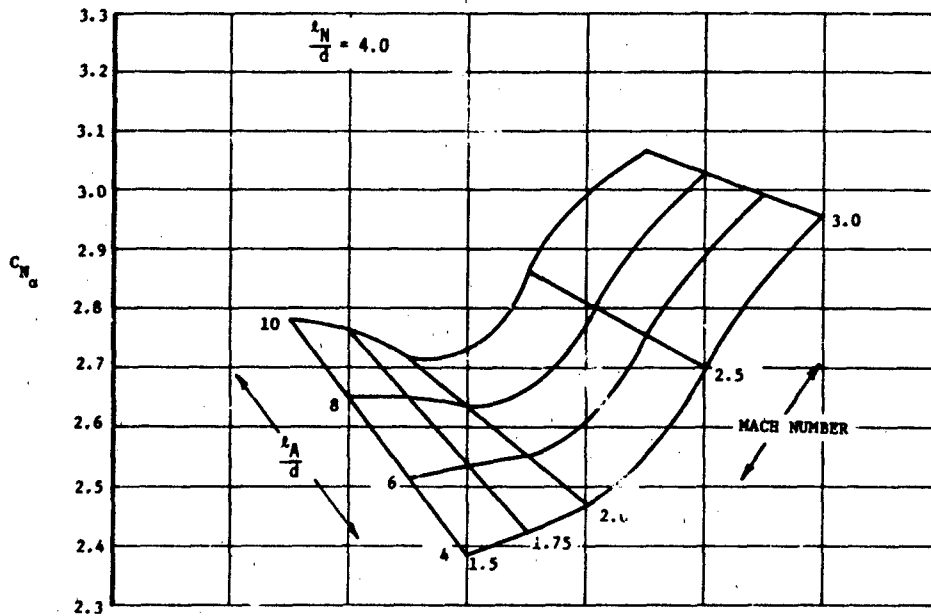


Figure 18d. Curves for Supersonic C_{N_α} ($l_N/d = 4.0$)

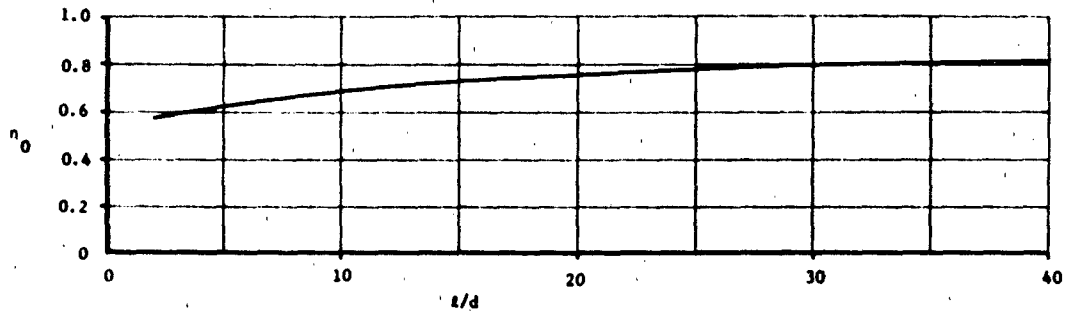


Figure 19. Correlation Factor for End Effects

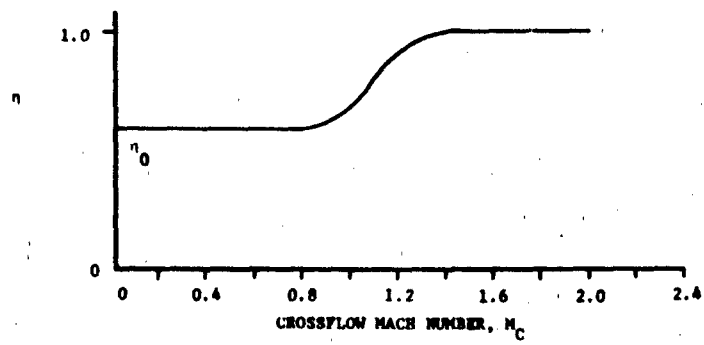


Figure 20. Variation of η With Mach Number

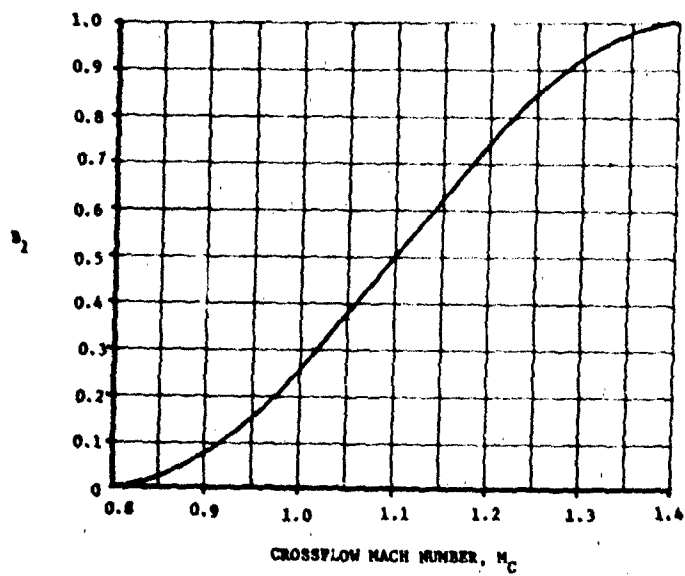
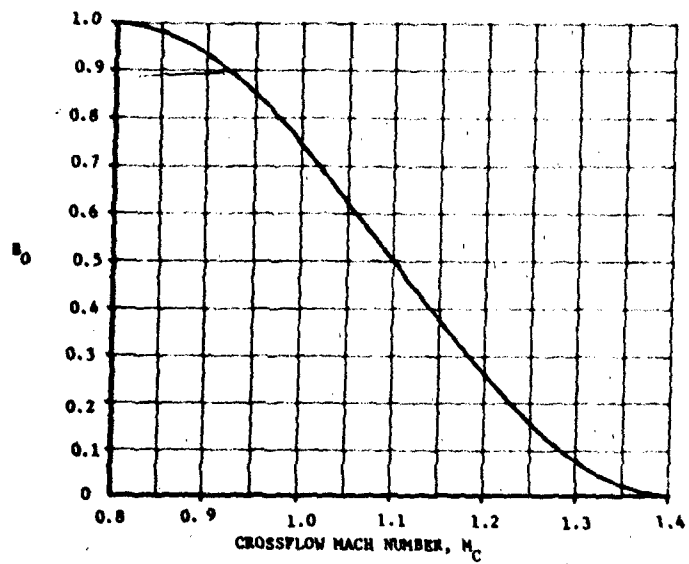


Figure 21. Curves for Determining Transonic Values of η

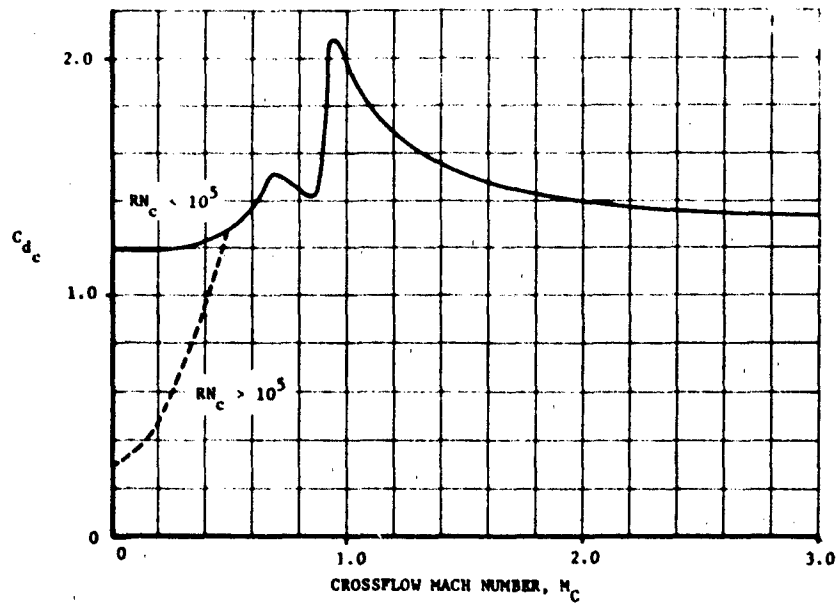


Figure 22a. Basic Values of C_{dc}

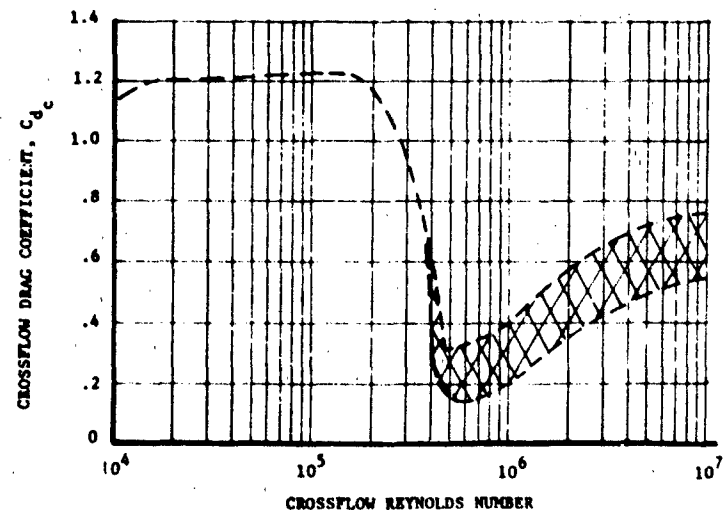


Figure 22b. Crossflow Drag Coefficient (Subcritical Crossflow, $M_c < 0.4$)

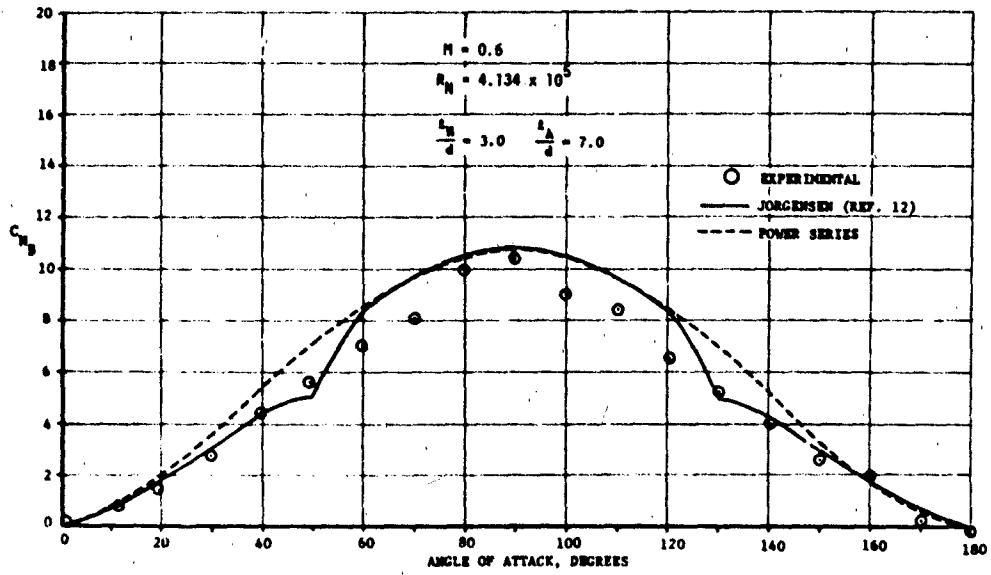


Figure 23. Comparison of Experimental and Predicted Results (C_{N_B}), Mach = 0.6

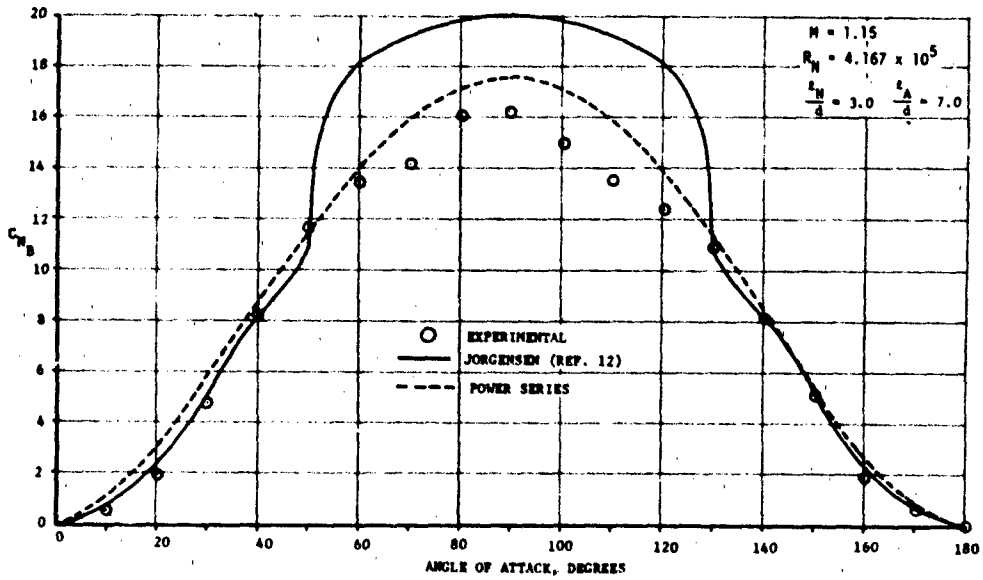


Figure 24. Comparison of Experimental and Predicted Results (C_{N_B}), Mach = 1.15

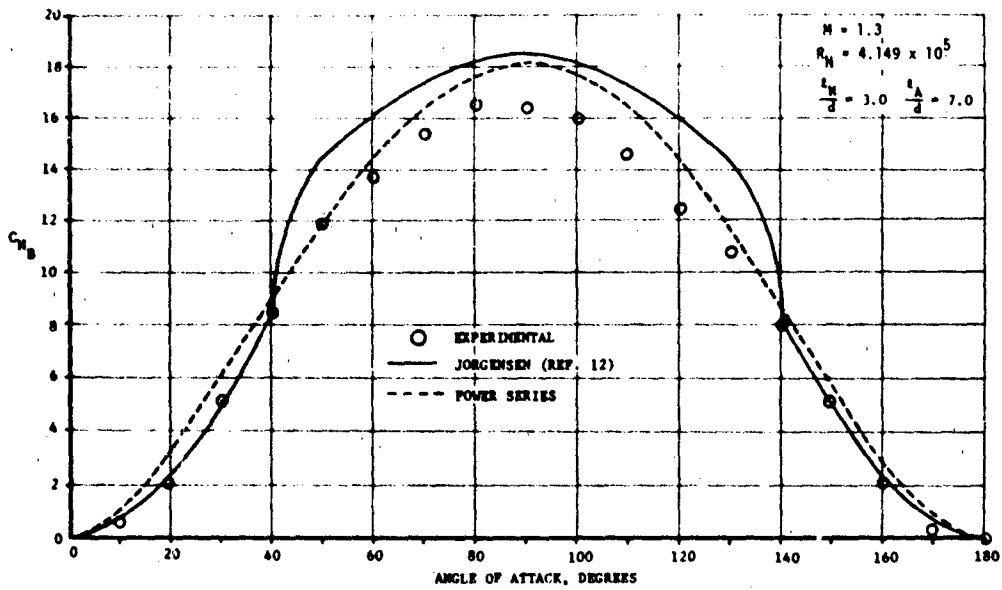


Figure 25. Comparison of Experimental and Predicted Results (C_{NB}), Mach = 1.30

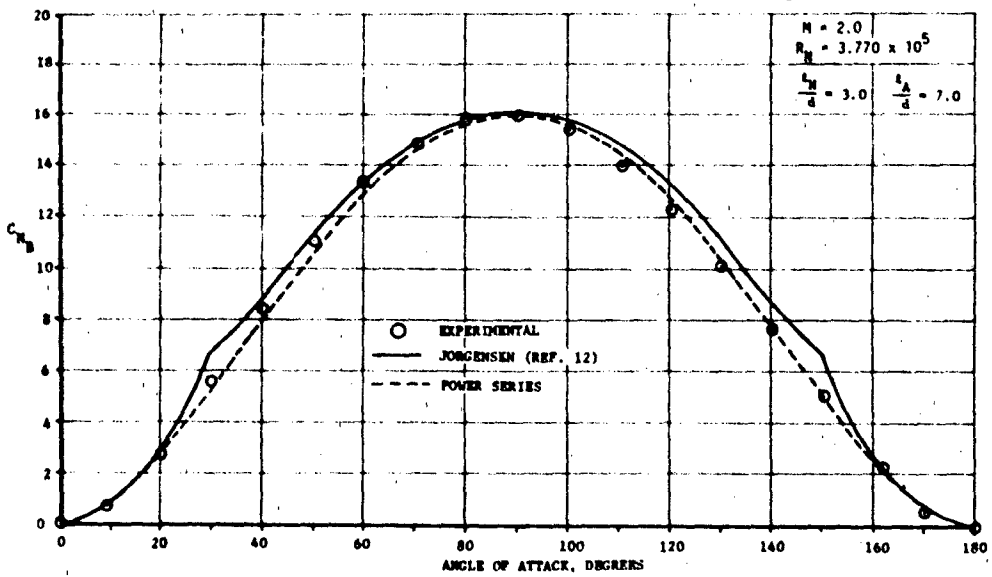


Figure 26. Comparison of Experimental and Predicted Results (C_{NB}), Mach = 2.0

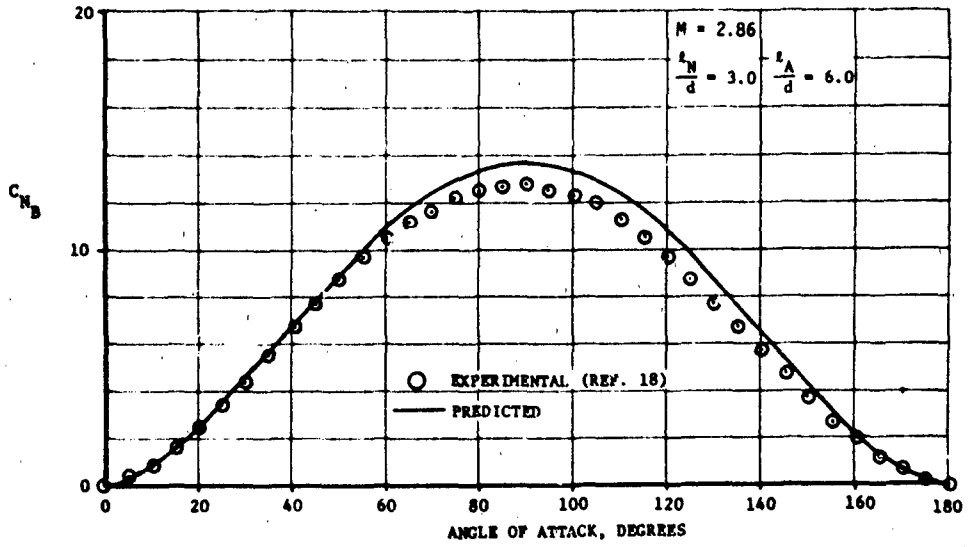


Figure 27. Comparison of Experimental and Predicted Results (C_{NB}), Mach = 2.86

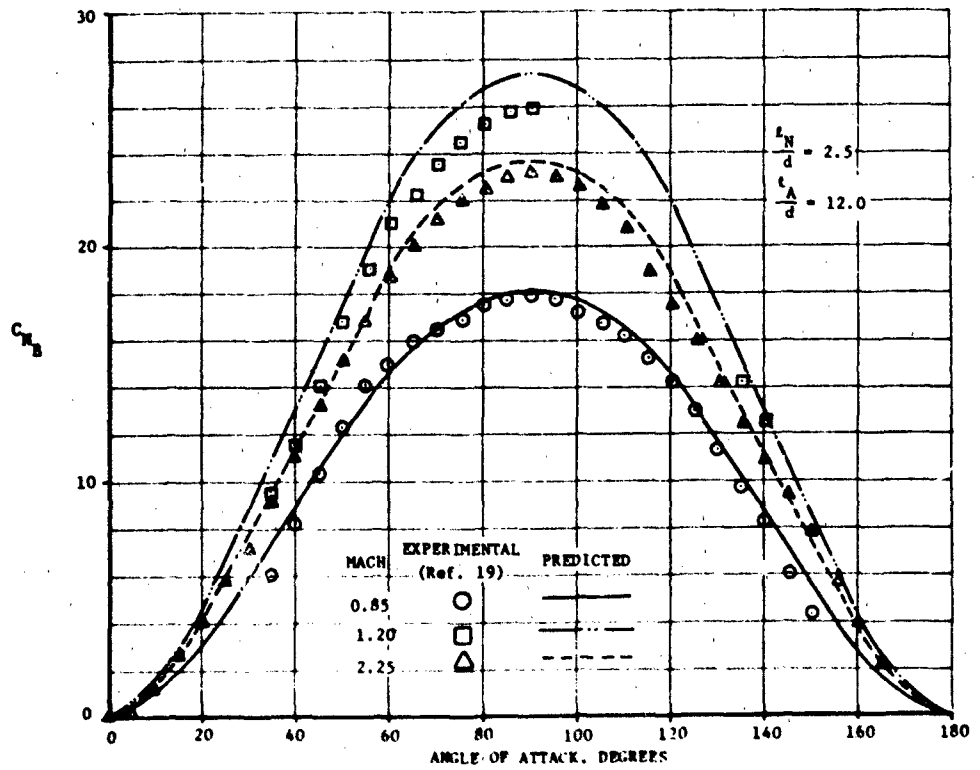


Figure 28. Comparison of Experimental and Predicted Results (C_{NB}), Mach = 0.85, 1.20, and 2.25

5.1.2 Body Center of Pressure

Summary

A method is presented for predicting isolated body center of pressure, X_{CP_B} , for angles of attack between 0 and 180 degrees and Mach numbers from 0.6 up to 3.0. Comparisons between predicted results and experimental data show good agreement.

Background

New highly maneuverable missiles will encounter extreme angles of attack. In some cases angles of attack may approach 180 degrees in either the transonic or supersonic Mach regimes.

Effective evaluation of proposed configurations will require methods for predicting aerodynamic characteristics at extreme angles of attack over a wide range of Mach numbers. Current predictive techniques are limited to angles of attack less than 30 degrees. New methods are required to fill the void between existing and required capabilities. This section deals specifically with a method for predicting body center of pressure, X_{CP_B} . The method presented is applicable to Mach numbers between 0.6 and 3.0 and angles of attack between 0 and 180 degrees.

Method Development

The method for predicting X_{CP} was developed using an empirical approach. The initial step involved a survey of available data (References 13, 18, and 19). The data displayed characteristics which were unique to specific Mach number and angle of attack ranges. For Mach numbers of 1.0 or greater, X_{CP} displayed a rapid rearward movement between angles of attack of 0 and 20 degrees, followed by a nearly linear progression of X_{CP} between 20 and 160 degrees and passes through the centroid of the planform area at 90 degree. Finally, between 160 and 180 degrees, another

rapid rearward movement of X_{CP} was observed. Experimental data showed that the X_{CP} left the body between 170 and 180 degrees. As the body approaches 180 degrees, a couple is produced as the positive potential normal force on the forward facing portion of the body becomes equal to the negative potential force on the trailing nose portion of the body. This couple subjects the body to a moment and to a zero net normal force. Under these circumstances, calculated values of X_{CP} tend to become infinitely large.

For Mach numbers less than 1.0, X_{CP} displayed the same characteristics between 0 and 20 degrees and 160 and 180 degrees. However, the location of X_{CP} tended to remain essentially constant between 20 and 50 degrees, followed by a rearward movement which is linear between 50 and 160 degrees and passes through the centroid of the planform area at 90 degrees.

A power series approach was used to develop the method between 0 and 20 degrees. In the usual way boundary conditions were sought. The center of pressure at $\alpha = 0$ degrees was taken as the first boundary condition. Curves presenting $\left. \frac{X_{CP}}{d} \right|_0$ as a function of $\frac{l_N}{d}$, $\frac{l_A}{d}$, and k in the transonic Mach regime are presented in Reference 3. For the sake of completeness these are presented again here in Figure 29. Similar data in the supersonic Mach regime ($1.5 \leq M \leq 4.5$) were found in Reference 16 and are presented in Figure 30. For a second boundary condition it can be shown that for symmetrical bodies $\left. \frac{\partial X_{CP}/d}{\partial \alpha} \right|_0 = 0.0$. A third boundary condition was defined by the center of pressure at 20 degrees. This was defined as the center of pressure at zero degrees plus an increment. Using data from References 3, 13, and 20, the

percentage of body length by which X_{CP} shifted between 0 and 20 degrees was determined as a function of Mach number (see Figure 31). As a final boundary condition, $\frac{\partial X_{CP}/d}{\partial \alpha}$ at 20 degrees was assumed to equal the slope of the linear variation between 20 and 90 degrees angle of attack. Experimental data indicated that the center of pressure at 90 degrees could be approximated as the centroid of the planform area. At 90 degrees, when the flow is separated along the entire length of the body, the normal force will be due entirely to crossflow drag (Reference 3). Assuming a constant C_{dc} along the body, the centers of pressure and of planform area should then coincide.

Collecting boundary conditions and applying them to the following polynomial expansion

$$\frac{X_{CP}}{d} = x = a_0 + a_1 \alpha + a_2 \alpha^2 + a_3 \alpha^3$$

yielded

$$x = \left[1 + \frac{7\alpha^3}{28000} - \frac{21\alpha^2}{2800} \right] x_0 + \left[\frac{23\alpha^2}{2800} - \frac{8\alpha^3}{28000} \right] x_{20} + \left[\frac{\alpha^3}{28000} - \frac{2\alpha^2}{2800} \right] x_{\pi/2}$$

which can be rewritten as

$$x = A_0 x_0 + A_1 x_{20} + A_2 x_{\pi/2} \quad (17)$$

Where

$$A_0 = 1 + \frac{7\alpha^3}{28,000} - \frac{21\alpha^2}{2800}$$

$$A_1 = \frac{23\alpha^2}{2800} - \frac{8\alpha^3}{28000}$$

$$A_2 = \frac{\alpha^3}{28000} - \frac{2\alpha^2}{2800} \quad , \alpha \text{ in radians}$$

Values of A_0 , A_1 and A_2 are plotted as a function of angle of attack in Figure 32.

Equation 17 was developed based on the characteristics of X_{CP} at Mach numbers of 1.0 or greater. Applying Equation 17 for Mach numbers less than 1.0 will produce good results even though $\frac{\partial X_{CP}}{\partial \alpha}$ at $\alpha=20$ degrees will be in error.

As indicated earlier, the variation in X_{CP} between 20 and 160 degrees is dependent upon Mach number. For Mach numbers less than 1.0, the location of X_{CP} remains constant between 20 and 50 degrees and then moves linearly toward the rear to the value of X_{CP} at 160 degrees, passing through the centroid of the planform area at 90 degrees. For Mach numbers of 1.0 or greater, X_{CP} varies linearly between the locations at 20 and 160 degrees, passing through the centroid of the planform area at 90 degrees. Using this information, the following equations were derived for determining the slope of the linear variation and the value of χ at 160 degrees.

$$\frac{\partial X}{\partial \alpha} = \frac{X_{\alpha'} - X_{\pi/2}}{\alpha' - 90} \quad (18)$$

$$X_{160} = 70 \frac{\partial X}{\partial \alpha} + X_{\pi/2} \quad (19)$$

where α' , the angle marking the bound of the low angle region, is 20 degrees for Mach numbers of 1.0 or greater and 50 degrees for Mach numbers less than 1.0.

A power series approach was used to develop the method between 160 and 180 degrees and in the usual way boundary conditions were sought. The center of pressure at 160 degrees was taken as the first boundary condition.

This can be calculated using Equation 19. A second boundary, $\frac{\partial x}{\partial \alpha}$ (written χ_α) at 160 degrees was assumed to equal the slope of the linear variation between α' and 160 degrees. This value can be calculated using Equation 18. Also, as a third boundary condition it can be shown that at 180 degrees $\frac{\partial x_{CP}}{\partial \alpha} = 0$. As a final boundary condition, the center of pressure at 180 degrees was assumed equal to the body length, rather than trying to define it as some point off the body as indicated earlier. This assumption will introduce no significant errors since the resulting forces and moments are small.

Collecting these boundary conditions and applying them to the following polynomial expansion

$$\frac{x_{CP}}{d} = x = a_0 + a_1 \alpha + a_2 \alpha^2 + a_3 \alpha^3$$

yielding

$$x = \left[\frac{-51840000 + 900000 \alpha - 5200 \alpha^2 + 10 \alpha^3}{4000} \right] \chi_{\alpha 160} + \left[\frac{4864000 - 86400 \alpha + 510 \alpha^2 - \alpha^3}{4000} \right] l/d + \left[\frac{-4860000 + 86400 \alpha - 510 \alpha^2 + \alpha^3}{4000} \right] \chi_{160}$$

which can be rewritten as

$$x = B_0 \chi_{\alpha 160} + B_1 l/d + B_2 \chi_{160} \quad (20)$$

where

$$B_0 = \frac{-51840000 + 900000 \alpha - 5200 \alpha^2 + 10 \alpha^3}{4000}$$

$$B_1 = \frac{4864000 - 86400 \alpha + 510 \alpha^2 - \alpha^3}{4000}$$

$$B_2 = \frac{-4860000 + 86400 \alpha - 510 \alpha^2 + \alpha^3}{4000}$$

Values of B_0 , B_1 , and B_2 are shown as a function of angle of attack in Figure 33.

Use of Method

The method for predicting isolated body center of pressure is applied as follows:

- 1 Depending upon the Mach regime, use either Figures 29 or 30 to determine χ_0 as a function of l_N/d and l_A/d . Linearly interpolate for values of χ_0 between Mach 1.2 and 1.5.
- 2 Using Figure 31 determine the rearward shift in center of pressure between 0 and 20 degrees for the appropriate l/d and M. Add this value to the result of Step 1 to determine χ_{20} .
- 3 Calculate the distance from the nose to the centroid of the planform area using

$$\bar{X} = \frac{\bar{X}_N S_{PN} + \bar{X}_A S_{PA}}{S_{PN} + S_{PA}}$$

and where S_{PN} and S_{PA} are the planform areas of the nose and cylindrical sections respectively in the case of a tangent-ogive cylinder body

$$S_{PN} = l_N \sqrt{-l_N^2 + R^2} + R^2 \sin^{-1} \frac{l_N}{R} - 2(R-r) l_N$$

$$\bar{X}_N S_{PN} = 2 \left[\frac{-R^3}{3} + \frac{(R^2 - l_N^2) \sqrt{R^2 - l_N^2}}{3} + \frac{l_N^2 \sqrt{R^2 - l_N^2}}{2} + \frac{l_N R^2}{2} \sin^{-1} \frac{l_N}{R} \right] - (R-r) l_N^2$$

$$R = \frac{d}{4} + \frac{l_N^2}{d}$$

$$S_{PA} = l_A * d$$

and

$$\bar{X}_A S_{PA} = \left(l_N + \frac{l_A}{2} \right) (l_A * d)$$

Note that $\chi_{\pi/2} = \frac{\bar{X}}{d}$

- 4 Using Equation (17), the results of steps 1, 2, and 3, and Figure 32, calculate the centers of pressure between 0 and 20 degrees.
- 5 Calculate the slope of χ at 160 degrees using Equation (18).
- 6 Calculate the value of χ at 160 degrees using Equation (19)
- 7 Using Equation (20), the results of Steps 5 and 6, and Figure 53, calculate the centers of pressure between 160 and 180 degrees.
- 8 Depending upon the Mach number range of interest, determine the variation of χ between 20 and 160 degrees.
 - a. For $M \geq 1.0$, extend a straight line from χ_{20} to χ_{160} .
 - b. For $M < 1.0$, maintain a constant value of χ from 20 to 50 degrees and then extend a straight line between the values of χ at 50 degrees and 160 degrees.

Numerical Example

Calculate χ between 0 and 180 degrees at $M = 2.86$ for a body with the following characteristics:

$$l_N/d = 3.0 \text{ tangent - ogive}$$

$$l_A/d = 6.0$$

$$l/d = 9.0$$

$$d = 1.5 \text{ inches}$$

- 1 Interpolating between the values of Figure 30b and 30c, χ_0 was calculated to be 1.93 calibers aft of the nose.
- 2 Using Figure 31, $\Delta\chi/l/d = 0.285$ at $M = 2.86$. Therefore, for $l/d = 9$, $\Delta\chi = 2.565$.

$$\chi_{20} = \chi_0 + \Delta\chi$$

$$\chi_{20} = 4.495$$

3 For the configuration of interest

$$x_{\pi/2} = 4.96$$

4 Use the following equation and Figure 32 to calculate the centers of pressure between 0 and 20 degrees.

$$x = A_0 x_0 + A_1 x_{20} + A_2 x_{\pi/2}$$

α	A_0	A_1	A_2	x
0	1.0	0	0.0	1.93
5	0.85	0.17	-0.0125	2.343
10	0.5	0.53	-0.036	3.169
15	0.15	0.88	-0.04	4.047
20	0.0	1.0	0.0	4.495

5 Using the following equation, calculate the slope of the linear variation between 90 and 160 degrees.

$$x_{\alpha_{160}} = \frac{x_{\alpha'} - x_{\pi/2}}{\alpha' - 90}$$

$$x_{\alpha_{160}} = 0.0066 \text{ } ^\circ/\text{deg}$$

6 Using the following equation, calculate the value of x at 160 degrees.

$$x_{160} = 70 \left[\frac{x_{\alpha'} - x_{\pi/2}}{\alpha' - 90} \right] + x_{\pi/2}$$

$$x_{160} = 5.425$$

7 Using the following equation and Figure 33, calculate the centers of pressure between 160 and 180 degrees.

$$x = B_0 x_{\alpha_{160}} + B_1 x/d + B_2 x_{160}$$

α	B_0	B_1	B_2	χ
160	0.0	0	1.0	5.425
165	2.81	0.154	0.846	5.994
170	2.5	0.5	0.5	7.229
175	0.91	0.846	0.154	8.455
180	0.0	1.0	0.0	9.0

8 Graphically determine values of χ between 20 and 160 degrees by connecting χ_{20} and χ_{160} with a straight line.

Data Comparisons

The results of the numerical example are compared against experimental data from Reference 18 in Figure 34. Because the data were not involved in the development of the methods, this comparison represents an independent check of the methods. Agreement is good throughout the angle of attack range. Figures 35, 36, 37 and 38 present further comparisons with other experimental data (References 13 and 19). Again agreement is quite good in all cases, except for the higher angles of attack in Figure 36.

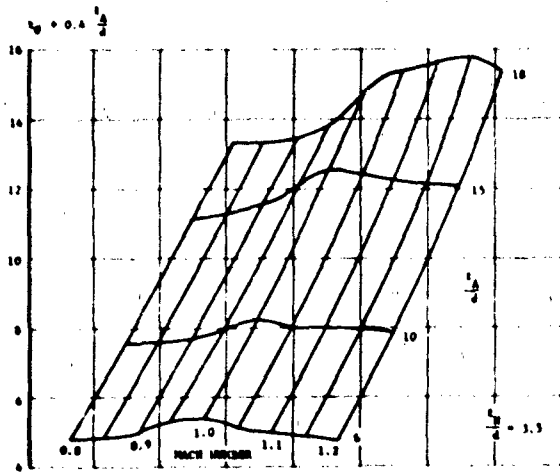


Figure 29a. Transonic Tangent Ogive-Cylinder Zero Angle of Attack Centers of Pressure ($l_N/d = 3.5$)

Figure 29b. Transonic Tangent Ogive-Cylinder Zero Angle of Attack Centers of Pressure ($l_N/d = 2.5$)

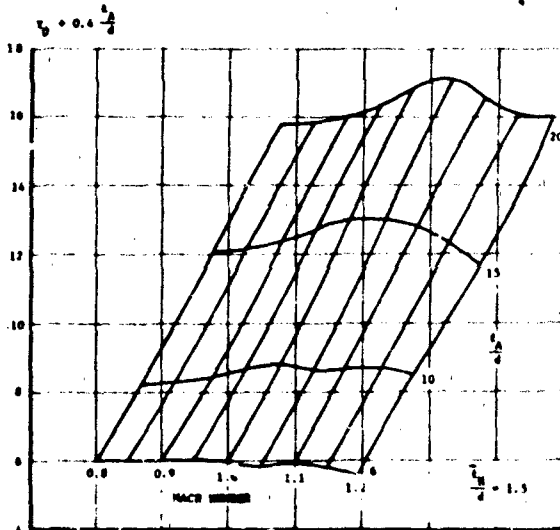
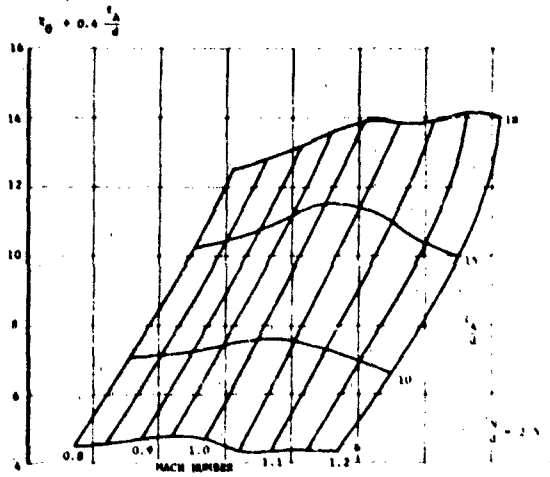
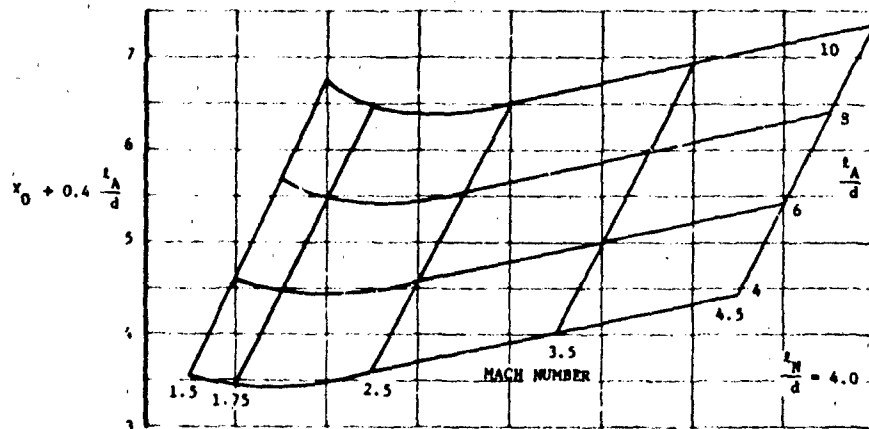
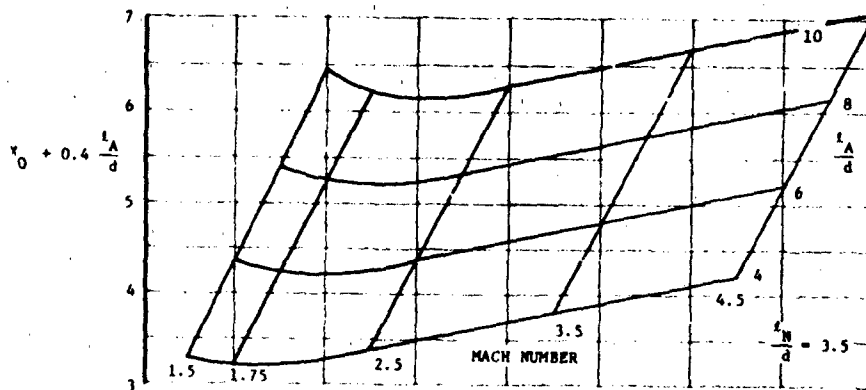


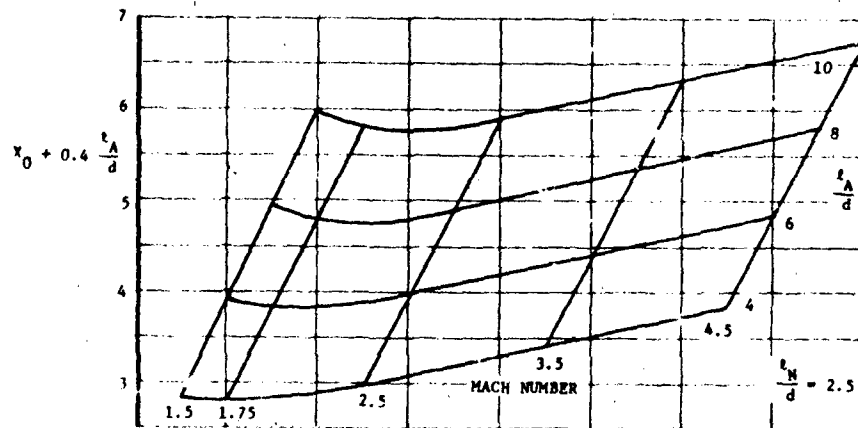
Figure 29c. Transonic Tangent Ogive-Cylinder Zero Angle of Attack Centers of Pressure ($l_N/d = 1.5$)



(a)



(b)



(c)

Figure 30. Tangent Ogive-Cylinder Zero Angle of Attack Centers of Pressure

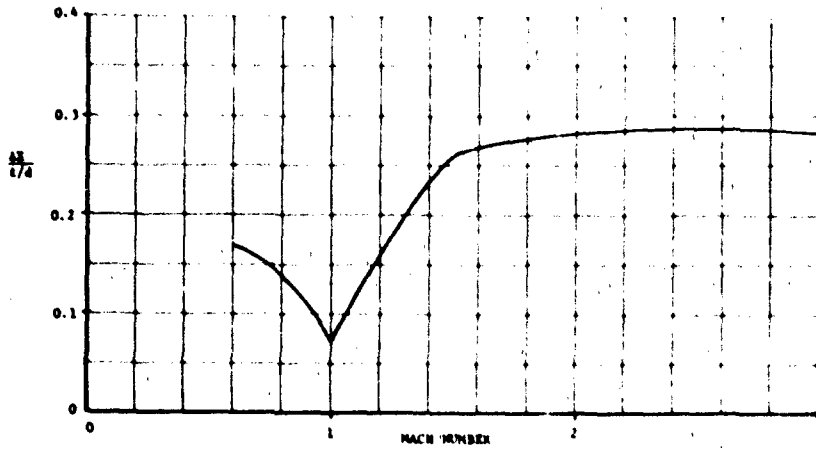


Figure 31. Increment in Center of Pressure Between Angles of Attack of 0 and 20 Degrees

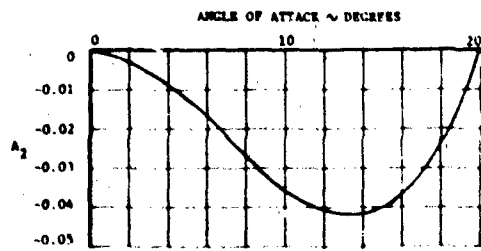
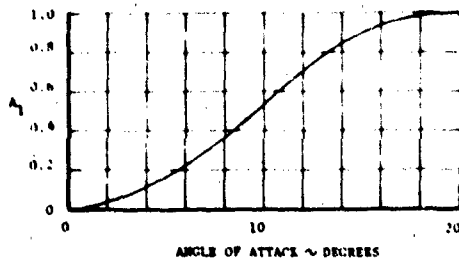
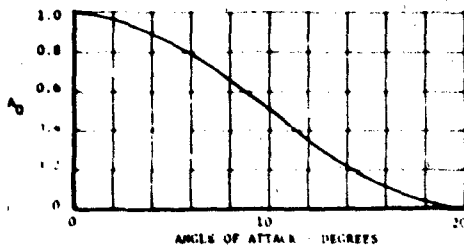


Figure 32. Polynomial Coefficients, Low Angle of Attack

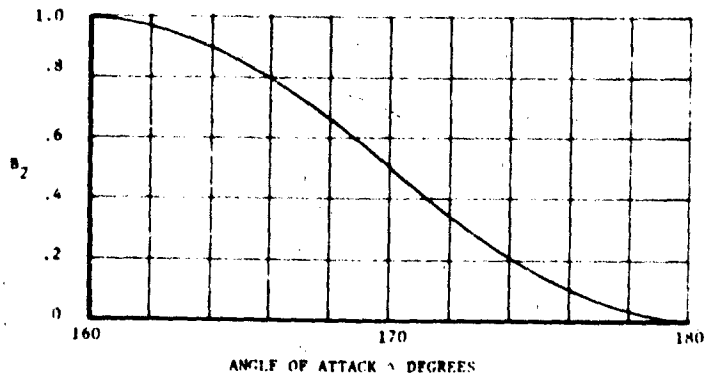
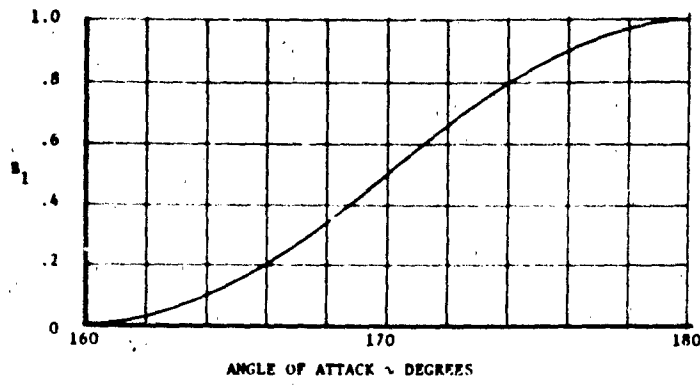
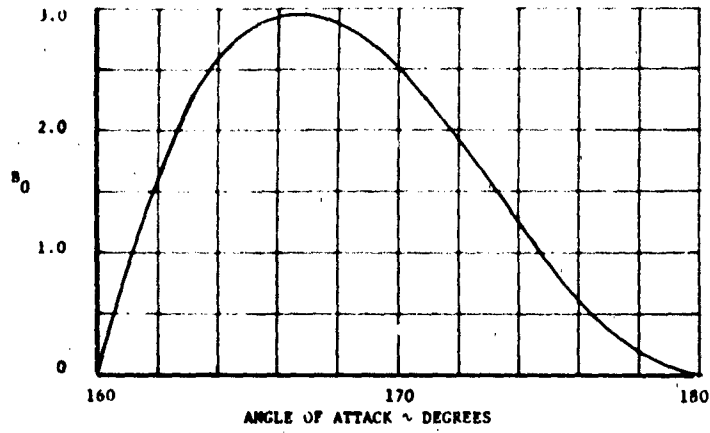


Figure 33. Polynomial Coefficients, High Angle of Attack

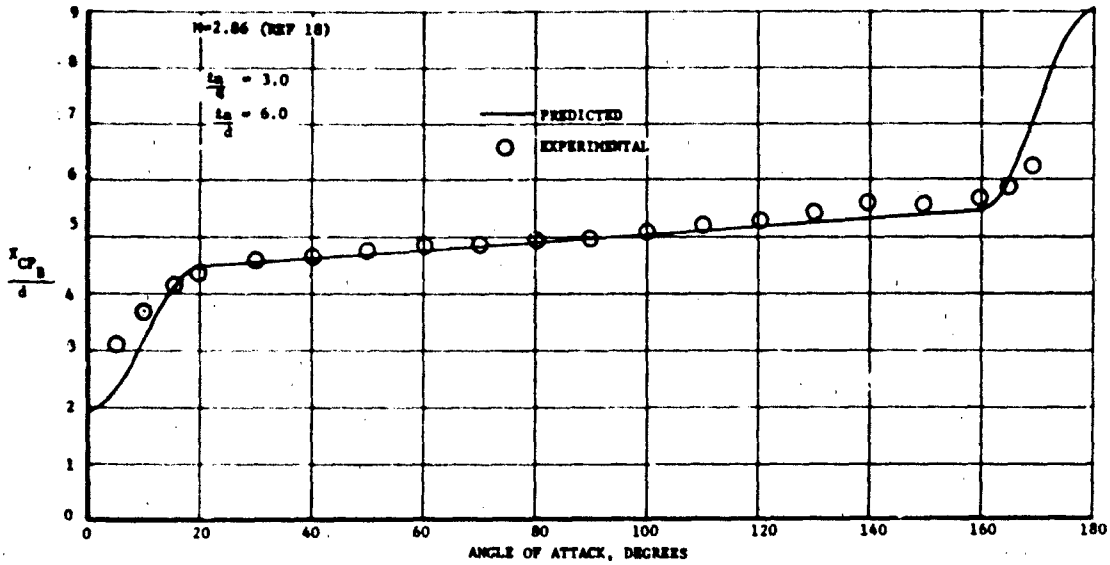


Figure 34. Comparisons Between Predictions and Experimental Data
 X_{CP}/d , Mach = 2.86

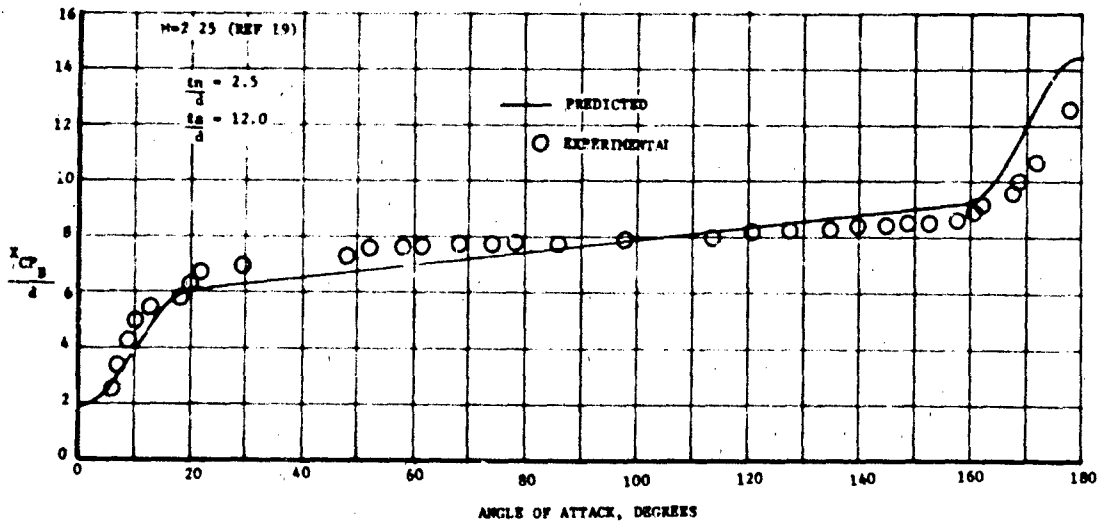


Figure 35. Comparisons Between Predictions and Experimental Data
 X_{CP}/d , Mach 2.25

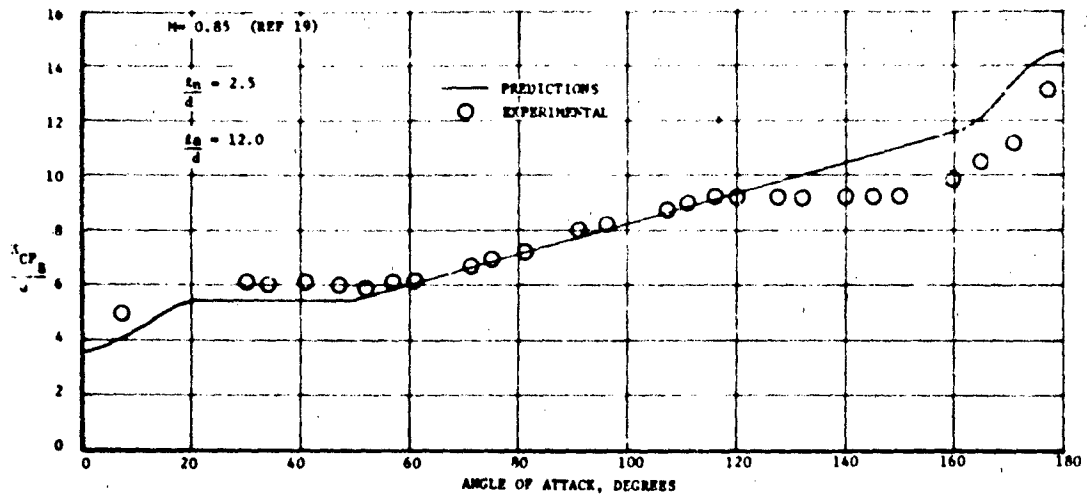


Figure 36. Comparison Between Predictions and Experimental Data
 X_{CP_B}/d , Mach = 0.85

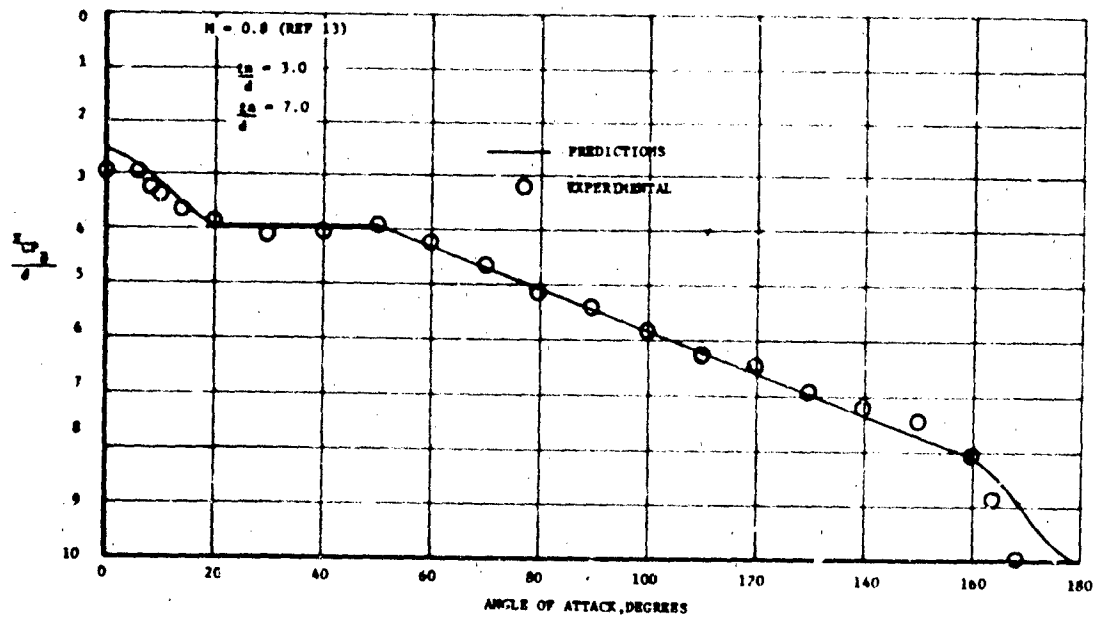


Figure 37. Comparisons Between Predictions and Experimental Data
 X_{CP_B}/d , Mach = 0.80

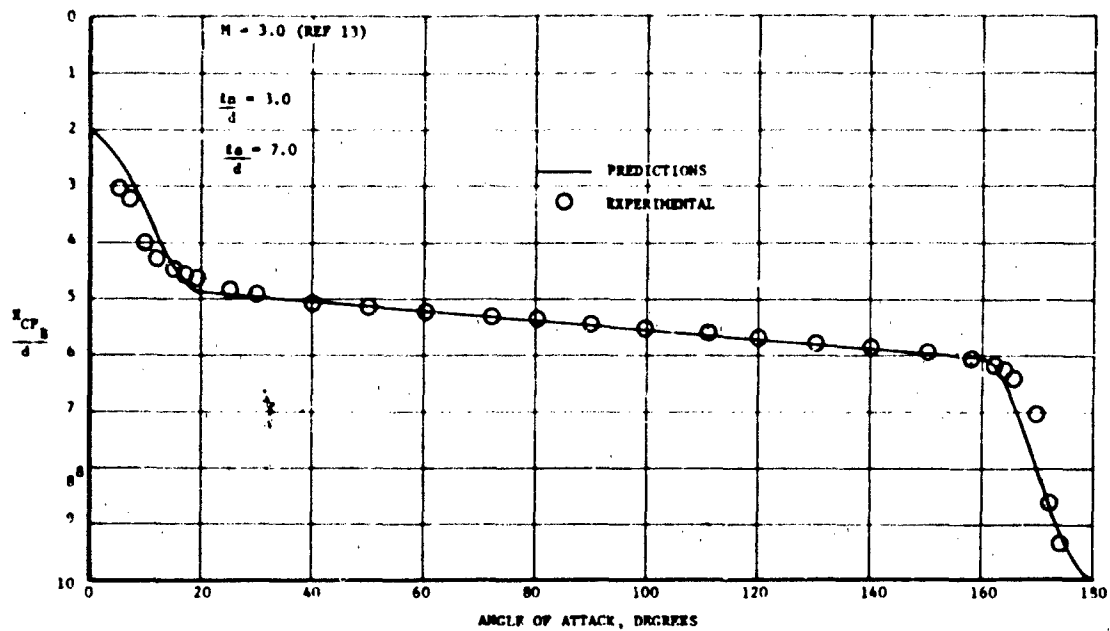


Figure 38. Comparisons Between Predictions and Experimental Data
 X_{CP_B}/d , Mach = 3.0

5.1.3 Body Axial Force

Summary

Methods are presented for predicting C_A , the isolated body axial force coefficient. Angle of attack and Mach ranges are 0 - 180 degrees and 0.6 - 3.0, respectively. Two methods are used. In the supersonic range a modification of an existing technique due to Jorgensen (Reference 12) is recommended; in the transonic range, a new method based on an extension of a previous technique has been constructed. The overall performance of the methods is shown to be good.

Background

An examination of existing methods for calculating body axial force coefficient from 0 - 180 degrees disclosed the following:

- 1 The method of Jorgensen (Reference 12), which applies over the entire angle of attack range, is applicable only to supersonic Mach numbers.
- 2 The method of Saffell, Howard and Brooks (Reference 21), which uses almost the same formulations as Jorgensen, deals with lift and drag, rather than normal and axial force components.
- 3 The method of Fidler and Bateman (Reference 3), which applies over the angle of attack range 0 - 90 degrees, is applicable to transonic speeds.

Because of its inconvenience, plus its strong similarity to the Jorgensen method, the work of Reference 21 was not considered further. Instead, References 3 and 12 were examined to determine whether the former needed to be improved for supersonic speeds and the latter could be modified to apply from 0 - 180 degrees for transonic speeds. The supersonic and transonic ranges are discussed separately. C_A is taken positive when directed towards the base.

Method Development (Transonic Mach Numbers)

The basic method here is that of Reference 3 which applies from 0 to 90 degrees. The basic formulation of the prediction equation is:

$$C_A = C_{A_0} + f(M, \alpha)$$

where $f(M, \alpha) = f(M, 90) = 0$, and

$$C_{A_0} = C_{A_1} + C_{A_{\text{base}}} \quad (C_{A_1} \text{ includes wave and friction effects})$$

Charts will be presented for estimating all the quantities required.

For 90 - 180 degrees, the following formulations were devised empirically, i.e., by choosing functional forms which are consistent with the patterns observed in the test data.

$$C_A = C_{A_0} - (C_{A_0} - C_{A_\pi}) \sin \alpha', \quad 90^\circ \leq \alpha \leq 160^\circ$$
$$\alpha' = \frac{9}{7} (\alpha - 90) \text{ deg.}$$

$$C_A = C_{A_\pi}, \quad 160^\circ \leq \alpha \leq 180^\circ.$$

The base drag contribution is obtained from Section 4.2.3.1 of Ref. 17.

$C_{A_\pi} = C_A$ for blunt cylinders and is obtained from Reference 6, from which Figure 39 is reproduced.

Use of the basic and modified formulations of Reference 3 provides the estimates which are compared with data in Figures 40a - f. It will be seen that matching is quite good overall and this method is recommended for use.

Use of Method (Transonic Mach Numbers)

Restating the basic equations:

$$C_A = C_{A_0} + f(M, \alpha)$$

$$C_{A_0} = C_{A_1} + C_{A_{\text{base}}}$$

C_{A_1} is obtained from Figures 41a - c as follows:

1 From Figures 41a, b, and c determine $C_{A_{1b}}$, the basic axial force coefficient (excluding base drag) at $Re_b = 15.8 \times 10^6$.

2 From Figure 42 determine the scaling factor $C_{A_1}/C_{A_{1b}}$ at the required Re , then $C_{A_1} = C_{A_{1b}} \frac{C_{A_1}}{C_{A_{1b}}}$.

3 From Section 4.2.3.1 of Reference 17, find $C_{A_{base}}$

$$C_{A_0} = C_{A_1} + C_{A_{base}}$$

$f(M, \alpha)$ is a power series containing α and $\overline{C_A}$, the value of C_A at $\alpha = 70^\circ$, as a free variable. The power series is:

$$C_A = -0.844\alpha + 1.92 \alpha^2 - 1.44 \alpha^3 + 0.360 \alpha^4 + \overline{C_A} [0.147\alpha - 1.842 \alpha^2 + 4.913 \alpha^3 - 2.419 \alpha^4].$$

For convenience, Figures 43 and 44 are given which are sufficient to calculate $f(M, \alpha)$. Figure 44 presents $f(M, \alpha)$ for various $\overline{C_A}$. Figure 43 presents $\overline{C_A}$ values for various transonic Mach numbers. Use of the curves is as follows:

4 At the appropriate M , read $\overline{C_A}$ from Figure 43

5 In Figure 44 estimate $f(M, \alpha)$ over the angle range at the appropriate $\overline{C_A}$.

Numerical Example

Calculate the axial force coefficient variation between 0 and 180 degrees for a missile body having a 3 caliber tangent ogive nose followed by a 7 caliber cylindrical section. Mach number is 1.15. $Re = 3.8 (10^{-6})$

1 From Figure 41 (interpolating) $C_{A_{1b}} = 0.215$.

2 From Figure 42, $C_{A_1} / C_{A_{1b}} = 1.88$

$$C_{A_1} = 0.215 \times 1.88 = 0.405$$

3 From Section 4.2.3.1 of Reference 17, $C_{A_{base}} = 0.05$.

$$\text{Hence, } C_{A_0} = C_{A_1} + C_{A_{base}}$$

$$= \underline{0.455}$$

The variation in the axial force coefficient with angle of attack is determined as follows:

0 - 90°

4 Now $M = 1.15$, hence $\overline{C_A} = -0.52$ (Figure 43)

5

α (deg)	$f(M, \alpha)$ (Fig. 44)	$C_A = C_{A_0} + f(M, \alpha)$
0	0	0.455
20	-0.11	0.345
40	-0.26	0.195
60	-0.46	-0.005
70	-0.52	-0.065
80	-0.42	0.035
90	0	0.455

See Figure 41.

90 - 160°

<u>α (deg)</u>	<u>C_A</u>
90	0.455
100	0.156
110	-0.324
120	-0.664
140	-1.162
160	-1.34 See Figure 41a.

160 - 180°

$$C_A = C_{A_{\pi}} = -1.34 \text{ (Figure 39)}$$

Method of Development (Supersonic Mach Numbers)

In Reference 12, equations and charts are presented from which the axial force coefficient on an isolated body may be estimated. The equations used are

$$C_A = C_{A_0} \cos^2 \alpha \quad 0^\circ \leq \alpha \leq 90^\circ$$

$$C_A = C_{A_{\pi}} \cos^2 (180 - \alpha) \quad 90^\circ \leq \alpha \leq 180^\circ$$

The zero-angle coefficient is expressed as:

$$C_{A_0} = C_{A_W} + C_{A_{SF}} + C_{A_{base}}$$

where C_{A_W} , $C_{A_{SF}}$ and $C_{A_{base}}$ are the contributions due to forebody pressure, skin friction and base drag, respectively, while the 180 degree coefficient (flat base into flow) is given by:

$$C_{A_{\pi}} = -C_s$$

Charts are presented for estimating all the above quantities except $C_{A_{SF}}$. For purposes of the present work, the skin friction was estimated from Section 4.1.5.1 of Reference 17, assuming a turbulent boundary layer.

Predictions of C_A over the entire angle of attack range were made using the Jorgensen formulations. Comparisons between predictions and data are shown across the supersonic Mach number range in Figures 45a - d. It should be noted that the AEDC wind tunnel data (Reference 13) are uncorrected for base pressure effects. It will be seen that matching is reasonably good, but obvious discrepancies are evident. For example, from 0 - 90 degrees the data do not approach zero as predicted. They either remain fairly constant or C_A increases slightly. Also, from 90 - 180 degrees some discrepancies are observable.

It was decided that a simple modification to the method could easily be accomplished to improve its performance. Based on the formulations which were found to work for the transonic case, the following empirical equations are used.

$$C_A = C_{A_0} \quad 0^\circ \leq \alpha \leq 90^\circ$$

$$C_A = C_{A_0} - (C_{A_0} - C_{A_\pi}) \sin \alpha' \quad 90^\circ \leq \alpha \leq 160^\circ$$

$$\alpha' = \frac{9}{7} (\alpha - 90)$$

$$C_A = C_{A_\pi} \quad 160^\circ \leq \alpha \leq 180^\circ$$

C_{A_0} is still obtained from the techniques of Reference 12.

The results of applying these equations are shown in Figures 45a - d. Clearly the overall matching is better than before. The modified equations are recommended for use instead of Reference 12.

Numerical Example

Estimate the axial force coefficient variation from 0 - 180 degrees for a missile body having a 3:1 caliber tangent ogive nose with a 7:1 caliber cylindrical afterbody. Mach number is 2.0.

$$\begin{aligned} \text{Now } C_{A_o} &= C_{A_n} + C_{A_{SF}} + C_{A_{base}} \\ &= 0.357 \text{ (Reference 12)} \end{aligned}$$

$$C_{A_n} = -1.66 \text{ (Reference 12)}$$

0 - 90° $C_A = 0.357$

90° - 160° 160° - 180° $C_A = -1.66$

α	C_A
90	0.357
100	-0.092
110	-0.518
120	-0.901
140	-1.46
160	-1.66

See Figure 45b

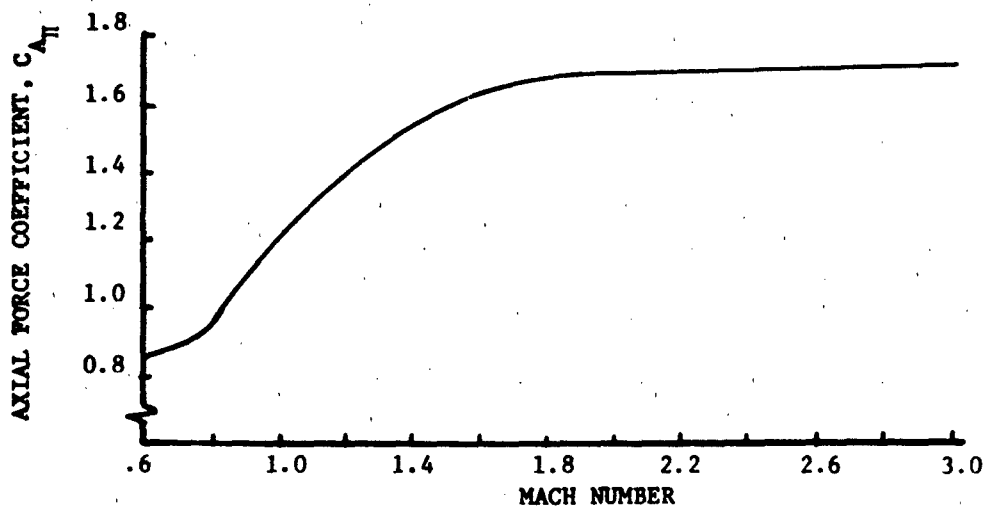


Figure 39. Variation With Mach Number of 180-Degree Axial Force Coefficient (Reference 6)

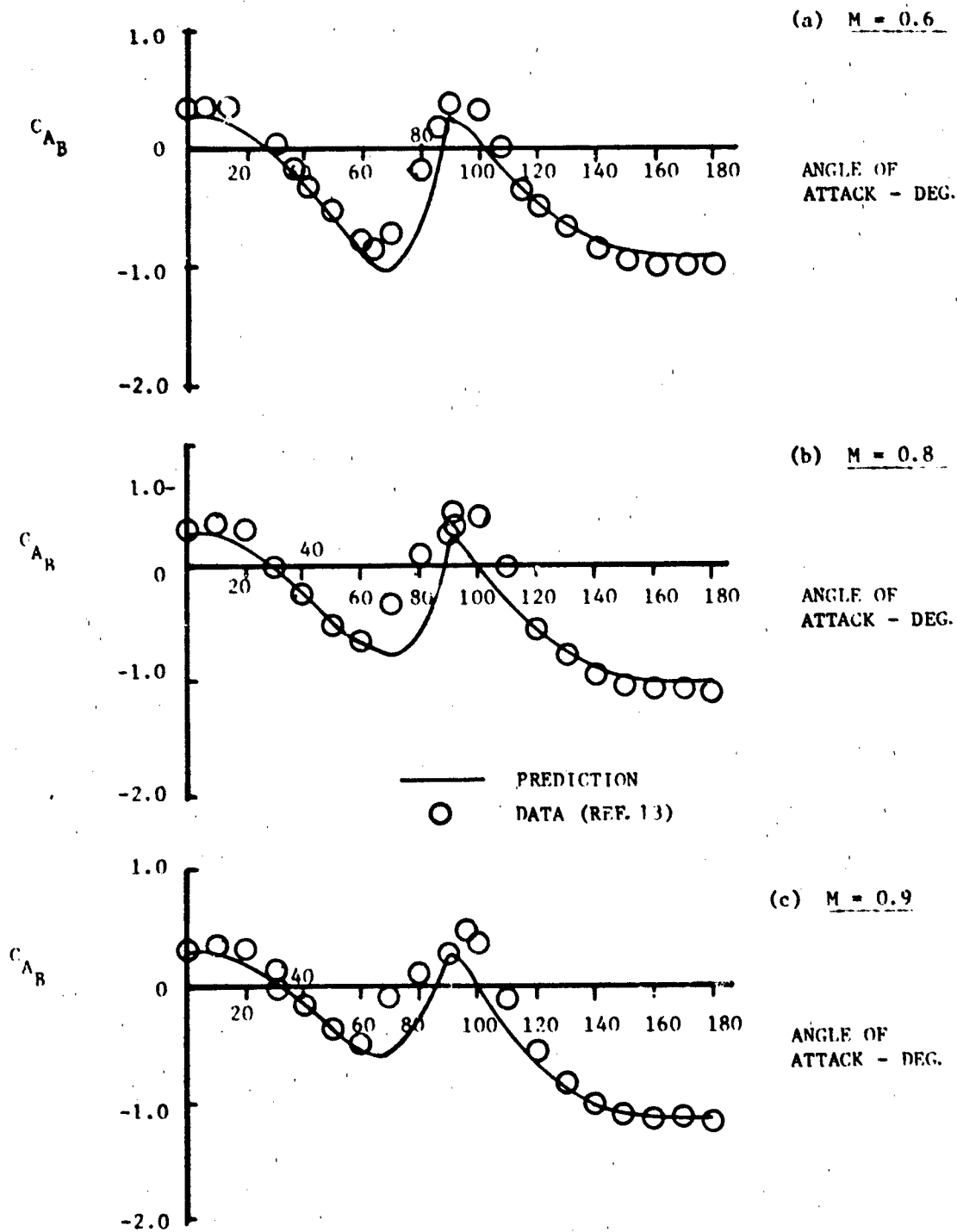


Figure 40. Comparison Between Predicted and Experimental C_{AB} (Transonic)

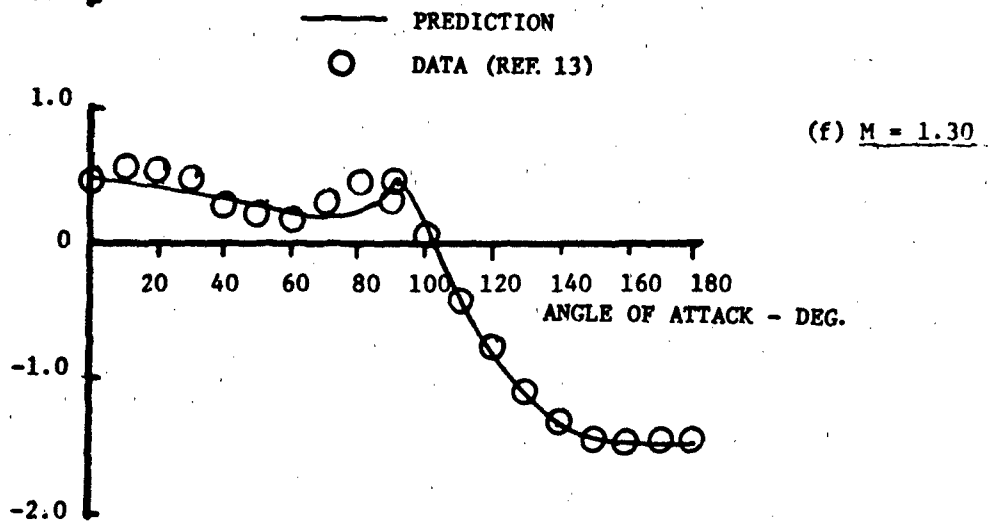
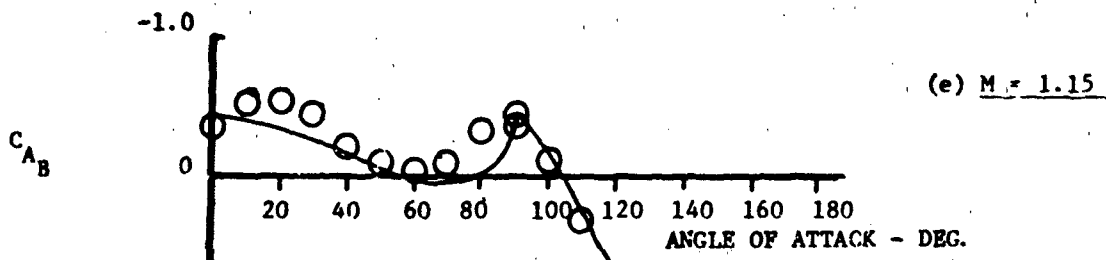
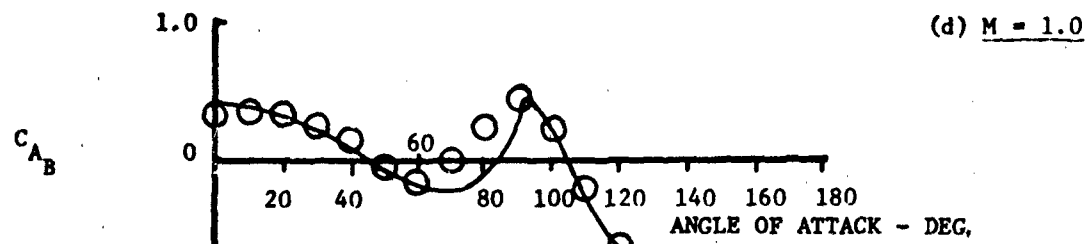


Figure 40. Continued

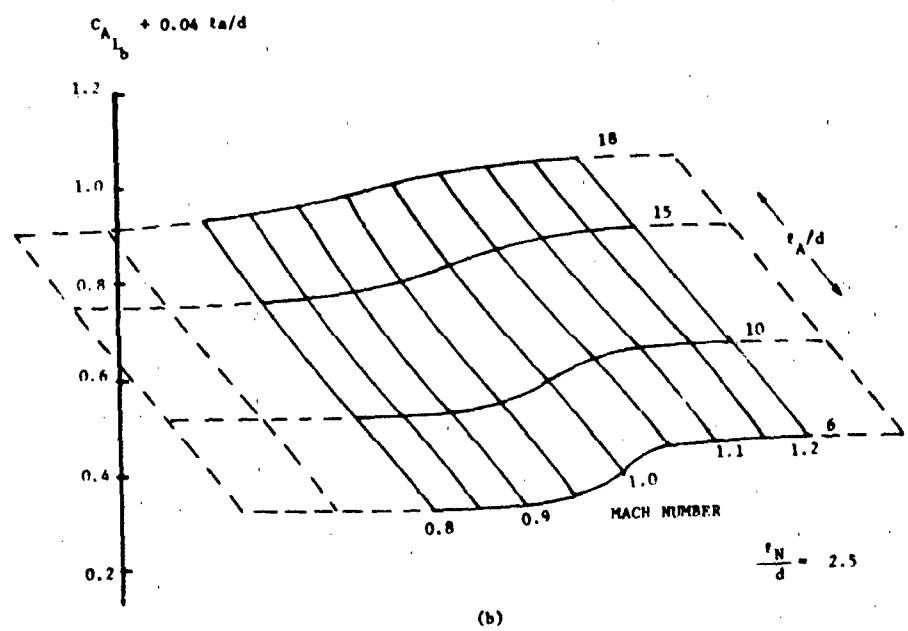
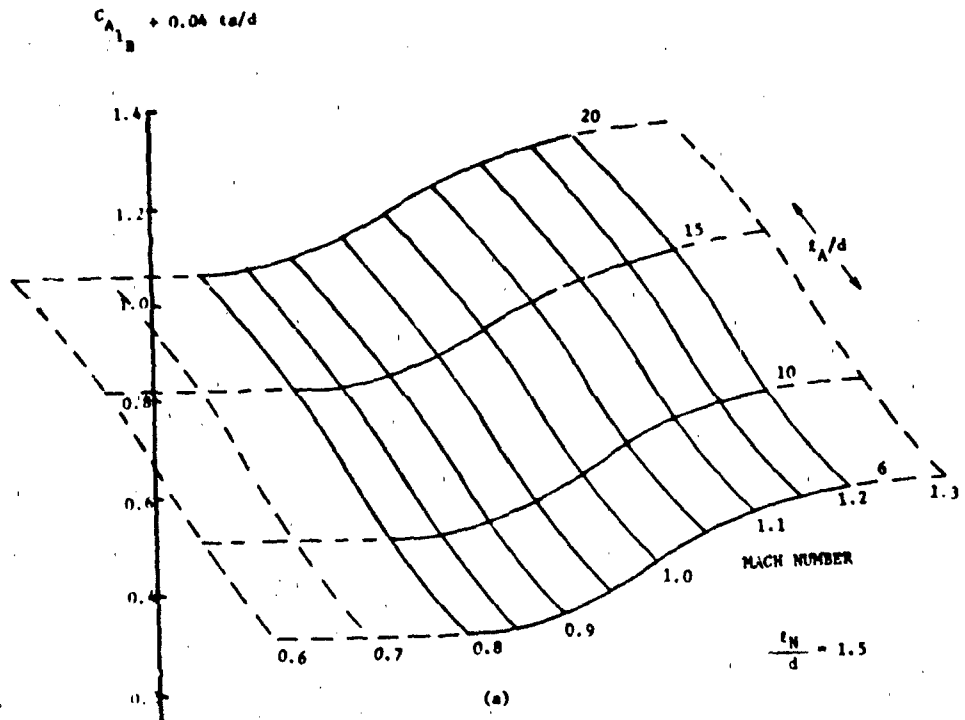


Figure 41. Curves for Determining C_{A1B}

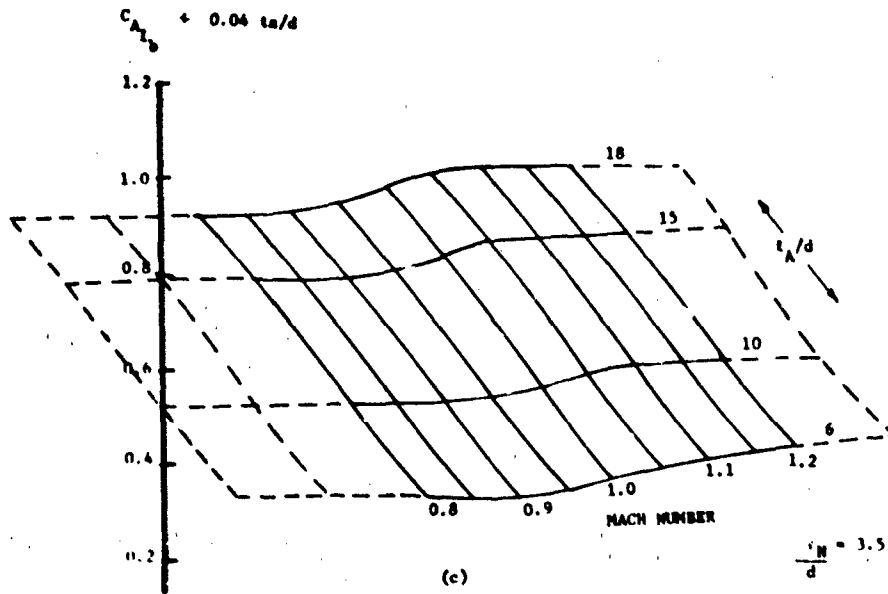


Figure 41. Continued

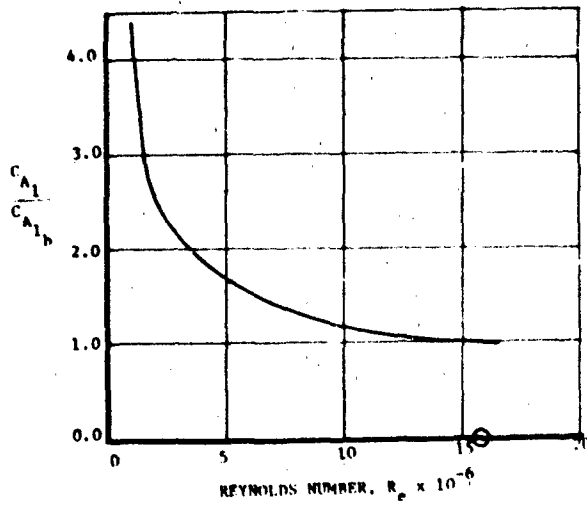


Figure 42. Scaling Factor for C_{A1B}

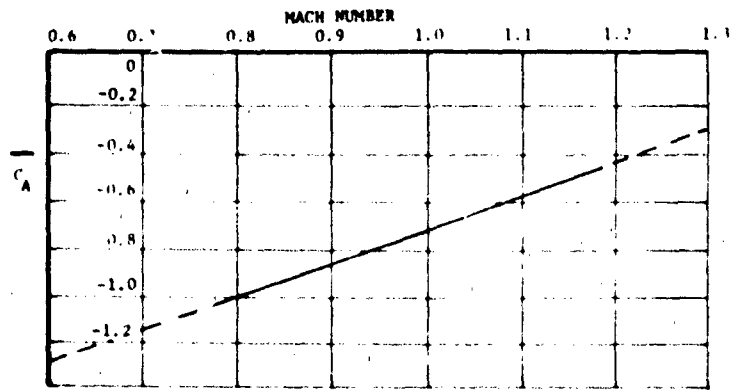


Figure 43. Variation Of \overline{C}_L With Mach Number

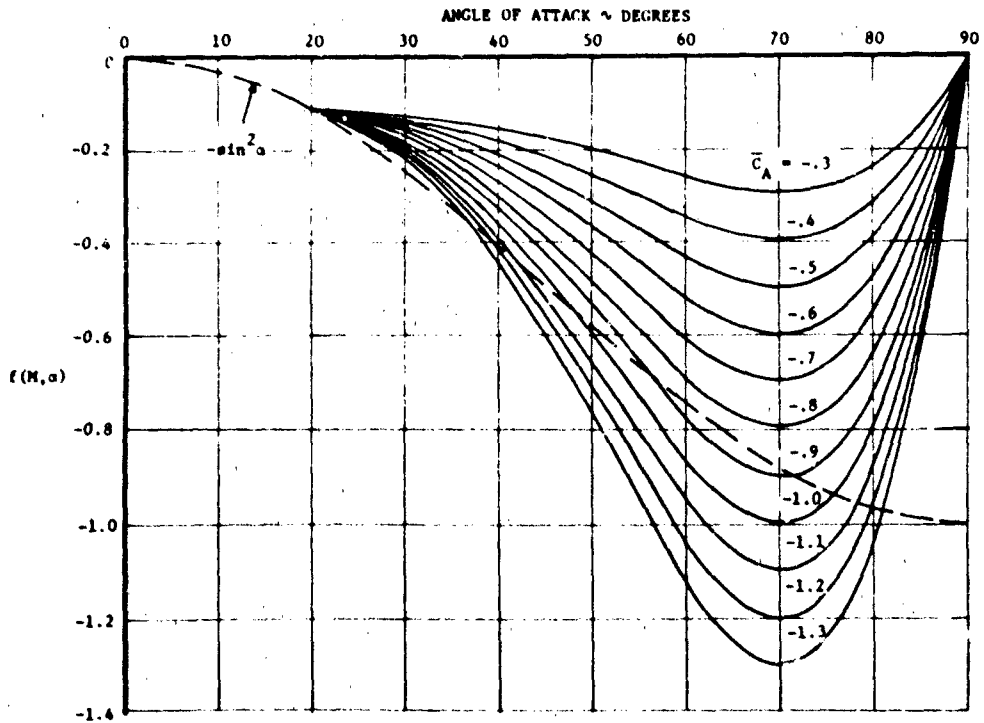


Figure 44. Basic Curves of $f(M, \alpha)$ Calculated From Power Series

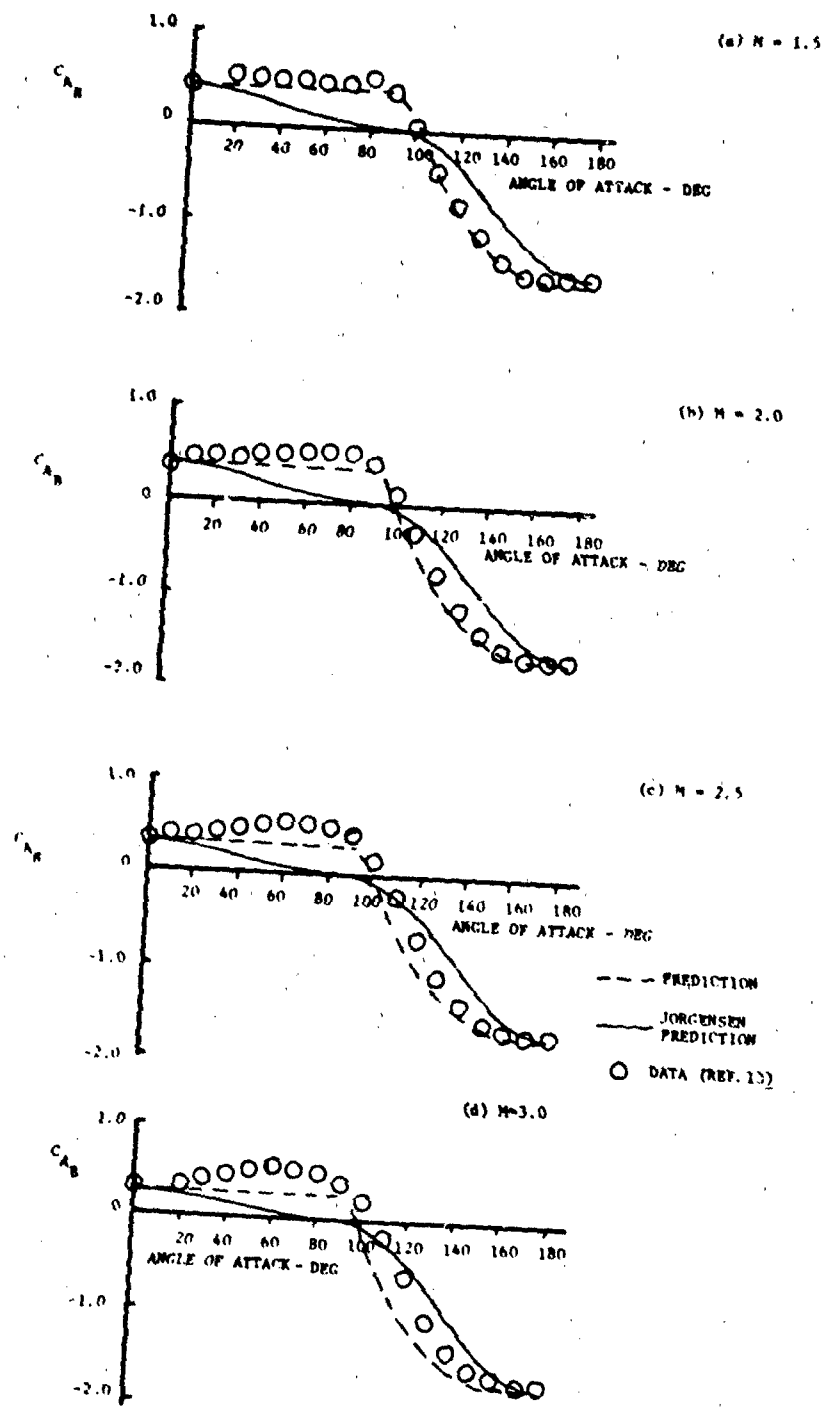


Figure 45. Comparisons Between Prediction and Experimental C_D (Supersonic)

5.1.4 Fin Normal Force

Summary

The normal force coefficient of an isolated tail panel C_{N_T} , can be predicted by the empirical methods developed in Reference 2 and extended by the correlations presented in this section. The applicable range of the methods is now:

Angle of attack	-	0 to 180 degrees
Mach number	-	0.60 to 3.0
Aspect ratio	-	≤ 2.0
Taper ratio	-	0 to 1.0

Comparisons between predictions and test data show generally good agreement, normal force coefficient being predicted usually well within 10 percent.

Background

This method allows the normal force coefficient of low aspect ratio fins to be calculated for angles of attack from 0 to 180 degrees and for Mach numbers ranging from 0.6 to 3.0. The method is an extension of the method presented in Reference 2, Section 3.3.1, made possible by the acquisition of additional test data. Typically, the method consists of two operations: 1) a procedure to estimate C_{N_T} up to 30 degrees, and 2) a procedure to extend the estimate to 90 degrees. It is shown that a mirror image of the curve so obtained provides a good estimate to 180 degrees. At supersonic Mach numbers greater than about 2.5, a single procedure is shown to fit the test data adequately within 10 percent.

Method Development

A full development of this method is contained in Reference 2. A portion of that material will be included here for completeness.

The flow about low aspect ratio fins at angles of attack greater than a few degrees is characterized by non-linear phenomena that cannot be described by linear theory techniques. Techniques have been developed for prediction of the aerodynamic characteristics of low aspect ratio fins in the presence of upper surface vortices, e.g., References 22, 23, 24, 25. However, for the general case where vortices, both coherent and burst, and a laminar separation bubble are present (Reference 26), methods are not available.

The method developed here is derived from the popular crossflow drag based methods as typified by Reference 23 which employs the formulation:

$$C_N = C_1 \alpha + C_2 \alpha^2 \quad (21)$$

In this expression C_1 is the zero angle of attack normal force curve slope and C_2 is a constant chosen to force the expression to fit experimental data.

This equation may be regarded as a truncated power series in α . Since it contains two constants, it should fit two boundary conditions on C_N , the condition, $(C_N)_{\alpha=0} = 0$ having already been satisfied. One condition is that $(\partial C_N / \partial \alpha)_{\alpha=0}$ must equal the normal force curve slope at $\alpha=0$. This determines C_1 . The second condition, the one determining the value of C_2 , is usually chosen so that the experimental data are fitted at some high angle of attack. The expression is then reasonably accurate up to that angle of attack, provided that the curvature of the data curve always has the same sign. In the general case, an expression such as Equation (21) cannot adequately describe the shape of the normal force curve above a few degrees angle of attack.

Since this form of solution leaves many boundary conditions unsatisfied, an obvious means of improving this situation is to retain the power series form of expansion, but to include as many terms as the boundary conditions permit.

Six boundary conditions are identified for use in a more general expression for C_{NT} along with a comment as to the basis for the chosen value.

$$C_{NT}(0) = 0, \text{ theoretical and empirical}$$

$$C_{NT\alpha}(0) \quad \text{theoretical}$$

$$C_{NT}(\pi) = 0, \text{ empirical}$$

$$C_{NT\alpha}(\pi) = -C_{NT\alpha}(0)$$

$$C_{NT\alpha}(\pi/2) = 0$$

$$C_{NT}(\pi/2) \text{ from test data}$$

The quantity $C_{NT}(0)$ is set to zero on the basis of linear theory predictions as well as test data whereas the values of the other five quantities are based on a review of test data. As indicated below, the resulting power series is expressed in terms of the two non-zero boundary conditions, i.e., $C_{NT\alpha}(0)$ and $C_{NT}(\pi/2)$.

Power Series Solution

With the six boundary conditions available, a power series containing six unknown coefficients may be used. The power series is assumed to be of the form:

$$C_{NT}(\alpha) = \sum_0^5 A_n \alpha^n \quad (22)$$

from which, with the aid of the boundary conditions, the six unknown constants A_0 through A_5 may be determined. Substitution of boundary conditions and rearrangement of the equation yields:

$$\begin{aligned} C_{NT}(\alpha) = & C_{NT\alpha}(0) \alpha + \left\{ \frac{16 C_{NT}(\pi/2)}{\pi^2} - \frac{5 C_{NT\alpha}(0)}{\pi} \right\} \alpha^2 \\ & + \left\{ \frac{8 C_{NT\alpha}(0)}{\pi^2} - \frac{32 C_{NT}(\pi/2)}{\pi^3} \right\} \alpha^3 \\ & + \left\{ \frac{16 C_{NT}(\pi/2)}{\pi^4} - \frac{4 C_{NT\alpha}(0)}{\pi^3} \right\} \alpha^4 \end{aligned} \quad (23)$$

where α is in radians.

To facilitate computation of the power series, Equation (23) has been rearranged in the form:

$$C_{NT}(\alpha) = A(\alpha)C_{NT}(0) + B(\alpha)C_{NT}(\pi/2) \quad (24)$$

where the values of $A(\alpha)$ and $B(\alpha)$ as a function of angle of attack are shown in Figure 46.

The term $C_{NT}(0)$ must be obtained from linear theory or Reference 27 from which Figures 47a through 47d are taken. The $C_{NT}(\pi/2)$ term is obtained through comparison of $C_{NT}(\alpha)$ with experimental data.

The quantity $C_{NT}(\pi/2)$ is empirically derived and presented in Figure 48. It is important to note that the numerical values assigned to the boundary condition $C_{NT}(\pi/2)$ are not actual normal force data but rather expediently chosen numbers which produced good agreement in the angle of attack range between 0 and 30 degrees. Even so, this approach does not work uniformly for all geometries and Mach numbers and yet another device is required to complete the portion of the model up to 30 degrees. Toward this end a quantity α' is defined which marks the upper bound angle of attack to which Equation 24 applies. If the value of α' found in Figure 49 is less than 30 degrees, then the value of C_{NT} for α between α' and 30 degrees is obtained by adding an increment (ΔC_N) to the value of C_{NT} obtained at α' . That is, for angles of attack between α' and 30 degrees, let:

$$C_{NT} = C_{NT} \Big|_{\alpha=\alpha'} + \Delta C_N$$

where:
$$\Delta C_N = \left(\frac{\Delta C_N}{\Delta C_{N_M}} \right) \Delta C_{N_M}$$

The quantity $\Delta C_N / \Delta C_{N_M}$ is an empirically determined factor (Figure 50) ranging from 0 to 1 indicating the fraction of the maximum correction (ΔC_{N_M}) required.

The quantity ΔC_{N_M} is an empirically determined parameter (Figure 51) representing

the largest difference found between the C_{N_T} calculated at any α' and the test values at $\alpha = 30$ degrees.

Use of Method

The normal force coefficient method consists of Equation (23) or (24), together with values of $C_{N_T}(\pi/2)$ from Figure 48, supplemented with additional information from Figures 49 through 51 where required. The following steps must be adhered to.

- 1 Calculate $C_{N_{T\alpha}}(0)$ using Figures 47a - 47d (or $\pi AR/2$ for lowest AR's)
- 2 Find $C_{N_T}(\pi/2)$ from Figure 48, interpolating where necessary
- 3 Calculate $C_{N_T}(\alpha)$ up to α' as obtained from Figure 49. (If $\alpha' = 30$ degrees, calculations are now complete. If $\alpha' < 30$ degrees, go on to Step 4).
- 4 For Mach numbers under consideration, obtain values of $\Delta C_N / \Delta C_{N_M}$ at various $(\alpha - \alpha') / (30 - \alpha')$ from Figure 5C.
- 5 From Figure 51 find ΔC_{N_M} ; use this to calculate values of ΔC_N and distribute these over the α range from α' to 30 degrees.

Numerical Example

Two examples illustrate application of the method.

Calculate the variation of normal force coefficient with angle of attack to 30 degrees for a wing as follows:

$$AR = 0.52, \lambda = 0, M = 0.8$$

- 1 $C_{N_{T\alpha}}(0) = \pi AR/2 = 0.819$ from Slender Body Theory
- 2 $C_{N_T}(\pi/2) = 2.4$ (Figure 48)
- 3 Figure 49, $\alpha' = 30$ degrees, hence calculate $f(\alpha)$ up to this value.

Using Equation (23), the following table may be constructed:

α (deg)	$C_{N_T}(\alpha)$	
5	0.091	A comparison between these values and experimental data taken from Reference 24 is shown in Figure 52. Also shown is the result of applying the method of Reference 17. The present method yields better matching with data.
10	0.216	
15	0.368	
20	0.541	
25	0.727	
30	0.927	

Calculate the variation of normal force coefficient with angle of attack to 30 degrees for a wing as follows:

$$AR = 2.0, \lambda = 1.0, M = 0.98$$

$$C_{N_{T_a}}(0) = 3.04 \text{ (Figure 47a)}$$

$$C_{N_T}(\pi/2) = 3.6 \text{ (Figure 48)}$$

From Figure 49, $\alpha' = 12$ degrees, which is < 30 degrees; hence, C_N is calculated only up to $\alpha = 12$ degrees:

α (deg)	C_{N_T}
5	0.28
10	0.568
12	0.689

4 Figures 50 and 51 must be used for $\alpha > 12$ degrees. Therefore, from Figure 50,

a table of $\Delta C_N / C_{N_M} \sim (\alpha - \alpha') / (30 - \alpha')$ is constructed:

$(\alpha - \alpha') / (30 - \alpha')$	$\Delta C_N / \Delta C_{N_M}$
0	0
0.2	0.47
0.4	0.69
0.6	0.83
0.8	0.93
1.0	1.0

5 Now $\alpha' = 12$ degrees, and from Figure 51, $\Delta C_{N_M} = 0.41$, hence ΔC_N and α may be calculated.

$(\alpha - \alpha')$ deg	α deg	ΔC_N	C_N
0	12	0	.689
3.6	15.6	0.193	.882
7.2	19.2	0.283	.972
10.8	22.8	0.341	1.030
14.4	26.4	0.382	1.071
18	30	0.41	1.099

The most direct way to obtain the normal curve is to draw C_{N_T} up to α' and then add on the remaining C_N increments. This curve is compared with experimental data in Figure 53.

One further check case is shown in Figure 54 for a fin of $AR = 0.86$, $\lambda = 0.4$, and $M = 1.02$. Again data matching is quite good. These data were obtained from Reference 28.

Extension of Method to 90 Degrees

In extending the method to 90 degrees angle of attack, a second power series is used along with data (References 5 and 29) at angles between 30 degrees and 90 degrees. Due to the lack of detailed high angle data at low supersonic speeds, it has not been possible to check the method at all Mach numbers. However, check cases using the high angle transonic data referred to earlier have shown the method to yield reasonable accuracy.

The procedure used to extend the method to 90 degrees introduces a series (similar to Equation (23)) which joins the curve for C_{N_T} at 30 degrees to the point at 90 degrees (C_{N_C}). Experimental values of C_{N_C} from transonic tests on the fins described in Reference 2, and supersonic values from

Reference 6 combine to produce the curve in Figure 55.

Boundary conditions used in construction of the new series are:

- 1 At $\alpha = 30$ degrees, $C_{NT}(30)$ may be determined from the first part of this method.
- 2 At $\alpha = 30$ degrees, C_{NT} may be determined from the differential form of Equation (23).

$$\begin{aligned}
 C_{NT_\alpha} = C_{NT_\alpha}(0) &+ 2 \left\{ \frac{16 C_{NT}(\pi/2)}{\pi^2} - \frac{5 C_{NT_\alpha}(0)}{\pi} \right\} \alpha \\
 &+ 3 \left\{ \frac{8 C_{NT_\alpha}(0)}{\pi^2} - \frac{32 C_{NT}(\pi/2)}{\pi} \right\} \alpha^2 \\
 &+ 4 \left\{ \frac{16 C_{NT}(\pi/2)}{\pi^4} - \frac{4 C_{NT_\alpha}(0)}{\pi^3} \right\} \alpha^3
 \end{aligned}$$

with $\alpha = 0.523$ rads (30 degrees) for $M > 1$.

For Steps 1 and 2, however, values of $C_{NT}(30)$ and $C_{NT_\alpha}(30)$ have been obtained from the experimental data and are given in Figures 56 and 57, respectively.

- 3 At $\alpha = 90$ degrees, C_{NC} is determined from experimental data as shown in Figure 55.
- 4 At $\alpha = 90$ degrees, $\partial C_N / \partial \alpha = 0$

Using these boundary conditions in the series of Equation (22) yields:

$$\begin{aligned}
 C_{NT}(\alpha) = & \left\{ -1.178111 C_{NT_\alpha}(30) + C_{NT}(\pi/2) - C_{NT}(30) + C_{NT}(30) \right\} \\
 & + \left\{ 3.7501 C_{NT_\alpha}(30) - 4.29731 [C_{NT}(\pi/2) - C_{NT}(30)] \right\} \alpha \\
 & + \left\{ -3.342356 C_{NT_\alpha}(30) + 5.471487 [C_{NT}(\pi/2) - C_{NT}(30)] \right\} \alpha^2 \\
 & + \left\{ 0.911921 C_{NT_\alpha}(30) - 1.74626 [C_{NT}(\pi/2) - C_{NT}(30)] \right\} \alpha^3
 \end{aligned} \tag{25}$$

It should be noted that Equation (25) has been reevaluated and the constants are somewhat different from those in Reference 2.

For ease in calculating $C_{N_T}(\alpha)$ from 30-90 degrees, the form of Equation (25) has been rearranged as follows:

$$C_{N_T} = C(\alpha) C_{N_T}(30) + D(\alpha) C_{N_C} + E(\alpha) C_{N_{T_\alpha}}(30) \quad (26)$$

with the three terms, $C(\alpha)$, $D(\alpha)$, and $E(\alpha)$ shown in Figure 58 as a function of angle of attack.

Use of Method ($30^\circ \leq \alpha \leq 90^\circ$)

Between 30 and 90 degrees angle of attack, the method is used as follows:

- 1 Find $C_{N_T}(30)$ from Figure 56
- 2 Find $C_{N_{T_\alpha}}(30)$ from Figure 57
- 3 Determine C_{N_C} from Figure 55
- 4 Calculate $C_{N_T}(\alpha)$ using Equation (25) or (26)

It is recommended that C_{N_T} be calculated from Equation (25) or (26) beginning at $\alpha = 50$ degrees and that the portions of the curve from 0 - 30 degrees and from 50 - 90 degrees be faired together. As an example, the variation from 0 to 90 degrees angle of attack is calculated for a fin having aspect ratio 1.0 and taper ratio 1.0 at a Mach number of 1.10:

$$C_{N_C} = 1.42 \text{ (Figure 55)}$$

$$C_{N_{T_\alpha}}(30) = 1.98 \text{ (Figure 57)}$$

$$C_{N_T}(30) = 1.23 \text{ (Figure 56)}$$

Substituting the above values in Equation (26) yields:

$$C_{N_T} = 1.23 C(\alpha) + 1.43 D(\alpha) + 1.98 E(\alpha)$$

This equation is used to construct the following table:

<u>α(deg)</u>	<u>C_{N_T}</u>
50	1.589
60	1.589
70	1.532
80	1.463
90	1.430

The comparison between these estimates and the high angle data (Reference 5) is shown in Figure 59. While exact matching is not achieved, the curve does follow the data quite well.

The method as described has been found to require a minor modification for fins of taper ratio 0 and aspect ratio 1.0 when Mach number is less than 1.0. When estimating the normal force coefficient of an isolated fin having this geometry at $M \leq 1.0$ the following modification to the method is suggested.

- i) Use the first part of the method, as described, up to $\alpha = 30$ degrees
- ii) Instead of using the second power series given by Equation (25) or Equation (26) for fairing from 30 - 90 degrees follow the steps below:

Estimate ΔC_{N_T} for angles between 30 and 40 degrees from Figure 60 and add to the value at $\alpha = 30$, from (i) above.
Fair the curve from the value at 40 degrees to the 90 degree value, C_{N_C} from Figure 55.

Example

Estimate values of C_{N_T} between 30 and 40 degrees for an isolated fin of taper ratio 0, aspect ratio 1.0 at $M = 0.9$.

From Figure 60, the portion AB of the curve is used exactly as shown, i.e., add the increment taken from AB directly to the value calculated at $\alpha = 30$ degrees. The portion BC of the curve applies between $\alpha = 35$ and 40 degrees and must be scaled by the factor 0.78 (Figure 60b). Between $\alpha = 35$

and 40 degrees the increment is equal to the product of the scale factor and Δ_{BC} . The resulting curve is shown in Figure 61. Point "A" must now be placed at the value of C_{NT} at 30 degrees from (1) above, and the curve from point "C" must be faired to C_{NT} at 90 degrees.

Extension of Method to 180 Degrees Angle of Attack

The availability of additional test data on low aspect ratio tail panels to 180 degrees angle of attack has permitted the prediction methods to be extended to this new range. The validity of the method in the transonic and low supersonic speed range is further demonstrated in Figure 62 and Figure 63. In these figures, the prediction method employs the power series of Equation (24) up to 30 degrees angle of attack, and Equation (26) from 50 to 90 degrees, with the curve faired from 30 to 50 degrees as described earlier. Note that test data from 90 to 180 degrees are plotted on these figures, indicating near symmetry of the data about 90 degrees angle of attack. The prediction is shown to closely approximate test data over the angle of attack range from 0 to 180 degrees.

A typical application of the method at subsonic speeds, $M = 0.6$, and from 0 to 180 degrees angle of attack is shown in Figure 64 indicating the prediction method used for the various segments of the curve. The data are again seen to be nearly symmetrical about 90 degrees and closely approximated by the prediction methods.

Extension of Prediction Methods to $M = 3.0$

Supersonic test data to Mach 3.0 and 180 degrees angle of attack for the family of low aspect ratio, low taper ratio panels were examined for compatibility with the prediction methods used for the subsonic and transonic cases. It should be noted here that during supersonic tests some of the isolated panels on the reflection plane encountered flow separation when the fins were

nearly normal to the flow. The fins behaved like forward facing steps, with the result that C_N was reduced. Here the C_N value at 90 degrees was obtained from the flat plate data of Figure 55 and the test data were faired through the apparent separation region.

Examination of the developed methods indicate that as the curve fit parameter $C_{N_T}(\pi/2)$ of Figure 48 approximates the actual value of normal force at 90 degrees, C_{N_C} , of Figure 55, and single power series method of Equation (24) should adequately predict the variation of C_{N_T} with alpha. Typical examples will be presented at Mach 2.0, 2.5, and 3.0 to illustrate the capabilities of the two power series approach, and to show that the single power series of Equation (24) is a reasonable prediction method as the Mach number approaches the 2.5 to 3.0 range. The mirror image characteristic of the supersonic data about 90 degrees is also evident from the test data, permitting the prediction to be applied to 180 degrees at these Mach numbers.

A typical configuration example will be examined at Mach 2.0 where the value of $C_{N_T}(\pi/2)$ is somewhat larger than C_{N_C} . In this case, the two power series approach yields a very good match with test data as seen in Figure 65. Had the method of Equation (24) been extended above 30 degrees the equation would have predicted a value of $C_{N_T}(\pi/2)$ which at this Mach number would be somewhat high. This and other test cases indicate that at Mach 2.0 the prediction should include both power series, Equation (24) and Equation (26), in order to obtain the best data fit.

At Mach 2.5 the requirement for using the two segment prediction method begins to disappear as the values of $C_{N_T}(\pi/2)$ and C_{N_C} start to converge. A typical example of a single curve fit from Equation (24) is shown in Figure 66, and is seen to reasonably match the test data. The dashed line of Figure 66

shows that the curve fit can be improved slightly by the application of the second power series, Equation (26), from 50-90 degrees angle of attack. In general, the single curve fit, Equation (24), should begin to be acceptable at this Mach number and above.

The application of the single power series, Equation 24, prediction method at Mach 3.0 is shown in Figure 67 and Figure 68 for two typical tail panel configurations, indicating good agreement with test data.

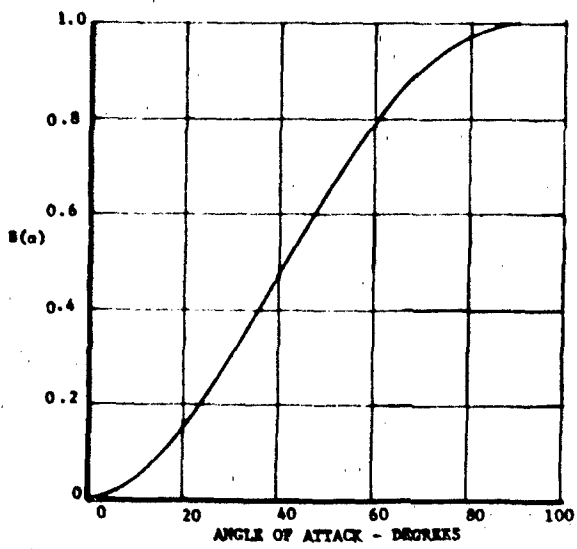
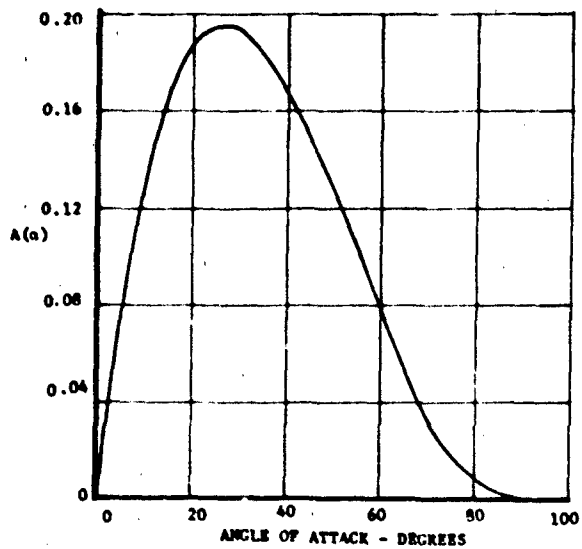


Figure 46. Power Series Parameters for Equation (24)

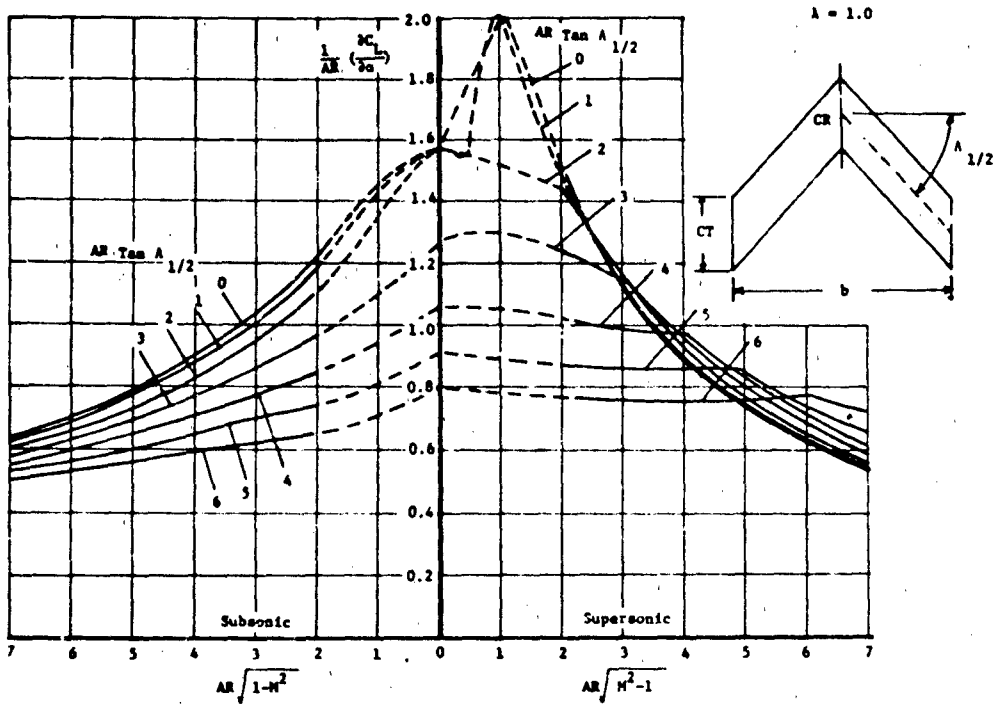


Figure 47a. Lift Curve Slope for Taper Ratio = 1.0

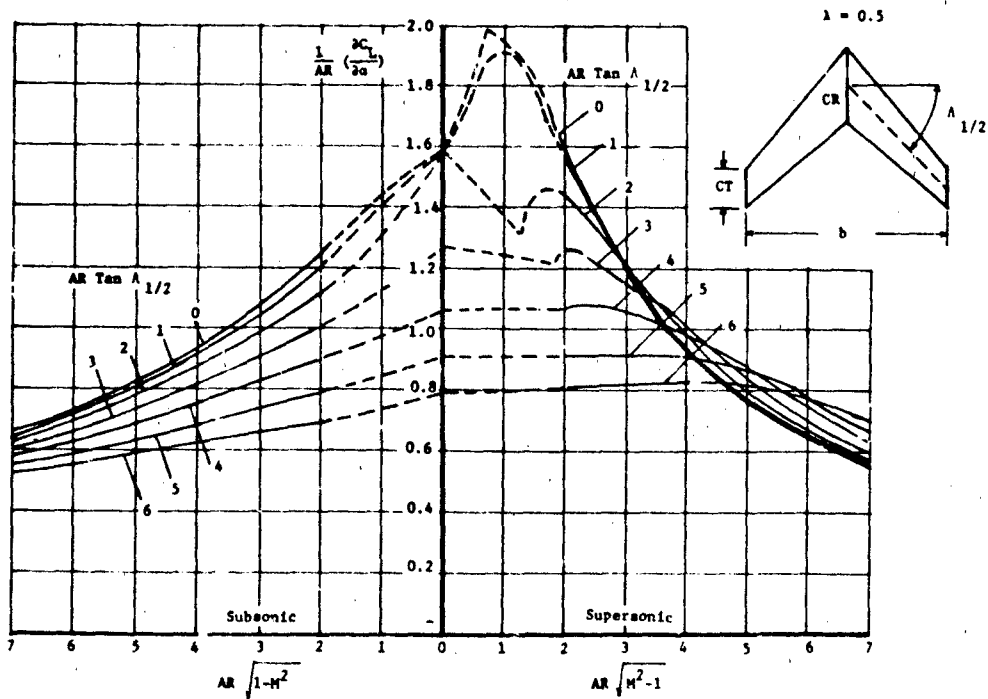


Figure 47b. Lift Curve Slope for Taper Ratio = 0.5

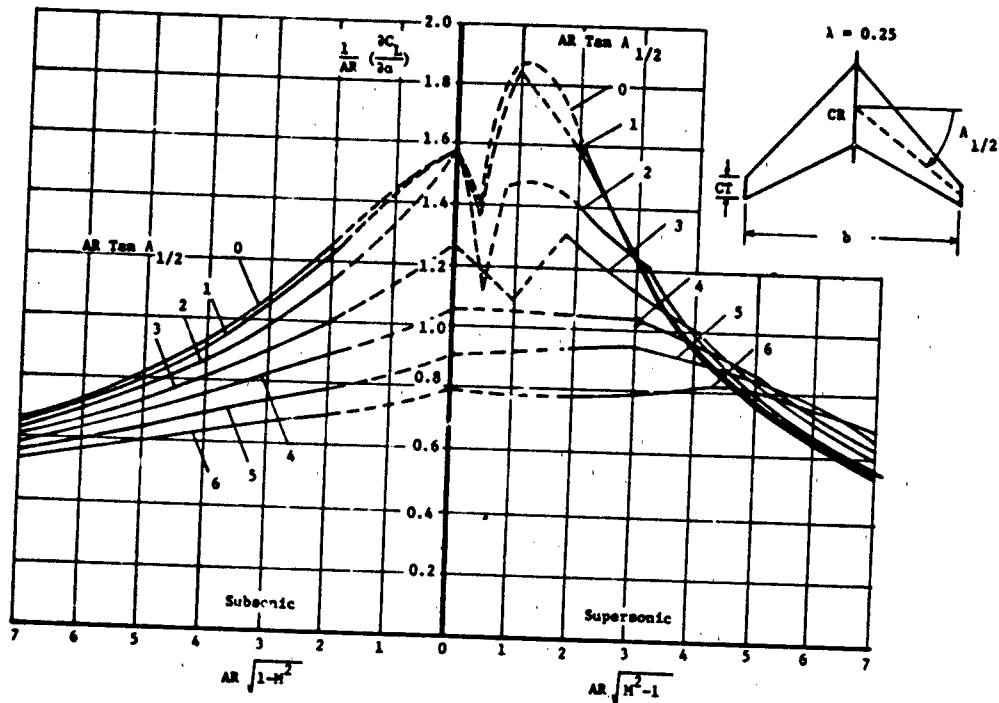


Figure 47c. Lift Curve Slope for Taper Ratio = 0.25

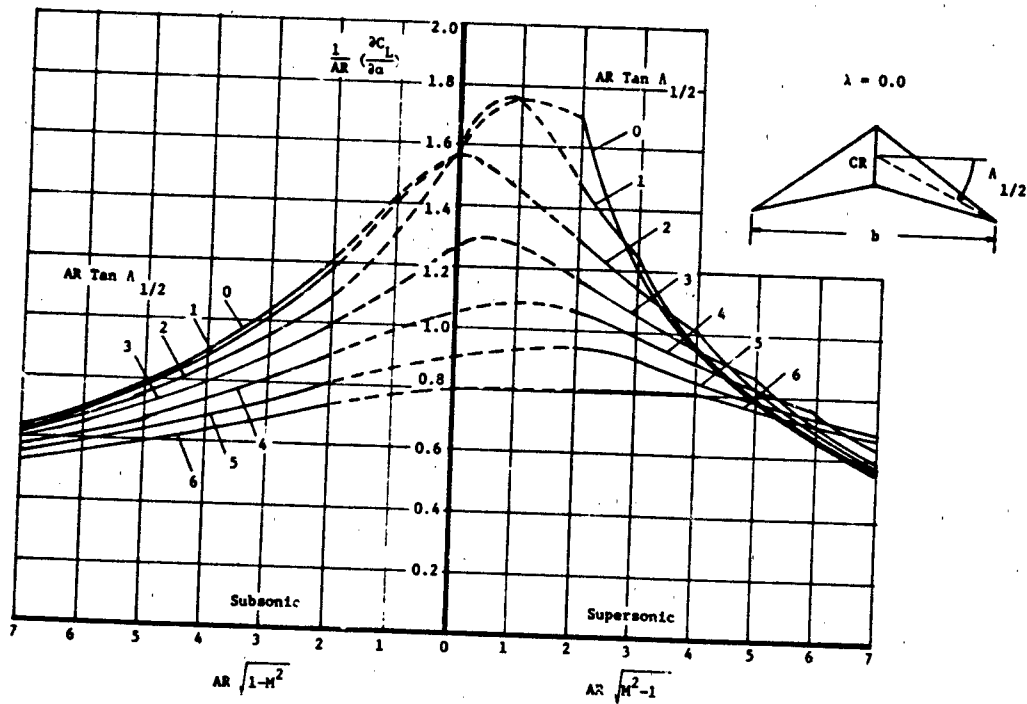


Figure 47d. Lift Curve Slope for Taper Ratio = 0.0

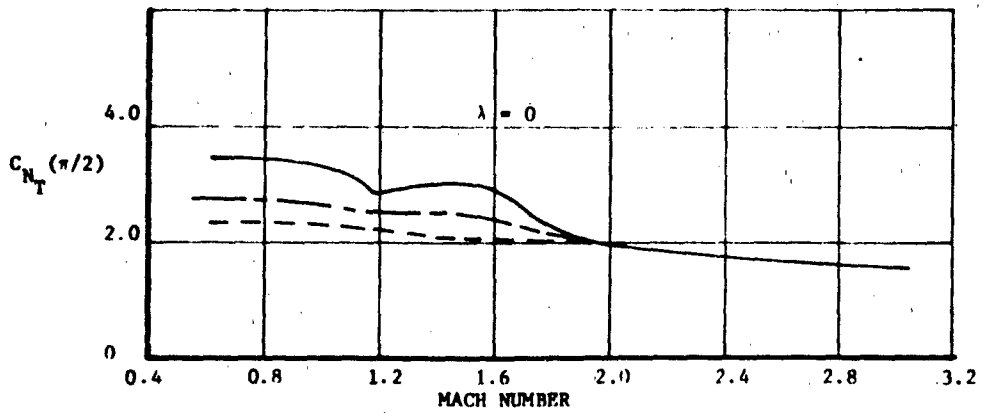
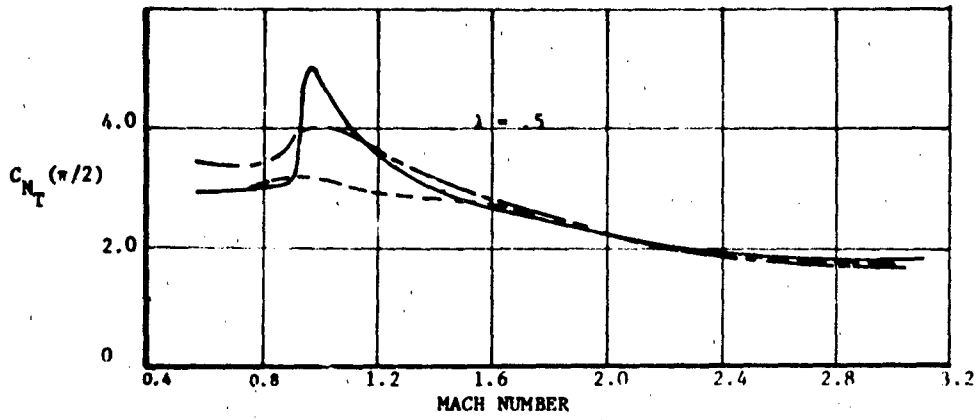
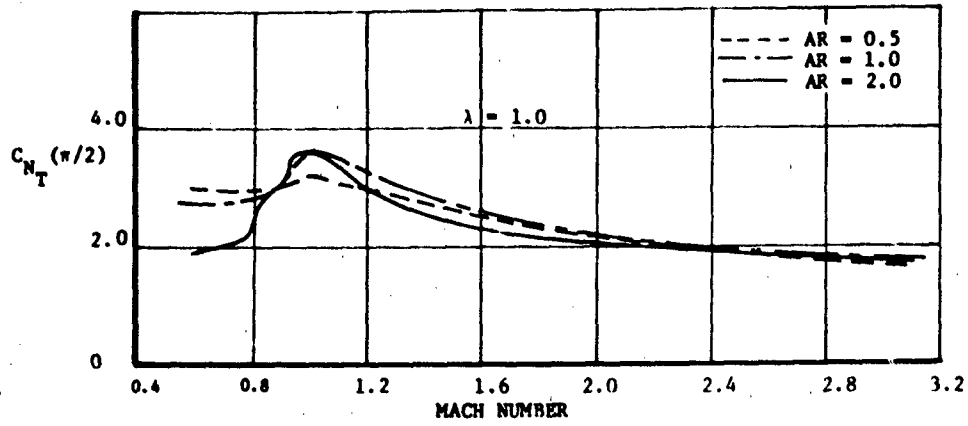


Figure 48. Variation of $C_{N_T} (\pi/2)$ With Mach Number

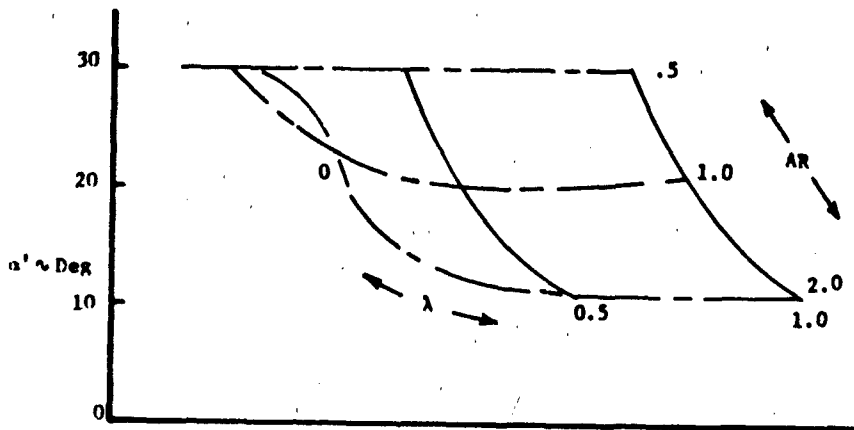


Figure 49. α' , Angle of Attack Above Which ΔC_N Must Be Applied (Subsonic Only)

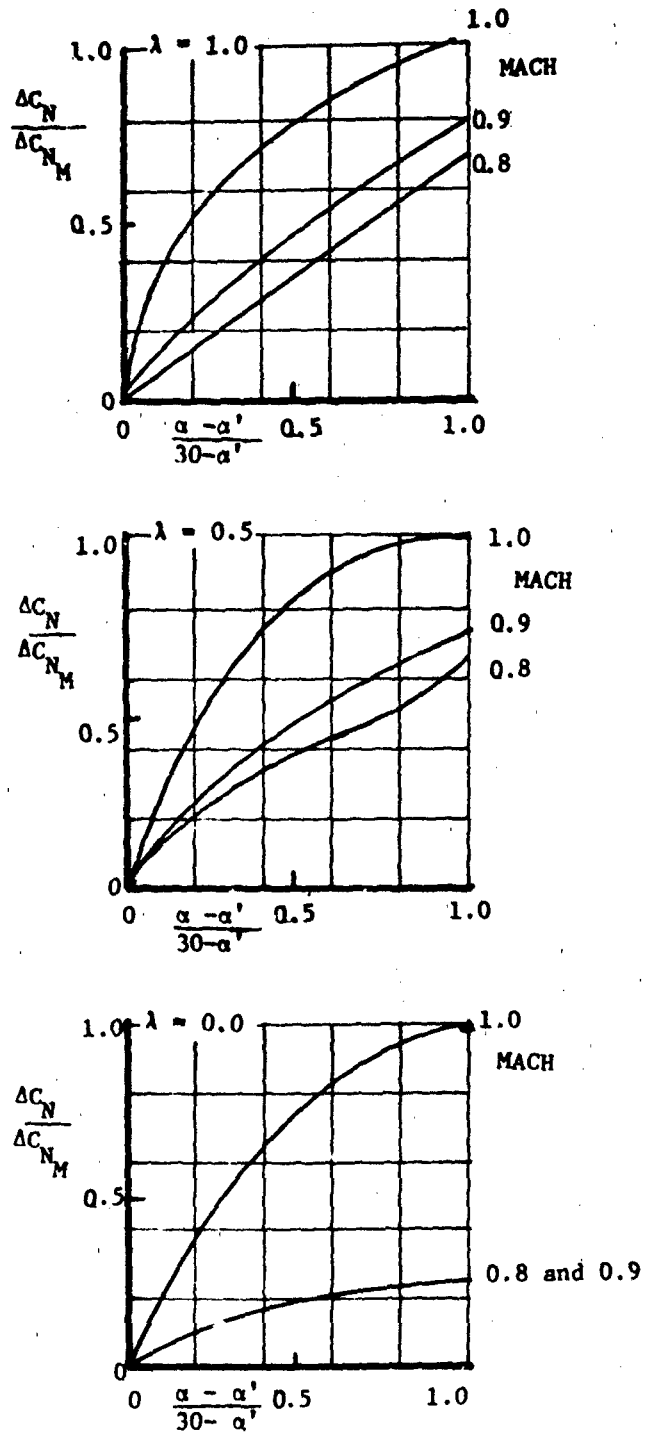


Figure 50. Dimensionless C_N Increment Above α'

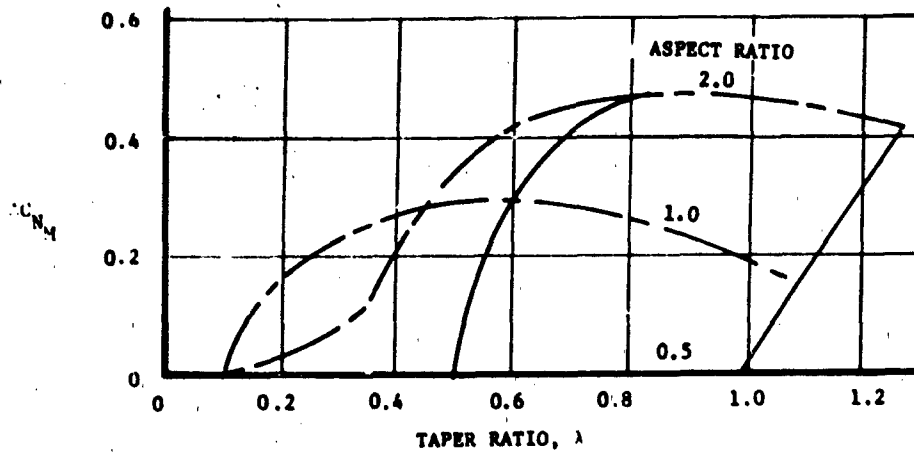


Figure 51. ΔC_{NM} Maximum Increment of Normal Force Above α' (Subsonic Only)

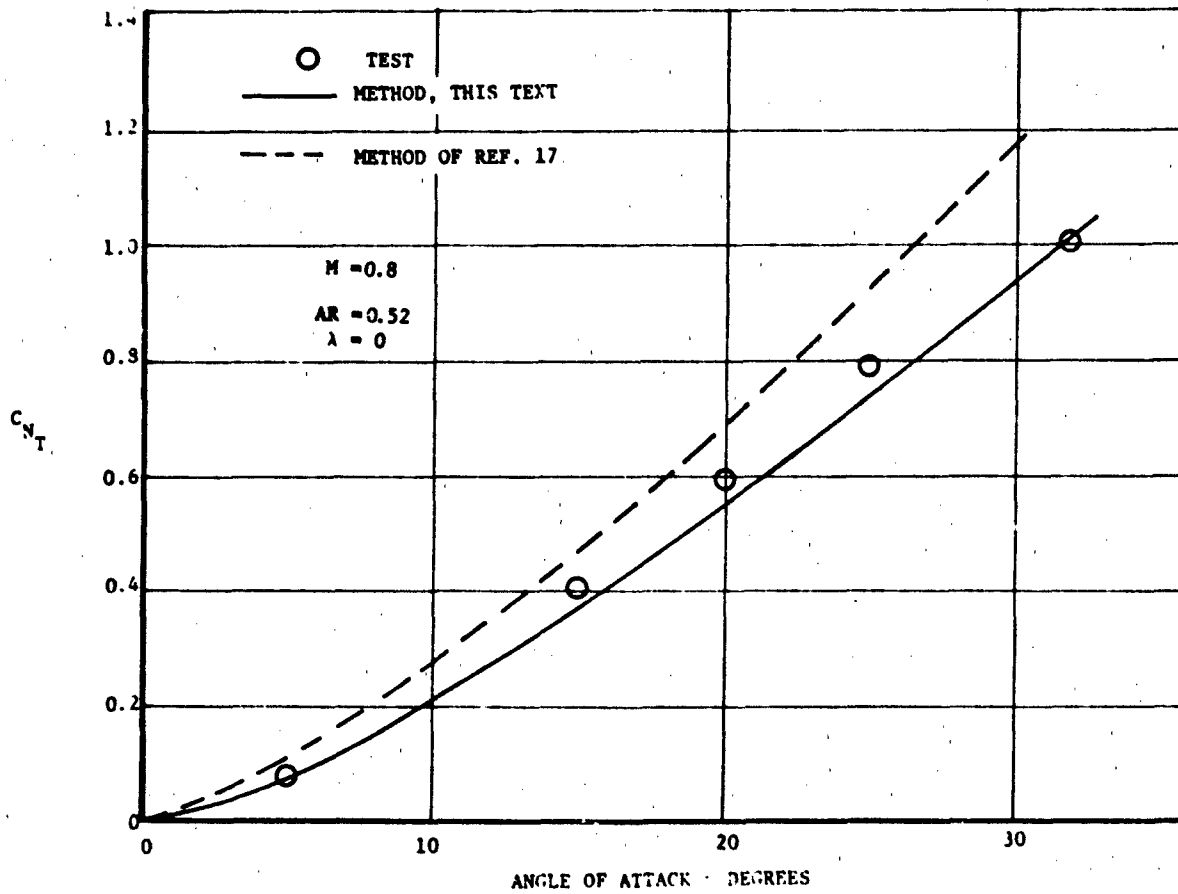


Figure 52. Comparison of Predicted and Experimental C_{NT} , Mach = 0.8

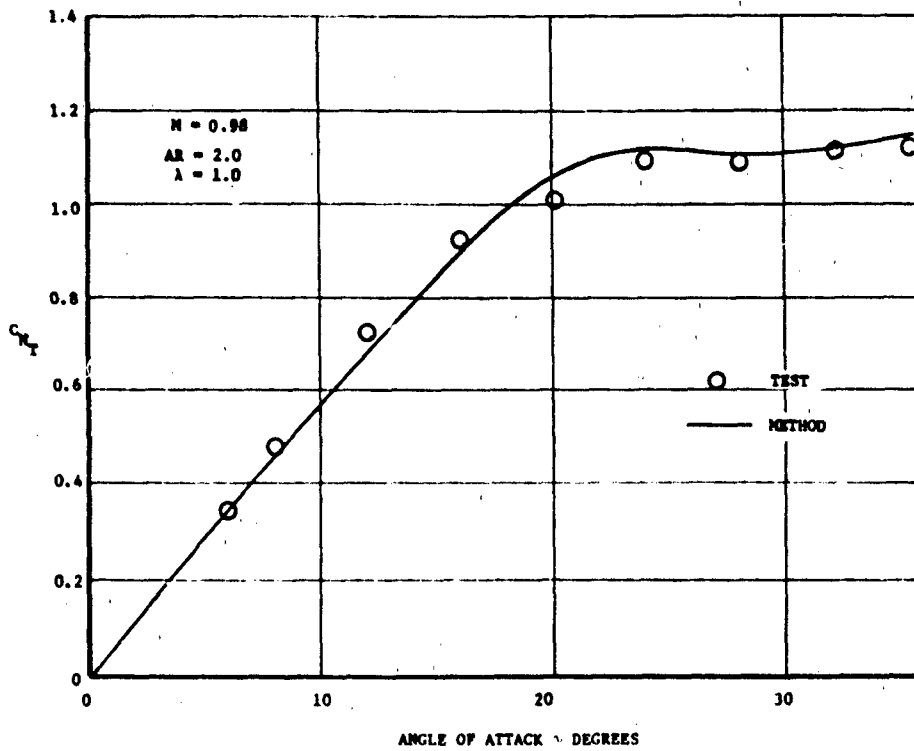


Figure 53. Comparison of Predicted and Experimental C_{N_T} ,
Mach = 0.98

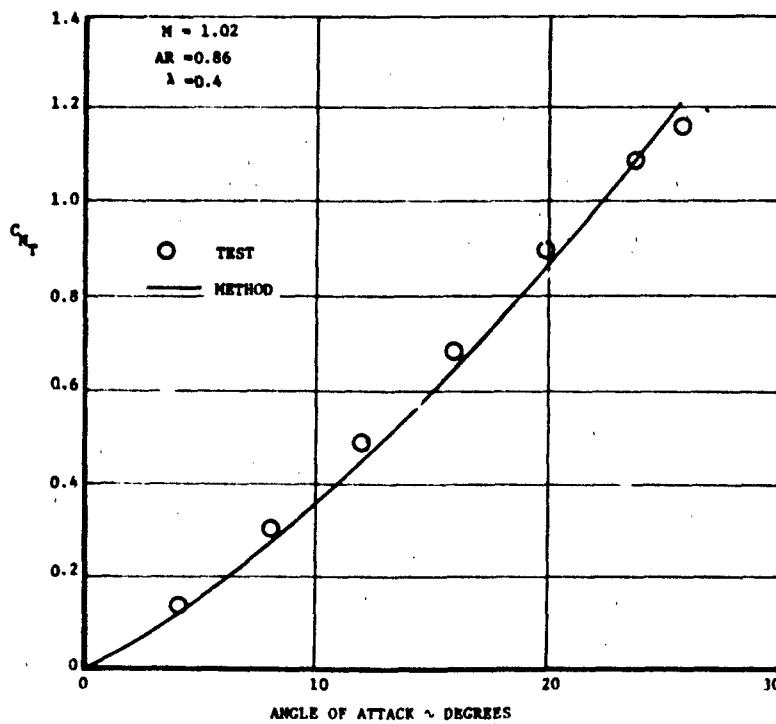


Figure 54. Comparison of Predicted and Experimental C_{N_T} ,
Mach = 1.02

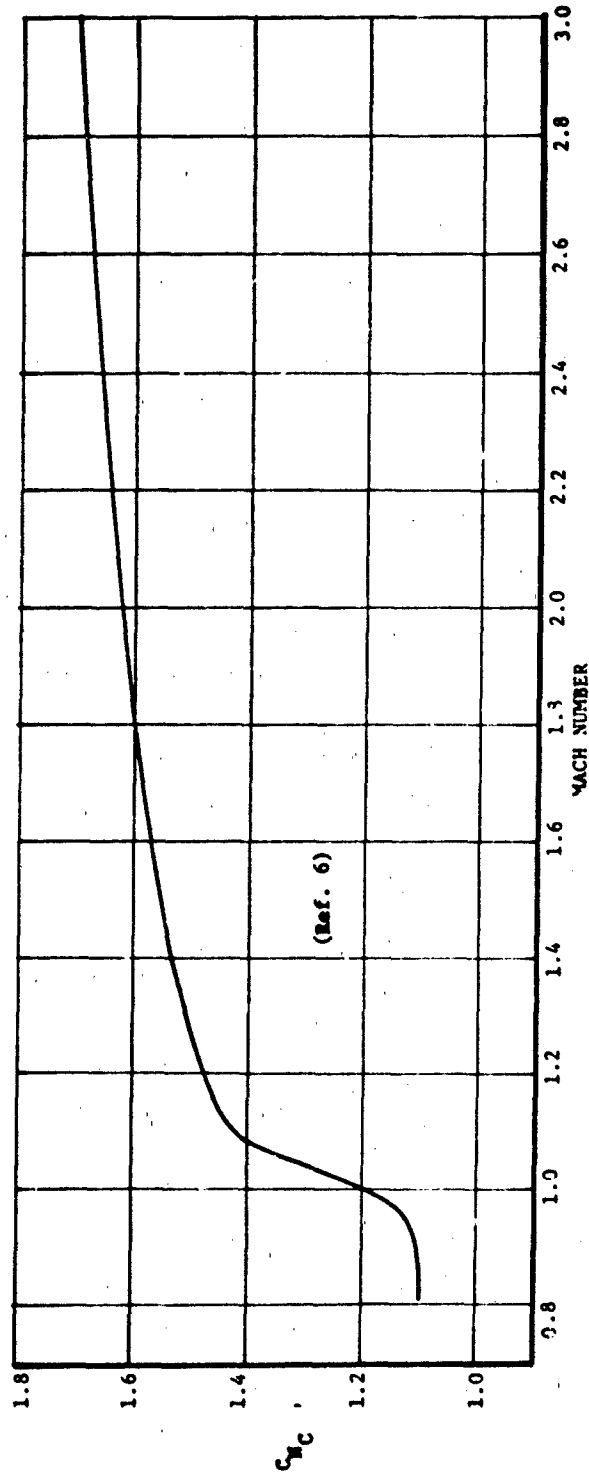


Figure 55. Variation of Pin Normal Force at $\alpha = 90$ Degrees With Mach Number

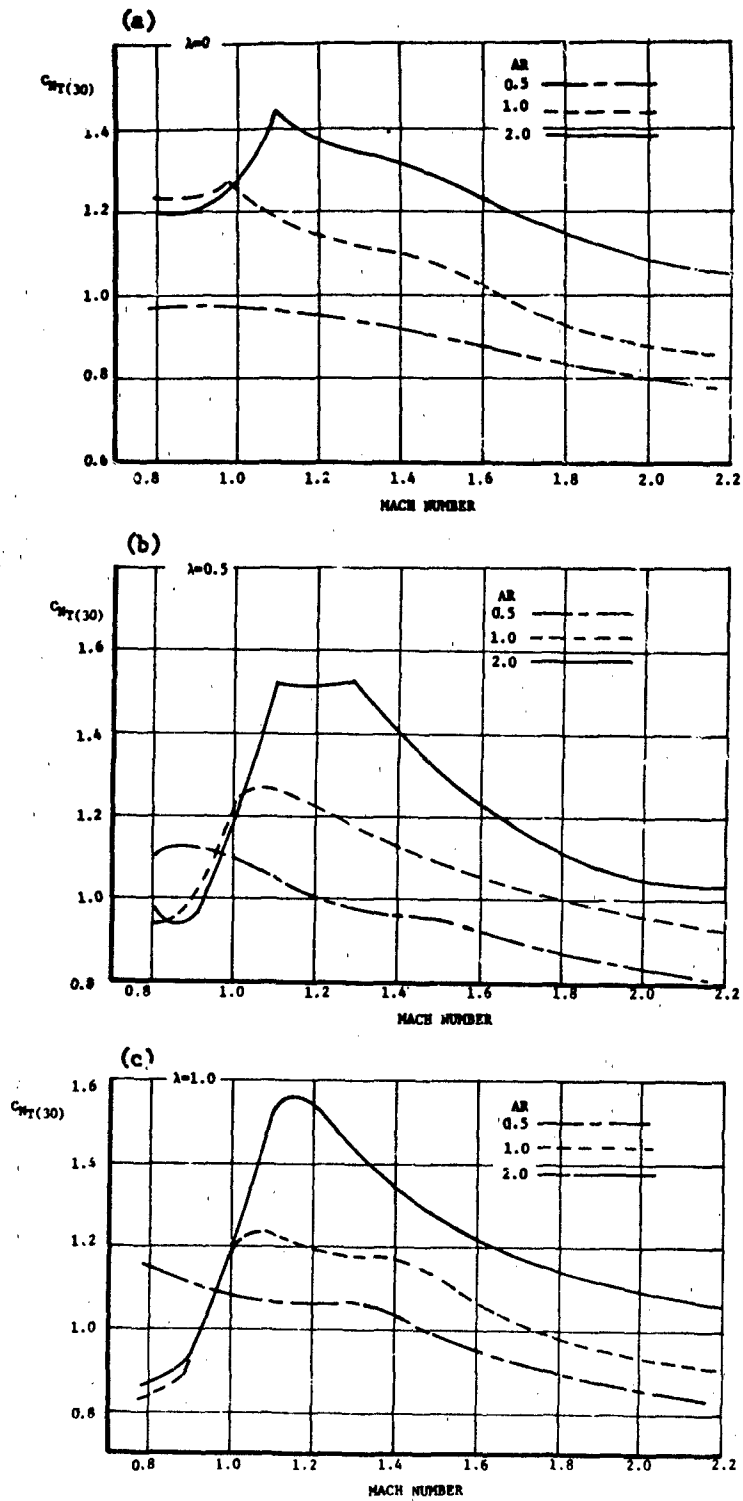


Figure 56. Variation of Normal Force Coefficient $C_{N_T}(30)$, With Mach Number, $\alpha = 30$ Degrees

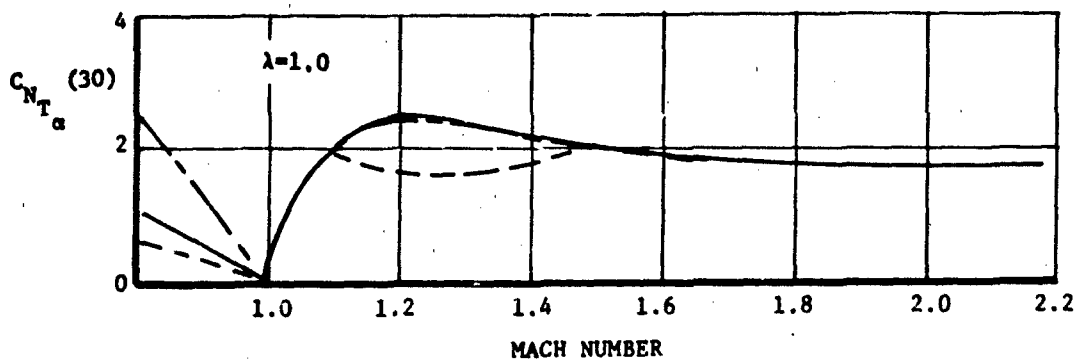
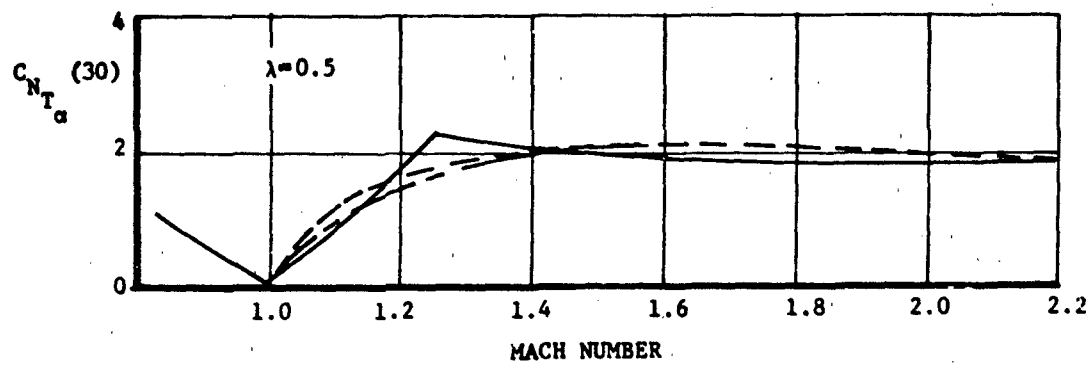
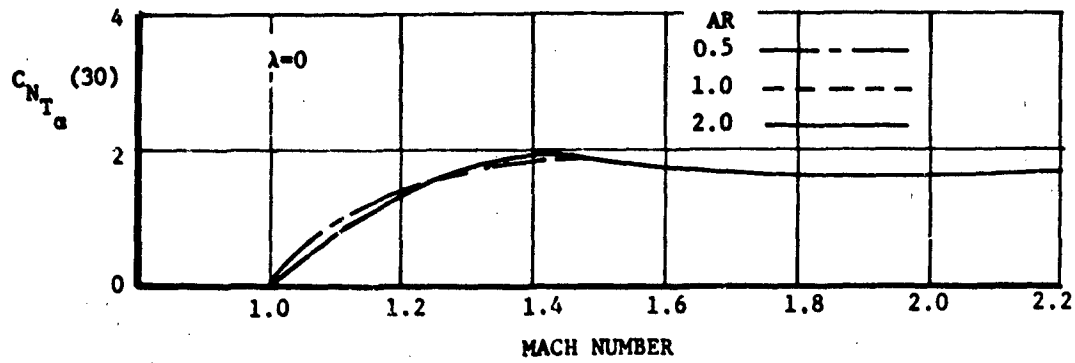


Figure 57. Variation of $C_{N_{T_a}} (30)$ With Mach Number

$$30 \leq \alpha \leq 90$$

$$C_{N_T} = C(\alpha)C_{N_T(30)} + D(\alpha)C_{N_C} + E(\alpha)C_{N_{T\alpha}(30)}$$

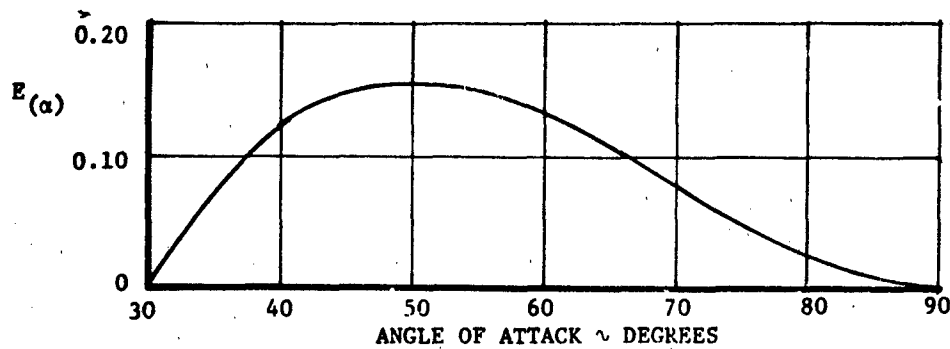
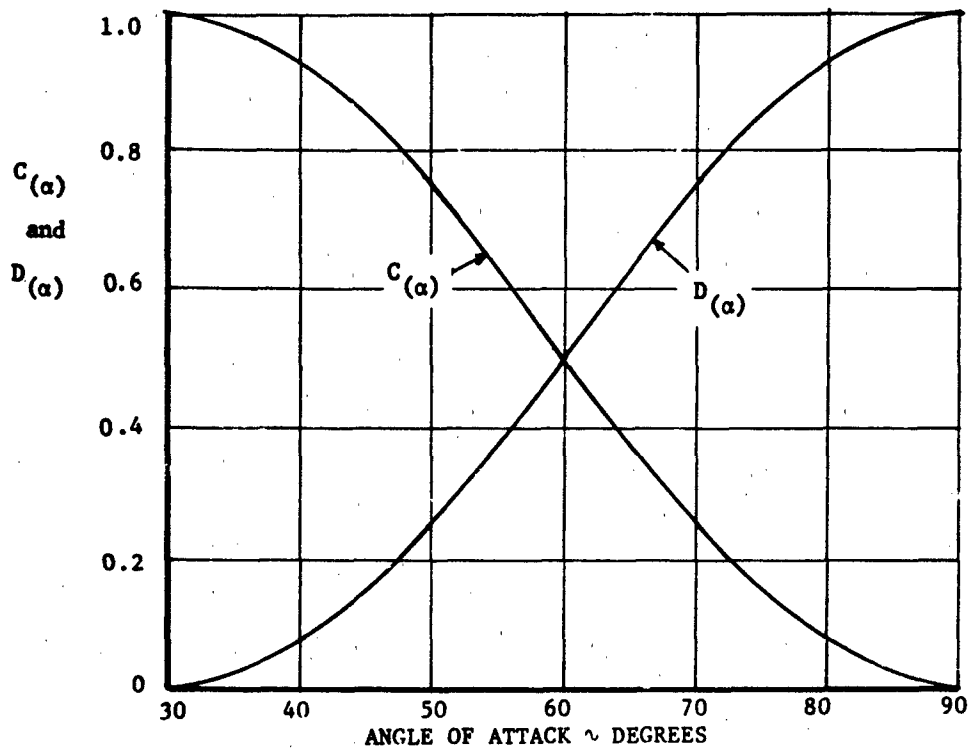


Figure 58. Power Series Parameters for Equation (26)

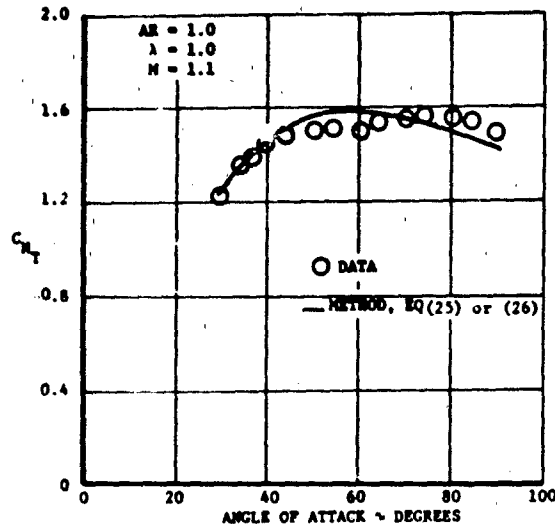


Figure 59. Comparison of Predicted and Experimental C_{N_T} From 30 to 90 Degree

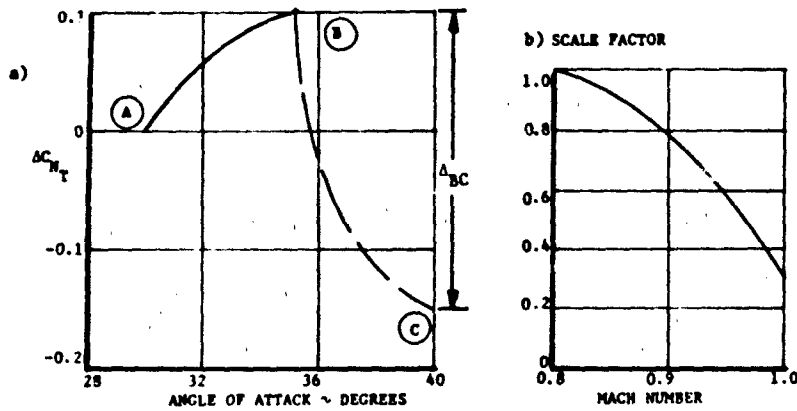


Figure 60. Curves for Modifying C_N Method ($\lambda=0$, $AR=1.0$, Subsonic)

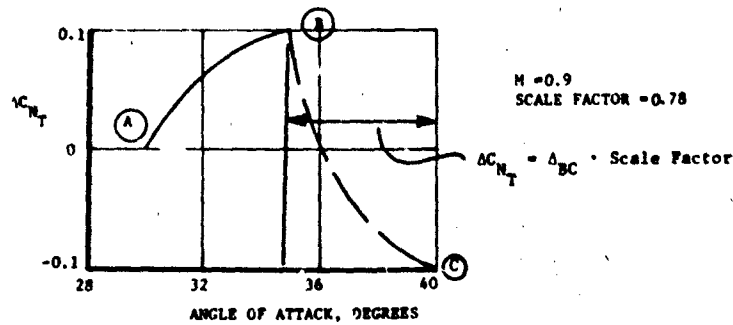


Figure 61. An Example Using ΔC_{N_T}

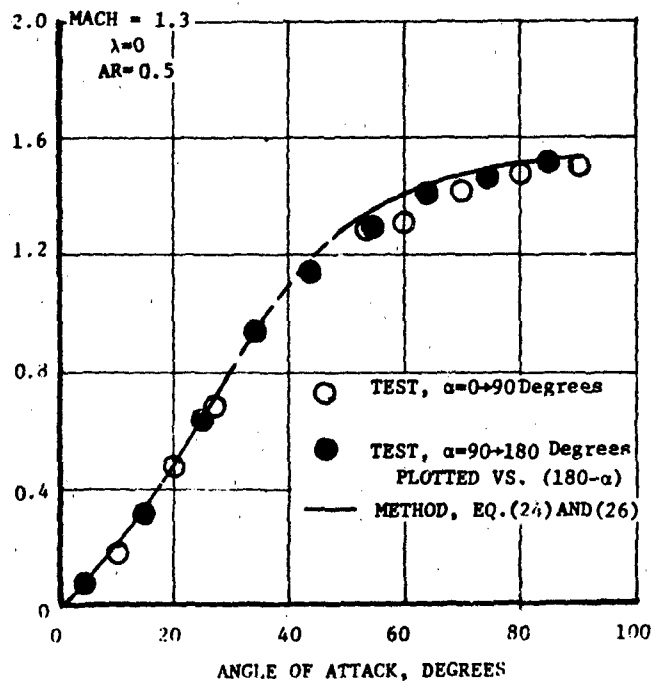
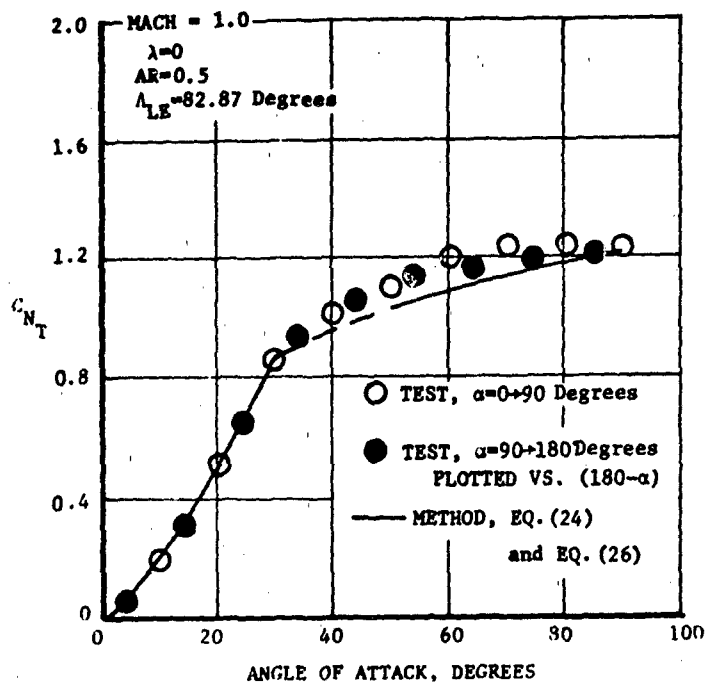


Figure 62. Comparison of Method and Test, C_{N_T} at $M = 1.0$ and 1.3 ($\lambda = 0, AR = 0.5$)

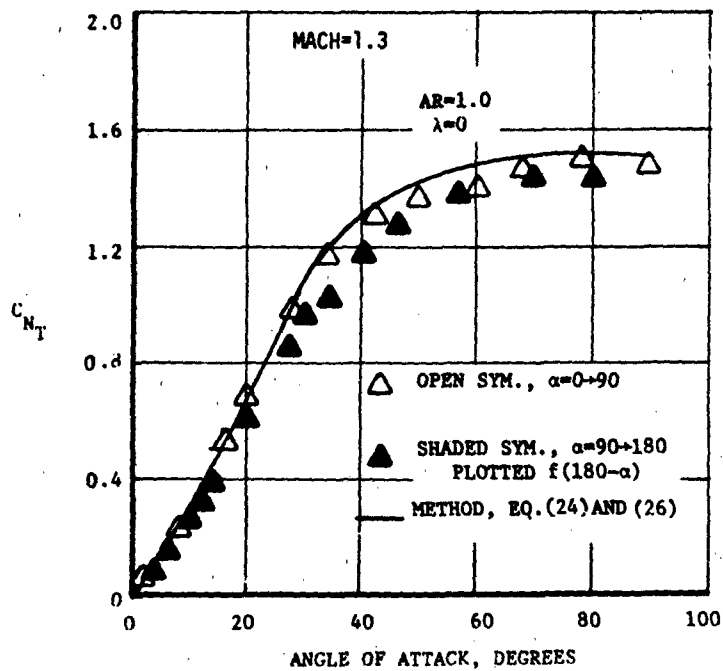
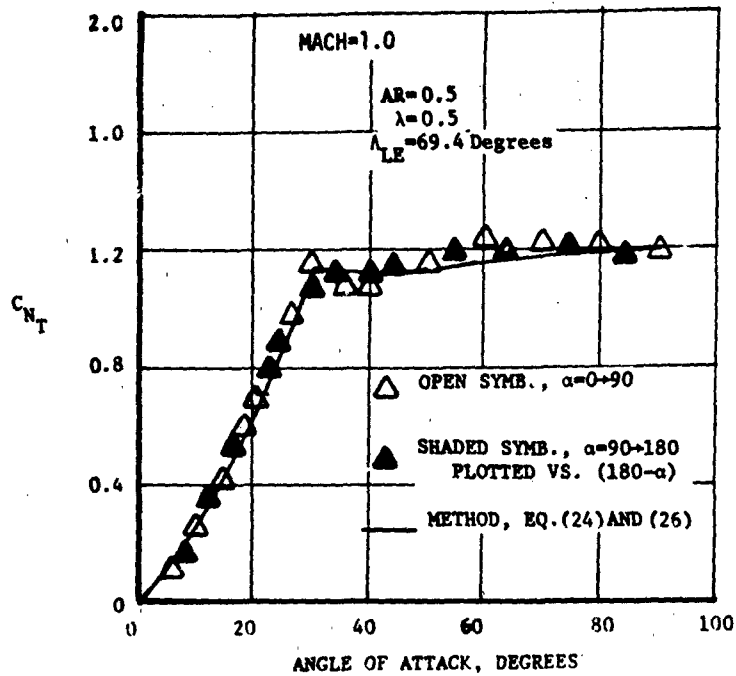


Figure 63. Comparison of Method and Test, C_{NT} at
 $M = 1.0$ ($\lambda = 0.5$, $AR = 0.5$) and
 $M = 1.3$ ($\lambda = 0.0$, $AR = 1.0$)

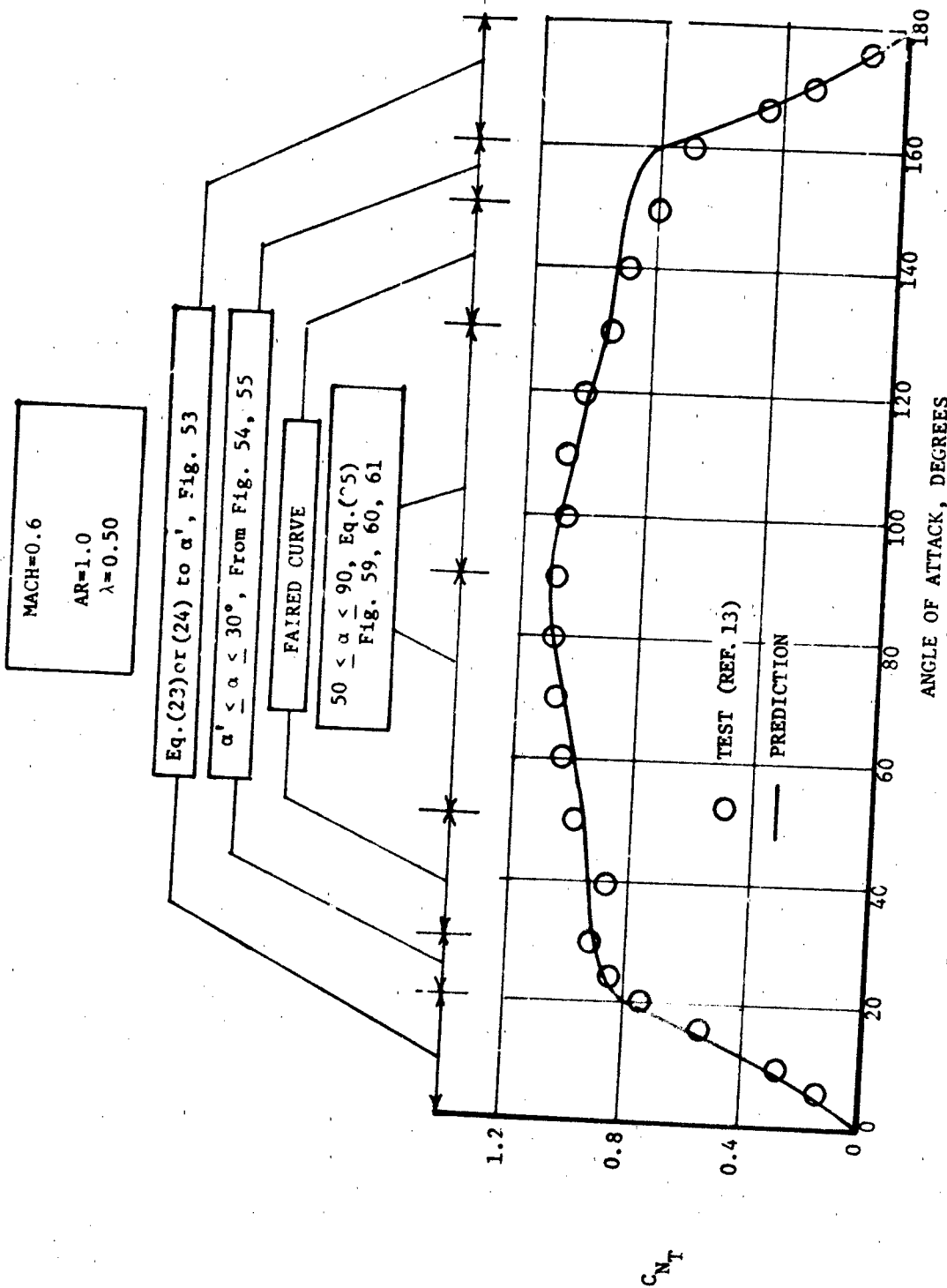


Figure 64. Comparison of Test to Prediction to 180 Degrees, Mach 0.6 (C_{N_T})

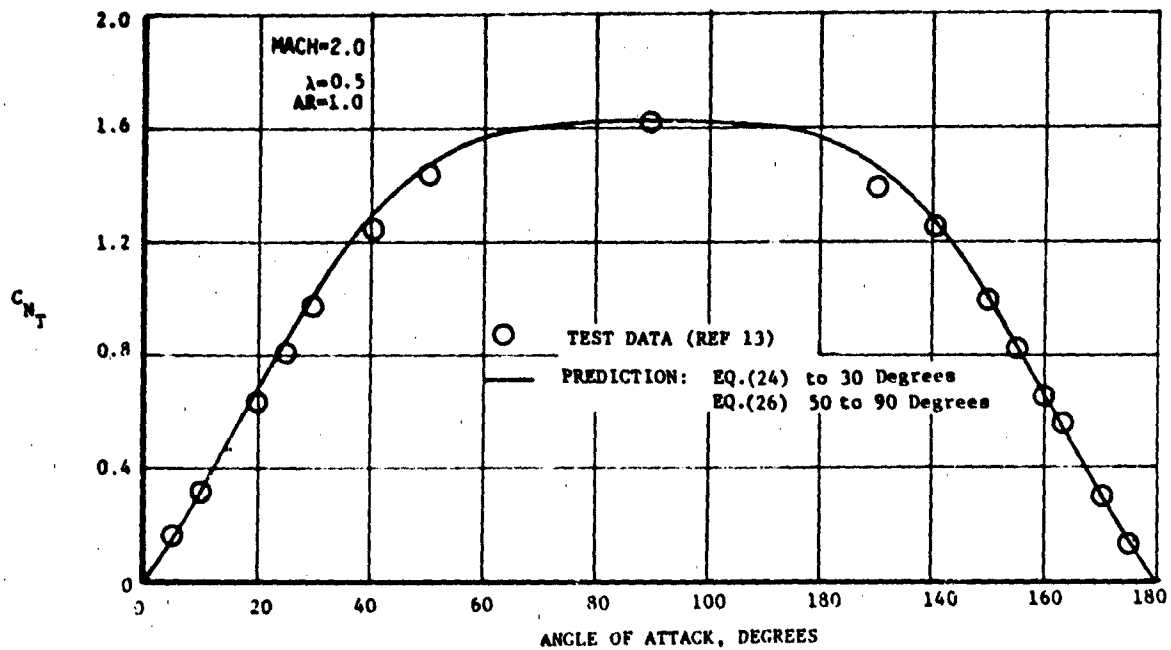


Figure 65. Comparison of Test and Method, Mach = 2.0 (C_{N_T})

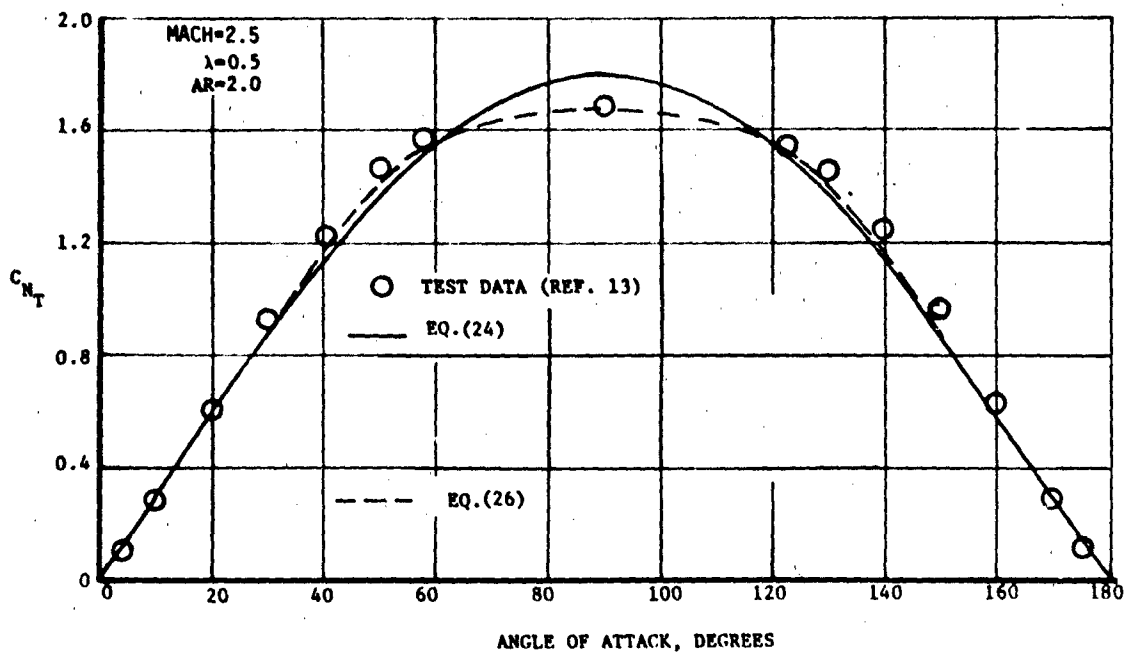


Figure 66. Comparison of Test and Method, M = 2.5 (C_{N_T})

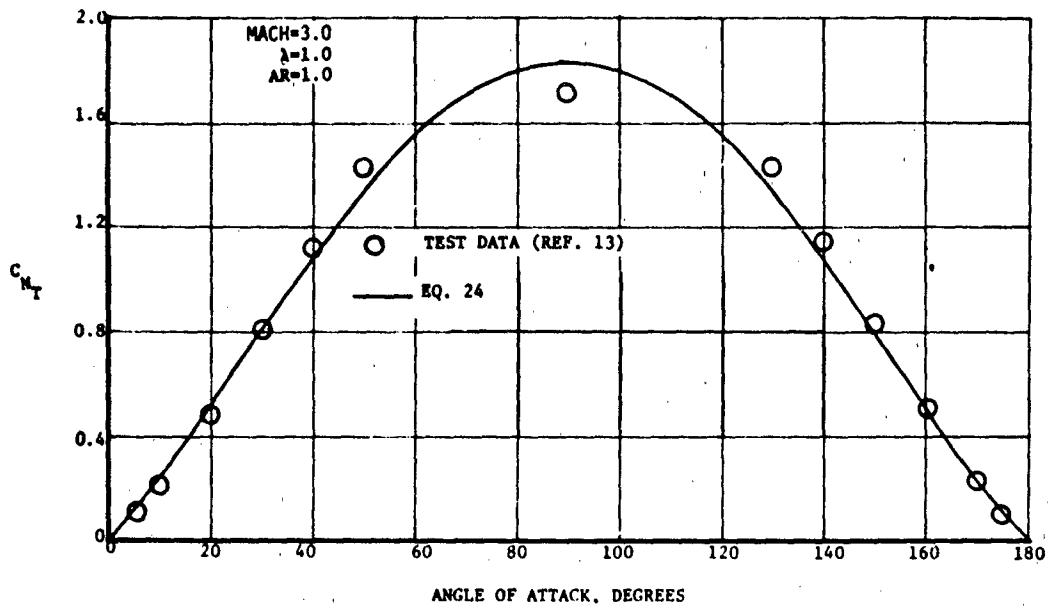


Figure 67. Comparison of Test and Method, Mach = 3.0
 (C_{N_T}) , $\lambda = 1.0$, AR = 1.0

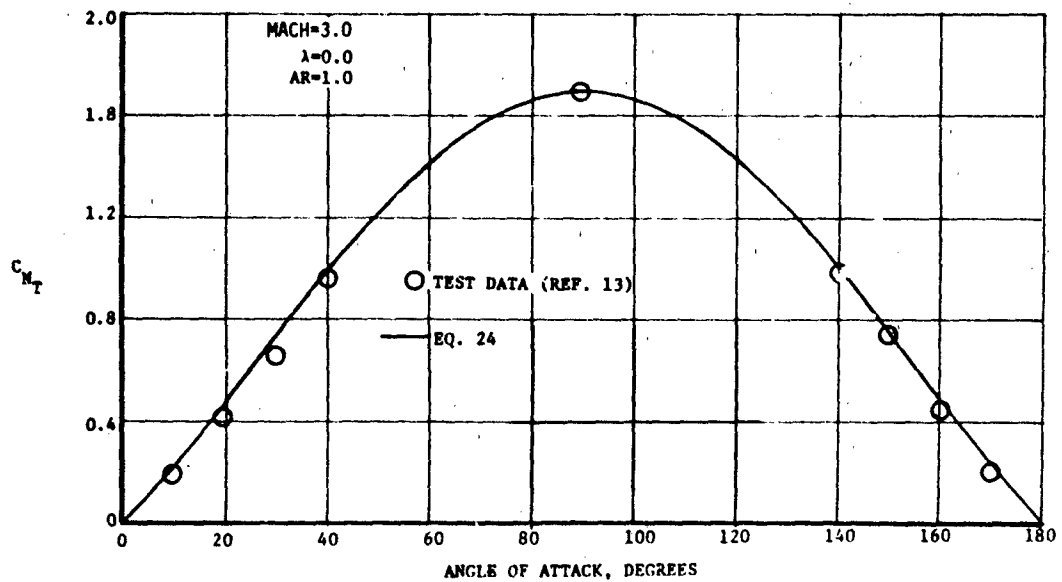


Figure 68. Comparison of Test and Method, Mach = 3.0
 (C_{N_T}) , $\lambda = 0.0$, AR = 1.0

5.1.5 Fin Chordwise Center of Pressure

Summary

A method is presented to predict X_{CP_T} , the chordwise center of pressure for low aspect ratio fins. The method is valid for angles of attack up to 180 degrees, and for Mach numbers in the range of 0.60 to 3.0. The method is an extension of the method presented in Reference 2, Section 3.3.2, and was made possible by the additional test data of Reference 13. The correlation method is shown to predict satisfactorily center of pressure location on typical missile fins. The results of this study apply to isolated lifting surfaces as well as to undeflected wings or tails fixed to missile bodies. The latter assertion is based on comparisons presented in Reference 2. The method is divided into two main divisions: 1) A procedure for estimating chordwise center of pressure at angles of attack to 90 degrees, and 2) A procedure for extending the estimates for angles between 90 and 180 degrees.

Background

The development of the first part ($\alpha = 0$ to 90 degrees) of the method is contained in Reference 2. A portion of that material will be included here for completeness.

Three basic theories: 1) Slender body theory, 2) Strip theory, and 3) Linear (fin alone) theory, are currently used in predicting chordwise center of pressure. These theories have been found to provide fair results at low angles of attack. However, as angle of attack is increased beyond the linear lift curve slope region the results become erroneous. Slender body and strip theory have been combined in developing a method for predicting chordwise center of pressure of a fin that is attached to a

cylindrical body. For a triangular fin, Reference 30 shows that all three methods give essentially the same results for the chordwise center of pressure of a fin in the presence of the body. This might have been expected, since the presence of a body induces an upwash that changes fin loading in the spanwise direction, thus having little effect on the chordwise load distribution. Reference 30 also showed that the fin alone linear theory is best for representing the chordwise center of pressure of low aspect ratio fins. However, due to the inability of this theory to predict accurately fin center of pressure beyond the region of linear lift, additional prediction methodology in this area obviously is needed.

Method Development

To generate the methods, center of pressure chordwise location for a tail alone was calculated from normal force and hinge moment test data (References 13 and 31). These tests featured isolated tail panels mounted on reflection planes that were deflected (rotated) throughout a range of $\alpha = 0$ to 180 degrees. The Mach number range of these test data is from Mach 0.60 to 3.0. Tail panel geometric parameters include three aspect ratios (AR = 0.5, 1.0 and 2.0) and three taper ratios ($\lambda = 0.0, 0.5$ and 1.0). The chordwise center of pressure location is referenced to the juncture of the tail panel leading edge and reflection plane, and the resulting center of pressure is non-dimensionalized on the basis of panel root chord.

The data were analyzed for similarities and significant parameters, knowing that the expression for the location of the center of pressure is, in general,

$$\frac{X_{CP}}{C_R} = \frac{X_{CP}}{C_R} (M, \alpha, \lambda, AR). \quad (27)$$

Examination of the data showed that AR was the least significant of the above parameters. This implies that the dependency of hinge moment on AR is due to the dependency of normal force on this quantity. Keeping in mind that AR is not a strong parameter, the expression for $\frac{X_{CP}}{C_R}$ is defined as a function of α and λ at selected values of AR and Mach 0.98.

The description of the method proceeds as follows. Presented first is the technique used to correlate the variation in center of pressure position with angle of attack at a fixed Mach number (basic Mach 0.98) for various combinations of aspect ratio and taper ratio. It is noted that the variation with α is subdivided into four subsets consisting of; $\alpha = 90^\circ$, $0 \leq \alpha < 90^\circ$, $90^\circ < \alpha \leq 160^\circ$ and $160^\circ < \alpha \leq 180^\circ$.

Following the correlation at $M = 0.98$, a technique is presented which permits calculation of the $\frac{X_{CP}}{C_R}$ for Mach numbers between 0.6 and 3.0.

Region I ($\alpha = 90$ degrees)

The chordwise center of pressure of a tail panel at 90 degrees can be thought of as the focal point or basis for the correlation method. The aerodynamic loading of a tail panel positioned normal to the flow ($\alpha = 90$ degrees) is considered to be uniform. To the extent that this is true, $\frac{X_{CP}}{C_R}$ of the tail will coincide with the centroid of the panel area. In addition, this relationship should be independent of Mach number. References 13 and 31 show this assessment to be valid. The test data for a $\lambda = 0.5$ tail panel can be seen in Figure 69. As shown, the area centroid of the panel and center of pressure nearly coincide at $\alpha = 90$ degrees. Therefore, at $\alpha = 90$ degrees the chordwise center of pressure (X_{CP}/C_R) will be determined by the area centroid. For a nonswept trailing edge planform,

area centroid is only a function taper ratio as shown in Figure 70.

It should be noted here that boundary layer separation occurred on the reflection plane in front of the tails during some of the supersonic tests when the fins were nearly normal to the flow. The fins behaved like forward facing steps, with the result that the C_{NT} data is rendered meaningless and so was discarded. To fill the gap, the data from the subsonic tests, where separation did not occur, were supplemented with supersonic data from Reference 6 on flat plates normal to the stream in place of the supersonic test data where separation occurred. The latter data proved to be compatible with the data generated during Martin Marietta test programs.

Region II ($\alpha < 90$ degrees)

Examination of the $\alpha = 0$ to 180 degree data, as shown in Figure 69, shows a smooth variation in center of pressure in the vicinity of $\alpha = 90$ degrees. The method used for predicting X_{CP}/C_R at angles of attack below 90 degrees was presented in Reference 2. This procedure has been extended in Mach number and will be restated for completeness.

The relationship between X_{CP}/C_R and α is plotted in Figure 71 for the three test aspect ratios ($AR = 0.5, 1.0$ and 2.0) at the basic Mach number 0.98 . Mach number effects on X_{CP}/C_R must be included in such a manner that will allow its influence to vanish at $\alpha = 90$ degrees. Thus, for the region $\alpha < 90$ degrees, the chordwise center of pressure is given by:

$$\frac{X_{CP}}{C_R} = \left. \frac{X_{CP}}{C_R} \right|_{\alpha=90} - \left(\Delta \frac{X_{CP}}{C_R} \right)_{\alpha<90} [1 + F(\text{Mach})] \quad (28)$$

where

$$\left(\Delta \frac{X_{CP}}{C_R} \right)_{\alpha<90} = \left. \frac{X_{CP}}{C_R} \right|_{\alpha=90} - \left. \frac{X_{CP}}{C_R} \right|_{\alpha<90}$$

Therefore, at any angle of attack less than 90 degrees, the difference in X_{CP}/C_R between the particular α in question and that at 90 degrees, is subtracted from the 90 degree (centroid of area) value. For Mach 0.98, $F(\text{Mach})$ is equal to zero. Center of pressure variations for Mach numbers other than 0.98 will be discussed following the complete range ($\alpha = 0$ to 180 degrees) of angle of attack effects. It should be noted that Equation 28 has been revised slightly from its presentation in Reference 2 due to evaluation of additional test data in Reference 13.

Region III ($\alpha > 90$ to 160 degrees)

Upon close examination of the test data (Reference 13 and 31) it was found that a linear variation could be adopted between $\alpha = 90$ and 160 degrees. Thus, the magnitude of X_{CP}/C_R for each end condition ($\alpha = 90$ and 160 degrees) will be required. The value of X_{CP}/C_R at $\alpha = 90$ degrees, as previously stated, coincides with the panel centroid of area. The value of X_{CP}/C_R at $\alpha = 160$ degrees for the basic Mach number 0.98 can be obtained directly from Figure 71. Although the value of X_{CP}/C_R at $\alpha = 90$ degrees is independent of Mach number, the value at $\alpha = 160$ degrees is not. This Mach number variation, while differing from that associated with region II ($\alpha < 90$ degrees), also will be forthcoming.

Region IV ($\alpha > 160$ to 180 degrees)

For the region between 160 and 180 degrees angle of attack a power series approach was used in lieu of the graphical type solution of region II ($\alpha < 90$ degrees). Test data indicate that tail normal force and hinge moments are linear from $\alpha = 175$ to 180 degrees; thus center of pressure is constant. Chordwise center of pressure data for $\alpha = 175$ to 180 degrees are presented in Figure 72 and are the basis for the second half ($\alpha > 90$ degrees)

of the correlation method. A power series solution was used in establishing the center of pressure variation between the two angles of attack ($\alpha = 160$ to 175 degrees). Upon examination of the available test data in this region a third order series equation was considered satisfactory and in the usual way boundary conditions were sought. Magnitudes of X_{CP}/C_R at $\alpha = 160$ and 175 degrees were used to fix both ends of the curve. The slopes of X_{CP}/C_R at these end conditions, viz.,

$$\frac{\partial \left(\frac{X_{CP}}{C_R} \right)}{\partial \alpha} = \left[\frac{\left. \frac{X_{CP}}{C_R} \right|_{\alpha=160} - \left. \frac{X_{CP}}{C_R} \right|_{\alpha=90}}{\left(\frac{70}{180} \right) \pi} \right] \text{ at } \alpha = 160^\circ, \text{ and}$$

$$\frac{\partial (X_{CP}/C_R)}{\partial \alpha} = 0 \text{ at } \alpha = 175^\circ, \text{ were used as the third and fourth boundary conditions.}$$

Applying these boundary conditions to the following power series:

$$X_{CP}/C_R = A_0 + A_1 \alpha + A_2 \alpha^2 + A_3 \alpha^3 \quad (29)$$

yielded the equation:

$$\frac{X_{CP}}{C_R} = \left. \frac{X_{CP}}{C_R} \right|_{\alpha=175} + B(\alpha) \left(\Delta \frac{X_{CP}}{C_R} \right)_{\alpha > 90} + C(\alpha) \left[\frac{\left. \frac{X_{CP}}{C_R} \right|_{\alpha=160} - \left. \frac{X_{CP}}{C_R} \right|_{\alpha=90}}{\left(\frac{70}{180} \right) \pi} \right] \quad (30)$$

$$\text{where } B(\alpha) = 112.75928 - 81.4741(\alpha) + 14.58789(\alpha^2)$$

$$C(\alpha) = -32.57471 + 22.32592(\alpha) - 3.81911(\alpha^2)$$

$$\left(\Delta \frac{X_{CP}}{C_R} \right)_{\alpha > 90} = \left. \frac{X_{CP}}{C_R} \right|_{\alpha=175} - \left. \frac{X_{CP}}{C_R} \right|_{\alpha=160}$$

$$\left. \frac{X_{CP}}{C_R} \right|_{\alpha=160} = \left. \frac{X_{CP}}{C_R} \right|_{\alpha=160} + \Delta_1 \left(\frac{X_{CP}}{C_R} \right)$$

$M=0.98$

The $\Delta_1(X_{CP}/C_R)$ term accounts for Mach number effects at Mach numbers other than Mach 0.98. It should be noted that Mach number corrections are limited to the term X_{CP}/C_R at 160 degrees in equation 30 because X_{CP}/C_R at 175 degrees (Figure 72) is already Mach number dependent. Values of $B(\alpha)$ and $C(\alpha)$ versus angle of attack are given in Figure 73. Thus equation 30 permits calculation of X_{CP}/C_R as a function of α in the range from $\alpha = 160$ to $\alpha = 175$ degrees.

Effect of Mach Number Variation on X_{CP}/C_R

The influence of Mach number on the center of pressure has been accounted for by two methods. These methods are dependent upon the angle of attack region, i.e., $\alpha < 90$ degrees or $\alpha > 90$ degrees. This results from the fact that the center of pressure is independent of Mach number at $\alpha = 90$ degrees.

Effect of Mach Number Variation at $\alpha < 90^\circ$

For angles of attack below 90 degrees the effect of Mach number is presented as a percent change in the basic $(\Delta X_{CP}/C_R)_{\alpha < 90}$ value of equation (28). It is recalled that the basic $(\Delta \frac{X_{CP}}{C_R})_{\alpha < 90}$ value, which represents the increment in X_{CP}/C_R existing between $\alpha = 90$ degrees to any $\alpha < 90$ degrees, corresponds to the basic Mach 0.98. The Mach number variation parameter $F(\text{Mach})$ of equation (28), which is determined by the measured difference in X_{CP}/C_R between Mach 0.98 and the other Mach numbers, is shown in Figure 74 as a function of aspect ratio. Thus, for angles of attack less than 90 degrees, the basic X_{CP}/C_R value can be modified to reflect the effects of Mach number from Mach 0.6 to 3.0.

Effect of Mach Number Variation at $\alpha > 90^\circ$

Mach number variations of X_{CP}/C_R for angles of attack greater than 90 degrees are accounted for in a slightly different manner. As previously

mentioned, the value of $X_{CP}/C_R \Big|_{\alpha=160}$ in equation (30) is not Mach number dependent and must be modified to include the effect of Mach number. This is accomplished by adjusting the basic X_{CP}/C_R value at $\alpha = 160$ degrees as follows:

$$\frac{X_{CP}}{C_R} \Big|_{\alpha=160} = \frac{X_{CP}}{C_R} \Big|_{\substack{\alpha=160 \\ M=0.98}} + \Delta_1 \left(\frac{X_{CP}}{C_R} \right).$$

The $\Delta_1(X_{CP}/C_R)$ term, which is merely an increment applied to the basic value of center of pressure at $\alpha = 160$ degrees, was determined by fairing a curve through the measured difference between X_{CP}/C_R at $M = 0.98$ and $M > 0.98$ for $\alpha = 160$ degrees. The magnitude of $\Delta_1(X_{CP}/C_R)$ for Mach > 1.0 is shown in Figure 75. For Mach < 0.98 no correction is required.

The effect of Mach number at $\alpha = 175$ degrees is accounted for as shown in Figure 72. Thus, the correction for Mach number at $\alpha = 160$ degrees completes Mach number variation for angles of attack greater than 90 degrees.

Use of Method

This section will demonstrate the use of the method in predicting X_{CP}/C_R for angles of attack from 0 to 180 degrees at $M = 1.15$ where the physical characteristics of the fin are:

$$AR = 1.0$$

$$\lambda = 0.5$$

First a general description of the method will be presented. This will be followed by a numerical example. The results will be compared against experimental data.

1 Calculate X_{CP}/C_R at $\alpha = 0$ to 90 degrees:

- a Using Figure 70 find X_{CP}/C_R at $\alpha = 90$ degrees;
- b Using Figure 71 find X_{CP}/C_R at desired angle of attack;
- c Calculate $(\Delta X_{CP}/C_R)_{\alpha < 90}$ at the desired angle of attack by using the following expression

$$\left(\Delta \frac{X_{CP}}{C_R} \right)_{\alpha < 90} = \frac{X_{CP}}{C_R} \Big|_{\alpha=90} - \frac{X_{CP}}{C_R} \Big|_{\alpha < 90}$$

- d Using Figure 74 find the function $F(\text{Mach})$ at the desired Mach number;

- e Using equation (28) calculate X_{CP}/C_R :

$$\frac{X_{CP}}{C_R} = \frac{X_{CP}}{C_R} \Big|_{\alpha=90} - \left(\Delta \frac{X_{CP}}{C_R} \right)_{\alpha < 90} [1 + F(\text{Mach})].$$

2 Calculate X_{CP}/C_R at $\alpha > 90$ to 180 degrees:

- a Use value from 1(a) above for X_{CP}/C_R at $\alpha = 90$ degrees;
- b Using Figure 71 find X_{CP}/C_R at $\alpha = 160$ degrees;
- c Using Figure 72 find X_{CP}/C_R at $\alpha = 175$ degrees;
- d Using Figure 75 find $\Delta_1 (X_{CP}/C_R)$ for desired Mach number;
- e Calculate X_{CP}/C_R at $\alpha = 160$ for desired Mach number

as follows

$$\frac{X_{CP}}{C_R} \Big|_{\alpha=160} = \frac{X_{CP}}{C_R} \Big|_{\alpha=160} + \Delta_1 \left(\frac{X_{CP}}{C_R} \right);$$

$M=0.98$

- f Calculate $(\Delta X_{CP}/C_R)_{\alpha > 90}$ as follows

$$\left(\Delta \frac{X_{CP}}{C_R} \right)_{\alpha > 90} = \frac{X_{CP}}{C_R} \Big|_{\alpha=175} - \frac{X_{CP}}{C_R} \Big|_{\alpha=160}$$

a Calculate initial slope at $\alpha = 160$ degrees;

$$\text{Initial Slope} = \frac{\left[\frac{X_{CP}}{C_R} \Big|_{\alpha=160} - \frac{X_{CP}}{C_R} \Big|_{\alpha=90} \right]}{(70/180)\pi}$$

h Using Figure 73 find $B(\alpha)$ and $C(\alpha)$ at desired α ;

i Calculate X_{CP}/C_R using equation 30

$$\frac{X_{CP}}{C_R} = \frac{X_{CP}}{C_R} \Big|_{\alpha=175} + B(\alpha) \left(\frac{X_{CP}}{C_R} \Big|_{\alpha>90} \right) + C(\alpha) \left[\frac{\frac{X_{CP}}{C_R} \Big|_{\alpha=160} - \frac{X_{CP}}{C_R} \Big|_{\alpha=90}}{(70/180)\pi} \right]$$

3 Using the results of steps 1 and 2 combined with X_{CP}/C_R for $\alpha = 90$ degrees, the chordwise center of pressure for a given fin can be determined throughout an angle of attack range of $\alpha = 0$ to 180 degrees.

Numerical Example

Following are the results obtained when the previous procedures are applied:

1 Calculate X_{CP}/C_R variation with α ($\alpha = 0$ to 90 degrees) for the following fin geometry at $M = 1.15$.

$$AR = 1.0$$

$$\lambda = 0.5$$

a Using Figure 70, $X_{CP}/C_R \Big|_{\alpha=90} = 0.611$

b Using Figure 71, X_{CP}/C_R at various α 's up to 90 degrees;

α ($^\circ$ deg)	$\left(\frac{X_{CP}}{C_R}\right)_{M=0.98}$
0-5	0.407
10	0.455
20	0.505
30	0.542
40	0.550
60	0.583
90	0.611

c Calculating $(\Delta \frac{X_{CP}}{C_R})_{\alpha < 90}$ from the results of (a) and (b)

α ($^\circ$ deg)	$(\Delta \frac{X_{CP}}{C_R})_{\alpha < 90}$
0-5	0.204
10	0.156
20	0.106
30	0.069
40	0.061
60	0.028
90	0.0

d Using Figure 74, $F(\text{Mach}) = -0.160$

e Using equation (28), X_{CP}/C_R is:

α ($^\circ$ deg.)	$\left.\frac{X_{CP}}{C_R}\right _{\alpha=90}$	$\left(\Delta \frac{X_{CP}}{C_R}\right)_{\alpha < 90}$	$1 + F(\text{Mach})$	$\frac{X_{CP}}{C_R}$
0-5	0.611	0.204	0.84	0.4396
10	0.611	0.156	0.84	0.4800
20	0.611	0.106	0.84	0.5220
30	0.611	0.069	0.84	0.5530
40	0.611	0.061	0.84	0.5598
60	0.611	0.028	0.84	0.5875
90	0.611	0.0	0.84	0.611

2 Calculate the remaining variation with alpha ($90 < \alpha \leq 180$ degrees) at $M = 1.15$

a From step 1a, $\left(\frac{X_{CP}}{C_R}\right)_{\alpha=90} = 0.611$

b Using Figure 71, $\left(\frac{X_{CP}}{C_R}\right)_{\alpha=160} = 0.748$
 $M=0.98$

c Using Figure 72, $\left(\frac{X_{CP}}{C_R}\right)_{\alpha=175} = 0.907$

d Using Figure 75, $\Delta_1 \left(\frac{X_{CP}}{C_R}\right) = -0.010$

e Calculate X_{CP}/C_R at $\alpha = 160^\circ$ for $M = 1.15$

$$\left.\frac{X_{CP}}{C_R}\right|_{\alpha=160} = \left.\frac{X_{CP}}{C_R}\right|_{\alpha=160} + \Delta_1 \left(\frac{X_{CP}}{C_R}\right) = 0.748 - 0.010 = 0.738$$

$M=0.98$

f Calculate $\left(\Delta \frac{X_{CP}}{C_R}\right)_{\alpha > 90}$ for $M = 1.15$

$$\left(\Delta \frac{X_{CP}}{C_R}\right)_{\alpha > 90} = \left.\frac{X_{CP}}{C_R}\right|_{\alpha=175} - \left.\frac{X_{CP}}{C_R}\right|_{\alpha=160} = 0.907 - 0.738 = 0.169$$

g Calculate initial slope at $\alpha = 160$ degrees

$$\text{Initial Slope} = \left[\frac{\left.\frac{X_{CP}}{C_R}\right|_{\alpha=160} - \left.\frac{X_{CP}}{C_R}\right|_{\alpha=90}}{(70/180)\pi} \right] = \left[\frac{0.738 - 0.611}{(70/180)\pi} \right] = 0.10395$$

h Using Figure 73, $B(\alpha)$ and $C(\alpha)$ are;

α (deg)	$B(\alpha)$	$C(\alpha)$
90	-	-
160	-1.0	0
165	-0.885	0.058
170	-0.550	0.058
175-180	0	0

i Using equation (30) to calculate X_{CP}/C_R

$$\frac{X_{CP}}{C_R} = \frac{X_{CP}}{C_R} \Big|_{\alpha=175} + B(\alpha) \left(\Delta \frac{X_{CP}}{C_R} \Big|_{\alpha>90} \right) + C(\alpha) \left[\frac{X_{CP}}{C_R} \Big|_{\alpha=160} - \frac{X_{CP}}{C_R} \Big|_{\alpha=90} \right] \frac{1}{(70/180)\pi}$$

$$\frac{X_{CP}}{C_R} = 0.907 + B(\alpha) (0.169) + C(\alpha) (0.10395)$$

α (deg)	X_{CP}/C_R
90	0.611
160	0.738
165	0.768
170	0.820
175-180	0.907

Data Comparisons

The results of the numerical example are compared with experimental data in Figure 76. Clearly, it would be desirable to show comparisons between the results determined by the method and completely independent test data. Unfortunately, due to the lack of such data, comparisons are restricted to the experimental data sources that were used in developing the correlation method. However, the specific test data used for comparisons were not directly used in the construction of the method. Additional comparisons are shown for a triangular fin of 0.5 aspect ratio at subsonic and transonic Mach numbers. A comparison at Mach 0.80 is shown in Figure 77 and Figure 78 shows a comparison at Mach 1.30. Agreement is quite good throughout the angle of attack range for all comparisons. Some data scatter is noticed near the extreme ends ($\alpha = 0$ and 180 degrees) of the angle of attack range. As may

be expected, scatter of this type usually results from the order of magnitude effects associated with very small forces and moments used in determining the center of pressure location. In general, the correlation method agrees within 2.5 percent of the experimental data with the possible exception of a few isolated areas. These areas usually involve only a very small segment of the α range such as shown in Figure 77 near $\alpha = 40$ degrees. A deviation of approximately 3 percent was noticed from $\alpha \sim 130$ to 150 degrees for the fin in Figure 76.

ASPECT RATIO 1.0

TAPER RATIO 0.5

MACH NUMBER 1.0

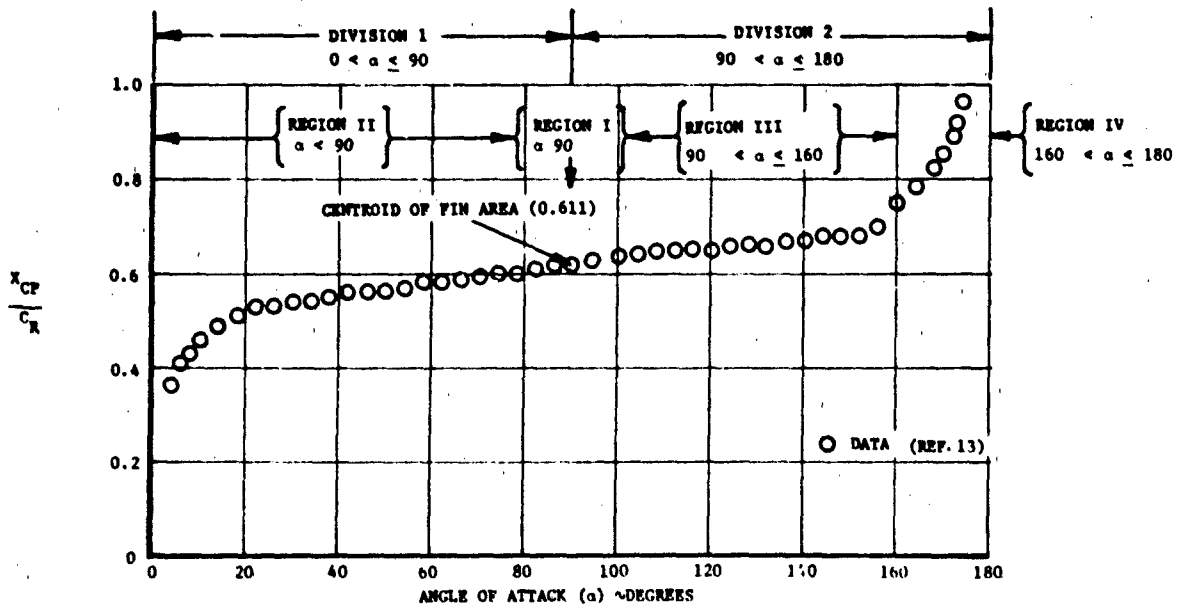


Figure 69. Chordwise Center of Pressure Variation to 180 Degrees

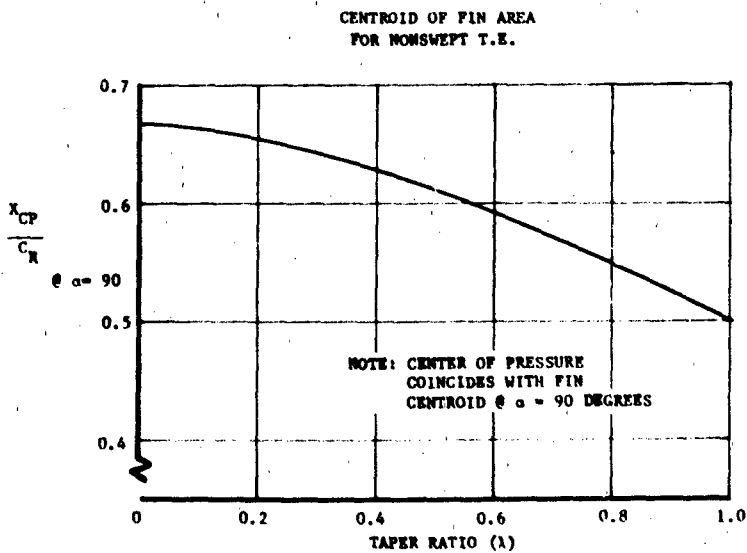


Figure 70. Chordwise Center of Pressure Variation with Taper Ratio at Alpha of 90 Degrees

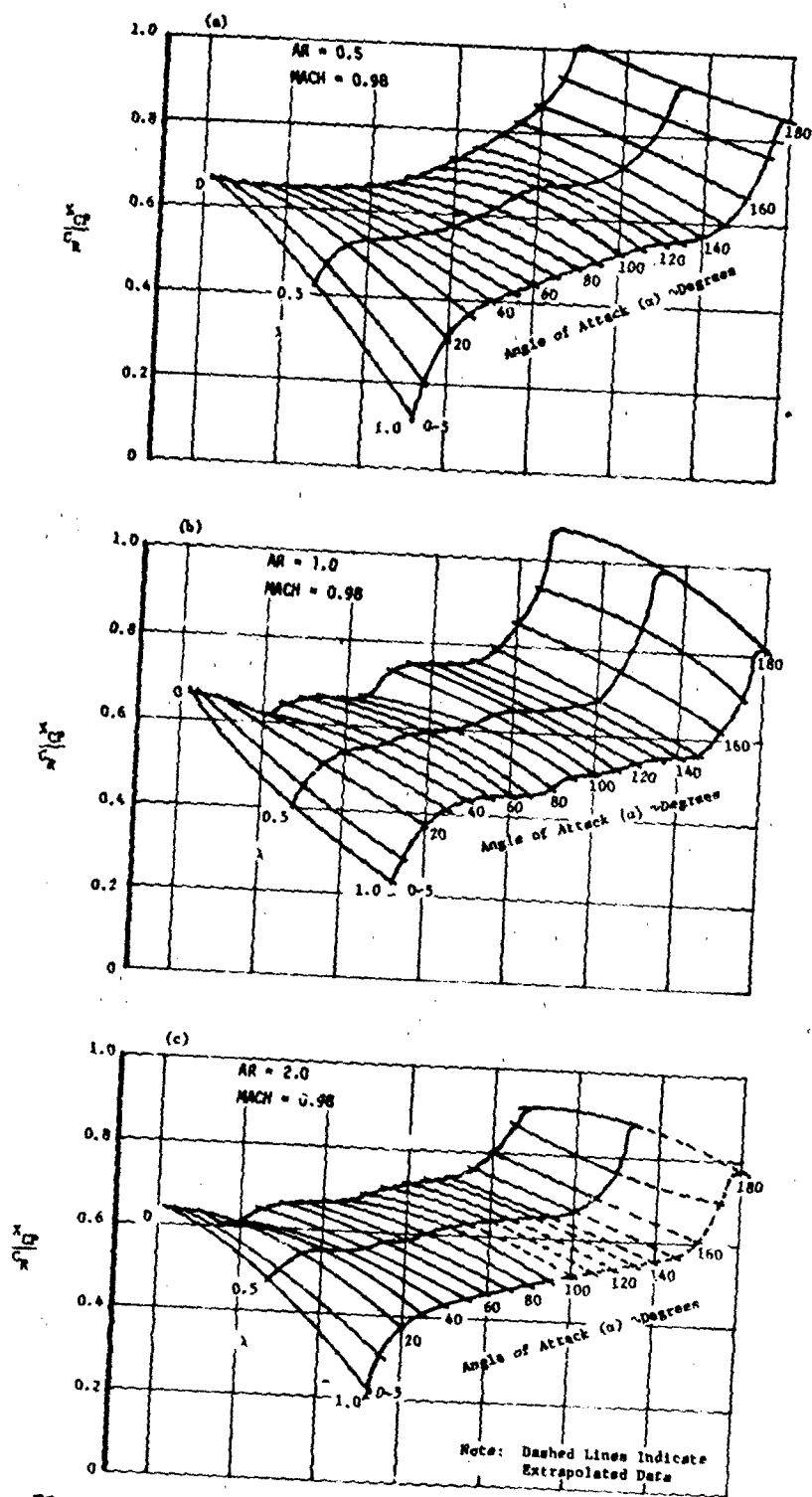


Figure 71. Basic Curves for X_{CP}/C_R at Reference Mach Number 0.98 (0 to 180 Degrees)

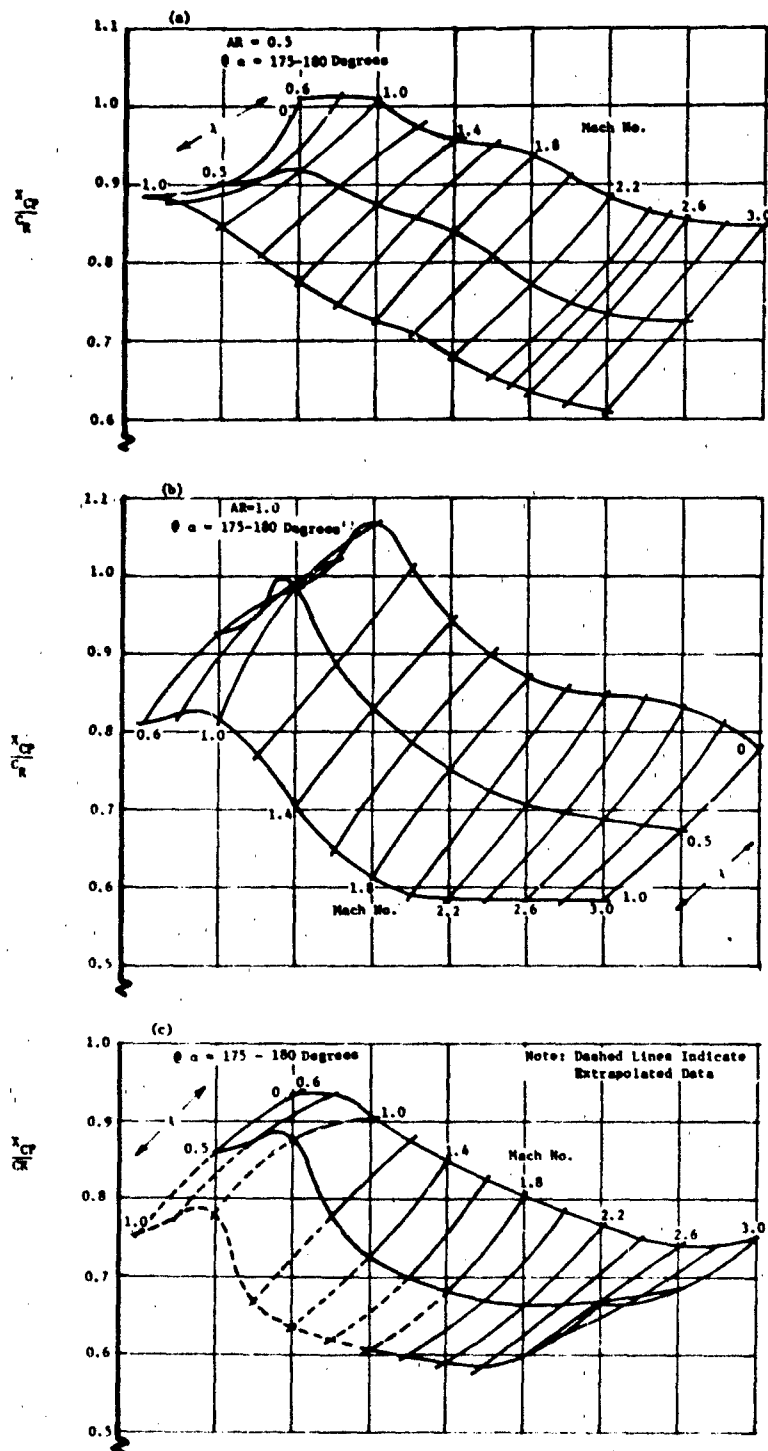


Figure 72. Basic Curves for X_{CP}/C_R at Reference Angle of Attack 175 to 180 Degrees ($M = 0.6$ to 3.0)

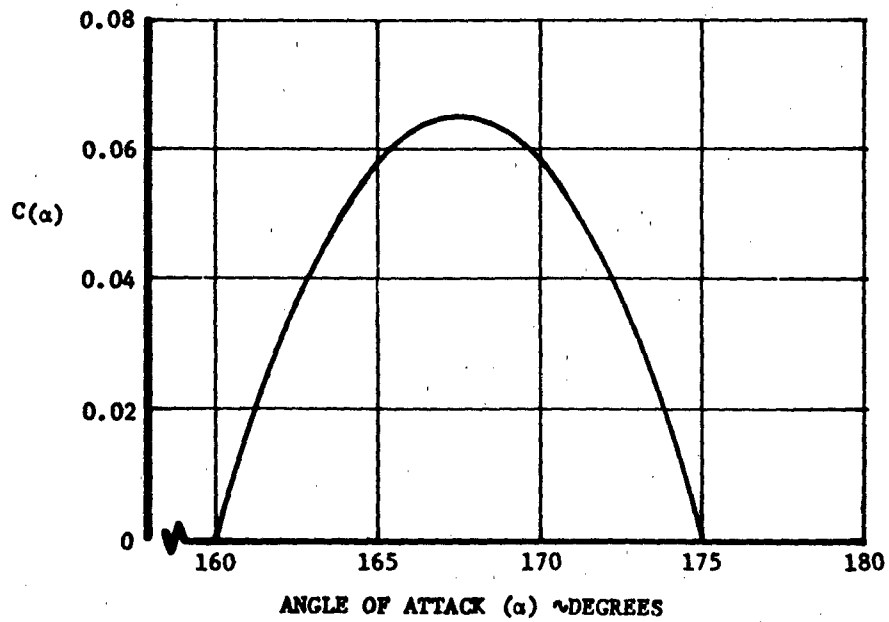
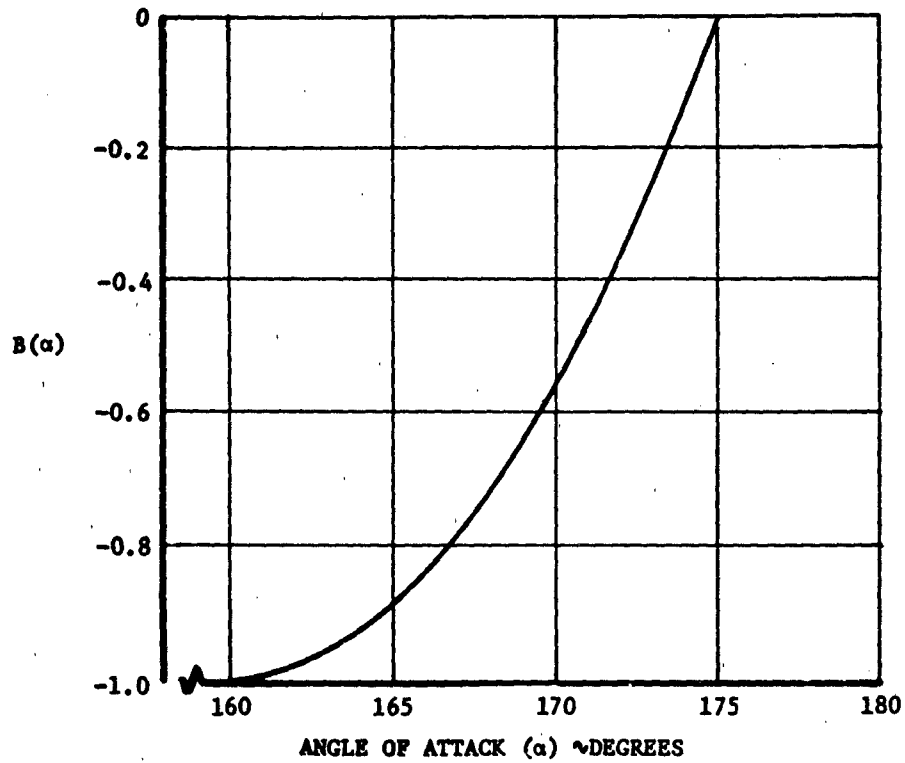


Figure 73. Power Series Constants versus Angle of Attack

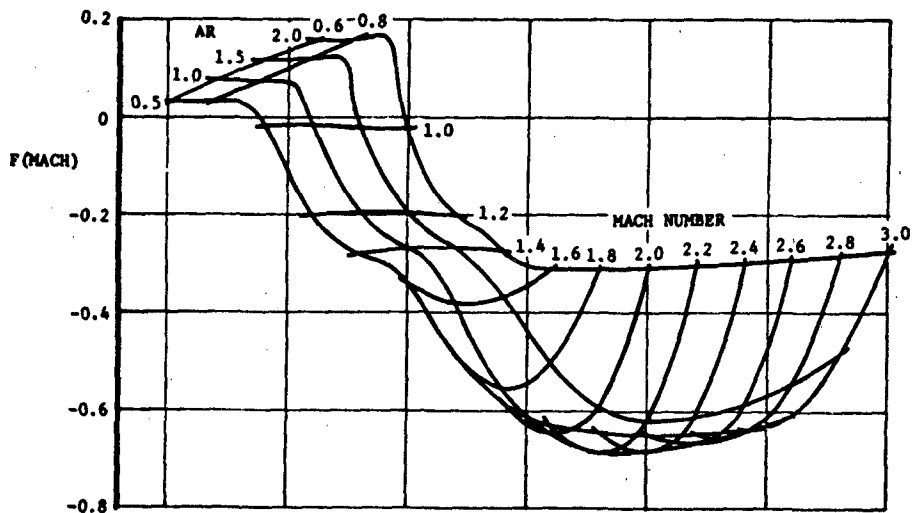


Figure 74. Mach Number Correction Factor for $\alpha < 90$ Degrees

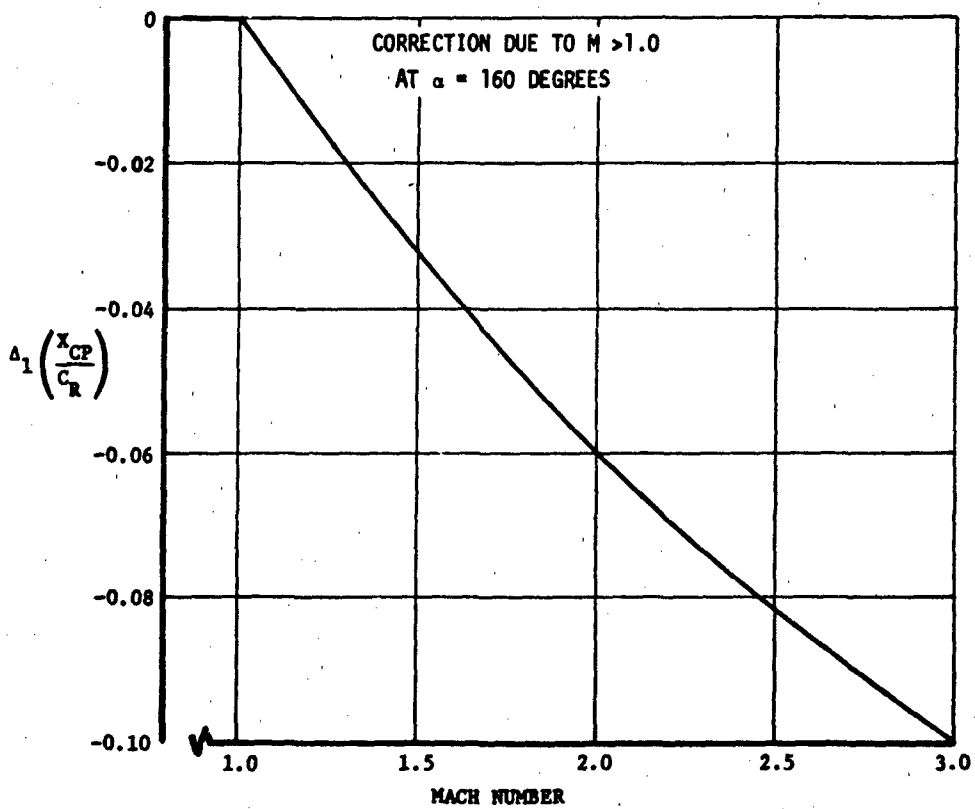


Figure 75. Variation of $\Delta_1 \left(\frac{X_{CP}}{C_R} \right)$ With Mach Number at Alpha of 160 Degrees

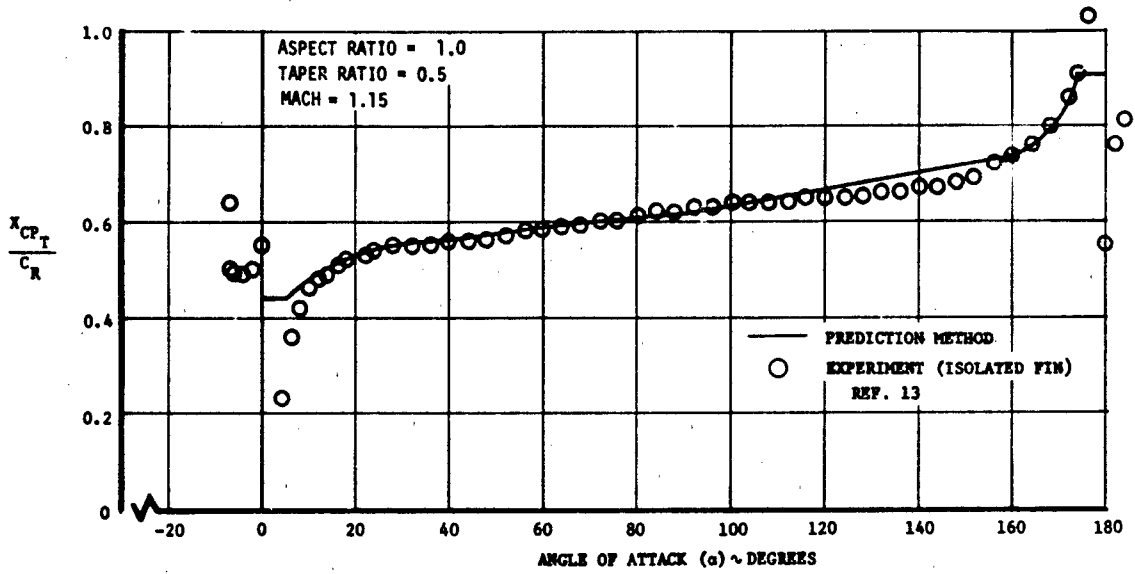


Figure 76. Comparison of Predicted and Experimental Center of Pressure Location, (X_{CP_T} / C_R) , Mach = 1.15

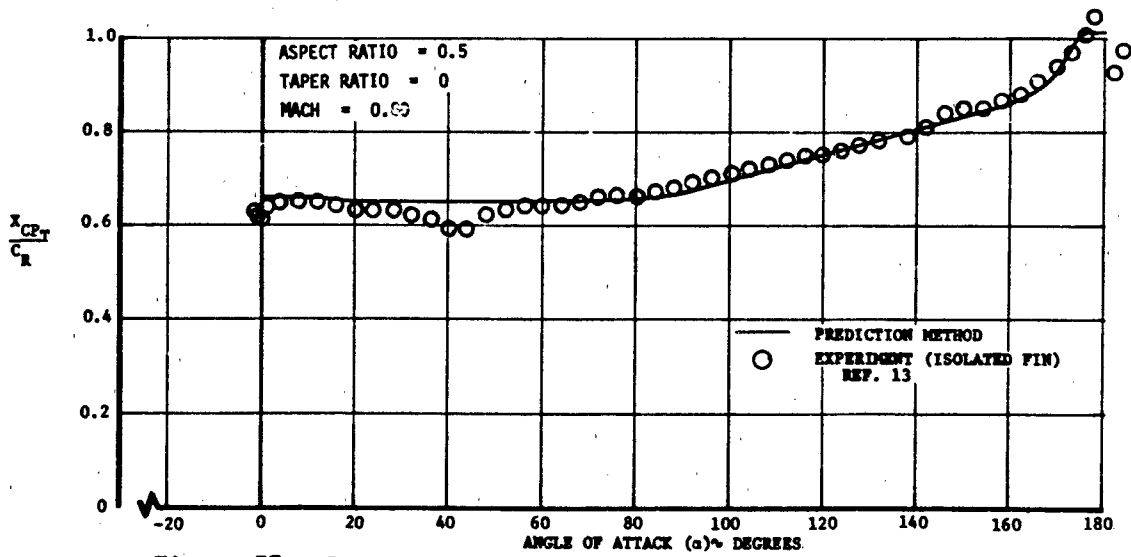


Figure 77. Comparison of Predicted and Experimental Center of Pressure Location (X_{CP_T} / C_R) , Mach = 0.80

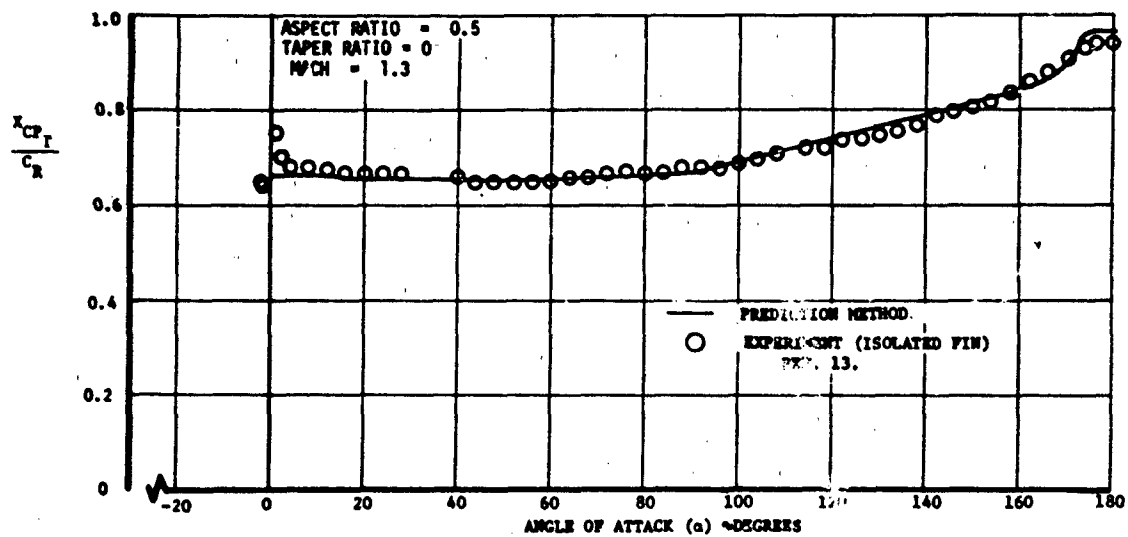


Figure 78. Comparison of Predicted and Experimental Center of Pressure Location (X_{CP_T} / C_R), Mach = 1.30

5.2 Body-Tail Configurations

5.2.1 Tail-On-Body Normal Force

Summary

A method is presented to predict $C_{N_{T(B)}}$, the normal force coefficient on the horizontal, undeflected tails of body-tail configurations. The method is applicable to "plus" configurations at Mach numbers between 0.6 and 3.0 and angles of attack from 0 to 180 degrees. The method consists of a procedure for calculating an interference factor, $R_{T(B)}$, which can be applied to isolated fin data or the results of Section 5.1.4 to determine tail-on-body normal force coefficients, $C_{N_{T(B)}}$. Agreement between predicted and experimental results were found to be quite good.

Background

The normal force on a tail fixed to a body differs from that on an isolated tail at the same angle of attack. This difference is attributable to the interference of body-induced upwash and lee-side vortex downwash on the tail flow field. To predict tail-on-body normal force, it is necessary to correct isolated fin data for these interference effects. Methods are available which predict each interference term separately (Reference 17) or combine the two into a single interference factor (Reference 3). However, these methods are not applicable over the entire angle of attack ($0^\circ - 180^\circ$) and Mach number (0.6 to 3.0) ranges. The method of Reference 17 is limited to angles of attack below that at which the body lee-side vortex pattern becomes asymmetric ($\alpha < 30^\circ$). In its present form, the method of Reference 3 is limited to angles of attack less than 60 degrees and to transonic Mach numbers.

Method Development

Due to the complicated nature of the flow field an analytic approach to method development was not considered. An empirical approach was selected.

The data of Reference 13 were insufficient to distinguish the contribution of each type of interference to the total; therefore, an extension of the method of Reference 17 was not practical. The nature of the instrumentation used to collect the data of Reference 13 did provide sufficient information to calculate the total interference as the ratio $R_{T(B)} = (\text{tail-on-body normal force } C_{N_{T(B)}}) / \text{tail alone normal force } C_{N_T}$. These data could be correlated and presented in a form like that of Reference 3. However, the resultant method would be awkward and time consuming to use. In order to develop a simple, easy to use preliminary design tool, a power series approach to method development was selected. In the usual way boundary conditions were sought. As indicated in Reference 3 the value of $R_{T(B)}$ at $\alpha = 0$ degrees can be set equal to the value of $K_{T(B)}$ predicted by potential flow theory. Values of $K_{T(B)}$ are presented in Reference 30 but for the sake of completeness are presented again here in Figure 79. As a second boundary condition, the value of $R_{T(B)}$ at $\alpha = 180$ degrees can be assumed equal to 1.0 in the absence of any forebody effects. A survey of $R_{T(B)}$ data (Reference 13) versus angle of attack yielded further boundary conditions. At $\alpha = 30$ degrees, the value of $R_{T(B)}$ was observed consistently to be 1.0 with $\frac{\partial R_{T(B)}}{\partial \alpha}$ equal to zero. It was also noted that at $\alpha = 130$ degrees, the value of $R_{T(B)}$ in Figure 79 with $\frac{\partial R_{T(B)}}{\partial \alpha}$ again equal to zero. The value of $R_{T(B)}$ at $\alpha = 90$ degrees was taken as a final boundary condition. The data showed that the value of $R_{T(B)}$ at 90 degrees was not constant; therefore, it was left as a free variable, $R_{T(B)}_{\pi/2}$.

Applying these boundary conditions to the following power series expansion

$$R_{T(B)} = a_0 + a_1\alpha + a_2\alpha^2 + a_3\alpha^3 + a_4\alpha^4 + a_5\alpha^5 + a_6\alpha^6$$

yielded

$$R_{T(B)} = (3.98080\alpha - 3.67990\alpha^2 - 1.95429\alpha^3 + 3.37838\alpha^4 - 1.32994\alpha^5 + 0.16987\alpha^6) + (1-7.34322\alpha + 20.55753\alpha^2 - 27.31747\alpha^3 + 17.64447\alpha^4 - 5.28848\alpha^5 + 0.58856\alpha^6) K_{T(B)} + (3.36248\alpha - 16.87764\alpha^2 + 29.27176\alpha^3 - 21.02285\alpha^4 + 6.61842\alpha^5 - 0.75843\alpha^6) R_{T(B)}_{\pi/2}$$

which can be rewritten as :

$$R_{T(B)} = A_0 + A_1 K_{T(B)} + A_2 R_{T(B)}_{\pi/2} \quad (31)$$

where

$$A_0 = 3.98080\alpha - 3.67990\alpha^2 - 1.95429\alpha^3 + 3.37838\alpha^4 - 1.32994\alpha^5 + 0.16987\alpha^6$$

$$A_1 = 1 - 7.34322\alpha + 20.55753\alpha^2 - 27.31747\alpha^3 + 17.64447\alpha^4 - 5.28848\alpha^5 + 0.58856\alpha^6$$

$$A_2 = 3.36248\alpha - 16.87764\alpha^2 + 29.27176\alpha^3 - 21.02285\alpha^4 + 6.61842\alpha^5 - 0.75843\alpha^6$$

Values of A_0 , A_1 and A_2 are plotted as a function of angle of attack in Figures 80, 81 and 82.

Correlation of the calculated values of $R_{T(B)}_{\pi/2}$ showed that this quantity varied with both Mach number and tail taper ratio. Values of $R_{T(B)}_{\pi/2}$ are presented in Figure 83 as a function of Mach number and taper ratio as obtained by fairing curves through the test data of Reference 13.

In the course of checking results predicted by Equation 31 against experimental data, a problem was encountered both subsonically and transonically for angles of attack between 0 and 30 degrees. The variation in $R_{T(B)}$ with angle of attack as predicted by Equation 31 was much more rapid than the experimental data tended to indicate. To account for this, a

second power series was used to develop a method applicable to subsonic and transonic Mach numbers over this range of angles of attack. As before, the values of $R_{T(B)}$ at $\alpha = 0$ and 30 degrees were taken to be $K_{T(B)}$ and 1.0, respectively. As a third boundary condition, it can be shown that $\frac{\partial R_{T(B)}}{\partial \alpha} =$ zero at $\alpha = 0$ degrees.

Applying these boundary conditions to the following power series expansion

$$R_{T(B)} = a_0 + a_1 \alpha + a_2 \alpha^2$$

yielded

$$R_{T(B)} = 3.64756\alpha^2 + (1 - 3.64756\alpha^2) K_{T(B)}$$

which can be rewritten as

$$R_{T(B)} = A_0 + A_1 K_{T(B)} \quad (32)$$

where

$$A_0 = 3.64756\alpha^2$$

$$A_1 = 1 - 3.64756\alpha^2$$

Values of A_0 and A_1 are also included in Figures 80 and 81.

Use of Method

A general description of how to apply this method will be presented in this section. This will be followed by a numerical example in which $R_{T(B)}$ will be calculated and applied to isolated fin data to determine $C_{NT(B)}$.

- 1 Using Figure 79 determine the value of $K_{T(B)}$ at the appropriate value of d/s .
- 2 Using Figure 83 determine the value of $R_{T(B)}_{\pi/2}$ at the appropriate Mach number and taper ratio.

- 3 Using the results of steps 1 and 2 and Figures 80, 81 and 82 apply Equation 31 (for subsonic and transonic Mach numbers use Equation 32 for angles up to 30 degrees) to calculate values of $R_{T(B)}$ for angles of attack between 0 and 180 degrees.
- 4 To determine the normal force coefficients for a tail fixed to a body, multiply isolated fin data or the results of Section 5.1.4 (p. 91 ff) by the values of $R_{T(B)}$.

Numerical Example

Calculate $C_{N_{T(B)}}$ for the following body tail configuration at $M = 0.6$.

Body:

$$\frac{l}{d} = 10.0 \quad \frac{l_N}{d} = 3.0 \quad d = 1.25 \text{ in.}$$

Tail:

$$\lambda = 0.5 \quad AR = 2.0 \quad d/s = 0.3 \quad \Lambda_{T.E.} = 0$$

- 1 Using Figure 79 or $d/s = 0.3$

$$K_{T(B)} = 1.25$$

- 2 Using Figure 83 for $M = 0.6$ and $\lambda = 0.5$

$$R_{T(B)_{\pi/2}} = 1.21$$

- 3 For $M = 0.6$ apply Equation 32 for $0^\circ < \alpha \leq 30^\circ$ and Equation 31 for $30^\circ < \alpha \leq 180^\circ$. Use Figures 80, 81 and 82 to determine general coefficients A_0 , A_1 and A_2 .

α	A_0	A_1	A_2	$R_{T(B)}$
0	0.0	1.0	0.0	1.25
10	0.111	0.8889	-	1.222
20	0.4444	0.5556	-	1.139
30	1.0	0.0	-	1.0

} Equation 32

3 (Continued)

α (deg)	A_0	A_1	A_2	$R_{T(B)}$
40	0.925	-0.02	0.095	1.015
50	0.735	-0.09	0.355	1.052
60	0.500	-0.18	0.685	1.104
70	0.275	-0.228	0.955	1.146
80	0.105	-0.175	1.07	1.181
90	0.0	0.0	1.0	1.210
100	-0.04	0.285	0.755	1.230
110	-0.035	0.615	0.425	1.248
120	-0.011	0.888	0.115	1.238
130	0.0	1.0	0.0	1.250
140	-0.011	0.865	0.140	1.240
150	-0.035	0.475	0.555	1.230
160	0.015	-0.055	1.045	1.211
170	0.280	-0.415	1.145	1.147
180	1.0	0.0	0.0	1.0

Equation 31

4 Using isolated fin data obtained from Reference 13, calculate $C_{NT(B)}$

α (deg)	$R_T(b)$	C_{NT}	$C_{NT(B)}$
0	1.25	0.0	0.0
10	1.222	0.45	0.550
20	1.139	0.76	0.866
30	1.0	0.76	0.760
40	1.015	0.9	0.914
50	1.052	0.99	1.041
60	1.104	1.04	1.148
70	1.146	1.04	1.192

4 (Continued)

<u>α (deg)</u>	<u>$R_T(B)$</u>	<u>C_{NT}</u>	<u>$C_{NT}(B)$</u>
80	1.181	1.07	1.264
90	1.21	1.08	1.307
100	1.230	1.08	1.328
110	1.248	1.08	1.348
120	1.238	1.03	1.275
130	1.250	0.96	1.2
140	1.240	0.83	1.029
150	1.230	0.68	0.836
160	1.211	0.58	0.702
170	1.147	0.40	0.459
180	1.0	-0.05	-0.05

Data Comparisons

The results of the numerical example are compared against experimental data in Figure 84. Further comparisons for a variety of Mach numbers and tail geometries are presented in Figures 85-89. Agreement is quite good in all cases.

Reference 30

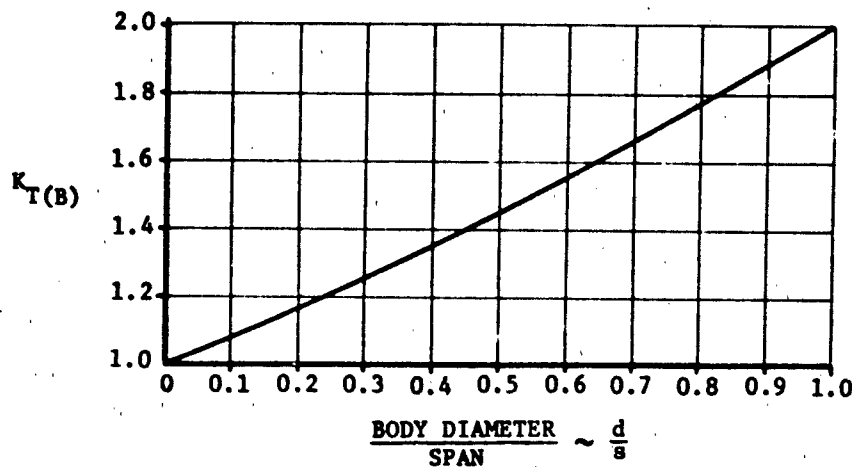


Figure 79. $K_{T(B)}$ Ratio At Zero Angle of Attack

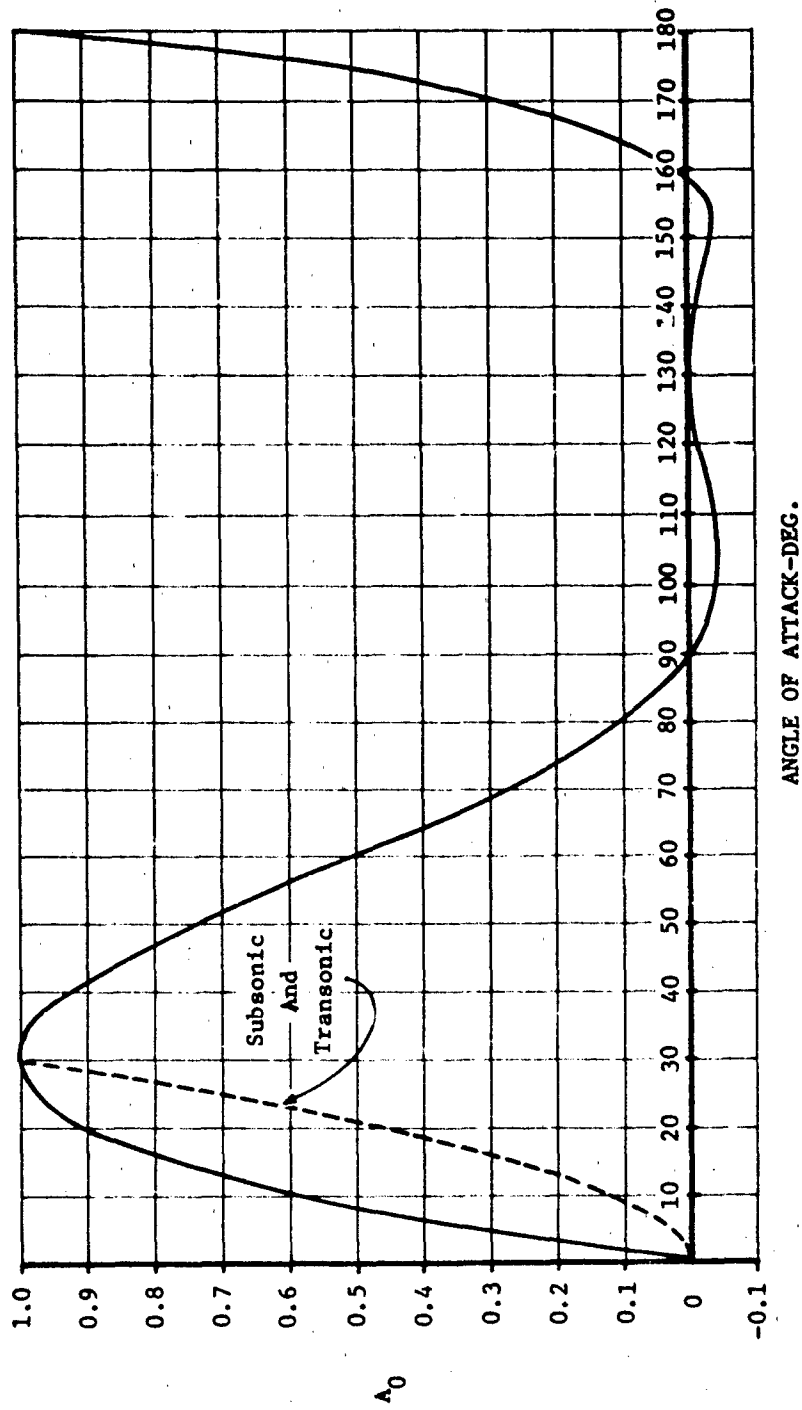


Figure 80. General Coefficients For Calculation Of $R_T(B)$

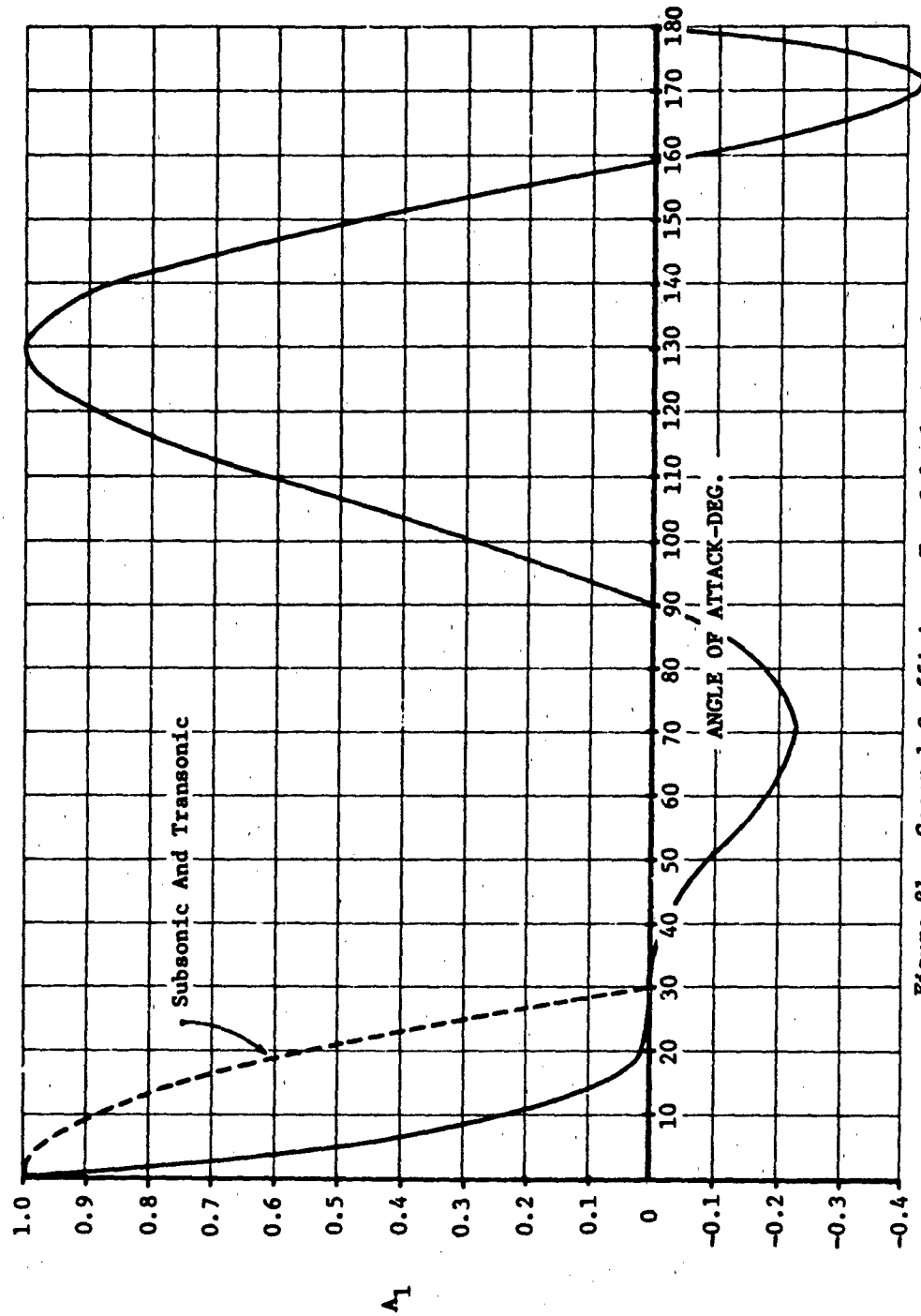


Figure 81. General Coefficients For Calculation Of $R_T(B)$

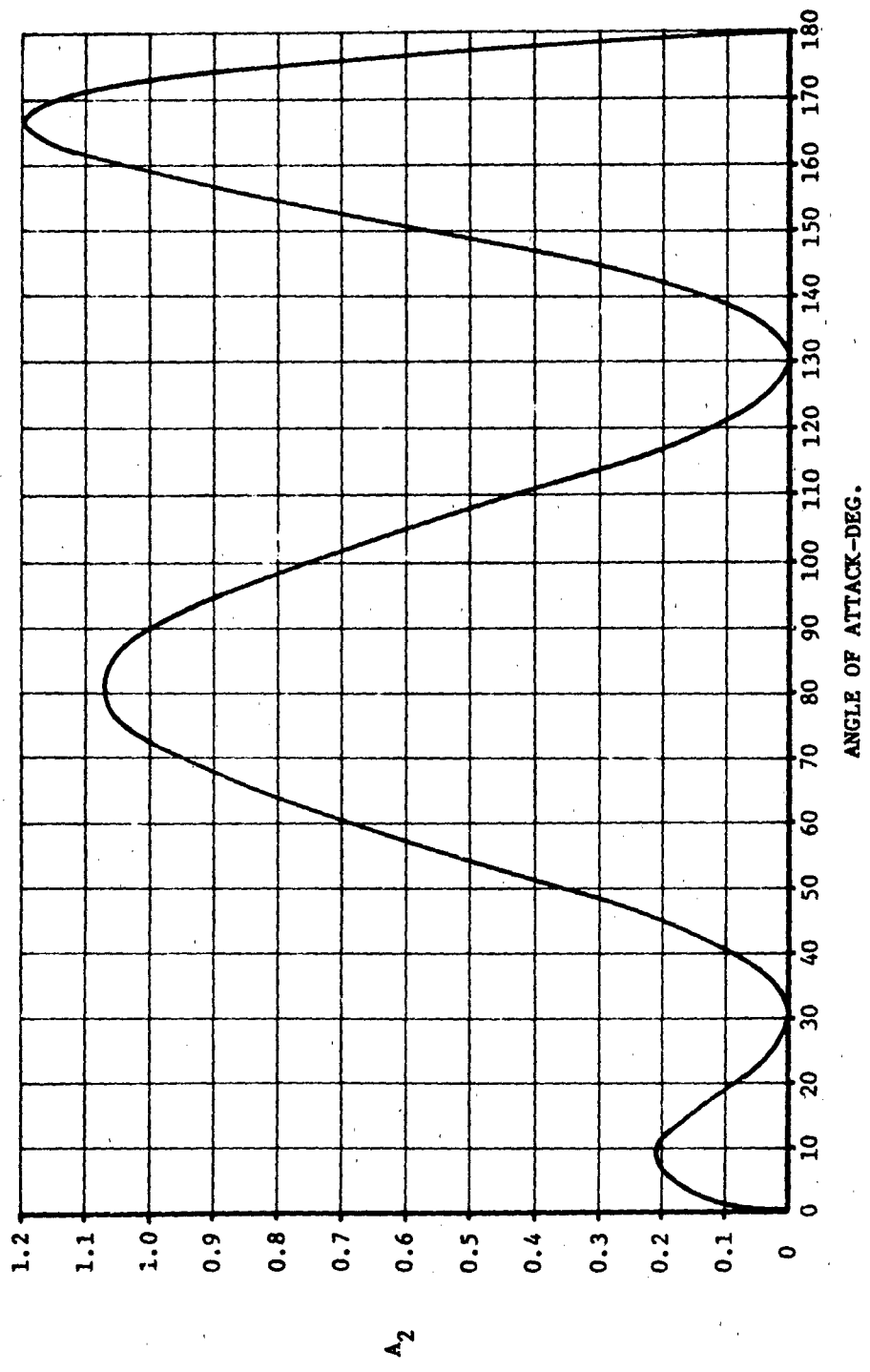


Figure 82. General Coefficients For Calculation Of $R_T(B)$

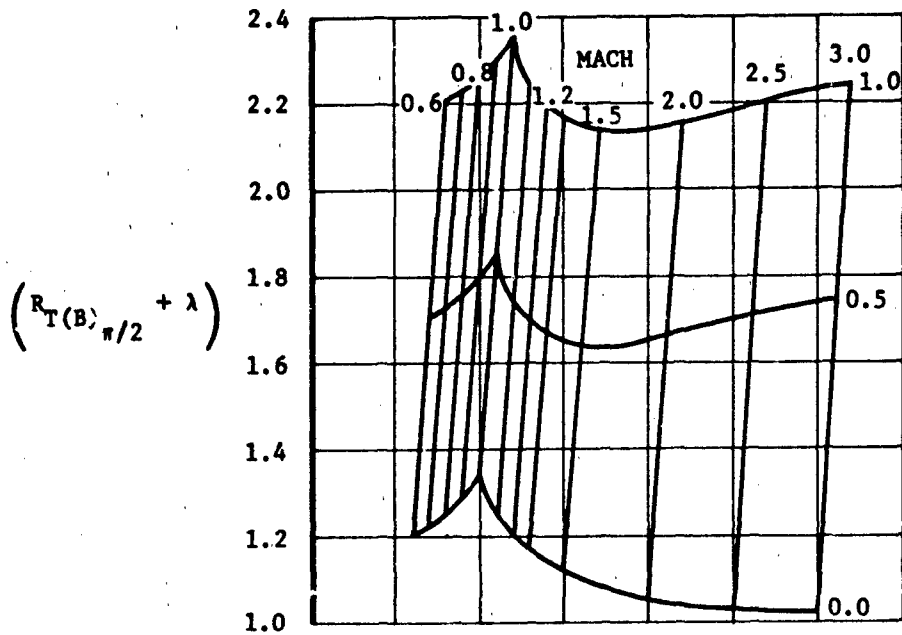


Figure 83. Interference Factor At Angle of Attack at 90 Degrees

M = 0.6

Body Tail

$\frac{l}{d} = 10.0$ $\lambda = 0.5$

$\frac{d}{s} = 0.3$

$\frac{A_N}{d} = 3.0$ AR = 2.0

○ Experimental (Ref. 13)

— Predicted

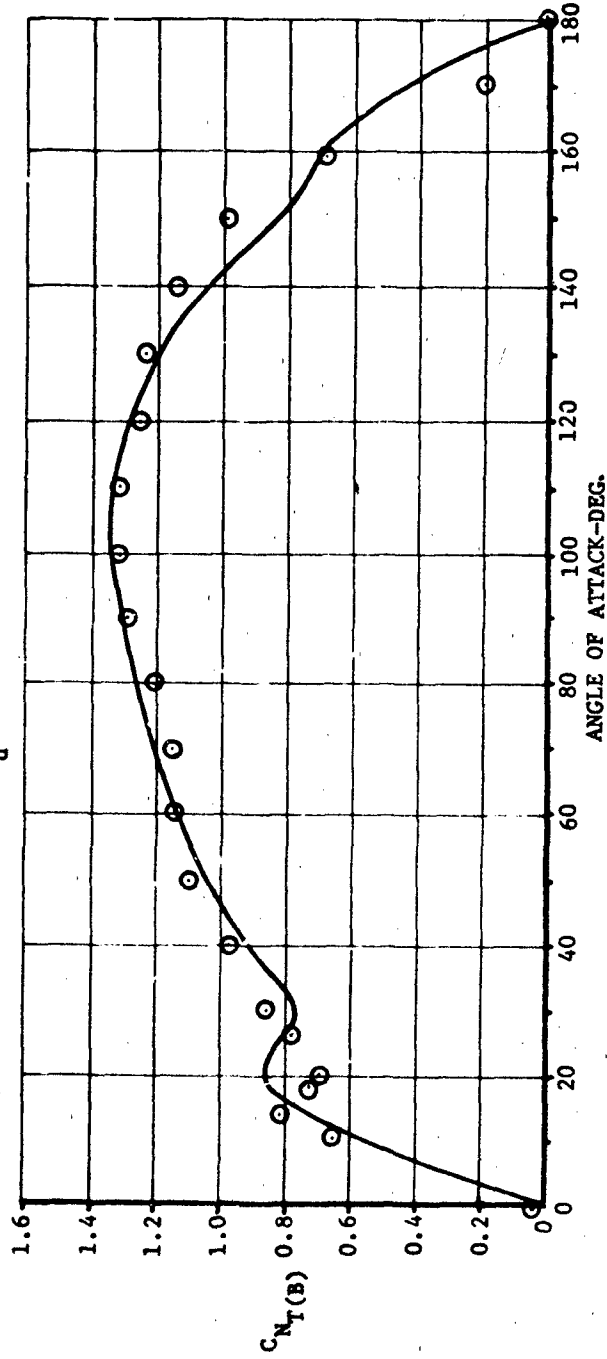


Figure 84. Comparison Of Experimental And Predicted Results, $C_{N_T(B)}$, M = 0.6

$M = 3.0$
 Body $l/d = 10.0$ Tail $\lambda = 0.0$
 $l_N/d = 3.0$ $d/s = 0.5$ $AR = 1.0$
 ○ Experimental (Ref. 13)
 — Predicted

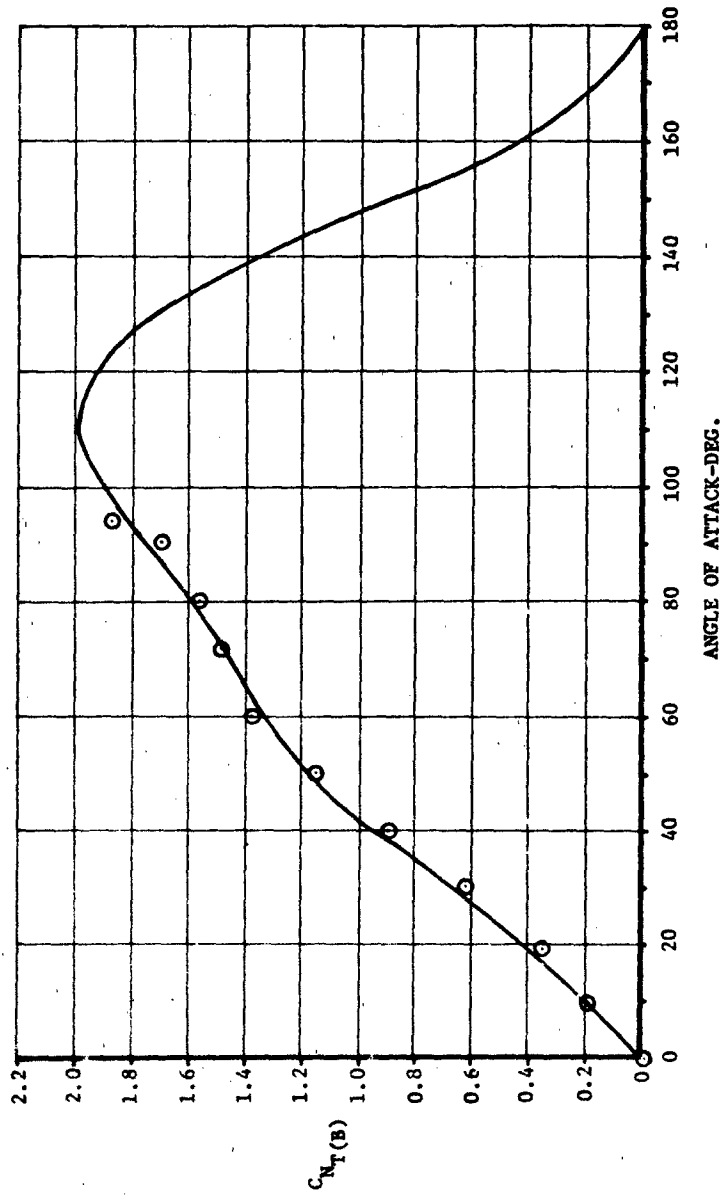


Figure 85. Comparison of Experimental and Predicted Results, $C_{N T(B)}$, $M = 3.0$

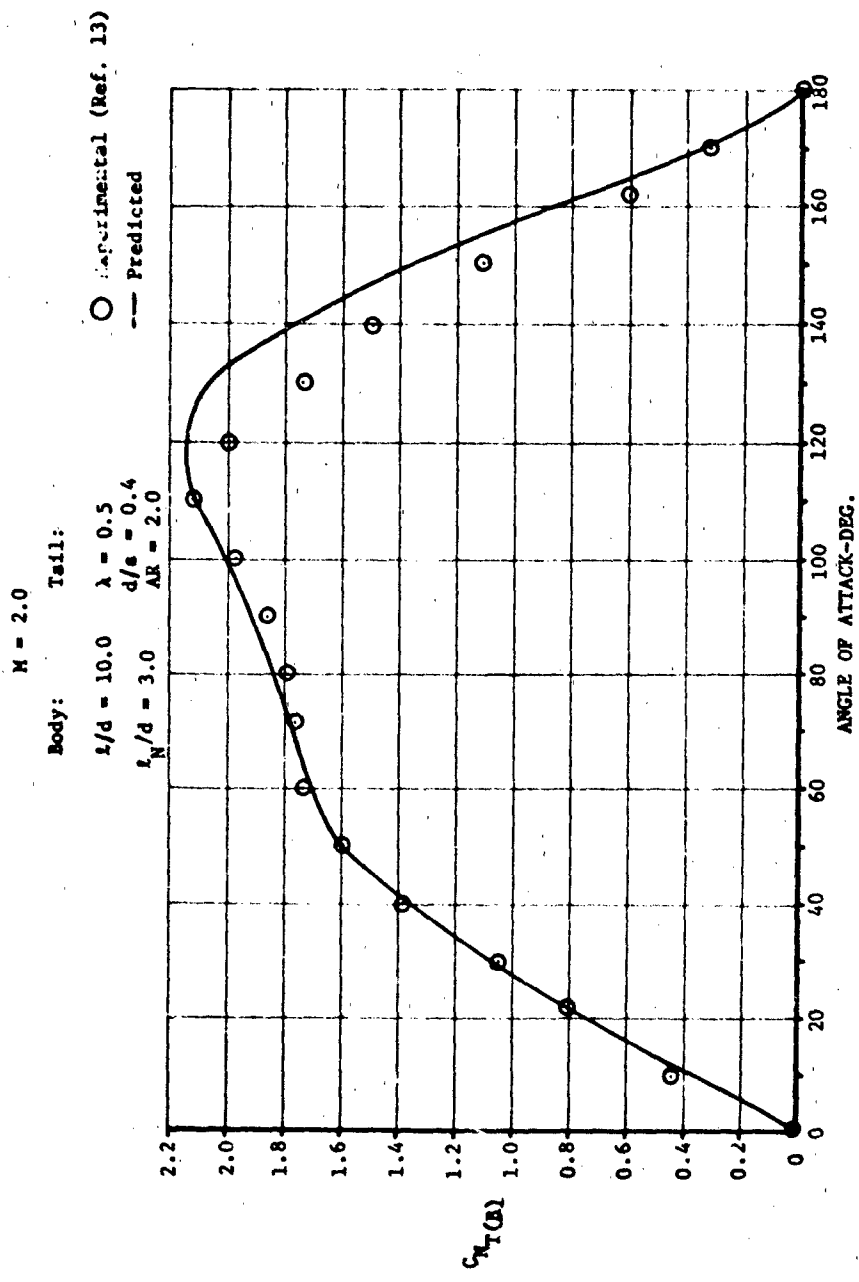


Figure 86. Comparison of Experimental and Predicted Results, $C_{N(B)}$, $M = 2.0$

$M = 3.0$
 Body: $l/d = 10.0$ $AR = 3.0$ $d/s = 0.5$
 Tail: $\lambda = 1.0$ $AR = 1.0$

○ Experimental (Ref. 13)
 — Predicted

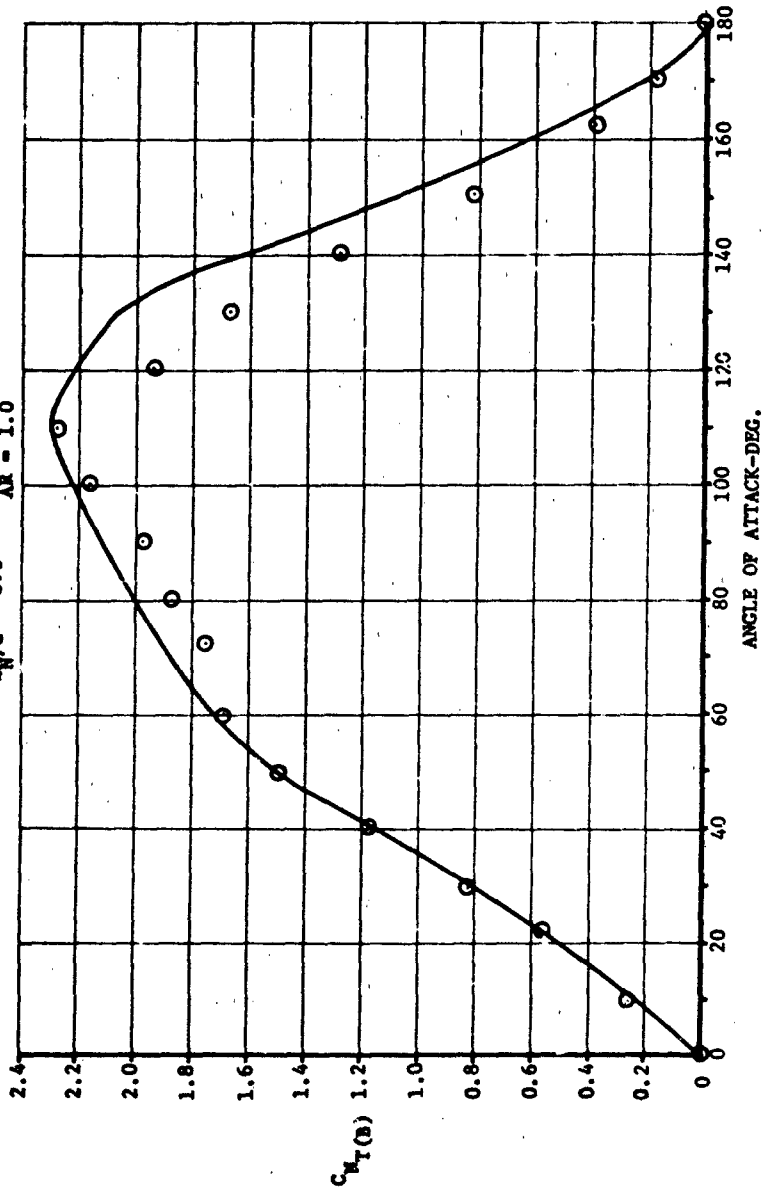


Figure 87. Comparison of Experimental and Predicted Results, $C_{N(B)}$, $M = 3.0$

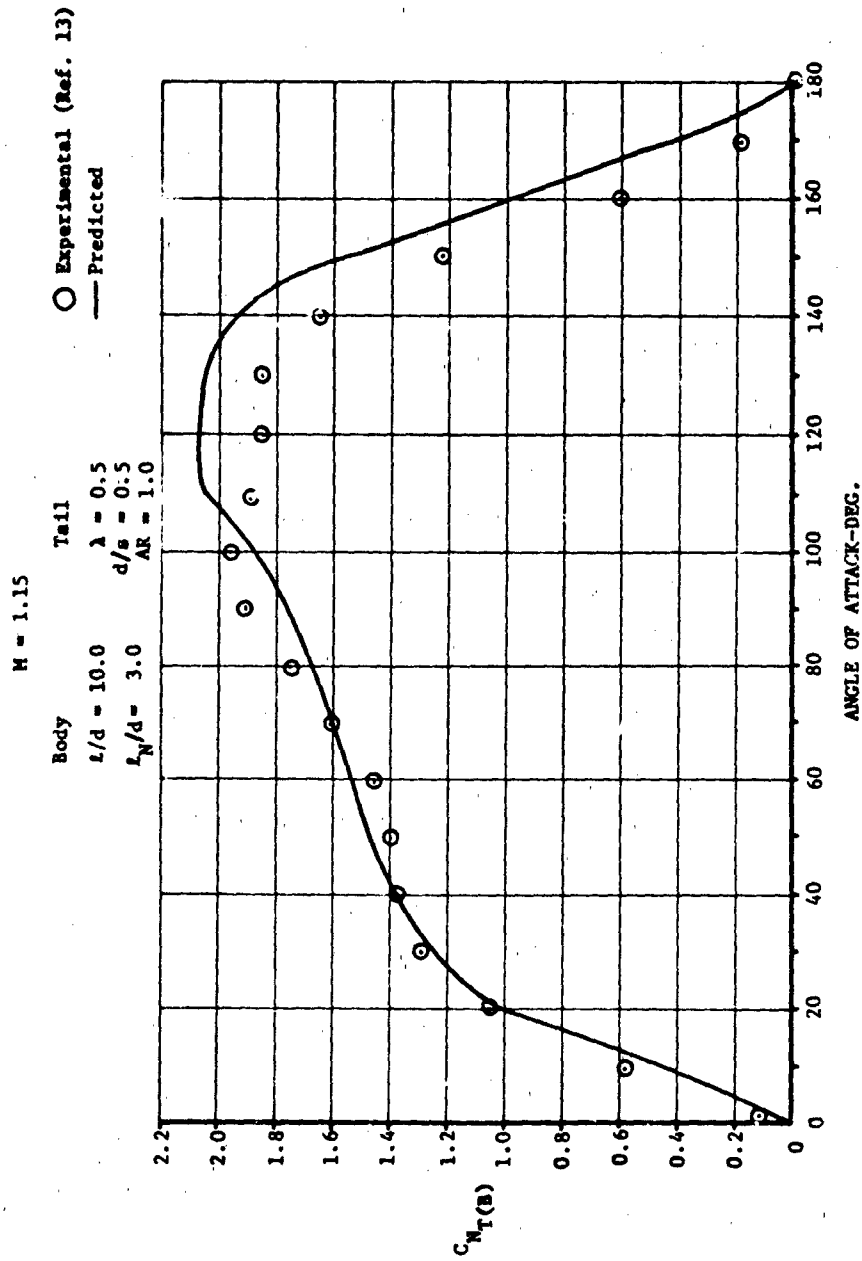


Figure 88. Comparison Of Experimental And Predicted Results, $C_{M_T}(B)$, $M = 1.15$

$M = 0.8$
 Body $s/d = 10.0$ $\lambda = 0.0$
 $t_N/d = 3.0$ $d/s = 0.5$
 Tail $AR = 1.0$

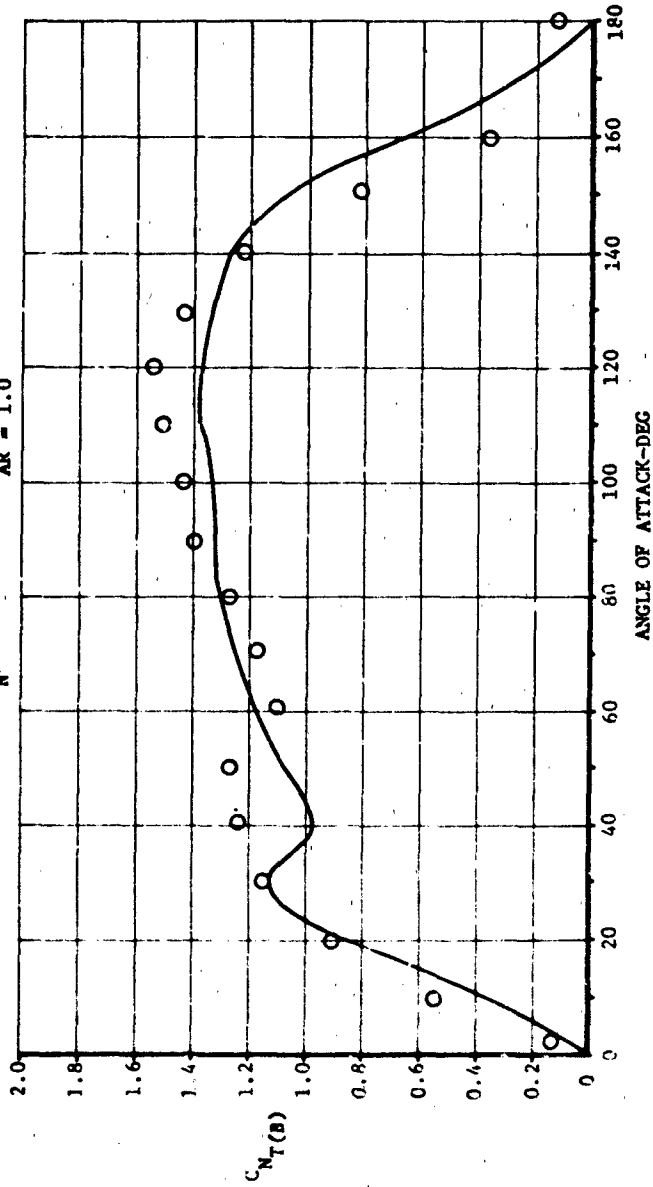


Figure 89. Comparison of Experimental And Predicted Results, $C_{N_T(B)}$, $M = 0.8$

5.2.2 Tail-to-Body Carryover Normal Force

Summary

A method is described to predict $I_{B(T)}$, the tail-to-body carryover normal force coefficient. The method applies over the Mach range 0.6 - 3.0 at angles of attack from 0 - 180 degrees.

Background

When load-carrying lifting surfaces are fixed to a body, loading also appears on the body due to carryover effects. The normal force thus generated is denoted here by $I_{B(T)}$ (see Section 4.0). In potential flow near zero angle of attack, $I_{B(T)}$ reduces to $K_{B(T)}$, which is determinable by linearized theory (Reference 30). Use is made of $K_{B(T)}$ in the present method.

Method Development

Separate methods are presented for the transonic ($0.6 \leq M \leq 1.3$) and supersonic ($2.0 \leq M \leq 3.0$) regimes, respectively. Interpolation should be used for Mach numbers between 1.3 and 2.0.

Transonic Mach No.:

The general form of the $I_{B(T)}$ curves, as derived from experimental data, is shown schematically in Figure 90. Three major values are used in power series development, I_a , I_b , and I_c . Note that at zero and 180 degrees angle of attack $I_{B(T)}$ is zero. The basic power series for portions A and B of the curve is:

$$I_{B(T)} = a_0 + a_1\alpha + a_2\alpha^2 + a_3\alpha^3$$

The division of the angle of attack range and the points used as boundary conditions are chosen by observation of the trend in the test data.

Boundary conditions are:

$$\begin{array}{l}
 \text{A} \left\{ \begin{array}{l}
 \alpha = 0, I_{B(T)} = 0 \\
 \alpha = 50^\circ, I_{B(T)} = I_a, \frac{dI}{d\alpha} = 0 \\
 \alpha = 130^\circ, I_{B(T)} = I_b \\
 \alpha = 130^\circ, I_{B(T)} = I_b \\
 \text{B} \left\{ \begin{array}{l}
 \alpha = 160^\circ, I_{B(T)} = I_c \\
 \alpha = 180^\circ, I_{B(T)} = 0
 \end{array} \right.
 \end{array} \right.
 \end{array}$$

Substitution of these conditions into the power series yields:

Portion A (α in radians)

$$\begin{aligned}
 I_{B(T)} = & [0.172 I_b + 2.562 I_a] \alpha \\
 & - [0.394 I_b + 1.930 I_a] \alpha^2 \\
 & + [0.353 I_a + 0.226 I_b] \alpha^3
 \end{aligned} \tag{33}$$

Portion B (Using only first 3 terms in series) (α in radians)

$$\begin{aligned}
 I_{B(T)} = & 19.592 I_b - 39.869 I_c \\
 & + [30.271 I_c - 13.286 I_b] \alpha \\
 & + [2.244 I_b - 5.596 I_c] \alpha^2
 \end{aligned} \tag{34}$$

Correlation of data can then proceed with attention concentrated on I_a , I_b , and I_c .

In general, I_a , I_b , and I_c are functions of configuration geometry and flow conditions, i.e.,

$$I_{a,b,c} = I_{a,b,c}(\lambda, AR, d/s, M)$$

The assumption is made that the variables are separable, so that the equation may be written

$$I_i = I_{i \text{ Basic}} F_i(\lambda) F_i(AR) F_i(d/s) F_i(M)$$

and the form of each separate function is obtained by examination of the experimental data. Sometimes correlation does not require use, or complete separation, of all the variables. For example, the following representations of I_a , I_b , and I_c were found to be sufficient:

$$I_a = I_{a \text{ Basic}} F_a(\text{AR}) F_a(M)$$

$$I_b = I_b(\text{AR}, M)$$

$$I_c = I_{c \text{ Basic}} F_c(\text{AR})$$

Examination of the test data of Reference 13 showed that correlations of the quantities I_a , I_b , and I_c made it possible to generate boundary conditions for the $I_{B(T)}$ function which leads to good agreement between the model and the test data.

The correlations of I_a , I_b , and I_c are presented in Figure 91a, b, and c.

Use of Method (Transonic)

Suppose it is required to estimate the tail-to-body carryover normal force for a configuration as follows:

$$\text{Tail: AR} = 0.5 \quad \lambda = 0.0 \quad d/s = 0.5$$

$$M = 0.8$$

From Figure 91:

$$\begin{aligned} I_a &= I_{a \text{ Basic}} F_a(\text{AR}) F_a(M) \\ &= 1.0 \times 2.6 \times (1.65 - 0.5) \\ &= 2.99 \end{aligned}$$

$$I_b = 0$$

$$\begin{aligned} I_c &= I_{c \text{ Basic}} F_c(\text{AR}) \\ &= 0.3 \times 2.5 \\ &= 0.75 \end{aligned}$$

Hence, the Equations (33) and (34) become:

$$I_{B(T)} = 7.66\alpha - 5.77\alpha^2 + 1.05\alpha^3 \quad (\alpha \text{ in radians}) \quad (33A)$$

$$I_{B(T)} = -29.902 + 22.703\alpha - 4.197\alpha^2 \quad (34A)$$

α°	$I_{B(T)}$
0	0
10	1.167
20	2.016
40	2.894
50	2.992
70	2.67
90	1.886
110	0.908
130	0
145	0.673
160	0.768
170	0.511
180	0

(33A)

(34A)

The results are compared with experimental data in Figure 92. It will be seen that matching is quite good.

Supersonic Mach No.

For supersonic Mach numbers the procedures for calculating $I_{B(T)}$ are generally simpler than for the transonic case. However the $I_{B(T)}$ curve is divided into three, rather than two, parts and is shown schematically in Figure 93. This is the form that the test data takes and the curve represents a fairing of the data.

The three major portions, A, B, and C are shown, along with the important correlation inputs, I_1 , I_2 , and I_3 . The following representations are used.

$$A: I_{B(T)} = I_1 \sin \alpha \quad (35) \left. \begin{array}{l} \alpha \text{ in} \\ \text{degrees} \end{array} \right\}$$

$$B: I_{B(T)} = I_1 - (I_1 - I_2) \sqrt{\frac{\alpha - 90}{25}} \quad (36) \left. \begin{array}{l} \alpha \text{ in} \\ \text{degrees} \end{array} \right\}$$

$$C: I_{B(T)} = -19.325 I_3 + 11.926 I_2 + \left[15.813 I_3 - 8.382 I_2 \right] \alpha + \left[1.46 I_2 - 3.076 I_3 \right] \alpha^2 \quad (37) \left. \begin{array}{l} \alpha \text{ in} \\ \text{degrees} \end{array} \right\}$$

The last equation was obtained from the usual power series representation with boundary conditions:

$$\alpha = 115^\circ \quad I_{B(T)} = I_2$$

$$\alpha = 149^\circ \quad I_{B(T)} = I_3$$

$$\alpha = 180^\circ \quad I_{B(T)} = 0$$

Again, using separation of variables,

$$I_1 = I_1 \text{ Basic } F_1 (d/s)$$

$$I_2 = I_2 \text{ Basic } F_2 (M) F_2 (d/s)$$

$$I_3 = I_3 \text{ Basic } F_3 (AR)$$

These quantities are presented in Figure 94a, b, and c, respectively.

Use of Method (Supersonic)

Suppose it is required to estimate the tail-to-body carryover normal force for a configuration as follows:

$$\text{Tail:} \quad AR = 2.0, \lambda = 0.5, d/s = 0.3$$

$$M = 2.5$$

From Figures 94a, b, and c:

$$\begin{aligned} I_1 &= I_1 \text{ Basic } F_1 (d/s) \\ &= 0.75 \times 1.0 = 0.75 \end{aligned}$$

$$\begin{aligned} I_2 &= I_2 \text{ Basic } F_2 (M) F_2 (d/s) \\ &= -2 \times 1.0 \times 1.0 = -2.0 \end{aligned}$$

$$\begin{aligned} I_3 &= I_3 \text{ Basic } F_3 (AR) \\ &= 0.5 \times 1.0 = 0.5 \end{aligned}$$

Portion A, $I_{B(T)} = 0.75 \sin \alpha$

$\alpha(\text{deg})$	$I_{B(T)}$
0	0.0
20	0.257
40	0.482
60	0.650
80	0.739
90	0.750

Portion B, $I_{B(T)} = 0.75 - (0.75 + 2.0) \sqrt{\frac{\alpha-90}{25}}$

$\alpha(\text{deg})$	$I_{B(T)}$
90	0.75
100	-0.988
110	-1.71
115	-2.0

Portion C, $I_{B(T)} = -33.515 + 24.672\alpha - 4.4574\alpha^2$

$\alpha(\text{deg})$	$I_{B(T)}$
115	-2.0
130	-0.481
149	0.5
165	0.56
180	0.0

Data Comparisons

A comparison between prediction and experiment is shown in Figure 95.

It will be seen that matching is quite good.

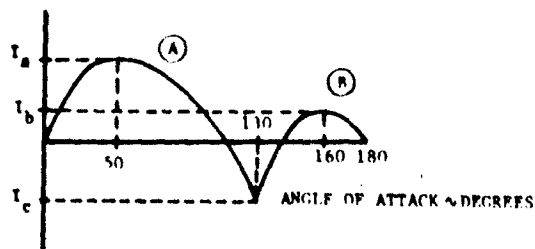


Figure 90. Transonic $I_{B(T)}$ Schematic

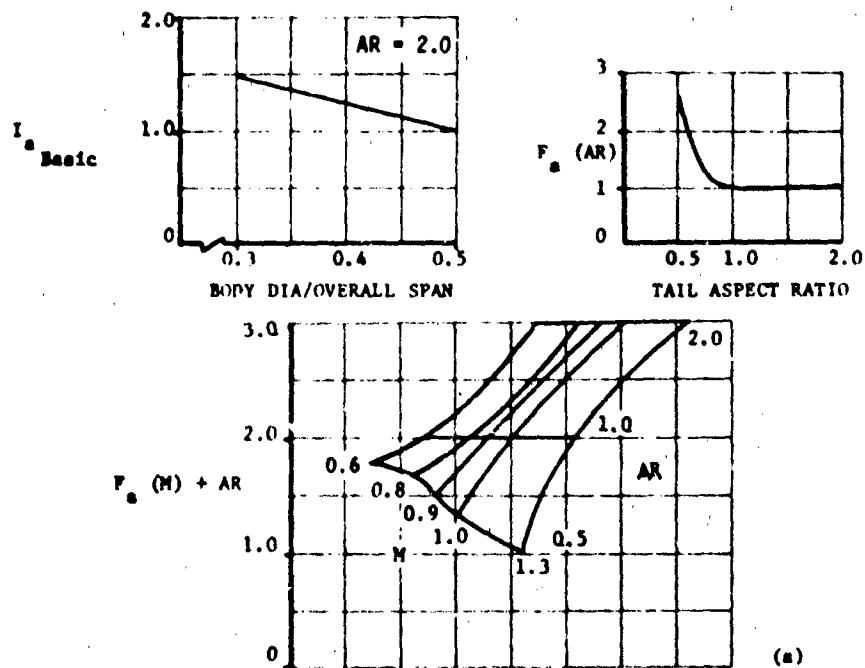


Figure 91a. Curves for Estimation of Transonic I_a (All λ)

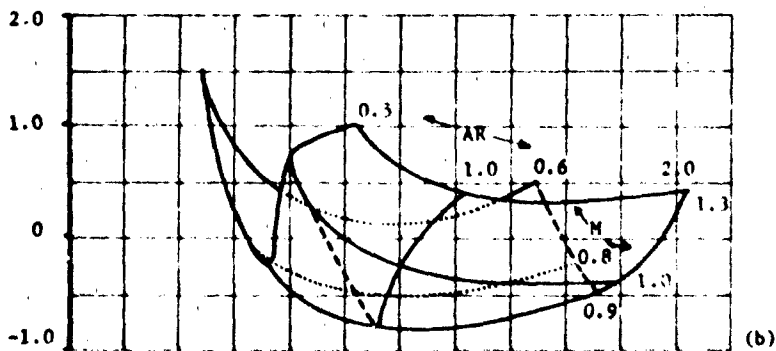


Figure 91b. Curves for Estimation of Transonic I_b (All λ and d/a)

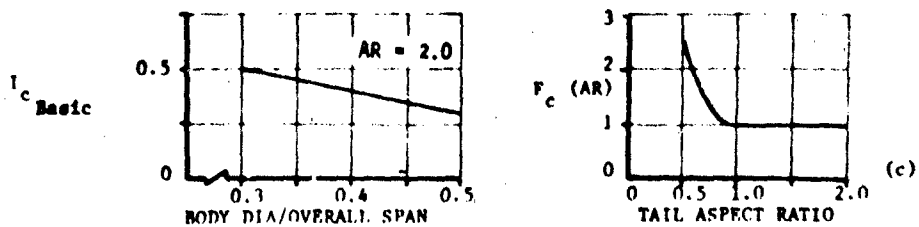


Figure 91c. Curves for Estimation of Transonic I_c (All λ and Mach Numbers)

$\lambda = 0, AR = 0.5, d/s = 0.5$

$M = 0.8$

○ Experiment (Ref. 13)

— Prediction

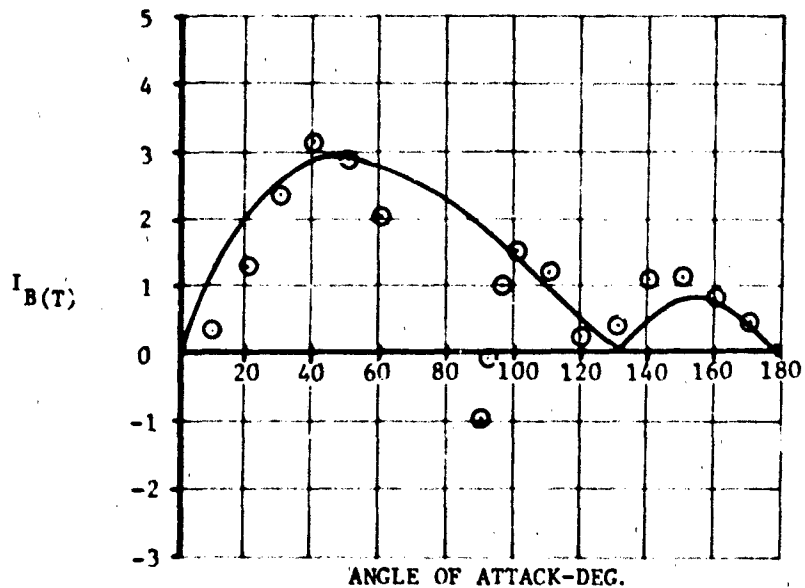


Figure 92. Comparison Between Predicted And Experimental I_{BT}

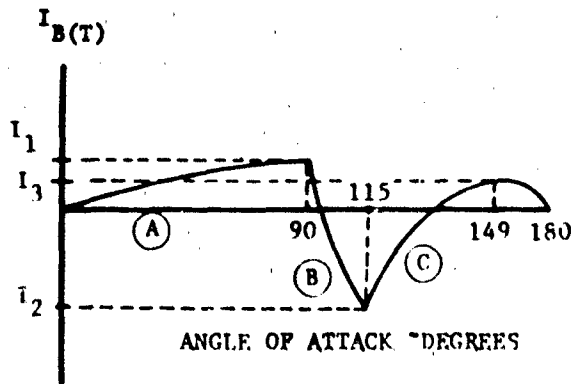


Figure 93. Supersonic $I_{B(T)}$, Schematic

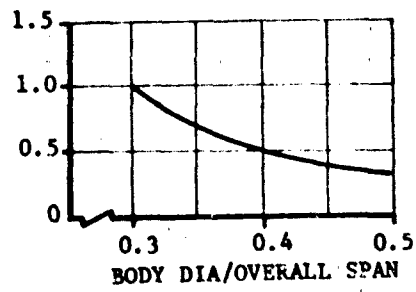
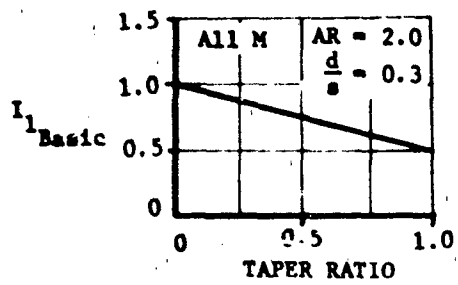


Figure 94a. Curves for Estimation of Supersonic I_1

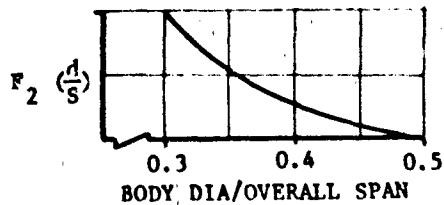
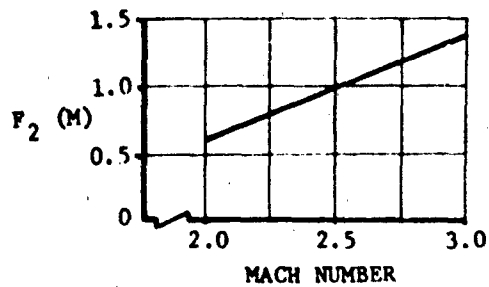
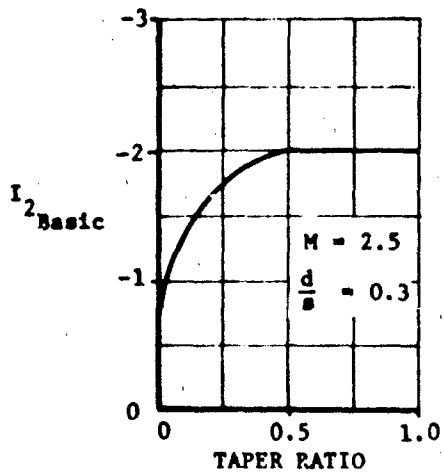


Figure 94b. Curves for Estimation of Supersonic I_2

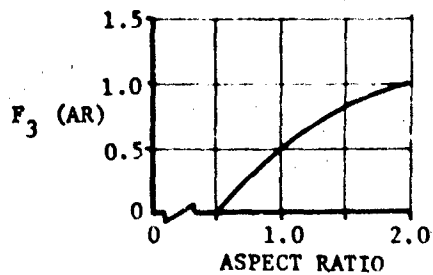
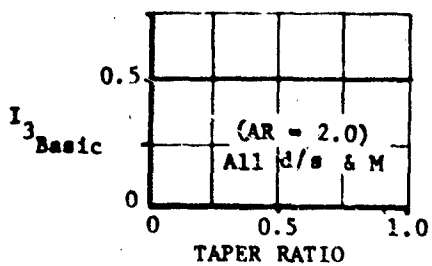


Figure 94c. Curves for Estimation of Supersonic I_3

M = 2.5

$\lambda = 0.5, AR = 2.0, \frac{d}{s} = 0.3$

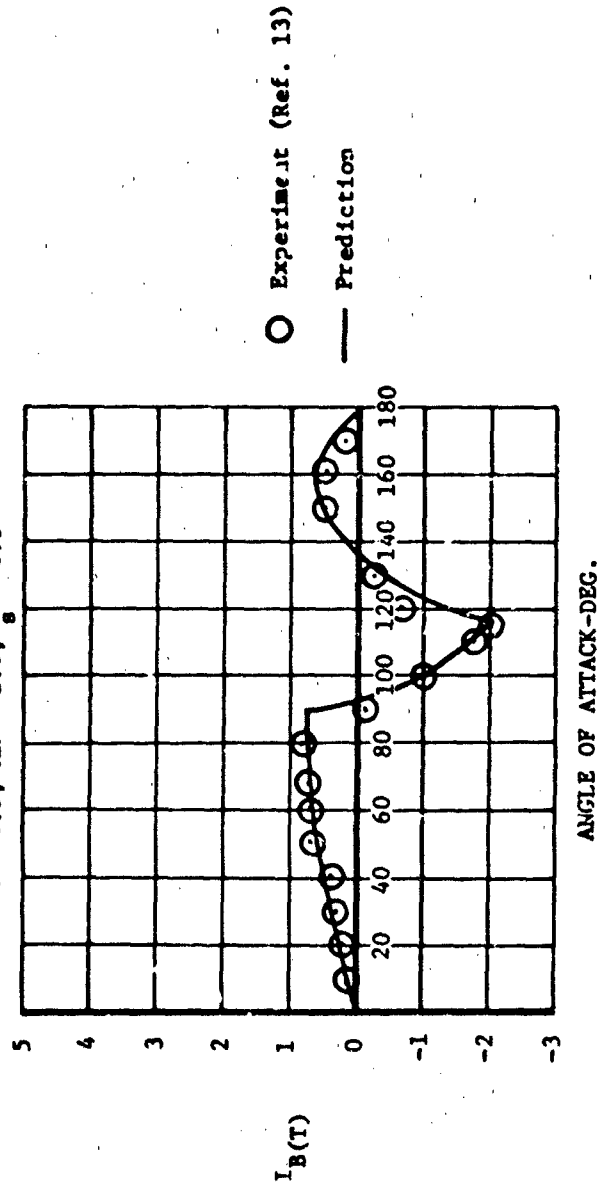


Figure 95. Comparison Between Predicted And Experimental $I_B(T)$

5.2.3 Tail-To-Body Carryover Normal Force Center of Pressure

Summary

A method is described to predict $X_{CP_{I(T)}}$, the center of pressure of normal force carried over to a body from horizontal tails. The method is an extension of an existing technique. It is valid for angles of attack from 0 - 180 degrees in the Mach range 0.6 - 2.0

It should be noted that $X_{CP_{I(T)}}$ is the axial distance from the missile nose to the point of application of the carryover force. The same point located relative to the surface leading edge is defined as $X_{CP_{B(T)}}$.

Background

An existing method, Reference 4, which applies to the angle range 0 - 90 degrees at Mach numbers from 0.8 - 1.2 was available as a starting point. The formulations of this method were such that the procedure was easily extendable to the angle range 0 - 180 degrees and the Mach number range 0.6 - 2.0.

The original method was based partly on the theoretical results of Reference 30 from which values of $X_{CP_{B(T)}}$ near zero angle were obtained. These results were used originally for the condition of a tail with no afterbody. However, when angle of attack has reached 180 degrees, the lifting surface does have an "afterbody" and the Reference 4 method was modified to reflect this.

Since the boundary conditions on the curve of $(X_{CP_{B(T)}}/C_R)$ versus angle of attack are easily determined, a power series approach to correlation was used.

Boundary conditions are:

$$\alpha = 0, (X_{CP_{B(T)}}/C_R)_0 \text{ given by Reference 30 (see below)}$$

$$\frac{\partial}{\partial \alpha} (X_{CP_{B(T)}}/C_R)_0 = 0 \text{ (linear theory)}$$

$$\alpha = 90^\circ, (X_{CP_{B(T)}}/C_R)_{\frac{\pi}{2}} = 0.5 \text{ (mid-chord point)}$$

$$\frac{\partial}{\partial \alpha} (X_{CP_{B(T)}}/C_R)_{\frac{\pi}{2}} = 0$$

$$\alpha = 180^\circ, (X_{CP_{B(T)}}/C_R)_\pi \text{ given by Reference 30 (see below)}$$

$$\frac{\partial}{\partial \alpha} (X_{CP_{B(T)}}/C_R)_\pi = 0 \text{ (linear theory)}$$

It is shown in Reference 30 that curves of $(X_{CP_{B(T)}}/C_R)_0$, the load location near zero angle of attack, can be constructed for various radius/semi-span ratios on the basis of βAR for configurations with afterbodies. It is noted that the ratio a/p used in Reference 30 is equivalent to $(d/2)/(s/2)$ or d/s in the terminology of this report. These curves are presented in Figures 96a, b, and c. The major reason for this representation is to use the slender body theory results for $\beta AR = 0$. Reference 30 indicates that the same representation can be employed for configurations with no afterbodies at supersonic speeds, but does not present the actual curves. It does, however, present information (Chart 14b of Reference 30) which can be used to construct partially the curves of $(X_{CP_{B(T)}}/C_R)_0$ away from the $\beta AR = 0$ point. Chart 14b presents data on load location as a function of $\beta d/C_R$ which may be written in terms of β , aspect ratio and body radius/semi-span ratio if tail taper ratio is known. For example, for triangular planform tails with no trailing edge sweep, the equality $d/C_R = AR/2(p/a-1)$ holds.

From relations like this, Chart 14b was converted to Figure 97a, b, and c of this report in which values of $(X_{CPB(T)}/C_R)_0$ are presented. In Figures 96 and 97 the values of load location at $\delta AR = 0$ were taken from slender body theory under the assumption that no tail force was developed aft of the maximum span. Values for $a/p = 0$ (tail with no body) were taken from supersonic wing theory.

For subsonic speeds, Figures 98 and 99, taken directly from Reference 30, may be used.

Rather than attempting to fit a single equation to the entire angle of attack range, it was divided into two sections, 0-90 degrees and 90-180 degrees.

0 - 90°

The functional form chosen empirically to represent $X_{CPB(T)}/C_R$ is:

$$\frac{X_{CPB(T)}}{C_R} = a_0 + a_1\alpha + a_2\alpha^2 + a_3\alpha^3$$

When the first four of the boundary conditions defined above are used, the series takes the following form.

$$\frac{X_{CPB(T)}}{C_R} = \frac{X_{CPB(T)}}{C_R} \Big|_0 + \left\{ \frac{2\alpha^3}{\left(\frac{\pi}{2}\right)^3} - \frac{3\alpha^2}{\left(\frac{\pi}{2}\right)^2} \right\} \left\{ \frac{X_{CPB(T)}}{C_R} \Big|_0 - \frac{X_{CPB(T)}}{C_R} \Big|_{\frac{\pi}{2}} \right\} \quad (38)$$

(α in rads)

The value of $X_{CPB(T)}/C_R$ represents, in non-dimensional form, the distance from the fin root chord leading edge to the center of pressure of the load generated on the body due to the presence of a tail. The second coefficient $2\alpha^3/(\pi/2)^3 - 3\alpha^2/(\pi/2)^2$ has been evaluated between 0 and 90 degrees and is shown in Figure 100.

90° - 180°

By now measuring the force location from the trailing edge ($\bar{x}_{CPB(T)}$) and defining the quantity $\bar{\alpha} = \pi - \alpha$, it is possible to derive an expression directly analogous to Equation (38) by utilizing the last four boundary conditions.

$$\frac{\bar{x}_{CPB(T)}}{C_R} = \frac{\bar{x}_{CPB(T)}}{C_R} \Big|_{\pi} + \left\{ \frac{2\bar{\alpha}^3}{\left(\frac{\pi}{2}\right)^3} - \frac{3\bar{\alpha}^2}{\left(\frac{\pi}{2}\right)^2} \right\} \left\{ \frac{\bar{x}_{CPB(T)}}{C_R} \Big|_{\pi} - \frac{\bar{x}_{CPB(T)}}{C_R} \Big|_{\frac{\pi}{2}} \right\} \quad (39A)$$

where \bar{x} is measured from the tail trailing edge and

$$\frac{x_{CPB(T)}}{C_R} = 1 - \frac{\bar{x}_{CPB(T)}}{C_R} \quad (39B)$$

Use of Method

Use of the method for predicting $x_{CPB(T)}$ will be demonstrated in conjunction with the other methods required to predict the center of pressure of a complete body-tail configuration. Initially, the method for predicting $x_{CPB(T)}$ will be described generally. Then a numerical example will be given of $x_{CPB(T)}$ calculations, plus the other calculations necessary to predict centers of pressure on a complete configuration.

1 Calculate $x_{CPB(T)}$ for $0^\circ \leq \alpha \leq 90^\circ$ using Equation 38.

a Depending upon Mach number, determine

$\frac{x_{CPB(T)}}{C_R} \Big|_0$ using either Figures 97 or 98.

b Using Figure 100, determine values of

$\frac{2\alpha^3}{\left(\frac{\pi}{2}\right)^3} - \frac{3\alpha^2}{\left(\frac{\pi}{2}\right)^2}$ at selected angles of attack.

2 Calculate $\bar{X}_{CPB(T)}$ for $90^\circ \leq \alpha \leq 180^\circ$ using Equation 39A and $X_{CPB(T)}$ with 39B

a Depending upon Mach number, determine $\frac{X_{CPB(T)}}{C_R} \left| \pi \right.$ using either Figures 96 or 99.

b Using Figure 100, determine values of $\frac{\bar{\alpha}^3}{\left(\frac{\pi}{2}\right)^3} - \frac{\bar{\alpha}^2}{\left(\frac{\pi}{2}\right)^2}$

where $\bar{\alpha} = 180 - \alpha$

Numerical Example

Calculate the centers of pressure at $M = 0.9$ for a body-tail configuration having the following characteristics:

Body:

$$\frac{l_N}{d} = 2.5$$

$$\frac{l_A}{d} = 7.5$$

$$d = 1.25 \text{ inches}$$

Tail:

$$\lambda = 0.5$$

$$AR = 1.0$$

$$d/s = 0.5$$

$$C_R = 1.667 \text{ inches}$$

$$\frac{X_{LE}}{d} = 8.666$$

1 Calculate C_{NB}

a At transonic Mach numbers, use the method of Reference 12

for $0^\circ \leq \alpha \leq 40^\circ$

<u>α (deg)</u>	<u>C_{NB}</u>
0	0
10	0.633
20	1.767
30	3.42
40	5.587

b For $50^\circ \leq \alpha \leq 180^\circ$, use the method of Section 5.1.1 (p. 39 ff)

<u>α (deg)</u>	<u>C_{NB}</u>
50	8.754
60	10.574
70	12.025
80	12.906
90	13.224
100	12.903
110	12.005
120	10.512
130	8.614
140	6.374
150	4.116
160	2.105
170	0.613
180	0.0

2 Calculate X_{CP_B} using the method of Section 5.1.2 (p. 61 ff)

<u>α (deg)</u>	<u>X_{CP_B} / d</u>
0	2.70
10	3.17
20	3.80
30	3.80
40	3.80
50	3.80
60	4.20
70	4.60
80	5.00
90	5.39
100	5.80
110	6.19
120	6.60
130	6.98
140	7.37
150	7.78
160	8.18
170	9.19
180	10.00

3 Using the methods of Section 5.1.4 (p. 91 ff) and 5.2.1 (p. 143 ff)

calculate $C_{NT(B)}$

$\alpha(\text{deg})$	C_{NT}	$R_T(B)$	$C_{NT(B)}$	$S_{\text{ref}} = S_T$
0	0	1.460	0	
10	0.369	1.400	0.517	
20	0.873	1.238	1.081	
30	1.085	1.000	1.085	
40	1.09	1.019	1.111	
50	1.08	1.058	1.143	
60	1.094	1.127	1.233	
70	1.100	1.181	1.299	
80	1.106	1.233	1.364	
90	1.1	1.300	1.430	
100	1.106	1.106	1.502	
110	1.1	1.415	1.557	
120	1.094	1.445	1.581	
130	1.080	1.460	1.577	
140	1.090	1.433	1.562	
150	1.085	1.379	1.496	
160	0.873	1.301	1.136	
170	0.369	1.158	0.427	
180	0.0	1.0	0.0	

4 Using the method of Section 5.1.5 (p. 122 ff) calculate $\frac{X_{CPT(B)}}{d}$

α (deg)	$\frac{X_{CPT(B)}}{C_R}$	$\frac{X_{CPT}}{d}$
0	0.391	9.188
10	0.439	9.252
20	0.498	9.330
30	0.535	9.380
40	0.546	9.394
50	0.557	9.409
60	0.578	9.437
70	0.589	9.452
80	0.599	9.465
90	0.615	9.486
100	0.635	9.513
110	0.650	9.533
120	0.670	9.560
130	0.690	9.586
140	0.710	9.613
150	0.725	9.633
160	0.745	9.670
170	0.863	9.817
180	0.995	9.993

where $\frac{X_{CPT}}{d} = \frac{X_{LE}}{d} + \frac{X_{CPT(B)}}{C_R} \cdot \frac{C_R}{d}$

5 Using the method of Section 5.2.2 (p. 161 ff), Calculate $I_B(T)$

<u>α (deg)</u>	<u>$I_B(T)$</u>
0	0
10	0.375
20	0.657
30	0.851
40	0.964
50	1.000
60	0.965
70	0.865
80	0.704
90	0.489
100	0.226
110	-0.082
120	-0.427
130	-0.800
140	-0.215
150	0.156
160	0.315
170	0.263
180	0.0

6 Using the procedure outlined above, calculate $\frac{X_{CP_I(T)}}{d}$

α (deg)	$\frac{X_{CP_B(T)}}{C_R}$	$\frac{X_{CP_I(T)}}{d}$
0	0.28	9.040
10	0.289	9.052
20	0.306	9.074
30	0.333	9.110
40	0.368	9.157
50	0.405	9.206
60	0.440	9.253
70	0.471	9.294
80	0.491	9.321
90	0.5	9.338
100	0.517	9.356
110	0.556	9.408
120	0.618	9.490
130	0.685	9.580
140	0.758	9.677
150	0.827	9.769
160	0.878	9.837
170	0.913	9.884
180	0.93	9.907

where $\frac{X_{CP_I(T)}}{d} = \frac{X_{LE}}{d} + \frac{X_{CP_B(T)}}{C_R} \cdot \frac{C_R}{d}$ for $\alpha \leq 90^\circ$

and $\frac{X_{CP_I(T)}}{d} = \frac{X_{LE}}{d} + \left(1.0 - \frac{X_{CP_B(T)}}{C_R}\right) \frac{C_R}{d}$ for $\alpha \geq 90^\circ$

7 To calculate $\frac{X_{CP_{BT}}}{d}$, the center of pressure of the body-tail combination, apply the results of Steps 1-6 to the following equation:

$$\frac{X_{CP_{BT}}}{d} = \frac{C_{N_B} \frac{X_{CP_B}}{d} + 2 C_{N_{T(B)}} \frac{S_T}{S_{ref}} \frac{X_{CP_{T(B)}}}{d} + I_{B(T)} \cdot \frac{X_{CP_I(T)}}{d}}{C_{N_B} + 2 C_{N_{T(B)}} \frac{S_T}{S_{ref}} + I_{B(T)}}$$

α (deg)	C_{N_B}	$\frac{X_{CP_B}}{d}$	$C_{N_{T(B)}}$	$\frac{X_{CP_{T(B)}}}{d}$	$I_{B(T)}$	$\frac{X_{CP_I}}{d}$	$C_{N_{BT}}$	$\frac{X_{CP_{BT}}}{d}$
0	0	2.7	0	9.188	0	9.040	0	-
10	.633	3.170	.577	9.252	.375	9.052	1.839	6.896
20	1.767	3.800	1.081	9.330	.657	9.074	3.800	6.715
30	3.42	3.800	1.085	9.380	.851	9.110	5.652	5.963
40	5.587	3.800	1.111	9.374	.964	9.157	7.966	5.442
50	8.754	3.80	1.143	9.409	1.000	9.206	11.209	5.011
60	10.574	4.20	1.233	9.437	.965	9.253	13.109	5.199
70	12.025	4.60	1.299	9.452	.865	9.294	14.544	5.431
80	12.906	5.00	1.364	9.465	.704	9.321	15.347	5.703
90	13.224	5.392	1.430	9.486	.489	9.330	15.534	5.996
100	12.903	5.80	1.502	9.513	.226	9.356	15.041	6.326
110	12.005	6.19	1.557	9.533	-.082	9.408	13.905	6.648
120	10.512	6.60	1.581	9.560	-.427	9.490	12.098	6.991
130	8.614	6.98	1.577	9.586	-.800	9.580	9.823	7.301
140	6.374	7.37	1.562	9.613	-.215	9.677	8.148	7.857
150	4.116	7.78	1.496	9.633	.156	9.769	6.177	8.402
160	2.105	8.178	1.136	9.660	.315	9.837	3.866	8.868
170	.613	9.189	.427	9.817	.263	9.884	1.420	9.558
180	0.0	10.0	0.0	9.993	0.0	9.907	0.0	

Data Comparisons

The results of this test case ($C_{N_{BT}}$ and $\frac{X_{CP_{BT}}}{d}$) are compared against experimental data in Figures 101 and 102. Good agreement is obtained between the predictions and experimental data.

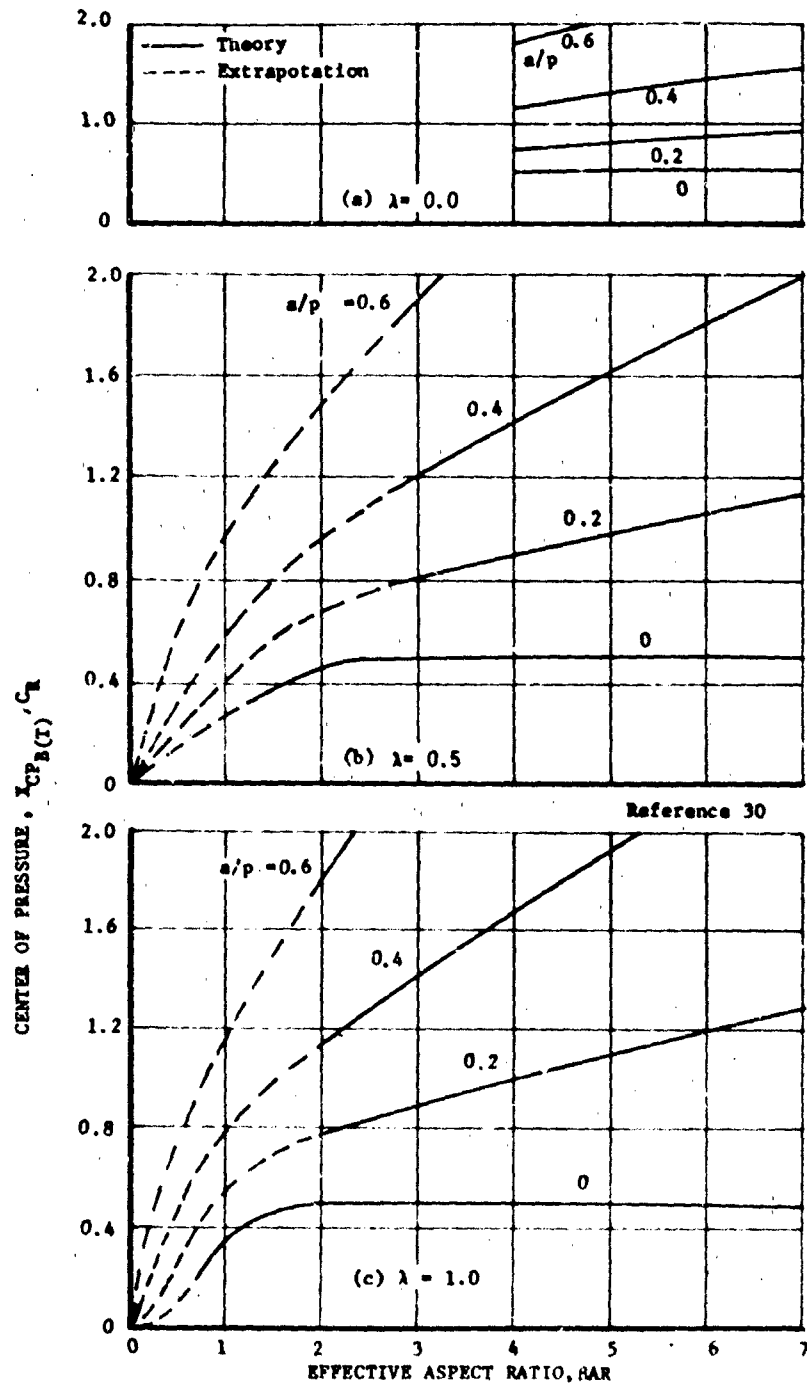


Figure 96. Curves for Determining $X_{CP_B(T)}/C_R$ With Afterbodies for Supersonic Speeds

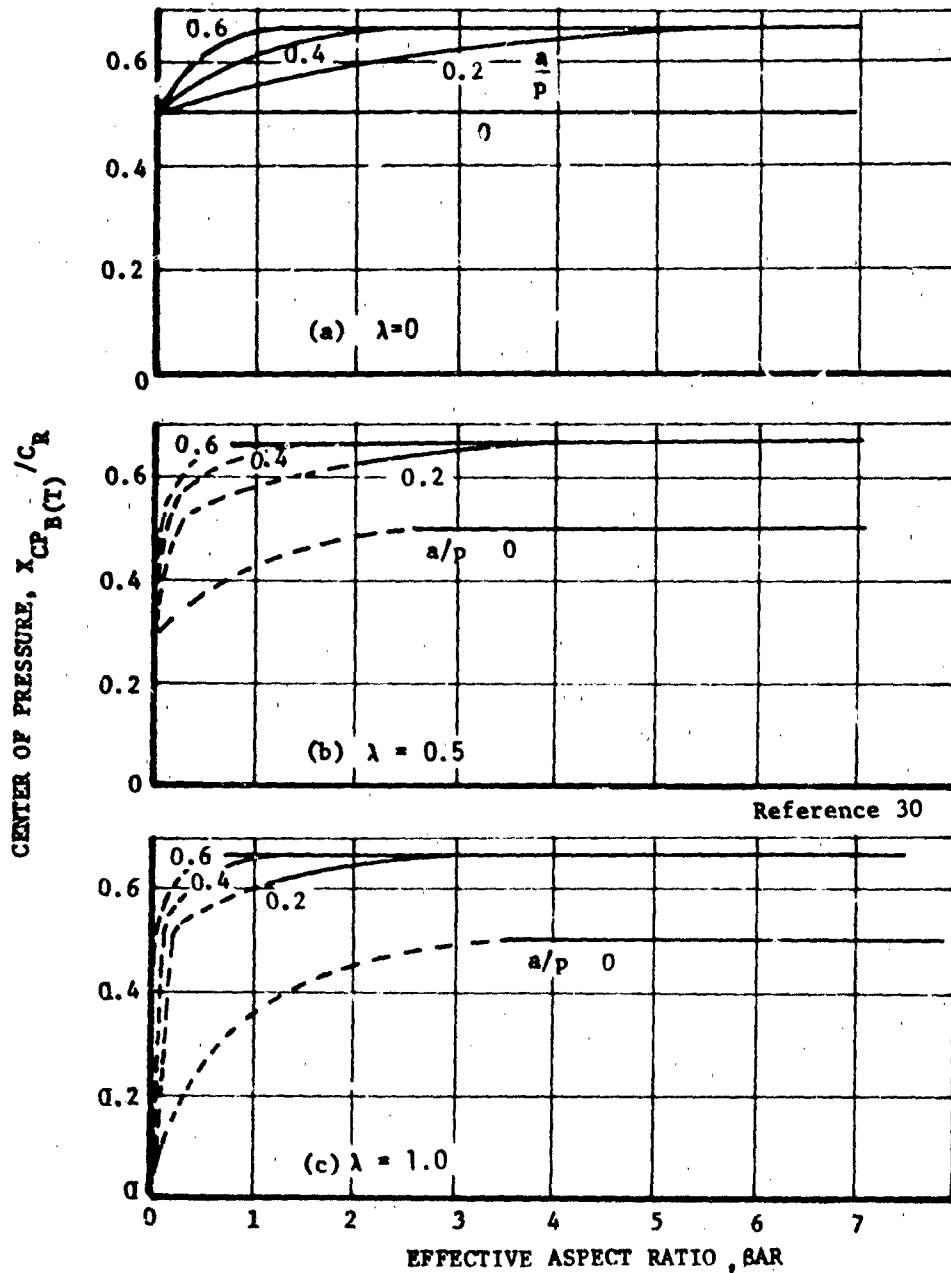


Figure 97. Curves for Determining $X_{CPB(T)}/C_R$ for No Afterbodies at Supersonic Speeds

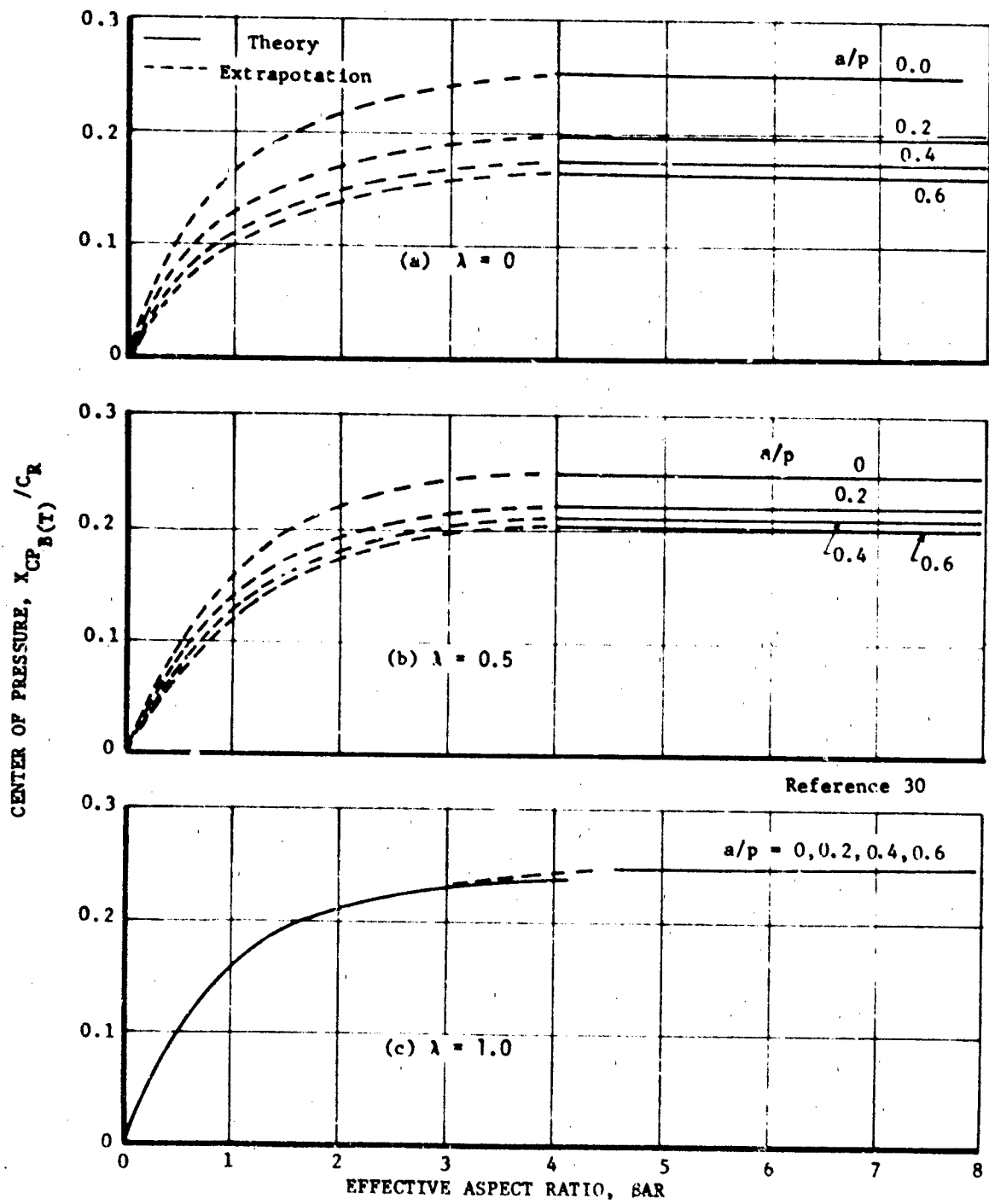


Figure 98. Curves for Determining $X_{CPB(T)}/C_R$ for Subsonic Speeds
(Zero Leading Edge Sweep)

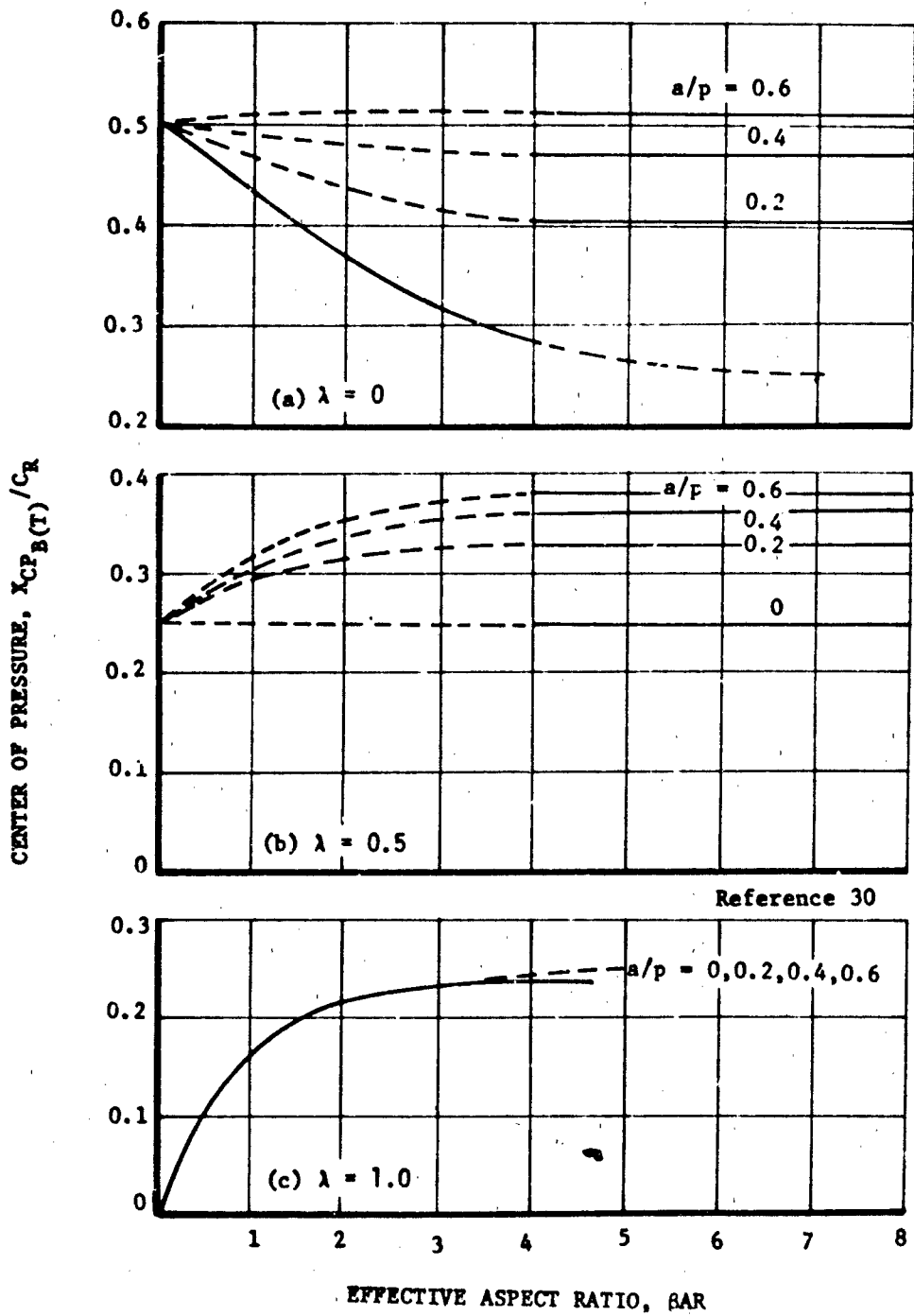


Figure 99. Curves for Determining $X_{CPB(T)}/C_R$ for Subsonic Speeds (Zero Trailing Edge Sweep)

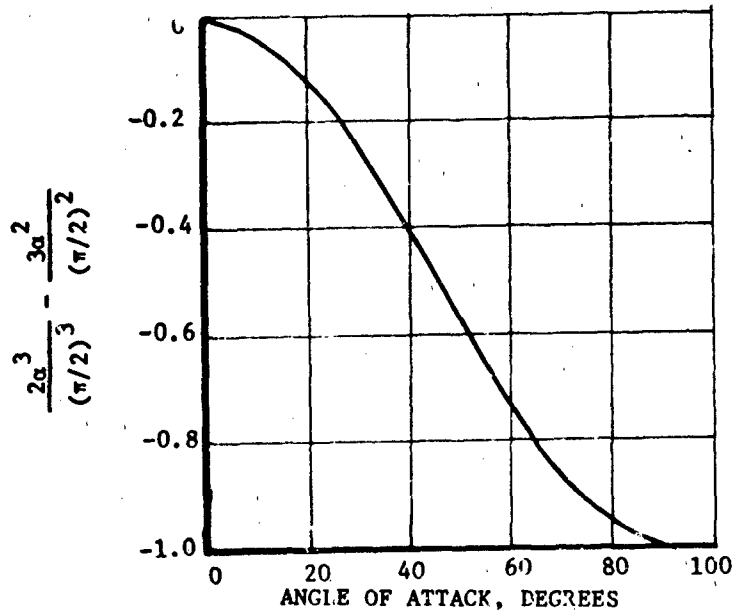


Figure 100. Coefficients Required for Evaluation of $x_{CP_{B(T)}}/C_R$

M = 0.9

Body

Tail

$l_N/d = 2.5$

$\lambda = 0.5$

$l_A/d = 7.5$

AR = 1.0

$d = 1.25$ Inches

$d/s = 0.5$

$C_R = 1.667$ Inches

○ Experimental (Ref. 13)
— Predicted

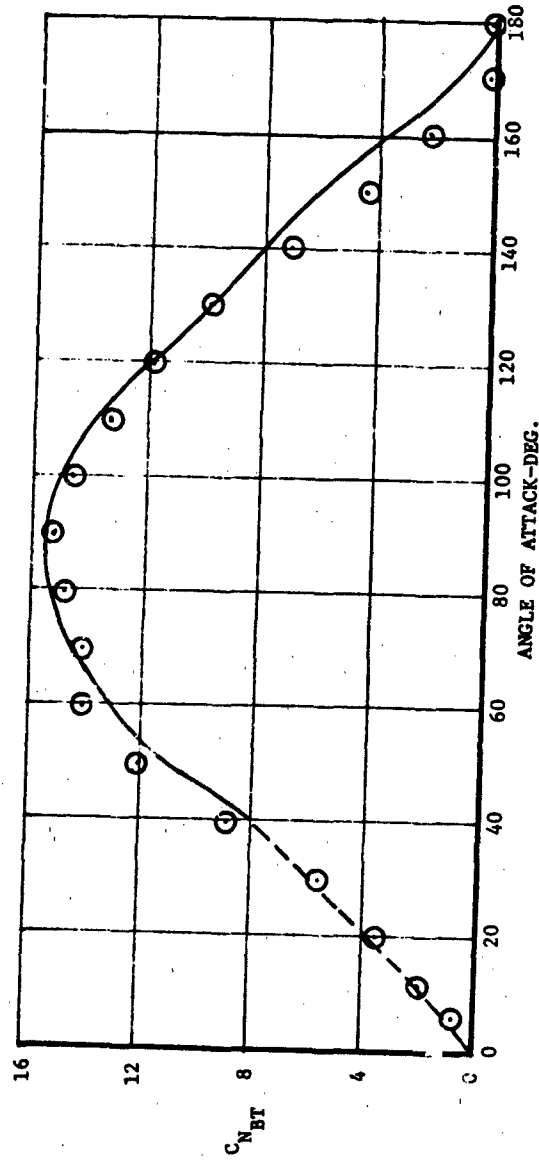


Figure 101. Comparison Between Predicted and Experimental Data, $C_{N_{BT}}$

$M = 0.9$
 Body
 $l_N/d = 2.5$
 $l_A/d = 7.5$
 $d = 1.25$ Inches
 Tail
 $\lambda = 0.5$
 $AR = 1.0$
 $d/s = 0.5$
 $C_R = 1.667$ Inches

○ Experimental (Ref. 13)
 — Predicted

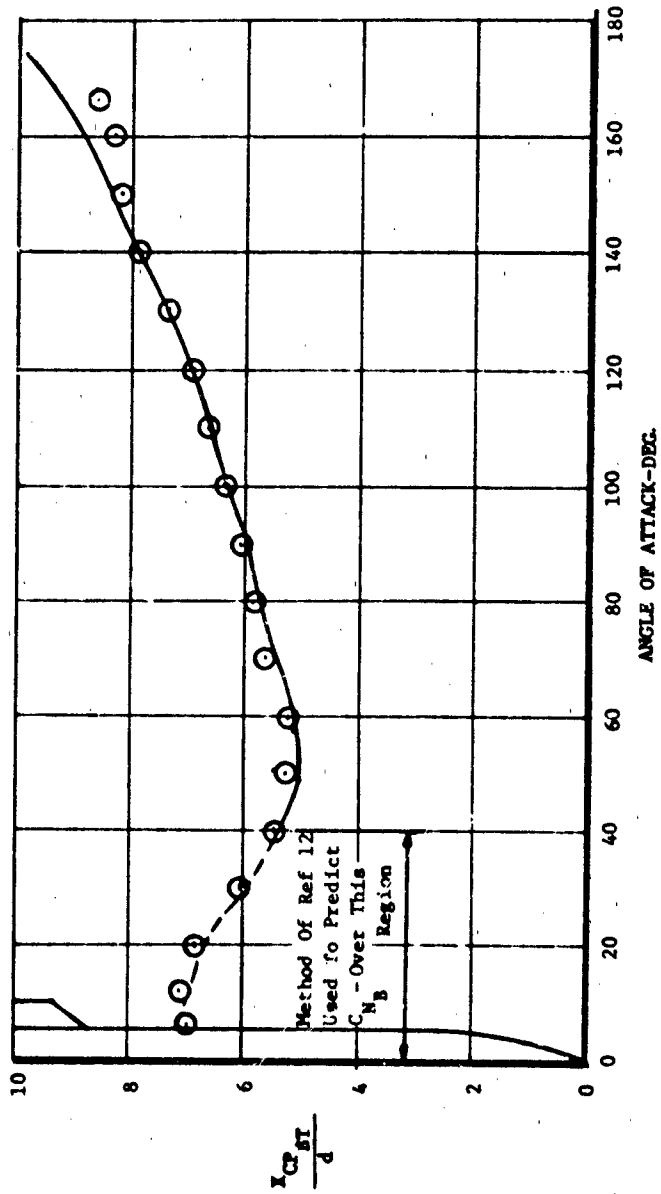


Figure 102. Comparison Between Predicted and Experimental Data, $X_{CP BT}$

5.3 Body-Strake-Tail Configurations

5.3.1 Incremental Normal Force Due to Strakes

Summary

A method is presented for estimating the total incremental normal force coefficient, $\Delta C_{N_{BS}}$, due to low aspect-ratio strakes on a slender tangent-ogive-cylinder body at a roll angle of zero (+ orientation). This method covers angles of attack up to 180 degrees and a Mach number range of 0.50 to 2.2 and represents an extension of an existing low-angle technique.

Background

The addition of strakes to a body produces an increased normal force which is a function of strake size relative to the body and strake aspect ratio. The incremental normal force may be estimated at low angles of attack from Section 4.3.1.2 of Reference 17. At higher angles no methods exist for calculating the increase. This section describes the construction of such a method. The data forming the basis for correlation were obtained from tests on a particular USAF missile design. Since the strakes used were not instrumented to record normal force, the following formulation was used:

$$C_{N_{BS}} = C_{N_B} + \Delta C_{N_{BS}}$$

$\Delta C_{N_{BS}}$ was determined directly from test data at Mach 0.6, 0.85, and 1.2. Due to a lack of body plus strake data at zero roll angle, values of $\Delta C_{N_{BS}}$ at Mach 1.8 and 2.2 were derived using available total configuration and body alone data at those Mach numbers in conjunction with a factor from Mach 1.2 data defining relative tail and strake contributions. A curve-fit procedure was used for data correlation.

Method Development

Examination of data available at five Mach numbers (0.60, 0.95, 1.20, 1.85, and 2.2) revealed several features useful in curve fitting (see Figure 103). A curve of $\Delta C_{N_{BS}}$ versus alpha at each Mach number exhibits peaks of approximately equal magnitude at $\alpha = 57^\circ$ and $\alpha = 135^\circ$. The value of $\Delta C_{N_{BS}}$ at these peaks is Mach number dependent. Between $\alpha = 80^\circ$ and $\alpha = 120^\circ$, the value of $\Delta C_{N_{BS}}$ oscillates about a mean value which is independent of Mach number. The slopes ($\Delta C_{N_{BS\alpha}}$) at $\alpha = 0^\circ$ and $\alpha = 180^\circ$ appear to be about equal in magnitude but with opposite signs. A power series formulation using the aforementioned curve qualities as boundary conditions was the approach selected to fit a general curve to the data.

A third-order power series of the form

$$\Delta C_{N_{BS}} = a_0 + a_1\alpha + a_2\alpha^2 + a_3\alpha^3$$

was used with the following boundary conditions:

$$\Delta C_{N_{BS}} = 0 \text{ at } \alpha = 0^\circ \text{ and } 180^\circ$$

$$\Delta C_{N_{BS\alpha}} = J_1 \text{ at } \alpha = 0^\circ$$

$$\Delta C_{N_{BS\alpha}} = -J_1 \text{ at } \alpha = 180^\circ$$

$$\Delta C_{N_{BS}} = K \text{ at } \alpha = 57.3^\circ \text{ and } 135^\circ$$

$$\Delta C_{N_{BS}} = L \text{ at } \alpha = 80^\circ \text{ and } 120^\circ$$

where

$$J_1 = \Delta C_{N_{BS\alpha}} \text{ at } \alpha = 0^\circ$$

$$= (K_{B(W)} + K_{W(B)}) \left(\frac{S_B}{S_{ref}} \right) \left(\frac{\pi}{2} AR_B \right) \text{ [Reference 17, Section 4.3.1.2]}$$

$K_a = \Delta C_{N_{BS}}$ peak value at $\alpha = 57.3^\circ$ and 135°

$$= \left[\frac{K_a}{(S_{S+B}/S_{ref})} \right] \frac{S_{S+B}}{S_{ref}}$$

The bracketed term is an empirical correlation presented in Figure 104

$L =$ mean value of $\Delta C_{N_{BS}}$, $80^\circ \leq \alpha \leq 120^\circ$

$$= 0.461 \left(\frac{S_{S+B}}{S_{ref}} \right)$$

$S_a =$ Strake single span exposed area

$S_{ref} =$ Reference area for $\Delta C_{N_{BS}}$ (equal to body cross sectional area)

$S_{S+B} =$ Area of two strakes + planform area of body between strakes

Note that the boundary condition J_1 has been generalized by the presence of aspect ratio, $K_{B(W)}$ and $K_{W(B)}$, the latter to be a function of d/s . Planform area was found to be an effective correlating parameter for the quantities K_a and L .

To simplify the power series solution and improve the accuracy of the estimate, the power series was formulated for three intervals: $0 \leq \alpha \leq 80^\circ$, $80^\circ \leq \alpha \leq 120^\circ$, and $120^\circ \leq \alpha \leq 180^\circ$. Solution of the third order power series yielded a_0 , a_1 , a_2 , and a_3 as functions of J_1 , K_a , and L for the three angle of attack ranges. Upon separating terms, an equation of the form

$$\Delta C_{N_{BS}} = A_1 J_1 + A_2 K_a + A_3 L$$

was derived. Equations for A_1 , A_2 , and A_3 are as follows:

$$0 \leq \alpha \leq 80^\circ$$

$$A_1 = \alpha - 1.7162 \alpha^2 + 0.7162 \alpha^3$$

$$A_2 = 3.5238 \alpha^2 - 2.5238 \alpha^3$$

$$A_3 = -1.2945 \alpha^2 + 1.2945 \alpha^3$$

($\alpha \sim$ radians)

$$80^\circ \leq \alpha \leq 120^\circ$$

$$A_1 = 0.$$

$$A_2 = 0.$$

$$A_3 = 1.0$$

$$120^\circ \leq \alpha \leq 180^\circ$$

$$A_1 = 18.8191 - 22.9603\alpha + 9.2150\alpha^2 - 1.2138\alpha^3$$

$$A_2 = -127.8802 + 142.4405\alpha - 51.8098\alpha^2 + 6.1836\alpha^3$$

$$A_3 = 80.9455 - 85.8667\alpha + 30.0601\alpha^2 - 3.4789\alpha^3$$

($\alpha \sim$ radians)

Values of A_1 , A_2 and A_3 have been plotted versus angle of attack (Figure 105)

to facilitate use of this method. Peak values $\frac{K}{S_{S+B}/S_{REF}}$ have been

determined empirically and are plotted versus Mach number in Figure 104.

Use of Method

The method is used as follows:

Given a tangent-ogive-cylinder body with low aspect ratio strakes of the following characteristics:

body diameter = d

body reference area = $\frac{\pi d^2}{4} = S_{ref}$

strake single span exposed area = S_s

strake root chord = C_{RS}

strake aspect ratio = AR_s

strake exposed semi-span = $b/2$

Proceed thus:

1 compute $J_1 = (K_{B(W)} + K_{W(B)}) \left(\frac{S_s}{S_{ref}} \right) \left(\frac{\pi}{2} AR_s \right)$ [Ref. 17, Sect. 4.3.1.2]

2 Find $\left(\frac{K_a}{S_{S+B}/S_{ref}} \right)$ from Figure 104 for the desired Mach number.

Compute $K_a = \frac{K_a}{(S_{S+B}/S_{ref})} * \frac{S_{S+B}}{S_{ref}}$ where $S_{S+B} = (2*S_s) + (C_{RS} * d)$

3 Compute $L = 0.461 \left(\frac{S_{S+B}}{S_{ref}} \right)$

4 Look up A_1 , A_2 , and A_3 for the desired angle of attack in Figure 105.

5 Substitute in the relationship.

$$\Delta C_{N_{BS}} = A_1 J_1 + A_2 K_a + A_3 L$$

Numerical Example

Calculate $\Delta C_{N_{BS}}$ at Mach 0.85 for a body - strake combination having the following properties:

$d = 3.667$ in. $AR_s = 0.040$

$S_{ref} = 10.56$ sq.in. $b/2 = 0.40$ in.

$S_s = 8.06$ sq.in. $C_{RS} = 14.33$ in.

1 from Ref. 17 $K_{B(W)} = 1.43$, $K_{W(B)} = 1.76$

$$J_1 = (1.43 + 1.76) \left(\frac{8.06}{10.56} \right) \left(\frac{\pi}{2} \right) (0.040) = 0.151/\text{radian}$$

2 from Figure 104, $\frac{K_a}{S_{S+B}/S_{ref}} = 0.66$ at Mach 0.85

$$S_{S+B} = (2*8.06) + (14.33*3.667) = 68.67 \text{ sq.in.}$$

$$K_a = 0.661 \left(\frac{68.67 \text{ sq.in.}}{10.56 \text{ sq.in.}} \right) = 4.30$$

3 $L = 0.461 \left(\frac{68.67}{10.56} \right) = 3.00$

4 From Figure 104

α	A_1	A_2	A_3	$A_1 J_1$	$A_2 K_a$	$A_3 L$	ΔC_{NBS}
0	0	0	0	0	0	0	0
20	0.17	0.32	-.10	0.03	1.38	-.30	1.11
40	0.11	0.87	-.19	0.02	3.75	-.57	3.20
60	-.02	0.95	0.07	0.00	4.09	0.21	4.30
80	0.00	0.00	1.00	0.00	0.00	3.00	3.00
100	0.00	0.00	1.00	0.00	0.00	3.00	3.00
120	0.00	0.00	1.00	0.00	0.00	3.00	3.00
140	0.03	1.05	-.14	0.00	4.53	-.42	4.11
160	0.12	0.52	-.19	0.02	2.24	-.57	1.67
180	0.00	0.00	0.00	0.00	0.00	0.00	0.00

Data Comparisons

In Figure 106 the results of this method are plotted along with those data used in formulating the method. It can be seen that the power series solution yields good correlation with test data across the Mach range tested. A lack of independent data in the desired high angle of attack range prevents further comparisons.

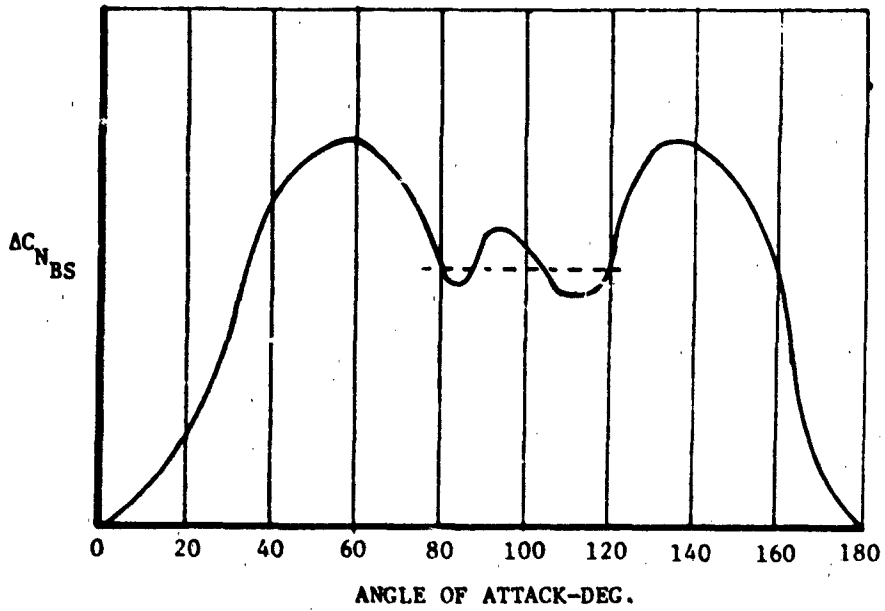


Figure 103. $\Delta C_{N_{BS}}$ General Curve Form

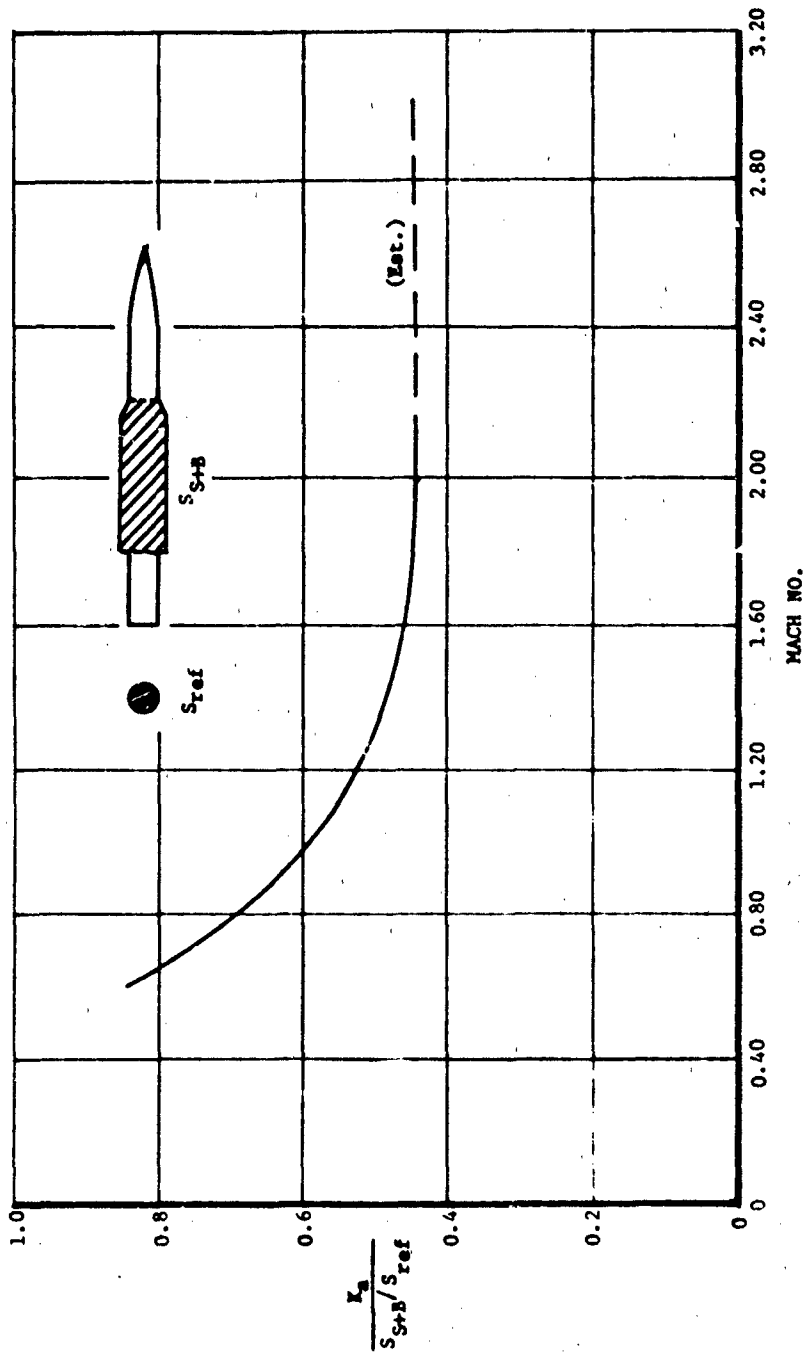


Figure 104. $\Delta C_{N_{BS}}$ Peak Factor K

$$\Delta C_{N_{BS}} = A_1 J_1 + A_2 K_2 + A_3 L$$

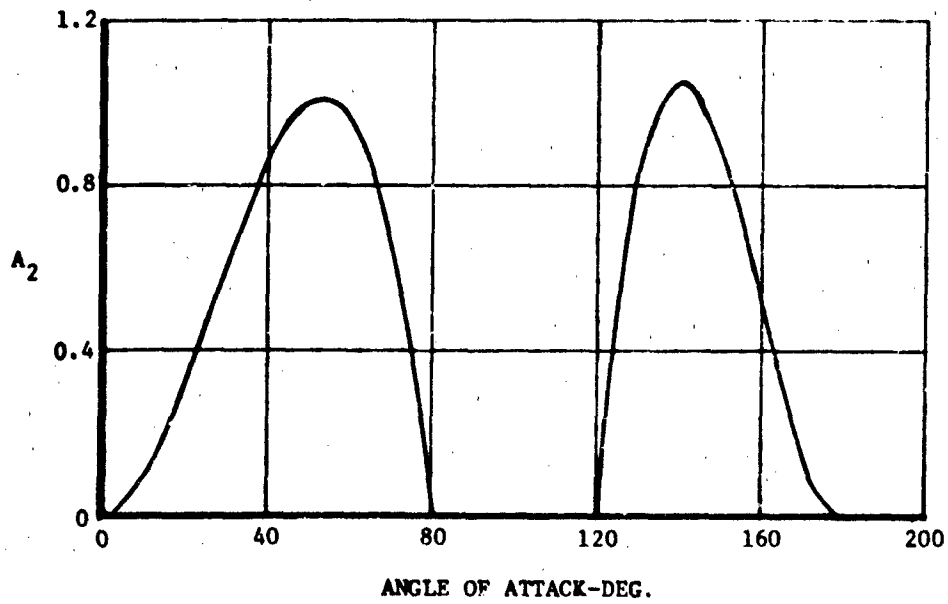
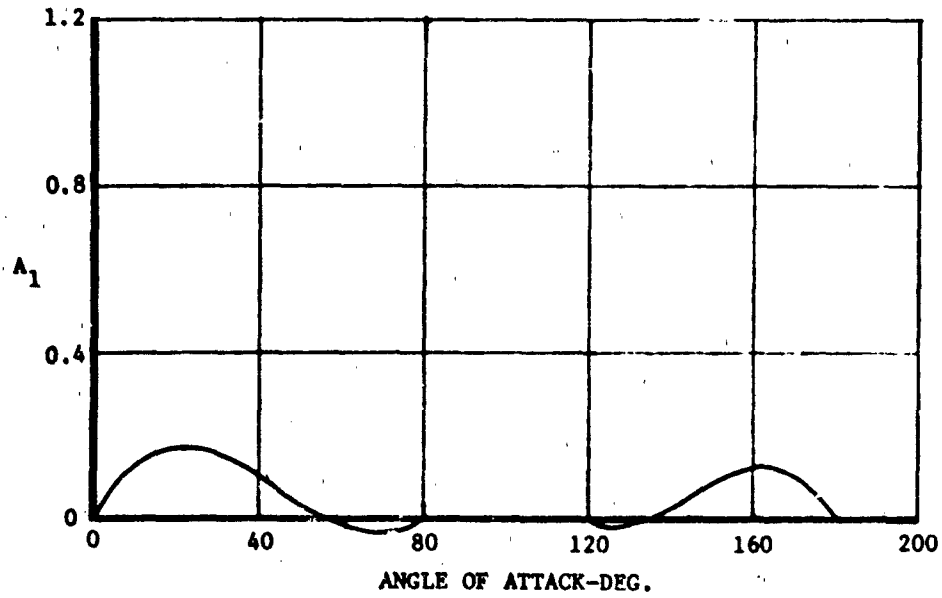


Figure 105. Coefficients for Calculating $\Delta C_{N_{BS}}$

$$\Delta C_{N_{BS}} = A_1 J_1 + A_2 K_2 + A_3 L$$

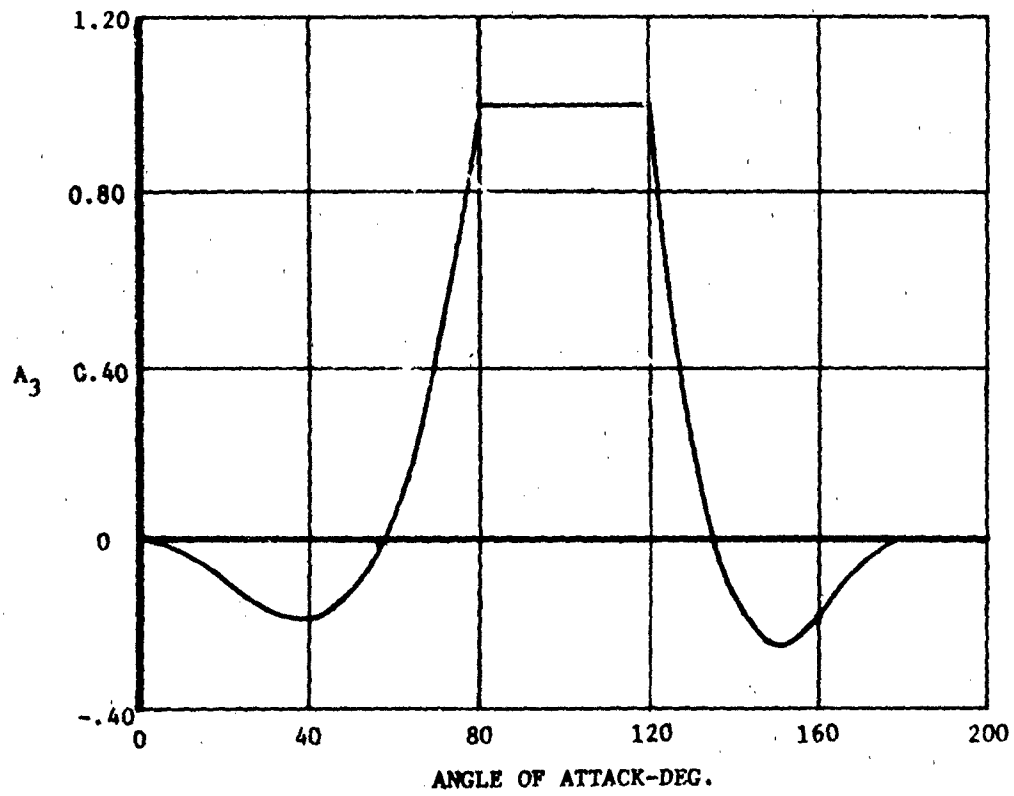
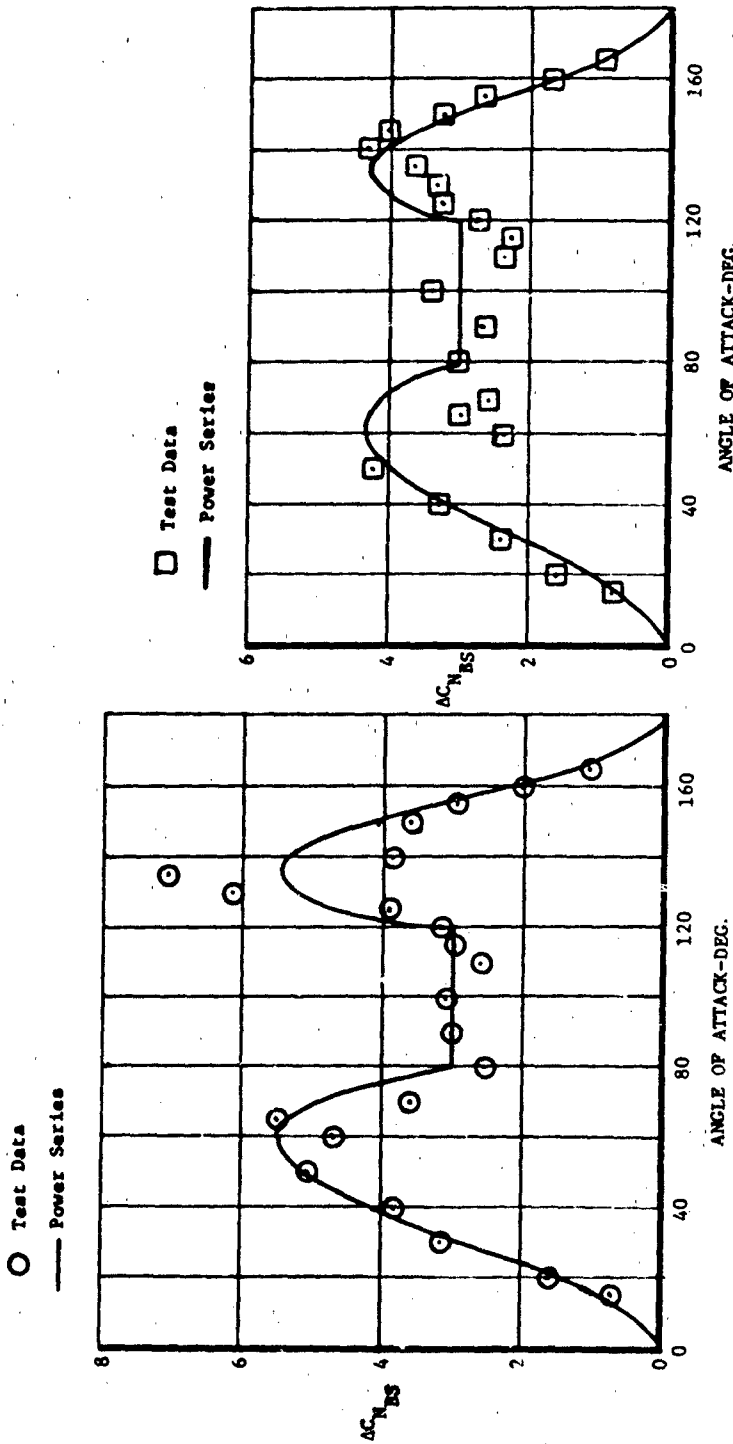


Figure 105 (Cont.). Coefficients for Calculating $\Delta C_{N_{BS}}$



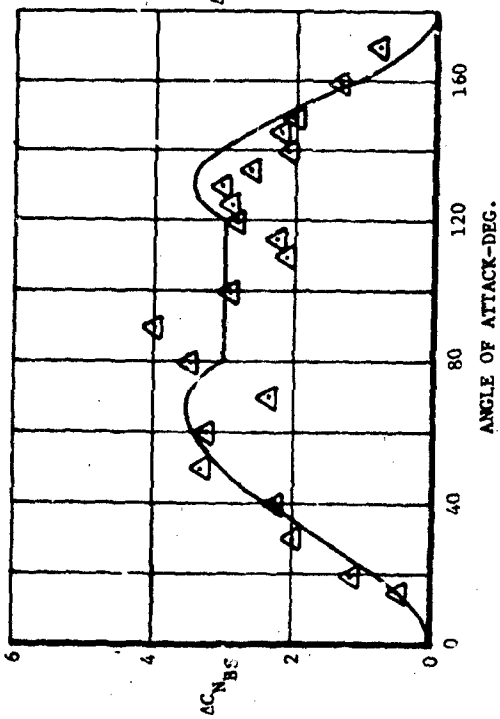
a. Mach 0.60

b. Mach 0.85

Figure 106. Comparison of Test Data And Method, $AC_{N_{BS}}$

Mach 1.2

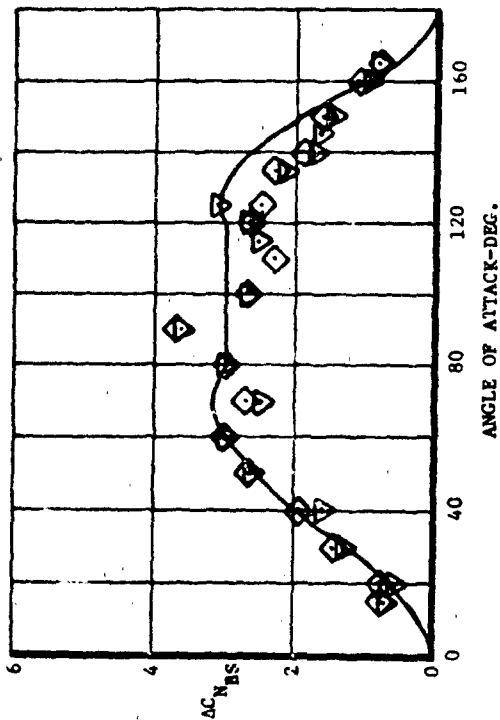
△ Test Data
— Power Series



c. Mach 1.20

Mach 1.8, 2.2

◇ Test Data, Mach 1.8
▽ Test Data, Mach 2.2
— Power Series



d. Mach 1.80, 2.20

Figure 105 (Cont.). Comparison of Test Data and Method, $AC_{N_{BS}}$

5.3.2 Center of Pressure for Incremental Normal Force Due to Strakes

Summary

A method is presented to predict $X_{CP_{\Delta BS}}$, the effective center of pressure of the incremental normal force ($\Delta C_{N_{BS}}$) due to a low aspect-ratio strake on a slender tangent ogive-cylinder body at a roll angle of zero (+ orientation). This method covers angles of attack up to 180 degrees and a Mach number range of 0.60 to 2.20 and represents an extension of an existing low-angle technique.

Background

The addition of strakes to a body produces a change in the center of pressure location which is related to the strake effective center of pressure location, $X_{CP_{\Delta BS}}$, the strake normal force coefficient including carryover, $\Delta C_{N_{BS}}$, and the body alone normal force coefficient, C_{N_B} , and center of pressure, X_{CP_B} . The strake center of pressure location may be estimated for low angles of attack by the methods of Section 4.1.4.2 of Reference 17. The present work describes the formulation of a method for predicting strake center of pressure location at angles of attack up to 180 degrees. The data forming the basis for correlation were obtained from tests on a particular USAF missile design.

Since the strakes tested were not instrumented for center of pressure determination, the following equation was used for the summation of moments:

$$C_{N_{BS}} \cdot X_{CP_{BS}} = C_{N_B} \cdot X_{CP_B} + \Delta C_{N_{BS}} \cdot X_{CP_{\Delta BS}}$$

$X_{CP_{\Delta BS}}$ represents the center of pressure of the entire strake normal force contribution, including interference effects, and was determined directly from test data at Mach 0.60, 0.85, and 1.2. Due to a lack of body plus strake data for zero roll angle at Mach 1.8 and 2.2, values of $X_{CP_{\Delta BS}}$ were derived using available total configuration and body alone data at those Mach numbers

in conjunction with a factor from Mach 1.2 data defining relative tail and strake contributions. A curve-fit procedure was used for data correlation.

Method Development

Figure 107 shows the general form of a curve of $X_{CP_{ABS}}$ versus angle of attack as derived from test data. This general curve shows that $X_{CP_{ABS}}$ moves from its $\alpha = 0^\circ$ location to a point near the strake centroid at $\alpha \sim 30^\circ$, then moves forward as $\alpha + 60^\circ$. At $\alpha \sim 120^\circ$, $X_{CP_{ABS}}$ attains its farthest aft position, from which it moves forward to a point near the centroid at $\alpha \sim 180^\circ$. Center of pressure locations at 0, 60, and 120 degrees exhibited a dependence on Mach number. A power series formulation using these curve qualities as boundary conditions was the approach selected to fit a general curve to the data.

$X_{CP_{ABS}}$ was considered to be a function of Mach number and strake geometry. Since the strake tested had two distinct segments, the area centroids of the forward portion (\bar{X}_A) and of the aft portion (\bar{X}_B) were incorporated along with the area centroid location of the entire strake (\bar{X}_S) and the strake root chord length (C_{RS}). Figure 108 illustrates the strake parameters used in this analysis.

The equation for the apparent location of the incremental force due to the addition of a strake is:

$$\frac{X_{CP_{ABS}}}{d} = \frac{X_{LE}}{d} + \frac{X_{CP_S}}{d}$$

where X_{CP_S}/d is a function of angle of attack and Mach number, and X_{LE} is the axial distance from the body nose to the leading edge of the strake.

Note that X_{CP_S}/d represents the center of pressure of the strake total normal force ($AC_{N_{BS}}$) and is measured from the leading edge of the strake root ,

whereas $X_{CP_{ABS}}$ is measured from the body nose. A second-order power series of the form

$$\frac{X_{CP_S}}{d} = a_0 + a_1\alpha + a_2\alpha^2$$

was used with the following boundary conditions:

$$\frac{X_{CP_S}}{d} = \frac{X_{CP_{S_0}}}{d} \text{ at } \alpha = 0^\circ$$

$$\frac{X_{CP_S}}{d} = \frac{\bar{X}_S}{d} \text{ at } \alpha = 30^\circ$$

$$\frac{X_{CP_S}}{d} = R \text{ at } \alpha = 60^\circ$$

$$\frac{X_{CP_S}}{d} = \frac{\bar{X}_S}{d} \text{ at } \alpha = 90^\circ$$

$$\frac{X_{CP_S}}{d} = T \text{ at } \alpha = 120^\circ$$

$$\frac{X_{CP_S}}{d} = \frac{\bar{X}_B}{d} \text{ at } \alpha = 145^\circ$$

$$\frac{X_{CP_S}}{d} = \frac{\bar{X}_S}{d} \text{ at } \alpha = 180^\circ$$

where $X_{CP_{S_0}}$ = center of pressure at $\alpha = 0^\circ$ [Ref. 17, Section 4.1.2.2]

$$\frac{X_{CP_{S_0}}}{d} = \frac{0.25C_R}{d} \text{ for } M < 1.0$$

$$= \frac{\bar{X}_S}{d} \text{ for } M \geq 1.0$$

A review of the test data suggested the following formulations.

R = CP location at $\alpha = 60^\circ$

$$= \frac{\bar{X}_S}{d} - J_2 \left(\frac{\bar{X}_S}{d} - \frac{\bar{X}_A}{d} \right)$$

T = CP location at $\alpha = 120^\circ$

$$= \frac{\bar{X}_B}{d} + K_b \left(\frac{C_{RS}}{d} - \frac{\bar{X}_B}{d} \right)$$

where J_2 and K_b are functions of Mach number.

Note that the equations for R and T have been generalized by the presence of the terms \bar{X}_A , \bar{X}_B , and \bar{X}_S and that, for the limiting case of a rectangular strake,

$$\bar{X}_A = 0, \bar{X}_B = \bar{X}_S, \text{ and } \bar{X}_S = 0.5C_{RS}.$$

To simplify the power series solution and improve the accuracy of the estimates, the series was formulated for three intervals: $0 \leq \alpha \leq 60^\circ$; $60^\circ < \alpha < 120^\circ$; and $120^\circ \leq \alpha \leq 180^\circ$. Solution for the second order power series coefficients yielded a_0 , a_1 , and a_2 as functions of $\frac{X_{CP S_0}}{d}$, $\frac{\bar{X}_S}{d}$, R, T, and $\frac{\bar{X}_S}{d}$. Upon separating terms, a function of the form

$$\frac{X_{CP S}}{d} = A_1 \left(\frac{X_{CP S_0}}{d} \right) + A_2 \left(\frac{\bar{X}_S}{d} \right) + A_3 (R) + A_4 (T) + A_5 \left(\frac{\bar{X}_S}{d} \right)$$

was derived. Equations for A_1 , A_2 , A_3 , A_4 and A_5 are as follows:

$$0 < \alpha < 60^\circ$$

$$A_1 = 1. - 2.864\alpha + 1.8238\alpha^2$$

$$A_2 = 3.8197\alpha - 3.6476\alpha^2$$

$$A_3 = -.9549\alpha + 1.8238\alpha^2$$

$$A_4 = 0$$

$$A_5 = 0$$

(α - radians)

$$60^\circ < \alpha < 120^\circ$$

$$A_1 = 0$$

$$A_2 = -8.0 + 11.4597\alpha - 3.6476\alpha^2$$

$$A_3 = 6.0 - 6.6846\alpha + 1.8238\alpha^2$$

$$A_4 = 3.0 - 4.7747\alpha + 1.8238\alpha^2$$

$$A_5 = 0$$

(α - radians)

$$120^\circ < \alpha < 180^\circ$$

$$A_1 = 0$$

$$A_2 = 8.2877 - 7.2318\alpha + 1.5636\alpha^2$$

$$A_3 = 0$$

$$A_4 = 17.4063 - 12.4193\alpha + 2.1896\alpha^2$$

$$A_5 = -24.6940 + 19.6512\alpha - 3.7532\alpha^2$$

(α - radians)

Values of A_n have been plotted as a function of angle of attack in Figure 109 to facilitate use of this method. Peak value factors J_2 and K_b have been determined empirically and are plotted versus Mach number in Figure 110.

Use of Method

The method is used as follows:

Given a tangent-ogive cylinder with low aspect-ratio strakes of the following characteristics:

body diameter = d

strake root chord = C_{RS}

strake leading edge station = X_{LE}

distance from LE to segment A centroid = \bar{X}_A

distance from LE to segment B centroid = \bar{X}_B

distance from LE to net strake centroid = \bar{X}_S

Proceed thus:

1 determine $X_{CP_{SO}}$ ($=0.25C_{RS}$ for $M < 1.0$; [Section 4.1.4.2 of Ref. 17]
 $= \bar{X}_S$ for $M \geq 1.0$)

2 determine J_2 and K_b for the appropriate Mach number (Figure 110).

3 compute $R = \frac{\bar{X}_B}{d} - J_2 \left(\frac{\bar{X}_S}{d} - \frac{\bar{X}_A}{d} \right)$
 $T = \frac{X_B}{d} + K_b \left(\frac{C_{RS}}{d} - \frac{X_B}{d} \right)$

4 look up $A_1, A_2, A_3, A_4,$ and A_5 for the desired angles of attack (Figure 109).

5 compute

$$\frac{X_{CP_S}}{d} = A_1 \left(\frac{X_{CP_{SO}}}{d} \right) + A_2 \left(\frac{\bar{X}_S}{d} \right) + A_3 (R) + A_4 (T) + A_5 \left(\frac{\bar{X}_B}{d} \right)$$

6) Compute

$$\frac{X_{CP_{ABS}}}{d} = \frac{X_{LE}}{d} + \frac{X_{CP_S}}{d}$$

Numerical Example

Given the following parameters, compute $\frac{X_{CP\Delta BS}}{d}$ for a body-strake combination at Mach 1.2:

$$d = 3.667$$

$$\bar{X}_A/d = 2.000$$

$$S_S = 7.978 \text{ in}^2$$

$$C_{RS}/d = 7.772$$

$$\bar{X}_B/d = 5.850$$

$$AR_S = .040$$

$$X_{LE}/d = 5.181$$

$$\bar{X}_S/d = 4.721$$

$$b/2 = 0.4 \text{ in.}$$

1 $X_{CPSO}/d = \frac{\bar{X}_S}{d} = 4.721$ since $M > 1.0$

2 from Figure 110: $J_2 = 0.0$

$$K = .64$$

3 $R = \frac{\bar{X}_S}{d} - J_2 \left(\frac{\bar{X}_S}{d} - \frac{\bar{X}_A}{d} \right) = 4.721$

$$T = \frac{\bar{X}_B}{d} + .64 \left(\frac{C_{RS}}{d} - \frac{\bar{X}_B}{d} \right) = 5.85 + .64 (7.72 - 5.85) = 7.120$$

4 from Figure 109

α	A_1	A_2	A_3	A_4	A_5
0	1.00	0.	0.	0.	0.
30	0.	1.00	0.	0.	0.
60	0.	0.	1.00	0.	0.
90	0.	1.00	0.	0.00	0.
120	0.	0.	0.	1.00	0.
150	0.	.07	0.	-.10	1.03
180	0.	1.0	0.	0.	0.

5-6 Substituting in $\frac{X_{CPS}}{d} = A_1 \left(\frac{X_{CPSO}}{d} \right) + A_2 (\bar{X}_S) + A_3 (R) + A_4 (T) + A_5 \left(\frac{\bar{X}_B}{d} \right)$

and $\frac{X_{CP\Delta BS}}{d} = \frac{X_{LE}}{d} + \frac{X_{CPS}}{d}$

α	$\frac{X_{CP_S}}{d}$	$\frac{X_{CP_{\Delta BS}}}{d}$
0	4.72	9.90
30	4.72	9.90
60	4.72	9.90
90	4.72	9.90
120	7.12	12.30
150	5.64	10.82
180	4.72	9.90

Data Comparisons

In Figure 111 method results are plotted along with those data used in formulating the method. The power series yields a good approximation of $X_{CP_{\Delta BS}}/d$ across the Mach range. A lack of independent data at high angles of attack makes further comparisons impossible at this time.

It is now appropriate to compare the center of pressure location of the body plus strake configuration as indicated by test data with that determined using previously derived methods. The following equation will be used:

$$C_{N_{BS}} \left(\frac{X_{CP_{BS}}}{d} \right) = C_{N_B} \left(\frac{X_{CP_B}}{d} \right) + \Delta C_{N_{BS}} \left(\frac{X_{CP_{\Delta BS}}}{d} \right)$$

or

$$\frac{X_{CP_{BS}}}{d} = \left(\frac{1}{C_{N_B} + \Delta C_{N_{BS}}} \right) \left[C_{N_B} \left(\frac{X_{CP_B}}{d} \right) + \Delta C_{N_{BS}} \left(\frac{X_{CP_{\Delta BS}}}{d} \right) \right]$$

The methods used in determining the various components of the basic equation are as follows:

Component	Source
C_{N_B}	Section 5.1.1 (p. 39 ff)
$\Delta C_{N_{BS}}$	Section 5.3.1 (p. 190 ff)
X_{CP_B}	Section 5.1.2 (p. 61 ff)
$X_{CP_{\Delta BS}}$	Preceding analysis

Relevant body parameters are:

$$\frac{l_N}{d} = 2.5$$

$$\frac{l}{d} = 14.5$$

$$\frac{l_A}{d} = 12.0$$

$$S_{ref} = 10.56 \text{ in}^2$$

strake parameters are as contained in the numerical example preceding.

Use of the four methods and application of the basic equation yields the following results at Mach 1.2:

α	C_{NB}	$\frac{X_{CPB}}{d}$	ΔC_{NBS}	$\frac{X_{CP\Delta BS}}{d}$	$\frac{X_{CPBS}}{d}$
5°	.70	3.56	.10	9.90	3.06
20	4.70	5.52	.82	9.90	5.03
40	13.30	6.14	2.35	9.90	6.69
60	22.0	6.76	3.42	9.90	7.19
80	26.8	7.38	3.00	9.63	7.61
100	26.7	8.00	3.00	10.43	8.25
120	21.9	8.62	3.00	12.30	9.06
140	13.0	9.24	3.13	11.25	9.65
160	4.3	9.83	1.20	10.45	9.96
175	.50	13.81	15	10.02	12.71

Data Comparisons

Figure 112 compares the results of these empirical methods with actual test data for the body/strake configuration. Very good correlation is shown across the angle of attack range at Mach 1.2.

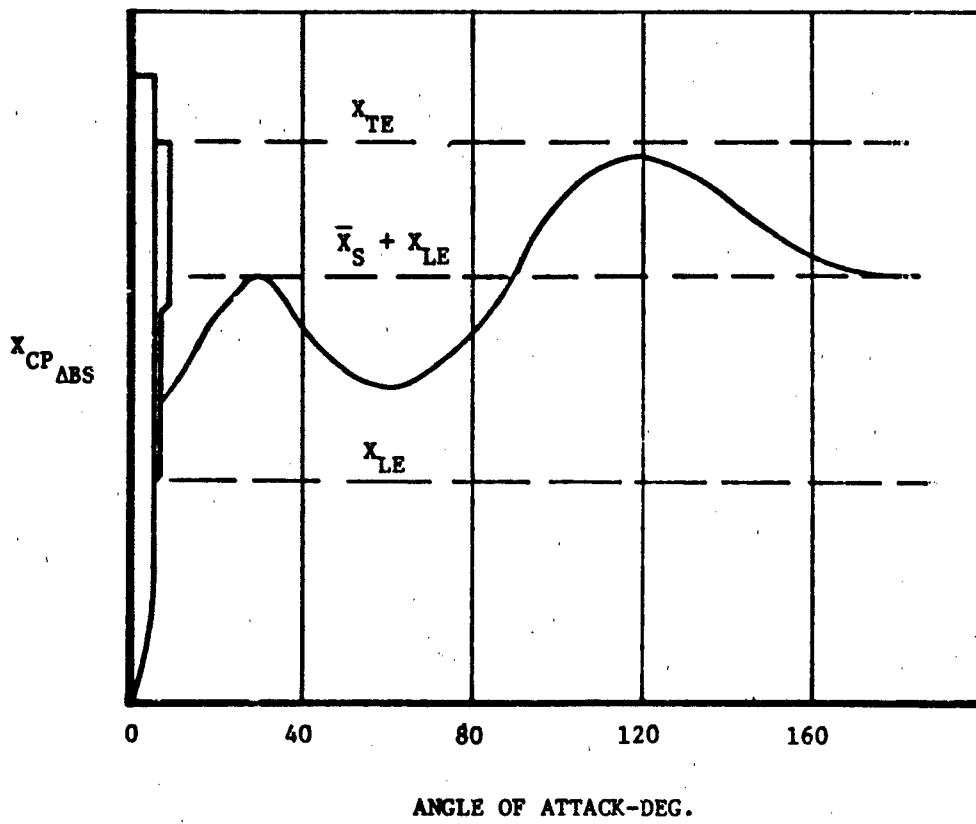


Figure 107. General Curve Form, X_{CP_ABS}

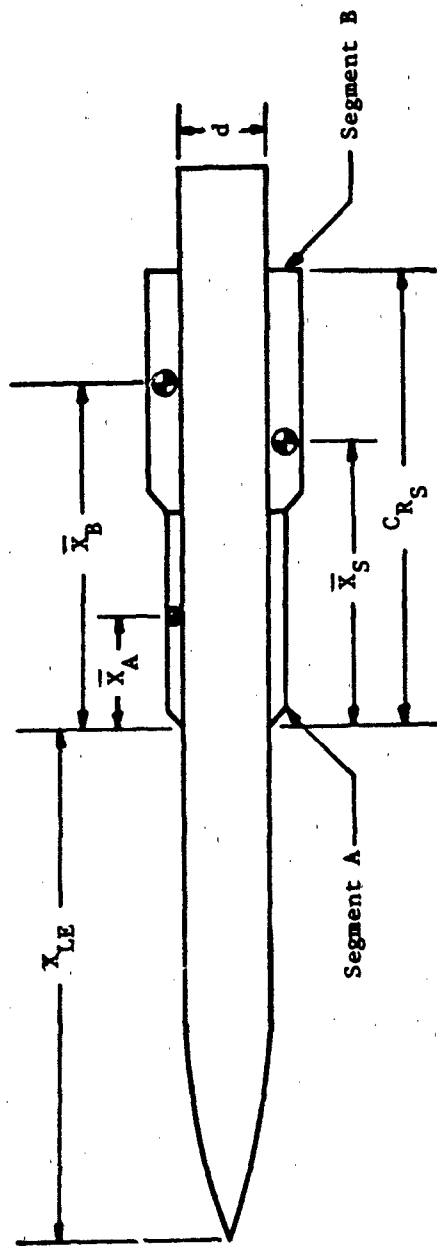
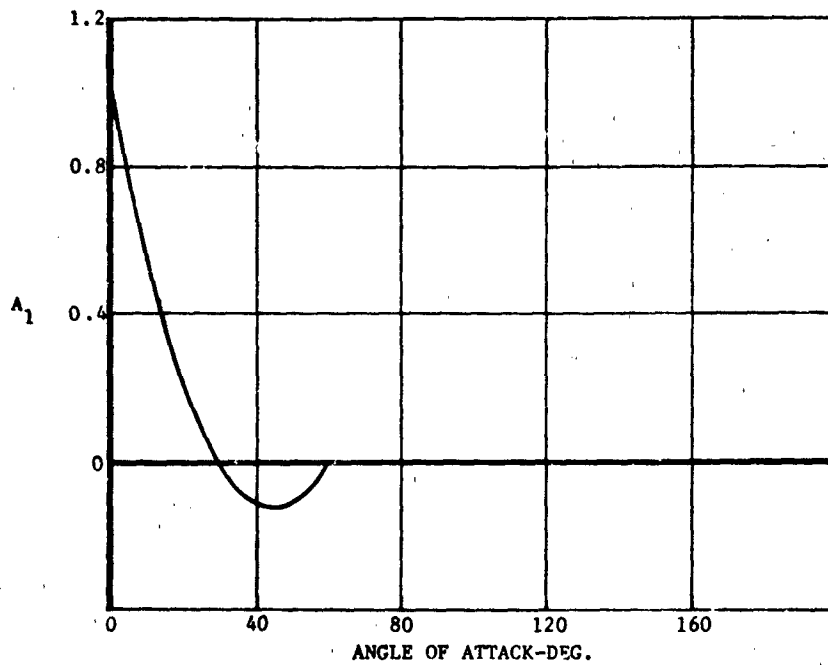


Figure 108. Strake Parameters



$$\frac{x_{CP_S}}{d} = A_1 \left(\frac{x_{CP_{S_0}}}{d} \right) + A_2 \left(\frac{\bar{x}_S}{d} \right) + A_3 (R) + A_4 (T) + A_5 \left(\frac{\bar{x}_B}{d} \right)$$

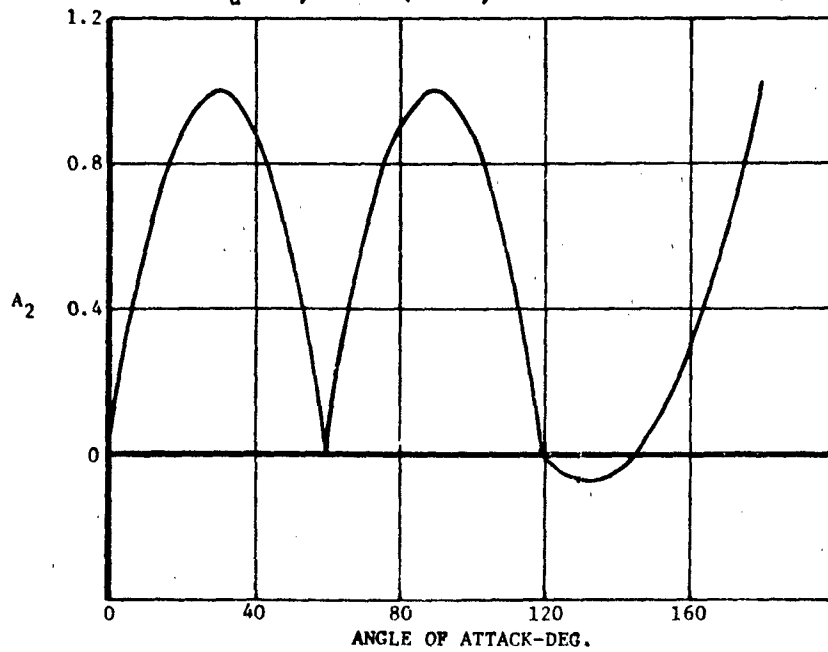
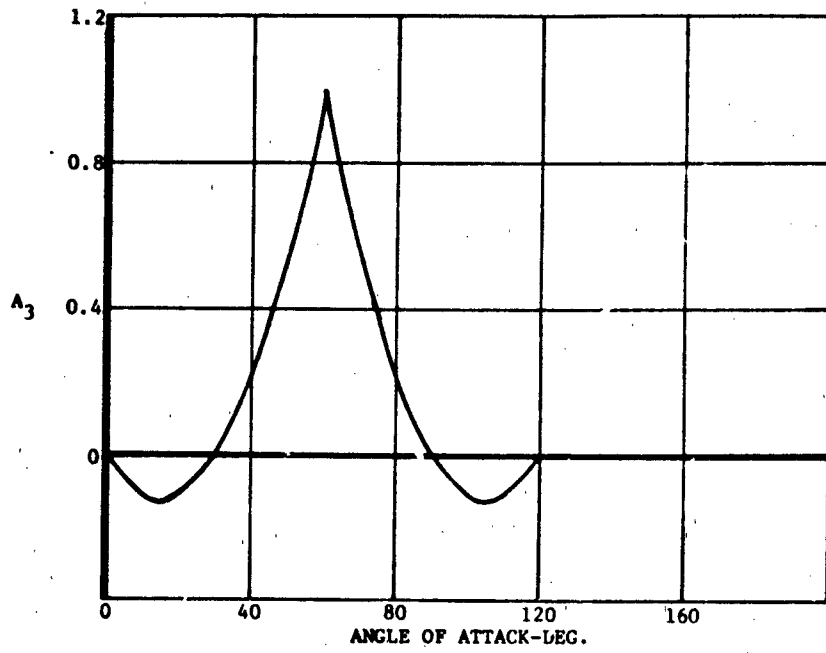


Figure 109. Polynomial Coefficients for Calculating $x_{CP_{ABS}}$



$$\frac{x_{CP_S}}{d} = A_1 \left(\frac{x_{CP_{S_0}}}{d} \right) + A_2 \left(\frac{\bar{x}_S}{d} \right) + A_3 (R) + A_4 (T) + A_5 \left(\frac{\bar{x}_B}{d} \right)$$

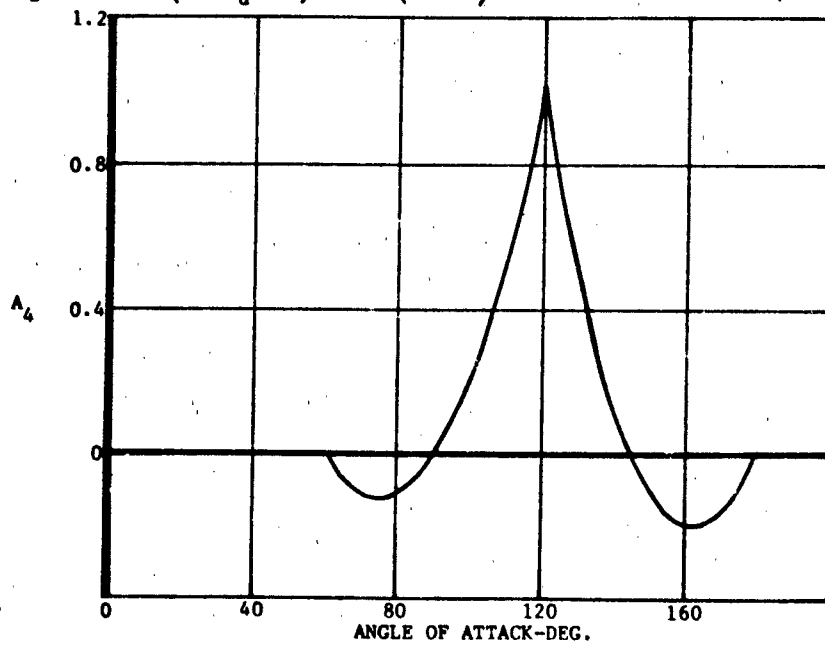
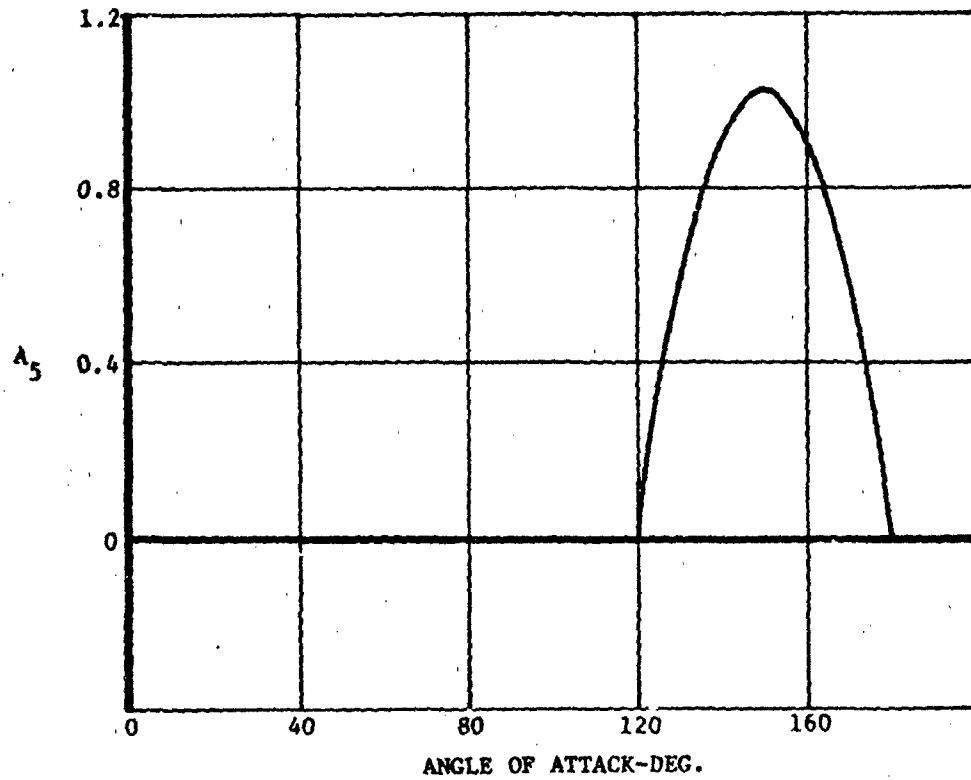


Figure 109 (cont.). Polynomial Coefficients for Calculating $x_{CP_{ABS}}$



$$\frac{\bar{x}_{CPS}}{d} = A_1 \left(\frac{\bar{x}_{CPS0}}{d} \right) + A_2 \left(\frac{\bar{x}_S}{d} \right) + A_3 (R) + A_4 (T) + A_5 \left(\frac{\bar{x}_B}{d} \right)$$

Figure 109 (Cont.). Polynomial Coefficients for Calculating

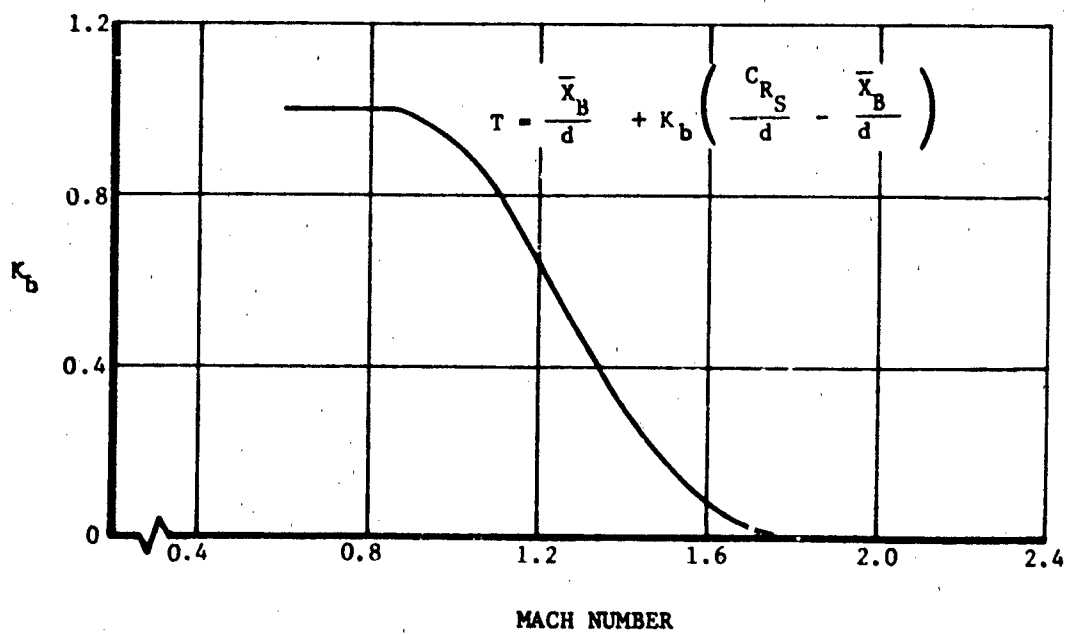
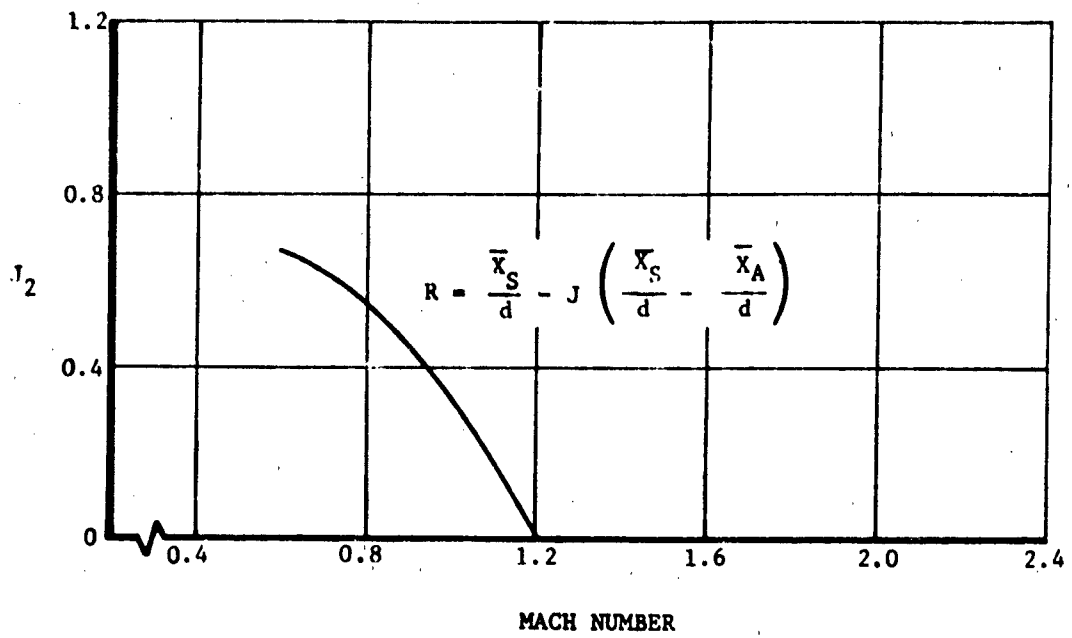


Figure 110. J and K Values for Calculating $X_{CP_{\Delta BS}}$

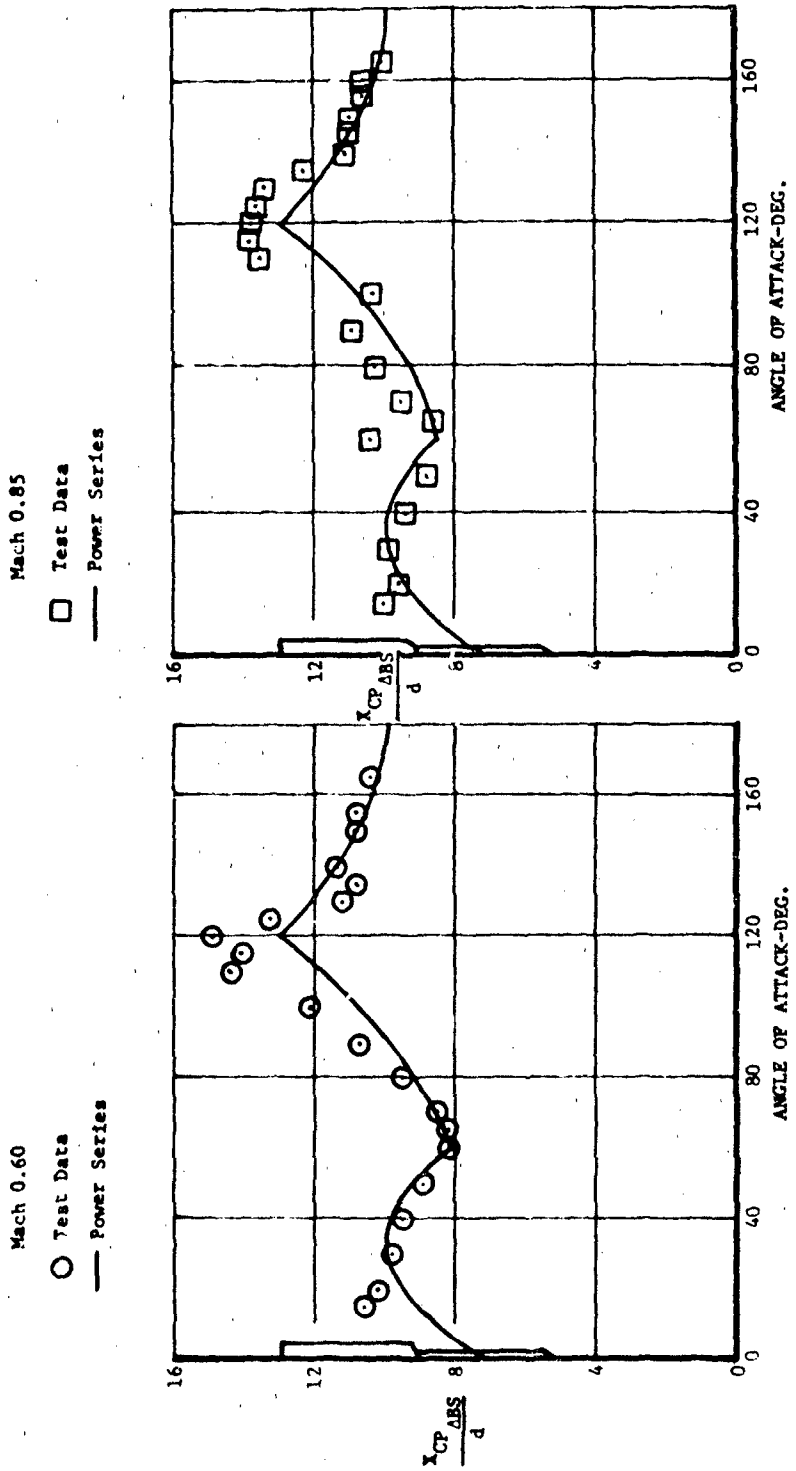
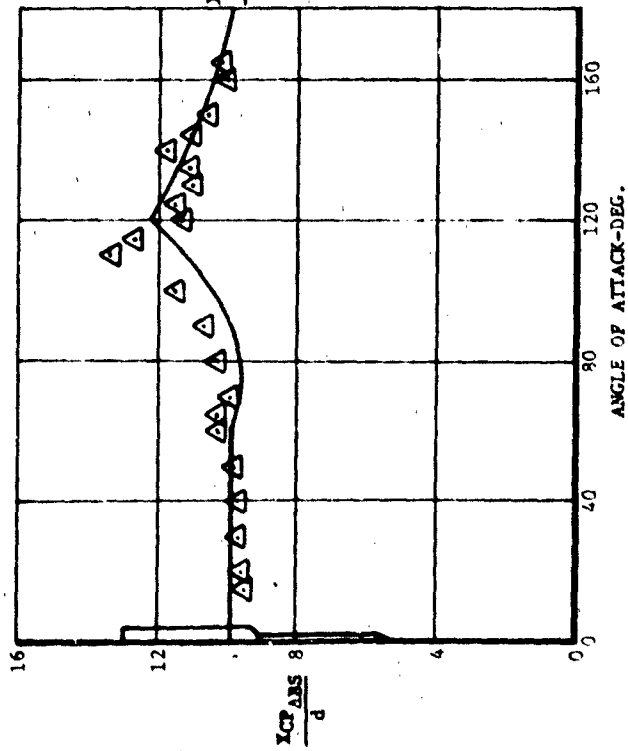


Figure 111. Comparison of Test Data and Method, X_{CP_ABS}/d

Mach 1.20

△ Test Data
— Power Series



Mach 1.8, 2.2

◇ Test Data, Mach 1.8
▽ Test Data, Mach 2.2
— Power Series

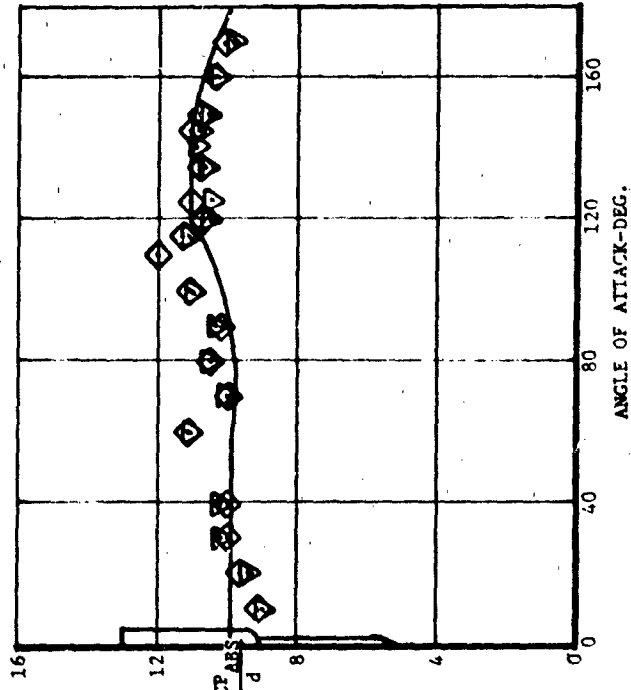


Figure 111(Cont.). Comparison of Test Data And Method, $\frac{X_{CP_ABS}}{d}$

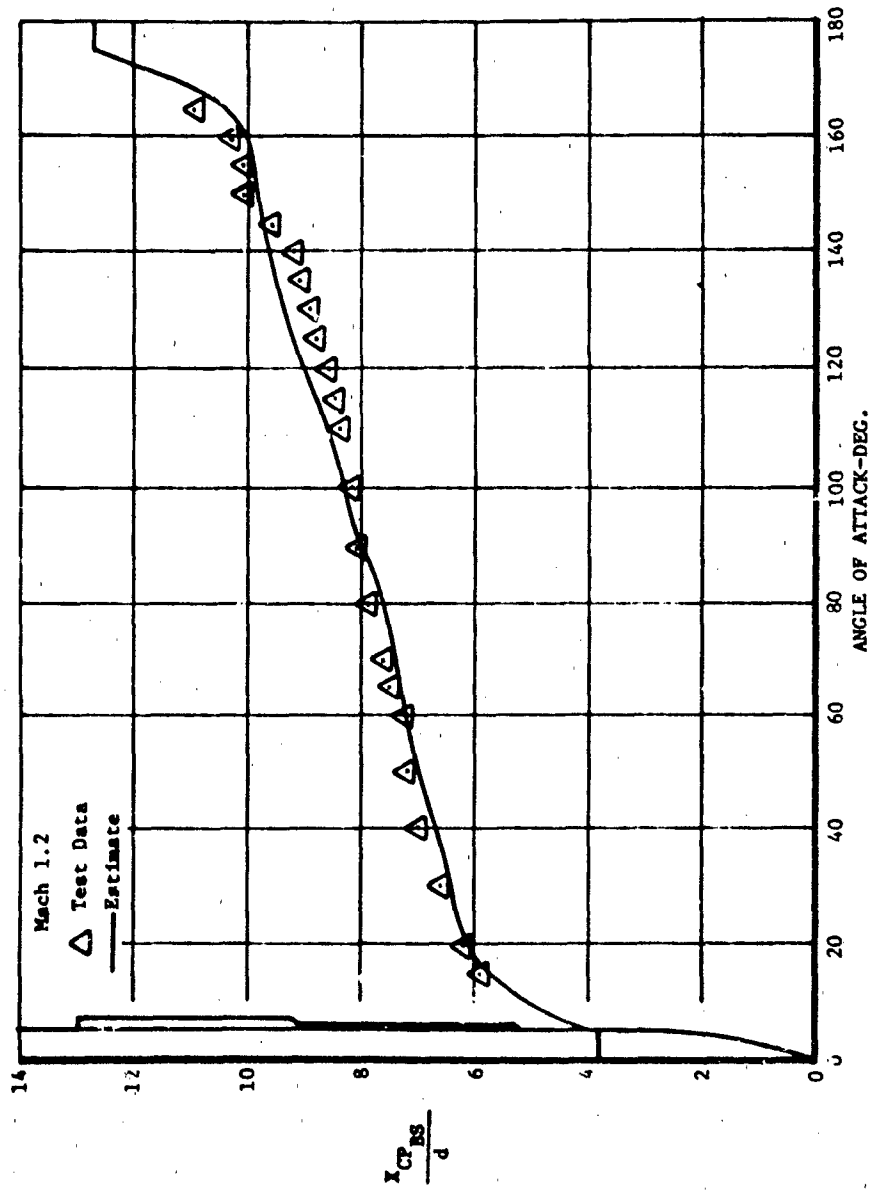


Figure 112. Comparison Of Test Data And Method, $X_{CP_{BS}}/d$

5.3.3 Incremental Normal Force Due to Tails

Summary

A method is presented for predicting $\Delta C_{N_{BST}}$, the total increment caused by the addition of tails to a body-strake configuration. Note that $\Delta C_{N_{BST}}$ includes the forces on the tails as well as the carryover to the body-strakes. The angle of attack range is 0 to 180 degrees and the Mach number range is 0.6 to 2.2. Comparisons between predicted and experimental results show good agreement. This method is an extension of existing methods which are accurate at angles of attack approaching 0 and 180 degrees.

Background

The normal force on a body-strake-tail configuration can be expressed as the sum of the forces on the isolated components plus interference-produced effects and carryover between the various components. This section deals with the development of an empirical method which extends the present DATCOM method for predicting the increment in normal force due to the tails of a body-strake-tail configuration. The extended method covers the entire 0 to 180 degree angle of attack range. Inputs to the method were obtained from DATCOM (Reference 17) at the lower angles and experimental data correlations at the higher angles.

At low to moderate angles of attack, say up to 20 degrees, the DATCOM method extends the basic theoretical procedures to account for the effects of separated flow in the form of symmetric steady vortices. Since the flow pattern in the 0-180 degrees range usually contains asymmetric and/or unsteady vortices, a modification of the DATCOM extension is inappropriate. Instead, a new extension of the basic theoretical procedures is desired. The new method will predict $\Delta C_{N_{BST}}$, which includes the combined effects of

interference and carryover. The nature of the instrumentation and configurations tested dictated the following formulation of the tail contribution to normal force:

$$\Delta C_{N_{BST}} = C_{N_{BST}} - C_{N_{BS}}$$

where $C_{N_{BS}}$ is determined by the method of Section 5.3.2.

Method Development

A power series approach was used and in the usual way boundary conditions were sought. First, values of $\Delta C_{N_{BST}}$ were extracted from wind tunnel data on an Air Force body-strake-tail configuration tested at angles of attack between 0 and 180 degrees and Mach numbers between 0.6 and 2.2. Using these data as a guide, the values of $\Delta C_{N_{BST}}$ at 0 and 180 degrees and $\frac{\partial \Delta C_{N_{BST}}}{\partial \alpha}$ at 90 degrees were taken as zero. The derivative $\frac{\partial \Delta C_{N_{BST}}}{\partial \alpha}$ at 0 and 180 degrees and the value of $C_{N_{T(B)}}$ at 90 degrees were left as free variables; viz., $C_{N_{\alpha_0}}$, $C_{N_{\alpha_\pi}}$ and $C_{N_{\pi/2}}$, respectively.

Applying these boundary conditions to the power series expansion

$$\Delta C_{N_{BST}} = a_0 + a_1 \alpha + a_2 \alpha^2 + a_3 \alpha^3 + a_4 \alpha^4 + a_5 \alpha^5$$

yielded

$$\begin{aligned} \Delta C_{N_{BST}} = & \left[\alpha - \frac{6\alpha^2}{\pi} + \frac{13\alpha^3}{\pi^2} - \frac{12\alpha^4}{\pi^3} + \frac{4}{\pi^4} \alpha^5 \right] \Delta C_{N_{\alpha_0}} \\ & + \left[\frac{16\alpha^2}{\pi^2} - \frac{32\alpha^3}{\pi^3} + \frac{16\alpha^4}{\pi^4} \right] \Delta C_{N_{\pi/2}} \\ & + \left[-\frac{1}{\pi} \alpha^2 + \frac{5\alpha^3}{\pi^2} - \frac{8\alpha^4}{\pi^3} + \frac{4\alpha^5}{\pi^4} \right] \Delta C_{N_{\alpha_\pi}} \end{aligned}$$

which can be rewritten as

$$\Delta C_{N_{BST}} = A_1 \Delta C_{N_{\alpha_0}} + A_2 \Delta C_{N_{\pi/2}} + A_3 \Delta C_{N_{\alpha_\pi}}, \quad (40)$$

where

$$\begin{aligned} A_1 &= \alpha - \frac{6\alpha^2}{\pi} + \frac{13\alpha^3}{\pi^2} - \frac{12\alpha^4}{\pi^3} + \frac{4\alpha^5}{\pi^4} \\ A_2 &= \frac{16\alpha^2}{\pi^2} - \frac{32\alpha^3}{\pi^3} + \frac{16\alpha^4}{\pi^4} \\ A_3 &= -\frac{1\alpha^2}{\pi} + \frac{5\alpha^3}{\pi^2} - \frac{8\alpha^4}{\pi^3} + \frac{4\alpha^5}{\pi^4} \end{aligned} \quad \alpha \text{ in radians}$$

Values of A_1 , A_2 and A_3 are plotted as a function of angle of attack in Figures 113, 114 and 115.

Values of $\Delta C_{N_{\alpha_0}}$ and $\Delta C_{N_{\alpha_\pi}}$ can be determined using the methods of References 12 and 30. The generalized expression suggested in Reference 30 used to predict the magnitude of $\Delta C_{N_{\alpha_0}}$ and $\Delta C_{N_{\alpha_\pi}}$ is as follows:

$$\Delta C_{N_{\alpha}} \Big|_1 = [K_{T(B)} + K_{B(T)}] (C_{N_{T_\alpha}})_1 \frac{S_T}{S_{ref}}, \quad (41)$$

where $C_{N_{T_\alpha}}$, the normal force curve slope at either $\alpha = 0$ or $\alpha = \pi$, can be determined using the method of DATCOM or the RAS Data Sheets (Reference 27). In the case of $\Delta C_{N_{\alpha_0}}$, the values of $K_{T(B)}$ and $K_{B(T)}$ taken from Reference 30 can be determined from Figure 116. In the case of $\Delta C_{N_{\alpha_\pi}}$, $K_{B(T)}$ can be determined from Figure 116. However, at $\alpha = 180^\circ$ $K_{T(B)}$ is set equal to 1.0 since there will be no upwash due to a forebody at the "leading" edge of the tail. Note that the slope at $\alpha = \pi$ will be negative.

From the experimentally derived data, the value of $\Delta C_{N_{\pi/2}}$ was found to approximate 3.65 at all Mach numbers. This value applies only to the configuration tested. Assuming that the value at 90 degrees varies as the

ratio of planform areas, the following equation can be applied to determine values of $\Delta C_{N_{\pi/2}}$ for general configurations.

$$\Delta C_{N_{\pi/2}} = 1.156 \frac{S_P}{S_{\text{ref}}} \quad (42)$$

Use of Method

The method for predicting $\Delta C_{N_T(\text{BS})}$ is applied in the following way:

- 1 Determine $C_{N_{\alpha_T}}$ using either the method of DATCOM (Reference 17) or the RAS Data Sheets (Reference 27).
- 2 Calculate $\Delta C_{N_{\alpha_0}}$ and $\Delta C_{N_{\alpha_\pi}}$ using Equation 41 and Figure 116.
- 3 Calculate $\Delta C_{N_{\pi/2}}$ using Equation 42.
- 4 Using the results of steps 2 and 3, Equation 40, and Figures 113, 114 and 115 calculate $\Delta C_{N_T(\text{BS})}$ between 0 and 180 degrees angle of attack.

Numerical Example

Calculate $\Delta C_{N_{\text{BST}}}$ between 0 and 180 degrees angle of attack at $M = 0.6$ for a configuration with the following characteristics.

$$d = 3.667 \text{ in.}$$

$$b_T \text{ single panel} = 1.867 \text{ in.} \\ \text{exposed}$$

$$S_T \text{ single panel} = 8.883 \text{ sq. in.}$$

$$AR_T = 0.785 \text{ double panel}$$

$$\lambda_T = 0.687$$

- 1 Using the RAS Data Sheets for $\lambda = 0.687$ and $AR = 0.785$, the slope of the tail normal force curve was determined to be 1.173/rad.

2 Calculate $\Delta C_{N_{\alpha_0}}$ using Equation 41 and the results of step 1.

At $\alpha = 0$ degrees, using Figure 116 for $d/s = 0.495$, $K_{T(B)} = 0.8$

$$\Delta C_{N_{\alpha_0}} = [1.45 + 0.8] 1.173 * [2 * \frac{8.883}{10.56}]$$

$$\Delta C_{N_{\alpha_0}} = 4.44/\text{rad}; S_{\text{ref}} = S_{\text{base}}$$

3 Calculate $\Delta C_{N_{\alpha_\pi}}$ using Equation 41 and the results of step 1.

At $\alpha = 180$ degrees, there will be no upwash at the fin "leading edge" due to a forebody; therefore, $K_{T(B)} = 1.0$; from Figure 116

$$K_{B(T)} = 0.8.$$

$$\Delta C_{N_{\alpha_\pi}} = - [1.0 + 0.8] 1.173 * [\frac{2 * 8.883}{10.56}]$$

$$\Delta C_{N_{\alpha_\pi}} = -3.55 \text{ 1/rad}; S_{\text{ref}} = S_{\text{base}}$$

4 Calculate $\Delta C_{N_{\pi/2}}$ using the following equation.

$$\Delta C_{N_{\pi/2}} = 1.156 \frac{S_p}{S_{\text{ref}}}$$

$$\Delta C_{N_{\pi/2}} = 1.156 \frac{2 * 8.883 + 3.667 * 4.243}{10.56}$$

$$\Delta C_{N_{\pi/2}} = 3.65$$

5 Using Equation 40 the results of steps 2, 3 and 4 and Figures 113, 114 and 115, calculate $\Delta C_{N_{\text{BST}}}$ between 0 and 180 degrees angle of attack.

5 (Continued)

<u>a(deg)</u>	<u>A₁</u>	<u>A₂</u>	<u>A₃</u>	<u>ΔC_NBST</u>
0	0	0	0.0	0.0
10	0.123	0.045	-.007	0.735
20	0.166	0.15	-.020	1.356
30	0.161	0.305	-.032	1.942
40	0.13	0.48	-.038	2.464
50	0.092	0.645	-.034	2.883
60	0.052	0.79	-.026	3.207
70	0.022	0.905	-.015	3.454
80	0.005	0.98	-.005	3.617
90	0.0	1.0	0.0	3.65
100	0.005	0.98	-.005	3.617
110	0.014	0.905	-.002	3.373
120	0.026	0.79	-.052	3.184
130	0.034	0.645	-.089	2.821
140	0.037	0.48	-.131	2.381
150	0.032	0.305	-.162	1.830
160	0.021	0.15	-.167	1.234
170	0.007	0.045	-.123	0.632
180	0.0	0.0	0.0	0.0

Data Comparison

The results of the numerical example along with the results of other test cases are compared against experimental data in Figure 117. Considering the scatter in the data, agreement is good. Due to a lack of data on body-strake-tail configurations throughout the angle of attack range, independent checks of the method are not possible at this time.

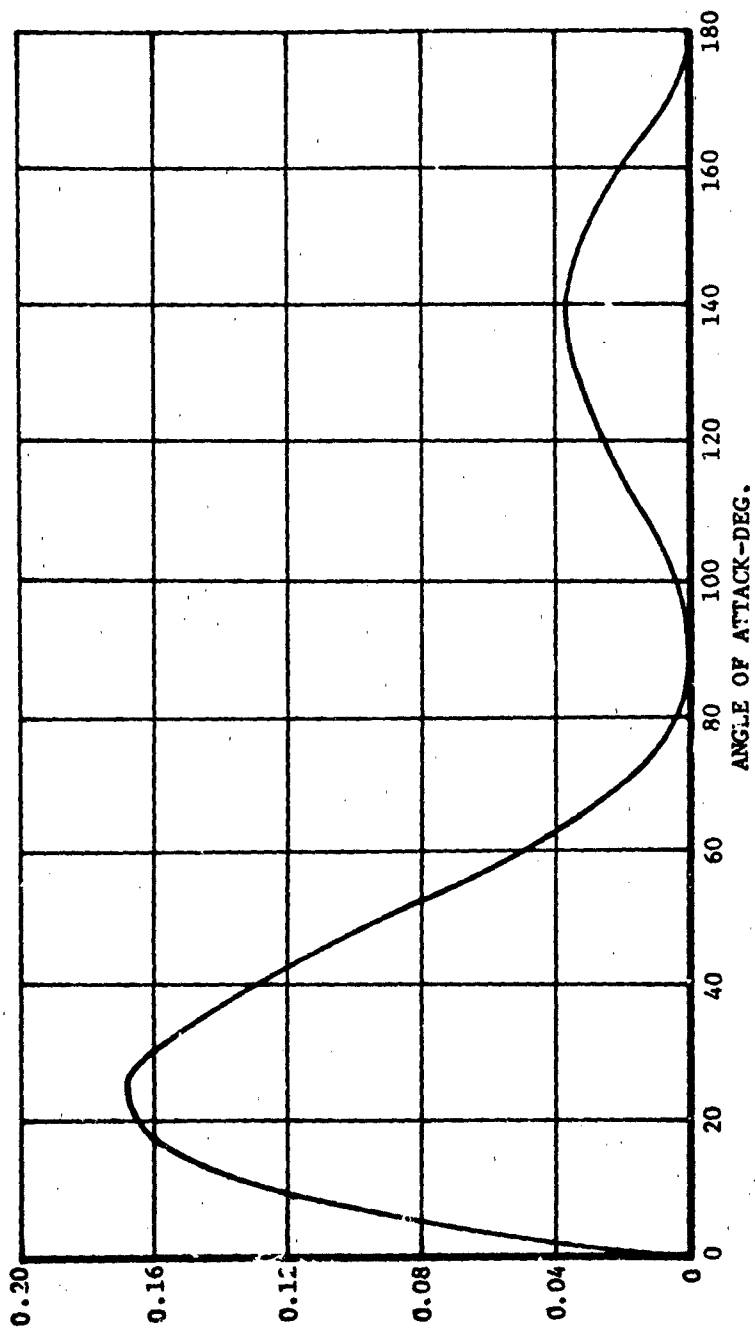


Figure 113. Coefficients for Calculation of $\Delta C_{N_{RST}}$

A1

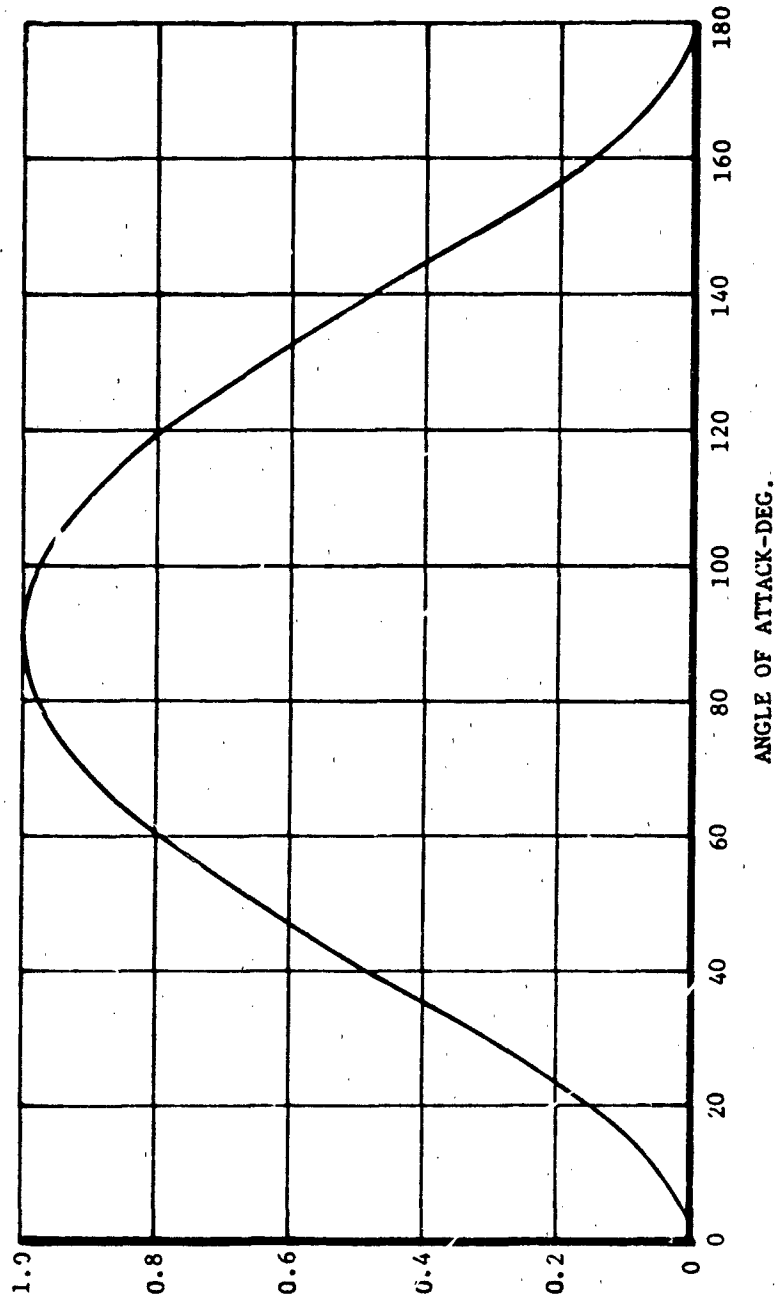


Figure 114. Coefficients For Calculation Of $AC_{N_{BST}}$

A_2

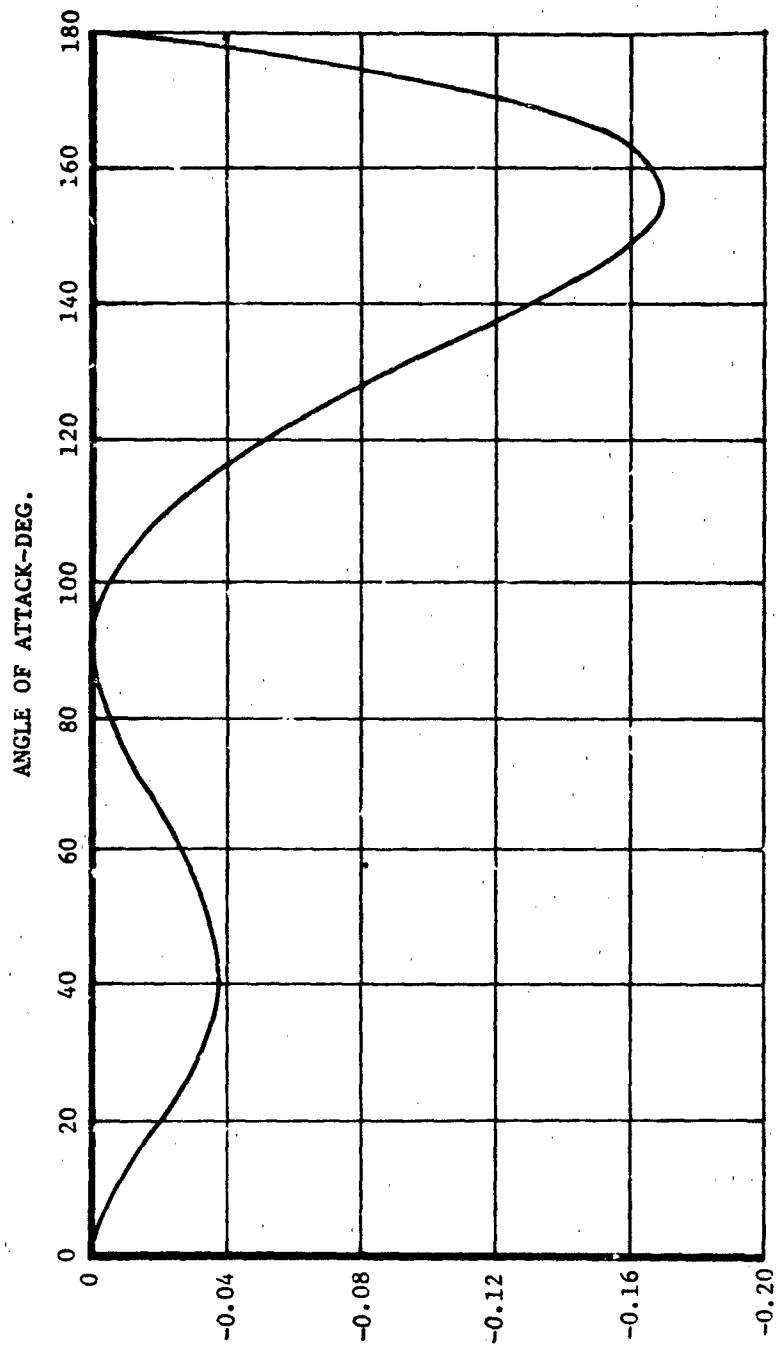


Figure 115. Coefficients For Calculation Of $\Delta C_{N_{BST}}$

A₃

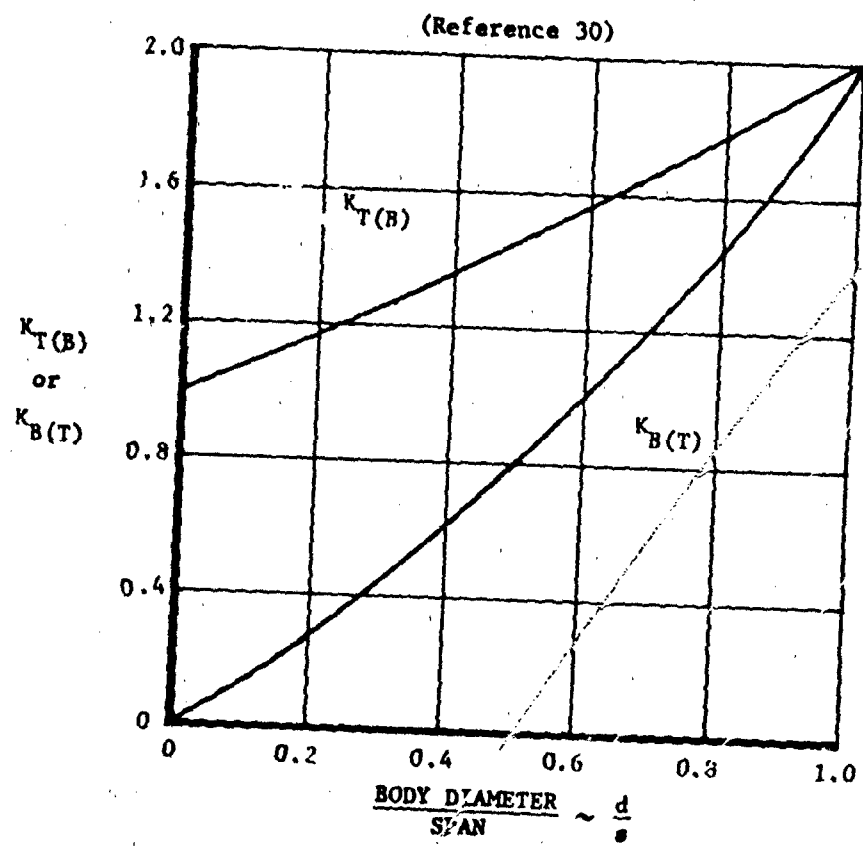


Figure 116. $K_{T(B)}$ And $K_{B(T)}$ Ratios (Slender Body Theory)

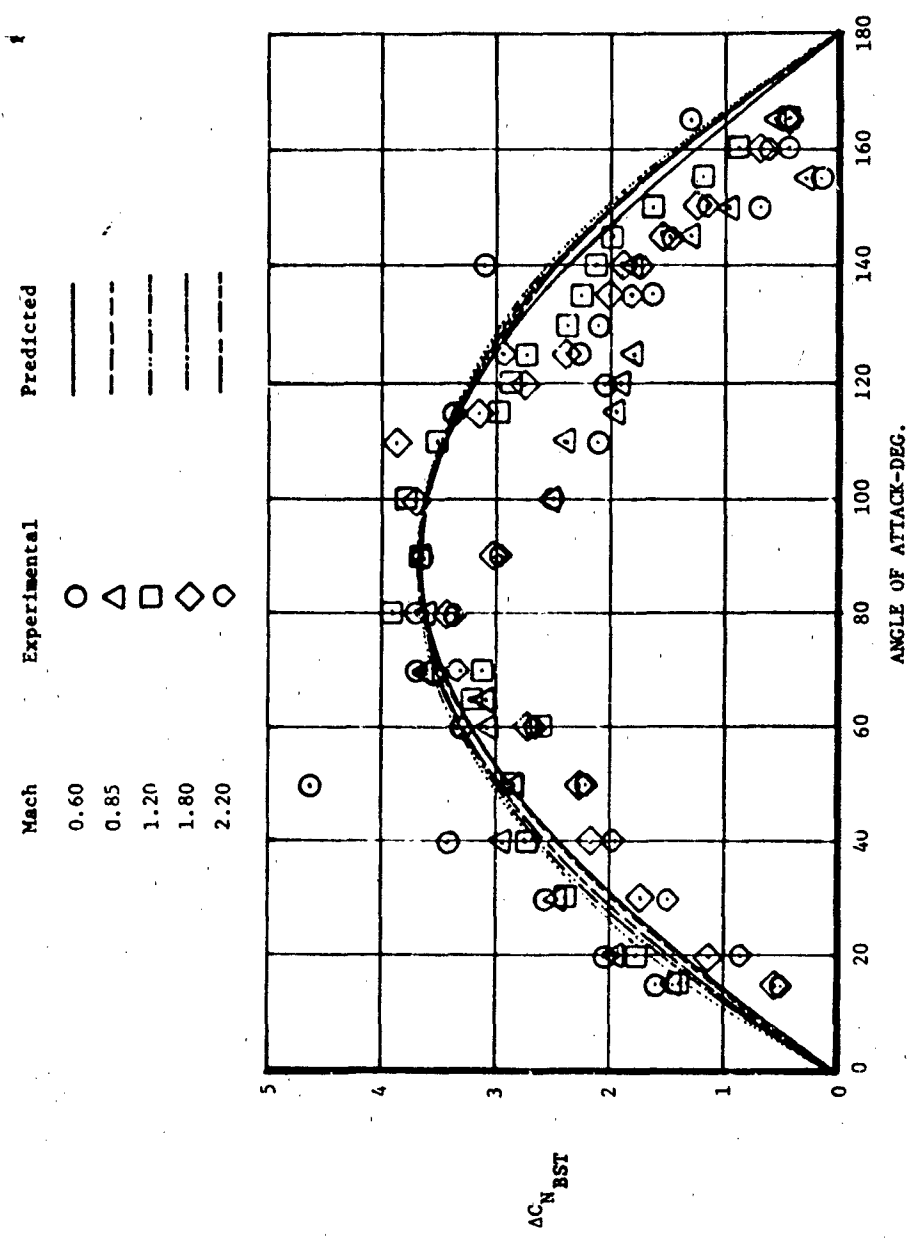


Figure 117. Comparisons of Predicted Results With Experimental Data, $\Delta C_{N_{BST}}$

5.3.4 Effective Center of Pressure for Incremental Normal Force Due to Tails

Summary

A method is presented to predict $X_{CP_{\Delta BST}}$, the effective center of pressure of the incremental normal force produced by adding tails to a body-strake configuration. The method is applicable to "plus" configuration at Mach numbers between 0.6 and 3.0 and angles of attack from 0 to 180 degrees. This method has been applied to the center of pressure calculations for a complete body-strake-tail configuration. Agreement between predicted and experimental results were found to be quite good. In some cases, it was found that predictions could be improved by using the Jorgensen technique for predicting C_{NB} up to 40 degrees angle of attack. Until enough comparisons are available to determine which method provides better results consistently, it is recommended that both the C_{NB} prediction method of Section 5.1.1 and that of Jorgensen (Reference 12) be used in $X_{CP_{\Delta BST}}$ calculations up to 40 degrees angle of attack.

Background

Current methods for predicting the effective center of pressure, $X_{CP_{\Delta BST}}$, of the increment in normal force due to the additions of tails to a body-strake configuration are not accurate over the entire 0 to 180 degree angle of attack range. In general, they are limited to angles of attack less than 30 degrees. These methods require separate procedures to calculate centers of pressure for the tail in the presence of the body, carryover from the tail to the body and strake-tail interference. Using this approach over the entire angle of attack range would require much more information than was available and would result in awkward and time consuming methods. In order to develop simple, easy to use methods for preliminary design purposes, a

method is presented for calculating a composite center of pressure for the total increment in normal force due to the addition of tails.

Method Development

An analytic approach to method development was ruled out due to the complicated nature of the flow field. A power series approach to method development was selected and, in the usual way, boundary conditions were sought. Available experimental data were of little use in determining boundary conditions. The only data available were total configuration pitching moment and normal force coefficients for body-strake-tail and body-strake configurations. Applying these data to the following equation yielded highly questionable results.

$$\frac{X_{CP \Delta BST}}{d} = \frac{C_{m_{BST}} - C_{m_{BS}}}{C_{N_{BST}} - C_{N_{BS}}}$$

At angles of attack greater than 90 degrees, calculated centers of pressure were off the body. This can be attributed to the effect of tail downwash on the strakes. Tail downwash will lower the normal force on the strakes and tend to move the strake X_{CP} aft. This results in a much larger change in moment due to the addition of tails than the change in normal force would tend to indicate. Keeping this in mind, other sources of boundary conditions were sought.

At $\alpha = 0$ degrees, the effective center of pressure of the incremental force due to the addition of tails can be approximated by summing the moments about the tail leading edge at the root.

$$\frac{X_{CP \Delta BST}}{C_R} = \frac{[K_{T(B)} \frac{X_{CP_{T(B)}}}{C_R} + K_{B(T)} \frac{X_{CP_{B(T)}}}{C_R}]}{[K_{T(B)} + K_{B(T)}]} \quad (43)$$

The important incremental forces are taken to be the force on the tail in the presence of the body and the force on body in the presence of the tail. Terms accounting for the effects of strake vortices on the tail are not included, since at $\alpha = 0$ degrees strake vortices will be weak or non-existent. Values of $K_{T(B)}$, $K_{B(T)}$, $\frac{X_{CP_{T(B)}}}{C_R}$, and $\frac{X_{CP_{B(T)}}}{C_R}$ can be found in References 4 and 30. However, for the sake of completeness, they are presented again here in Figures 118 through 122. At $\alpha = 180$ degrees, Equation 43 can again be used. $K_{T(B)}$ should be equal to 1.0 since there will be no upwash at the tail trailing edge due to the presence of a forebody. Values of $\frac{X_{CP_{T(B)}}}{C_R}$ can be taken from Figures 119 and 120. Values for $\frac{X_{CP_{B(T)}}}{C_R}$ are presented in Reference 30. Again for the sake of completeness these values are presented here in Figures 123 and 124. At $\alpha = 90$ degrees there will be no interference between the tails and strakes. Then the effective center of pressure can be assumed at the centroid of the fin planform area. This assumption is valid so long as the carryover from the tails to the body is small. Section 5.2.2 dealing with $I_{B(T)}$ has shown that the carryover is small.

Applying the above boundary conditions to the following power series expansion

$$\frac{X_{CP_{ABST}}}{C_R} = a_0 + a_1\alpha + a_2\alpha^2$$

yielded

$$\frac{X_{CP_{ABST}}}{C_R} = \left[1 - \frac{3\alpha}{\pi} + \frac{2\alpha^2}{\pi^2}\right] \frac{X_{CP_0}}{C_R} + \left[\frac{4\alpha}{\pi} - \frac{4\alpha^2}{\pi^2}\right] \frac{X_{CP_{\pi/2}}}{C_R} + \left[\frac{2\alpha^2}{\pi^2} - \frac{\alpha}{\pi}\right] \frac{X_{CP_{\pi}}}{C_R}$$

which can be rewritten as:

$$\frac{X_{CP\ ABST}}{C_R} = A_0 \frac{X_{CP\ 0}}{C_R} + A_1 \frac{X_{CP\ \pi/2}}{C_R} + A_2 \frac{X_{CP\ \pi}}{C_R} \quad (44)$$

where:

$$A_0 = 1 - \frac{3\alpha}{\pi} + \frac{2\alpha^2}{\pi^2}$$

$$A_1 = \frac{4\alpha^2}{\pi} - \frac{4\alpha^2}{\pi^2} \quad (\alpha \text{ in radians})$$

$$A_2 = \frac{2\alpha^2}{\pi^2} - \frac{\alpha}{\pi}$$

Values of A_0 , A_1 , and A_2 are plotted in Figures 125, 126 and 127.

Use of Method

A general description presenting the details of how to apply this method will be presented in this section. This will be followed by a numerical example in which this method is applied in conjunction with the other methods needed to calculate the X_{CP} of a complete body-strake-tail configuration.

1 Calculate $\frac{X_{CP\ 0}}{C_R}$

a Use Figure 118 to determine values of $K_{T(B)}$ and $K_{B(T)}$ at the appropriate value of d/s .

b Depending upon the Mach number, use either Figure 119 or 120 to determine $\frac{X_{CP\ T(B)}}{C_R}$.

c Depending upon the Mach number, use either Figure 121 or 122 to determine $\frac{X_{CP\ B(T)}}{C_R}$.

- d Apply the results of steps a, b and c to Equation 43. The calculated center of pressure is measured from the leading edge to the fin root chord.
- 2 Calculate $\frac{X_{CP_n}}{C_R}$
- a Use Figure 118 to determine $K_{B(T)}$ and assume $K_{T(B)} = 1.0$.
- b Depending upon the Mach number, use either Figure 119 or 120 to determine $\frac{X_{CP_{T(B)}}}{C_R}$.
- c Depending upon the Mach number use either Figure 123 or 124 to determine $\frac{X_{CP_{B(T)}}}{C_R}$.
- d Apply the results of Steps a, b and c to Equation 43. The calculated center of pressure is measured from the trailing edge of the fin root chord.
- e Using the results of step d determine the center of pressure as measured from the leading edge of the fin root chord.
- 3 Calculate the centroid of the fin planform area as measured from the leading edge of the fin root chord.
- 4 Apply the results of steps 1, 2 and 3 to Equation 44 to determine the $\frac{X_{CP_{\Delta BST}}}{C_R}$ of $\Delta C_{N_{BST}}$ for angles of attack between 0 and 180 degrees.

Numerical Example

Calculate the center of pressure for the following body-strake-tail configuration at $M = 0.6$.

Body:

$$d = 3.667 \text{ in.} \quad \frac{\ell}{d} = 14.5 \quad \frac{R_N}{d} = 2.5 \begin{matrix} \text{(tangent)} \\ \text{ogive} \end{matrix}$$

Strakes:

$$C_{R_S} = 14.33 \text{ in.} \quad S_s = 8.06 \text{ sq.in.} \quad AR_s = 0.040$$

$$\frac{b}{2} = 0.40 \text{ in.}$$

Tails:

$$C_{R_T} = 5.96 \text{ in.} \quad S_T = 8.883 \text{ sq.in.} \quad AR_T = 0.785$$

$$b_T = 1.867 \text{ in.} \quad \Lambda_{TE} = 0^\circ \quad \Lambda_{LE} = 45^\circ$$

$$\lambda = 0.687 \quad \frac{d}{s} = 0.495 \quad \frac{l}{d_{LE}} = 13.22$$

1 Calculate $\frac{X_{CP_{\Delta BST}}}{d}$

a Calculate $\frac{X_{CP_0}}{C_R}$

i. Using Figure 118 for $\frac{d}{s} = 0.495$,

$$K_{T(B)} = 1.45$$

$$K_{B(T)} = 0.8$$

ii. From Figure 119 for $\Lambda_{T.E.} = 0^\circ$ and $\lambda = 0.687$;

$$\frac{X_{CP_{T(B)}}}{C_R} = 0.309$$

iii. From Figure 121 for $\lambda = 0.687$, $\frac{d}{s} = 0.495$ and no afterbody:

$$\frac{X_{CP_{B(T)}}}{C_R} = 0.226$$

iv. Applying the results of steps i through iii to Equation 43 yields:

$$\frac{x_{CP0}}{C_R} = 0.279$$

b Calculate $\frac{x_{CP_T}}{C_R}$

i. As in the previous step $K_{D(T)} = 0.8$; however, $K_{T(B)} = 1.0$ in the absence of a forebody.

ii. From Figure 119 for $\lambda = 0.687$ and $\Lambda_{LE} = 0^\circ$ (i.e., Fin T.E. facing forward)

$$\frac{x_{CP_{T(B)}}}{C_R} = 0.175.$$

iii. From Figure 123 for $\frac{d}{s} = 0.495$, $\lambda = 0.687$ and $\Lambda_{LE} = 0^\circ$ (i.e., Fin trailing edge forward):

$$\frac{x_{CP_{B(T)}}}{C_R} = 0.101.$$

iv. Apply the results of steps i through iii to Equation 43 yields:

$$\frac{x_{CP_T}}{C_R} = 0.142 \text{ (measured from T.E.)}$$

$$\frac{x_{CP_T}}{C_R} = 0.858 \text{ (measured from L.E.)}$$

c Calculate $\frac{x_{CP_{W/2}}}{C_R}$

i. $\frac{x_{CP_{W/2}}}{C_R} = \bar{x}_T = 0.555$

d Apply the results of steps a, b and c to Equation 44
for angles of attack between 0 and 180 degrees.

α (deg)	A_0	A_1	A_2	$\frac{X_{CP_{ABST}}}{C_R}$	$\frac{X_{CP}}{d}$
0	1.0	0.0	0.0	0.279	13.67
10	0.8395	0.2099	-0.0494	0.308	13.72
20	0.6914	0.3951	-0.0864	0.338	13.77
30	0.5556	0.5556	-0.1111	0.368	13.82
40	0.4321	0.6914	-0.1235	0.398	13.87
50	0.3210	0.8025	-0.1235	0.429	13.92
60	0.2222	0.8889	-0.1111	0.460	13.97
70	0.1358	0.9506	-0.0864	0.491	14.02
80	0.0617	0.9877	-0.0498	0.523	14.07
90	0.0	1.0	0.0	0.555	14.12
100	-0.0494	0.9877	0.617	0.587	14.17
110	-0.0864	0.9506	0.1358	0.620	14.23
120	-0.1110	0.8889	0.2222	0.653	14.28
130	-0.1235	0.8025	0.3210	0.686	14.33
140	-0.1235	0.6914	0.4321	0.720	14.39
150	-0.1111	0.5556	0.5556	0.754	14.45
160	-0.0864	0.3951	0.6914	0.788	14.50
170	-0.0494	0.2099	0.8395	0.823	14.56
180	0.0	0.0	1.0	0.858	14.61

Where $\frac{X_{CP}}{d} = \frac{t}{d} \text{ L.E.} + \frac{X_{CP_{ABST}}}{C_R} \cdot \frac{C_R}{d}$

2 Calculate $\Delta C_{N_{BST}}$ using the method of Section 5.3.3 (p. 220 ff)

α	$\Delta C_{N_{BST}}$
0	0
10	0.711
20	1.178
30	1.909
40	2.438
50	2.865
60	3.186
70	3.450
80	3.616
90	3.65
100	3.616
110	3.441
120	3.178
130	2.814
140	2.374
150	1.824
160	1.229
170	0.631
180	0.0

3 Calculate ΔC_{NBS} and $X_{CP_{ABS}}$ using the methods of Sections 5.3.1

and 5.3.2, respectively. (p. 190 ff)

α	ΔC_{NBS}	$X_{cp/d}$
0	0	7.124
10	0.45	8.560
20	1.5	9.486
30	2.9	9.902
40	4.2	9.807
50	5.15	9.202
60	5.5	8.087
70	4.95	8.554
80	3.0	9.159
90	3.0	9.901
100	3.0	10.781
110	3.0	11.798
120	3.0	12.952
130	5.2	12.074
140	5.35	11.342
150	4.15	10.759
160	2.3	10.325
170	0.7	10.040
180	0.0	9.904

4 Calculate C_{NB} and $\frac{X_{CP}}{d}$ using the methods of Sections 5.1.1 (p. 39 ff) and 5.1.2 (p. 61 ff), respectively

α (deg)	C_{NB}	$\frac{X_{CP}}{d}$
0	0	3.6
10	1.09	4.75
20	3.10	6.15
30	5.74	6.15
40	8.50	6.15
50	12.09	6.15
60	13.79	6.5
70	15.69	6.88
80	16.76	7.25
90	17.18	7.6
100	16.76	8.0
110	15.67	8.35
120	13.73	8.72
130	11.94	9.1
140	8.26	9.48
150	5.41	9.85
160	2.72	10.2
170	0.79	12.5
180	0.0	14.5

- 5 Calculate the centers of pressure between 0 and 180 degrees for the complete body-strake-tail configuration using the following equation:

$$\left. \frac{X_{CP}}{d} \right|_{BST} = \frac{C_{NB} \left(\frac{X_{CP_B}}{d} \right) + \Delta C_{N_{BS}} \left(\frac{X_{CP_{\Delta BS}}}{d} \right) + \Delta C_{N_{BST}} \left(\frac{X_{CP_{\Delta BST}}}{d} \right)}{C_{NB} + \Delta C_{N_{BS}} + \Delta C_{N_{BST}}}$$

except at $\alpha = 0$ and 180 degrees

$$\text{when } \left[\frac{X_{CP}}{d} \right]_{BST} = \frac{C_{M_\alpha}}{C_{N_\alpha}}$$

α (deg)	C_{m_B}	$C_{m_{\Delta BS}}$	$C_{m_{\Delta BST}}$	C_{NB}	$\Delta C_{N_{BS}}$	$\Delta C_{N_{BST}}$	$(X_{CP}/d)_{BST}$
0	0	0	0	0	0	0	
10	5.18	3.85	9.75	1.09	0.45	0.71	8.32
20	19.07	14.23	24.43	3.10	1.50	1.18	10.00
30	35.30	28.72	26.38	5.74	2.90	1.91	8.57
40	52.28	41.19	33.82	8.50	4.20	2.44	8.41
50	74.35	47.39	39.88	12.09	5.15	2.87	8.04
60	89.64	44.48	44.51	13.79	5.5	3.19	7.95
70	107.95	42.34	48.37	15.69	4.95	3.45	8.25
80	121.51	27.48	50.88	16.76	3.0	3.62	8.55
90	130.58	29.70	51.54	17.18	3.0	3.65	8.89
100	134.08	32.34	51.24	16.76	3.0	3.62	9.31
110	130.84	35.39	48.97	15.67	3.0	3.44	9.73

α (deg)	C_{m_B}	$C_{m_{ABS}}$	$C_{m_{ABST}}$	C_{N_B}	$\Delta C_{N_{BS}}$	$\Delta C_{N_T(RS)}$	$(X_{CP}/d)_{BST}$
120	119.73	38.86	45.38	13.73	3.0	3.18	10.24
130	108.65	62.79	40.32	11.94	5.2	2.81	10.61
140	78.30	60.68	34.16	8.26	5.35	2.37	10.83
150	53.29	44.65	26.36	5.41	4.15	1.82	10.92
160	27.74	23.75	17.82	2.72	2.3	1.23	11.09
170	9.88	7.03	9.19	.79	.7	.63	12.31
180	0	0	0	0	0	0	

Data Comparisons

The results of the numerical example are compared with experimental data at Mach 0.8 in Figure 128. As can be seen, agreement is quite good. The results obtained using Jorgensen's C_{N_B} predictions up to 40 degrees are also presented. The results of further check cases at other Mach numbers are shown in Figures 129, 130, and 131. As noted in Section 5.1.1, Jorgensen's method is recommended for predicting C_{N_B} up to angles of attack of 40 degrees.

Reference 30

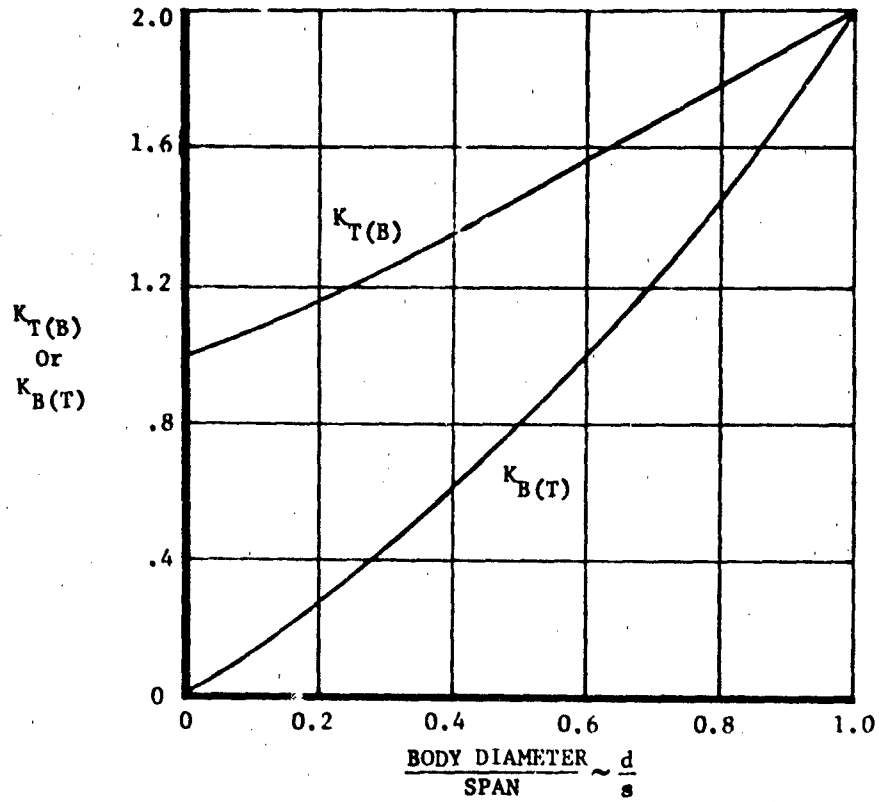
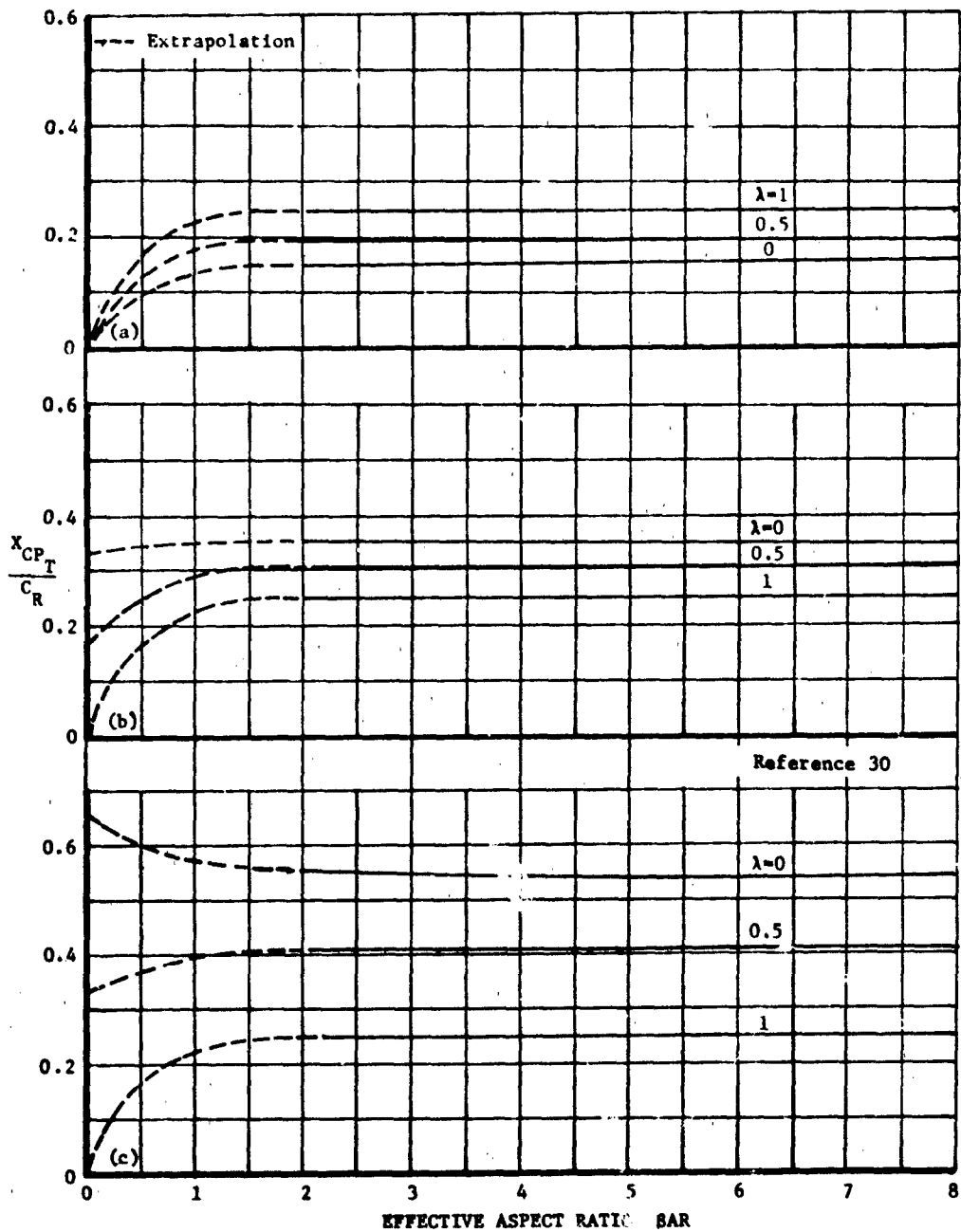


Figure 118. $K_{T(B)}$ and $K_{B(T)}$ Ratios (ry)



(a) No Leading-Edge Sweep (b) No Midchord Sweep (c) No Trailing-Edge Sweep

Figure 119. Tail Alone Center of Pressure at Subsonic Speeds

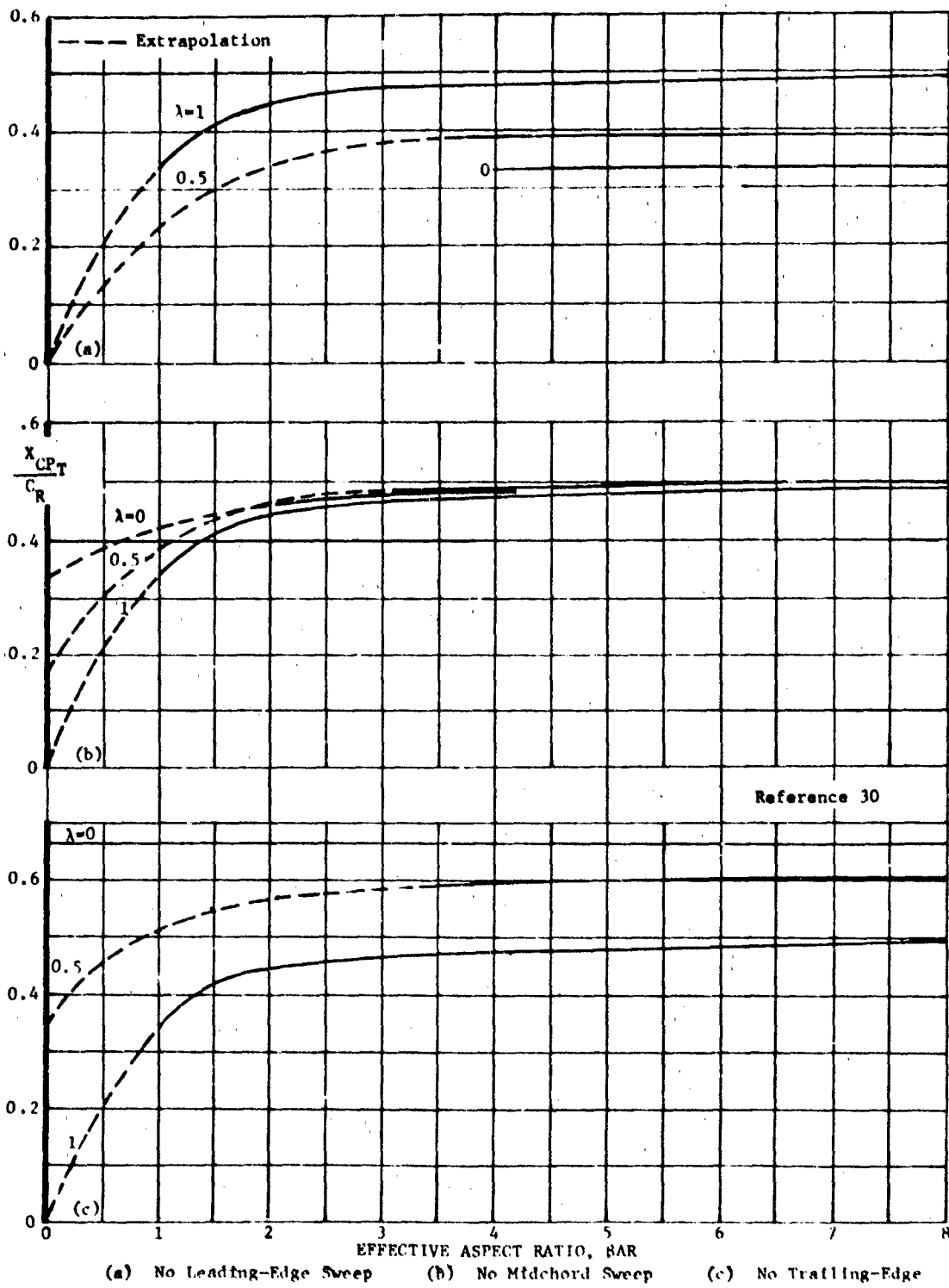


Figure 120. Tail Alone Center of Pressure at Supersonic Speeds

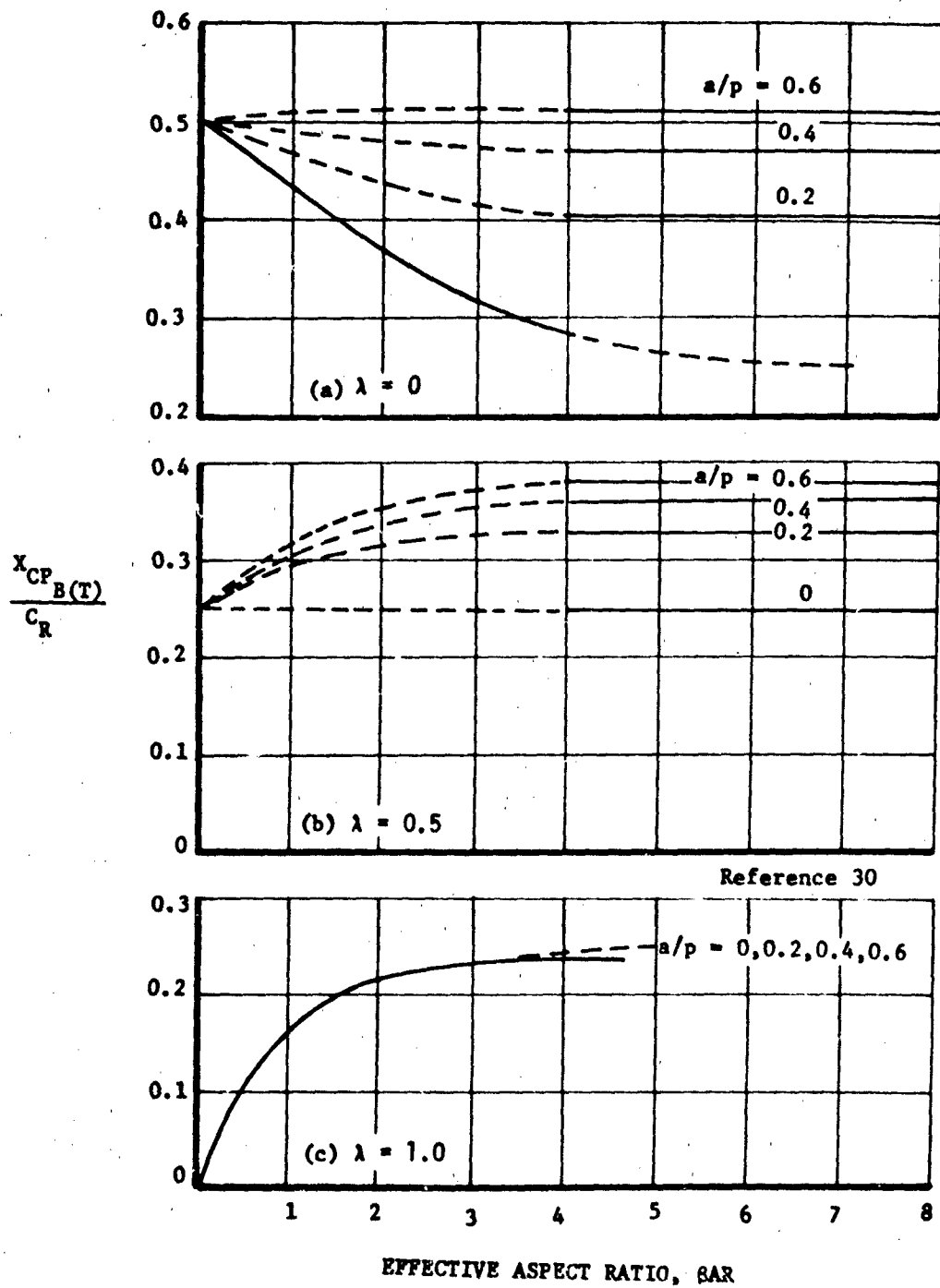


Figure 121. Curves for Determining $X_{CP_B(T)}/C_R$ for Subsonic Speeds
(Zero Trailing Edge Sweep)

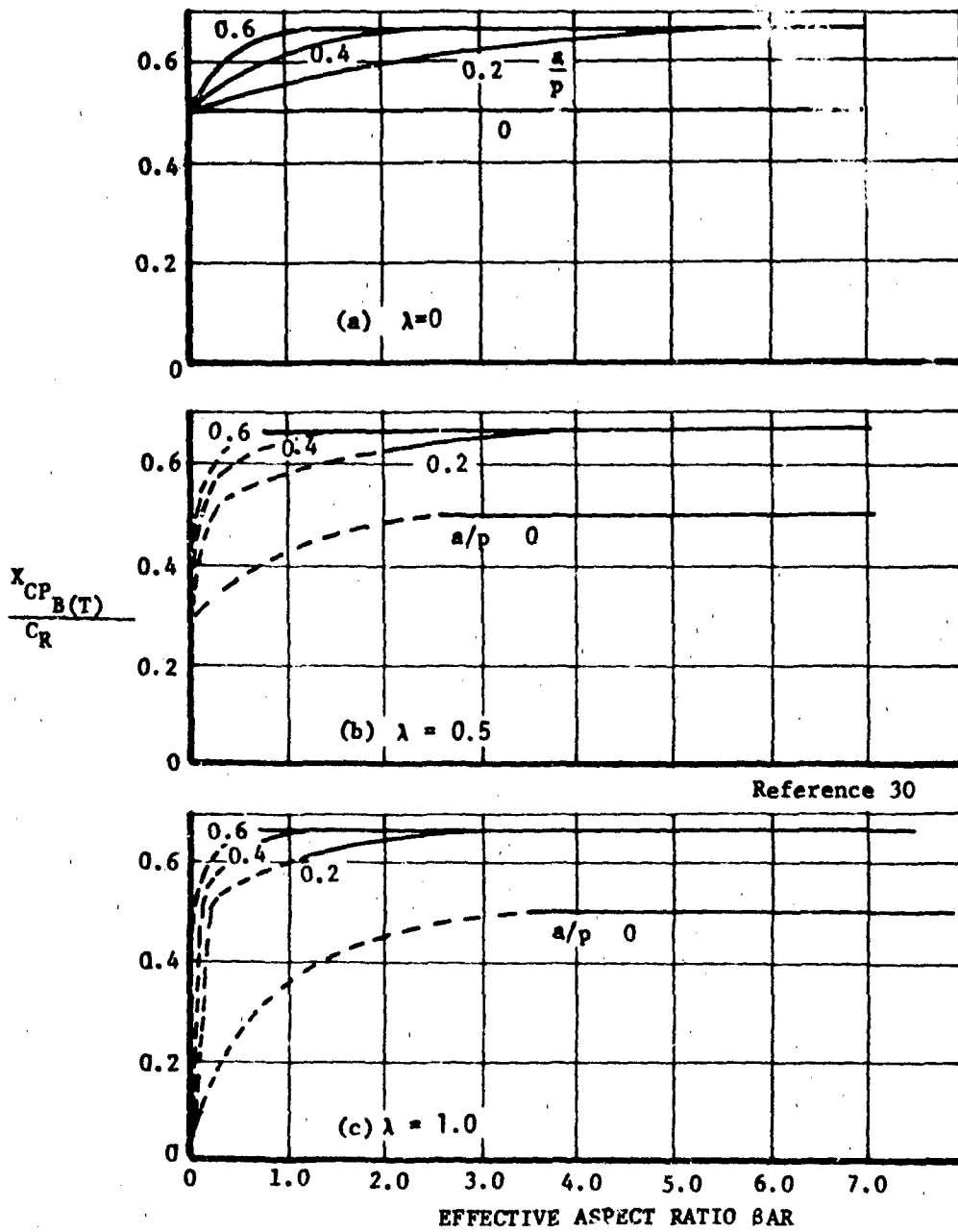


Figure 122. Curves for Determining $X_{CP_{B(T)}}/C_R$ for No-Afterbody at Supersonic Speeds

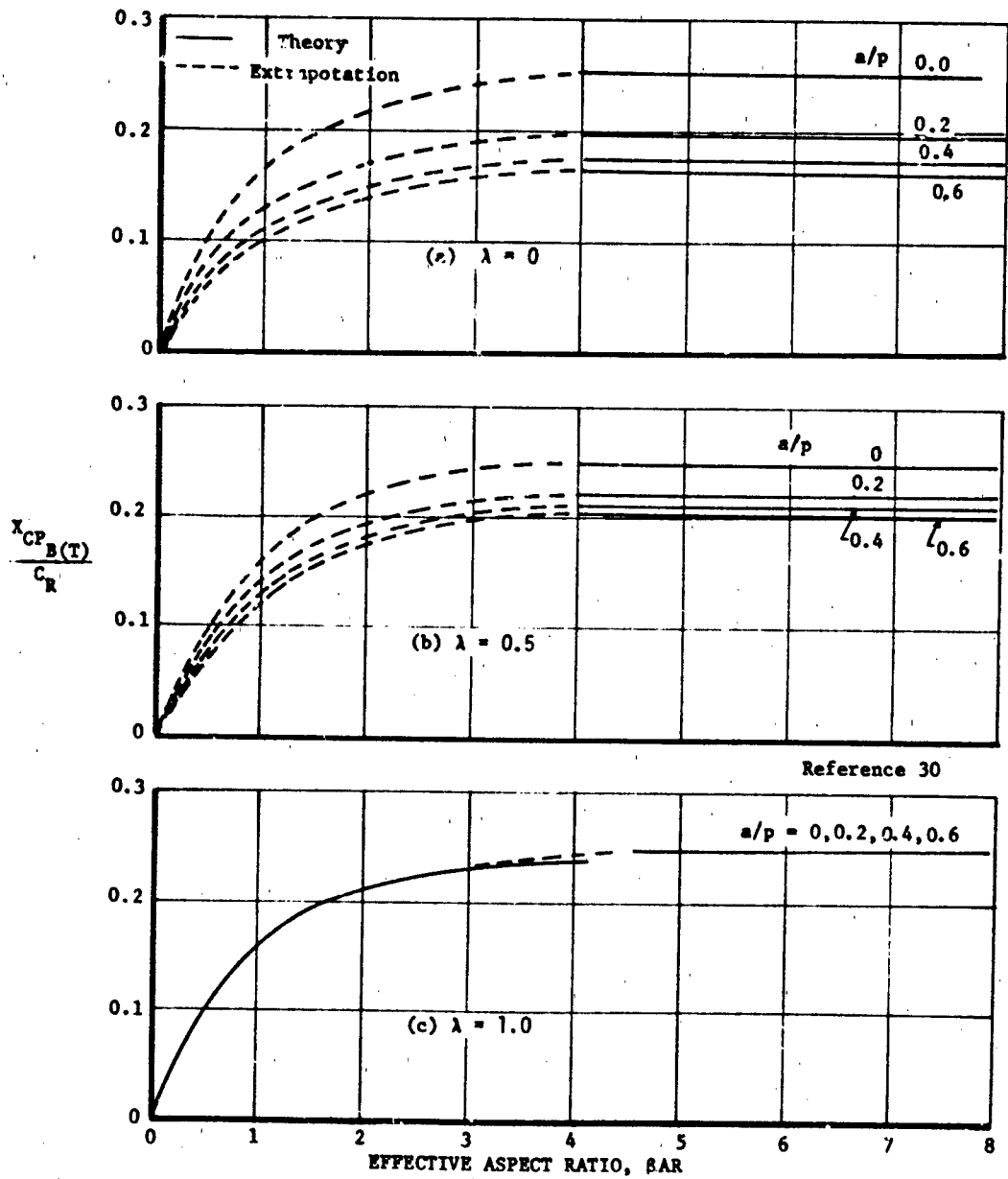


Figure 123. Curves for Determining $X_{CP_{B(T)}}/C_R$ for Subsonic Speeds
 (Zero Leading Edge Sweep)

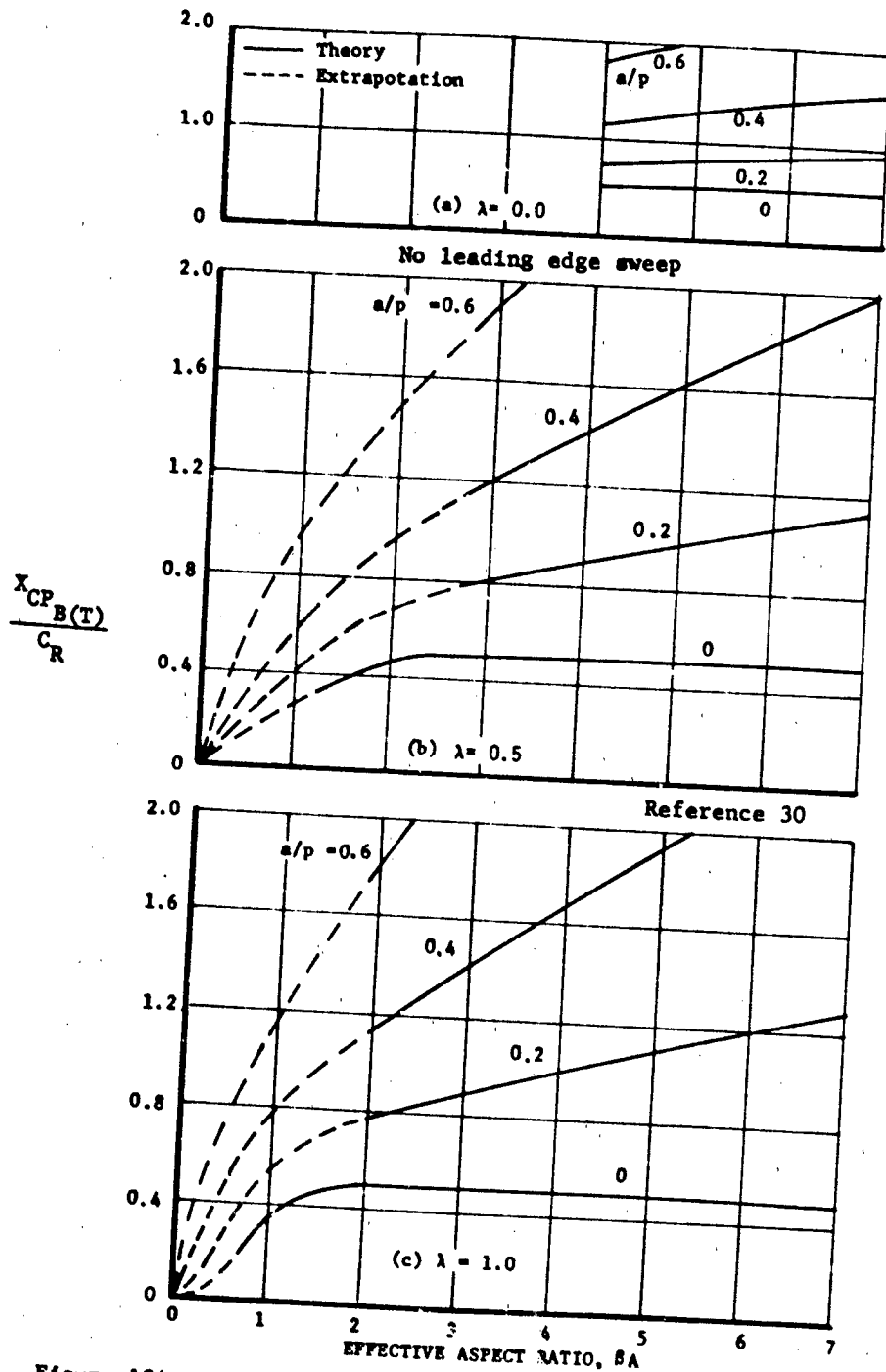
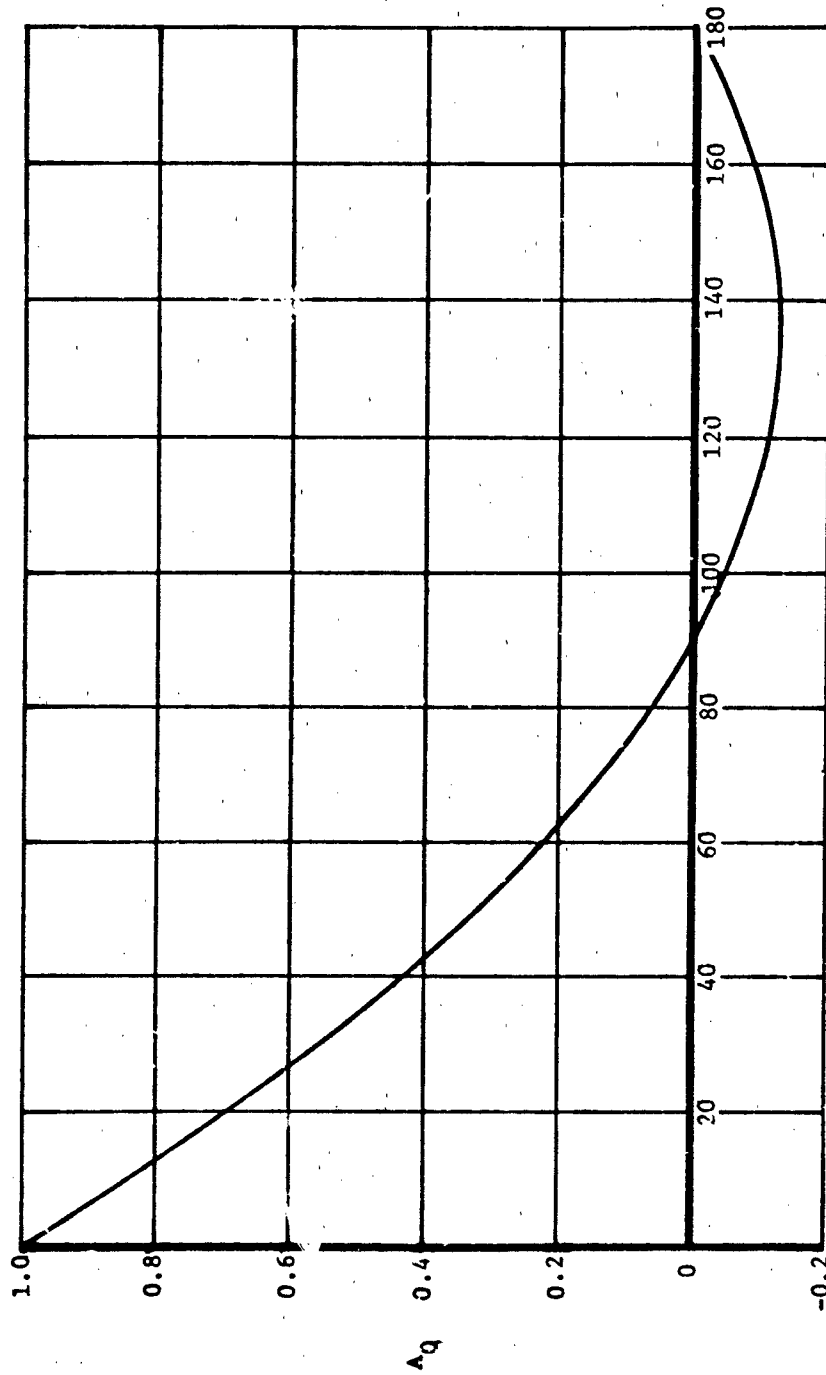


Figure 124. Curves for Determining $\frac{X_{CP_B(T)}}{C_R}$ with Afterbodies at Supersonic Speeds



ANGLE OF ATTACK-DEG.

Figure 125. Coefficients For Calculation Of $\frac{X_{CP}}{C_R}$

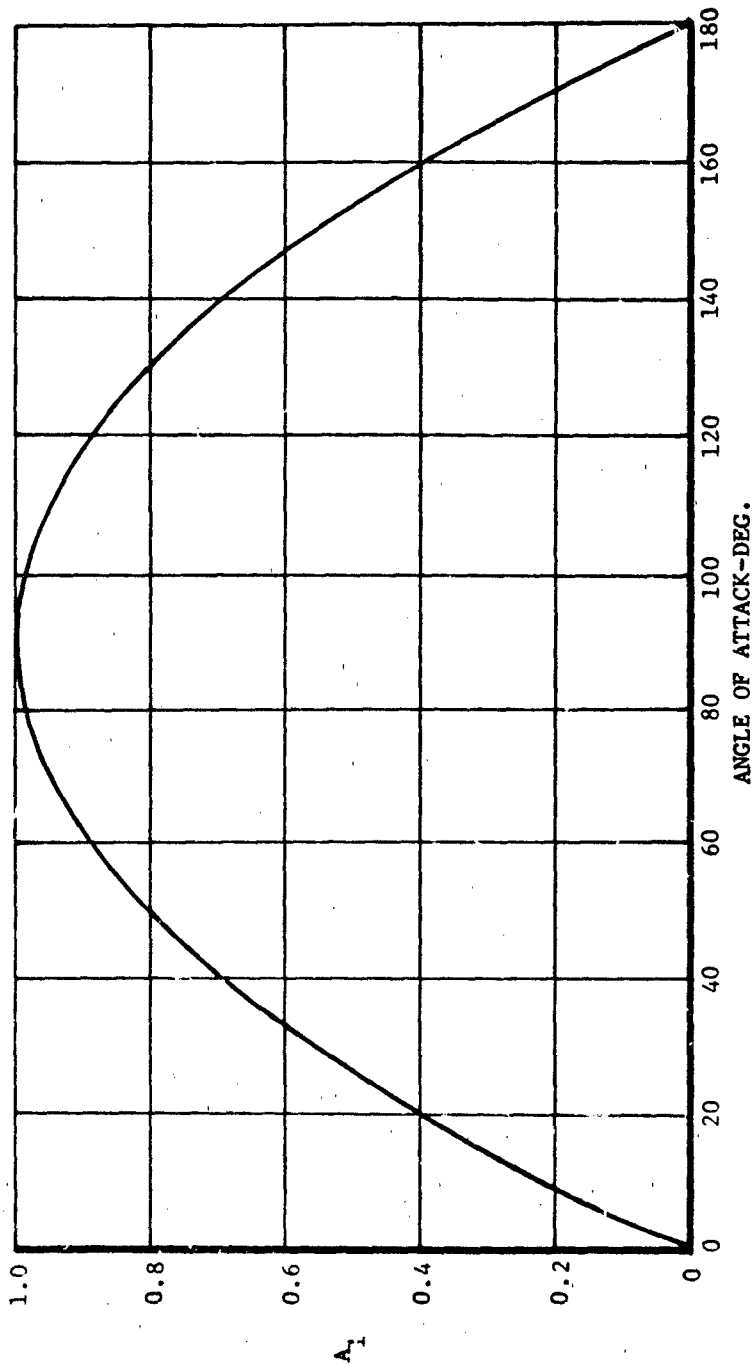
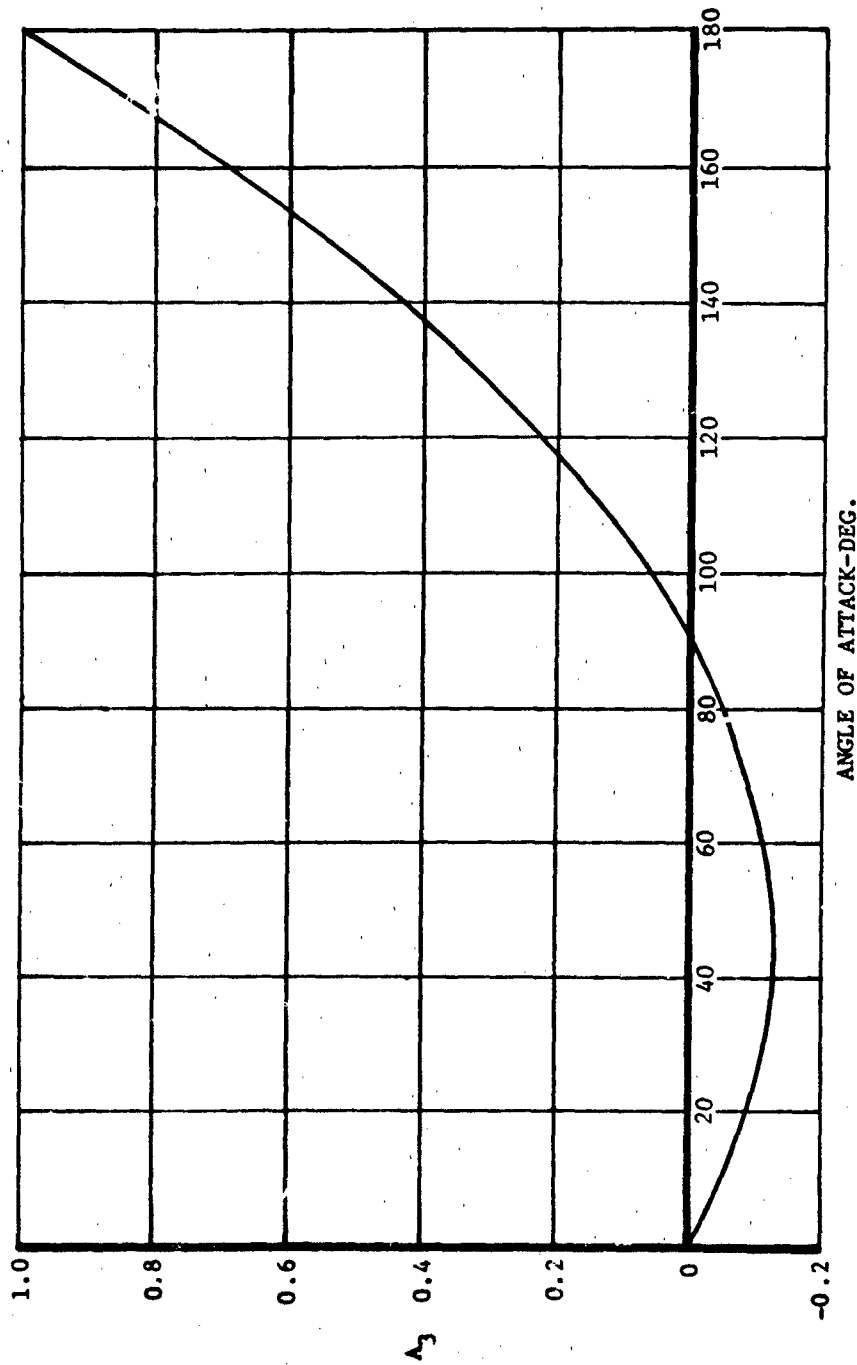


Figure 126. Coefficients For Calculation Of $\frac{X_{CP}}{C_R}$



ANGLE OF ATTACK-DEG.

Figure 127. Coefficients For Calculation Of $\frac{X_{CP}}{C_R}$

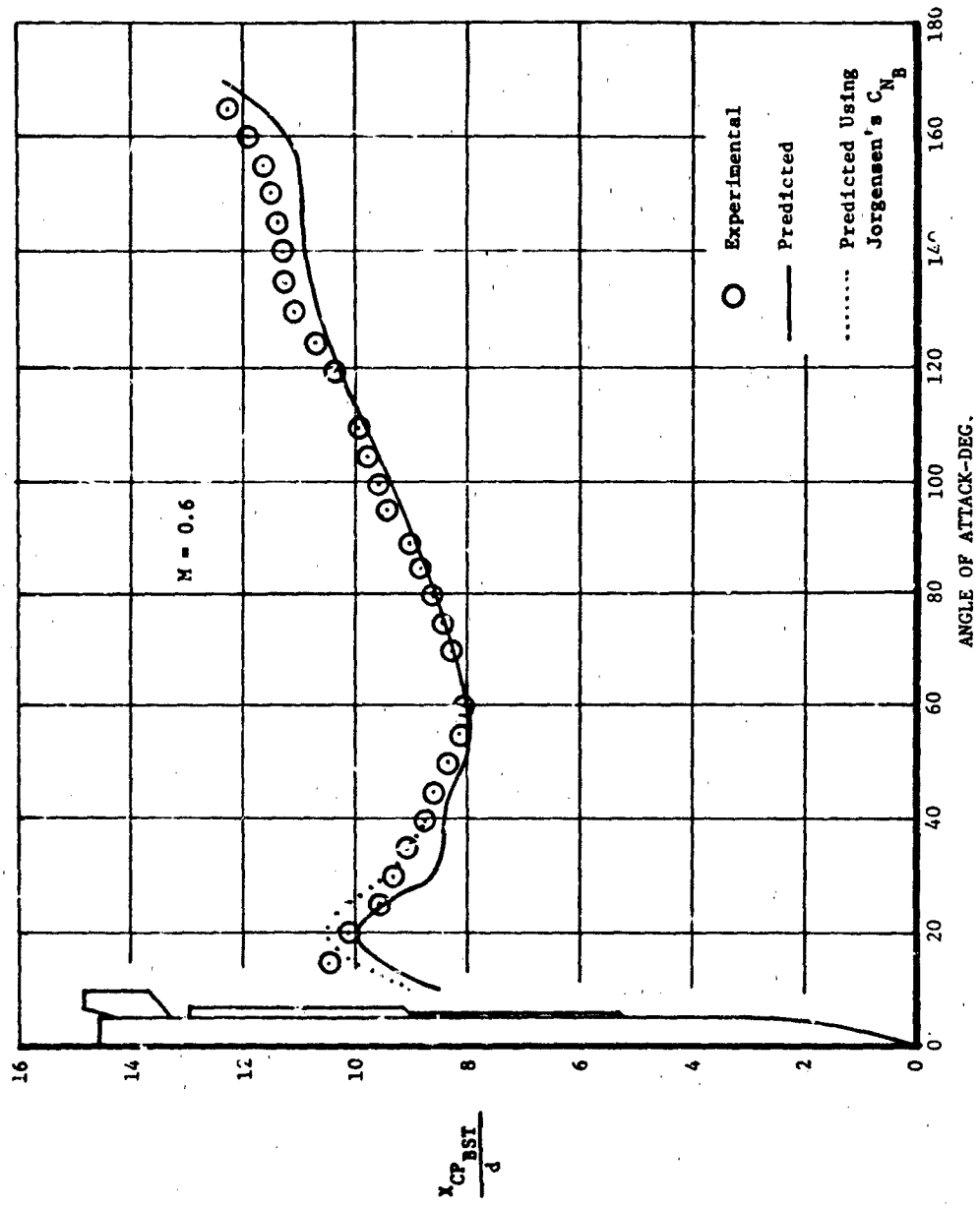


Figure 128. Comparison Between Predicted And Experimental Results, X_{CP_BST}/d , $M = 0.6$

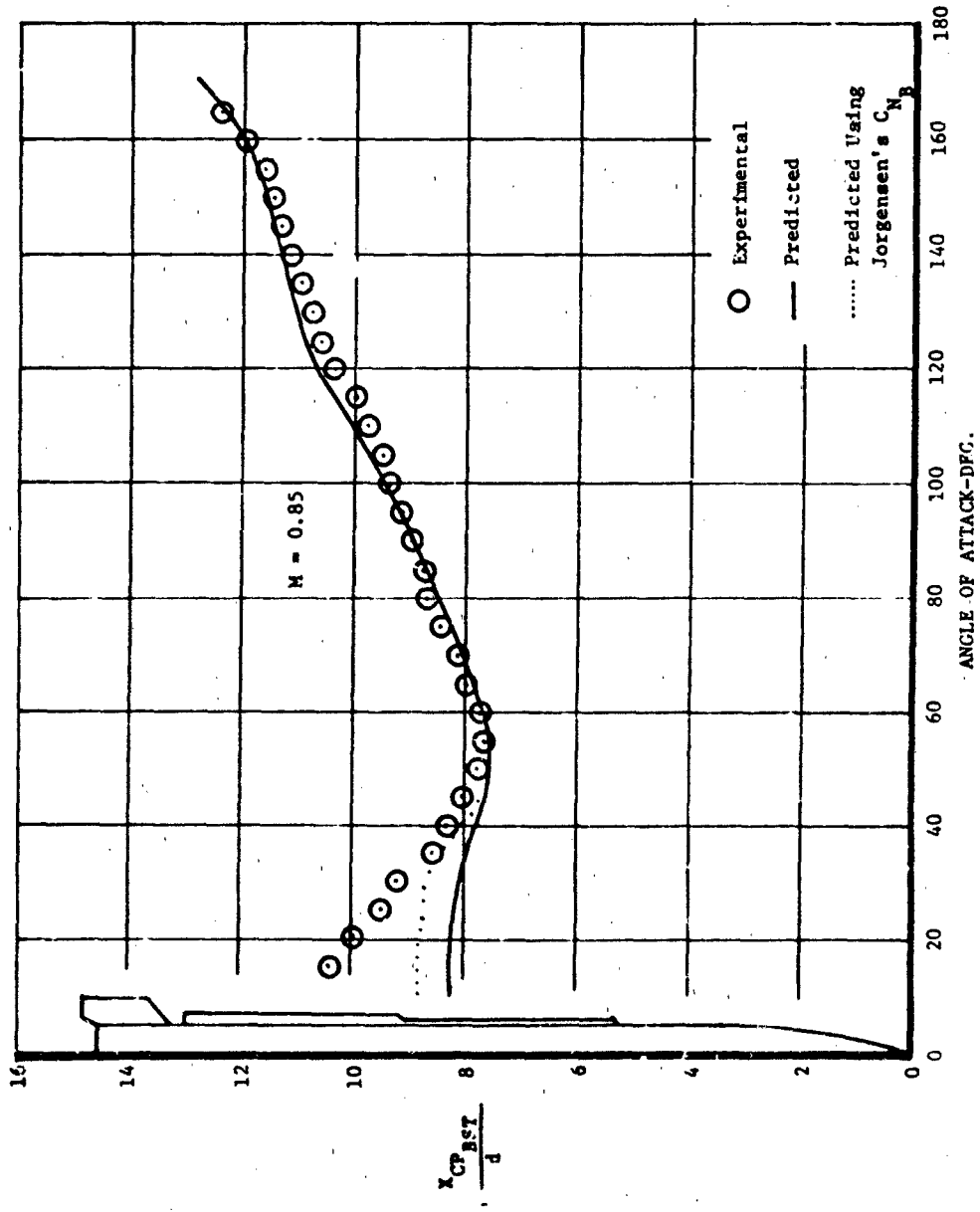


Figure 129. Comparison Between Predicted And Experimental Results, X_{CP_BST} , $M = 0.85$

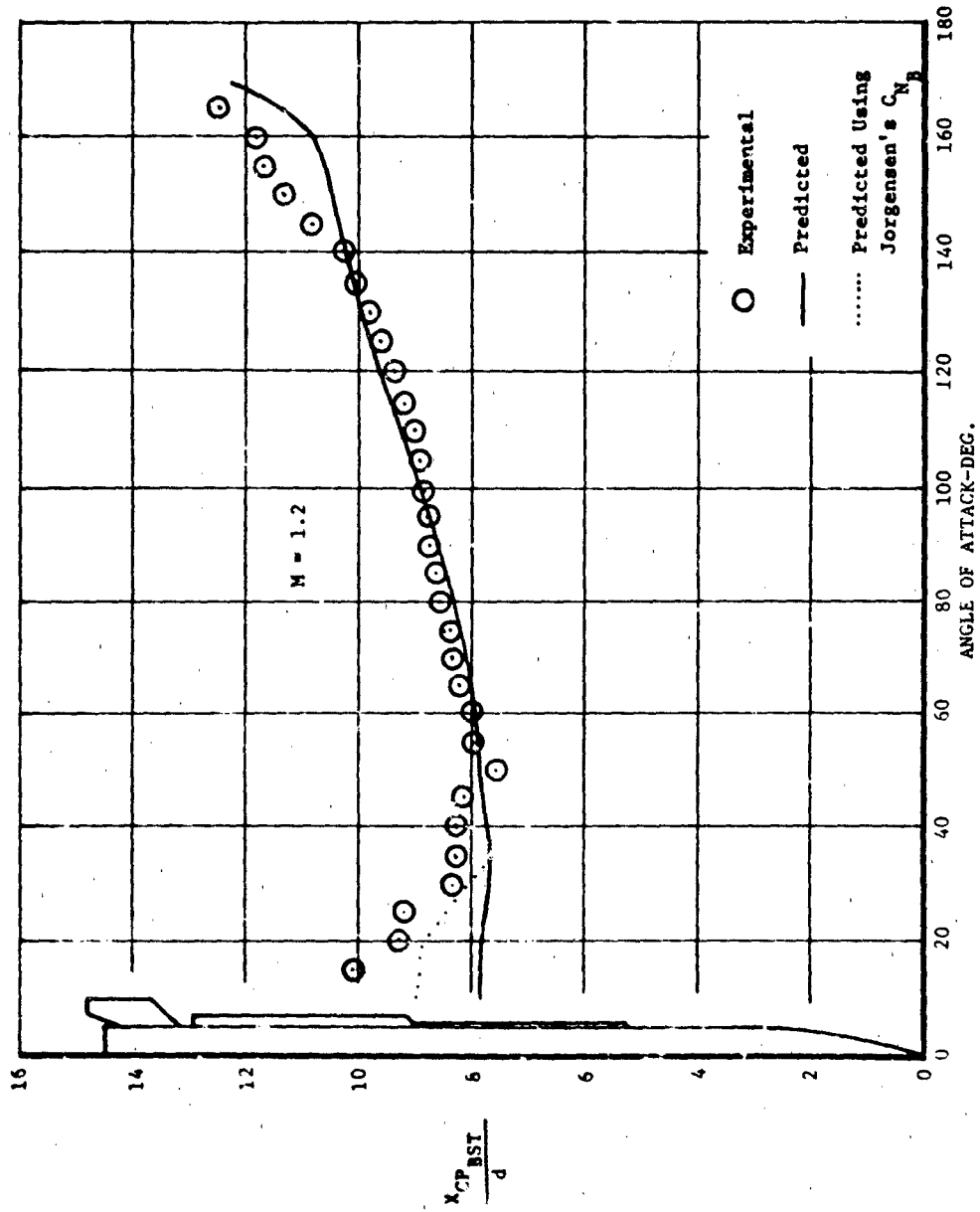


Figure 130. Comparison Between Predicted and Experimental Results, $\frac{X_{CP_BST}}{d}$, $M = 1.2$

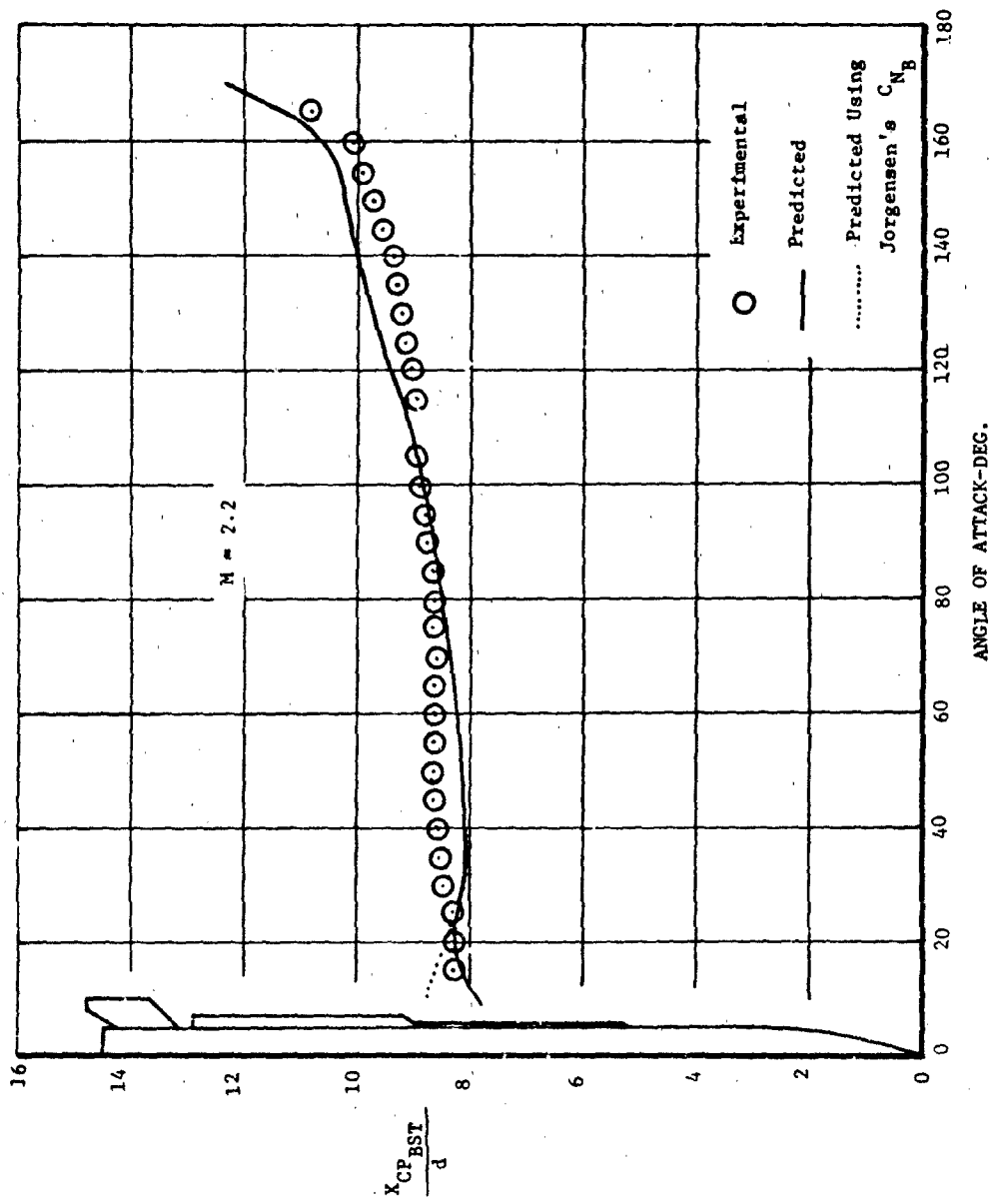


Figure 131. Comparison Between Predicted And Experimental Results, X_{CP_BST}/d , $M = 2.2$

5.4 Body-Wing-Tail Configurations

5.4.1 Incremental Normal Force Due to Wings

Summary

A method is presented to predict $\Delta C_{N_{BW}}$, the total increment in normal force due to the addition of wings to a body. The method is applicable to Mach numbers between 0.6 and 3.0 and angles of attack from 0 to 30 degrees. Comparisons between predicted results and experimental data show good agreement for all cases except Mach numbers less than 1.0. The maximum difference between predicted and experimental values for these subsonic cases occurs at an angle of attack of 30 degrees and can amount to an underprediction of between 30 and 40 percent. A discussion of some possible sources of the discrepancy is presented in connection with the comparisons between test and predicted values.

Background

Addition of wings to a body will produce an increase in normal force. This increase differs from the normal force produced on the isolated wing under identical free stream conditions. The difference is attributable to mutual interferences between configuration components. At low angles of attack ($\alpha < 6^\circ$), the interference effects are due largely to body upwash on the wings, normal force carry-over from the wings to the body and downwash imposed on the body aft of the wings due to trailing wing vortices. As angle of attack is increased beyond 6 degrees, the body crossflow boundary layer begins to separate and roll up into symmetrically disposed vortices on either side of the body. Downwash from these vortices has an additional effect on wing loading. Body vortices grow in size and strength with increases in angle of attack; therefore, their influence varies with angle

of attack. At angles of attack greater than 30 degrees, the vortex wake will become asymmetric due to the alternate shedding and growth of additional vortices. An asymmetric body vortex wake will alter the downwash which each wing experiences. This in turn will alter the loading on each wing inducing a configuration rolling moment. This problem is more acute in the subsonic and transonic Mach regimes.

Method Development

A method is required to predict the increment in normal force due to the addition of wings to a body, ΔC_{NBW} . The method is to be applicable to Mach numbers between 0.6 and 3.0 and angles of attack to 30 or 40 degrees. The method must account for wing non-linear normal force characteristics and mutual component interferences.

The existing method of DATCOM (Reference 17) predicts isolated wing normal force as a function of angle of attack, including non-linear effects. Wing normal force predictions are corrected for interference effects using the slender body interference factors of Reference 30. Body vortex effects on the wings are predicted separately and added to these results. The procedure for predicting body vortex effects requires the prediction of vortex location and strength in order to determine vortex interference factors. Body vortex interference factors are applied to wing linear normal force characteristics only. In Figure 132 the method of DATCOM has been applied to a body wing configuration and the results compared with experimental data of Reference 30. The comparison between predicted and experimental results is quite good up to 20 degrees angle of attack. However, to extend the predictions past 20 degrees requires extrapolation. For the comparison of Figure 132 the predictions were extended to 25 degrees. The

comparison shows that past 20 degrees, predictions and experimental data diverge. Due to this angle of attack limitation and difficulties encountered with the body vortex interference prediction methods, a new ΔC_{NBW} method was developed.

The method of this section predicts isolated wing normal force coefficients as a function of angle of attack and then corrects for interference effects. Utilizing the concept of the interference factors according to References 17 and 30, the incremental normal force due to the addition of a wing to a body is:

$$\Delta C_{NBW} = [R_{W(B)} + K_{B(W)}] \frac{S_w}{S_{ref}} C_{N_w} \quad (45)$$

where $C_{N_w}(\alpha)$ represents the isolated surface coefficients. $R_{W(B)}$ and $K_{B(W)}$ are interference factors. Methods for predicting $C_{N_w}(\alpha)$ and $R_{W(B)}$ are presented in Sections 5.1.4 and 5.2.1, respectively. Empirical inputs to these methods were developed using the data of Reference 13. $R_{W(B)}$ is an interference factor which when applied to isolated panel data predicts the normal force on the wing in the presence of the body. $R_{W(B)}$ empirically accounts for body upwash and body vortex downwash on the wing and can be predicted as a function of M , d/s , λ and α . $R_{W(B)}$ replaces the $K_{W(B)}$ and body vortex term in the method of Reference 17. The normal force on the wing in the presence of the body is believed to be the dominating factor in the ΔC_{NBW} term. Therefore for the purposes of this method, the normal carry-over from the wing to the body can be predicted with sufficient accuracy using the carry-over factor $K_{B(W)}$ of Reference 30. For the sake of completeness, values of $K_{B(W)}$ are presented again in Figure 133.

Use of Method

A general description of how to apply the method will be presented in this section. This will be followed by a numerical example demonstrating the use of the method.

- 1 Calculate isolated wing normal force coefficients as a function of angle of attack using the method of Section 5.1.4.
- 2 Calculate the interference factor $R_{W(B)}$ using the method of Section 5.2.1. (p. 143 ff).
- 3 Use Figure 133 to determine $K_{B(W)}$ at the appropriate value of d/s .
- 4 Apply the results of Steps 1-3 to Equation 45.

Numerical Example

The method for predicting $\Delta C_{N_{RW}}(\alpha)$ will be applied to a configuration with the following characteristics at $M=1.1$.

Body:

$$l/d = 10.0$$

$$l_N/d = 3.0 \text{ tangent-ogive}$$

$$d = 3.75 \text{ in.}$$

Wing:

$$\lambda = 0.0$$

$$AR = 2.0$$

$$d/s = 0.4$$

$$\Lambda_{L.E.} = 63.43^\circ$$

$$X_{L.E.} = 16.75 \text{ in.}$$

$$S_w/S_{ref} = 1.432$$

The steps are as follows:

- 1 Calculation of C_{N_W} using the method of Section 5.1.4 (p. 91 ff).

$$C_{N_{W\alpha}}(\alpha) = 2.93/\text{rad from R.A.S. Data Sheets (Reference 27)}$$

$$C_{N_{W\alpha}}(\pi/2) = 3.1$$

α (deg)	C_{N_T}
0	0
5	0.281
10	0.520
15	0.787
20	1.028
25	1.281
30	1.511

2 Calculation of $R_{W(B)}$ using the method of Section 5.2.1 (p. 143 ff)

$$R_{W(B)} = K_{W(B)} = 1.36 \quad @ \quad \alpha = 0^\circ$$

α (deg)	$R_{W(B)}^*$
0	1.36
5	1.351
10	1.319
15	1.26
20	1.191
25	1.108
30	1.0

* Using Transonic method

3 Using Figure 133:

$$K_{B(W)} = 0.61 \quad d/s = 0.4$$

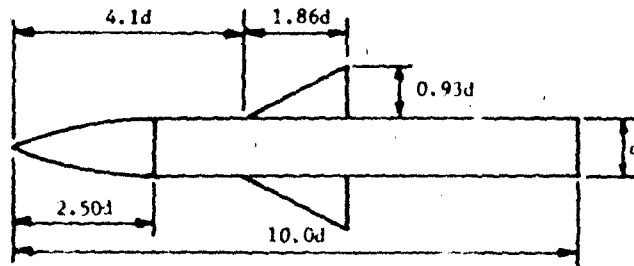
4 Apply the results of Steps 1-3 to Equation 45.

<u>α (deg)</u>	<u>ΔC_{NBW}</u>
0	0
5	0.789
10	1.437
15	2.108
20	2.651
25	3.152
30	3.484

Data Comparisons

The results of the numerical example are compared with experimental data in Figure 134. See Figure 135 for a sketch of the configuration. Further comparisons between predicted results and experimental data are presented in Figures 136 through 139. These comparisons cover a range of Mach numbers and configurations. The configurations of interest vary body length, relative wing size and wing planform. In all cases agreement between predicted and experimental data is quite good except at subsonic Mach numbers. See Figure 139. For the configurations of Figure 139, the predicted and experimental results begin to diverge rapidly between 22 and 30 degrees angle of attack. The maximum differences occur at 30 degrees where the predicted results are between 30 and 40 percent under the experimental values. At this time, the source of the difference cannot be determined. However, one aspect of the proposed method must be considered as suspect, namely the use of $K_{B(W)}$ from Reference 30 which strictly speaking applies at angles of attack near zero only. Since the wings were not instrumented in the tests which provided the basis for the current study, the variation in $K_{B(W)}$ with α cannot be evaluated. Therefore, $R_{W(B)}$, which

is the same as $R_{T(B)}$ (Section 5.2.1), accounts for the effects of α , but $K_{B(W)}$ does not. In order to explore the sensitivity of the result to $K_{B(W)}$, values of $K_{B(W)}$ were chosen such that agreement with the test data was achieved. The required value is twice the magnitude as expected for the particular body diameter to span ratio. For example, $R_{W(B)}$ for configuration 1 was set equal to 1.46 (the maximum value indicated by the data of Reference 13 for a fin with $d/s = 0.5$) and the value of $K_{B(W)}$ which would force matching was calculated. The value calculated was approximately 1.6 or twice the value of 0.8 predicted in Figure 133. As a result, a question can be raised concerning the accuracy of the test data. Further systematic data is necessary to determine if the differences observed in Figure 139 are due to inaccuracies in the experimental data or in the prediction method.



$\lambda = 0.0$
 $AR = 2.0$
 $d/s = 0.35$
 $\frac{S_w}{S_{ref}} = 2.19$

$M = 1.1$

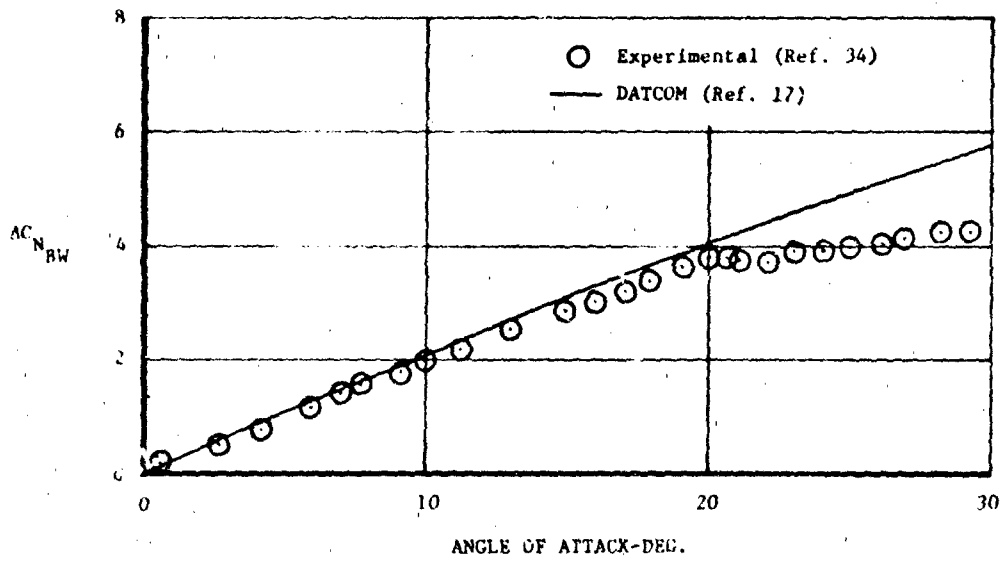


Figure 132. Comparison Of Existing Method Predictions With Experimental Data, AC_{NBW}

Reference 30

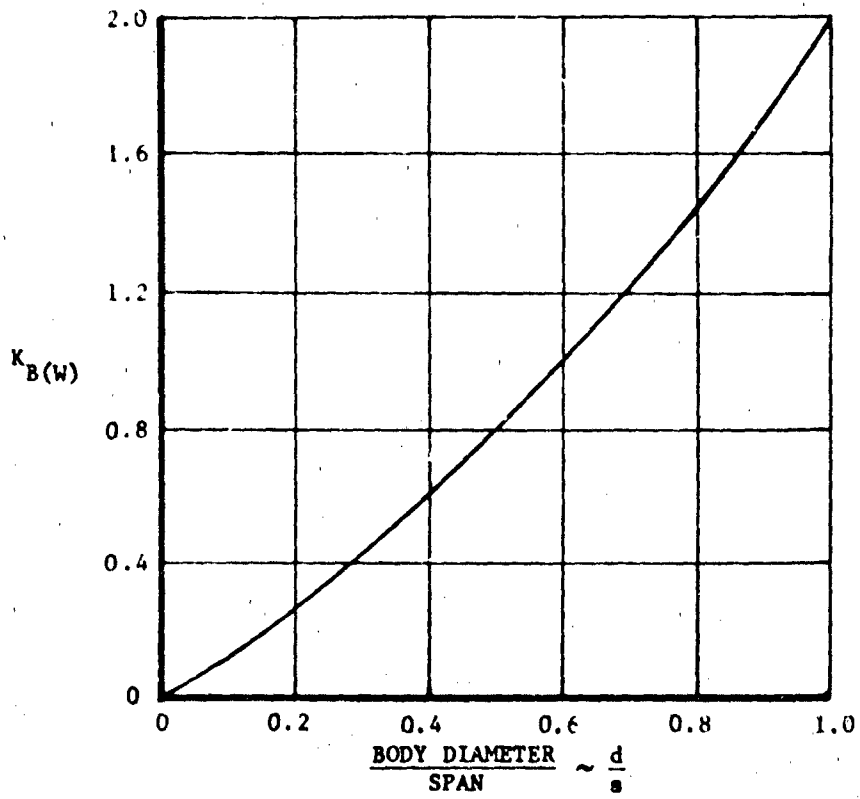


Figure 133. $K_B(w)$ Ratio at Zero Angle of Attack

Configuration 2

M = 1.1

AR = 2.0

$\lambda = 0.0$

d/s = 0.4

$\frac{S_w}{S_{ref}} = 1.432$

□ Experimental (Ref. 34)
— Predicted

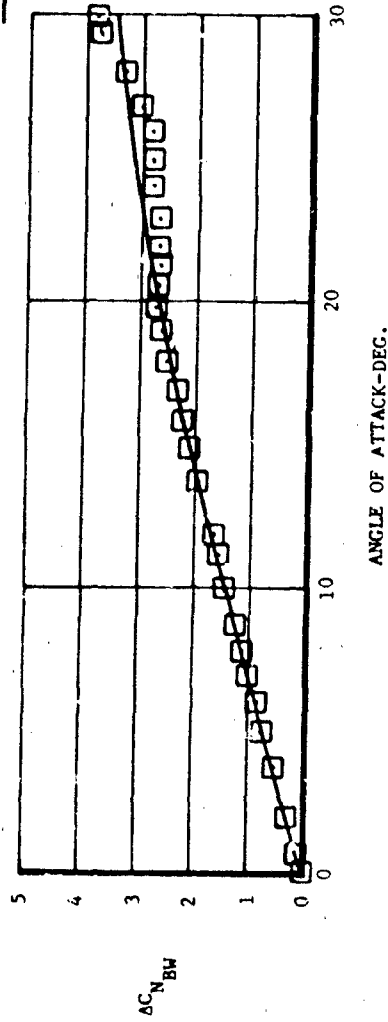


Figure 134. Comparison Between Predicted And Experimental Results, $\Delta C_{N_{BW}}$

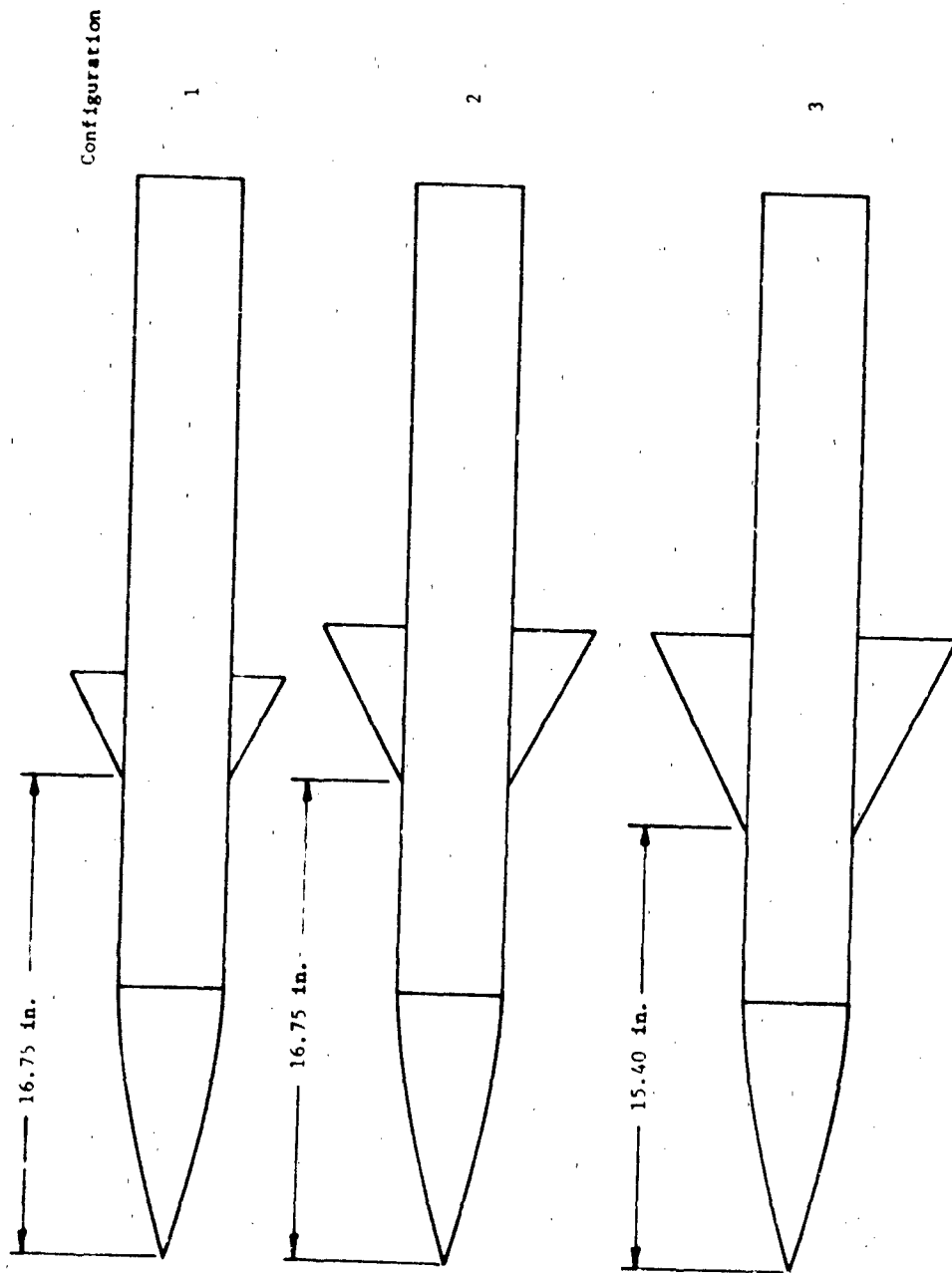


Figure 135. Configurations (Body + Wing)

M = 1.1

Config.	$\frac{S_w}{S_{ref}}$	d/s	λ	AR	Experimental Predicted (Ref. 34)
3	2.193	0.35	0.0	2.0	Δ - - - -
1	0.6366	0.5	0.0	2.0	\circ - - - -

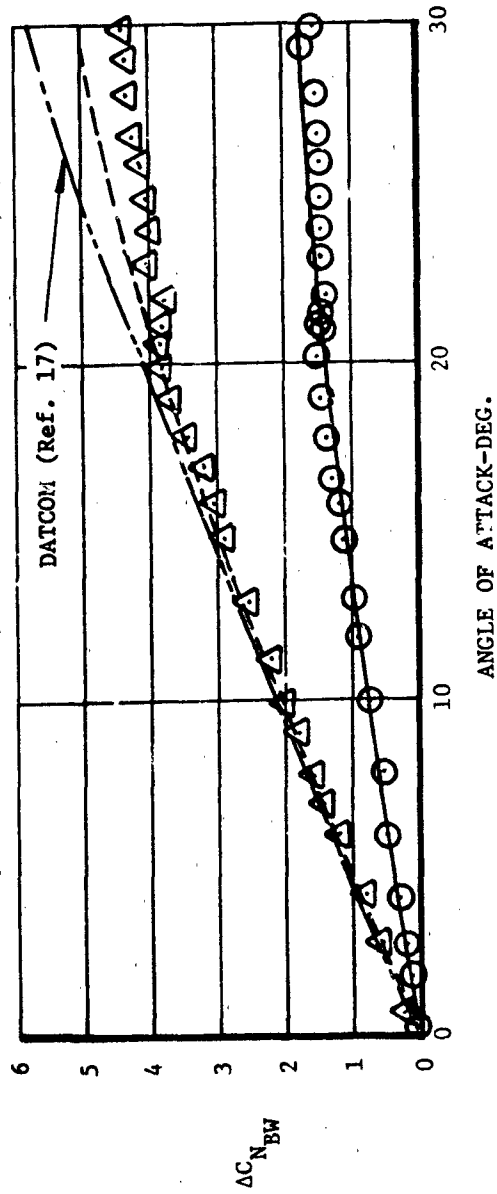


Figure 136. Comparison Between Experimental And Predicted Results, $\Delta C_{N_{BW}}$, M=1.1

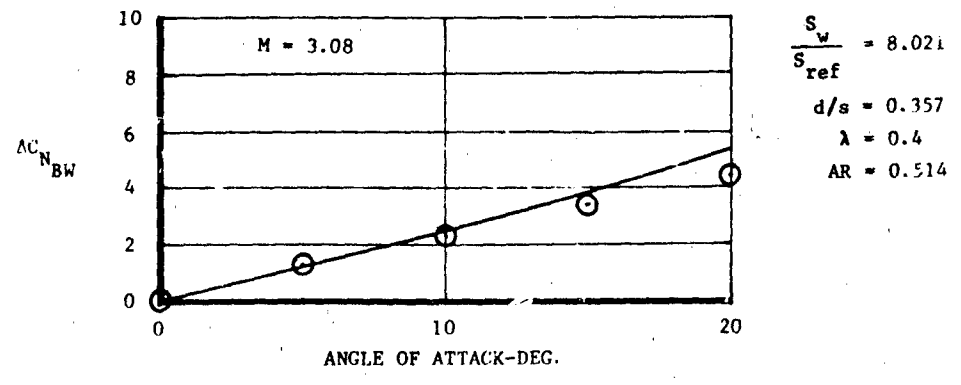
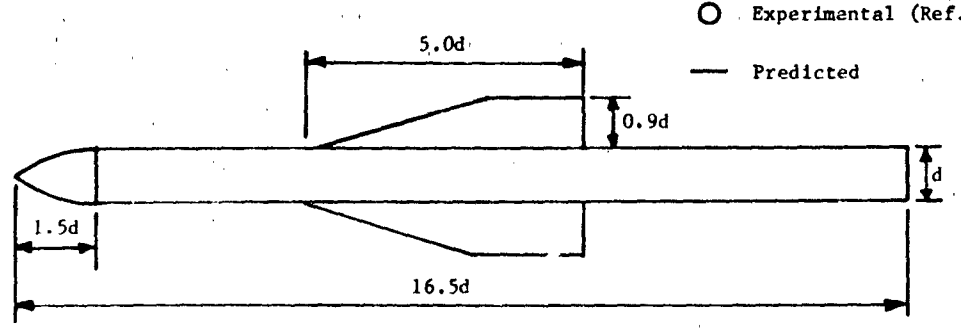
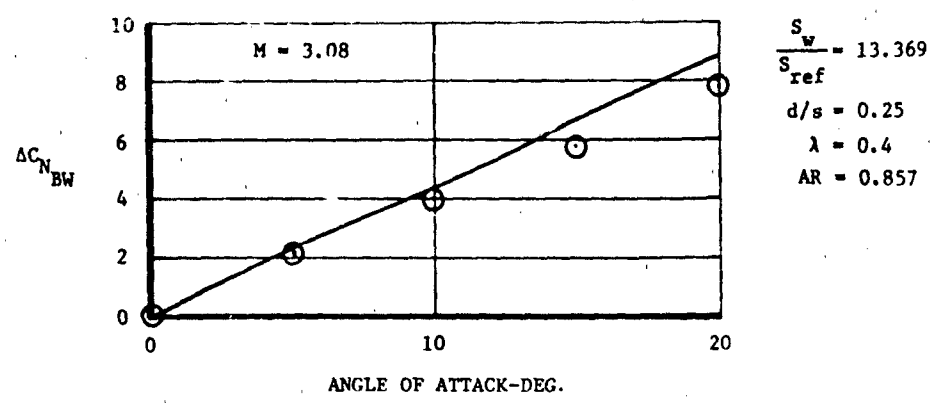
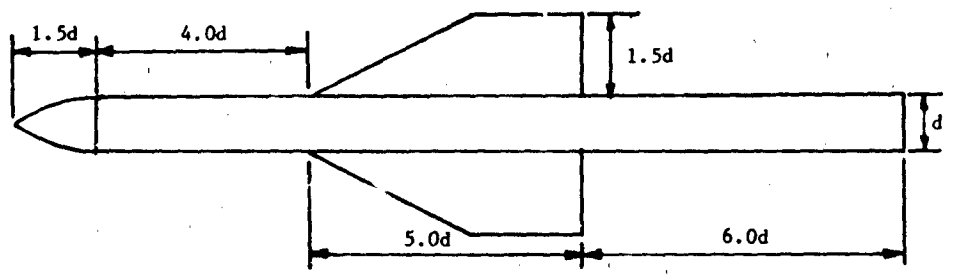
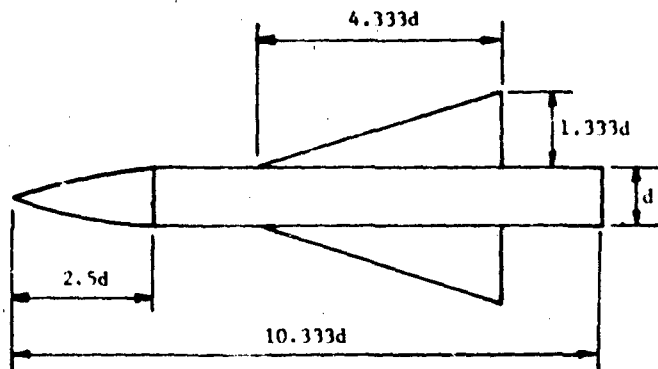


Figure 137. Comparison Between Experimental And Predicted Results, $\Delta C_{N_{BW}}$, $M=3.08$



$$\lambda = 0$$

$$AR = 1.231$$

$$d/B = 0.273$$

$$\frac{S_w}{S_{ref}} = 7.354$$

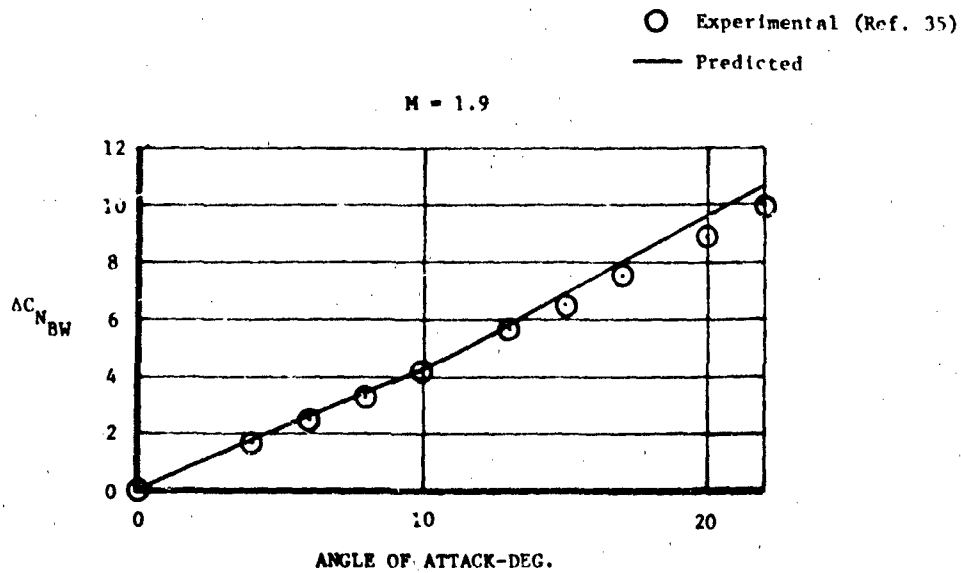


Figure 138. Comparison Between Experimental And Predicted Results, $\Delta C_{N_{BW}}$, $M=1.9$

M = 0.85

Config.	$\frac{S_w}{S_{REF}}$	d/s	AR	λ	Experimental (Ref. 34)	Predicted
1	0.637	0.5	2.0	0.0	○	—
2	1.432	0.4	2.0	0.0	□	- - -
3	2.193	0.35	2.0	0.0	△	- - -

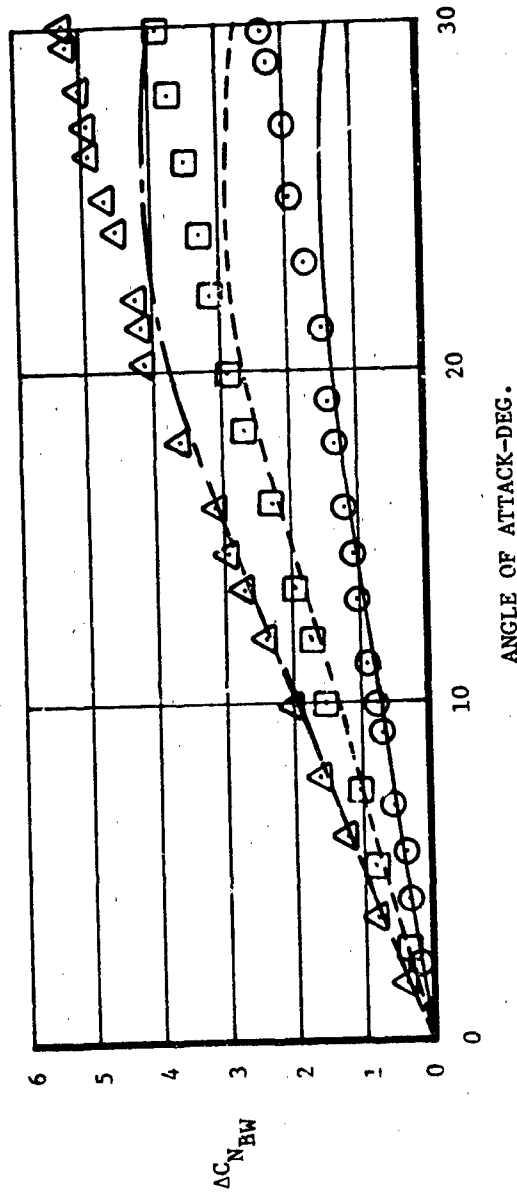


Figure 139. Comparison Between Experimental And Predicted Results, AC_{NBW} , M=0.85

5.4.2 Effective Center of Pressure for Incremental Normal Force Due to Wings

Summary

A method to predict the effective center of pressure, $X_{CP \Delta BW}$, of the incremental normal force, $\Delta C_{N_{BW}}$, is presented. $\Delta C_{N_{BW}}$ includes normal force on the wing in the presence of the body plus any carry-over from the wing to the body. The method is applicable to Mach numbers from 0.6 to 3.0 and angles of attack from 0 to 30 degrees for body-wing configurations. Comparisons between predictions and experimental data have shown good agreement.

Background

The addition of wings to a body produces an incremental normal force, $\Delta C_{N_{BW}}$. This incremental normal force includes the normal force on the wing in the presence of the body plus any carry-over from the wing to the body. See Section 5.4.1. When attempting to predict wing-body configuration aerodynamic stability characteristics, it is necessary to determine the effective center of pressure, $X_{CP \Delta BW}$ of $\Delta C_{N_{BW}}$. For preliminary design purposes, it is desired that the method for predicting this center of pressure be easy to use. The current method of Reference 17 is awkward to employ. Therefore a more elementary, easy to use method will be presented in this section.

Method Development

Development of the method began with an analysis of experimental data of References 20 and 34, consisting of normal force and pitching moment coefficients for isolated bodies and body-wing configurations. Experimental

values of the $X_{CP_{\Delta BW}}$ were determined using the following equation:

$$\frac{X_{CP_{\Delta BW}}}{d} = \frac{C_{N_{BW}} \frac{X_{CP_{BW}}}{d} - C_{N_B} \frac{X_{CP_B}}{d}}{\Delta C_{N_{BW}}} \quad (46)$$

where center of pressure is measured in diameters from the nose. The results showed that $X_{CP_{\Delta BW}}/d$ remained essentially constant for angles of attack between 0 and 30 degrees. Therefore, the method will rely on predicting X_{CP} at $\alpha = 0$ degrees and letting it remain constant between 0 and 30 degrees.

To make the method independent of forebody length, the procedure defines the center of pressure location as a percentage of the wing root chord measured from the root chord leading edge. Based on the discussions of Reference 30, $X_{CP_{\Delta BW}}/C_R$ at $\alpha = 0^\circ$ can be expressed as:

$$\frac{X_{CP_{\Delta BW}}}{C_R} = \frac{\left(K_{W(B)} \frac{X_{CP_{W(B)}}}{C_R} + K_{B(W)} \frac{X_{CP_{B(W)}}}{C_R} \right)}{[K_{W(B)} + K_{B(W)}]} \quad (47)$$

where $C_{N_{\alpha W}}$ terms cancel and $K_{W(B)}$, $K_{B(W)}$, $X_{CP_{W(B)}}/C_R$ and $X_{CP_{B(W)}}/C_R$ terms, as derived from slender body theory, are presented in Figures 140 through 144.

Use of Method

To illustrate fully the use of the method for predicting $\frac{X_{CP_{\Delta BW}}}{C_p}$, a general description of the procedure is presented, followed by a step by step numerical example.

1 Using Figure 140, determine the values of $K_{W(B)}$ and $K_{B(W)}$ for the d/s of interest.

2 Depending upon the Mach number, use either Figure 141, 142 to determine $\frac{X_{CP_{W(B)}}}{C_R}$.

3 Depending upon the Mach number, use either Figure 143 or 144 to determine $\frac{X_{CP_{B(W)}}}{C_R}$ for wings with afterbodies.

4 Using Equation 47, calculate $\frac{X_{CP_{\Delta BW}}}{C_R}$ at $\alpha = 0$ degrees. $\frac{X_{CP_{\Delta BW}}}{C_R}$ remains fixed for angles of attack between 0 and 30 degrees.

5 To express $\frac{X_{CP_{\Delta BW}}}{C_R}$ in terms of diameters from the nose use the following equation.

$$\frac{X_{CP_{\Delta BW}}}{d} = \frac{X_{L.E.}}{d} + \frac{X_{CP_{\Delta BW}}}{C_R} \frac{C_R}{d}$$

Numerical Example

Calculate $\frac{X_{CP_{\Delta BW}}}{d}$ at $M = 0.85$ for a body-wing configuration with the following characteristics.

$$\frac{l}{d} = 10 \quad d = 3.75 \text{ in.} \quad X_{LE} = 16.75 \text{ in.}$$

$$\lambda = 0 \quad AR = 2.0 \quad d/s = 0.5 \quad C_R = 3.75 \text{ in.}$$

1 From Figure 140, for $d/s = 0.5$

$$K_{W(B)} = 1.46$$

$$K_{B(W)} = 0.8$$

2 Since $M = 0.85$, use Figure 141 to determine $\frac{X_{CPW}}{C_R}$ for $\lambda = 0$.

$$\frac{X_{CPW}}{C_R} = 0.57$$

3 Since $M = 0.85$, use Figure 143 to determine $\frac{X_{CPB(W)}}{C_R}$ for $\lambda = 0$ and $d/s = 0.5$.

$$\frac{X_{CPB(W)}}{C_R} = 0.5.$$

4 Apply the results of Steps 1 - 3 to Equation 47.

$$\frac{X_{CP\Delta BW}}{C_R} = \frac{(1.46)(0.57) + (0.8)(0.5)}{1.46 + 0.8} = 0.55$$

5 Express $\frac{X_{CP\Delta BW}}{C_R}$ in terms of diameter, from the nose.

$$\frac{X_{CP\Delta BW}}{d} = \frac{16.75}{3.75} + 0.55 \frac{(3.75)}{(3.75)} = 5.02$$

Data Comparisons

A sketch of the configuration used in the numerical example is presented in Figure 145. The values of $X_{CP\Delta BW}/C_R$ calculated in the numerical example plus results for the other configurations of Figure 145 are compared with experimental data (Reference 34) in Figure 146. Further comparisons are presented in Figure 147 for the same configurations at $M = 1.1$. Figures 148 and 149 compare predictions with experimental (Reference 35) centers of pressure. The predicted values of center of pressure for the body-wing combination requires: the method of Section 5.1.1 for the body normal force coefficient (C_{NB}), the method of Section 5.1.2 for the

center of pressure X_{CP_B} of C_{N_B} , the method of Section 5.4.1 for the incremental normal force coefficient due to the addition of a wing to a body ($\Delta C_{N_{BW}}$), and finally the method described in this section for the effective center of pressure $X_{CP_{\Delta BW}}$ of $\Delta C_{N_{BW}}$. The components are combined as follows to obtain the total configuration center of pressure.

$$\frac{X_{CP}}{d} = \frac{C_{N_B} \left(\frac{X_{CP_B}}{d} \right) + \Delta C_{N_{BW}} \left(\frac{X_{CP_{\Delta BW}}}{d} \right)}{C_{N_B} + \Delta C_{N_{BW}}}$$

Reference 30

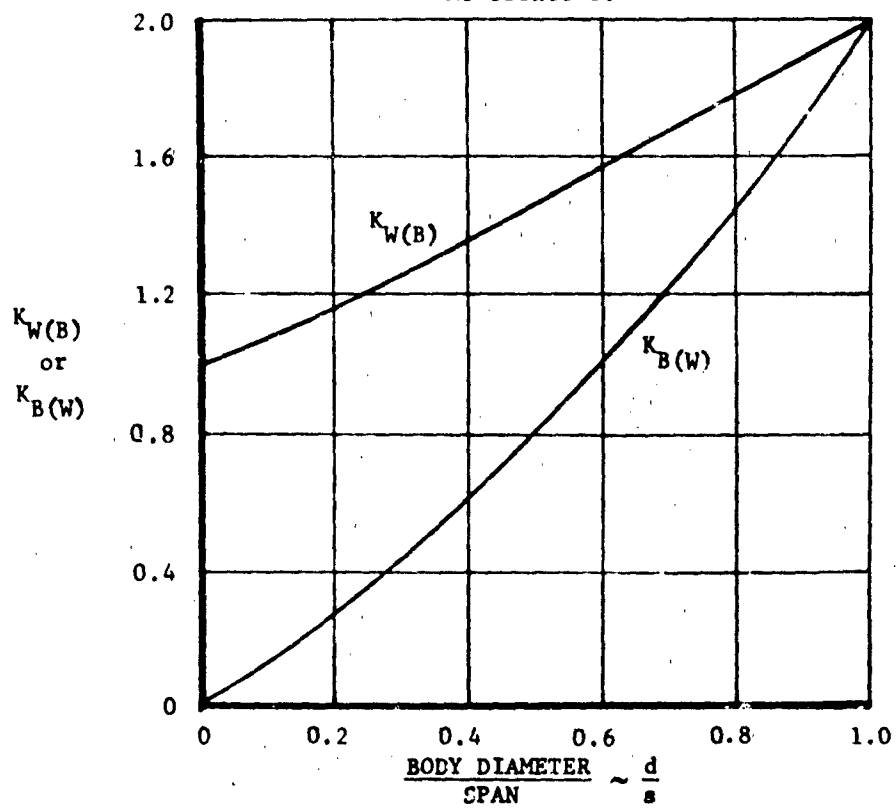
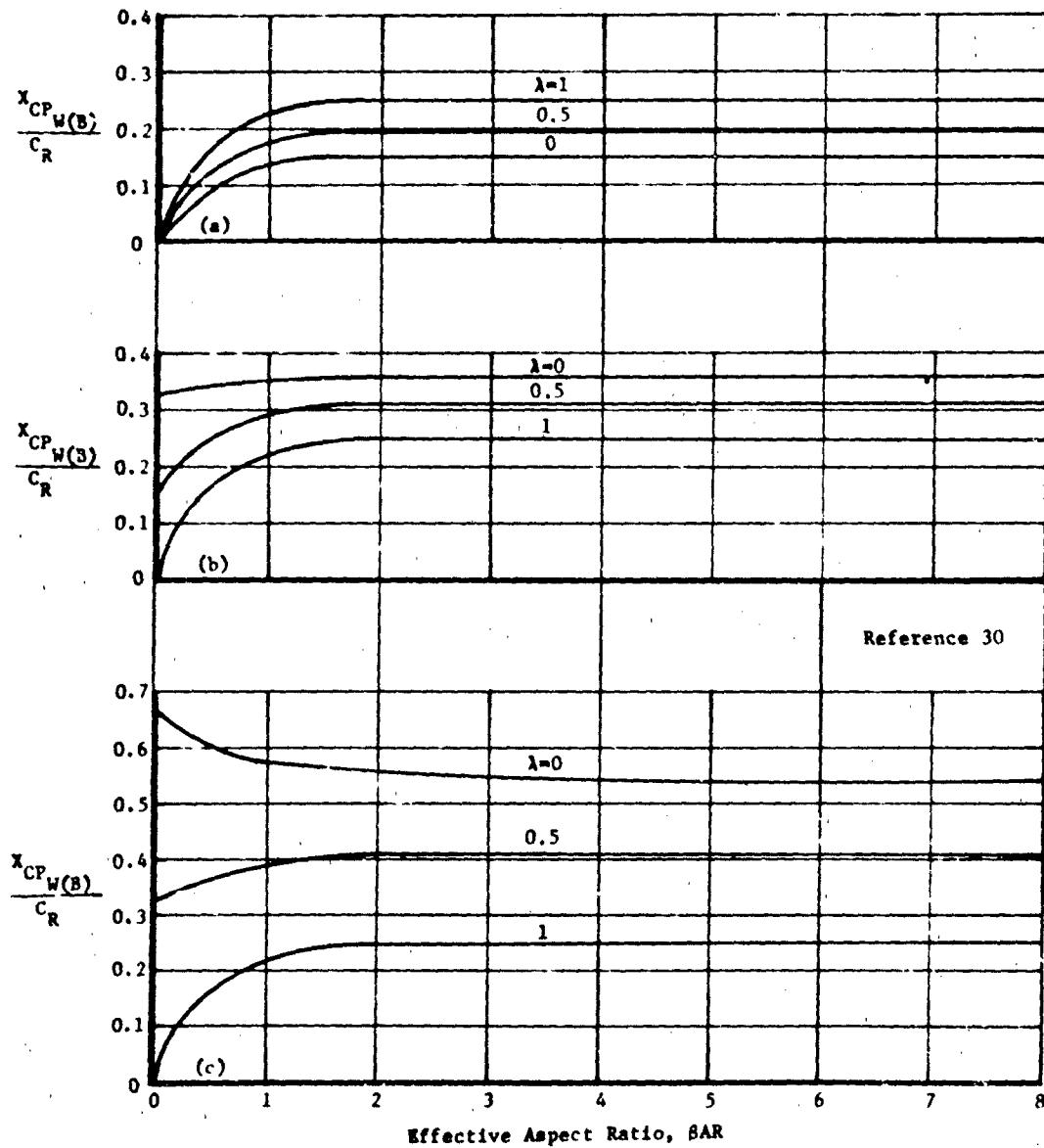
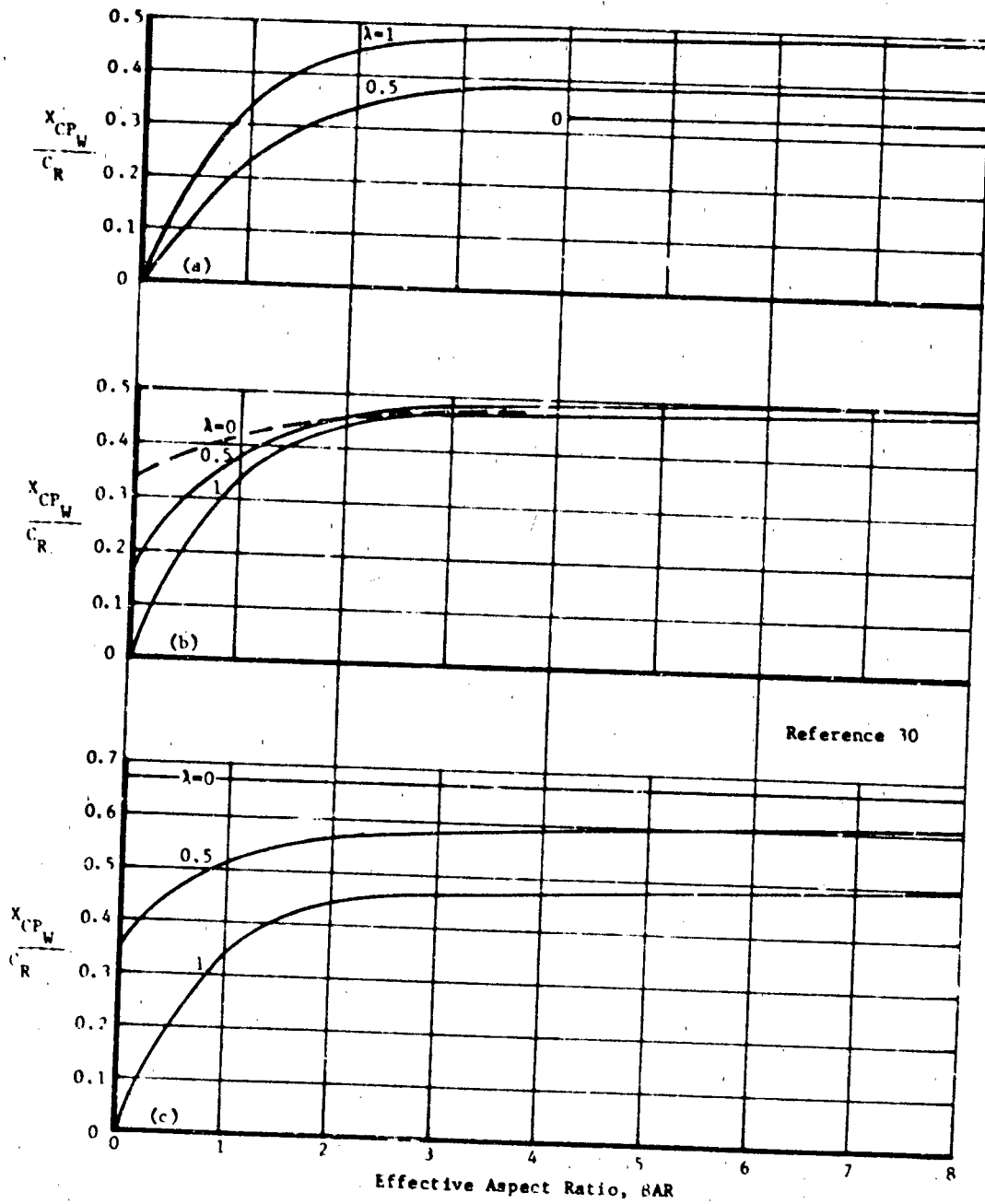


Figure 140. $K_{W(B)}$ And $K_{B(W)}$ Ratios (Slender Body Theory)



(a) No Leading-Edge Sweep (b) No Mid-Chord Sweep (c) No Trailing-Edge Sweep

Figure 141. Wing Alone Center Of Pressure At Subsonic Speeds



(a) No Leading-Edge Sweep (b) No Midchord Sweep (c) No Trailing-Edge Sweep

Figure 142. Wing Alone Center Of Pressure At Supersonic Speeds

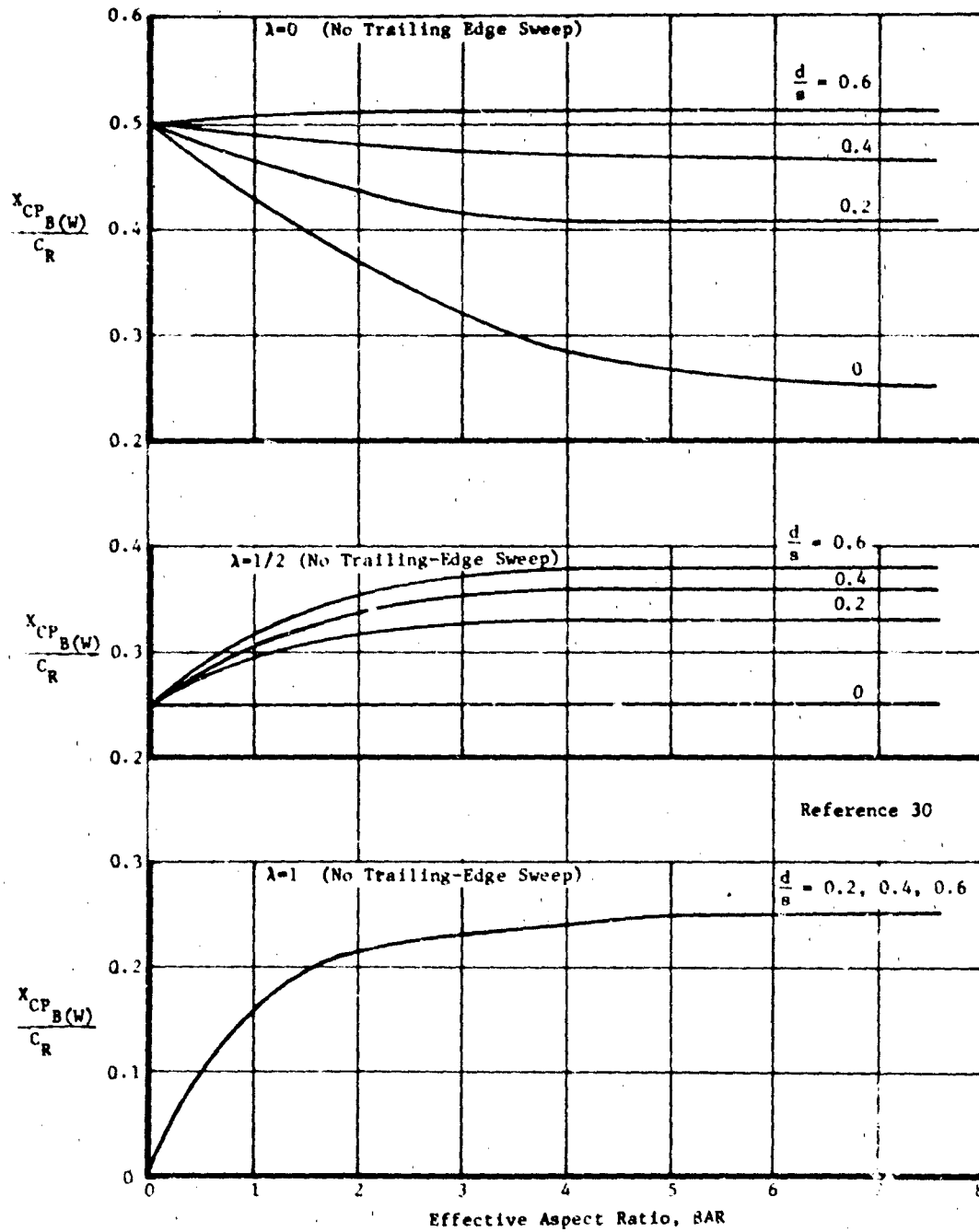


Figure 14. Curves for Determining $X_{CP_E(W)}/C_R$ at Subsonic Speeds

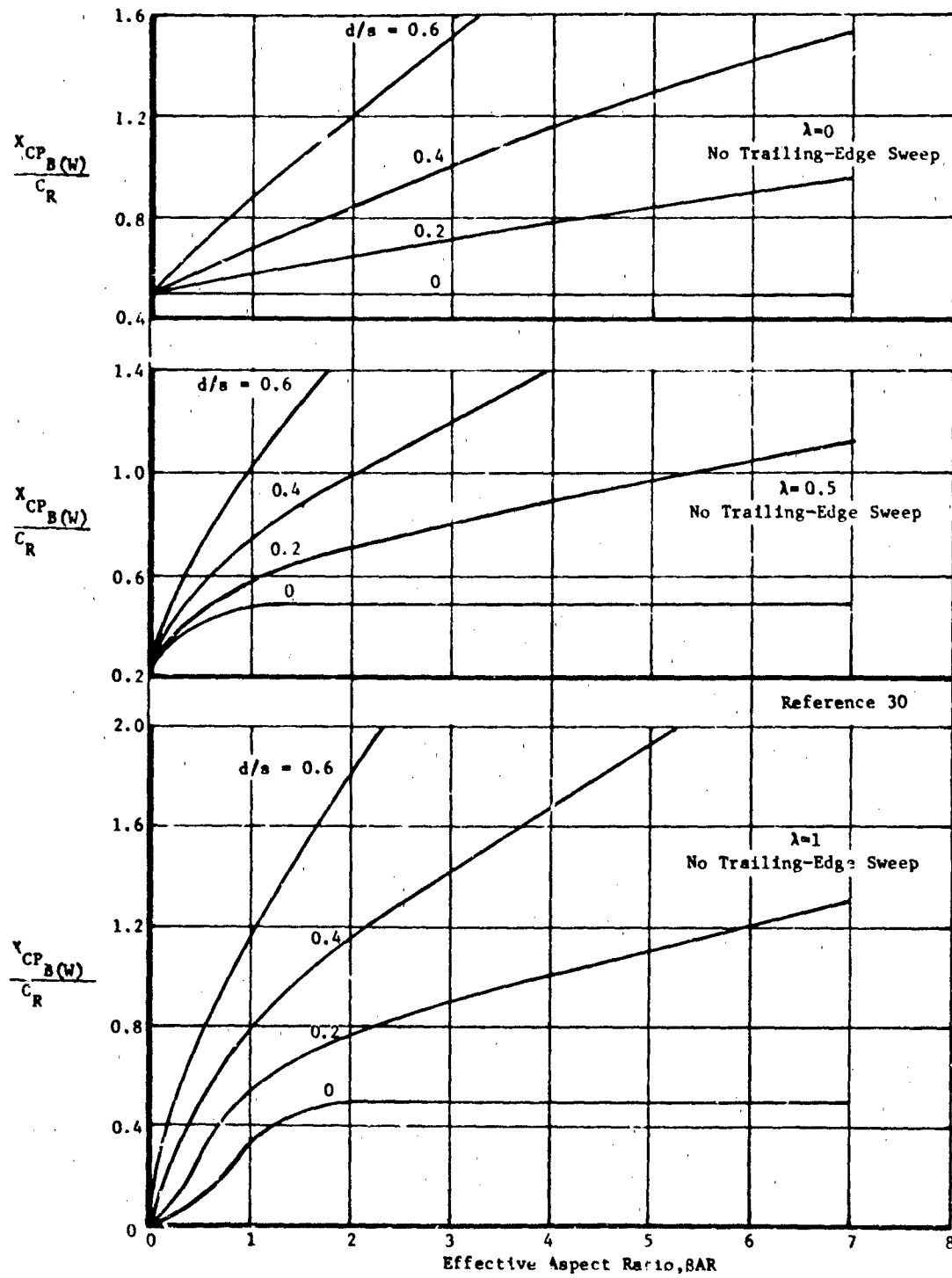


Figure 144. Curves for Determining $X_{CP_B(W)}/C_R$ with Afterbody at Supersonic Speeds

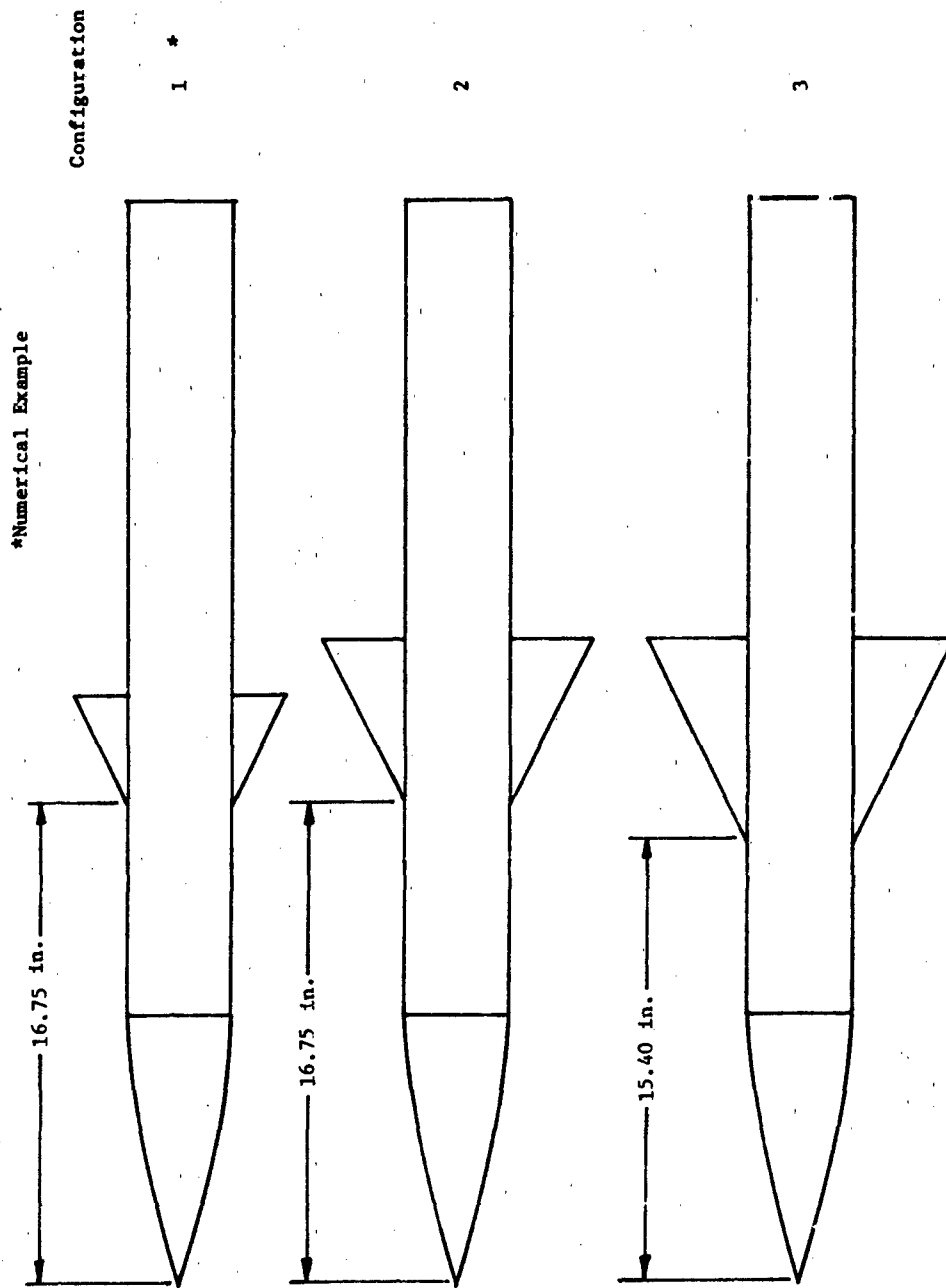


Figure 145. Configurations (Body + Wing)

Configuration Experimental
 (Ref. 34)

1 ○ □ △
 2 ○ □ △
 3 ○ □ △

Predicted
 ———
 - - -
 - - -

$M = 0.85$

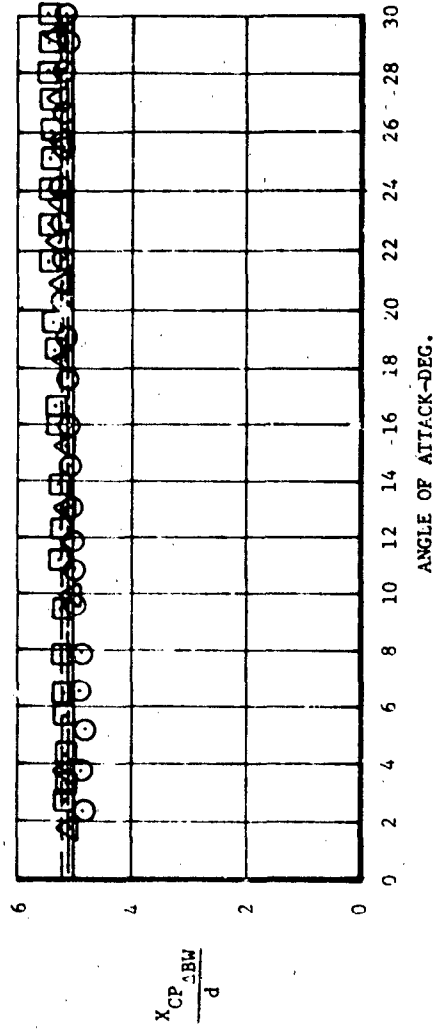


Figure 146. Comparison Between Predictions And Experimental Data, $X_{CP_{ABW}}/d$

Configuration Experimental (Ref. 34) Predicted

1 ○ □ ▽

2 — — — —

3 — — — —

M = 1.1

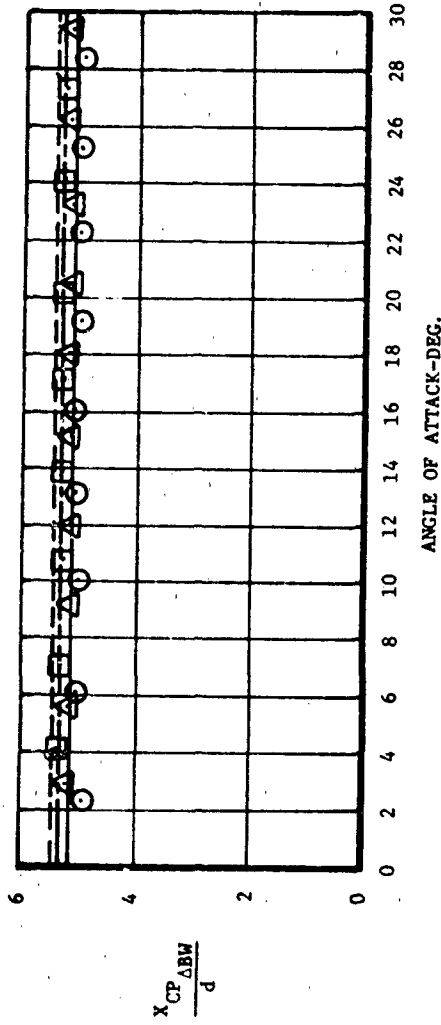


Figure 147. Comparison Between Predictions And Experimental Data, $X_{CP \Delta BW} / d$

M = 1.9

$l/d = 10.33$ $\lambda = 0$

$C_R = 4.333d$ $AR = 1.231$

$l_N/d = 2.5$ $d/s = 0.273$

○ Experimental (Ref. 35)

— Predicted

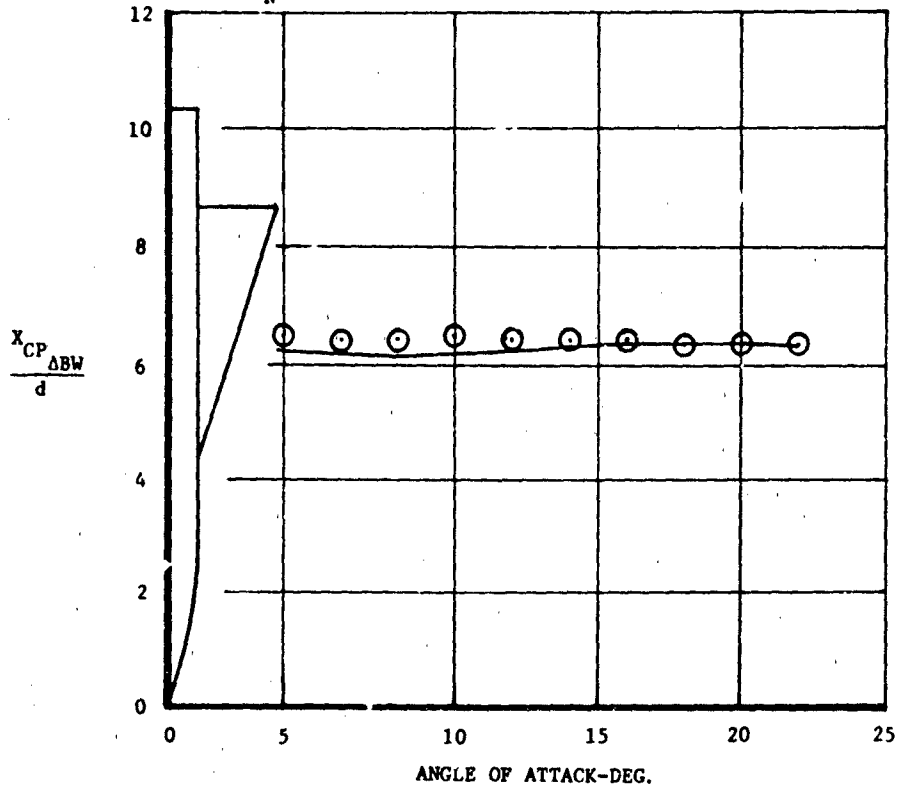


Figure 148. Comparison Between Predictions And Experimental Data, X_{CP_ABW}/d

M=2.86

$t/d = 10.333$ $\lambda = 0$
 $C_R = 4.333d$ $AR = 1.231$
 $t_N/d = 2.5$ $d/s = 0.273$

○ Experimental (Ref. 35)

— Predicted

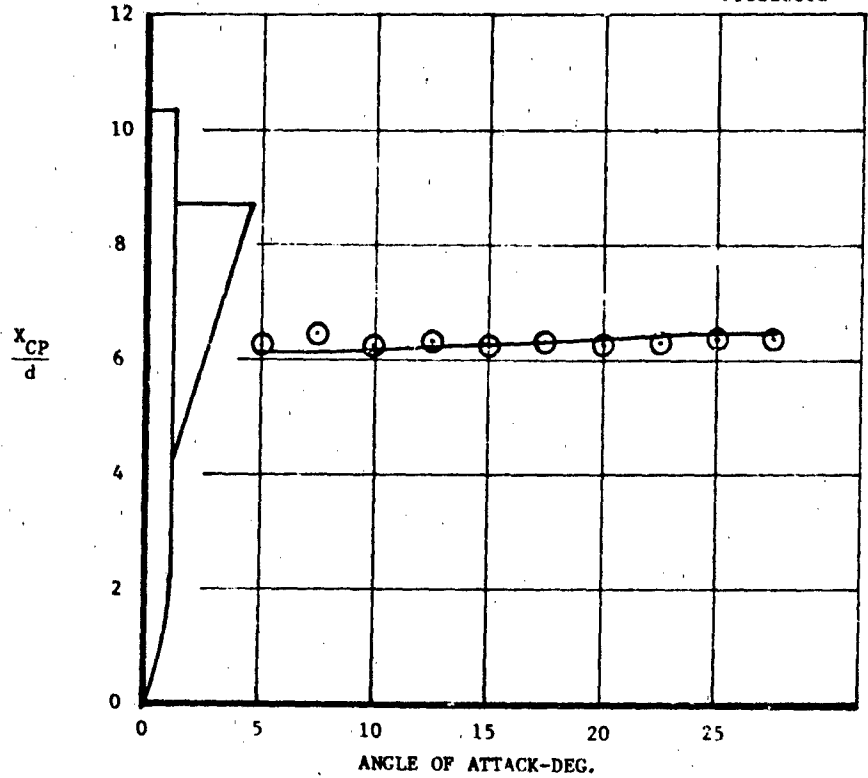


Figure 149. Comparison Between Predictions And Experimental Data, X_{CP}/d

5.4.3 Tail Incremental Normal Force Due to Wing-Vortex Interference

Summary

A method is presented for predicting $\Delta C_{N_{TW}}$, the incremental normal force produced on a tail due to wing-vortex interference. The method predicts a vortex induced angle of attack at the tail, ϵ , which can be used in conjunction with isolated tail normal force data to define $\Delta C_{N_{TW}}$. The method accounts for variations in wing-tail spacing for angles of attack to 30 degrees in the transonic regime. Supersonic capabilities, however, are limited to 24 degrees angle of attack. Insufficient data were available for correlation at angles greater than 24 degrees. Data available for correlation in both Mach number regimes represented limited variations of wing and tail geometries. However, comparisons between predicted and experimental results for geometries not used in the correlation have demonstrated applicability over a wide range of wing and tail geometries. Reasonable results have been obtained in all check cases.

Background

Tail loads for body-wing-tail configurations differ from those of body-tail configurations. The difference is due to wing-tail interference caused by vortices trailing aft in the free stream direction from a lifting wing. According to the Kutta-Joukowski relationship, the strength of these trailing vortices is related to wing lift. As the vortices stream aft they are displaced laterally and vertically by body crossflow and mutual vortex interactions. These trailing vortices alter the flowfield encountered by a tail surface and therefore change the tail loading. Assuming potential vortices ($V_t = \Gamma/r$), vortex influence on the tail diminishes with increased separation distance between the vortex core and the tail surface. To

develop a method for predicting the incremental normal force (ΔC_{NTW}) on a tail due to wing vortices it will be necessary to account for vortex strengths and variations in vortex-tail separation distances.

Method Development

Values of ΔC_{NTW} were extracted from experimental data using the following expression:

$$\Delta C_{NTW} = \frac{\text{Tail in presence of body and wing + carryover}}{(C_{NBWT} - C_{NBW})} - \frac{\text{Tail in presence of body + carryover}}{(C_{NBT} - C_{NB})} \quad (48)$$

The quantities C_{NBWT} , C_{NBW} , C_{NBT} and C_{NB} represent main balance data from configuration build-up tests. The assumption was made that the total increment in normal force, obtained using Equation 48, is applied to the tail panels only. According to Reference 30, the portion of the incremental normal force carried over to the body will generally be a small fraction of the total increment.

Data which could be applied to Equation 48 were limited. Most of the data were from a transonic body-wing-tail build-up test (Reference 34) for angles of attack to 30 degrees. Wings and tails tested were limited to aspect ratio 2.0 and taper ratio 0; however, wing d/s and wing-tail axial spacing were systematically varied as illustrated in Figure 150. Supersonic data were not available for the same configuration tested transonically. See Reference 20 for a description of the supersonic test configurations. Supersonic data were limited to 22 degrees angle of attack.

To analyze the results obtained by applying transonic test data to Equation 48, ΔC_{NTW} was equated to the normal force produced by an isolated tail at an angle attack, α . Therefore, α is analogous to the effective tail angle of attack, ϵ , induced by the presence of a trailing wing vortex.

Using the values of $\Delta C_{N_{TW}}$ extracted from the transonic test data and isolated fin data, values of ϵ were determined.

The method presented in this section was designed to predict ϵ . This angle can be used in conjunction with isolated fin data to determine $\Delta C_{N_{TW}}$. Important parameters which must be considered when attempting to predict ϵ are vortex-tail separation distance and vortex strength.

Vortex-tail separation distance is a function of configuration angle of attack and wing-tail axial separation distance (See Figure 151). A wing vortex sheds at a lateral position approximated by $\bar{y}_w = \frac{\pi b}{4}$, the position predicted by slender body theory for low aspect ratio fins. According to Reference 30 the vortices trail aft from the wing trailing edge at an angle of attack equal to the free stream angle of attack. The vertical distance h , separating the vortex center and tail is defined at the point where the vortex breaks the plane of the tail leading edge at a lateral position \bar{y}_w . In the case where \bar{y}_w is greater than the tail semispan, this position is defined as the point at which the vortex core intersects a plane perpendicular to the body center line and passing through the intersection of the tail leading edge and the tip chord. The vertical distance separating the vortex core and tail is expressed non-dimensionally as:

$$\frac{h}{d} = \frac{l_a}{d} \tan \alpha \quad (49)$$

where l_a is defined as the axial distance between the wing trailing edge and the tail leading edge.

According to the Kutta-Joukowski relationship, vortex strength is related to lift. Therefore, normal force on the wing in the presence of the body, $C_{N_{W(B)}}$, was utilized as the measure of vortex strength. Variations in vortex strength due to Mach number, planform and angle of attack can be

reflected by $C_{NW(B)}$.

The measured values of ϵ correlated well with $(\frac{d}{h})^{1/2} C_{NW(B)}$, (Figure 152a). This term incorporates the major parameters relating vortex strength and vortex-tail separation distance to vortex influence on the tail. For angles of attack up to 16 degrees, ϵ was found to vary linearly with the parameter $(\frac{d}{h})^{1/2} C_{NW(B)}$. At angles of attack of 16 to 24 degrees, values of ϵ/ϵ_{16} were found to correlate as a function of angle of attack and to be independent of Mach number. However, for angles of attack greater than 24 degrees, ϵ/ϵ_{16} became a strong function of Mach number in the transonic range. See Figure 152b. Note that ϵ_{16} in Figure 152b corresponds to the vortex induced angle of attack at $\alpha = 16$ degrees.

There were insufficient data available to determine what caused the change in induced angle of attack characteristics past $\alpha = 16$ degrees. According to Reference 2, the vortex shed from an aspect ratio 2.0 delta wing will begin to burst at the leading edge of the tail in the 14 to 16 degree angle of attack range for the various wing-tail separation distances tested. Vortex bursting can best be described as the rapid breakdown of a vortex into random turbulence. Reference 2 indicates that aspect ratio and Mach number have a strong influence on vortex bursting. Decreases in aspect ratio and supersonic Mach numbers tend to delay the bursting of vortices shed from delta wings. The data available were not systematic enough to show whether or not vortex bursting could be related to the changes in ϵ .

Insufficient supersonic data were available to conduct an analysis like that for the transonic data. Data from Reference 20 were available to produce values of ϵ which compared with those obtained from the transonic data up to 22 degrees angle of attack. No supersonic data were available to determine how ϵ varied in the 22 to 30 degree range. In the transonic case most of

this region was highly Mach number sensitive; therefore, use of Figure 152b for angles greater than 22 degrees in the supersonic regime is not advised.

Use of Method

To illustrate the use of the method for predicting $\Delta C_{N_{TW}}$, a general description of the procedure is presented, followed by a step-by-step numerical example.

- 1 Determine the distance, l_g , between the wing trailing edge and the leading edge of the tail at a lateral position defined by $\bar{Y}_w = \frac{\pi b}{4}$
- 2 Determine the vertical distance between the vortex core and the tail surface as a function of alpha using Equation (49).
- 3 Using Sections 5.1.4 and 5.2.1 calculate $C_{N_{W(B)}}$ using the calculated quantities C_{N_w} and $R_{W(B)}$
- 4 For angles of attack to 16 degrees, use the results of steps 2 and 3 to calculate $(\frac{d}{h})^{1/2} C_{N_{W(B)}}$. Note that in this step $S_{ref} = S_{base}$.
- 5 Using the results of step 4 and Figure 152a determine values of ϵ for angles of attack to 16 degrees.
- 6 For transonic Mach numbers use Figure 152b for angles of attack between 16 and 30 degrees. ($\epsilon_{16} = \epsilon$ at $\alpha = 16^\circ$)
Supersonically, use of Figure 152b to determine values of ϵ for angles of attack beyond 22 degrees is not advised.
- 7 Using Section 5.1.4, calculate C_{N_T} as a function of α .

8 Using the results of Steps 5, 6 and 7, determine values of

$$\Delta C_{N_{TWV}} \text{ where } \alpha = \epsilon.$$

Numerical Example

Calculate $\Delta C_{N_{TWV}}$ at $M = 1.1$ for the body-wing-tail configuration with the following characteristics.

Body:

$$\frac{l_N}{d} = 2.5 \qquad \frac{l}{d} = 10.0 \qquad d = 3.75 \text{ inches}$$

Wings:

$$\begin{aligned} AR &= 2.0 & \lambda &= 0.0 & \frac{d}{s} &= 0.35 \\ S_{WSP} &= 12.11 \text{ sq. in.} & s &= 3.48 \text{ inches} \\ C_R &= 6.96 \text{ inches} & \Lambda_{T.E.} &= 0^\circ \\ X_{LE} &= 15.40 \text{ inches} \end{aligned}$$

Tails:

$$\begin{aligned} AR &= 2.0 & \lambda &= 0.0 & \frac{d}{s} &= 0.4 \\ S_{TSP} &= 7.909 \text{ sq. in.} & s &= 2.812 \text{ inches} \\ C_R &= 5.625 \text{ inches} & \Lambda_{T.E.} &= 0^\circ \\ X_{L.E.} &= 31.872 \text{ inches} \end{aligned}$$

1 Calculate \bar{Y}_w

$$\bar{Y}_w = \frac{\pi s}{r} = 2.733 \text{ inches}$$

2 Calculate h/d as a function of α

$$l_s = 14.98 \text{ @ } \bar{Y}_w = 2.733$$

$$\frac{h}{d} = \frac{t}{d} \tan \alpha$$

α	h/d
0	0
4	0.279
8	0.561
12	0.849
16	1.145
20	1.454
24	1.779
28	2.124
30	2.306

3 Using Section 5.1.4 (p.91ff) and 5.2.1 (p.143ff) calculate $C_{N_{W(B)}}$

α	C_{N_W}	$R_{W(B)}$	$C_{N_{W(B)}}$
0	0	1.3	0
4	0.224	1.296	0.290
8	0.421	1.241	0.522
12	0.535	1.244	0.790
16	0.835	1.213	1.013
20	1.028	1.152	1.184
24	1.235	1.099	1.357
28	1.421	1.027	1.459
30	1.511	1.0	1.511

$S_{ref} = S_w$

- 4 Calculate $\left(\frac{d}{h}\right)^{1/2} C_{N_{W(B)}}$ where $S_{ref} = S_{base}$ using results of steps 2 and 3.

α	h/d	$C_{N_{W(B)}}$	$\left(\frac{d}{h}\right)^{1/2} C_{N_{W(B)}}$	
0	0	0	0	
4	0.279	0.318	0.602	
8	0.561	0.572	0.764	
12	0.849	0.866	0.940	$S_{ref} = S_{base}$
16	1.145	1.111	1.038	

- 5 Using the results of Step 4 and Figure 152a determine

ϵ at $\alpha = 16$ degrees.

α	$\left(\frac{d}{h}\right)^{1/2} C_{N_{W(B)}}$	ϵ
0	0	0
4	0.602	- 6.3
8	0.764	- 8.0
12	0.940	- 9.9
16	1.038	-10.4

- 6 Determine ϵ for angles of attack between 16 and 30 degrees at $M=1.1$ using Figure 152b. Utilizing the value of ϵ at $\alpha = 16$ degrees, the values of ϵ are obtained at α greater than 16 degrees.

α	c/c_{16}	z
16	1.0	-10.4
20	0.8	- 8.32
24	0.37	- 3.85
28	0.57	- 5.93
30	1.0	-10.4

7 Using Section 5.1.4 (p.91ff) calculate $C_{N_T}(\alpha)$ at $K = 1.1$

α	C_{N_T}
0	0
4	.224
8	.421
12	.635
16	.835
20	1.028
24	1.235
28	1.421
30	1.511

8 Using the results of Step 5, 6, and 7 determine $\Delta C_{N_{TWV}}$.

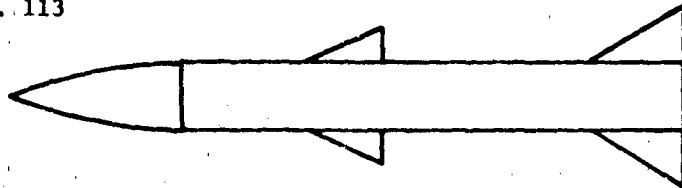
α	c	$(S_{ref} = S_T)$	$(S_{ref} = S_{base})$
		$\Delta C_{N_{TWV}} \text{ S.P.}$	$\Delta C_{N_{TWV}} \text{ D.P.}$
0	0	0	0
4	- 6.3	- 0.34	- 0.487
8	- 8.0	- 0.42	- 0.602

α	ϵ	$\Delta C_{N_{TWV}}$ S.P.	$\Delta C_{N_{TWV}}$ D.P.
12	- 9.9	- 0.52	- 0.745
16	-10.4	- 0.55	- 0.788
20	- 8.32	- 0.44	- 0.630
24	- 3.85	- 0.22	- 0.315
28	- 5.93	- 0.32	- 0.458
30	-10.4	- 0.55	- 0.788

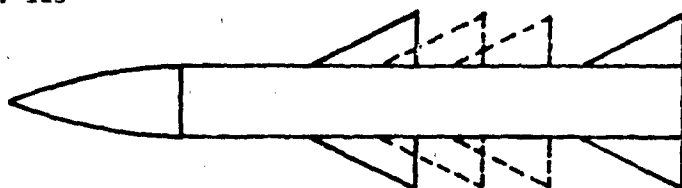
Data Comparisons

The results of the numerical example are compared with experimental data in Figure 153. The results show good agreement. Further comparisons are presented in Figures 154, 155 and 156. These latter figures compare normal force coefficients for complete body-wing-tail configurations with experimental data. These predictions required the use of several methods in conjunction with the method for predicting $\Delta C_{N_{TWV}}$. A range of Mach numbers and configuration geometries were covered and good agreement was obtained in all cases. Figures 155 and 156 represent independent comparisons since these data were not used to development the method.

Config. 113



Config. 123



Config. 133

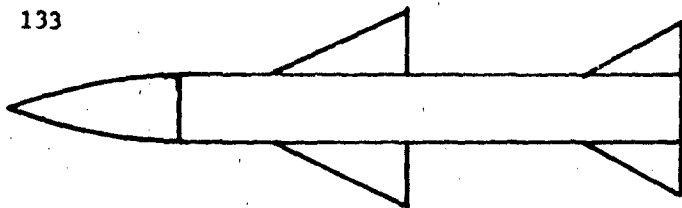
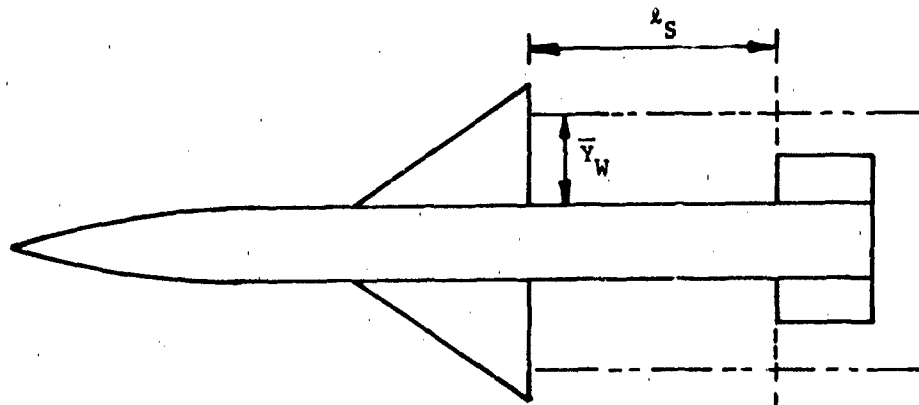
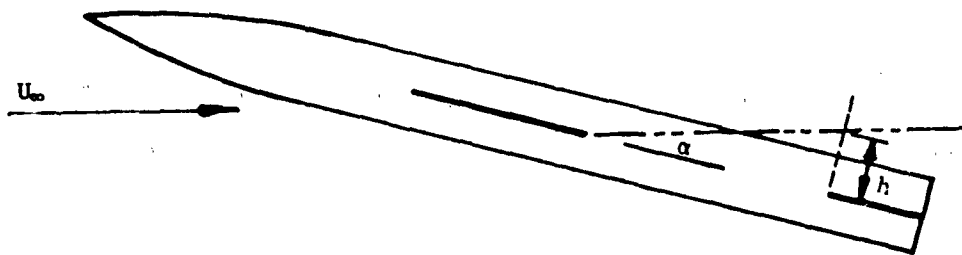


Figure 150. Transonic Wind Tunnel Test Configurations



——— Vortex Path
 - - - Tail Leading Edge Plane

Figure 151. Wing Vortex Location

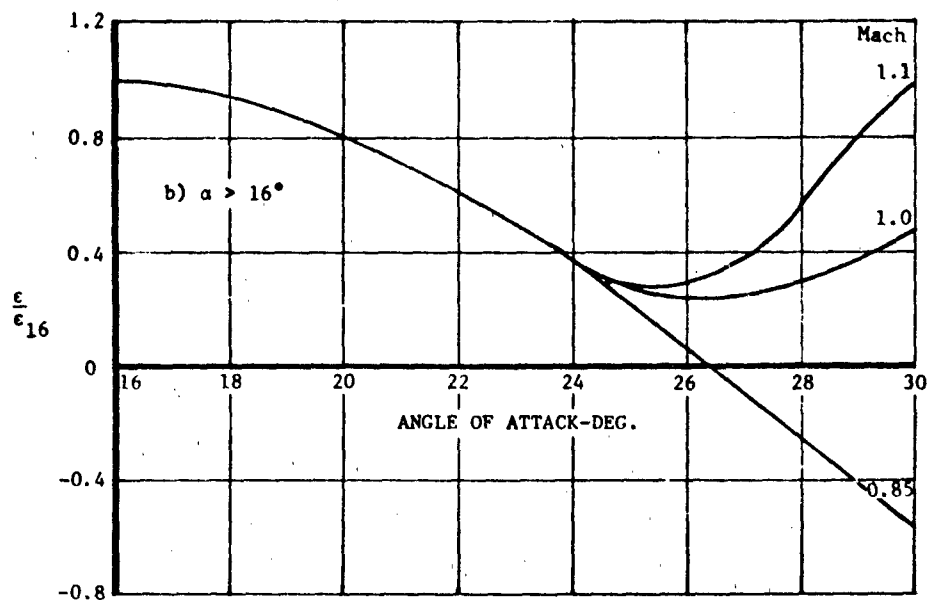
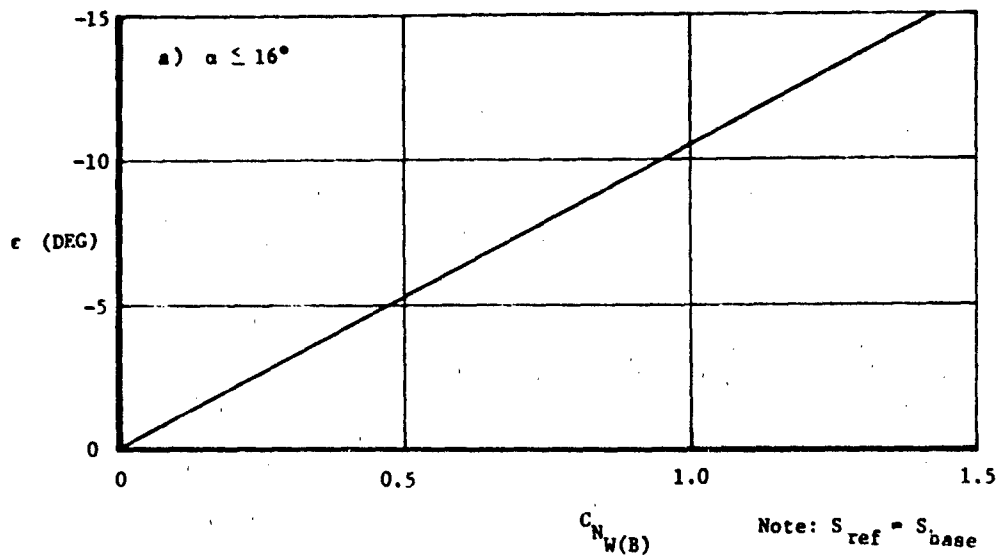


Figure 152. Wing Vortex Induced Tail Angle of Attack

○ Experimental (Ref. 34)

— Predicted

M = 1.1

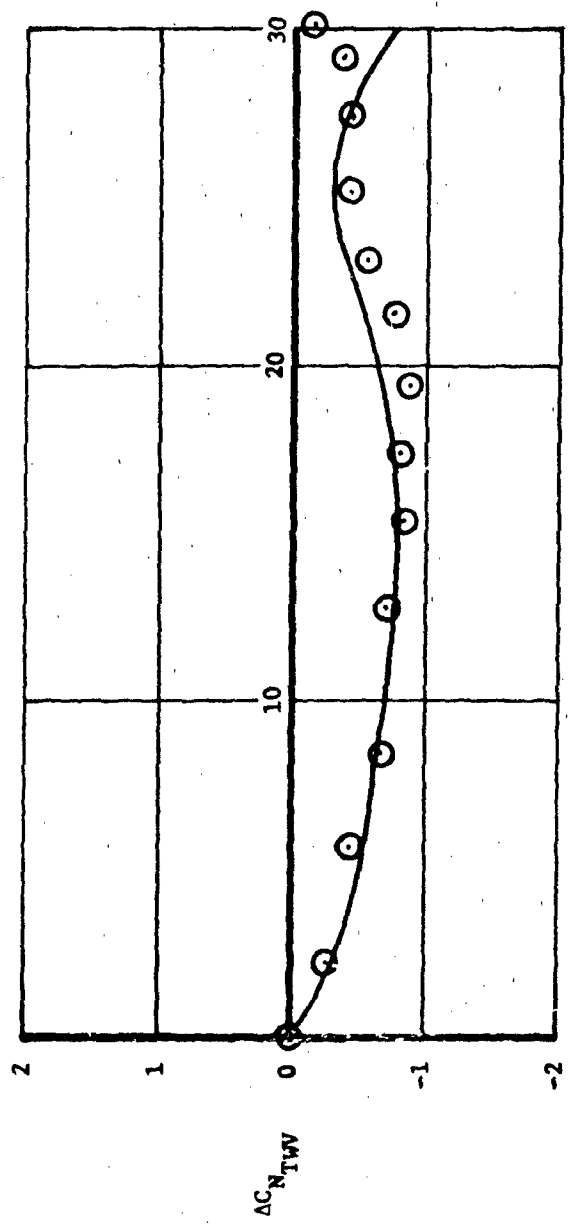
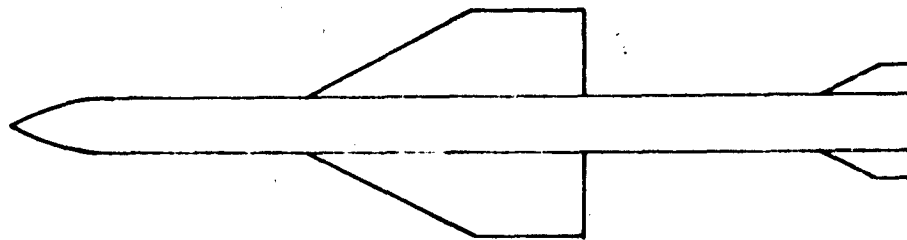


Figure 153. Comparison Between Predicted and Experimental Results, $\Delta C_{N_{TW}}$, M=1.1



○ Experimental (Ref. 20)

— Predicted

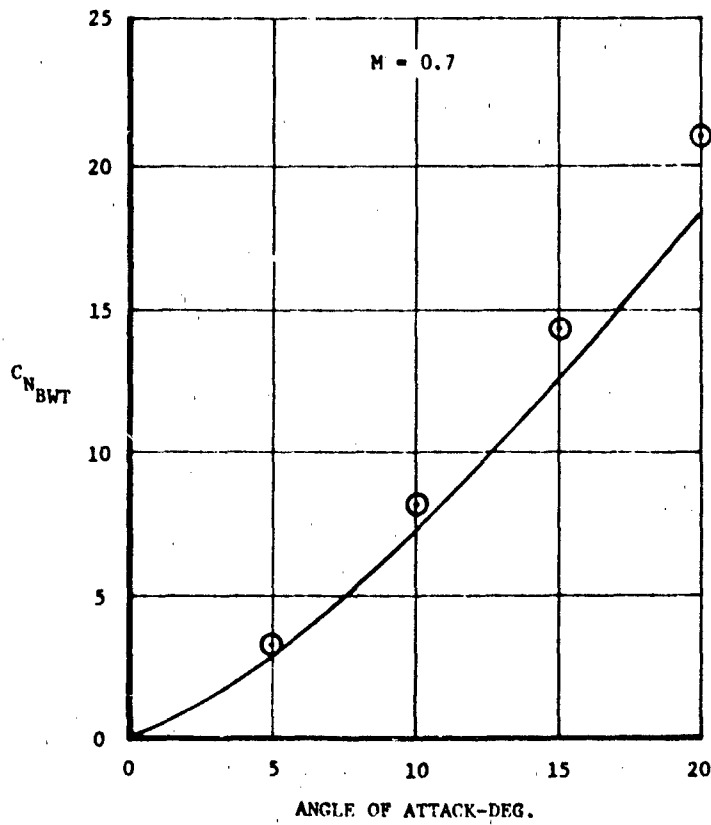


Figure 154. Comparison Between Predicted And Experimental Results, $C_{N_{BWT}}$, $M=0.7$

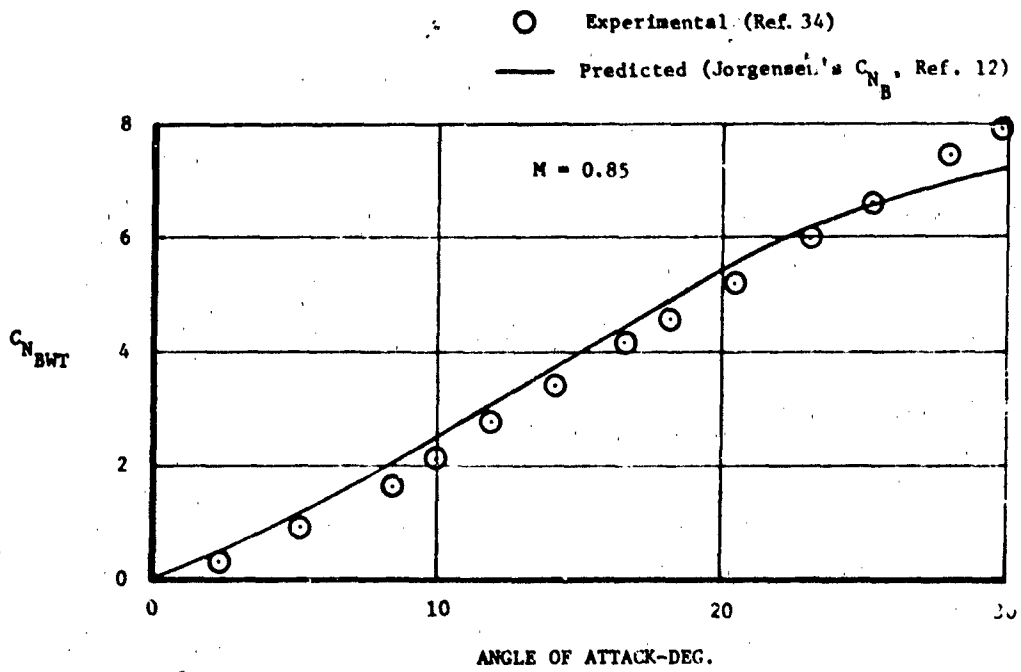
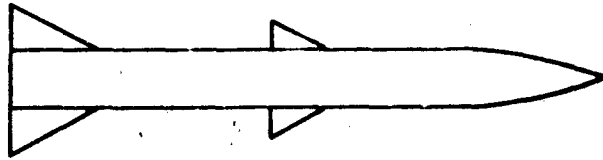
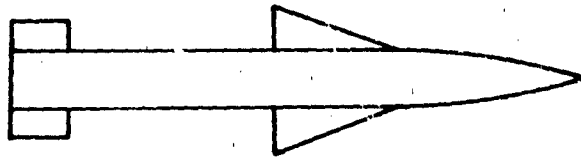


Figure 155. Comparison Between Predicted And Experimental Results, C_{NBWT} , $M=0.85$



○ Experimental (Ref. 36)
— Predicted

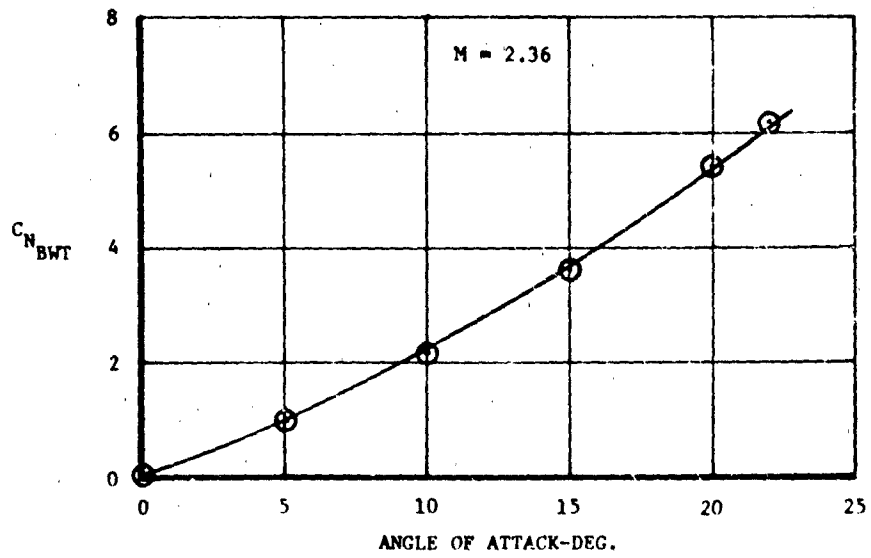


Figure 156. Comparison Between Predicted And Experimental Results, $C_{N_{BWT}}$, $M=2.36$

5.4.4 Effective Center of Pressure of the Incremental Tail Normal Force Due to Wings

Summary

A method is presented for predicting the effective center of pressure, $X_{CP\Delta TWV}$, of the incremental force produced on a tail due to the addition of wings to the body. This force results from the effective angle of attack, ϵ , induced on the tail due to the vortices emanating from the wing. The available data made it possible to identify correlations up to angles of attack of 30 degrees in transonic flow and to approximately 22 degrees in supersonic flow.

Background

The addition of wings to a body-tail configuration alters the normal force produced by the tails in the presence of a body by an amount identified as $\Delta C_{N_{TWV}}$. This incremental normal force is attributed to the effect of wing vortices on the tail. Wing vortices produce a change in the flowfield encountered by the tails. The net effect is to induce an effective angle of attack on the tails, thereby altering the tail angle of attack. Section 5.4.3 presents a method for predicting the vortex induced angle of attack, ϵ , and the corresponding value of $\Delta C_{N_{TWV}}$. To account for the effects of $\Delta C_{N_{TWV}}$ on total configuration center of pressure a method is required to predict its effective center of pressure, $X_{CP\Delta TWV}$.

Method Development

According to Reference 30, $X_{CP\Delta TWV}$ can be treated in a way that is analogous to the effect of body upwash on the tail, i.e., that both the upwash and downwash alter the loads on the tail but do not change the chordwise distribution appreciably. Therefore, $X_{CP\Delta TWV} = X_{CP_{T(B)}} = X_{CP_T}$. The

procedure for predicting X_{CP_T} is outlined in Section 5.1.4 (p. 91 ff).

The following expression was used to calculate $\frac{X_{CP_{BWT}}}{d}$.

$$\frac{X_{CP_{BWT}}}{d} = \frac{C_{N_B} \frac{X_{CP_B}}{d} + \Delta C_{N_{BW}} \frac{X_{CP_{\Delta BW}}}{d} + 2C_{N_T} R_{T(B)} \frac{S_T}{S_{ref}} \frac{X_{CP_{T(B)}}}{d} + \Delta C_{N_{TWV}} \frac{X_{CP_{\Delta TWV}}}{d} + I_{BT} \frac{X_{CP_{I(T)}}}{d}}{C_{N_B} + \Delta C_{N_{BW}} + 2C_{N_T} R_{T(B)} \frac{S_T}{S_{ref}} + \Delta C_{N_{TWV}} + I_{BT}}$$

This equation requires the use of a number of the predictive methods described earlier which will not be repeated here.

Data Comparisons

Figures 157 and 158 show comparisons of the use of the effective center of pressure, $X_{CP_{\Delta TWV}}$ for the incremental normal force of the tail due to wing vortex interference. In these cases the $X_{CP_{\Delta TWV}}$ was used in an overall prediction of the center of pressure, $X_{CP_{BWT}}$, for the complete body-wing-tail. Comparison between the predicted and experimental results are good in both transonic and supersonic regimes, at least for the two cases examined.

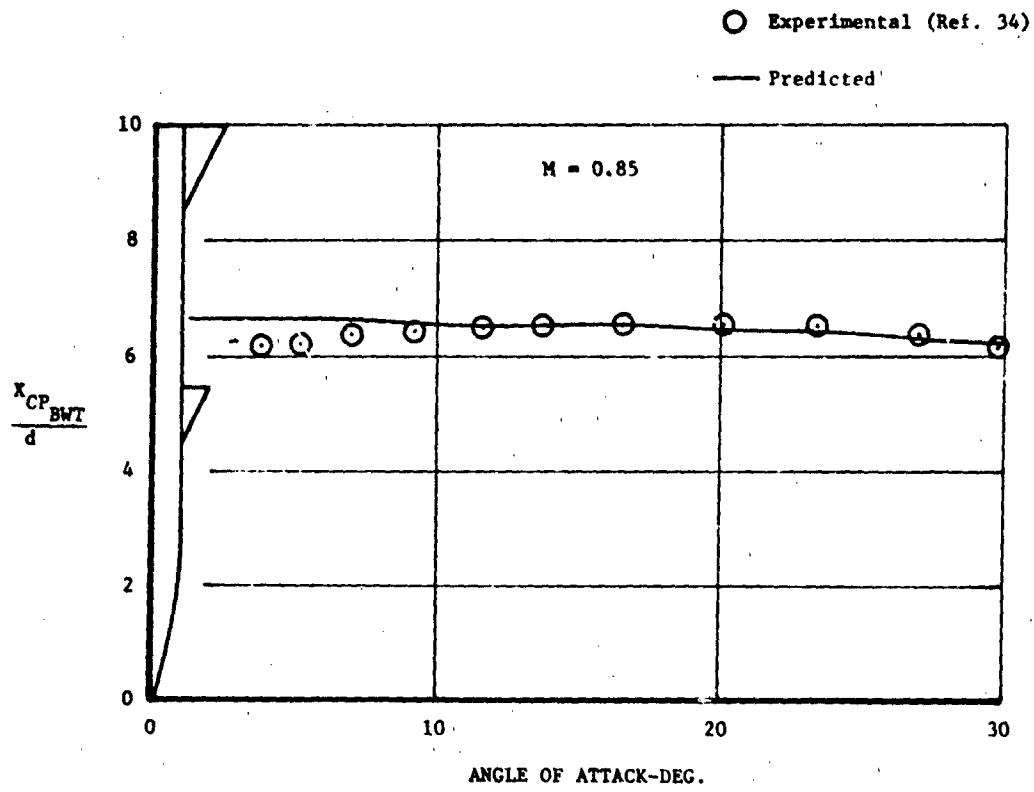


Figure 157. Comparison Between Predicted And Experimental Data, $\frac{X_{CP_{BWT}}}{d}$, $M=0.85$

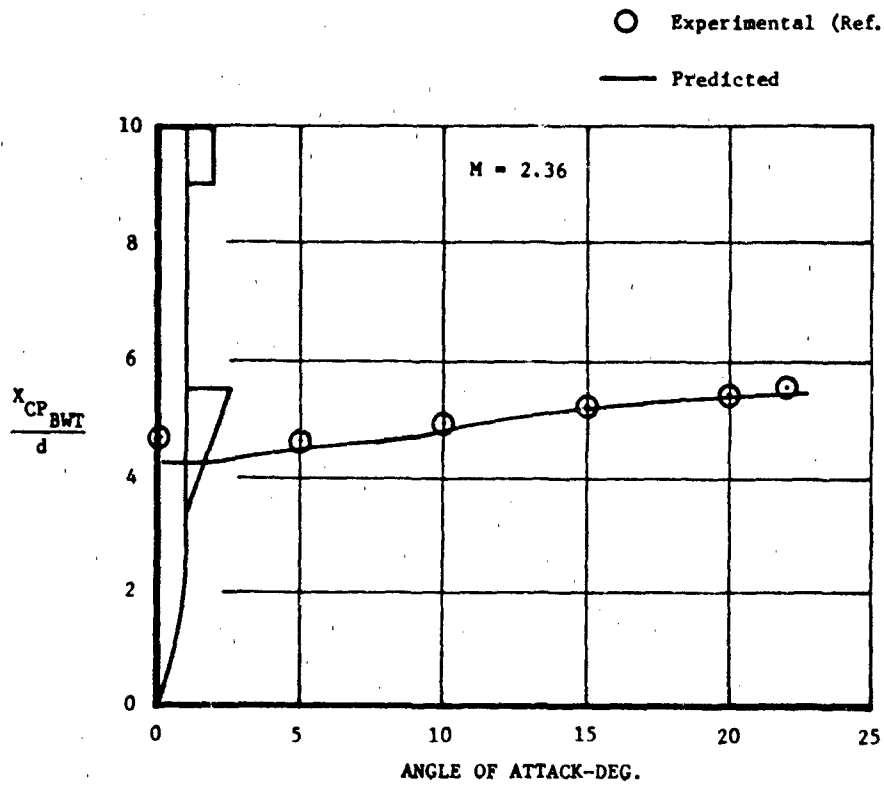


Figure 158. Comparison Between Predicted and Experimental Data, $\frac{X_{CP_{BWT}}}{d}$, M=2.36

5.5 Thrust Vector Control Effects

5.5.1 Incremental Normal Force Due to Plume Effects

Summary

A method is presented for estimating $\Delta C_{N_{BP}}$, the incremental normal force coefficient on a slender tangent ogive-cylinder body due to a flowing main jet ($\Delta C_{N_{BP}}$). This method covers angles of attack to 180 degrees and a Mach number range of 0.60 to 2.20.

Background

The addition of a flowing jet to a body produces a change in the body normal force coefficient due to impingement of the jet plume on the body and the effects of the jet on the flow field about the body. The magnitude of this incremental normal force coefficient ($\Delta C_{N_{BP}}$) is dependent on the following: Mach number, angle of attack, and the strength of the jet relative to the free stream (defined here as the momentum ratio M_R). No previously derived method was found which predicted the effects of a flowing main jet across the desired angle of attack range. The present work describes the formulation of a method for predicting $\Delta C_{N_{BP}}$ up to $\alpha = 180^\circ$ at Mach numbers from 0.60 to 2.20. Data from tests on a particular USAF missile design form the basis for this analysis.

The incremental normal force coefficient on a body due to a jet plume is defined as:

$$\Delta C_{N_{BP}} = C_{N_{BP}} - C_{NB}$$

Test data were available at Mach numbers 0.60 to 2.20 and angles of attack from 15 to 165 degrees. Jet momentum ratios tested were as follows:

Mach	M_R
0.60	60.1
0.85	30.1
1.20	19.1
1.80	73.6
2.20	49.3

Jet-on data were available only for a body-strake-tail configuration, with jet-off data obtained on body alone and body-strake-tail configurations. It would obviously have been desirable to have tested the body alone with jet-on. Since this is not available it was necessary to derive body alone jet-on normal force coefficients ($C_{N_{BP}}$) from available data. The available data consist of parameters measured by integrating surfaces pressures, including normal force coefficients for the body in the presence of strakes and tails, jet-on and jet-off ($C_{N_{B(ST)P}}$ and $C_{N_{B(ST)}}$); body alone normal force coefficient, jet-off (C_{N_B}); tail normal force coefficient, jet-on and jet-off ($C_{N_{TP}}$ and C_{N_T}); and strake normal force coefficient, jet-on and jet-off ($C_{N_{SP}}$ and C_{N_S}). The procedure used was as follows:

- 1 Compute the incremental normal force due to presence of strake and tail with the jet off.

$$I_{B(ST)} = C_{N_{B(ST)}} - C_{N_B}$$

- 2 Assuming that the increment in normal force, due to the strake plus tail, jet-on, is proportional to the increment in normal force coefficient, jet-off, compute jet-on strake plus tail increment:

$$I_{B(ST)P} = I_{B(ST)} \left(\frac{C_{N_{SP}} + C_{N_{TP}}}{C_{N_S} + C_{N_T}} \right)$$

- 3 Subtract the calculated jet-on increment from the measured normal force coefficient of the body in the presence of strakes and tails with jet on:

$$C_{N_{BP}} = C_{N_{B(ST)P}} - I_{B(ST)P}$$

- 4 Compute

$$\Delta C_{N_{BP}} = C_{N_{BP}} - C_{N_B}$$

Method Development

Figure 159 shows the general form of a curve of $\Delta C_{N_{BP}}$ versus angle of attack. This curve shows that there is no significant jet effect at angles of attack less than 40 degrees. The term $\Delta C_{N_{BP}}$ reaches a peak about $\alpha = 70^\circ$, then decreases to a minimum value at $\alpha = 90^\circ$. Jet effects increase again as alpha approaches 145° , then decrease to a value of zero at $\alpha = 180^\circ$. The value and sign of $\Delta C_{N_{BP}}$ at $\alpha = 70^\circ$ and $\alpha = 145^\circ$ are Mach number dependent. A power series formulation incorporating the effects of angle of attack, Mach number, and momentum ratio was the approach selected to fit a general curve to the data. The term $\Delta C_{N_{BP}}$ was considered to be linearly dependent on jet momentum ratio for a given Mach number.

Power series for the variation of ΔC_{NBP} with α , in which values of zero occur at $\alpha = 40^\circ, 90^\circ$ and 180° and values of 1.0 occur at 70° and 145° were then constructed. The form of the equation is:

$$\Delta C_{NBP} = M_R * K * A$$

where

$$M_R = \text{Jet momentum ratio} = q_j / q_\infty$$

$$K = \text{Amplification factor} = K(M)$$

$$= K_{70} \text{ for } 40^\circ \leq \alpha \leq 90^\circ$$

$$= K_{145} \text{ for } 90^\circ < \alpha < 180^\circ$$

$$A = \text{Power series defining curve form}$$

The complexity of the variation with alpha necessitates dividing the angle of attack range into three intervals: $0 \leq \alpha \leq 40^\circ$, $40^\circ \leq \alpha \leq 90^\circ$ and $90^\circ \leq \alpha \leq 180^\circ$. Parameters in each range are as follows:

$$0 \leq \alpha \leq 40^\circ$$

$$A = 0$$

$$\Delta C_{NBP} = 0$$

$$40^\circ \leq \alpha \leq 90^\circ$$

$$K = K_{70}$$

$$A = 23.4450 - 89.88886\alpha + 121.1061\alpha^2 - 66.9524\alpha^3 + 12.8829\alpha^4 \quad (\alpha \text{ radians})$$

$$90^\circ \leq \alpha \leq 180^\circ$$

$$K = K_{145}$$

$$A = 45.6283 - 82.7136\alpha + 53.6644\alpha^2 - 14.6512\alpha^3 + 12.8829\alpha^4 \quad (\alpha \text{ radians})$$

The quantity $\Delta C_{N_{BP}}/M_R$, as determined from the test data, was non-dimensionalized by the value at $\alpha = 70^\circ$ in the range of alpha between 40 and 90 degrees. In the alpha range from 90 to 180 degrees, the value at $\alpha = 145^\circ$ was used to non-dimensionalize $\Delta C_{N_{BP}}/M_R$. Figure 160 shows the curve which was faired through the non-dimensionalized test data. The data for all Mach numbers is combined in arriving at Figure 160. The Mach number effect is obtained by plotting the values of $(\Delta C_{N_{BP}}/M_R)$ at $\alpha = 70^\circ, 145^\circ$ and then fairing curves through these data to obtain Figure 161.

It should be noted that available test data incorporated only one jet momentum ratio at each test Mach number. While these represent realistic values for the configuration tested, estimates obtained for a missile with greatly different jet momentum ratios should be used with caution. Also of importance is the fact that the effects of nozzle exit diameter on $\Delta C_{N_{BP}}$ cannot be determined from existing data. The ratio of nozzle exit diameter to body diameter $\left(\frac{d_{noz}}{d_{ref}}\right)$ for the configuration tested was 0.87. It is reasonable to assume that this analysis is valid for cases in which the nozzle exit diameter approximates that of the body.

Use of Method

The method is utilized as follows:

Given: a tangent ogive-cylinder body with a main jet momentum ratio, M_R , at the desired Mach number.

Proceed thus:

- 1 Determine K_{70} and K_{145} for the appropriate Mach number (Figure 161)
- 2 Look up values of A for the desired angles of attack (Figure 160)
- 3 Compute

$$\Delta C_{N_{BP}} = M_R * K * A$$

$$\text{where } K = K_{70} \text{ for } 40^\circ \leq \alpha \leq 90^\circ$$

$$= K_{145} \text{ for } 90^\circ \leq \alpha \leq 180^\circ$$

Numerical Example

Given the following parameters, compute $\Delta C_{N_{BP}}$ for a slender tangent ogive cylinder body at Mach 0.85:

$$\frac{d_{noz}}{d_{ref}} = 0.90$$

$$M_R = 30.1 \text{ @ Mach } 0.85$$

1 From Figure 161: $K_{70} = 0.074$

$$K_{145} = 0.044$$

- 2-3 Utilizing Figure 160 to obtain values of A the following table is generated.

α	A	M_R	K	$\Delta C_{N_{BP}} = M_R * K * A$	
0	0.	30.1	0.074	0.	
40	0.	↓	↓	0.	
60	0.73			1.63	
70	1.00			2.23	
80	0.75			1.67	
90	0.			0.	
100	0.07			0.044	0.09
120	0.62			0.82	
140	0.99			1.31	
145	1.00			1.32	
160	0.76			1.01	
180	0.			0.	

Data Comparisons

In Figure 162 method results are plotted along with those data used in formulating the method. It can be seen that the curve fitting approach used yields a good approximation of $\Delta C_{N_{BP}}$ across the Mach range. A lack of independent body alone jet-on data at high angles of attack makes further detailed comparisons impossible at this time. Independent data presented in Reference 37 for a body plus tail configuration tend to support this analysis in that no jet effects are evident at angles of attack less than about 40 degrees, the magnitude of $\Delta C_{N_{BP}}$ is small relative to total C_N , and the value of $\Delta C_{N_{BP}}$ decreases with increasing Mach number.

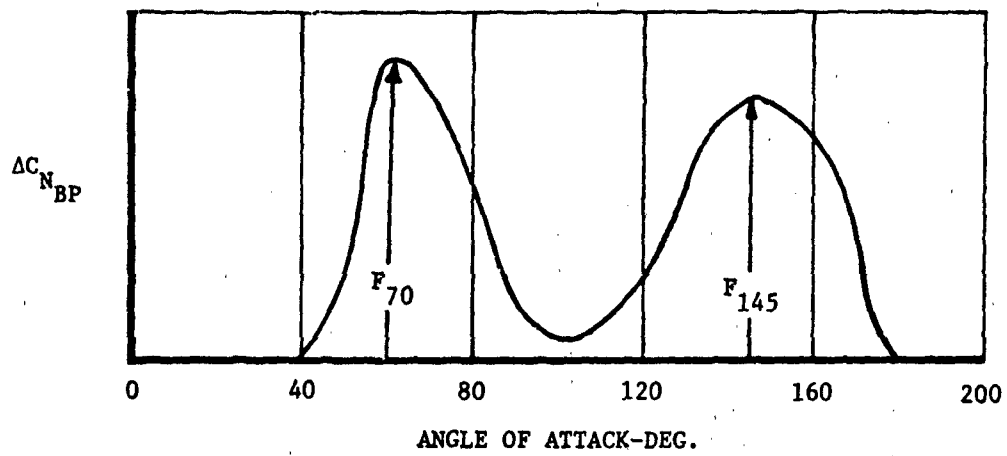


Figure 159: General Curve Form, ΔC_{NBP}

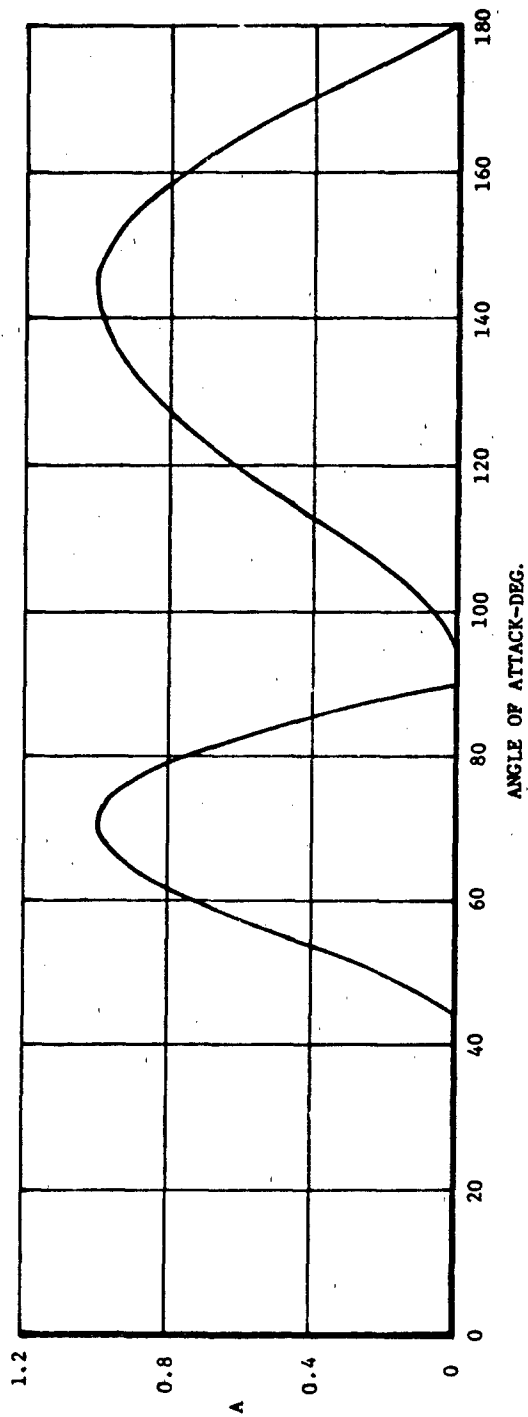


Figure 160. Power Series A for Calculating $\Delta C_{H_{EP}}$

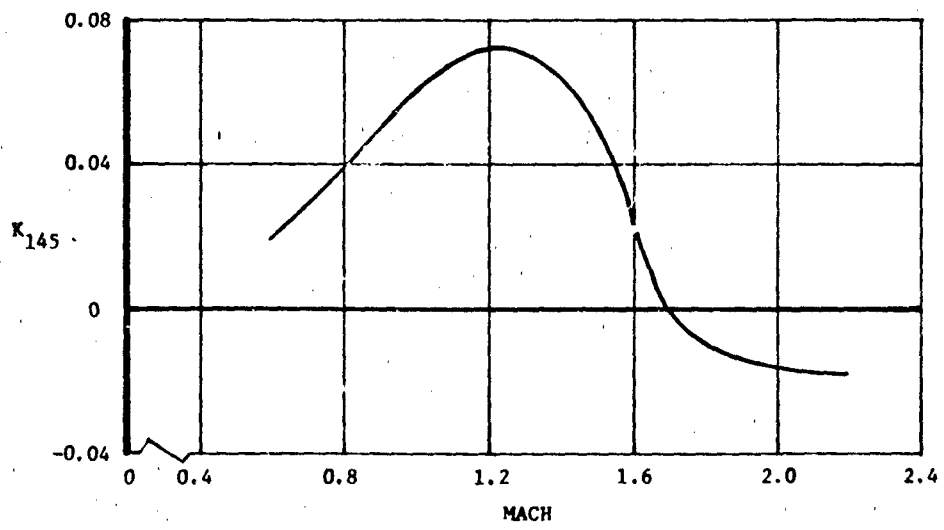
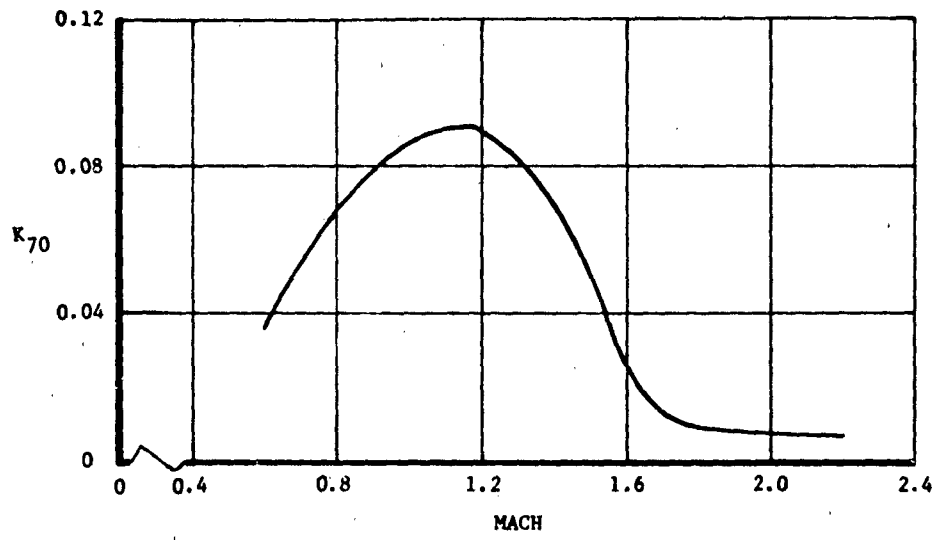
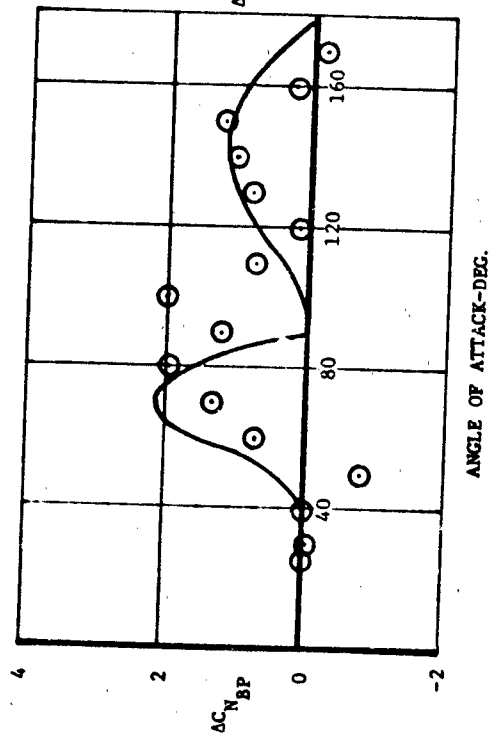


Figure 161. Amplification Factors for Calculating $\Delta C_{N_{BP}}$

a) Mach 0.60
 ○ Test Data
 — Estimate



b) Mach 0.85
 □ Test Data
 — Estimate

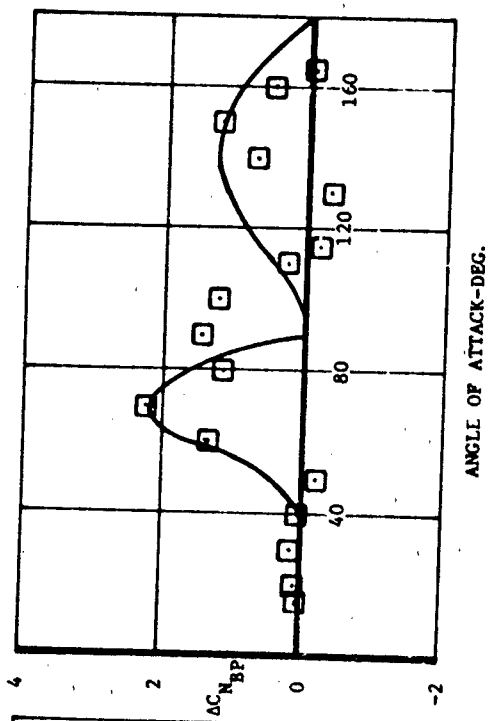
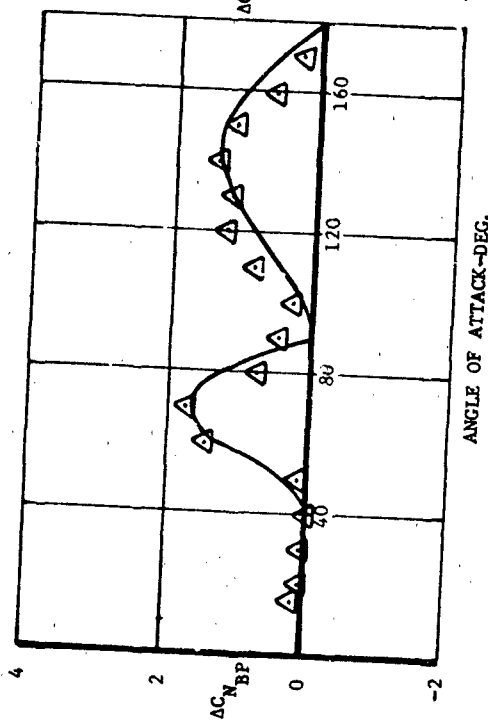


Figure 162. Comparison Between Predictions And Experimental Data, AC_{NBP}

c) Mach 1.20
 \triangle Test Data
 — Estimate



d) Mach 1.80
 \diamond Test Data
 — Estimate

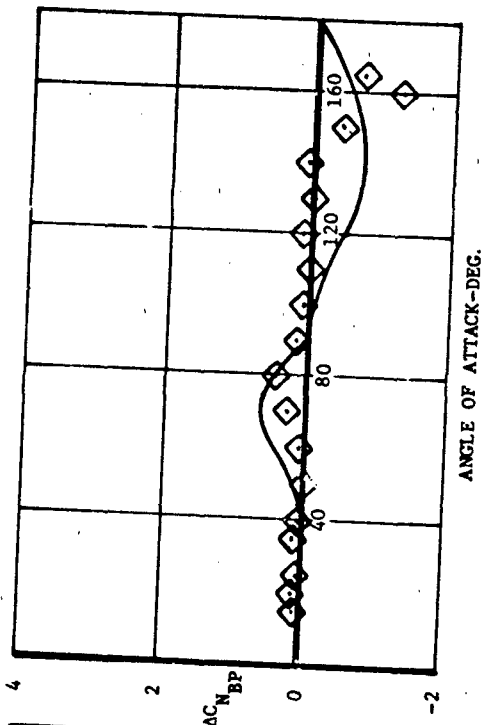


Figure 162 (Cont.). Comparison Between Predictions And Experimental Data, AC_{NBP}

e) Mach 2.2

▽ Test Data

— Estimate

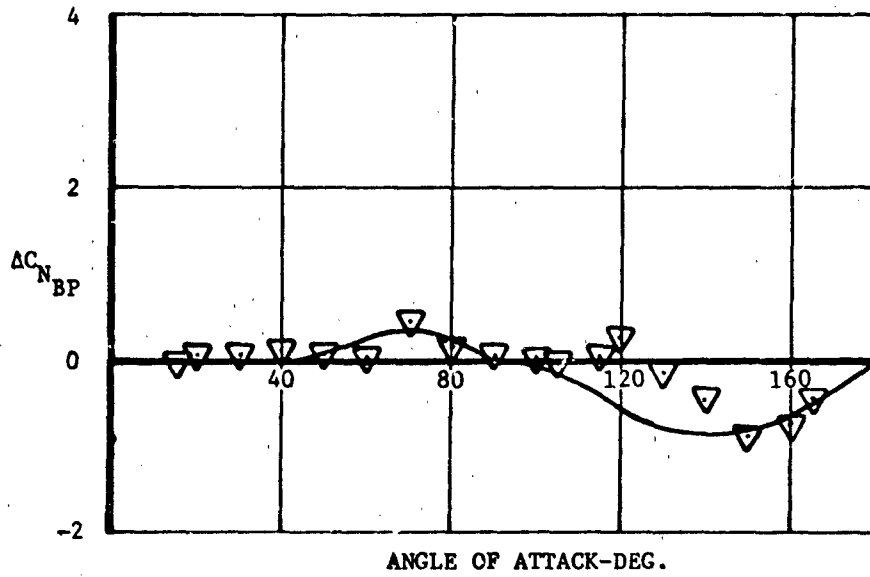


Figure 162 (Cont.). Comparisons Between Predictions And Experimental Data, $\Delta C_{N_{BP}}$

5.5.2 Effective Center of Pressure for Incremental Body Normal Force Due to Plume Effects

Summary

A method is presented for estimating $X_{CP_{BP}}$, the effective center of pressure of the incremental force on a slender tangent ogive-cylinder body due to a flowing main jet. This method applies for angles of attack to 180 degrees and a Mach number range of 0.60 to 2.20.

Background

The addition of a flowing main jet to a body produces a change in the body center of pressure location due to plume impingement on the body and plume interaction with the flowfield about the body. No methods were found to predict the center of pressure location over the desired high angle of attack range. The present work describes the formulation of such a method. The data forming the basis for this correlation were obtained from tests on a particular USAF missile design.

Test data were available at Mach numbers 0.60 to 2.20 and angles of attack from 15 to 165 degrees. Jet momentum ratios tested were as follows:

<u>Mach</u>	<u>M_R</u>
0.60	60.1
0.85	30.1
1.20	19.1
1.80	73.6
2.20	49.3

For the configuration tested, $\frac{l_N}{d} = 2.5$ and $\frac{l}{d} = 14.45$.

Jet-on data were available only for a body-strake-tail configuration, with jet-off data obtained on body alone and body-strake-tail configurations. It was therefore necessary to derive $X_{CP_{BP}}$ using available

data. Specifically the quantities obtained experimentally were measured by integrating pressure distributions and consisted of normal force coefficients and centers of pressure of the body alone (jet-off), of the strakes and tails, and the body in the presence of the strakes and tails (jet-on and jet-off). The derivation of jet-on values of the incremental C_N on the body due to strake and tail carryover ($I_{B(ST)P}$) is described in the method presented for determining ΔC_{NBP} . The procedure developed to calculate X_{CPBP} is as follows.

Method Development

Figure 163 shows the basic data used in formulating the jet-on center of pressure prediction method. Due to a lack of test data in which body fineness ratio (l/d) was varied, it was decided to base the prediction method on jet-off values of X_{CPB} which may be calculated using the method of Section 5.1.2.

Examination of the data in Figure 163 reveals that the flowing main jet has essentially no effect on the body center of pressure location at angles of attack less than about 100 degrees at all Mach numbers. At $M=1.2$ and below, X_{CPBP} falls about 0.5 calibers forward of X_{CPB} for $100^\circ \leq \alpha \leq 160^\circ$. At supersonic Mach numbers, X_{CPB} and X_{CPBP} are essentially equal up to $\alpha = 120^\circ$, then are symmetrical about the value at $\alpha = 120^\circ$.

The method developed simply approximates the curves of Figure 163 as described above. For Mach numbers less than or equal to 1.2:

$$\begin{aligned}
 0^\circ \leq \alpha \leq 100^\circ: & \quad X_{CPBP}/d = X_{CPB}/d \\
 110^\circ \leq \alpha \leq 180^\circ: & \quad X_{CPBP}/d = (X_{CPB}/d) - 0.50 \\
 100^\circ < \alpha < 110^\circ: & \quad \text{Linearly interpolate between values at } \alpha = 100^\circ \text{ and } \\
 & \quad 110^\circ
 \end{aligned}$$

For Mach numbers greater than 1.2:

$$0^\circ \leq \alpha \leq 120^\circ: X_{CPBP}/d = X_{CPB}/d$$

$$120^\circ \leq \alpha \leq 180^\circ: \frac{X_{CPBP}}{d} = \frac{X_{CPB}}{d} - 2 \left(\frac{X_{CPB}}{d} - K_1 \right)$$

$$= 2 K_1 - \frac{X_{CPB}}{d}$$

where K_1 = value of $\frac{X_{CPB}}{d}$ at $\alpha = 120^\circ$

Use of Method

The method is used as follows:

Given a slender tangent ogive-cylinder body with a flowing main jet.

The jet momentum ratio M_R is of the same order of magnitude as those of the test data previously cited.

Proceed thusly:

1 Determine $\frac{X_{CPB}}{d}$ for the Mach and alpha range desired from test data or via the method of Section 5.1.2 (p. 61 ff).

2 If $M \leq 1.2$, $\frac{X_{CPBP}}{d} = \frac{X_{CPB}}{d}$ for $0 \leq \alpha \leq 100^\circ$

If $M > 1.2$, $\frac{X_{CPBP}}{d} = \frac{X_{CPB}}{d}$ for $0 \leq \alpha \leq 120^\circ$

3 If $M \leq 1.2$, $\frac{X_{CPBP}}{d} = \frac{X_{CPB}}{d} - 0.50$ for $110^\circ \leq \alpha \leq 180^\circ$

If $M > 1.2$, $\frac{X_{CPBP}}{d} = 2 K_1 - \frac{X_{CPB}}{d}$ for $120^\circ \leq \alpha \leq 180^\circ$

where K_1 = value of $\frac{X_{CPB}}{d}$ @ $\alpha = 120^\circ$

Numerical Example

Determine X_{CPBP}/d for a slender tangent ogive-cylinder body at Mach 0.85 and Mach 1.8; $M_R = 30.1$ at Mach 0.85, $M_R = 73.6$ at Mach 1.8.

Mach 0.85:

α (\sim deg)	(Step 1)	(Step 2)	(Step 3)
	$\frac{X_{CPB}}{d}$	$\frac{X_{CPBP}}{d} = \frac{X_{CPB}}{d}$	$\frac{X_{CPBP}}{d} = \frac{X_{CPB}}{d} - 0.50$
	(test data)		
20	3.84	3.84	
40	5.37	5.37	
60	6.30	6.30	
80	7.32	7.32	
100	8.20	8.20	
110	8.31		7.81
120	8.50		8.00
140	9.61		9.11
160	10.89		10.49

Mach 1.80:

α (\sim deg)	(Step 1)	(Step 2)	(Step 3)
	$\frac{X_{CPB}}{d}$	$\frac{X_{CPBP}}{d} = \frac{X_{CPB}}{d}$	$\frac{X_{CPBP}}{d} = 2 K_1 - \frac{X_{CPB}}{d}$
20	6.32	6.32	
40	7.15	7.15	
60	7.43	7.43	
80	7.64	7.64	
100	7.84	7.84	
120	8.02	8.02	8.02
140	8.16		7.88
160	9.25		6.79

Data Comparisons

In Figure 164, method results are compared with the jet-on data used in formulating the method. It can be seen that this relatively simple method yields a good approximation of X_{CPBP}/d across Mach number and angle of attack regime. A lack of independent body alone jet-on data at the necessary high angles of attack makes further detailed comparisons impossible at this time. Independent data presented in Reference 37 for a body plus tail configuration indicate trends similar to those noted in this analysis, i.e., little jet affect on X_{CPB} at angles of attack less than 100 degrees, then a forward shift in CP location with increasing angle of attack.

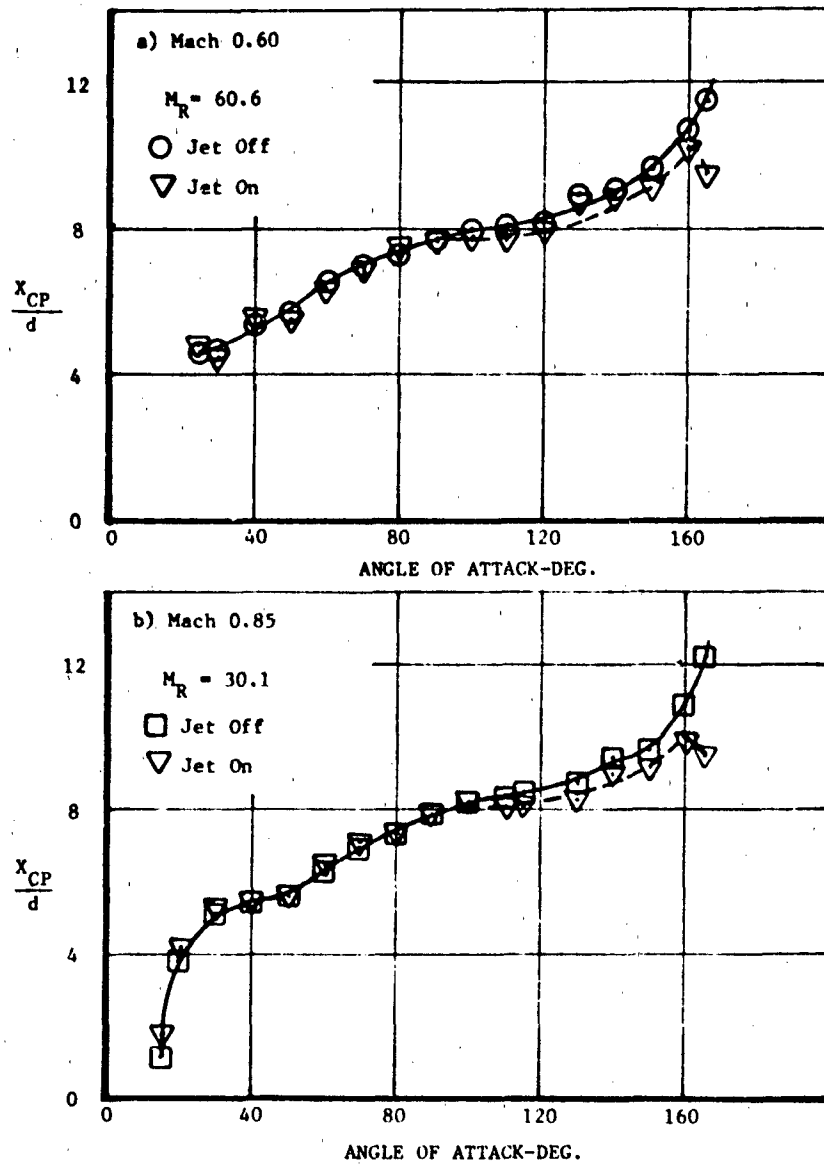


Figure 163. Comparison Of Body Alone $\frac{X_{CP}}{d}$ (Jet On Versus Jet Off)

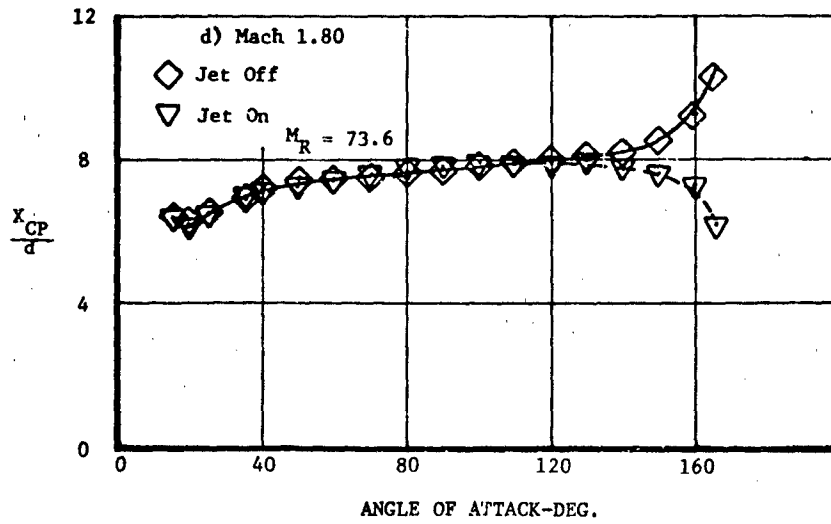
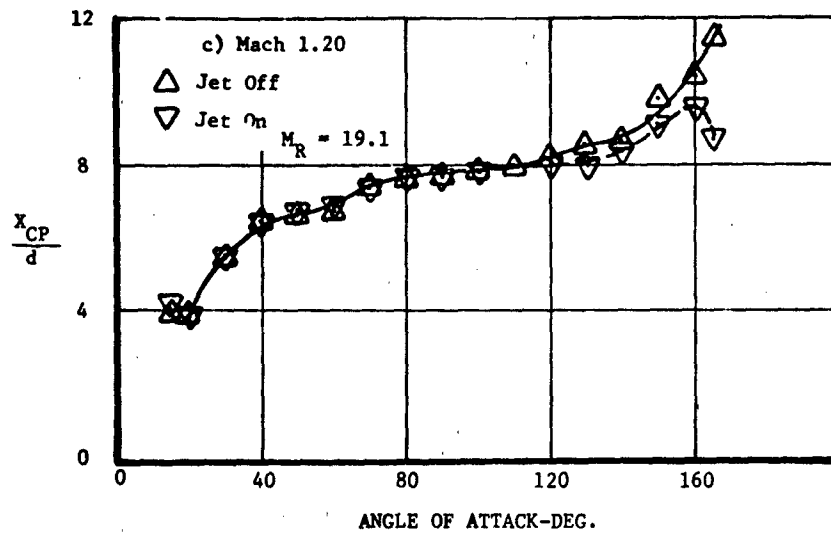


Figure 163 (Cont.). Comparison Of Body Alone $\frac{X_{CP}}{d}$ (Jet On Versus Jet Off)

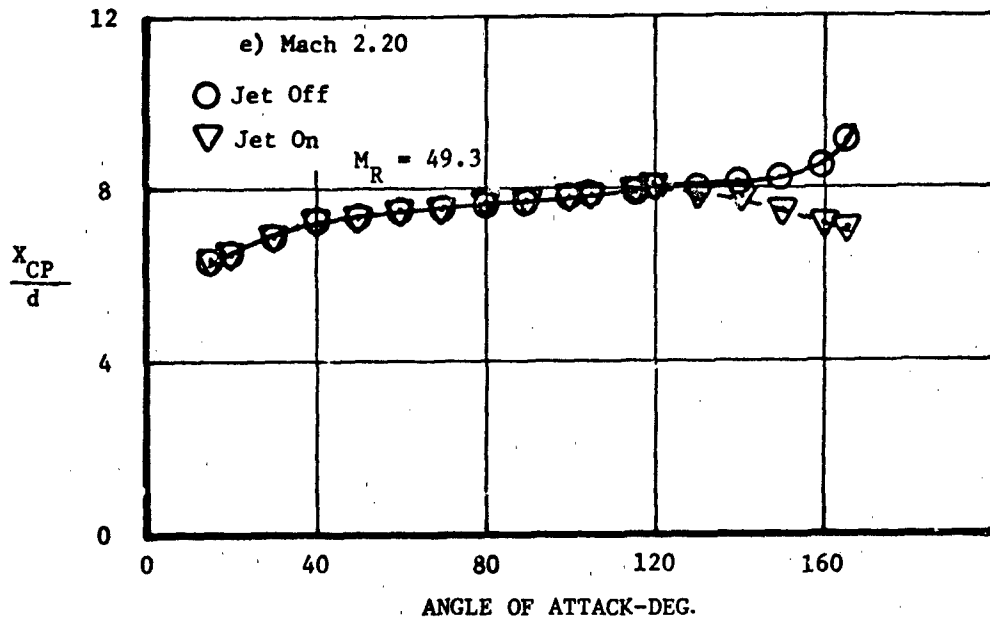


Figure 163 (Cont.). Comparison Of Body Alone $\frac{X_{CP}}{d}$ (Jet On Versus Jet Off)

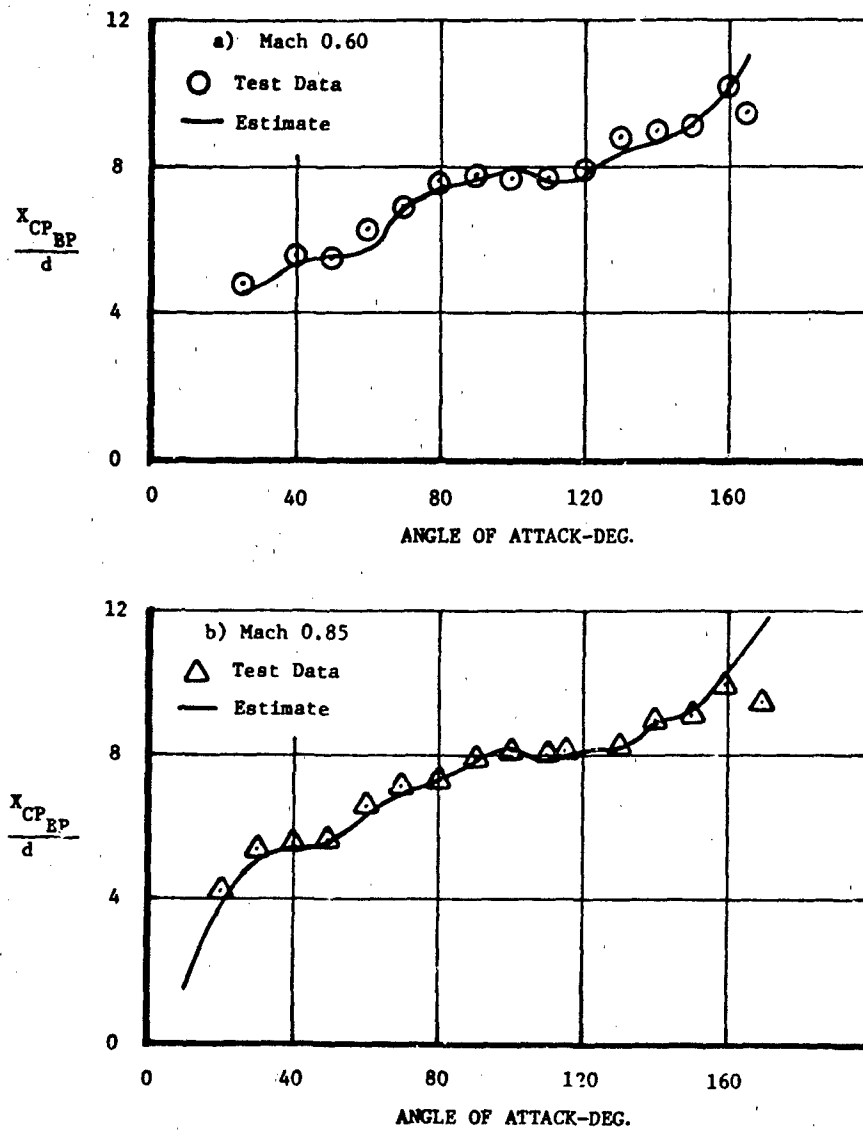


Figure 164. Comparison Between Predictions And Experimental Data, $\frac{X_{CP_{BP}}}{d}$

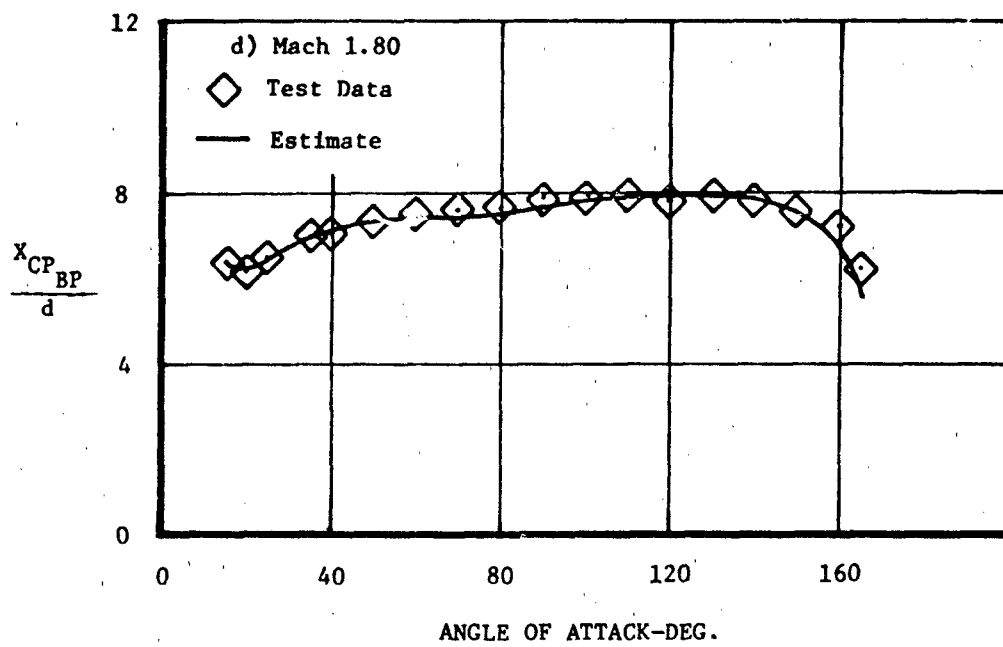
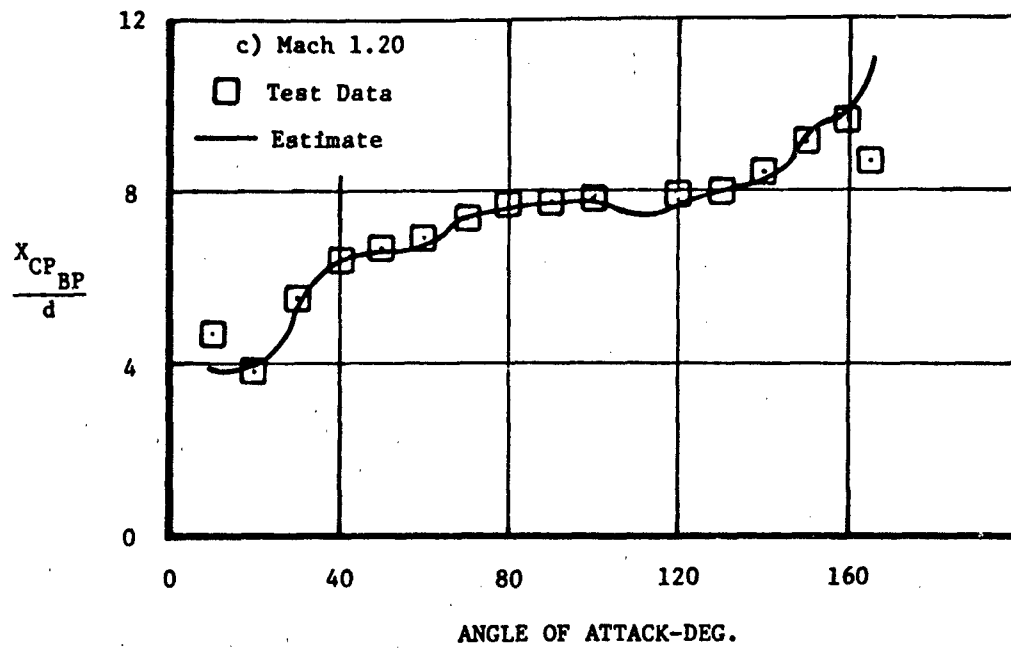


Figure 164 (Cont.). Comparison Between Predictions and Experimental Data, $\frac{X_{CP_{BP}}}{d}$

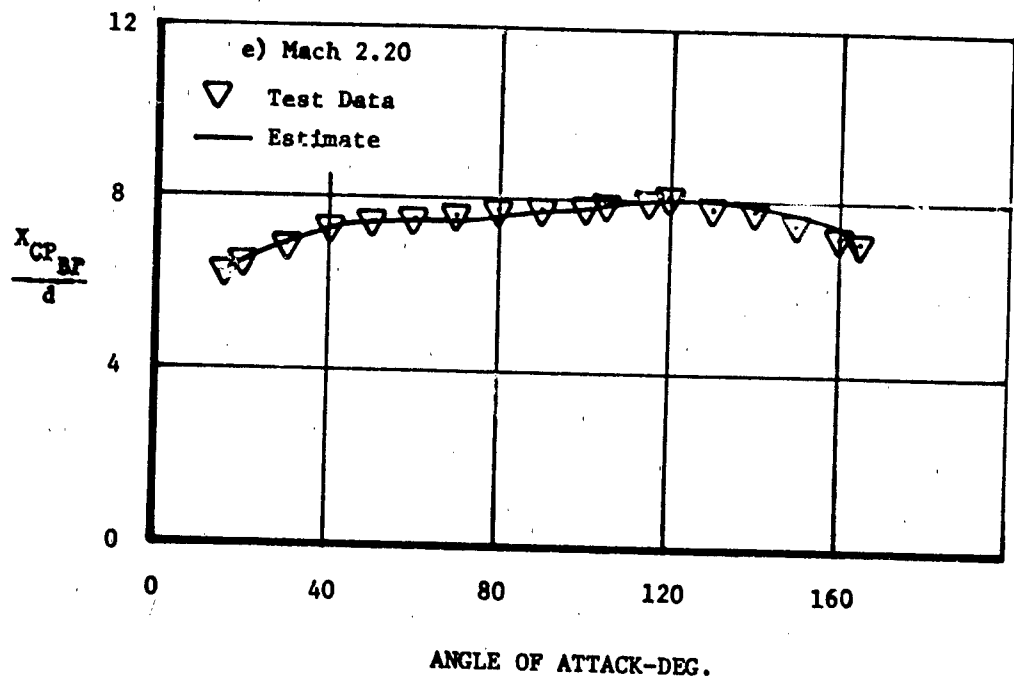


Figure 164 (Cont.). Comparison Between Predictions and Experimental Data, $\frac{X_{CP_{BP}}}{d}$

5.5.3 Incremental Tail Normal Force Due To Plume Effects

Summary

A method is presented to predict $\Delta C_{N_{TP}}$, the incremental normal force coefficient on horizontal tails on a slender tangent ogive-cylinder body due to a jet plume. The term $\Delta C_{N_{TP}}$ represents the change in total normal force coefficient on two tail panels plus the change in tail-on-body carryover normal force due to a flowing jet. The method is applicable at angles of attack up to 180 degrees at Mach numbers 0.60 to 2.20.

Background

The addition of a flowing jet to a body-tail configuration produces changes in the normal force on the tail and in the magnitude of the carryover normal force imposed on the body by the tails. The magnitude of this jet effect is dependent on such parameters as angle of attack, Mach number, tail size, and the strength of the jet relative to the free stream (defined here as the momentum ratio, M_R). No previously derived method was found which predicted the effects of a flowing jet on the tails at the desired high angles of attack. The present work describes the formulation of such a method for predicting the $\Delta C_{N_{TP}}$ at angles of attack up to 180 degrees and Mach numbers 0.60 to 2.20. Data from tests on a particular USAF missile configuration form the basis for this analysis.

The incremental normal force coefficient on a body-tail configuration due to jet effects on the tail is defined as:

$$\Delta C_{N_{TP}} = \left(C_{N_{T(B)P}} + I_{B(T)P} \right) - \left(C_{N_{T(B)}} + I_{B(T)} \right)$$

This is based on the premise that the total effect of a tail on a body-tail configuration is made up of the force on the tail itself plus the carry over to the body, and further that both quantities may be affected by the

presence of a plume.

Test data were available at Mach numbers 0.60 to 2.2 and angles of attack from 15 to 165 degrees. Jet momentum ratios tested were as follows:

<u>Mach</u>	<u>M_R</u>
0.60	60.1
0.85	30.1
1.20	19.1
1.80	73.6
2.0	49.3

Jet-on data were available only for a body-strake-tail configuration, with jet-off data obtained on body alone and body-strake-tails configurations.

It was, therefore, necessary to derive $\Delta C_{N_{TP}}$ from available data. Parameters measured by integrating surface pressures included normal force coefficients for the body in the presence of strakes and tails, jet-off and jet-on ($C_{N_{B(ST)}}$ and $C_{N_{B(ST)P}}$); body alone normal force coefficient, jet-off (C_{N_B}); total tail normal force coefficient in the presence of the body, jet-off and jet-on ($C_{N_{T(B)total}}$ and $C_{N_{T(F)Ptotal}}$); and total strake normal force coefficient, jet-off and jet-on ($C_{N_{S(B)total}}$ and $C_{N_{S(B)Ptotal}}$). The procedure for computing

$\Delta C_{N_{TP}}$ from known data is as follows:

Given the basic equation

$$\Delta C_{N_{TP}} = \left(C_{N_{T(B)Ptotal}} + I_{B(T)P} \right) - \left(C_{N_{T(B)total}} + I_{B(T)} \right) \quad (50)$$

The terms $C_{N_{T(B)Ptotal}}$ and $C_{N_{T(B)total}}$ may be determined directly from test data.

The equation may then be expressed as

$$\Delta C_{N_{TP}} = C_{N_{T(B)P_{total}}} - C_{N_{T(B)_{total}}} + \Delta I_{BTP}, \quad (51)$$

where $\Delta I_{B(T)P} = I_{B(T)P} - I_{B(T)}$

The incremental normal force coefficients, $I_{B(ST)}$ and $I_{B(ST)P}$, due to presence of strake and tail, were developed previously in Section 5.5.1

One can then define

$$\Delta I_{B(ST)P} = I_{B(ST)P} - I_{B(ST)} \quad (52)$$

It was assumed that the changes in tail carryover on the body due to the jet would be proportional to that for a strake plus tail in the same manner as the change in normal force on the tail due to a jet is proportional to that for a strake plus tail. Therefore:

$$\Delta I_{B(T)P} = \Delta I_{B(ST)P} \frac{\Delta C_{N_{T(B)}}}{\Delta C_{N_{S(B)}} \Delta C_{N_{T(B)}}} \quad (53)$$

The results of equation (53) may then be substituted into equation (51)

determine $\Delta C_{N_{TP}}$.

Method Development

Figure 165 shows the general form of curves of $|\Delta C_{N_{TP}}|$ versus angle of attack for $0.6 \leq M \leq 1.2$ and $1.2 < M \leq 2.2$. Both curves show no jet effects at angles of attack less than 20 degrees, followed by increasing $|\Delta C_{N_{TP}}|$ up to $\alpha = 55^\circ$. Jet effects decrease to approximately zero at $\alpha = 90^\circ$. Peaks for all Mach numbers tested occur at $\alpha = 110^\circ$ and $\alpha = 160^\circ$, while zero points fall at $\alpha = 135^\circ$ for $M \leq 1.2$ and at $\alpha = 120^\circ$ for $1.2 < M \leq 2.2$. $\Delta C_{N_{TP}}$ equals zero at $\alpha = 180^\circ$ at all Mach numbers due to symmetry. The value and sign of $\Delta C_{N_{TP}}$ at $\alpha = 55^\circ$, 110° , and 160° are Mach number dependent. A power series formulation incorporating the effects of angle of attack, Mach number, jet momentum ratio, and tail area was the approach selected to fit a general curve to the data.

Assuming $\Delta C_{N_{TP}}$ varies linearly with M_R and R_T , then

$$\frac{\Delta C_{N_{TP}}}{M_R * R_T} = A(\alpha)K(M),$$

where R_T = tail area ratio = $\frac{S_T}{S_{ref}}$.

$A(\alpha)$ is defined by the general curve forms in Figure 165, and varies in magnitude from zero to one. The magnitude of $A(\alpha)$ is scaled by the values of $(\Delta C_{N_{TP}} / M_R R_T)$ at $\alpha = 55^\circ, 110^\circ$ and 160° , respectively, in the three

ranges of angle of attack. Power series curves with a value of zero at $\alpha = 20^\circ, 90^\circ, 135^\circ$, and 180° and a value of 1.0 at $\alpha = 55^\circ, 110^\circ$, and 160° were then constructed for Mach numbers less than or equal to 1.20. Curves constructed for $M > 1.2$ had zero values at $\alpha = 90^\circ, 120^\circ$ and 180° . The final form of the equation is:

$$\Delta C_{N_{TP}} = M_R * R_T * K * A$$

where M_R = jet momentum ratio - q_j/q_∞

R_T = tail area ratio - S_T/S_{ref}

K = amplification factor

= K_{55} for $0^\circ \leq \alpha \leq 90^\circ$ ($0.6 \leq M \leq 2.2$)

= K_{110} { for $90^\circ < \alpha \leq 135^\circ$ ($0.6 \leq M \leq 1.2$)

 { for $90^\circ < \alpha \leq 120^\circ$ ($1.2 < M \leq 2.2$)

= K_{160} { for $135^\circ < \alpha \leq 180^\circ$ ($0.6 \leq M \leq 1.2$)

 { for $120^\circ < \alpha \leq 180^\circ$ ($1.2 < M \leq 2.2$)

A = Power series defining curve form.

Solution of the equation necessitates dividing the angle of attack range into four intervals. For Mach numbers from 0.60 to 1.2:

$$0 \leq \alpha \leq 20^\circ$$

$$A = 0 \quad \therefore \quad \Delta C_{N_{TP}} = 0$$

$$20^\circ \leq \alpha \leq 90^\circ$$

$$K = K_{55}$$

$$A = 2.4498 - 16.7515\alpha + 37.3514\alpha^2 - 29.8329\alpha^3 + 7.7740\alpha^4$$

[α ~ radians]

$$90^\circ \leq \alpha \leq 135^\circ$$

$$K = K_{110}$$

$$A = -256.1760 + 494.7937\alpha - 359.0437\alpha^2 + 116.7324\alpha^3 - 14.3837\alpha^4$$

[α ~ radians]

$$135^\circ \leq \alpha \leq 180^\circ$$

$$K = K_{160}$$

$$A = 1046.9190 - 1501.6280\alpha + 798.0073\alpha^2 - 185.0520\alpha^3 + 16.0493\alpha^4$$

[α ~ radians]

For $1.2 < M \leq 2.2$:

$$0 \leq \alpha \leq 20^\circ$$

$$A = 0 \quad \Delta C_{N_{TP}} = 0$$

$$20^\circ \leq \alpha \leq 90^\circ$$

$$K = K_{55}$$

$$A = 2.4498 - 16.7515\alpha + 37.3514\alpha^2 - 29.8329\alpha^3 + 7.7740\alpha^4$$

[α ~ radians]

$$90^\circ \leq \alpha < 120^\circ$$

$$K = K_{110}$$

$$A = -1840.2781 + 4055.1289\alpha - 3352.6751\alpha^2 + 1232.9331\alpha^3 - 170.1181\alpha^4$$

[α ~ radians]

$$120^\circ \leq \alpha < 180^\circ$$

$$K = K_{160}$$

$$A = -265.5403 + 417.9143\alpha - 248.1630\alpha^2 + 55.9331\alpha^3 - 6.5953\alpha^4$$

[α ~ radians]

Values of K_{55} , K_{110} , and K_{160} have been determined empirically and are plotted versus Mach number in Figure 166. Power series A is presented versus angle of attack in Figure 167a for $M \leq 1.2$ and in Figure 167b for $1.2 < M \leq 2.2$.

It should be noted that available test data incorporated only one jet momentum ratio at each Mach number. While these represent realistic values for the configuration tested, estimates obtained for a missile with greatly different jet momentum ratios should be used with caution. Also of importance is the fact that the effects of varying nozzle exit diameter and nozzle-to-tail distance cannot be derived from existing data. The ratio of nozzle exit diameter to body diameter (d_{noz}/d_{ref}) for the configuration tested was 0.87; the distance from the nozzle exit plane to the tail trailing edge was 0.42d. Variation of these parameters can be expected to have some as yet undetermined effects on the values of $\Delta C_{N_{TP}}$ predicted by this method.

Use of Method

The method is used as follows:

Given a tangent ogive-cylinder with horizontal tails of area ratio, R_T , and a main jet momentum ratio, M_R .

Proceed thus:

1 Determine K_{55} , K_{110} , and K_{160} for the desired Mach number.
(Figure 166)

2 Look up values of A for the desired angles of attack in the appropriate Mach range. (Figure 167)

3 Compute $\Delta C_{NBP} = M_R * R_T * K * A$

where $K = K_{55}$ for $0 \leq \alpha \leq 90^\circ$

= K_{110} for $90^\circ \leq \alpha \leq 135^\circ$ if $M \leq 1.2$

= K_{110} for $90^\circ < \alpha \leq 120^\circ$ if $1.2 < M \leq 2.2$

= K_{160} for $135^\circ < \alpha \leq 180^\circ$ if $M \leq 1.2$

= K_{160} for $120^\circ < \alpha \leq 180^\circ$ if $1.2 < M \leq 2.2$

Numerical Example

Given the following parameters, compute ΔC_{NTP} for a slender tangent ogive-cylinder body with horizontal tails from $\alpha = 0$ to $\alpha = 180^\circ$ at Mach 0.85 and Mach 1.80.

$$M_R = 30.1 \text{ at } M = 0.85$$

$$M_R = 73.6 \text{ at } M = 1.80$$

$$R_T = 0.84$$

At Mach 0.85:

1 From Figure 166:

$$K_{55} = 0.065, K_{110} = -0.028, K_{160} = 0.015$$

2-3

α	A	* M_R	* R_T	* K	ΔC_{NTP}
0	0.	30.1	0.84	0.065	0
20	0.				0
40	0.67				1.10
55	1.0				1.64
70	0.65				1.07
90	0.				0
110	1.0			-0.028	-0.71
120	0.83				-0.59
135	0.				0
150	0.65			0.015	0.25
160	1.0				0.38
170	0.80				0.30
180	0.				0

(Figure 167a)

At Mach 1.8.

1 From Figure .166:

$$K_{55} = 0.004, K_{110} = 0.004, K_{160} = -0.021$$

<u>2-3</u>	α	A	* M_R	* R_T	* K	ΔC_{NTP}	
		(Fig. 167b)					
	0	0.	73.6	0.85	0.004	0.	
	20	0.	↓	↓	↓	0.	
	40	0.67				0.17	
	55	1.0				0.25	
	70	0.65				0.16	
	90	0.				0.	
	100	0.86				0.004	0.21
	110	1.0				0.25	
	120	0.				0.	
	140	0.74				-0.021	-0.96
	160	1.0				-1.30	
	180	0.	0.				

Data Comparisons

In Figure 168, method results are plotted along with those data used in formulating the method. The curve-fitting approach used yields a good approximation of ΔC_{NTP} across the Mach range tested. A lack of independent data makes further comparisons impossible at this time.

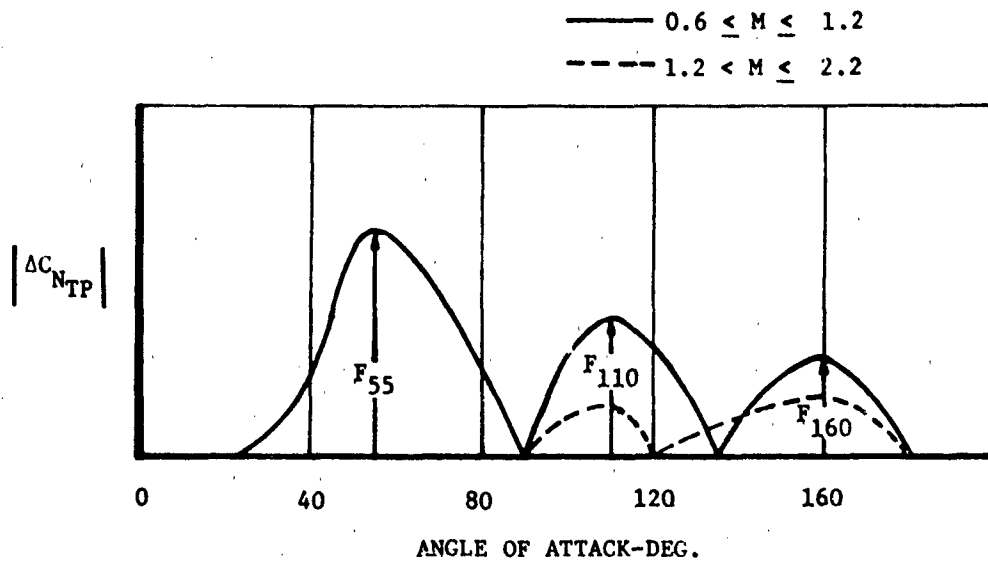


Figure 165. General Curve Forms, $|\Delta C_{NTP}|$

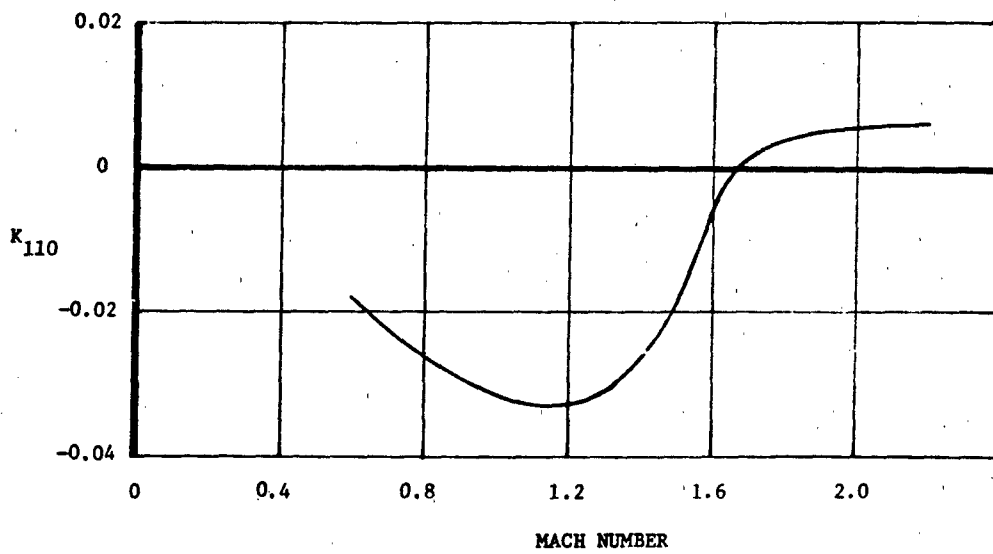
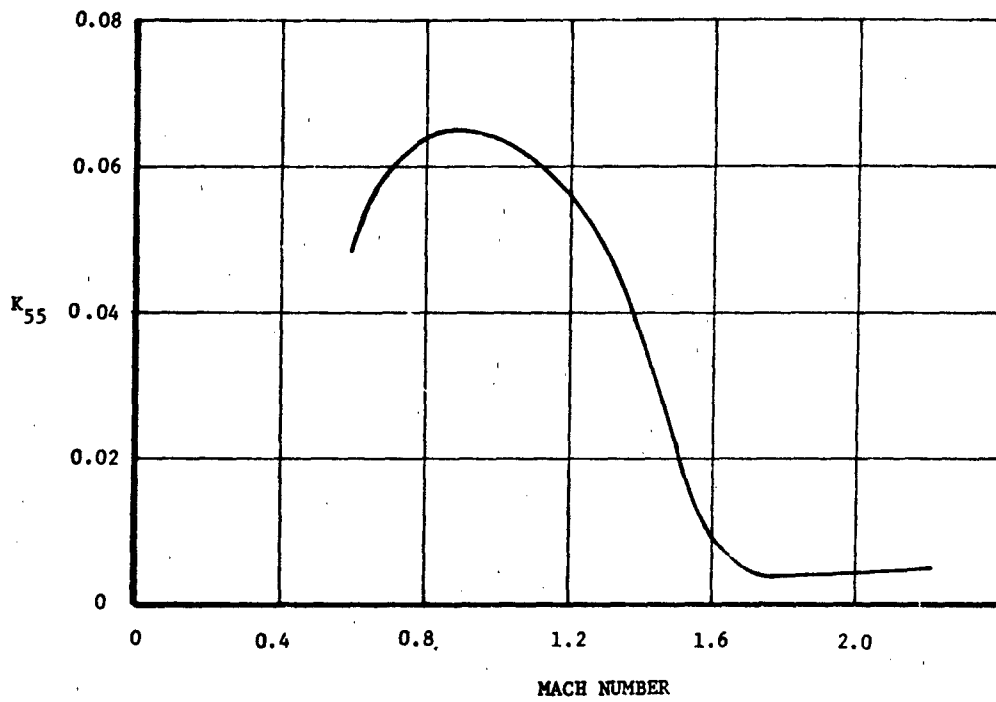


Figure 166. Amplification Factors for Calculating $\Delta C_{N_{TP}}$

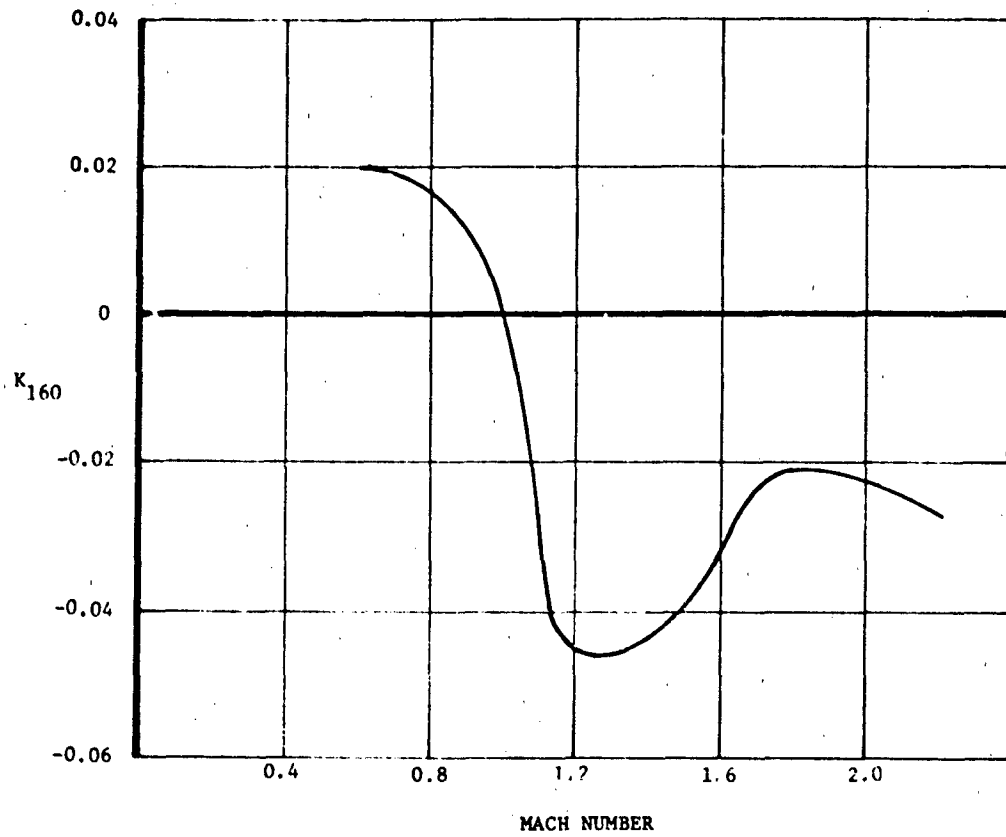


Figure 166 (Cont.). Amplification Factors for Calculating $\Delta C_{N_{TP}}$

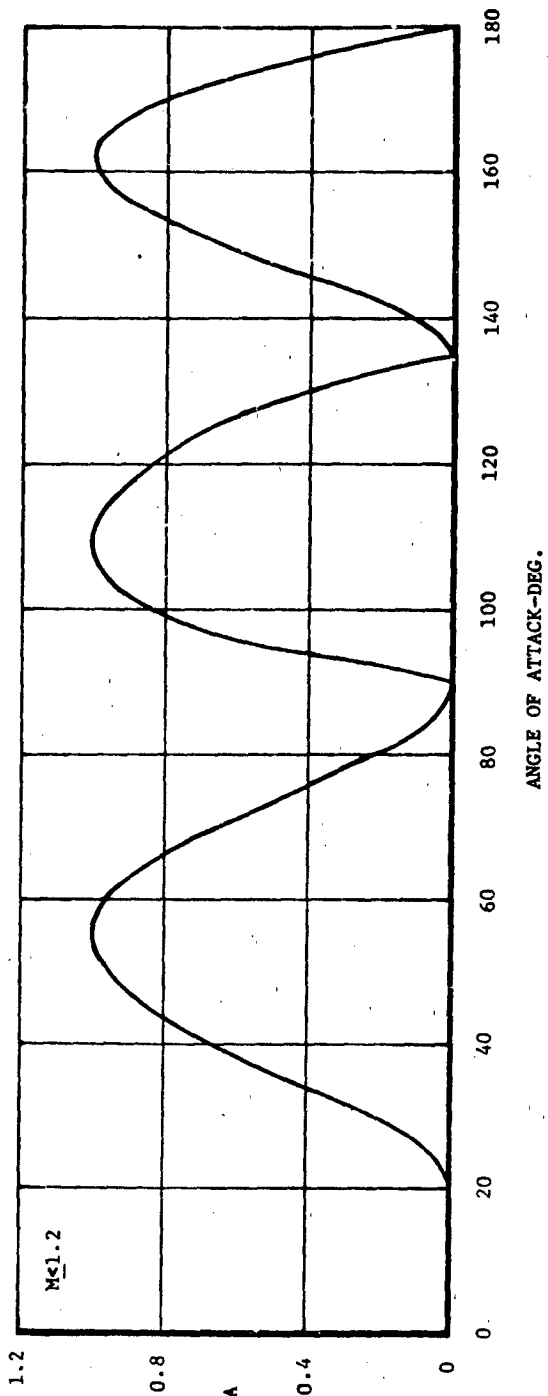


Figure 167a. Power Series A for Calculating ΔC_{NTP} ($M_{1.2}$)

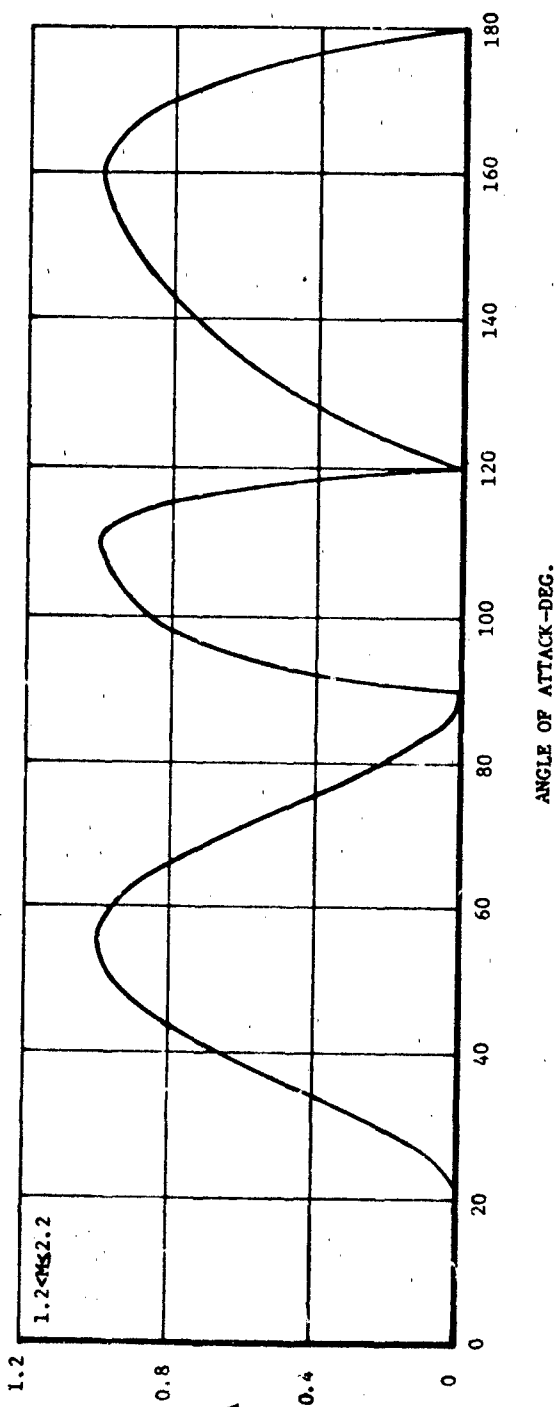
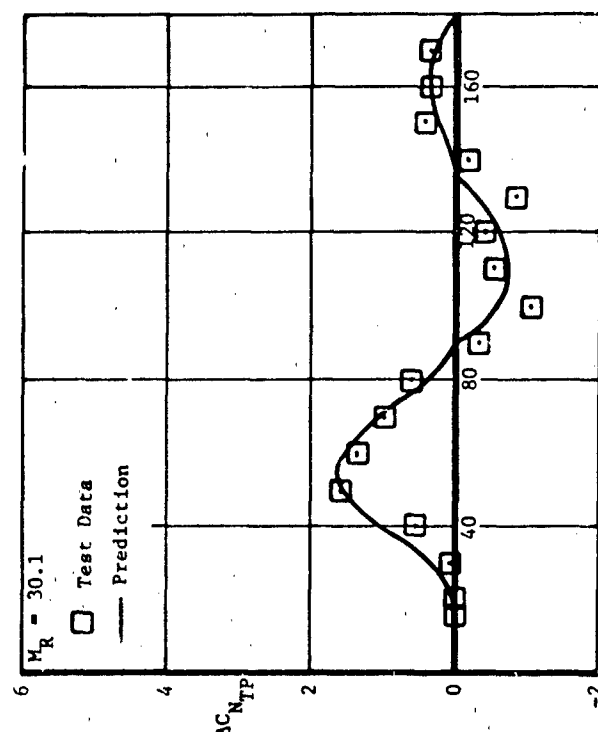
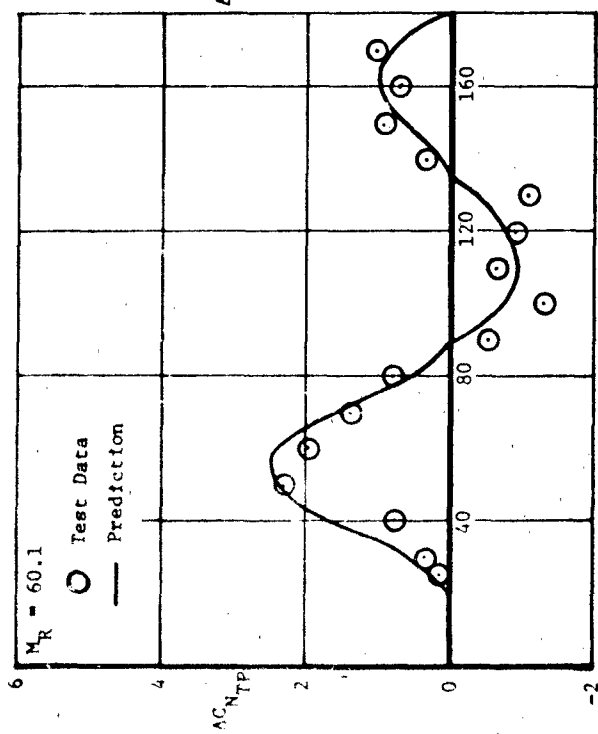


Figure 167b. Power Series A for Calculating $\Delta C_{N_{IP}}$ (1.2442.2)



a) Mach 0.60



b) Mach 0.85

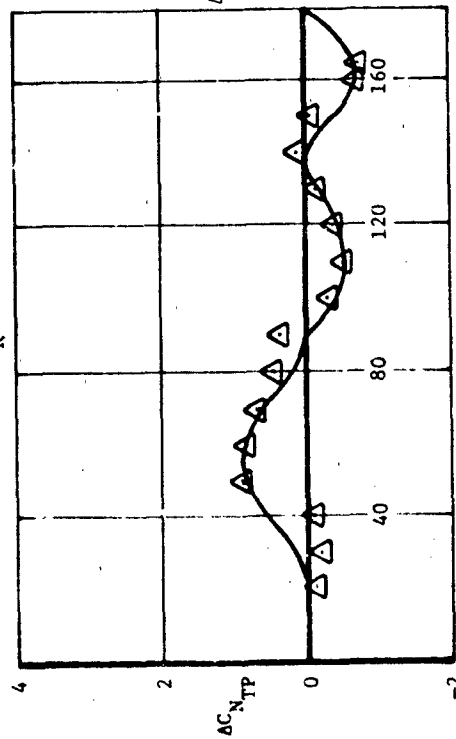
Figure 168. Comparisons Between Predictions And Experimental Data, AC_{NTP}

c) Mach 1.20

△ Test Data

— Prediction

$M_R = 19.14$



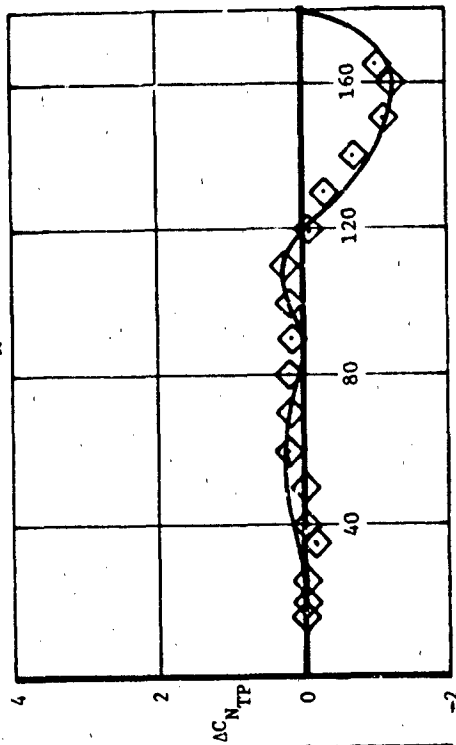
ANGLE OF ATTACK-DEG.

d) Mach 1.8

◇ Test Data

— Prediction

$M_R = 73.6$



ANGLE OF ATTACK-DEG.

Figure 168 (Cont.). Comparisons Between Predictions And Experimental Data, $\Delta C_{N_{TP}}$

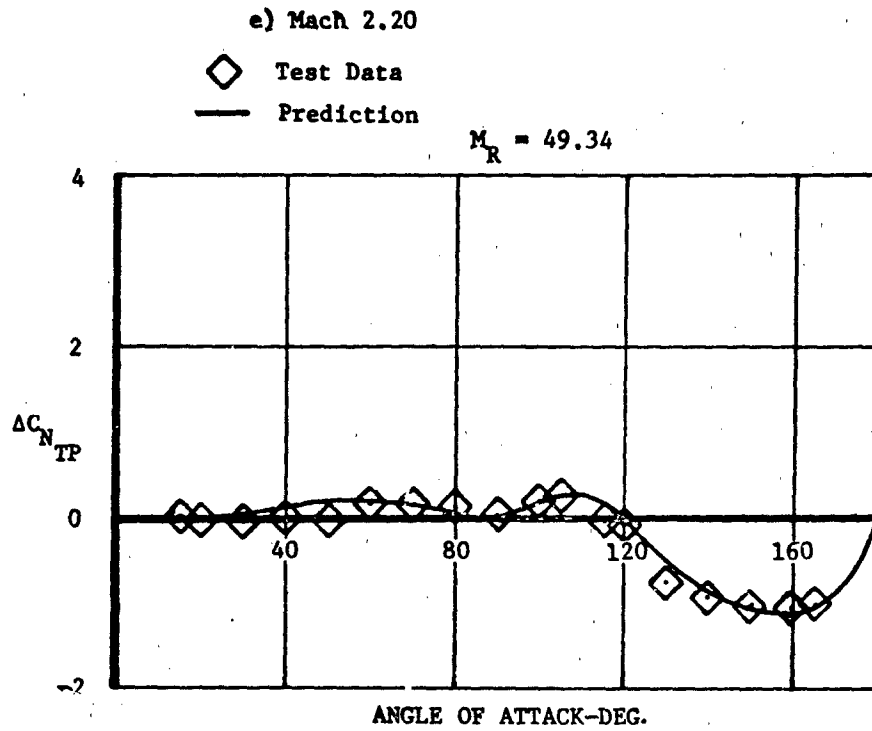


Figure 168 (Cont.). Comparisons Between Predictions And Experimental Data, $\Delta C_{N_{TP}}$

5.5.4 Effective Center of Pressure of Incremental Tail Normal Force Due to Plume Effects

Summary

A method is presented for predicting $X_{CP_{T(B)P}}$, the effective center of pressure of the incremental tail normal force due to plume effects. Data comparisons showed no difference between jet-on and jet-off tail chordwise center of pressure for Mach numbers between 0.6 and 2.2 and angles of attack to 180 degrees. Therefore, it is not necessary to develop a new method and it is recommended that the existing method of Section 5.1.5 be used to calculate X_{CP_T}/C_R which is equivalent to $X_{CP_{T(B)P}}/C_R$.

Background

When predicting the aerodynamic characteristics for a missile at high angles of attack, the presence of an exhaust plume must be taken into account. At high angles of attack, the plume produced by a thrusting missile can alter local surface pressures through either direct impingement or by its influence on the flowfield forward of the plume. Methods for predicting plume effects on body normal force, body center of pressure, and tail normal force have been presented in Sections 5.5.1 through 5.5.3. This section deals specifically with the effects of a plume on tail chordwise center of pressure.

A study has been completed on the effects which rocket motor exhaust plumes have on tail center of pressure. Data used in the study were obtained from wind tunnel tests of a particular USAF body-strake-tail missile configuration. Tests were conducted using a pressure model with and without main jet simulation at Mach numbers from 0.6 to 2.2 and angles of attack from 15 to 135 degrees. The ratio of jet total pressure to free stream total pressure and the ratio of jet dynamic pressure to free stream dynamic pressure

simulated in the tests were as follows:

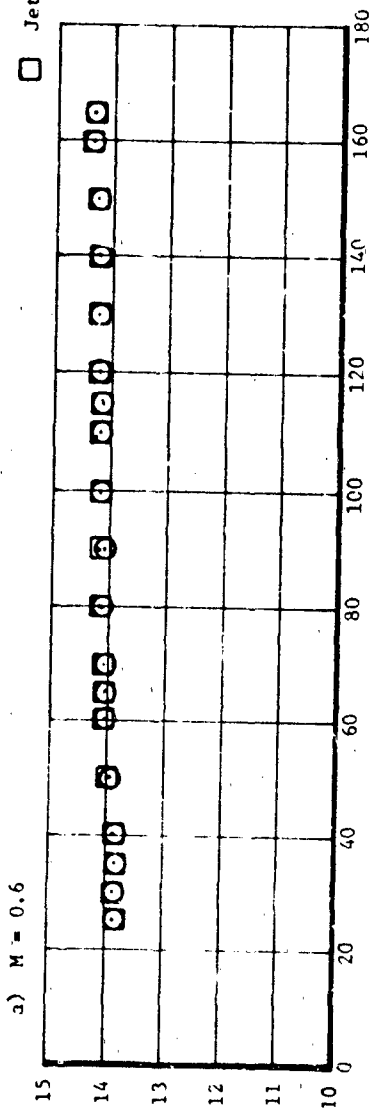
<u>Mach</u>	<u>P_{TJ}/P_{T∞}</u>	<u>q_J/q_∞</u>
0.6	135	60.58
0.85	107	30.10
1.2	89	19.14
1.8	328	73.63
2.2	176	49.34

Integrated pressure data provided total configuration normal force and center of pressure plus normal force and center of pressure on each component, including interference effects. Comparisons of tail chordwise centers of pressure on the horizontal fins of a cruciform configuration in the "plus" altitude with and without jet simulation are presented in Figure 169. These comparisons, covering the entire Mach number range (0.6-2.2) and angle of attack range (15 to 165 degrees) tested, indicate that for the conditions tested, the presence of a plume has little or no impact on chordwise center of pressure. No additional method is required to account for the effects of a plume on tail center of pressure. Therefore, as in the case of no plume, the method of Section 5.1.5 can be used to predict $X_{CP_{T(B)}}$ / C_R which can be expressed in terms of body diameters by the appropriate geometric relationships, i.e.,:

$$\frac{X_{CP_{T(BS)}}}{d} = \frac{X_{T.L.E.}}{d} + \frac{X_{CP_{T(B)}}}{C_R} \cdot \frac{C_R}{d}$$

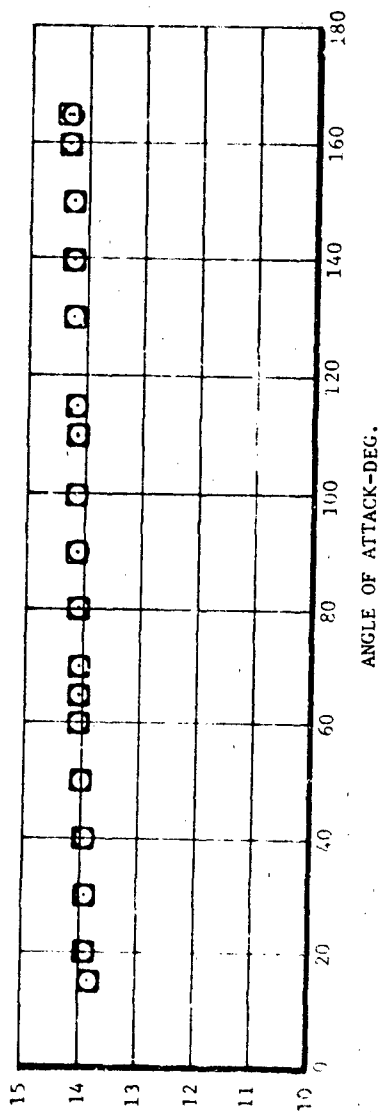
○ Jet-On

□ Jet-Off



ANGLE OF ATTACK-DEG.

b) $M = 0.85$



ANGLE OF ATTACK-DEG.

Figure 169. Comparison Between Jet-On and Jet-Off Tail Centers of Pressure

○ Jet-On
 □ Jet-Off

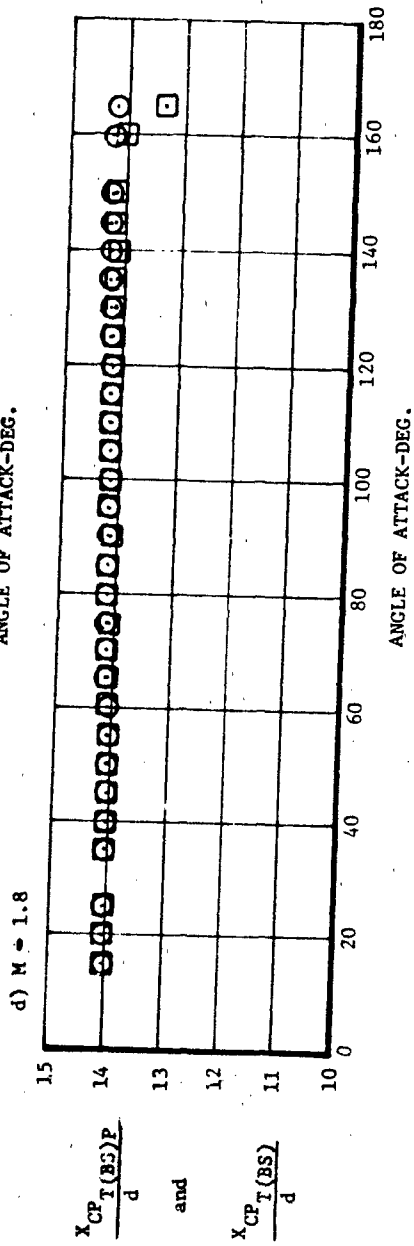
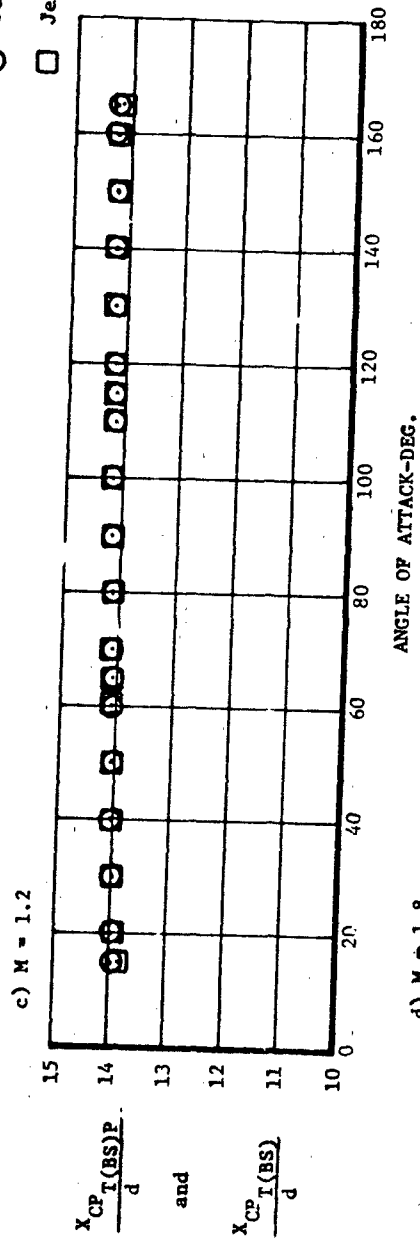


Figure 169 (Cont.) Comparison Between Jet-On and Jet-Off Tail Centers of Pressure

○ Jet-On
 □ Jet-Off

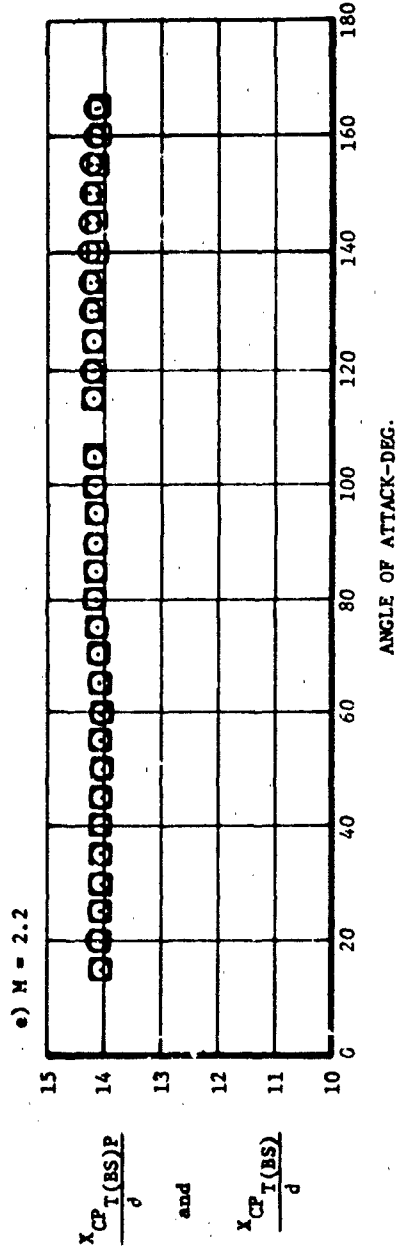


Figure 169 (Cont.). Comparison Between Jet-On and Jet-Off Tail Centers Of Pressure

6.0 CONCLUSIONS AND RECOMMENDATIONS

This study shows that the availability of systematic test data permits the development of methodology to predict reasonably accurate aerodynamic characteristics. The applicability of the methods is limited only by the range of the test data. As for any semi-empirical method, the methods should not be used beyond the range of the test data base until the real limits of applicability can be ascertained. This can only be accomplished over a period of time as additional test data becomes available.

Experience gained in using the methods shows that although they are suitable for "hand" calculations, it is desirable to computerize them. This was not included as part of the present contract, and is therefore recommended for future consideration.

The success of the methods developed here supports the view that this approach could well be extended as the systematic data base grows. Areas which were identified as deficient in data or as fertile ground for the continuation of the effort begun here are summarized below:

- 1 Since wind tunnel testing does not, in general, match flight Reynolds numbers and Mach numbers simultaneously, this causes a question about the accuracy with which Reynolds number effects can be accounted for in the methods. This uncertainty manifests itself primarily in the modeling of the viscous contribution to the body normal force. Additional tests aimed specifically at assessing the viscous effects on body normal force are recommended.
- 2 Since maneuverability implies the use of a control system, the test data base and methods should now be extended to

deal with deflected control surfaces.

- 3 Certain geometric features, e.g., boattails and nose bluntness, should also be tested systematically to complement the current data base.
- 4 The effects of arbitrary roll angle should be treated systematically beyond angles of attack of 45 degrees which was treated in the recent Martin Marietta study (Reference 38) conducted for the U. S. Army. One of the problem areas of particular interest in this regard is the prediction of hinge moments on the leeward surfaces even at small angles of attack wherein the occurrence of couples complicates the prediction of the center of pressure on the tail.
- 5 Finally it should be recalled that this study dealt only with static aerodynamics, whereas similar methods can and should be developed for some of the dynamic stability derivatives.

7.0 REFERENCES

1. Fidler, J.E., "A Systematic Experimental Approach to Upgrading Missile Aerodynamic Methodology" 9th U.S. Navy Symposium on Aero-ballistics, May 1972.
2. Fidler, J.E. and Bateman, M.C., "Aerodynamic Methodology (Isolated Fins and Bodies)", Final report on U.S.A. MICOM contract DAAH03-72-C-0487, 1973
3. Fidler, J.E. and Bateman, M.C., "Aerodynamic Methodology (Bodies with and without Tails in Transonic Flow)". Report issued under U.S. Navy NAVAIR Contract, N00019-73-C-0108, 1974.
4. Fidler, J.E. and Bateman, M.C., "Aerodynamic Methodology (Bodies with Tails at Arbitrary Roll Angle)" OR 13,375-1, Final Report on U.S. Army MICOM Contract DAAH01-74-C-0621, 1974
5. Fidler, J.E., "Data Report" (issued under USAF Flight Dynamic Laboratory Contract No. F33615-75-C-3052, CDRL Item No. A005)
6. Hoerner, S.F., "Fluid Dynamic Drag", published by author, 1965 Ed.
7. Fidler, J.E. and Bateman, M.C., "Asymmetric Vortex Effects on Missile Configurations", presented at AIAA 13th Aerospace Sciences Meeting, Jan 1975, AIAA Paper 75-209
8. Briggs, M.M., Clark, W.H., and Peoples, J.R., "Occurrence and Inhibition of Large Yawing Moments during High Incidence Flight of Slender Missile Configurations," AIAA Second Atmosphere Flight Conference, Palo Alto, CA, Sept. 1972.
9. Ward, G.N., "Supersonic Flow Past Slender Pointed Bodies," Quarterly Journal of Mechanics and Applied Mathematics, Vol. II, Pt. 1, 1949.
10. Allen, H.J. and Perkins, E.W., "Characteristics of Flow Over Inclined Bodies of Revolution," NACA RM A50L07, March 1951.
11. Kelly, H.R., "The Estimation of Normal Force, Drag and Pitching Moment Coefficients for Blunt Based Bodies of Revolution a Large Angles of Attack," J. Aero. Sci., Vol. 21, No. 8, August 1954, P 549-555.
12. Jorgensen, L.H., "Prediction of Static Aerodynamic Characteristics for Space-Shuttle-Like and Other Bodies at Angles of Attack from 0° to 180°" NASA TN D-6996, January 1973
13. Baker, W., Static Aerodynamic Characteristics of a Series of Generalized Slender Bodies with and without Fins at Mach Numbers from 0.6 to 3.0 and Angle of Attack from 0 to 180 Deg., AEDC-TR-75-124, May 1976.

14. Barth, H., "Datenblätter zur Ermittlung Aerodynamischer Beiwerte Schlanker Bug-Zylinder-Konfigurationen im transsonischen geschwindigkeitsbereich." (Data Sheets for Determining the Aerodynamic Coefficients of Slender Nose Cylinder-Configurations in the Transonic Speed Range), Messerschmitt-Bolkow-Blohm GMBH, TN WE12-88/70, 1970.
15. Barth H., "Datenblätter zur Ermittlung von Normalkraft-Momenter-und Tangentialkraftcharakteristiken Schlanker Bug-Zylinder-Konfigurationen im transsonischem geschwindigkeitsbereich." (Data Sheets for Determining the Normal Force, Moments - and Axial Force Characteristics of Slender Nose-Cylinder-Configurations in the Transonic Speed Range), MBB, TN WE2-97/69, 1969.
16. Spring, D.J., "The Effect of Nose Shape and Afterbody Length on the Normal Force and Neutral Point Location of Axisymmetric Bodies at Mach Numbers from 0.80 to 4.50," Report No. RF-TR-64-13, U.S. Army Missile Command, July 1964.
17. U.S. Air Force Stability and Control DATCOM.
18. Jernell, L.S., "Aerodynamic Characteristics of Bodies of Revolution at Mach Numbers from 1.5 to 2.86 and Angles of Attack to 180°," "NASA TM X-1658, 1968.
19. Fleeman, E.L. and Nelson, R.C., "Aerodynamic Forces and Moments on a Slender Body with a Jet Plume for Angles of Attack up to 180 Degrees," AIAA 12th Aerospace Sciences Meeting, Paper No. 74-110, January 1974.
20. Gudmundson, S.E. and Torngren, L., "Supersonic and Transonic Wind Tunnel Tests on a Slender Ogive-Cylinder Body in Single and in Combination with Cruciform Wings and Tails of Different Sizes," The Aeronautical Research Institute of Sweden, FFA-AU-772, 1972.
21. Saffell, B.F. Jr., Howard, M.L. and Brooks, E.N. Jr., "A Method for Predicting the Static Aerodynamic Characteristics of Typical Missile Configurations for Angles of Attack to 180 Degrees," R&E RPT. 3645 Naval Ship R&D Center, 1971.
22. Gersten, K., "Calculation of Non-Linear Aerodynamic Stability Derivatives of Aeroplanes" NATO, AGARD Report 342, 1961.
23. Bartlett, G. E. and Vidal, R. J., "Experimental Investigation of the Influence of Edge Shape on the Aerodynamic Characteristics of Low-Aspect-Ratio Wings at Subsonic and Transonic Speeds", Cornell Aero. Lab Report AF-743-A-8, 1956.
24. Brown, C.E. and Michael, W.H., "Effects of Leading - Edge Separation on the Lift of a Delta Wing", Jour. Aero. Sci. 21, 1954, pp 690-694.

25. Flax, A.H. and Lawrence, H.R. "The Aerodynamics of Low-Aspect-Ratio Ratio Wings and Wing-Body Combinations", Cornell Aero. Labs, Rept. CAL-37, 1951.
26. Wickens, R.H., "The Vortex Wake and Aerodynamic Load Distribution of Slender Rectangular Plates. The Effects of 20-Degree Bend at Midchord", Nat. Res. Coun. of Can. Aero., Rept. 1976.
27. Royal Aeronautical Society, Data Sheets, Wings 5.01.03.03, 5.01.03.04, 5.01.03.05 and 5.01.03.06.
28. Emerson, H.F., "Wind Tunnel Investigation of the Effect of Clipping the Tips of Triangular Wings of Different Thickness, Camber and Aspect Ratio - Transonic Bump Method", TN3671, 1956, NACA.
29. Kirkpatrick, D.L.I., "Analysis of the Static Pressure Distribution on a Delta Wing in Subsonic Flow", RAE Farmborough, R&M No. 3619, 1970.
30. Pitts, W. C., Nielsen, J. N., and Kaatari, G. E., "Lift and Center of Pressure on Wind-Body-Tail Combinations at Subsonic, Transonic, and Supersonic Speeds," NACA Report 1307, 1957.
31. Unpublished test data taken at NASA Langley Unitary Tunnel using Martin Marietta model, 1968.
32. "Monthly Contract Status Report for Aerodynamic Stability Technology for Maneuverable Missiles," period ending May 24, 1975.
33. Ibid, period ending June 24, 1975
34. Martin Marietta/NSRDC Tail Effectiveness Test Data, 1968.
35. Fournier, R. H. and Spearman, M. L., "Effects of Nose Bluntness on the Static Aerodynamic Characteristics of a Cruciform-Wing Missile at Mach numbers 1.50 to 2.86," NASA TMX-2289, July 1971.
36. Graves, E. B., "Supersonic Aerodynamic Characteristics of a Low-Aspect Ratio Missile Model with Wing and Tail Controls and with Tails in Line and Interdigitated" NASA TMX-2531, 1972.
37. Carter, S. K., et al "Aerodynamic Characteristics of a Missile Configuration in the Presence of an Exhaust Plume at Angles of Attack to 180 Degrees (θ)," MDAC Paper WD 2521, July 1975.
38. Aiello, G. F., "AERODYNAMIC METHODOLOGY, Bodies with Arbitrary Roll Angles (Transonic and Supersonic)," AR 14,145, Final Report on U.S. Army MICOM Contract F33615-75-C-3052, 1976.
39. Aiello, G. F. and Bateman, M. C., Asymmetric Vortex Effects Computer Program, Martin Marietta Report OR 14028, December 1975.